

Electroanalytical Methods for Forensic Evaluation of Firearm Generated Evidence



A Thesis Submitted to Maynooth University in Fulfilment of the
Requirements for the Degree of

Doctor of Philosophy

By

Colm McKeever, B.Sc., M.Sc.

Department of Chemistry,

Maynooth University,

Maynooth,

Co. Kildare Ireland.

February 2024

Research Supervisor: Dr. Eithne Dempsey

Head of Department: Prof. Denise Rooney

Declaration

I hereby certify that this thesis has not been submitted before, in whole or part, to this or any other university for any degree, and is, except where stated otherwise, the original work of the author.

Signed _____ Date _____

Colm McKeever, B.Sc., M.Sc.

Abstract

Firearm related violence is a cause for concern in an ever-turbulent world. In this thesis, innovative electrochemical approaches to forensic evaluation of firearm generated evidence is presented using a two-prong approach. Firstly, development of an electroanalytical method for the detection of characteristic compounds found within the organic fraction of firearms residue (OFAR) was explored. This involved electrochemical analysis of diphenylamine (DPA) and ethyl centralite (EC) in both organic and aqueous supporting electrolytes revealing the formation of secondary products at the electrodes surface such as diphenylurea and primary amine degradation products. A novel sensing approach followed with the aid of magnetic nanoparticles of magnetite (MNPs) formed using controlled electrooxidation and chemical co-precipitation processes. Quantitative analysis using differential pulse voltammetry (DPV) revealed limits of detection (LODs) and quantification (LOQs) for EC and DPA at 4.39 ± 0.28 and 14.6 ± 0.95 μM and 3.51 ± 0.15 and 11.7 ± 0.47 μM respectively with sensitivities of 0.0637 ± 0.0044 and 0.0801 ± 0.0034 $\mu\text{A}\cdot\mu\text{M}^{-1}$. The method was applied to unburnt ammunition and real FAR samples while data from custom-designed screen-printed electrodes (SPE) highlighted the feasibility of onsite OFAR determination. Secondly, the deposition of conducting/redox active polymers for visualising latent finger-marks on brass ammunition casings was explored. This aspect exploited the electrodeposition of 3,4-ethylenedioxythiophene (EDOT), thionine Acetate (Th), neutral red (NR), and their mixtures at a range of transducers including sheet and cartridge brass. EDOT-Th emerged consistently as the most effective combination, revealing latent finger-marks at the highest level of detail (level 3), including pores within the ridges, on brass sheets using a rapid (120 s) and low-potential (0.1 V) approach. Successful visualisation of groomed latent finger-marks was achieved following exposure to temperatures of 700 °C and up to 16-month room temperature aging, with evidence for a robust methodology suitable for forensic practice. Bespoke electrochemical cells designed to facilitate the use of ammunition casings as working electrodes produced exceptional results via CV, resulting in pristine visualised latent finger-marks of grade 4 with visible level 3 features. Overall, the research advances the state of the art with respect to electroanalytical tools for OFAR measurement of signature analytes with the potential for extension to multiplexed operation.

Acknowledgements

First and foremost, I would like to thank my supervisor Dr. Eithne Dempsey for replying to my email over 4 years ago and allowing me to set out on this journey. Your unbound curiosity was contagious and has thoroughly become a core principle in my own research philosophy. Thank you for all the help, guidance and leeway over the years. I hope we continue to collaborate in the future.

To the “electrochem crew”, my sincerest thank you for making the lab a place that someone is excited to come into and work. Saurav, your wealth of knowledge and kindness never dwindled the entire time you were in the lab, thank you for all the encouragement and chats over coffee and flooring me with the out of the bag one liners. Big boss (Athira), while we may never truly know if all fish are indeed mammals, we did break some ground on the electrochemistry stuff. While I wasn't totally appreciative at the time, thank you for all the tediously specific questions you had over the years. You made me a better chemist for it, having to study just in case I heard the word “Ceistana” from around the corner the next day. The lab crew are yours now to take care of, keep the new folk in check.

To my parents, Marie and John, thank you for all the patience and support I have had in my entire life. Thank you for the constant encouragement and telling me to just “go for it” and “all you can do is your best”. I don't think I would have made it through this without you two in my corner, but I swear I am finished school now.

To my siblings, Martina, Susan, John and Caroline, thank you for the laughs and chats and making sure I don't get too big of a head (egotistically, the actual size of my head just looks big because of the hair). Here's hoping that it will be easier to answer the question “what does your brother do?” in future.

To the technical and admin staff at MU, in every way possible you made this journey easier. With your expertise, helpfulness and just general soundness, it has been a pleasure. Thank you, Noel, for facilitating nearly every wild idea I had, you allowed creativity to never be stopped when coming up with solutions to problems I faced in the lab.

To the other postgrads and postdocs who I have had the pleasure to meet in the department during my time at MU. Thanks for the laughs, the moans, the essential tier lists, “stimulating conversations” and endless meetings for continual improvement, of course

they finally get a bench when we leave. Remember there's always a space in the gaff for anyone that needs it.

Cay, during all the long days and late nights writing, figuring out problems, making slides, preparing for teaching, the lab or anything else that was due (usually the next day...) you were there. Thank you for holding my sanity together (albeit with duct-tape and hope) as we took this journey together. I'm sure it will all be worth it.

Table of Contents

Chapter 1: Introduction	1
1.1 Firearms Residue.....	2
1.1.1 Ammunition Propellant Formulation	4
1.1.2 Inorganic Firearms Residue	8
1.1.3 Organic Firearms Residue.....	10
1.1.4 Current Trends in Analysis of Organic Firearms Residue	14
1.2 Finger-mark Evidence	17
1.2.1 Types of Finger-Mark Evidence and Surfaces of Application	17
1.2.2 Scoring of Finger-mark Evidence	19
1.2.3 Visualisation Methods for Latent Finger-marks.....	22
1.2.4 Ammunition Casings.....	25
1.2.5 Finger-marks on Ammunition Casings	26
1.2.6 Conducting and Redox Polymers.....	30
1.3 Research Goals for this Work.....	33
1.4 References	35
Chapter 2: Theory Behind Experimental Techniques	50
2.1 Electrochemical methods	51
2.2 Mass Transport.....	53
2.3 Electrochemical Experimental Techniques	56
2.3.1 Chronoamperometry	56
2.3.2 Linear Sweep Voltammetry	57
2.3.3 Cyclic Voltammetry.....	58
2.3.4 Differential Pulse Voltammetry.....	60
2.3.5 Electrodes used in the Electrochemical Cell.....	62
2.4 Additional analytical techniques used in this thesis.....	63

2.4.1 Scanning Electron Microscopy	63
2.4.2 Energy-dispersive X-ray Spectroscopy	64
2.4.3 X-ray Photoelectron Spectroscopy	65
2.4.4 Ultraviolet–visible spectroscopy	66
2.4.5 Infra-Red Spectroscopy (IR)	68
2.4.6 Thermogravimetric analysis	69
2.4.7 Differential Scanning Calorimetry	70
2.5 References:	71
Chapter 3: Electroanalysis of Organic Firearm Residue Species.....	73
3.1 Chapter Aims.....	74
3.2 Introduction	74
3.3 Experimental	76
3.3.1 Materials and Reagents	76
3.3.2 Instrumentation and Software	76
3.3.3 Procedures	77
3.4 Results and Discussion.....	80
3.4.1 Optimisation of Electrochemical Synthesis for Magnetic Nanoparticle Formation	80
3.4.2 Electrochemical Analysis of Diphenylamine	94
3.4.3 Electrochemical Analysis of Ethyl-Centralite.....	105
3.5 Conclusion	118
3.6 References	120
Chapter 4: Electrochemical Analysis of Analytes Found Within OFAR with the Extension to Real Sample Analysis	131
4.1 Chapter Aims.....	132
4.2 Introduction	132
4.3 Experimental	134

4.3.1 Materials and Reagents	134
4.3.2 Instrumentation and Software	135
4.3.3 Procedures	135
4.4 Results and Discussion.....	139
4.4.1 Dual Analyte Analysis.....	139
4.4.2 Analysis of Firearms Residue generated from the Discharge of a Shotgun.	145
4.4.3 Development of Screen-Printed Electrodes for OFAR Detection.....	155
4.5 Conclusion	163
4.6 References	165
Chapter 5: Latent Finger-Mark Visualisation at a Brass Surface via Deposition of Conducting and Redox Polymers.....	171
5.1 Chapter Aims.....	172
5.2 Introduction	172
5.3 Experimental	181
5.3.1 Materials and Reagents	181
5.3.2 Instrumentation and software.....	182
5.3.3 Procedures	182
5.4 Results and Discussion.....	187
5.4.1 Electrochemical Investigation of Brass Substrate.....	187
5.4.2 X-ray Photoelectron Spectroscopy of a Brass Surface	205
5.4.3 Electrochemical and Optical Investigations of Phenazine, Phenothiazine and EDOT Deposition.....	208
5.5 Conclusion	246
5.6 References	247
Chapter 6: Visualisation of Latent Finger-Marks on Brass Surfaces	259
6.1 Chapter Aims.....	260
6.2 Introduction	260

6.3 Experimental	261
6.3.1 Materials and Reagents	261
6.3.2 Instrumentation and Software	261
6.3.3 Procedures	262
6.4 Results and Discussion.....	268
6.4.1 Screening of Monomers and Combinations for Effectivity of Visualisation.....	268
6.4.2 Potentiostatic Methods for Finger-mark Visualisation.....	280
6.4.3 Visualisation of Analogous Real Case Latent Finger-marks.....	290
6.4.4 Visualisation of Finger-marks on Ammunition Casings	299
6.5 Conclusion	303
6.6 References	304
Chapter 7: Conclusions and Future work.....	309
7.1 Conclusion:	310
7.1.1 Development of an Electroanalytical Method for the Detection of Organic Firearms Residue.....	310
7.1.2 Development of an electrochemical method for the visualisation of latent finger-marks on brass ammunition casings.....	314
7.2 Additional Components Completed During the PhD Programme	317
7.2.1 Modules Completed and Credits Achieved.....	317
7.2.2 Presentations	318
7.2.3 Publications.....	319
7.2.4 Outreach	320
7.2.5 Funding Awards.....	320
7.2.6 Prizes and Awards	320

List of Figures

Figure 1.1: Image of a firearm being discharged with the resulting plume of gas containing FAR ⁴	3
Figure 1.2: Chemical structures of common stabilisers found within propellant formulations	5
Figure 1.3: Chemical structures of common plasticisers found within propellant formulations	6
Figure 1.4: Structure of common primer compound lead styphnate.....	7
Figure 1.5: Cross section of bullet-based ammunition showing location and role of various components in smokeless powder and primer mixture.	7
Figure 1.6: Example of SEM and EDX data which are traditionally used for IFAR evidence analysis, showing SEM data for A) IFAR particles at x450 magnification and B) a single IFAR particle at x4000 magnification and C) EDX data for the IFAR particle observed in B).	8
Figure 1.7: Common nitrated derivatives of DPA formed during propellant stabilisation.	12
Figure 1.8: Photograph of a plastic finger-mark on a sample of malleable putty.	17
Figure 1.9: Photograph of a series of ink-based patent finger-marks on paper.....	18
Figure 1.10: Photograph of latent finger-marks on glass of the touch screen of a video game console, with a latent finger-mark highlighted within the red circle.....	19
Figure 1.11: Example of features found within the three levels of features within a finger-mark ⁸¹	21
Figure 1.12: Photographs of A) In house fabricated magna brush, B) latent finger-mark on glass visualised with magnetic powder and C) magnetic powder visualised finger-mark as seen in (B) at x1000 magnification.....	23
Figure 1.13: Example of brass ammunition, identifying casing and bullet.	25
Figure 1.14: Latent finger-mark visualised at 180 °C after 3 days of storage by Wightman & O'Connor ⁹⁷	26
Figure 1.15 Latent finger-mark visualised on an unfired ammunition casing held in a pH 7 buffer for 24 hours by Lui et al ⁹⁹	27
Figure 1.16: Sebaceous latent finger-mark on stainless steel under potentiostatic conditions in 1 M EDOT with 0.01 M H ₂ SO ₄ and 0.02 M sodium N-lauroylsarcosinate by Brown & Hillman ¹⁰⁶	29

Figure 1.17: Partial visualisation of a latent finger-mark on a fired ammunition casing via CV over the potential range of -0.3 to 0.6 V at 50 mV.s ⁻¹ for 6 cycles ¹⁰⁹	29
Figure 1.18: General energy difference between the valance band and conduction band for a insulator, semi-conductor and conductor.	30
Figure 1.19: Example of cyclic voltammogram for the formation of poly-N-ethylaniline on a glassy carbon electrode over the potential range of 0 to 1 V vs. Ag AgCl (3 M KCl) at 50 mV.s ⁻¹ for 50 cycles (showing cycles 1-10 and every subsequent fifth cycle, 15, 20....50) inset: Zoomed in area of electrochemical responses.	31
Figure 2.1: Electrical double layer containing the inner and outer Helmholtz planes and diffuse layer interface at an electrode surface, showing continuation into bulk solution.	52
Figure 2.2: Diagrams of the three principal mechanisms of mass transport: diffusion, migration and convection.	54
Figure 2.3: Overview of redox processes involved in the generation of an electrochemical signal.	54
Figure 2.4: Generic graph showing potential step (with respect to time) for a chronoamperometry experiment.	56
Figure 2.5: Generic graph showing the current response to time during a chronoamperometry experiment.	57
Figure 2.6: Generic examples of A) potential vs. time and B) current vs. potential during a LSV experiment for an oxidative process.	58
Figure 2.7: Generic examples of A) potential vs. time and B) current vs. potential for a reversable or Nernstian system.	59
Figure 2.8: Generic example of potential vs. time during DPV analysis, indicating the parameters of pulse increment, period, width, height and the locations of current measuring.	61
Figure 2.9: Simplified diagram of the components of a SEM.	64
Figure 2.10: Simplified image of X-ray generation during EDX analysis.	65
Figure 2.11: Simple diagram of XPS spectrometer.	66
Figure 2.12: Energy level transitions within UV-Vis indicating the occupied and unoccupied orbitals.	67

Figure 2.13: A) Simplified Jablonski diagram of 1) promotion of an electron to a higher energy level and 2) the subsequent release of that energy in the form of molecular vibrations with B) a chart of the types of molecular vibrations ¹⁴	68
Figure 2.14: Generic example of a TGA thermograph showing a % mass loss with increasing temperature.	69
Figure 3.1: Representation of iron anode and cathode rods immersed in tetramethylammonium chloride with electrochemical formation of Fe ₃ O ₄ upon application of 5 V for 30 min at 60 °C.....	78
Figure 3.2: Equipment for spectroelectrochemistry. From left to right, platinum mesh electrode, magnified image of mesh, spectroelectrochemical quartz cuvette used and an in-situ image of equipment.	79
Figure 3.3: Current-time response at E _{app} = +5 V for 1800 s, at three different temperatures of 45 °C (black), 65 °C (red) and 75 °C (blue), showing the process of MNP production at an iron cathode in 0.04 M tetramethylammonium chloride (typical trace).....	81
Figure 3.4: IR spectra for the MNP material produced at E _{app} = +5 V for 1800 s held at temperatures of 45, 60 and 75 °C during electrochemical synthesis, highlighting the region (purple) which the Fe-O bond is found (approximately 570 cm ⁻¹).	82
Figure 3.5: Current-time response at held potentials of E _{app} = +1 V (black) , +2.5 V (red) and +5 V (blue) for 1800 s, at 60 °C, observing the process of MNP production at an iron cathode in 0.04 M tetramethylammonium chloride (typical trace).....	83
Figure 3.6: IR spectra for the MNP material produced at E _{app} = +1, +2.5 and +5 V while being heated at 60 °C, highlighting peaks of interest with dropped dotted lines.	85
Figure 3.7: High resolution SEM images of MNP electrosynthesis via application of A) 1 V, B) 2.5 V and C & D) 5 V. With E) a particle size distribution based on 100 particles (1 V), 50 particles (2.5 and 5 V) samples.	86
Figure 3.8: EDX spectrum confirming Fe and O atomic composition from A) 1 V, B) 2.5 V and C) 5 V preparations.....	87
Figure 3.9: Plots of thermogravimetric (red-dash) and differential scanning calorimetry (blue-solid) data of a 12.35 mg Fe ₃ O ₄ sample (generated at E _{app} = +5 V at 60 °C) in air at a flow rate of 10 ml.s ⁻¹ with a temperature programme with an initial hold of 30 °C for 1 minute and an increasing ramp of 30 °C to 600 °C at 5 °C.min ⁻¹ (typical trace shown).	88
Figure 3.10: X-ray diffraction pattern of MNP generated from an electrosynthetic method of E _{app} = +5 V at 60 °C for 1800 s in 0.04 M tetramethylammonium chloride.	89

- Figure 3.11: Cyclic voltammogram (showing cycle 3) of MNP modified GCE and bare electrode over the potential range -1 to $+1$ V vs. Ag|AgCl at 50 mV.s^{-1} in 0.1 M KCl including A) modification material generated at different potentials, showing bare GCE (green), 5 V MNP modified GCE (blue), 2.5 V MNP modified GCE (red), and 1 V MNP modified GCE (black). And B) with modification material generated at different temperatures showing bare GCE (green), MNP modified GCE with material generated at $60 \text{ }^\circ\text{C}$ (blue), $75 \text{ }^\circ\text{C}$ (red) and $45 \text{ }^\circ\text{C}$ (black) (typical traces throughout). 90
- Figure 3.12: Cyclic voltammograms (showing cycle 3) over the potential range -1 to $+1$ V vs. Ag|AgCl at 50 mV.s^{-1} in $3:7$ methanol:sodium acetate buffer ($\text{pH} \sim 4.5$) of bare (black) and MNP modified (red) GCE in A) aerated and B) degassed solutions (typical traces). 91
- Figure 3.13: Cyclic voltammograms (showing cycle 3) of MNP modified GCE showing the influence of cathodic potential limit on MNP redox behaviour (typical traces). Potential ranges 0 to 1 V (blue), -0.5 to $+1 \text{ V}$ (red) and -1 to $+1 \text{ V}$ (black) vs. Ag|AgCl at a scan rate of 50 mV.s^{-1} in $3:7$ methanol:sodium acetate buffer ($\text{pH} \sim 4.5$) (typical traces). 92
- Figure 3.14: A) Cyclic voltammograms (showing cycle 3) over the potential range of -1 to $+1 \text{ V}$ vs. Ag|AgCl for a scan rate study for MNP modified GCE using scan rates from 20 to 200 mV.s^{-1} in $3:7$ methanol:sodium acetate buffer ($\text{pH} \sim 4.5$) (typical traces). B) Corresponding plot of current density vs. scan rate using data from (A) ($n=2$). 93
- Figure 3.15: A) Cyclic voltammogram (showing cycle 1) at an unmodified GCE over the potential range of -0.1 to $+1 \text{ V}$ vs. Ag|AgCl at a scan rate of 50 mV.s^{-1} . Concentration range of DPA was 0.05 to 1 mM in a $1:1$ solution of acetonitrile:methanol with 0.1 M LiClO_4 . B) corresponding plot of j (from peak I) vs. concentration of DPA ($n=1$). 94
- Figure 3.16: Cyclic voltammogram (showing cycle 3) over the potential range of 0.2 to 1 V vs. Ag|AgCl for scan rate study using a fresh GCE surface with each new scan rate over 5 to 50 mV.s^{-1} for 1 mM DPA in a $3:7$ methanol:sodium acetate buffer ($\text{pH} \sim 4.5$). Corresponding plots (for peaks I and II) of B) $\log j_p$ vs. $\log v$ confirming surface confined behaviour of the signal for the dimeric species formed following the first anodic sweep. C) Plot of j_p vs. v confirming surface confined behaviour of the signal for the dimeric species formed following the first anodic sweep. 97
- Figure 3.17: A) Cyclic voltammogram (showing cycle 3) over the potential range of 0.2 to 1 V vs. Ag|AgCl for a DPA concentration study using a fresh GCE surface with each

concentration over the range 0.1 to 0.5 mM DPA in a 3:7 methanol:sodium acetate buffer (pH ~4.5). B) Corresponding plot of j_p vs. concentration for response at $E_{pa} = 0.7$ V (peak I).	98
Figure 3.18: A) Cyclic voltammogram over the potential range of -1 to +1 V vs. Ag AgCl at 100 $mV.s^{-1}$ in a solution of 3:7 methanol:sodium acetate buffer (pH ~4.5) showing cycles 1-10 for the film formed after repeated cycling in 1 mM DPA in 3:7 methanol:sodium acetate buffer (pH ~4.5) (n=1). B) Reflectance microscopy image of formed film, pre-electrochemical measurements (of A), on a GCE (x1000 using dark field polarisation).....	98
Figure 3.19: Averaged UV-Vis spectra (n=4) of A) 1 mM DPA in a solution of 3:7 methanol:sodium acetate buffer (pH ~4.5) before (black) and after (red) cycling 100 times over the potential range -1 to +1 V at 100 $mV.s^{-1}$. Inset: zoomed in region between 350 and 550 nm. Indicative λ_{max} for DPA are 204 and 284 nm which decrease following film formation. B) Absorbance ratio spectra for pre and post cycling solution with (red) and without (black) platinum gauze. C) Overlaid spectra for Pt gauze in background electrolyte (grey) and following cycling (black). Red curve represents solution only spectrum (background reference cuvette containing 1 mM DPA).....	100
Figure 3.20: Cyclic voltammogram (showing cycle 3) of a 1 mM DPA solution in 3:7 methanol:sodium acetate buffer (pH ~4.5) at 50 $mV.s^{-1}$ over the potential range of A) 0 to 1, B) -0.5 to +1 V and C) -1 to +1 V vs. Ag AgCl at bare (black) and MNP modified (red) (typical traces).....	101
Figure 3.21: Linear sweep voltammogram over the potential range of -1 to +1 V vs. Ag AgCl at 50 $mV.s^{-1}$ for DPA concentration series (0.1 to 1 mM) in 3:7 in methanol:sodium acetate buffer (pH ~4.5) at a MNP modified GCE (typical trace). Inset: zoomed in region of 0.5 to 1 V for DPA oxidation.	102
Figure 3.22: Averaged data (n=3) for differential pulse voltammetry over the potential range of -1 to +1.5 V vs. Ag AgCl with additional parameters as per electrochemical procedures section (region of DPA peak 0.4 V to 0.9 V only shown). DPA concentration series (5 to 1000 μM) at A) bare and B) MNP modified GCE (with current standard deviations of ± 0.12 μA at bare and ± 0.16 μA at modified electrodes across the entire series).	103
Figure 3.23: Averaged data plots (n=3) of current vs. concentration of DPA in 3:7 methanol:sodium acetate buffer (pH ~4.5) (from Figure 3.21) at bare (blue) and modified	

(red) GCE over the concentrations of A) 5 to 1000 μM B) 50 to 1000 μM and C) 5 to 50 μM	104
Figure 3.24: Cyclic voltammogram of 1 mM EC in 0.1 M LiClO_4 in acetonitrile for 3 cycles at a GCE over the potential range 0 to 1.5 V vs. $\text{Ag} \text{Ag}^+$ (10 mM AgNO_3) at 100 $\text{mV}\cdot\text{s}^{-1}$. (Cycle 1: black/solid, Cycle 2: red/dash, Cycle 3: blue/dots) (typical trace). ..	106
Figure 3.25: A) Cyclic voltammogram (showing cycle 3) of 1 mM EC in 0.1 M LiClO_4 in acetonitrile at various scan rates 10 to 200 $\text{mV}\cdot\text{s}^{-1}$ (typical trace) with B) corresponding plot of current density vs $\sqrt{\text{scan rate}}$ for peaks I, II, III. Potential range 0 to 1.5 V vs. $\text{Ag} \text{Ag}^+$ (10 mM AgNO_3).....	107
Figure 3.26: Cyclic voltammogram of A) 1 mM EC in 3:7 methanol:sodium acetate buffer (pH ~ 4.5) at a GCE over the potential range 0 to 1.5 V at 50 $\text{mV}\cdot\text{s}^{-1}$ (showing all three cycles) (typical trace). B) Influence of the cathodic limit on the anodic process (first cycle shown) at 50 $\text{mV}\cdot\text{s}^{-1}$ over the potential range -1 (blue), 0 (black) and -0.5 (red) to +1.5 V (typical traces).....	108
Figure 3.27: Cyclic voltammogram over the potential range of -1 to +1.5 V vs. $\text{Ag} \text{AgCl}$ of A) 1 mM EC in 3:7 methanol:sodium acetate buffer (pH ~ 4.5) at a GCE (20 cycles shown) (typical trace) and B) 1 mM EC in 3:7 methanol:phosphate buffer (pH ~ 7.25) at a GCE (5 cycles shown) (typical trace). Inset: cycle 2 shown at 50 $\text{mV}\cdot\text{s}^{-1}$	109
Figure 3.28: A) Photographs (x40 magnification) of 1) bare GCE polished surface and a GCE surface following 50 cycles in 2) 1 mM and 3) 5 mM EC in 3:7 methanol:sodium acetate buffer (pH ~ 4.5) at 100 $\text{mV}\cdot\text{s}^{-1}$ over the range -1 to +1.5 V. Cyclic voltammogram over the potential range of -1 to +1 V vs. $\text{Ag} \text{AgCl}$ at 50 $\text{mV}\cdot\text{s}^{-1}$ for B) 5 mM EC and C) 1 mM EC in 3:7 methanol:sodium acetate buffer (pH ~ 4.5) at a GCE (50 cycles, showing cycles 1 to 10 and then every subsequent tenth cycle) (typical trace).	110
Figure 3.29: Cyclic voltammogram (showing cycle 1) over the potential range of -1 to +1.5 V vs. $\text{Ag} \text{AgCl}$ at 100 $\text{mV}\cdot\text{s}^{-1}$ in 3:7 methanol:sodium acetate buffer (pH ~ 4.5) of film formed following cycling in 1 mM EC (red) relative to bare GCE (black) (n=1).....	111
Figure 3.30: A) Cyclic voltammograms (showing cycle 1) for scan rate study of EC at a bare GCE over the potential range of -1 to +1.5 V vs. $\text{Ag} \text{AgCl}$, scan rates of 10 to 500 $\text{mV}\cdot\text{s}^{-1}$. First 3 cycles of 1 mM EC with 0.1 M LiClO_4 in 3:7 methanol:sodium acetate buffer (pH ~ 4.5) at B) 10 $\text{mV}\cdot\text{s}^{-1}$ and C) 200 $\text{mV}\cdot\text{s}^{-1}$	115
Figure 3.31: Average DPV data (n=3) of EC over the potential range of -1 to +1.5 V vs. $\text{Ag} \text{AgCl}$ with additional parameters as per electrochemical procedures section (region of	

EC peak 1 to 1.5 V only shown) for a concentration series (5 to 1000 μM) at A) bare and B) MNP modified GCE (with current standard deviations of $\pm 0.15 \mu\text{A}$ for bare and $\pm 0.20 \mu\text{A}$ for modified across the entire series).	116
Figure 3.32: Average data plots (n=3) of current vs. concentration of EC in 3:7 methanol:sodium acetate buffer (pH ~ 4.5) at bare (blue) and modified (red) GCE over the concentrations of A) 5 to 1000 μM , B) 50 to 1000 μM and C) 5 to 50 μM	117
Figure 4.1: Photograph of ELEY super game shotgun cartridges box with spent cartridges.	138
Figure 4.2: Image of gunshot hole in 65% polyester 35% cotton fabric.....	139
Figure 4.3: Average data (n=3) for DPV over the potential range -1 to +1.5 V vs. Ag AgCl (region of peaks 0.5 to 1.5 V only shown) with additional parameters as per electrochemical procedures section. Equal concentrations of DPA and EC over the range 1 to 1000 μM in a 3:7 methanol:sodium acetate buffer (pH ~ 4.5) at A) bare and B) MNP modified GCE (with current standard deviations of $\pm 0.15 \mu\text{A}$ for bare and $\pm 0.24 \mu\text{A}$ for modified across the entire series) with corresponding calibration curves for C) bare and D) modified electrodes.	140
Figure 4.4: Average DPV (n=3) over the potential range of -1 to +1.5 V vs. Ag AgCl for both individual and dual analyte systems with additional parameters as per electrochemical procedures section showing A) 1 mM EC peak and B) 1 mM DPA peak under the same conditions at both a bare and MNP modified GCE.	141
Figure 4.5: Plot of current vs. concentration for both DPA and EC in a mixed analyte system over the concentration range of 5 to 50 μM at MNP modified GCE.....	142
Figure 4.6: Overlaid DPVs over the potential range of -1 to +1.5 V vs. Ag AgCl with additional parameters as per electrochemical procedures section (region of peaks: 0.5 to 1.5 V only shown). MNP modified GCE response to 0.25 mM DPA (black), 0.25 mM EC (red), 0.25 mM DPU (blue) and 0.25 mM DMP (green) in individual solutions (typical traces).	145
Figure 4.7: SEM photographs of IFAR particles recovered from fabric via tape lifts using a carbon stub showing particles at A) x450 and B) x4000 magnification with EDX spectral analysis for IFAR particle in (B) showing presence of lead, antimony and barium.	146
Figure 4.8: Atomic force microscopy of tape lifted sample performed by Dr. Shane Murphy of Technological University Dublin, taken under ambient conditions using a	

benchtop AFM in tapping mode with 300 kHz, 40 N.m ⁻¹ cantilever using a scan speed of 0.2 lines.s ⁻¹ , drive frequency of 272 kHz and drive amplitude of 0.4 V.....	147
Figure 4.9: Photograph of unburnt propellant discs recovered from shotgun cartridge.	148
Figure 4.10: Average DPV data (n=3) over the potential range of -1 to +1.5 vs. Ag AgCl with additional parameters as per electrochemical procedures section. A) unburnt propellant sample at bare (black) and MNP modified (red) electrodes and 10 μM DPA standard at bare (blue) and MNP modified (green) electrodes with B) zoomed in region of interest for DPA peak.	149
Figure 4.11: Average DPV data (n=3) over the potential range of -1 to +1.5 V vs. Ag AgCl with additional parameters as per electrochemical procedures section of A) bare and B) MNP modified GCE with standard addition of DPA 19.6 to 56.6 μM in a solution of 5.91 mg unburnt propellant discs with C) standard addition analysis plots generated from DPV data in (A) and (B) (with current standard deviations of ± 0.092 μA for bare and ± 0.11 μA for modified across the entire series).	150
Figure 4.12: Average DPV data (n=3) over the potential range of -1 to +1.5 V vs. Ag AgCl with additional parameters as per electrochemical procedures section. A) bare and B) MNP modified GCE with standard addition of EC 19.6 to 56.6 μM in a solution of 32.2 mg unburnt propellant discs with C) standard addition analysis plots generated from DPV data in (A) and (B) (with current standard deviations of ± 0.14 μA for bare and ± 0.4 μA for modified across the entire series).	151
Figure 4.13: Average DPV data (n=3) over the potential range of -1 to +1.5 V vs. Ag AgCl with additional parameters as per electrochemical procedures section. A) bare and B) MNP modified GCE with standard addition of DPA 19.6 to 56.6 μM in a solution of FAR swabbed over an area of 50 cm ² with C) standard addition analysis plots generated from DPV data in (A) and (B) (current standard deviations of ± 0.02 μA for bare and ± 0.01 μA for modified across the entire series).	153
Figure 4.14: Average DPV data (n=3) over the potential range of -1 to +1.5 V vs. Ag AgCl with additional parameters as per electrochemical procedures section. A) bare and B) MNP modified GCE with standard addition of EC 19.6 to 56.6 μM in a solution of FAR swabbed over an area of 50 cm ² . C) standard addition analysis plots generated from DPV data in (A) and (B) (with current standard deviations of ± 0.31 μA for bare and ± 0.63 μA for modified across the entire series).	154

Figure 4.15: Three iterations of the SPE prototype design for the analysis of OFAR. .	156
Figure 4.16: FTIR spectra of (black) electrochemically and (red) chemically synthesised MNP.	157
Figure 4.17: Thermal analysis (DSC/TGA) in air at a flow rate of 10 mL.s ⁻¹ with a temperature programme of an initial hold at 30 °C for 1 minute and an increasing temperature ramp of 30 °C to 600 °C at 5 °C.min ⁻¹ for A) chemically prepared and B) electrochemically prepared MNPs.	157
Figure 4.18: Average DPV data (n=3) over the potential range of -0.5 to +2 V vs. Ag AgCl with additional parameters as per electrochemical procedures section. A) 1 mM DPA, B) 1 mM EC and C) 1 mM DPA and 1 mM EC in 3:7 methanol:sodium acetate buffer (pH ~ 4.5) comparing a bare (solid) and MNP modified (dash) SPE.....	159
Figure 4.19: Average DPV data (n=4) over the potential range of -0.5 to +2 V vs. Ag AgCl with additional parameters as per electrochemical procedures section. A) background electrolyte solution at bare (black) and MNP modified (red) SPE and B) 1 mM DPA and 1 mM EC in 3:7 methanol:sodium acetate buffer (pH ~4.5) background subtracted (using data from (A)) comparing a bare (solid) and MNP modified (dash) SPE.....	160
<i>Figure 4.20: DPV over the potential range of -0.5 to +2 V vs. Ag AgCl with additional parameters as per electrochemical procedures section. Of A) bare and B) modified SPE for 1 mM EC and DPA in 3:7 methanol:sodium acetate buffer (pH ~4.5) showing inter-electrode variability for n=4 individual strips.</i>	161
Figure 4.21: Average DPV data (n=3) over the potential range of -0.5 to +2 V vs. Ag AgCl with additional parameters as per electrochemical procedures section, of a sample of unburnt propellant at bare (solid) and MNP modified (dash) SPE (background subtracted).	162
Figure 4.22: Average DPV data (n=3) over the potential range of -0.5 to +2 V vs. Ag AgCl with additional parameters as per electrochemical procedures section of a sample of unburnt propellant recovered from a textile at bare (solid) and MNP modified (dash) SPE (both background subtracted).....	163
Figure 5.1: Chemical structures of monomers of interest for deposition.....	177
Figure 5.2: Generic structure of a phenazine and phenothiazine, where R groups (-H, -CH ₃ etc.) may or may not be present ³⁴	179
Figure 5.3: Structure of repeating unit of polythionine ⁴⁷	181

Figure 5.4: Diagram of brass strip with working area sectioned via insulating tape prior to electrochemical use.	183
Figure 5.5: Diagram of brass samples for XPS analysis.	185
Figure 5.6: Digitised finger-mark of finger used in analysis with common features labelled.	186
Figure 5.7: Cyclic voltammogram over the potential range -0.6 to +1 V vs. Ag AgCl for a brass sheet in 0.1 M H ₂ SO ₄ at 100 mV.s ⁻¹ for 3 cycles (Cycle 1: black, Cycle 2: red and Cycle 3: blue). Inset: showing crossover in cycle 1 at 0.11 V (typical trace).	189
Figure 5.8: Pourbaix diagram of zinc in an aqueous system at 25 °C ⁵⁰	190
Figure 5.9: Photograph of sebaceous finger-mark on a brass sheet visualised via cyclic voltammetry over the potential range of -0.6 to +1 V vs. Ag AgCl for 3 cycles at 100 mV.s ⁻¹ in 0.1 M H ₂ SO ₄ with B) high contrast black and white.	190
Figure 5.10: Chronoamperometry of brass sheets in 0.1 M H ₂ SO ₄ showing E _{app} = A) +1.1 V (black), +0.5 V (red) and +0.3 V (blue) and B) -0.5 V (black) and -0.1 V (red). Inset: zoomed in plot of -0.1 V.	192
Figure 5.11: Pourbaix diagram of copper in a SO ₄ ²⁻ rich environment ⁵² with the horizontal red lines indicating the potentials held (corrected for conversion to SHE) with vertical line representing pH of solution employed in this work.	193
Figure 5.12: Chronoamperometry of a brass sheet in 0.1 M H ₂ SO ₄ at E _{app} = 0.1 V for 60 s (black) and 300 s (red). Inset: representation of solution lines on a strip of brass post analysis in 0.1 M H ₂ SO ₄	194
Figure 5.13: A) Chronoamperometry of a brass sheet with a latent print of E _{app} = +0.1 V (black) and E _{app} = +0.2 V (red) for 300 s in 0.1 M H ₂ SO ₄ and corresponding photograph of visualised finger-marks via E _{app} = +0.2 V in B) full colour and C) high contrast black and white.	195
Figure 5.14: A) Chronoamperometry of a brass sheet of E _{app} = +0.1 V (black) and E _{app} = +0.2 V (red) for 300 s in 0.01 M EDOT with 0.1 M H ₂ SO ₄ and corresponding photograph of visualised finger-marks via E _{app} = +0.2 V in B) full colour and C) high contrast black and white.	197
Figure 5.15: Cyclic voltammogram over the potential range of -0.2 to +0.5 V vs. Ag AgCl for 3 cycles at 100 mV.s ⁻¹ for a brass sheet in A) 0.1 M H ₂ SO ₄ and B) 0.01 M EDOT with 0.1 M H ₂ SO ₄	198

Figure 5.16: Photographs of finger-marks on brass visualised via cyclic voltammetry over the potential range of -0.2 to +0.5 V vs. Ag AgCl for 3 cycles at 100 mV.s ⁻¹ showing A) the full colour image and B) the high contrast counterpart of a finger-mark visualised in 0.1 M H ₂ SO ₄ and C) a full colour and D) the high contrast counterpart visualised in 0.01 M EDOT in 0.1 M H ₂ SO ₄	199
Figure 5.17: Cyclic voltammogram of a brass sheet over the potential range of -0.2 to +0.5 V vs. Ag AgCl showing three cycles at 50 mV.s ⁻¹ in 0.1 M NaNO ₃	200
Figure 5.18: Photographs of A) finger-marks on brass visualised via cyclic voltammetry over the potential range of -0.2 to +0.5 V at 50 mV.s ⁻¹ for three cycles in 0.1 M NaNO ₃ with high contrast images underneath and B) level 3 features indicated by arrows on zoomed in region of one of the previously visualised finger-marks.	201
Figure 5.19: Pourbaix diagram of copper in an aqueous environment with the red intersecting lines showing the maximum and minimum of the potential ranges with the experimental parameters (corrected for conversion to SHE).	202
Figure 5.20: Cyclic voltammogram of a brass strip over the potential range -0.2 to +0.5 V vs. Ag AgCl showing three cycles at 50 mV.s ⁻¹ in a solution of 2 mM EDOT in 0.1 M NaNO ₃	203
Figure 5.21: Photographs of A) finger-marks visualised with 2 mM EDOT in 0.1 M NaNO ₃ with B) high contrast photographs C) zoomed in image of core of visualised finger-mark showing level 3 features (pores).	204
Figure 5.22: XPS spectra of brass showing A) full copper area scan of untreated (black) and treated in 0.1 M NaNO ₃ over the potential range -0.2 to +0.5 V vs. Ag AgCl for three cycles at 100 mV.s ⁻¹ (red) samples with B) untreated and C) treated brass.	206
Figure 5.23: XPS data of brass sheets showing the A) zinc region with untreated (black) and treated (red) brass B) the oxygen region of untreated brass and C) the oxygen region of treated brass.	207
Figure 5.24: A) Cyclic voltammogram of 2 mM EDOT in 0.1 M NaNO ₃ at a GCE over the potential range -0.8 to +1.2 V vs. Ag AgCl at 100 mV.s ⁻¹ showing cycles one (black), three (red) and five (blue). Inset of cycles three and five. B) PEDOT film on a GCE showing third cycle (black) against third cycle of a clean electrode (red dash) over the potential range -0.8 to +1.5 V vs. Ag AgCl at 100 mV.s ⁻¹ in 0.1 M NaNO ₃	210
Figure 5.25: A) Cyclic voltammogram of 1 mM Th in 0.1 M NaNO ₃ at a GCE over the potential range of -0.8 to +1.2 V vs. Ag AgCl at 100 mV.s ⁻¹ showing cycles one (black),	

three (red) and five (blue) and B) Th film on a GCE showing third cycle (black) against third cycle of a clean electrode (red dash) over the potential range of -0.8 to +1.5 V vs. Ag AgCl at 100 mV.s ⁻¹ in 0.1 M NaNO ₃	211
Figure 5.26: A) Cyclic voltammogram of 1 mM NR in 0.1 M NaNO ₃ at a GCE over the potential range -0.8 to +1.2 V vs. Ag AgCl at 100 mV.s ⁻¹ showing cycles one (black), three (red) and five (blue) B) NR film on a GCE showing third cycle (black) against third cycle of a clean electrode (red dash) over the potential range -0.8 to +1.5 V vs. Ag AgCl at 100 mV.s ⁻¹ in 0.1 M NaNO ₃	212
Figure 5.27: Cyclic voltammogram (showing cycle 1) over the potential range of -0.8 to +1.5 V vs. Ag AgCl at 100 mV.s ⁻¹ of 2 mM EDOT (black), 1 mM NR (blue) and EDOT-NR (2:1 mM) (red) in 3:7 methanol:sodium acetate buffer (pH ~ 4.5) (typical traces).	213
Figure 5.28: Cyclic voltammogram of A) 2 mM EDOT and 1 mM NR in 0.1 M NaNO ₃ at a GCE across the range of -0.8 to +1.2 V vs. Ag AgCl at 100 mV.s ⁻¹ showing cycles one (black), three (red) and five (blue). Inset: cycles three and five. B) PEDOT-NR film on a GCE showing third cycle (black) against third cycle of a clean electrode (red dash) across the range of -0.8 to +1.5 V vs. Ag AgCl at 100 mV.s ⁻¹ in 0.1 M NaNO ₃	214
Figure 5.29: Cyclic voltammogram (showing cycle 1) over the potential range -0.8 to +1.5 V vs. Ag AgCl at 100 mV.s ⁻¹ of 2 mM EDOT (black), 1 mM Th (blue) and EDOT-Th (2:1 mM) (red) in 3:7 methanol:sodium acetate buffer (pH ~ 4.5) (typical traces).	215
Figure 5.30: Cyclic voltammogram of A) 2 mM EDOT and 1 mM Th in 0.1 M NaNO ₃ at a GCE over the potential range -0.8 to +1.2 V vs. Ag AgCl at 100 mV.s ⁻¹ showing cycles one (black), three (red) and five (blue). B) PEDOT-Th film on a GCE showing third cycle (black) against third cycle of a clean electrode (red dash) over the potential range -0.8 to +1.5 V vs. Ag AgCl at 100 mV.s ⁻¹ in 0.1 M NaNO ₃	215
Figure 5.31: Cyclic voltammogram (showing cycle 1) over the potential range -0.8 to +1.5 V vs. Ag AgCl at 100 mV.s ⁻¹ of 1 mM NR (black), 1 mM Th (blue) and NR-Th (1:1 mM) (red) in 3:7 methanol:sodium acetate buffer (pH ~ 4.5) (typical traces).....	216
Figure 5.32: Cyclic voltammogram of A) 1 mM NR and 1 mM Th in 0.1 M NaNO ₃ at a GCE over the potential range -0.8 to +1.2 V vs. Ag AgCl at 100 mV.s ⁻¹ showing cycles one (black), three (red) and five (blue) and B) NR-Th film on a GCE showing third cycle (black) against third cycle of a clean electrode (red dash) over the potential range -0.8 to +1.5 V vs. Ag AgCl at 100 mV.s ⁻¹ in 0.1 M NaNO ₃	217

Figure 5.33: Example spectra of a 2 mM EDOT solution in 0.1 M NaNO ₃ showing how second derivative analysis can resolve a spectral peak.	219
Figure 5.34: Second derivative UV-Vis absorbance spectra of PEDOT and PEDOT containing films on a GCE using reflectance probe spectroscopy.	220
Figure 5.35: Second derivative UV-Vis absorbance spectra of Th and Th containing films on a GCE using reflectance probe spectroscopy.	221
Figure 5.36: Second derivative UV-Vis absorbance spectra of NR and NR containing films on a GCE using reflectance probe spectroscopy.	222
Figure 5.37: IR spectra of electrochemically deposited films on a GCE surface.	225
Figure 5.38: Series of IR spectra of films on a GCE with A) comparison of NR containing films, B) comparison of PEDOT containing films and C) comparison of Th containing films.	227
Figure 5.39: Cyclic voltammograms of an ITO electrode in A) 2 mM EDOT in 0.1 M NaNO ₃ over the potential range -0.5 to +1.2 V vs. Ag AgCl at 100 mV.s ⁻¹ showing cycles one (black), five (red), ten (blue), fifteen (green) and twenty (purple) (typical traces) and B) scan rate study of the film formed in (A) in 0.1 M NaNO ₃ over the potential range 0 to 1 V vs. Ag AgCl at 50 (black), 100 (red), 150 (blue), 200 (green) and 250 (purple) mV.s ⁻¹ (typical traces).	229
Figure 5.40: Cyclic voltammograms of an ITO electrode in A) 1 mM Th in 0.1 M NaNO ₃ over the potential range -0.5 to +1.2 V vs. Ag AgCl at 100 mV.s ⁻¹ showing cycles one (black), five (red), ten (blue), fifteen (green) and twenty (purple) (typical traces) and B) scan rate study of the Th film formed in (A) in 0.1 M NaNO ₃ over the potential range -0.5 to +0.5 V vs. Ag AgCl at 50 (black), 100 (red), 150 (blue), 200 (green) and 250 (purple) mV.s ⁻¹ (typical traces).	230
Figure 5.41: Plot of <i>jp</i> values I and II from Figure 5.40 vs. A) scan rate and B) √scan rate.	231
Figure 5.42: Cyclic voltammograms of an ITO electrode in A) 1 mM NR in 0.1 M NaNO ₃ over the potential range -0.5 to +1.2 V vs. Ag AgCl at 100 mV.s ⁻¹ showing cycles one (black), five (red), ten (blue), fifteen (green) and twenty (purple) (typical traces) and B) scan rate study of the NR film formed in (A) in 0.1 M NaNO ₃ over the potential range 0 to 1 V vs. Ag AgCl at 50 (black), 100 (red), 150 (blue), 200 (green) and 250 (purple) mV.s ⁻¹ (typical traces).	232

Figure 5.43: Cyclic voltammograms of an ITO electrode in A) 2 mM EDOT and 1 mM NR in 0.1 M NaNO ₃ over the potential range -0.5 to +1.2 V vs. Ag AgCl at 100 mV.s ⁻¹ showing cycles one (black), five (red), ten (blue), fifteen (green) and twenty (purple) (typical traces) and B) scan rate study of the film formed in (A) in 0.1 M NaNO ₃ over the potential range 0 to 1 V vs. Ag AgCl at 50 (black), 100 (red), 150 (blue), 200 (green) and 250 (purple) mV.s ⁻¹ (typical traces).....	233
Figure 5.44: Cyclic voltammograms of an ITO electrode in A) 2 mM EDOT and 1 mM Th in 0.1 M NaNO ₃ over the potential range -0.5 to +1.2 V vs. Ag AgCl at 100 mV.s ⁻¹ showing cycles one (black), five (red), ten (blue), fifteen (green) and twenty (purple) (typical traces) and B) scan rate study of the film formed in (A) in 0.1 M NaNO ₃ over the potential range -0.5 to +0.5 V vs. Ag AgCl at 50 (black), 100 (red), 150 (blue), 200 (green) and 250 (purple) mV.s ⁻¹ (typical traces) and C) plot of <i>I_{pc}</i> vs. $\sqrt{\text{scan rate}}$	234
Figure 5.45: Cyclic voltammograms of an ITO electrode in A) 1 mM NR and 1 mM Th in 0.1 M NaNO ₃ over the potential range -0.5 to +1.2 V vs. Ag AgCl at 100 mV.s ⁻¹ showing cycles cycles one (black), five (red), ten (blue), fifteen (green) and twenty (purple) (typical traces) and B) scan rate study of the film formed in (A) in 0.1 M NaNO ₃ over the potential range -0.5 to +0.5 V vs. Ag AgCl at 50 (black), 100 (red), 150 (blue), 200 (green) and 250 (purple) mV.s ⁻¹ (typical traces) and C) plot of <i>I_{pc}</i> vs. $\sqrt{\text{scan rate}}$	235
Figure 5.46: UV-Vis absorbance spectra for A) PEDOT containing films, B) Th containing films and C) NR containing films at an ITO surface.	237
Figure 5.47: IR spectra of A) NR containing films B) PEDOT containing films and C) Th containing films at an ITO surface.	239
Figure 5.48: Proposed structures indicating linkages between monomer units in combined films showing A) NR-Th, B) PEDOT-Th and C) PEDOT-NR.	241
Figure 5.49: Cyclic voltammograms of A) 2 mM EDOT, B) 1 mM Th, C) 1 mM NR, D) 2 mM EDOT and 1 mM NR, E) 2 mM EDOT and 1 mM Th and F) 1 mM NR and 1 M Th in 0.1 M NaNO ₃ at a brass surface over the potential range -0.2 to +0.5 V vs. Ag AgCl at 100 mV.s ⁻¹ (typical traces).....	242
Figure 5.50: UV-vis absorbance spectra of all individual and mixed monomer films at a brass surface, using reflectance probe spectroscopy.	244
Figure 5.51: IR spectra of electrochemically deposited films on a brass surface.	245
Figure 6.1: A) Photographs of ammunition casings in a drill B) before and after polishing surface of ammunition casings.....	263

Figure 6.2: Photograph of three electrode cell set-up with ammunition casing acting as the working electrode.	266
Figure 6.3: Photograph of photographic set-up of imaging for visualised finger-marks.	268
Figure 6.4: Cyclic voltammogram of a brass sheet A) without and B) with a latent finger-mark in 2 mM EDOT and 1 mM NR in 0.1 M NaNO ₃ over the potential range -0.2 to +0.5 V vs. Ag AgCl at 50 mV.s ⁻¹ for three cycles (Cycle 1: black, Cycle 2: red and Cycle 3: blue-dash) (typical traces).	269
Figure 6.5: High contrast photographs of latent finger-marks visualised at a brass sheet via cyclic voltammetry over the potential range -0.2 to +0.5 V vs. Ag AgCl at 50 mV.s ⁻¹ for three cycles in A) 0.1 M NaNO ₃ , and subsequent monomer solutions of 0.1 M NaNO ₃ with B) 2 mM EDOT, C) 1 mM Th and D) 1 mM NR.	270
Figure 6.6: High contrast photographs of latent finger-marks visualised at a brass sheet via cyclic voltammetry over the potential range -0.2 to +0.5 V vs. Ag AgCl at 50 mV.s ⁻¹ for three cycles in 0.1 M NaNO ₃ with mixed monomer solutions of A) EDOT-NR (2:1 mM), B) EDOT-Th (2:1 mM), C) NR-Th (1:1 mM).	271
Figure 6.7: Photographs of microscope images (x1000 magnification) of finger-mark cores visualised at a brass sheet via cyclic voltammetry over the potential range -0.2 to +0.5 V vs. Ag AgCl at 50 mV.s ⁻¹ for three cycles in 0.1 M NaNO ₃ containing the monomers A) 2 mM EDOT, B) 1 mM Th, C) 1 mM NR and the mixed monomer solutions of D) EDOT-NR (2:1 mM), E) EDOT-Th (2:1 mM) and F) NR-Th (1:1 mM).	274
Figure 6.8: XPS graphs from brass surface following cyclic voltammetry over the potential range -0.2 to +0.5 V vs. Ag AgCl at 50 mV.s ⁻¹ for three cycles in 0.1 M NaNO ₃ with EDOT-Th (solid lines) and Th (dashed lines), showing the binding energies of A) Nitrogen and B) Sulphur. C) Histogram showing the elemental % atomic quantification at surface for untreated brass (black) and brass surface following cyclic voltammetry over the potential range -0.2 to +0.5 V vs. Ag AgCl at 50 mV.s ⁻¹ for three cycles in 0.1 M NaNO ₃ (red), 2 mM Th (purple) and EDOT-Th (2:1 mM)(green).	279
Figure 6.9: Charge density vs. time plot for brass sheets held at E _{app} = +0.5 V vs. Ag AgCl in 1 mM Th with 0.1 M NaNO ₃ until a charge of 1 (black), 5 (red) and 10 (blue) C was reached.	280

Figure 6.10: Photographs x100 magnification of untouched surface, ridge details and dark field of a visualised latent finger-mark visualised upon $E_{app} = +0.5$ V vs. Ag AgCl in 0.1 M NaNO ₃ until a charge of A) 4, B) 5 and C) 6 C was reached.	284
Figure 6.11 Photographs x100 magnification of untouched surface, ridge details and dark field image of a visualised latent finger-mark visualised with $E_{app} = +0.5$ V vs. Ag AgCl in 1 mM Th in 0.1 M NaNO ₃ until a charge of A) 4, B) 5 and C) 6 C was reached.	285
Figure 6.12 Photographs x100 magnification of untouched surface, ridge details and dark field image of a visualised latent finger-mark visualised with $E_{app} = +0.5$ V vs. Ag AgCl in 2 mM EDOT with 1 mM Th in 0.1 M NaNO ₃ until a charge of A) 4, B) 5 and C) 6 C charge was reached.	287
Figure 6.13: Photograph and high contrast image of latent finger-mark on a brass surface visualised in 2 mM EDOT and 1 mM Th in 0.1 M NaNO ₃ at $E_{app} = +0.25$ V vs. Ag AgCl for 60 s.	288
Figure 6.14: Photograph and high contrast image of a latent finger-mark on a brass surface visualised in 2 mM EDOT and 1 mM Th in 0.1 M NaNO ₃ at $E_{app} = +0.1$ V vs. Ag AgCl for 120 s.	289
Figure 6.15: Photograph and high contrast image of a latent finger-mark on a brass surface visualised in 0.1 M NaNO ₃ at $E_{app} = +0.1$ V vs. Ag AgCl for 120 s.	289
Figure 6.16: Photograph and zoomed in high contrast image of visualised 5-month-old groomed latent finger-mark at $E_{app} = +0.1$ V vs. Ag AgCl for 120 s split across two brass sheets showing, left visualised in 0.1 M NaNO ₃ and right visualised in 2 mM EDOT with 1 mM Th in 0.1 M NaNO ₃	291
Figure 6.17: Natural (A and C) and groomed (B and D) 16-month-old latent finger-marks on a brass surface visualised in 2 mM EDOT with 1 mM Th in 0.1 M NaNO ₃ at $E_{app} = +0.1$ V vs. Ag AgCl for 120 s.	293
Figure 6.18: Phase diagram for brass with different compositions of copper and zinc, indicating both types of brass used within this work.	295
Figure 6.19: Photograph and high contrast image of latent finger-mark visualised in 2 mM EDOT with 1 mM Th in 0.1 M NaNO ₃ at $E_{app} = +0.1$ V vs. Ag AgCl for 120 s post heating to 100 °C for 25 minutes.	296
Figure 6.20: Photograph and high contrast image of latent finger-mark visualised in 2 mM EDOT with 1 mM Th in 0.1 M NaNO ₃ at $E_{app} = +0.1$ V vs. Ag AgCl for 120 s post heating to 300 °C for 0.5 minutes.	297

Figure 6.21: Photograph and high contrast image of latent finger-mark visualised in 2 mM EDOT with 1 mM Th in 0.1 M NaNO ₃ at $E_{app} = +0.1$ V vs. Ag AgCl for 120 s post heating to 700 °C for 0.5 minutes.	298
Figure 6.22: Photograph and high contrast image of latent finger-mark on a brass ammunition casing visualised at $E_{app} = +0.1$ V vs. Ag AgCl for 120 s in 2 mM EDOT with 1 mM Th in 0.1 M NaNO ₃	300
Figure 6.23: Visualised latent finger-mark on ammunition casing using cyclic voltammetry over the potential range of -0.2 to +0.5 V vs. Ag AgCl at 50 mV.s ⁻¹ for 6 cycles in 2 mM EDOT with 1 mM Th in 0.1 M NaNO ₃	302

List of Tables

Table 1.1: Classifications of characteristic components of OFAR as identified by Goudsmits et al. ⁴¹	11
Table 1.2: Finger-mark Grading system (as Defined by the UK Home Office) ⁷⁵	20
Table 1.3: Band gaps for conventional and polymeric semiconductors ¹¹¹	30
Table 1.4: Conductivity values for common metals and conducting polymers ¹¹¹	32
Table 2.1: Energy level transitions within UV-Vis analysis with examples of where transitions are commonly found ¹⁴	67
Table 3.1: Current density values throughout temperature study during MNP formation (n=2).....	81
Table 3.2 Current density values at Fe anode throughout the applied potential study of MNP formation (n=2).....	84
Table 3.3: Average particle size of MNP prepared via electrosynthesis.....	87
Table 3.4: XRD data for Magnetite MNP.....	89
Table 3.5: Comparison of LOD and LOQ values for DPA and EC at bare and MNP modified GCEs.....	118
Table 4.1: Non-electrochemical methods of analysis for DPA or EC.....	133
Table 4.2: Electrochemical methods for analysis of DPA or EC.....	134
Table 4.3: Maxam [®] CSB 3 powder specifications as per manufacturer.....	138
Table 4.4: LOD and LOQ comparison for bare and MNP modified electrodes.....	143
Table 4.5: Comparison of statistically significant differences for LOD and LOQ values obtained for DPA and EC at different electrode modifications.....	144
Table 4.6: Averaged results of standard addition analysis with unburnt propellant (n=3).	152
Table 4.7: Results of standard addition analysis with FAR sample swabbed from textile surface (n=3).	155
Table 4.8: DPA and EC peak data at four different SPEs.....	161
Table 5.1: Composition of common metals and averaged compositions found in cartridge brass. ^{3,4}	172
Table 5.2: Galvanic series of some example metals indicating nobility or activity ⁷	174
Table 5.3: Combinations of EDOT monomer, thionine acetate and neutral red employed.	184

Table 5.4: Binding energies and species found in full XPS survey data (untreated brass).	205
Table 5.5: Averaged total percentage of elements at the surfaces of brass samples	208
Table 5.6: Reagent combinations employed for electrodeposition experiments using conducting and redox polymers.	209
Table 5.7: Overview of electrochemical responses observed in cycle one of the various solutions used for this analysis.....	218
Table 5.8: Table of observed absorbance wavelengths within polymeric films on a GCE.	223
Table 5.9: Table of crossover and breakdown potentials observed in cycle 1 with a brass surface in various solutions of monomers.....	243
Table 6.1: Comparison of level features obtained from the visualisation of a groomed latent finger-mark on a brass surface in various solutions via cyclic voltammetry.	272
Table 6.2: Table of results from the split print method of application of finger-marks visualised via cyclic voltammetry.	275
Table 6.3: Identity of some sulphur binding energies found with Th and EDOT-Th deposition layers on a brass surface.	280
Table 6.4: Data from survey of $E_{app} = 0.5$ V at brass sheets in different visualisation solutions.	282
Table 6.5: Level features observed from visualisation of 5-month-old latent finger-marks.	292
Table 6.6: Level features observed from visualisation of 16-month-old latent finger-marks	294
Table 6.7: Overview of level features achieved from heat treated latent finger-marks on brass.	298
Table 6.8: Results of replicates of visualisation in EDOT-Th solution with $E_{app} = 0.1$ V for 120 s.	301
Table 6.9: Results of replicates of visualisation in EDOT-Th solution via cyclic voltammetry.....	302
Table 7.1: Modules completed, and credits awarded.	317

List of Schemes

Scheme 1.1: Possible degradation routes of ethyl centralite within propellant ammunition ⁵⁸	13
Scheme 1.2: Simplified mechanism of ninhydrin reaction with amino acids which can be present within latent finger-marks, resulting in a dark purple compound called Ruhemann's Purple ⁸⁷	24
Scheme 1.3: Simplified mechanism of 1,8-Diazafluoren-9-one (DFO) reaction with amino acids which can be present within latent finger-marks, resulting in a compound which can fluoresce under UV light ⁸⁹	24
Scheme 1.4: Oxidative and reductive processes of poly N-ethylaniline (adapted from Direksilp and Sirivat. ¹¹³)	32
Scheme 3.1: Typical example for a single step of drop cast modification of macroelectrode using a solution of 1 mg.mL ⁻¹ magnetite based MNP suspended in ethanol.	79
Scheme 3.2: Mechanism of diphenylbenzidine formation from diphenylamine showing (A) One electron oxidation of DPA to a radical cation (electrochemical step) followed by dimerisation (B (I)) (chemical step), and leads to the electroactive diphenylbenzidine species (electrochemical step) in non-aqueous electrolyte (B (II)).....	95
Scheme 3.3: I) Acid catalysed hydrolysis of EC with breakdown of ethyl(phenyl)carbamic acid, and II) further reaction of N-ethylaniline formed from hydrolysis and breakdown of carbamic acid.	112
Scheme 3.4: Various structures of poly(N-methylaniline) undergoing oxidation and reduction ⁷⁶	114
Scheme 4.1: Schematic showing fabrication process for screen printed electrode utilised within this work.	137
Scheme 5.1: Scheme showing a basic overview of the steps involved in the dezincification process.....	176
Scheme 5.2: Initial oxidation of EDOT and possible polymeric forms of PEDOT obtained via electrochemical means ³²	178
Scheme 5.3: Generic dimerisation of phenazine and phenothiazines ³⁴	179
Scheme 5.4: Mechanism of doping and de-doping of neutral red monomer.	180
Scheme 5.5: A) Application of a latent finger-mark on a brass surface and B) basic view of electrochemically deposited material onto the surface of brass using the latent finger-mark as a stencil.	188

Scheme 5.6: A) Initial reduction of neutral red with B) possible dimer and C) oligomer structures ⁴⁰	212
Scheme 5.7: Initial oxidation and dimerisation of thionine ⁷⁵	231
Scheme 6.1: Visualisation of the “split print” method for comparison of visualisation solutions.	264
Scheme 6.2: Application of finger-marks to ammunition casings.	265

List of Abbreviations

Abbreviation	Meaning
<i>AA</i>	Acetic acid
<i>AAS</i>	Atomic absorption spectroscopy
<i>ACN</i>	Acetonitrile
<i>Ak</i>	Akardite
<i>CA</i>	Chronoamperometry
<i>CE</i>	Counter electrode
<i>CMV</i>	Capillary microextraction of volatiles
<i>CV</i>	Cyclic voltammetry
<i>DESI-MS</i>	Desorption electrospray ionisation mass spectrometry
<i>DPA</i>	Diphenylamine
<i>DPV</i>	Differential pulse voltammetry
<i>DSC</i>	Differential scanning calorimetry
<i>E</i>	Potential
<i>E_{app}</i>	Applied potential
<i>E_p^{a/c}</i>	Peak potential (anodic/cathodic)
<i>EC</i>	Ethylcentralite (1,3-diethyl-1,3-diphenylurea)
<i>EDOT</i>	3,4-Ethylenedioxythiophene
<i>EDX</i>	Energy dispersive x-ray spectroscopy
<i>F</i>	Faradays constant
<i>FAR</i>	Firearms residue
<i>FBI</i>	Federal Bureau of Investigation
<i>FPLC</i>	Fast protein liquid chromatography
<i>GC</i>	Gas chromatography
<i>GCE</i>	Glassy carbon electrode
<i>HOMO</i>	Highest occupied molecular orbital
<i>I</i>	Current
<i>I_p^{a/c}</i>	Peak Current (anodic/cathodic)
<i>ICPS</i>	Inductively coupled plasma spectroscopy
<i>IFAR</i>	Inorganic firearms residue
<i>IMS</i>	Ion mobility spectrometer
<i>IR</i>	Infrared
<i>ITO</i>	Indium tin oxide
<i>j</i>	Current density
<i>LC</i>	Liquid chromatography
<i>LIBS</i>	laser induced breakdown spectroscopy
<i>LOD</i>	Limit of detection
<i>LOQ</i>	Limit of quantification
<i>LSV</i>	Linear sweep voltammetry
<i>LUMO</i>	Lowest unoccupied molecular orbital
<i>MC</i>	Methylcentralite
<i>MeOH</i>	Methanol

<i>MNP</i>	Magnetic nano particle
<i>MSI-TOF-SIMS</i>	Mass spectrometry imaging with time-of-flight secondary ion mass spectrometry
<i>NC</i>	Nitrocellulose
<i>NR</i>	Neutral red
<i>OFAR</i>	Organic firearms residue
<i>OSAC</i>	Organisation of Scientific Area Committee for Forensic Science
<i>Q</i>	Charge
<i>RE</i>	Reference electrode
<i>RSD</i>	Relative standard deviation
<i>SA</i>	Sodium acetate
<i>SEM</i>	Scanning electron microscopy
<i>SPE</i>	Screen printed electrode
<i>SPEC</i>	Spectro-electrochemical cell
<i>TEA</i>	Thermal energy analyser
<i>TGA</i>	Thermogravimetric analysis
<i>Th</i>	Thionine acetate
<i>UHPLC-MS</i>	Ultra high-pressure liquid chromatography mass spectrometry
<i>UV-vis</i>	Ultra-violet - Visible
<i>v</i>	Scan rate
<i>WE</i>	Working electrode
<i>XPS</i>	X-Ray photoelectron spectroscopy

Chapter 1: Introduction

Forensic science is the implementation of methods and techniques, from which data can be used by the courts to determine a suspect's involvement in a criminal case. Much like the pharmaceutical industry, it is simply the use of analytical techniques focused on a single sector, however, instead of analysing for “*quality of samples*”, forensic science analyses the “*strength of evidence*” for its ability to tell a narrative of events. The event of interest to this body of work is the discharge of a firearm.

Firearm related crime destroys the lives of the people involved and 2020 saw the highest increase of firearm violence in the USA from the previous year since the early 1990's¹. Unless the perpetrator of the violence is observed or filmed in the act of using the firearm other means are necessary to identify who was holding the weapon at time of discharge.

The act of discharging a firearm creates a wide variety of evidence types that forensic professionals are of interest in order to build a case. Toolmark analysis, ballistic trajectory determination, wound analysis and even blood-spatter analysis are all useful methods in determining things such as what firearm was used, where it was fired from and how close it was to the target². However, these specialities still do not place an individual at the firearm at the time of discharge. The desire to associate an *individual* with loading and firing the firearm requires both evidence types selected in this work i.e. firearms residue (FAR) and finger-mark evidence.

1.1 Firearms Residue

Any substance which has been deposited onto a surface from the discharge of a firearm is classified as firearm residue³. These residues can escape through openings in the gun, such as the muzzle, ejection port and hammer, being deposited on the shooter and nearby surfaces (**Figure 1.1**).



Figure 1.1: Image of a firearm being discharged with the resulting plume of gas containing FAR⁴.

FAR can be recovered from various sources, including the hands, face, and hair of a suspect, as well as from their clothing and surfaces like the interior of a vehicle used to transport the suspects, weapons, and cartridges after firing⁵. The persistence of residues on surfaces depends on activity; residues can remain indefinitely on undisturbed surfaces and enclosed spaces, but they can be lost quickly from hands^{6,7}. Persistence studies performed by Vander Pyl et al. found that inorganic material experienced losses of 9% while organic material resulted in losses of up to 25% six hours after the initial application (firing) when in controlled conditions. Acts of washing or rubbing hands off each other or different materials generated losses of 99% and 55% respectively⁸. In general, it is stated that the majority of FAR is lost between the time points of four and six hours⁹⁻¹³. Forensic scientists examine FAR to determine if the samples from the recovered evidence match those of the suspect(s). To maintain the integrity of the evidence, strict contamination control procedures and quality control checks are implemented in the laboratory to ensure no evidence is lost or deemed to be questionable after each stage of the analysis. FAR requires the firearm to be discharged, and during this period the propellant is ignited, and so to understand FAR we must first look at the components of firearm propellants.

1.1.1 Ammunition Propellant Formulation

Chemical explosives typically contain oxygen, nitrogen, and fuels (hydrocarbons), with oxygen often attached to nitrogen in groups such as NO, NO₂, and NO₃. During a reaction, nitrogen and oxygen molecules separate and then unite with fuel components, releasing large amounts of energy and hot gases. The heat released, or heat of reaction, results from the difference between the energy required to break the explosive molecule into its elements and the energy released upon recombination into stable compounds like CO₂, H₂O, and N₂. Propellants are combustible materials that contain all the oxygen needed for their combustion and burn rather than explode. This combustion is typically violent, accompanied by flames or sparks and a hissing or crackling sound, but lacks the sharp, loud bang characteristic of detonating explosives. Propellants are initiated by flame or spark and transition from a solid to a gaseous state over milliseconds¹⁴. One of the earliest forms of propellant used for firearms was black powder, which was a simple mixture generally consisting of sulphur, charcoal, and potassium nitrate¹⁵. While some version of black powder may be used in improvised explosives, most of the black powder use is now limited to the pyrotechnic industry, having been more refined for aesthetics of the ignition, instead of its ability to propel material. Modern propellant powders fall under the category of smokeless powders and were developed to be a much more energetic material with the possibility of expanding up to 1000 times its original volume, creating pressures > 0.29 GPa¹⁵, which is approximately 6% of the pressure needed to form lab grown diamonds (5 GPa)¹⁶. With this immense pressure and the possibility to propel some form of ammunition, the first component of propellants discussed here is the energetic material or base formulation.

1.1.1.1 Propellant Bases within Propellant Formulations

The term “base” in propellant formulations is not used in the chemical sense (referring to alkaline material). Instead, it refers to the energetic material contained in the formulation, falling into three categories: single, double, and triple base propellants. Single bases commonly contain only nitrocellulose, double bases utilise a nitro-glycerine gelatinised nitrocellulose derivative while triple bases use this gelatinised nitrocellulose with the addition of nitroguanidine to increase the propulsion power even further¹⁷. As evident from the mixes, each base formulation has different applications, with triple being used

exclusively for military purposes of high calibre firearms and artillery munitions^{18,19}. The general public are able to acquire double and single base formulations, with rifle and handgun ammunition commonly containing double base and shotgun shells containing single base propellant. While the presence of the energetic material does change the availability of the type of propellant to the public, one thing remains constant in all formulations of the propellant mixes, the stabilisers within the formulation.

1.1.1.2 Propellant Stabilisers within Propellant Formulations

Shelf life of propellant powders is a key factor for the ammunitions industry, ensuring that ammunition manufactured will still successfully fire months or years later. Propellants containing nitrocellulose will continuously decompose, releasing nitrogen oxides, in turn increasing the rate of decomposition by auto-catalysis²⁰. The stabilisers prevent auto-catalysis, reacting easily with the nitrogen oxides forming more stable compounds²¹ with some of the most common ones being diphenylamine (DPA), ethyl-centralite (EC), methyl-centralite (MC), akardite I (AK I) and akardite II (AK II) (**Figure 1.2**)

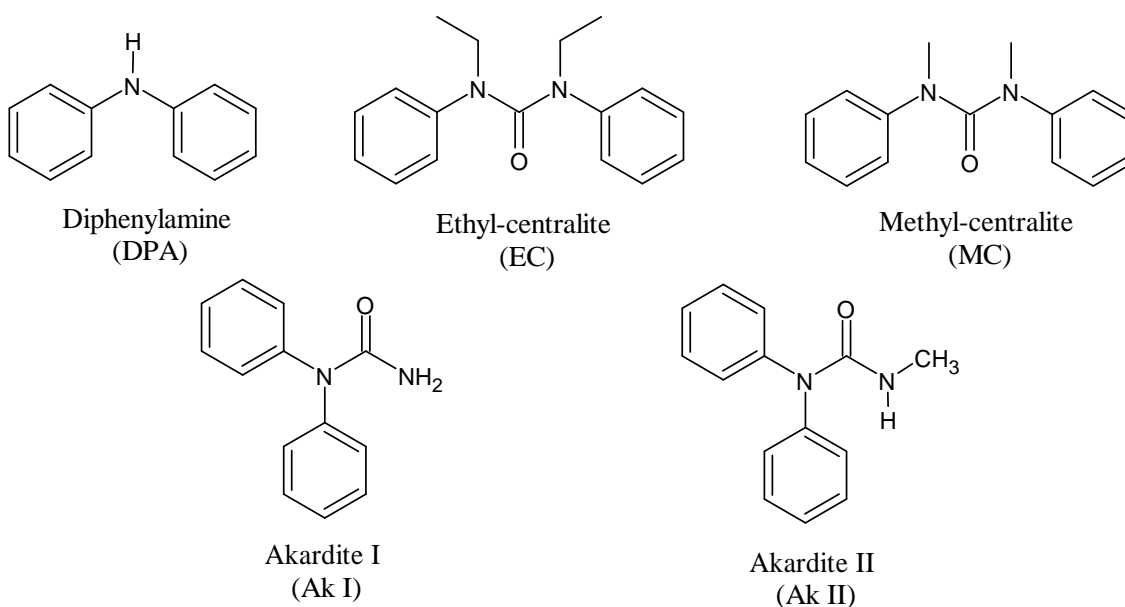


Figure 1.2: Chemical structures of common stabilisers found within propellant formulations

1.1.1.3 Plasticisers and Gelatinisers within Propellant Formulations

Plasticisers and gelatinisers are typically added to the formulation to facilitate processing and improve the mechanical properties. Within high energy ammunition (military grade), energetic versions of the material (nitrated compounds) can be utilised to increase the energy output and efficiency of the propellant²². Common plasticisers found in ammunition formulations include dimethyl-, diethyl-, dibutylphthalate and triacetin (Figure 1.3).

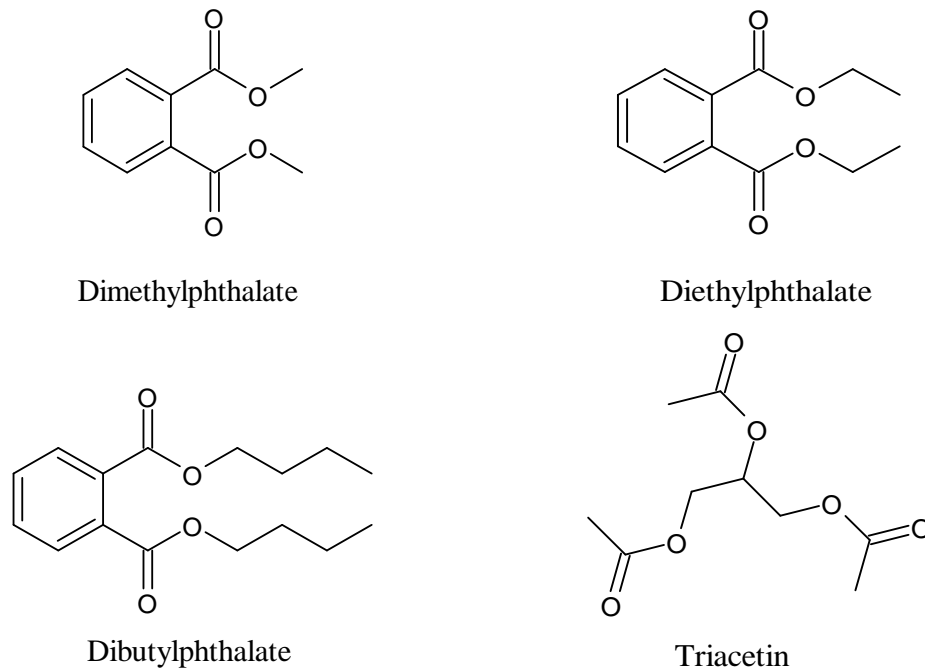
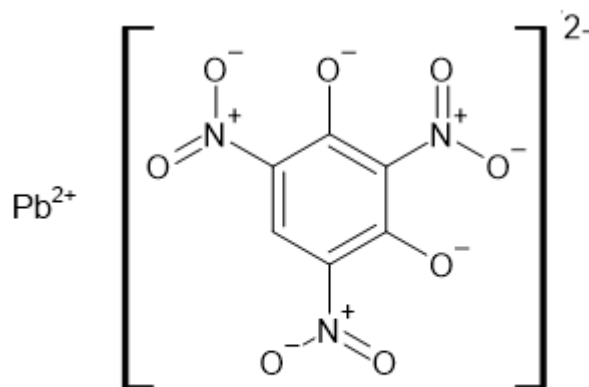


Figure 1.3: Chemical structures of common plasticisers found within propellant formulations

1.1.1.4 Primer Mixture within Ammunition

The primer is located directly under the rim of the ammunition casing and under the propellant powder. The primer contains a mixture of highly sensitive explosives with lead styphnate (Figure 1.4) being the primary explosive and barium nitrate the primary oxidiser²³. Once the primer is struck by the hammer of the firearm, a small explosion occurs which ignites the propellant increasing the pressure in the ammunition casing and ejecting the bullet from the casing and firearm.



Lead styphnate

Figure 1.4: Structure of common primer compound lead styphnate.

A generic list of components found within ammunition can be seen in **Figure 1.5**. Given this complex mixture of materials, it is interesting to note that the primer mixture is the main source of material which is needed for the current methods of identification of FAR, specifically the lead, barium and antimony which generates the inorganic fraction of FAR (IFAR).

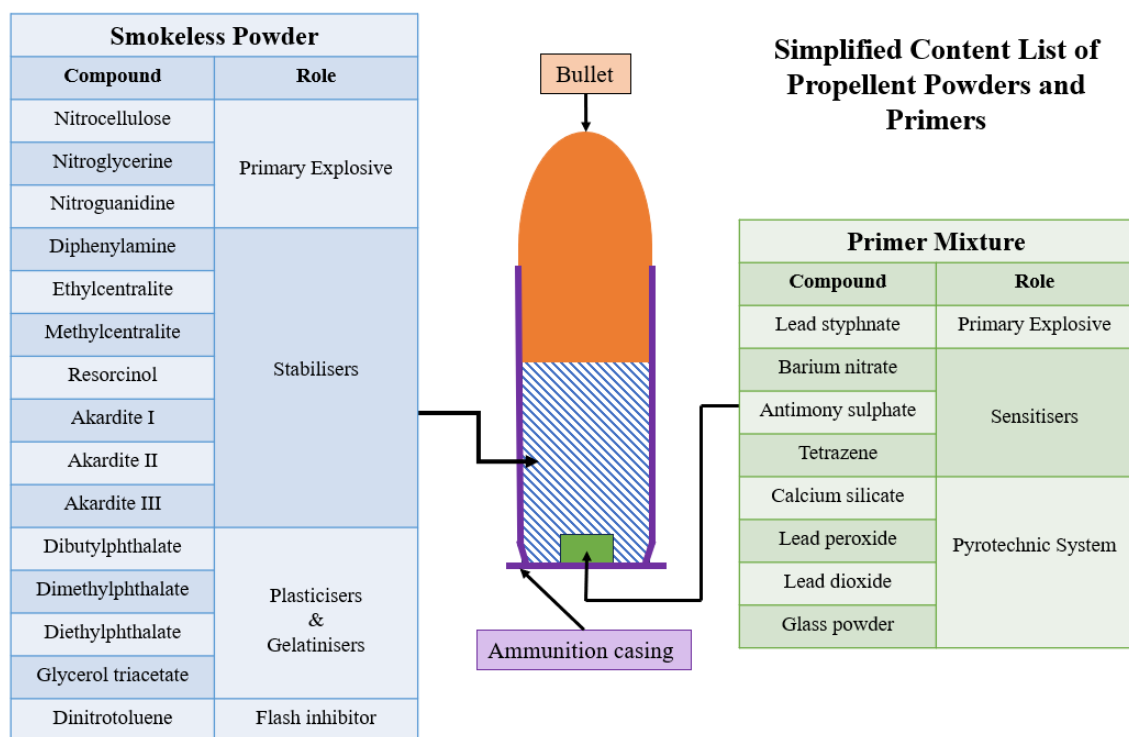


Figure 1.5: Cross section of bullet-based ammunition showing location and role of various components in smokeless powder and primer mixture.

1.1.2 *Inorganic Firearms Residue*

Within current methods of FAR analysis, the residue of interest is comprised of inorganic materials. IFAR particles are formed as a result of the materials that are present in the bullet, casing and primer cap undergoing the high temperatures and pressure associated with discharging a firearm²⁴. These particles are classified as one, two and three component particles. The components of these particles are lead, barium and antimony. In all classifications lead must be present with small particles of lead being indicative, while the multi-component particles are classified as FAR.

Scanning electron microscopy (SEM) in conjunction with energy dispersive x-ray (EDX) has been successfully used for observation of the morphological features of the particles along with elemental analysis respectively^{25–28} commonly being used by forensic professionals for FAR analysis (**Figure 1.6**). However, this is limited by the high cost and time-consuming nature of running the instrument for this technique.

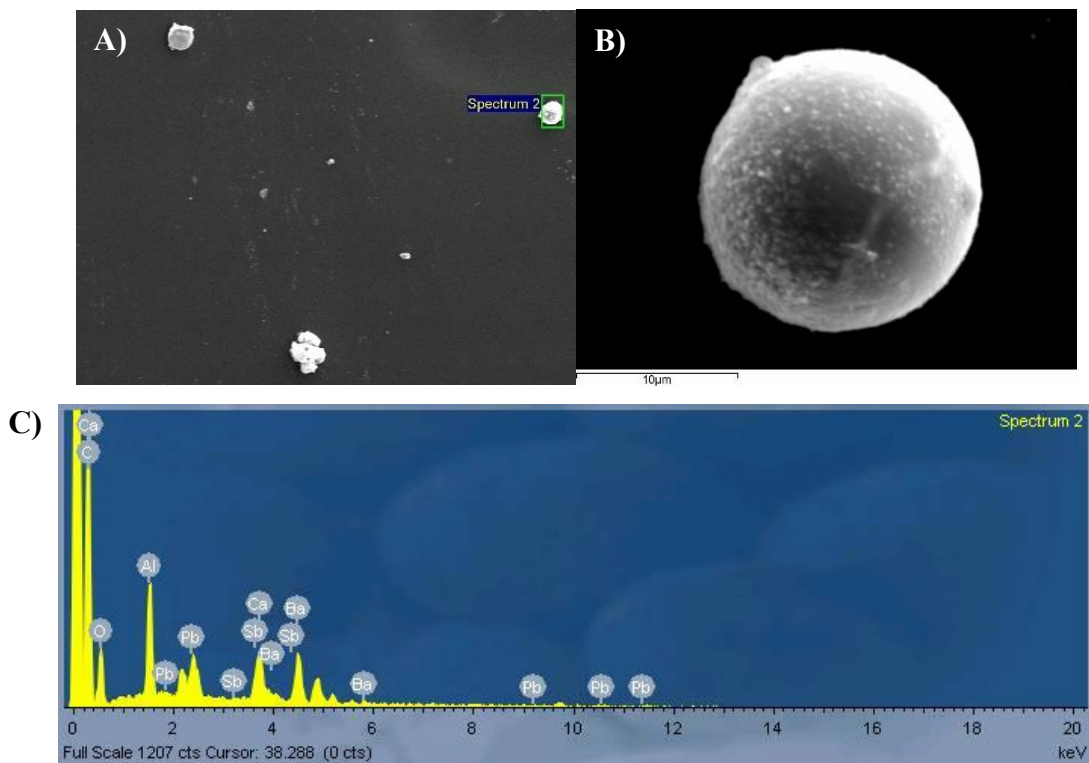


Figure 1.6: Example of SEM and EDX data which are traditionally used for IFAR evidence analysis, showing SEM data for A) IFAR particles at x450 magnification and B) a single IFAR particle at x4000 magnification and C) EDX data for the IFAR particle observed in B).

Other methods which have seen success in IFAR analysis are atomic absorption spectroscopy (AAS)^{29,30} and inductively coupled plasma spectroscopy (ICPS)^{6,31-34}. Both techniques boast excellent detection at trace levels (down to ng and pg levels) and successful analysis on 80-90% of samples processed. However, a major drawback which limited the use of these techniques for routine analysis was the significant amount of sample required and the destructive nature of the analysis. Destructive techniques are best avoided for forensic sample analysis, as evidence retention for a second opinion or re-analysis, contracted by either defence or prosecution teams is commonplace for evidence which may be used in a court case.

The components of these particles have been linked in the past to similar particles produced from braking systems on automobiles and those produced from cigarette lighters, indicating false positives in SEM/EDX analysis, calling into question the specificity of this type of sample for FAR. The case has been made that if the potential shooter was a mechanic for example, that any particle that meets the above criteria could be dismissed as the validity of its source is now in question. A European international study looked at the presence of IFAR like particles that may be present on the skin of the general public³⁵. This study removed the once thought bias that people who work in the automotive industry may be able to explain away the presence of IFAR like particles on their skin due to their work environment. The study found that IFAR like particles are nearly non-existent on the skin of the general public. Even law enforcement personnel which use firearms saw little to no presence of IFAR³⁵, cementing the specificity of the presence of these particles to the discharge of a firearm. However, while this study did indeed clarify that there is no cause for concern when using IFAR for the purposes of linking an individual to the firing of a weapon, the concern for the use of IFAR for forensic science purposes has been highlighted by the environmental sector.

Firearms in the hands of the general public, are never intended to be used for the purposes of harming other human beings, with the exception of military and law enforcement use of such items. Firearms are intended for one of two things, sports and hunting. While the sporting aspect can take place in ranges within buildings, hunting needs to take place outside and environmental groups and policy makers have focused on the need to remove heavy metal contamination in the soil in nature rich areas where hunting is commonly performed. As of the 15th of February 2023, the use of lead-based ammunition has been banned for use within 100 meters of wetlands across Europe, while Denmark and the

Netherlands have bans on the use of any lead-based ammunition³⁶. With this in mind, ammunition manufacturers will be incentivised to produce ammunition which does not contain lead if they still wish to have a European market share. However, if we recall from the above, all categories of IFAR contain lead. This means that that by the classifications currently in place, if lead is removed from the ammunition, IFAR particles won't exist for forensic professionals to analyse. The case to change the definition of IFAR to include any particle which contains the other elements of interest (Barium and Antimony) could be made, however, it won't be long before these metals are next for removal from ammunition manufacturing. So instead of constantly changing the definition of IFAR, looking at another type of material that is present in FAR would allow for a longevity in analysis methods and this is where organic firearms residue (OFAR) comes in.

1.1.3 Organic Firearms Residue

Organic Firearms residue (OFAR) is produced in the same manner as its inorganic counterpart, however, the source of the material which produces OFAR is the ammunition powder or propellant. This includes all the compounds mentioned within the previous ammunition propellant formulation described in **Section 1.1.1**.

Even when freshly manufactured, the propellant and primer mixtures are a complex matrix of materials to analyse. The number of potential compounds within the sample matrix is increased even further over time, with the production of nitrated derivatives by stabilisation mechanisms³⁷⁻³⁹ and the high heat and pressures of the discharge of the firearm. Classification of characteristic compounds of OFAR is necessary if the sample type is to be used by forensic professionals. One of the first listings of the group of compounds called OFAR was provided by Mach et al which classified ethylcentralite (EC), diphenylamine (DPA) and 2,4-dinitrotoluene as the three most characteristic components⁴⁰. However, in a systematic review by Goudsmits et al., 136 different compounds which could be associated with OFAR were found⁴¹, and of these a shortlist of 20 compounds were proposed, falling under three distinct categories (**Table 1.1**).

Table 1.1: Classifications of characteristic components of OFAR as identified by Goudsmits et al.⁴¹.

Category	Description	Compound	Common Function
1	Compounds that are very strongly associated with FAR with very few applications unrelated to GSR	Ethylcentralite	Stabiliser
		Methylcentralite	Stabiliser
		Nitroglycerine	Explosive
		Nitroguanidine	Explosive
2	Compounds that are strongly associated with FAR with a few other applications unrelated to GSR	Diphenylamine	Stabiliser
		2-Nitrodiphenylamine	Stabiliser
		4-Nitrodiphenylamine	Stabiliser
		2,4-dinitrotolouene	Flash suppressor
		Akardite II	Stabiliser
3	Compounds that are associated with FAR, but which are detected less frequently, with applications unrelated to GSR	Nitrocellulose	Explosive
		Other nitrotoluenes	Flash suppressor
		Other diphenylamine derivatives	Stabiliser
		Triacetin	Plasticiser

In this work the stabilisers of DPA and EC are the focus of initial method development, due to their category assignment within the list of “characteristic compounds”, their availability within the propellant formulation (~5% % w/w)⁴²⁻⁴⁵ and their common presence within OFAR analytical literature⁴⁶⁻⁵².

1.1.3.1 Diphenylamine as a Component of Organic Firearms Residue

DPA is predominantly used as a stabilising agent for ammunition and general nitrocellulose containing explosives⁵³. This species derivatises with the degradation products within the propellant formulation commonly forming mono-, di- and trinitro-DPA^{54,55} (**Figure 1.7**). DPA is also commonly used to aid in the storage of harvested apples, preventing a storage disorder called “scald”⁵⁶. DPA contamination has become

more prevalent in recent years as an emerging concern with regards to environmental pollution. The European Union first implemented a limit on the use of DPA in 2008 and Commission Regulation limits the presence of DPA on nearly all food items to 0.05 mg/kg, implemented from 1st of May 2019⁵⁷.

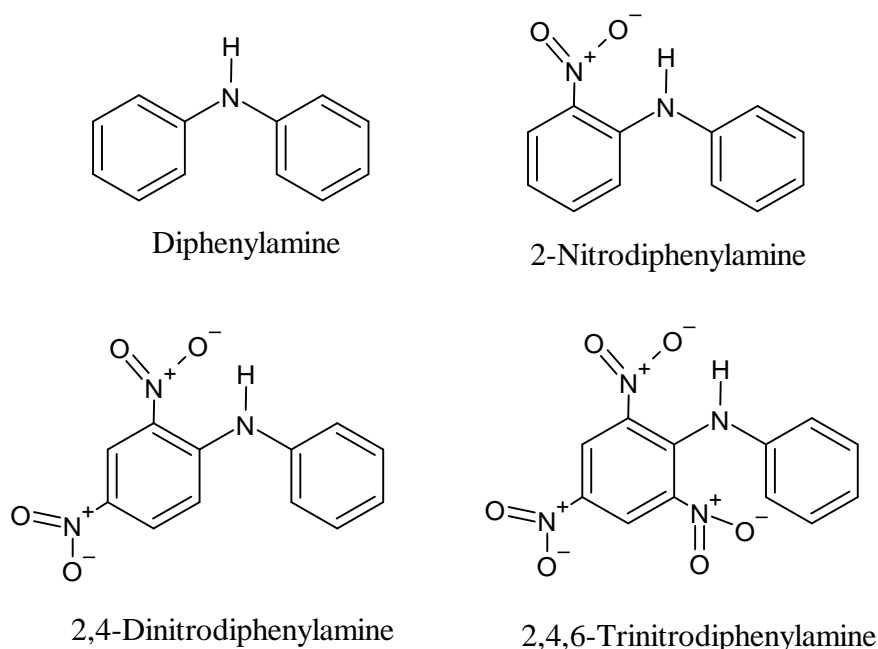
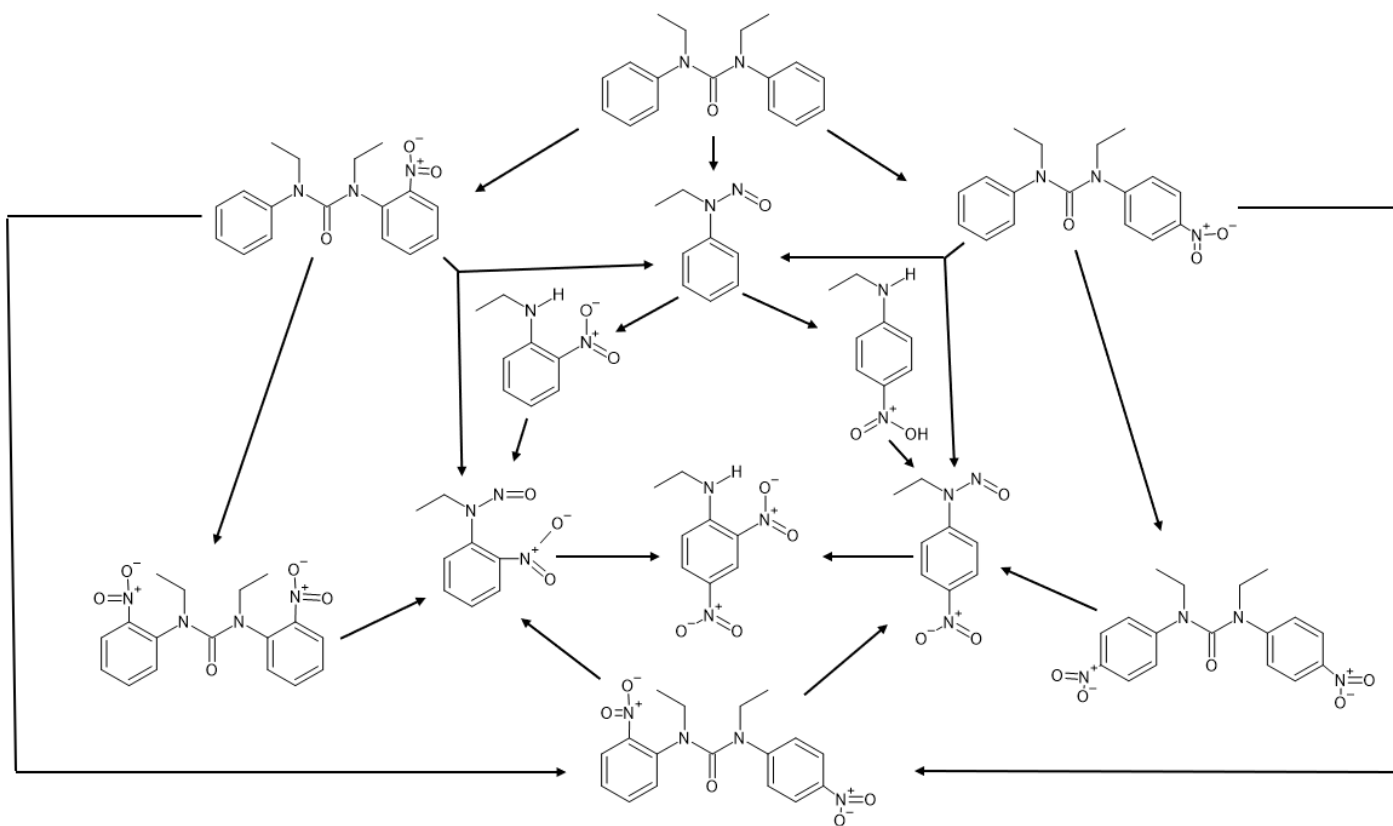


Figure 1.7: Common nitrated derivatives of DPA formed during propellant stabilisation.

1.1.3.2 Ethylcentralite as a Component of Organic Firearms Residue

Ethylcentralite (EC) appears to have no industrial use outside of propellant stabilisation. Like DPA, EC commonly reacts with nitrogen oxides forming a variety of EC and ethylaniline nitrated derivatives (**Scheme 1.1**), producing a complex mix of potential compounds within the propellant matrix.



Scheme 1.1: Possible nitration degradation routes of ethyl centralite within propellant ammunition⁵⁸.

1.1.4 Current Trends in Analysis of Organic Firearms Residue

As mentioned previously, OFAR is of growing interest for those involved with forensic practices. With the increased regulations around lead containing ammunition, the concern for the current standards of FAR analysis is that it may not be stringent enough to deal with the new sample types. As such, numerous analytical methods have been implemented in literature with the aim to improve the FAR analysis toolbox by incorporating OFAR, with the common targets of OFAR analysis normally being one of the compounds which Goudsmits et al. described as characteristic⁴¹ (**Table 1.1**).

Gas Chromatography (GC) was an obvious choice for these materials considering the process by which OFAR is generated. Wu et al. reported a GC method coupled with mass spectrometry (MS) with a detection time of less than 10 minutes and a limit of detection (LOD) of 0.05 to 1 ng for DPA and its various nitrated derivatives⁵⁹. In addition, Burleson et al. employed solid phase micro-extraction and a nitrogen phosphorus detector to develop a GC method detecting DPA and EC along with other characteristic compounds down to 10 ng in 2 mL⁶⁰. GC suffers from incompatibility with some of the characteristic compounds of OFAR, such as nitrocellulose (NC) not being sufficiently volatile and its presence accelerating the degradation of GC columns.

Bratin and Kissinger compared OFAR analysis by liquid chromatography (LC) and cyclic voltammetry (CV) of the more energetic material found within the residues (NC, DNT etc.) stating that the stabilisers would be of more importance within OFAR samples, as the methods they employed lacked sufficient LOD for the analytes of interest⁶¹. Chromatographic methods represent a strong group of techniques for the analysis for OFAR, with the possibility of optimisation of conditions for successful separation and detection of individual components within the sample matrix. Simple or preliminary studies of high-performance liquid chromatography (HPLC) methods are readily found within literature^{51,62,63}.

While analysis of FAR appears to be discussed in the inorganic and organic categories, development of methods which can observe both fractions of the evidence would prove invaluable to forensic professionals.

One of the first methods proposed for simultaneous detection of IFAR and OFAR was a capillary electrophoresis method developed by Morales and Vázquez⁶⁴. In this method, 10 inorganic and 11 organic analytes commonly found within FAR was targeted with

successful detection of the residues via collection from a shooter's hand with cotton swabs. However, sensitivity and selectivity appeared to be a limitation of the method with 17.95 % RSD observed for DPA⁶⁴. Other methods of simultaneous analysis employed mass spectrometry imaging with time-of-flight secondary ion mass spectrometry (MSI-TOF-SIMS). This method proved quite promising with chemical and morphological information of the sample with little damage in a single analysis⁴⁷. Electrochemistry has also been employed to analyse both evidence types, with square wave anodic stripping voltammetry successfully detecting inorganic and organic compounds on a carbon screen printed electrode^{48,65}.

While simultaneous analysis of FAR components may prove difficult with specific analytical methods, sequential analysis opens many avenues. An early method proposed by Dhal and Lott involved the use of fast protein liquid chromatography (FPLC) with electrochemical detection for OFAR (specifically DPA) and subsequent AAS for trace metals which may exist within the sample⁶⁶. Tape lifts were analysed with SEM/EDX for IFAR analysis and subsequent use of GC with a thermal energy analyser (TEA) and ion-mobility spectrometer (IMS) employed for detection⁶⁷. Other methods observed OFAR initially on carbon stubs, using desorption electrospray ionisation mass spectrometry (DESI-MS) and subsequent SEM/EDX for IFAR, however, this method produced LODs higher than the expected amounts in real samples⁵². Other groups used cotton swabs as the collection method, employing a capillary microextraction of volatiles (CMV) prior to the use of GC-MS for the initial OFAR analysis with subsequent laser induced breakdown spectroscopy (LIBS) for the IFAR⁵⁰. LIBS was used for the analysis of IFAR and square wave anodic stripping voltammetry for the detection of OFAR components, indicating that successful detection of both IFAR and OFAR could be performed by this sequential method⁶⁸.

Simultaneous or sequential methods of analysis do have their obvious drawbacks, however, another way of developing an analytical method for the analysis of both IFAR and OFAR from the same sample involved simply splitting the sample in half and performing different analysis types on each half. Taudte et al. employed a form of separation passing the sample in solution over a SEM stub and performing SEM/EDX analysis and using the remaining solution for ultra high-pressure liquid chromatography linked with mass spectrometry (UHPLC-MS) for detection of the organic components⁶⁹.

The scope of analysis of OFAR is wide ranging, however, the development of rapid onsite electroanalytical methods appears to be a welcome addition to the current state of analytical methods either as screening methods for samples prior to traditional analysis⁷⁰ or as the full suite analysis⁶⁵.

The development of an electroanalytical method for OFAR presents a promising avenue for reducing the required lab space and minimising the need for additional materials such as gases and solvents associated with more traditional methods of analysis such as chromatographic methods. Introducing not only a cost benefit to the method, but also a greener alternative to classical methods, electrochemical methods in general incorporate at least five out of the ten principles for green analytical chemistry including: *in-situ* analysis methods, increasing miniaturisation, reducing reagents and waste, less energy consumption and increasing safety⁷¹.

However, electroanalytical methods offer benefits to forensic science practitioners beyond the detection and identification of FAR components alone. In the next section, we will explore how electroanalytical methods can be adapted to enhance the analysis of impression evidence, specifically, latent finger-marks on ammunition casings, commonly encountered at crime scenes. By using electroanalytical techniques, forensic investigators can potentially overcome some of the challenges associated with traditional methods, including the preservation of evidence integrity and the need for extensive sample preparation. This approach may present an option to streamline forensic investigations, improve the accuracy of evidence analysis, and enhance the efficiency of criminal proceedings.

1.2 Finger-mark Evidence

Nomenclature of finger-mark evidence is interesting in the sense that, along with many other facets of forensic science, popular media has instead used the term “*fingerprint*” when relating to finger-mark evidence. The arbitrary difference between the terms seems of little importance, as most individuals will still understand what is being discussed. Within forensic literature, the term fingerprint refers to the actual physical ridges contained on a finger⁷², while the term finger-mark is the piece of evidence left on a surface after contact with a fingerprint. In order to stay in line with forensic scientific practice, the term finger-mark is used throughout this work.

1.2.1 Types of Finger-Mark Evidence and Surfaces of Application

Finger-mark evidence is broken into three distinct categories: plastic, patent, and latent finger-marks. Plastic finger-marks are formed when a finger is placed onto a malleable material, allowing for a cast of the ridge detail to remain (**Figure 1.8**).



Figure 1.8: Photograph of a plastic finger-mark on a sample of malleable putty.

Patent finger-marks (**Figure 1.9**) are formed when there is some form of material on the surface of the finger, be it blood, oil or dirt, before application to a surface. This results in an ink stamp like transfer of the finger-mark to the surface. This means that when law enforcement personnel take an individual's finger-marks using inks they are creating patent prints for their records.



Figure 1.9: Photograph of a series of ink-based patent finger-marks on paper.

Latent finger-marks (**Figure 1.10**) are formed by the natural secretions of the skin coating the finger and remaining behind on the surface after contact. These secretions are produced by eccrine and sebaceous glands which are present on the skin. While both produce material which is referred to as sweat, the contents of the material from each type of gland differ. Eccrine sweat is generally about 98% water, containing additional inorganic (chlorides, ammonias, phosphates, etc.) and organic (amino acids, urea, sugars, etc.) materials, while material produced from sebaceous glands contains mostly organic materials (glycerides, fatty acids, sterol esters, etc.)⁷³. The composition of both these secretions can change due to a number of physiological factors such as age, diet or individual medication⁷⁴. However, the production of a latent finger-mark involves the coating of this material on the finger surface, and study into the composition of the material is not currently of great interest to forensic professionals. Unlike patent prints, these latent prints are not normally visible to the naked eye (unless on the surface of touch screen devices to the dismay of their users).

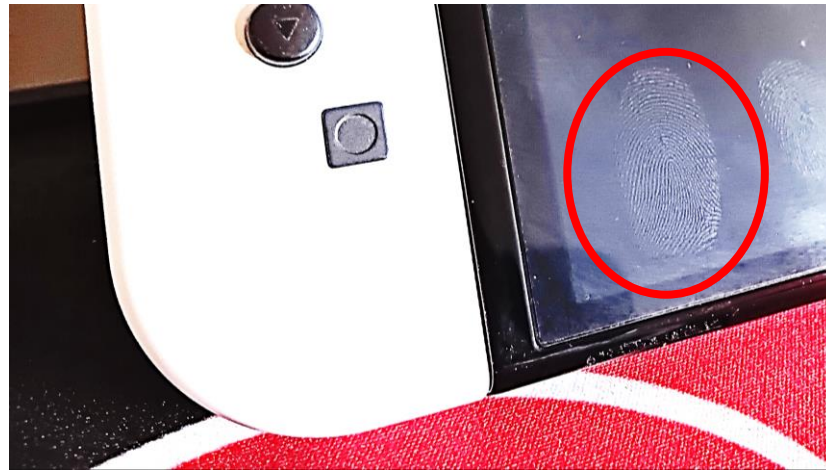


Figure 1.10: Photograph of latent finger-marks on glass of the touch screen of a video game console, with a latent finger-mark highlighted within the red circle.

Of these types of finger-mark evidence, plastic and patent finger-marks are easily collected by forensic professionals via photography, without the need for additional visualisation methods (apart from the correct lighting for the photograph) being used.

The most common type of finger-marks requiring additional steps to be seen are the latent finger-marks, which need various visualisation methods to be accurately imaged. However, before examining visualisation methods, the quality of produced finger-mark evidence will be discussed first.

1.2.2 Scoring of Finger-mark Evidence

The quality of a finger-mark recovered from a scene is scored on two different aspects grades and level features. The grade of the finger-mark is quantified by the amount of the original fingerprint represented by the mark. In **Table 1.2** the grading system used by the UK Home Office is shown⁷⁵. This is used to compare the quality of visualised or enhanced finger-marks on a surface, graded on a scale of 0 to 4, increasing in number as the quality or visible detail of the mark increases. In simple terms the system is broken down into three categories, not visible (Grade 0), visible but not enough detail to identify (Grade 1 and 2) and visible and enough detail to identify (Grade 3 and 4).

Table 1.2: Finger-mark Grading system (as Defined by the UK Home Office)⁷⁵.

Grade	Description
0	No ridge detail visible
1	Weak development: evidence of contact but no ridge detail
2	Limited development: about 1/3 of ridge details are present but probably cannot be used for identification purposes
3	Strong development: between 1/3 to 2/3 of ridge details, identifiable finger mark
4	Very strong development: full ridge details identifiable finger mark

Along with these grades there are three levels of features within a finger-mark (seen in **Figure 1.11**), level 1 details are the general ridge pattern and the overall shape of the finger-mark. While the Federal Bureau of Investigation (FBI) recognise eight different types of categories, these fingerprints fall into the general categories of loops, arches and whorls⁷². These level features are useful for eliminating or including potential suspects, however, it is not sufficient for an identification, as approximately 65% of the population contain loop features, while whorls and arches make up the remaining 30% and 5% respectively⁷⁶.

Level 2 features are the characteristics of individual ridge patterns such as location, ridge endings, ridge splits, width and shape. Individually, these details are not means for identification. However, when used collectively it increases the likelihood that an identification can take place. Each of these features are classified as “*points*” for matching to a reference finger-mark. The number of matching points to classify a match between the evidence and the reference image vary depending on the jurisdiction which the evidence is being analysed. Statistically, Roxburgh calculated the minimum number of matching points required to classify the evidence a match to the reference. In the worst-case scenario (bad evidence sample) 18 points were required to make a match to the reference if taking the population of the world, while best case scenario (very good evidence sample) 8 points would only be required for a match⁷⁷. Multiple models exist for finger-mark classification, ranging from the rarity of the actual details to the spatial relationship between points. While there does not appear to be any one industry standard

model for verification of a finger-mark, these level 2 details make up the majority of the points of comparison.

Level 3 features are the fine details within the ridge pattern such as pores, ridge edge contours or scars. These provide the highest level of detail and can carry more weight with their presence for claiming an identification. While level 3 features are rarely used in the previously mentioned models, interest specifically in the pores has been developed. Studies on relative location⁷⁸, size and shape⁷⁹ led to pore modelling⁸⁰, these minute details will see common use when visualisation techniques readily enhance these details.

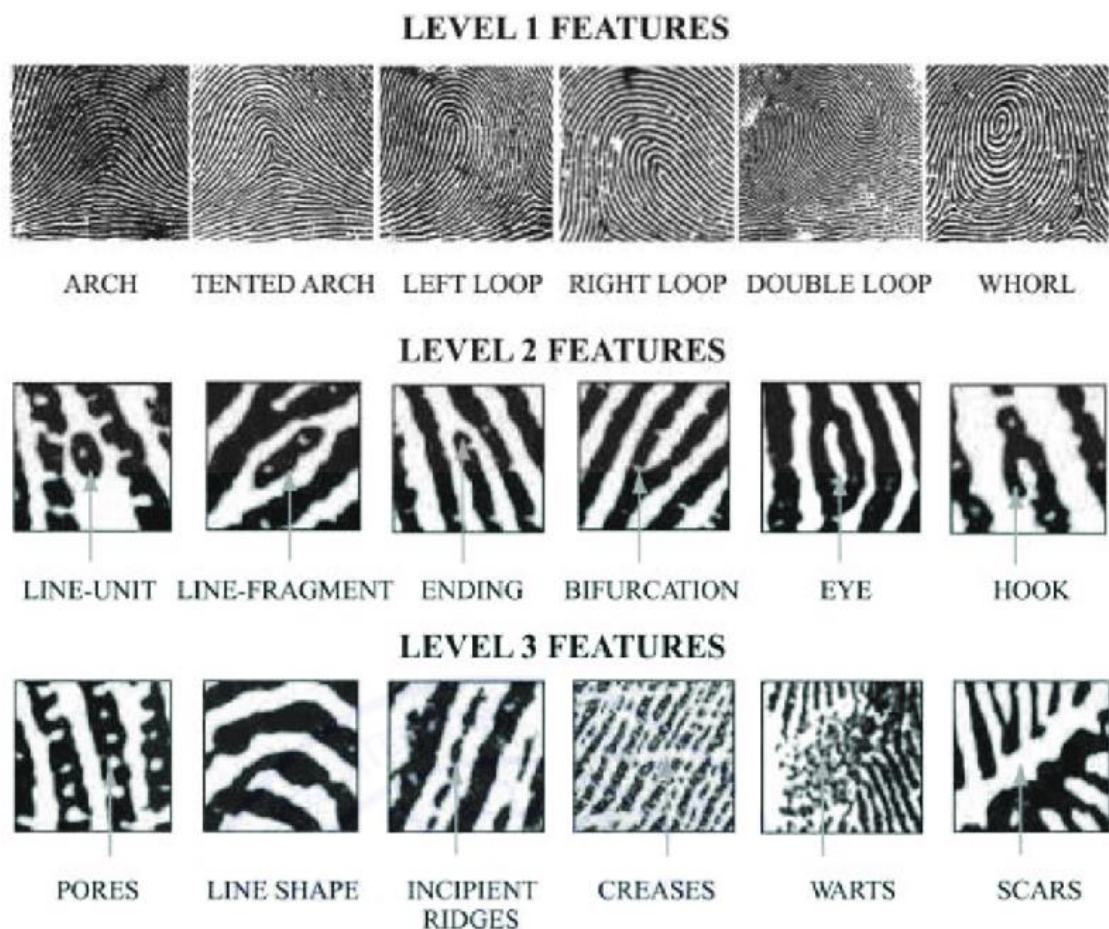


Figure 1.11: Example of features found within the three levels of features within a finger-mark⁸¹.

Given the above account of the criteria of high-quality visualisation of a finger-mark, the methods by which these marks are visualised are discussed below.

1.2.3 Visualisation Methods for Latent Finger-marks

There are a wide variety of visualisation techniques for finger-mark evidence at the disposal of forensic professionals, and in a lot of circumstances, the selection of the visualisation method relies on criteria such as:

- The type of surface the mark has been deposited on, i.e. porous or non-porous.
- The material on which the mark has been deposited, i.e. metallic, plastic, magnetic, glass, paper.
- The quality of the finger-mark, i.e. age, environmental degradation, smudging.

These common visualisation methods can be categorised as powder, light or chemical visualisation.

1.2.3.1 Powder Visualisation of Latent Finger-marks

Depending on the surface colour, different coloured powders can be used to aid in the contrast of the visualised finger-mark to the surface. Black powder is a fine carbon-based powder that is used to develop latent finger-marks on light or pale-coloured surfaces. While white powders, generally consisting of fine particulate of aluminium or zinc oxide, are used for dark or multi-coloured surfaces. In both cases, the powder is applied using a brush or a feather duster, adhering to the moisture and oils present in the finger-marks, making them visible⁸².

Another common type of powder which may be used are fluorescent powders. Fluorescent powders are a type of powder that emit a bright, fluorescent colour under ultraviolet (UV) light. It is useful for developing latent finger-marks on surfaces that do not respond well to other types of powders, such as fabrics⁸².

One final powder, which may act as the bristles of the brush during application is magnetic powder. This powder consists of magnetite iron particles (Fe_3O_4) and is applied using a wand with a small magnet located at the tip (magna-brush) (**Figure 1.12**). The particles within a magnetic field create bristles, allowing for a very soft and gentle dusting process for more delicate finger-marks⁸². This method is hindered if the material of interest is magnetic, as close proximity to the magna-brush can lead to accidental contact and possible damage of the mark.

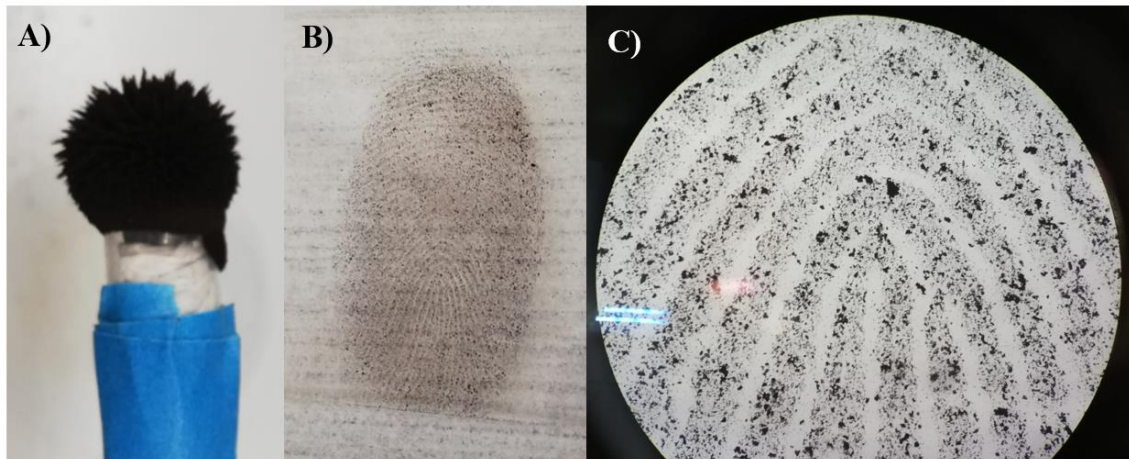


Figure 1.12: Photographs of A) In house fabricated magna brush, B) latent finger-mark on glass visualised with magnetic powder and C) magnetic powder visualised finger-mark as seen in (B) at x1000 magnification.

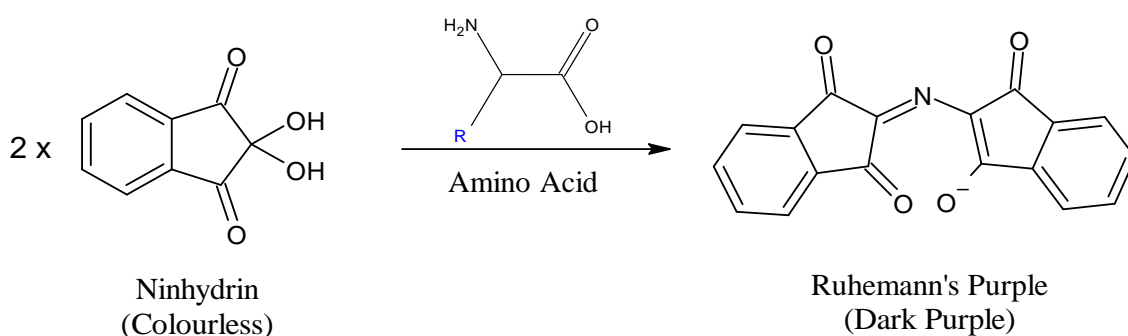
1.2.3.2 Light Sources for Latent Finger-mark Visualisation

Sometimes light sources can be utilised to allow for high quality photography of the finger-marks on a surface. White light is the most commonly used light source in finger-mark photography. It provides a broad spectrum of light that is useful for general observation and photography of finger-marks. White light may be used for locating finger-marks to be further visualised with the previously mentioned powders⁸³.

In conjunction with other forms of visualisation, UV light is particularly useful for visualising latent finger-marks that are not visible to the naked eye. UV light can be used in conjunction with powders, dyes or other light sources to enhance the visibility and detail of finger-marks. Infrared (IR) light can be used to visualise finger-marks on surfaces that are not visible under normal lighting conditions. IR light can penetrate some materials and reveal finger-marks that are not visible under white light or UV light⁸⁴. To gain more information about the topology of the finger-mark, polarised light can be used to reveal details about the orientation and thickness of the ridges. By using polarised light filters, the investigator can gather additional information that is not visible under normal lighting conditions⁸⁵.

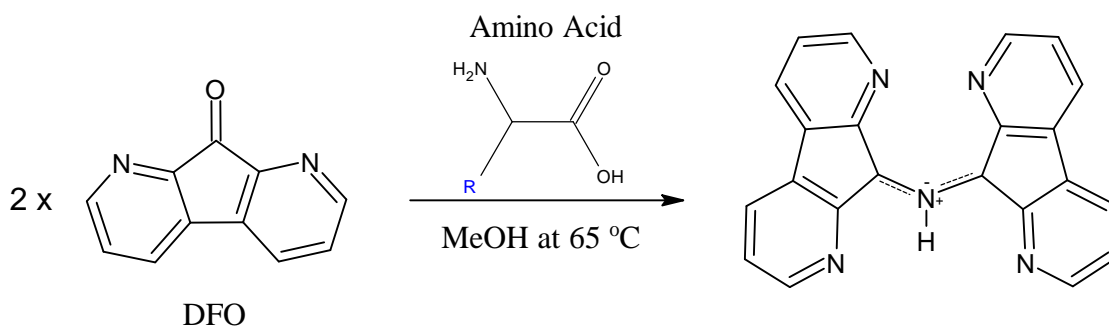
1.2.3.3 Chemical Methods for Latent Finger-mark Visualisation

When the more simplistic methods of visualisation (i.e. powders and light) do not produce sufficiently visible latent-finger-marks or they are not suitable for the surface type, chemical-based methods of visualisation can be employed. Ninhydrin reagent reacts with the amino acids present in latent finger-marks, producing a purple or blue colour (**Scheme 1.2**). This reaction can take several hours to develop, and the resulting prints are permanent allowing them to be photographed for further analysis⁸⁶.



Scheme 1.2: Simplified mechanism of ninhydrin reaction with amino acids which can be present within latent finger-marks, resulting in a dark purple compound called Ruhemann's Purple⁸⁷.

1,8-Diazafluoren-9-one (DFO) reacts with the amino acids present in finger-marks, producing a fluorescent colour that can be visualised using UV light (**Scheme 1.3**). DFO is particularly useful for developing finger-marks on dark or multi-coloured surfaces that do not respond well to other types of powders or chemicals.



Scheme 1.3: Simplified mechanism of 1,8-Diazafluoren-9-one (DFO) reaction with amino acids which can be present within latent finger-marks, resulting in a compound which can fluoresce under UV light⁸⁹.

Silver nitrate is a chemical reagent that reacts with the chloride ions present in sweat, producing a brown or black colour that can be visualised using UV light. This method is particularly useful for developing finger-marks on porous surfaces such as paper or cardboard⁸⁸. Possibly the most familiar method within popular media is cyanoacrylate fuming. Cyanoacrylate fuming involves exposing finger-mark evidence to cyanoacrylate vapours, which react with the moisture and oils present in the finger-marks, producing a white or light-coloured print. This method is particularly useful for developing finger-marks on nonporous surfaces such as glass or metal⁹⁰.

Throughout the visualisation methods, the surface to which the latent finger-mark was applied can be a deciding factor. The specific surface of interest for the work in this thesis is ammunition casings.

1.2.4 Ammunition Casings

Ammunition casings are the containers that hold all the other components together in a single unit (**Figure 1.13**). The material of choice for these casings are important for many factors including type of ammunition, area of use and reusability⁹¹. Plastics are utilised for casings such as shotgun shells, or synthetic polymer casings which have seen use in modern ammunition. Steel had been commonly used in World Wars I and II, due to its ease of fabrication, however, the steel casings would usually deform decreasing the reusability of the casings. Brass ammunition casings are still to this day the industry standard, as they are used to produce reliable and reusable ammunition casings. Brass is regularly used for this purpose, and a specific alloy composition called cartridge brass (70:30, Copper:Zinc)^{92,93} is used in the making of ammunition casings.



Figure 1.13: Example of brass ammunition, identifying casing and bullet.

1.2.5 Finger-marks on Ammunition Casings

While visualisation methods for latent finger-marks have been discussed previously, the application of these methods is dependent on the surface type the mark was applied to. SEM imaging has seen successful has been successfully used for the visualisation of latent finger-marks on a variety of metallic surfaces including brass⁹⁴. However, it is crucial to acknowledge that SEM may not be the optimal choice for analysing a large bulk of samples, primarily due to the challenges associated with accurately locating the area of interest, without the prior use of visualisation methods, such as metal deposition onto the mark⁹⁵, surface corrosion⁹⁶ or cyanoacrylate fuming⁹⁴.

Wightman and O'Connor utilised SEM to develop finger-marks on brass, aluminium, and steel surfaces, common materials in ammunition casings. Employing a low thermal mass furnace, they achieved favourable results, particularly with brass samples heated to 200 °C (**Figure 1.14**). The study also explored the influence of deposition time, yielding promising outcomes. However, limitations include a small sample size (three donors) and the inherently destructive nature of the method, potentially leading to the loss of donor-specific information⁹⁷.



Figure 1.14: Latent finger-mark visualised at 180 °C after 3 days of storage by Wightman & O'Connor⁹⁷.

Jasuja et al. investigated the development of eccrine and sebaceous sweat generated finger-marks on metallic surfaces using an immersion approach lasting 10–20 minutes. The metal substrates with latent finger-marks were immersed in solutions of varying pH, with some experiments involving a second metallic surface to expedite the reaction.

Favourable outcomes were observed on surfaces such as aluminium, zinc, copper, and brass. The authors noted that certain metals exhibited optimal development in slightly acidic solutions, while others required a more basic environment. Although the authors used their own grading scale, the method demonstrated effectiveness, successfully developing finger-marks from 10 different donors, including older marks of 10 days⁹⁸. This method was further applied to fired and unfired ammunition casings by Liu et al. While finger-mark development was successful for the majority of unfired casings, only a limited number (4 out of 60) yielded positive results on fired cases. The study indicated that the heat and friction associated with firing had a detrimental impact on finger-marks. Liu et al. further proposed that the visualisation of finger-marks improves with longer deposition times on cases, allowing for increased corrosion. In this specific investigation, the casings underwent a 24-hour immersion period (**Figure 1.15**). These findings shed light on the challenges posed by fired cases in finger-mark development and emphasise the importance of deposition duration in achieving optimal visualisation⁹⁹.

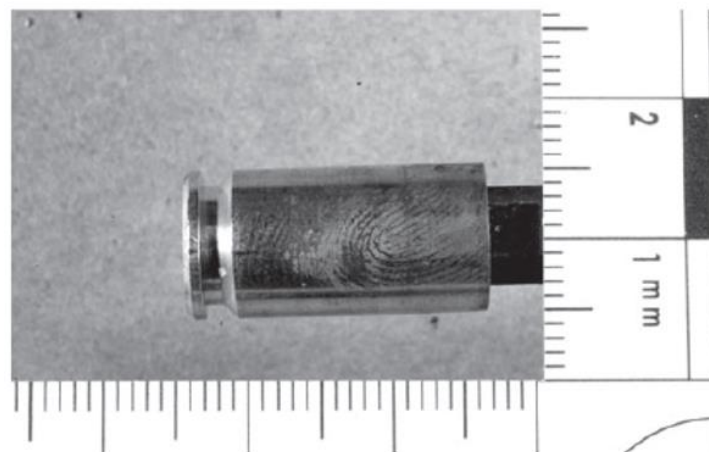


Figure 1.15 Latent finger-mark visualised on an unfired ammunition casing held in a pH 7 buffer for 24 hours by Lui et al⁹⁹.

These corrosion effects have also been exploited by electrochemical methods. Bond has been involved in a series of works which have employed electrochemical methods to aid in the visualisation of latent finger-marks. Initially, this involved depositing a conducting powder onto the latent finger-mark on a brass surface and applying a very large potential difference to the surface (1.4 kV). Observation of how the potential changed on the surface of the brass allowed for the identification of ridge detail¹⁰⁰, in a similar manner to how scanning electrochemical microscopy would function. In the next reported work, the

authors increased the applied voltage to 2.5 kV using ammunition casings as the substrate. Instead of measuring the ΔV , a more simplistic method of surface corrosion was employed allowing for patterns of finger-mark corrosion to be imaged on the surface of a fired brass ammunition casing^{101,102}. Sykes and Bond continued development by gathering a greater understanding of how these methods were affected by different alloys of brass, concluding that the composition of the brass can in fact inhibit the visualisation technique¹⁰³.

Other methodologies of latent finger-mark visualisation on metal substrates utilised the electrochemical deposition of material onto the surface. This allows the latent finger-mark to act as a mask or stencil on the surface, with the deposition of material in between the ridges of the finger-mark in turn visualising a “negative” of the mark. Conducting and redox polymers have been a prime choice for this deposition material. In a proof-of-concept study, Sapstead et al. investigated the insulating effect of finger-marks on metallic surfaces, particularly focusing on stainless steel films. They employed electro-oxidation of copolymers (pyrrole and EDOT) to enhance the visualisation of negative finger-marks, considering factors such as film colour, composition, and topography. Despite the preliminary nature of the study, the authors reported successfully visualised finger-marks achieving grades 3–4¹⁰⁴. Beresford and Hillman replicated successful outcomes by employing polyaniline films on stainless steel plates, demonstrating effectiveness on both aged and fresh finger-marks. The study, tested with only one donor, however, involved generating a variety of finger-marks under diverse sweat inducement times and deposition pressures. The practical utility of the method for forensic purposes was constrained, with only 40% of the produced finger-marks being deemed usable¹⁰⁵. Hillman continued with Brown using polymerised EDOT (PEDOT) alone, and various donors and deposition times were employed to evaluate the method's efficacy (**Figure 1.16**). Samples were also enhanced using established techniques for comparative analysis. The electrochromic deposition method achieved over 50% successful enhancements, with a 60% success rate noted for samples aged 7 days. These findings suggest that electrochromic deposition can complement the cyanoacrylate fuming method, particularly on substrates where this method proves unsuccessful¹⁰⁶.



Figure 1.16: Sebaceous latent finger-mark on stainless steel under potentiostatic conditions in 1 M EDOT with 0.01 M H_2SO_4 and 0.02 M sodium *N*-lauroylsarcosinate by Brown & Hillman¹⁰⁶.

More recently, Costas et al. employed PEDOT also, stating successful finger-mark visualisation on brass ammunition casings (grades 3 and 4) via low-potential chronocoulometric method, observing successful visualisation within 180 seconds¹⁰⁷. Broncová et al. took a different approach depositing polyneutral red at brass ammunition surfaces via cyclic voltammetry, resulting in successful visualisation on unfired casings, while partial or poor-quality visualisation was reported for marks on fired ammunition casings^{108,109} (**Figure 1.17**).

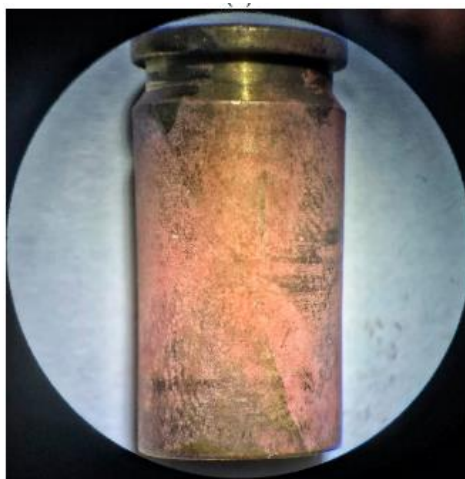


Figure 1.17: Partial visualisation of a latent finger-mark on a fired ammunition casing via CV over the potential range of -0.3 to 0.6 V at $50 \text{ mV}\cdot\text{s}^{-1}$ for 6 cycles¹⁰⁹.

As these conducting and redox polymers are the basis of the visualisation methods proposed in this work, they are described in more detail below, and in the introduction to **Chapter 5**.

1.2.6 *Conducting and Redox Polymers*

Polymers have seen a wide variety of uses in modern life, and are typically insulators, such as the coatings on wires. However, conducting polymers exist which exhibit conducting or semi-conducting properties. The conducting properties of polymers are described by the band gap theory of solids, electron delocalisation, and the choice of doping anions¹¹⁰. A simplified diagram of band gap energies is shown in **Figure 1.18**. This illustrates the highest occupied energy level (HOMO) for electrons, known as the valence band, and the lowest unoccupied level (LUMO), the conduction band. The energy required to transition an electron from the valence to the conduction band defines the band gap energy. For example, insulators form when the band gap energy is large (>10 eV), hindering electron promotion into the conduction band. Conversely, conductors emerge when the valence and conduction bands overlap, resulting in no band gap energy. Semi-conductors, with an energy gap of approximately 1 eV, facilitate electron promotion into the conduction band. Generally, conducting polymers exhibit a band gap energy close to 1 eV, rendering them semiconductors (**Table 1.3**).

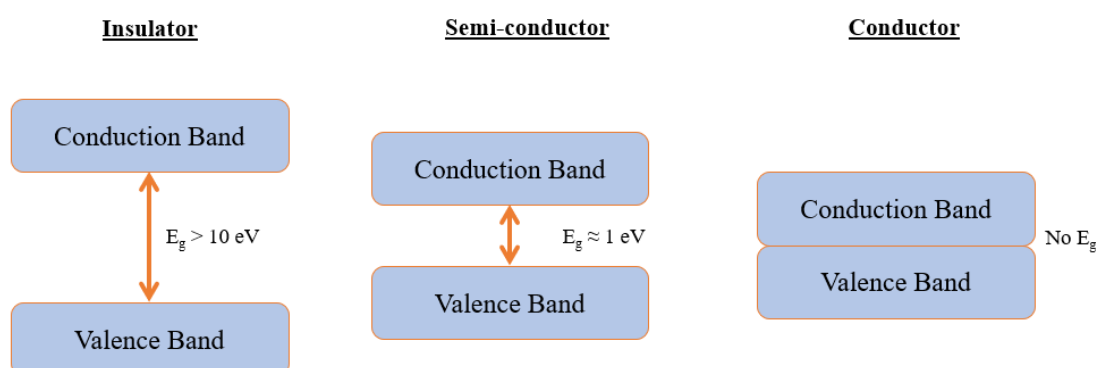


Figure 1.18: General energy difference between the valence band and conduction band for a insulator, semi-conductor and conductor.

Table 1.3: Band gaps for conventional and polymeric semiconductors¹¹¹.

Material	Band gap (eV)	Material	Band gap (eV)
Silicon	1.1	Polyacetylene	1.7
Germanium	0.7	Polypyrrole	3.2
Cadmium Sulfide	2.5	Polythiophene	2.0
Zinc Oxide	3.3	Polyparaphenylene	3.5

The conductivity of these polymers is not fully explained by band gap theory. Conducting polymers and redox polymers, while sharing some common features, serve distinct functions and display unique characteristics. Conducting polymers derive their conductivity from charge carrier movement, typically electrons or holes, along the polymer chain, giving them unique electrical and conducting properties¹¹². This mobility is facilitated by conjugated π -electron systems within the polymer structure, with the π -bonding molecular orbitals representing the valence bands and the π^* -antibonding molecular orbitals constituting the conduction band. While the band gap between these two bands can be used to inform the intrinsic electrical properties of the material, it should only be observed as a qualitative relationship between the size of the gap and the conductivity. Conductivity is dependent on the number and mobility of available charge carriers within the polymer¹¹¹ (**Figure 1.19**)(**Table 1.4**).

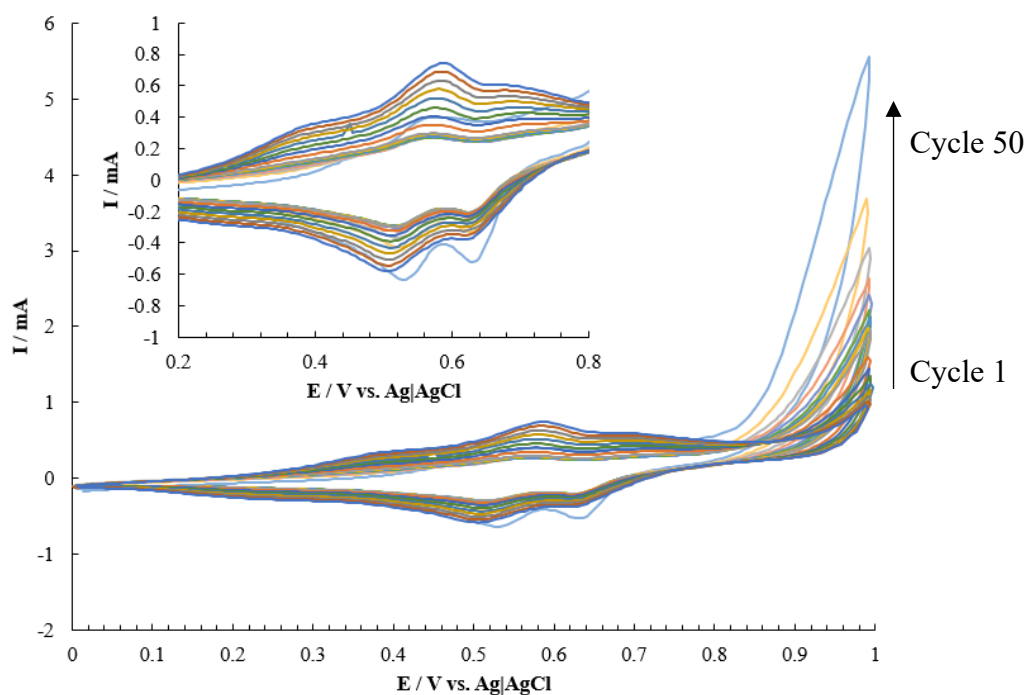
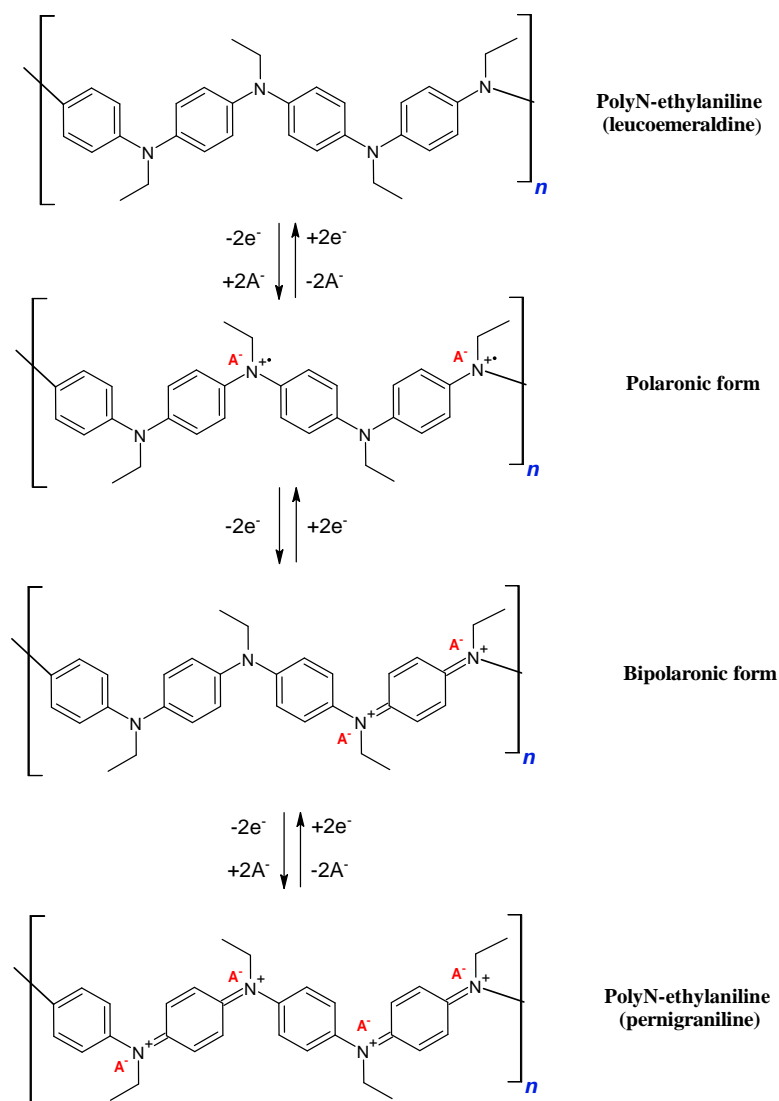


Figure 1.19: Example of cyclic voltammogram for the formation of poly-N-ethylaniline on a glassy carbon electrode over the potential range of 0 to 1 V vs. Ag|AgCl (3 M KCl) at $50 \text{ mV}\cdot\text{s}^{-1}$ for 50 cycles (showing cycles 1-10 and every subsequent fifth cycle, 15, 20.....50) inset: Zoomed in area of electrochemical responses.



Scheme 1.4: Oxidative and reductive processes of poly N-ethylaniline (adapted from Direksilp and Sirivat.¹¹³).

Table 1.4: Conductivity values for common metals and conducting polymers¹¹¹.

Metal	Conductivity (S.cm ⁻¹)	Polymer	Conductivity (S.cm ⁻¹)	
			Dedoped Form	Doped Form
Silver	6.29 x 10 ⁵	Polypyrrole	~10 ⁻¹⁰	10 ² – 10 ³
Copper	5.65 x 10 ⁵	Polythiophene	~10 ⁻¹⁰	10 ² – 10 ³
Platinum	1.00 x 10 ⁵	Polyparaphenylene	~10 ⁻¹²	5 x 10 ²
Mercury	1.04 x 10 ⁴	cis- Polyacetylene	~10 ⁻⁷	10 ³ – 10 ⁴

These polymers find applications in electronic devices, sensors, and conductive coatings, making them valuable in areas like flexible electronics and organic solar cells. In contrast, redox polymers undergo reversible redox reactions, with electrostatically and spatially localised redox sites that can be oxidised or reduced. Electrons are transported through an electron exchange reaction (electron hopping) between neighbouring redox sites, contingent on segmental motions enabling such movement¹¹⁴ (discussed further in **Chapter 6**). Redox polymers fall into subclasses, including those with covalently attached redox sites, either integrated into the chain or as pendant groups, often involving organic or organometallic molecules¹¹⁵. Another subclass comprises ion exchange polymeric systems or polyelectrolytes, where redox-active ions, typically complex compounds, are bound electrostatically. These polymers find applications in energy storage, electrochemical sensors, and bio electrochemical devices. The distinction lies in the electronic conductivity of conducting polymers, while redox polymers produce reversible redox reactions, making them crucial for processes requiring electron transfer. Polymers like these are utilised within this work to act as contrast agents, with the intention of generating the previously mentioned “negative” finger-mark, by observing the areas on the brass surface which do not contain the electrochemically deposited polymer.

1.3 Research Goals for this Work

Firearm related crime is prevalent across the world and development of rapid and reliable forensic techniques can aid in bringing those who perpetrate these crimes to justice.

The two overarching aims of this project are to:

- A) Develop a novel electroanalytical method for the detection of OFAR by:
 - i. Understanding the redox behaviour of characteristic analytes of interest found within OFAR, using cyclic voltammetry to advance insights into secondary product formation arising from electrochemical measurements or chemical degradation.
 - ii. Developing an electrochemical method capable of multi-analyte analysis at a chemically modified electrode with application to a genuine FAR sample.

- iii. Translating this method to a low-cost bespoke screen-printed electrode, suitable for onsite measurements of FAR.
- B) Develop an electrochemical method for the visualisation of latent finger-marks on a brass surface by:
- i. Understanding how the brass surface behaves electrochemically in selected environments.
 - ii. Electrodeposition of a range of materials and their combinations onto the surface of the brass and optimising the deposition solution for production of the highest quality finger-marks.
 - iii. Visualising latent finger-marks (groomed and donor samples) on brass surfaces following high temperature treatment and a room temperature aging study in order to mimic the firing of the weapon and aging of the finger-marks.
 - iv. Applying this rapid, innovative visualisation technique to ammunition casings for high quality visualisation of latent finger-marks.

1.4 References

- (1) Davis, A.; Geller, L.; Kim, R.; Villarreal, S.; McCourt, A.; Cubbage, J.; Crifasi, C. *A Year in Review 2020 GUN DEATHS in the U.S. The Johns Hopkins Center for Gun Violence Solutions*; John Hopkins Bloomberg School of Public Health: Center for Gun Violence Solutions, 2022; pp. 1–40. <https://publichealth.jhu.edu/gun-violence-solutions>. (accessed 2024-01-23).
- (2) Mattijssen, E. J. A. T.; Kerkhoff, W.; Hermsen, R.; Hes, R. A. G. Interpol Review of Forensic Firearm Examination 2019–2022. *Forensic Science International: Synergy* **2023**, *6* (2023), 100305. <https://doi.org/10.1016/j.fsisyn.2022.100305>.
- (3) Fay, J.; Patterson, D. *Contemporary Security Management*, 4th ed.; Butterworth-Heinemann: Oxford, 2018.
- (4) Hristov, T. *Person Firing a Gun*; 2019. <https://www.pexels.com/photo/person-firing-a-gun-5222282/> (accessed 2024-08-01).
- (5) Jalanti, T.; Henchoz, P.; Gallusser, A.; Bonfanti, M. S. The Persistence of Gunshot Residue on Shooters' Hands. *Science & Justice* **1999**, *39* (1), 48–52. [https://doi.org/10.1016/s1355-0306\(99\)72014-9](https://doi.org/10.1016/s1355-0306(99)72014-9).
- (6) Reis, E. L. T.; Souza Sarkis, J. E.; Neto, O. N.; Rodrigues, C.; Kakazu, M. H.; Viebig, S. A New Method for Collection and Identification of Gunshot Residues from the Hands of Shooters. *Journal of Forensic Sciences* **2003**, *48* (6), 2002441. <https://doi.org/10.1520/jfs2002441>.
- (7) Vinokurov, A.; Zeichner, A.; Glattstein, B.; Koffman, A.; Levin, N.; Rosengarten, A. Machine Washing or Brushing of Clothing and Its Influence on Shooting Distance Estimation. *Journal of Forensic Sciences* **2001**, *46* (4), 15072J. <https://doi.org/10.1520/jfs15072j>.
- (8) Vander Pyl, C.; Dalzell, K.; Menking-Hoggatt, K.; Ledergerber, T.; Arroyo, L.; Trejos, T. Transfer and Persistence Studies of Inorganic and Organic Gunshot Residues Using Synthetic Skin Membranes. *Forensic Chemistry* **2023**, *34* (2023), 100498. <https://doi.org/10.1016/j.forc.2023.100498>.

- (9) Maitre, M.; Horder, M.; Kirkbride, K. P.; Gassner, A.-L.; Weyermann, C.; Roux, C.; Beavis, A. A Forensic Investigation on the Persistence of Organic Gunshot Residues. *Forensic Science International* **2018**, *292*, 1–10. <https://doi.org/10.1016/j.forsciint.2018.08.036>.
- (10) Tahirukaj, M.; Surleva, A.; Vizureanu, P.; Olluri, B.; Sandu, A. V. Assessment of Persistence of Gunshot Residues Produced by Firearms from Criminal Cases in the Republic of Kosovo. *Applied Sciences* **2022**, *12* (20), 10477. <https://doi.org/10.3390/app122010477>.
- (11) Wallace, D. Transfer and Persistence of Gunshot Residue Particles. Thesis, West Virginia University, 2010, pp. 1–86. <https://researchrepository.wvu.edu/etd/4667>.
- (12) Blakey, L. S.; Sharples, G. P.; Chana, K.; Birkett, J. W. Fate and Behavior of Gunshot Residue-A Review. *Journal of Forensic Sciences* **2017**, *63* (1), 9–19. <https://doi.org/10.1111/1556-4029.13555>.
- (13) Krishna, S.; Ahuja, P. A Chronological Study of Gunshot Residue (GSR) Detection Techniques: A Narrative Review. *Egyptian Journal of Forensic Sciences* **2023**, *13* (1). <https://doi.org/10.1186/s41935-023-00369-8>.
- (14) Akhavan, J. *The Chemistry of Explosives*, 3rd ed.; Royal Society of Chemistry: Cambridge, 2012.
- (15) Walker, R. E. *Cartridges and Firearm Identification*, 1st ed.; Crc Press/Taylor & Francis: Boca Raton, 2013.
- (16) Werner, M.; Locher, R. Growth and Application of Undoped and Doped Diamond Films. *Reports on Progress in Physics* **1998**, *61* (12), 1665–1710. <https://doi.org/10.1088/0034-4885/61/12/002>.
- (17) Szala, M. Development Trends in Artillery Ammunition Propellants. *High Energy Materials* **2020**, *12* (2), 5–16. <https://doi.org/10.22211/matwys/0196>.

- (18) Ghosh, K.; Pant, C. S.; Sanghavi, R.; Adhav, S.; Singh, A. Studies on Triple Base Gun Propellant Based on Two Energetic Azido Esters. *Journal of Energetic Materials* **2008**, *27* (1), 40–50. <https://doi.org/10.1080/07370650802182542>.
- (19) Dahiwale, S.; Bhongale, C.; Roy, S.; Navle, P.; Asthana, S. Studies on the Ballistic Parameters of a Deterred Triple Base Propellant Used in Large Caliber Ammunition. *Central European Journal of Energetic Materials* **2019**, *16* (3), 449–467. <https://doi.org/10.22211/cejem/112374>.
- (20) Klapötke, T. M. *Chemistry of High-Energy Materials*, 6th ed.; Walter De Gruyter GmbH & Co KG, 2022.
- (21) Lussier, L. S.; Gagnon, H.; Bohn, M. A. On the Chemical Reactions of Diphenylamine and Its Derivatives with Nitrogen Dioxide at Normal Storage Temperature Conditions. *Propellants Explosives Pyrotechnics* **2000**, *25* (3), 117–125. [https://doi.org/10.1002/1521-4087\(200006\)25:3%3C117::aid-prep117%3E3.0.co;2-8](https://doi.org/10.1002/1521-4087(200006)25:3%3C117::aid-prep117%3E3.0.co;2-8).
- (22) Provatas, A. *Energetic Polymers and Plasticisers for Explosive Formulations - a Review of Recent Advances*; Defence Science and Technology Organisation, Aeronautical and Maritime Research Laboratory, 2000; pp. 1–46.
- (23) Serol, M.; Ahmad, S. M.; Quintas, A.; Família, C. Chemical Analysis of Gunpowder and Gunshot Residues. *Molecules* **2023**, *28* (14), 5550–5550. <https://doi.org/10.3390/molecules28145550>.
- (24) Saverio Romolo, F.; Margot, P. Identification of Gunshot Residue: A Critical Review. *Forensic Science International* **2001**, *119* (2), 195–211. [https://doi.org/10.1016/s0379-0738\(00\)00428-x](https://doi.org/10.1016/s0379-0738(00)00428-x).
- (25) French, J.; Morgan, R.; Davy, J. The Secondary Transfer of Gunshot Residue: An Experimental Investigation Carried out with SEM-EDX Analysis. *X-Ray Spectrometry* **2013**, *43* (1), 56–61. <https://doi.org/10.1002/xrs.2498>.

- (26) Gerard, R. V.; McVicar, M. J.; Lindsay, E.; Randall, E. D.; Harvey, E. The Long Range Deposition of Gunshot Residue and the Mechanism of Its Transportation. *Canadian Society of Forensic Science Journal* **2011**, *44* (3), 97–104. <https://doi.org/10.1080/00085030.2011.10768145>.
- (27) Brożek-Mucha, Z. On the Prevalence of Gunshot Residue in Selected Populations—an Empirical Study Performed with SEM-EDX Analysis. *Forensic Science International* **2014**, *237* (2014), 46–52. <https://doi.org/10.1016/j.forsciint.2014.01.020>.
- (28) Brożek-Mucha, Z. Chemical and Physical Characterisation of Welding Fume Particles for Distinguishing from Gunshot Residue. *Forensic Science International* **2015**, *254* (2015), 51–58. <https://doi.org/10.1016/j.forsciint.2015.06.033>.
- (29) Aliste, M.; Chávez, L. G. Analysis of Gunshot Residues as Trace in Nasal Mucus by GFAAS. *Forensic Science International* **2016**, *261* (2016), 14–18. <https://doi.org/10.1016/j.forsciint.2016.01.034>.
- (30) Yüksel, B. GFAAS Determination of Antimony, Barium, and Lead Levels in Gunshot Residue Swabs: An Application in Forensic Chemistry. *Atomic Spectroscopy* **2016**, *37* (4), 164–169. <https://doi.org/10.46770/as.2016.04.006>.
- (31) Costa, R. A.; Motta, L. C.; Destefani, C. A.; Rodrigues, R. R. T.; do Espírito Santo, K. S.; Aquije, G. M. F. V.; Boldrini, R.; Athayde, G. P. B.; Carneiro, M. T. W. D.; Romão, W. Gunshot Residues (GSR) Analysis of Clean Range Ammunition Using SEM/EDX, Colorimetric Test and ICP-MS: A Comparative Approach between the Analytical Techniques. *Microchemical Journal* **2016**, *129* (2016), 339–347. <https://doi.org/10.1016/j.microc.2016.07.017>.
- (32) Diaz, E.; Souza Sarkis, J. E.; Viebig, S.; Saldiva, P. Measurement of Airborne Gunshot Particles in a Ballistics Laboratory by Sector Field Inductively Coupled Plasma Mass Spectrometry. *Forensic Science International* **2012**, *214* (1-3), 44–47. <https://doi.org/10.1016/j.forsciint.2011.07.016>.

- (33) Reardon, M. R.; MacCrehan, W. A.; Rowe, W. F. Comparing the Additive Composition of Smokeless Gunpowder and Its Handgun-Fired Residues. *Journal of Forensic Sciences* **2000**, *45* (6), 14871J. <https://doi.org/10.1520/jfs14871j>.
- (34) Sarkis, J. E. S.; Neto, O. N.; Viebig, S.; Durrant, S. F. Measurements of Gunshot Residues by Sector Field Inductively Coupled Plasma Mass Spectrometry—Further Studies with Pistols. *Forensic Science International* **2007**, *172* (1), 63–66. <https://doi.org/10.1016/j.forsciint.2006.12.007>.
- (35) Stamouli, A.; Niewöhner, L.; Larsson, M.; Colson, B.; Uhlig, S.; Fojtasek, L.; Machado, F.; Gunaratnam, L. Survey of Gunshot Residue Prevalence on the Hands of Individuals from Various Population Groups in and Outside Europe. *Forensic Chemistry* **2021**, *23* (2021), 100308. <https://doi.org/10.1016/j.forc.2021.100308>.
- (36) Kanstrup, N.; Balsby, T. J. S.; Mellerup, K. A.; Hansen, H. P. Non-Lead Rifle Ammunition: Danish Hunters' Attitudes. *Environmental Sciences Europe* **2021**, *33* (1). <https://doi.org/10.1186/s12302-021-00485-z>.
- (37) Tong, Y.; Wu, Z.; Yang, C.; Yu, J.; Zhang, X.; Yang, S.; Deng, X.; Xu, Y.; Wen, Y. Determination of Diphenylamine Stabilizer and Its Nitrated Derivatives in Smokeless Gunpowder Using a Tandem MS Method. *The Analyst* **2001**, *126* (4), 480–484. <https://doi.org/10.1039/b010183o>.
- (38) Benito, S.; Abrego, Z.; Sánchez, A.; Unceta, N.; Goicolea, M. A.; Barrio, R. J. Characterization of Organic Gunshot Residues in Lead-Free Ammunition Using a New Sample Collection Device for Liquid Chromatography–Quadrupole Time-of-Flight Mass Spectrometry. *Forensic Science International* **2015**, *246* (2015), 79–85. <https://doi.org/10.1016/j.forsciint.2014.11.002>.
- (39) Ferdowsi, M.; Abolfazl Taghian; Najafi, A.; Moradi, M. Application of a Nanostructured Supramolecular Solvent for the Microextraction of Diphenylamine and Its Mono-Nitrated Derivatives from Unburned Single-Base Propellants. *Journal of separation science* **2014**, *38* (2), 276–282. <https://doi.org/10.1002/jssc.201401023>.

- (40) Mach, M. H.; Pallos, A.; Jones, P. F. Feasibility of Gunshot Residue Detection via Its Organic Constituents. Part I: Analysis of Smokeless Powders by Combined Gas Chromatography-Chemical Ionization Mass Spectrometry. *Journal of Forensic Sciences* **1978**, *23* (3), 10690J. <https://doi.org/10.1520/jfs10690j>.
- (41) Goudsmits, E.; Sharples, G. P.; Birkett, J. W. Preliminary Classification of Characteristic Organic Gunshot Residue Compounds. *Science & Justice* **2016**, *56* (6), 421–425. <https://doi.org/10.1016/j.scijus.2016.06.007>.
- (42) Stiles, S.; Luense, J. Methods of Making Double Base Casting Powder, November 30, 2010. <https://patents.google.com/patent/US7842144B1/en>.
- (43) Haury, V.; Frankel, M. Gun Propellant Containing Nitroplasticized Nitrocellulose and Triaminoguanidine Nitrate, May 8, 1973. <https://patents.google.com/patent/US3732131A/en>.
- (44) Pierce, E. Nitrocellulose Solid Propellant Composition with Load Additive to Reduce Radar Attenuation, April 30, 1974. <https://patents.google.com/patent/US3808061A/en>.
- (45) Hafner, M. T.; Balangué, R.; Clark, D.; Westbrook, J. W. Propellant Compositions Including Stabilized Red Phosphorus and Methods of Forming Same, May 22, 2014. <https://patents.google.com/patent/US20140137996A1/en>.
- (46) Gassner, A.-L.; Weyermann, C. LC–MS Method Development and Comparison of Sampling Materials for the Analysis of Organic Gunshot Residues. *Forensic Science International* **2016**, *264* (2016), 47–55. <https://doi.org/10.1016/j.forsciint.2016.03.022>.
- (47) Castellanos, A.; Bell, S.; Fernandez-Lima, F. Characterization of Firearm Discharge Residues Recovered from Skin Swabs Using Sub-Micrometric Mass Spectrometry Imaging. *Analytical Methods* **2016**, *8* (21), 4300–4305. <https://doi.org/10.1039/c6ay00096g>.

- (48) Dalzell, K. A.; Ott, C. E.; Trejos, T.; Arroyo, L. E. Comparison of Portable and Benchtop Electrochemical Instruments for Detection of Inorganic and Organic Gunshot Residues in Authentic Shooter Samples. *Journal of Forensic Sciences* **2022**, *67* (4), 1450–1460. <https://doi.org/10.1111/1556-4029.15049>.
- (49) Karahacane, D. S.; Dahmani, A.; Khimeche, K. Raman Spectroscopy Analysis and Chemometric Study of Organic Gunshot Residues Originating from Two Types of Ammunition. *Forensic Science International* **2019**, *301* (2019), 129–136. <https://doi.org/10.1016/j.forsciint.2019.05.022>.
- (50) Tarifa, A.; Almirall, J. R. Fast Detection and Characterization of Organic and Inorganic Gunshot Residues on the Hands of Suspects by CMV-GC–MS and LIBS. *Science & Justice* **2015**, *55* (3), 168–175. <https://doi.org/10.1016/j.scijus.2015.02.003>.
- (51) Zuy, Y.; Sweck, S. O.; Dockery, C. R.; Potts, G. E. HPLC Detection of Organic Gunshot Residues Collected with Silicone Wristbands. *Analytical Methods* **2020**, *12* (1), 85–90. <https://doi.org/10.1039/c9ay02305d>.
- (52) Morelato, M.; Beavis, A.; Ogle, A.; Doble, P.; Kirkbride, P.; Roux, C. Screening of Gunshot Residues Using Desorption Electrospray Ionisation–Mass Spectrometry (DESI–MS). *Forensic Science International* **2012**, *217* (1-3), 101–106. <https://doi.org/10.1016/j.forsciint.2011.10.030>.
- (53) Drzyzga, O. Diphenylamine and Derivatives in the Environment: A Review. *Chemosphere* **2003**, *53* (8), 809–818. [https://doi.org/10.1016/s0045-6535\(03\)00613-1](https://doi.org/10.1016/s0045-6535(03)00613-1).
- (54) Espinoza, E. O’N.; Thornton, J. I. Characterization of Smokeless Gunpowder by Means of Diphenylamine Stabilizer and Its Nitrated Derivatives. *Analytica Chimica Acta* **1994**, *288* (1), 57–69. [https://doi.org/10.1016/0003-2670\(94\)85116-6](https://doi.org/10.1016/0003-2670(94)85116-6).

- (55) Curtis, N. J.; Rogasch, P. E. Determination of Derivatives of Diphenylamine in Australian Gun Propellants by High Performance Liquid Chromatography. *Propellants, Explosives, Pyrotechnics* **1987**, *12* (5), 158–163. <https://doi.org/10.1002/prop.19870120505>.
- (56) Lurie, S.; Watkins, C. B. Superficial Scald, Its Etiology and Control. *Postharvest Biology and Technology* **2012**, *65*, 44–60. <https://doi.org/10.1016/j.postharvbio.2011.11.001>.
- (57) European Union. *COMMISSION REGULATION (EU) 2018/1515 of 10 October 2018 Amending Annexes III and V to Regulation (EC) No 396/2005 of the European Parliament and of the Council as Regards Maximum Residue Levels for Diphenylamine and Oxadixyl in or on Certain Product*.
- (58) Curtis, N. J. *Syntheses and Characterisations of Derivatives of Ethyl Centralite*; Defence Science and Technology Organisation, Weapons Systems Research Laboratory, 1987; pp. 1–30.
- (59) Wu, M.-S.; Wen, T.-C.; Gopalan, A. Electrochemical Copolymerization of Diphenylamine and Anthranilic Acid with Various Feed Ratios. *Journal of the Electrochemical Society* **2001**, *148* (5), D65–D65. <https://doi.org/10.1149/1.1366625>.
- (60) Burleson, G. L.; Gonzalez, B.; Simons, K.; Yu, J. C. C. Forensic Analysis of a Single Particle of Partially Burnt Gunpowder by Solid Phase Micro-Extraction–Gas Chromatography–Nitrogen Phosphorus Detector. *Journal of Chromatography A* **2009**, *1216* (22), 4679–4683. <https://doi.org/10.1016/j.chroma.2009.03.074>.
- (61) Bratin, K.; Kissinger, P. T.; Briner, R. C.; Bruntlett, C. S. Determination of Nitro Aromatic, Nitramine, and Nitrate Ester Explosive Compounds in Explosive Mixtures and Gunshot Residue by Liquid Chromatography and Reductive Electrochemical Detection. *Analytica Chimica Acta* **1981**, *130* (2), 295–311. [https://doi.org/10.1016/s0003-2670\(01\)93007-7](https://doi.org/10.1016/s0003-2670(01)93007-7).

- (62) Meng, H.; Caddy, B. Detection of N,N'-Diphenyl-N,N'-Diethylurea (Ethyl Centralite) in Gunshot Residues Using High-Performance Liquid Chromatography with Fluorescence Detection. *The Analyst* **1995**, *120* (6), 1759–1762. <https://doi.org/10.1039/an9952001759>.
- (63) MacCrehan, W. A.; Bedner, M. Development of a Smokeless Powder Reference Material for Propellant and Explosives Analysis. *Forensic Science International* **2006**, *163* (1-2), 119–124. <https://doi.org/10.1016/j.forsciint.2005.11.027>.
- (64) Bernal Morales, E.; Revilla Vázquez, A. L. Simultaneous Determination of Inorganic and Organic Gunshot Residues by Capillary Electrophoresis. *Journal of Chromatography A* **2004**, *1061* (2), 225–233. <https://doi.org/10.1016/j.chroma.2004.10.083>.
- (65) Ott, C. E.; Dalzell, K. A.; Calderón-Arce, P. J.; Alvarado-Gómez, A. L.; Trejos, T.; Arroyo, L. E. Evaluation of the Simultaneous Analysis of Organic and Inorganic Gunshot Residues within a Large Population Data Set Using Electrochemical Sensors. *Journal of Forensic Sciences* **2020**, *65* (6), 1935–1944. <https://doi.org/10.1111/1556-4029.14548>.
- (66) Dahl, D. B.; Lott, P. F. Determination of Black and Smokeless Powder Residues in Firearms and Improvised Explosive Devices. *Microchemical Journal* **1987**, *35* (1), 40–50. [https://doi.org/10.1016/0026-265x\(87\)90198-6](https://doi.org/10.1016/0026-265x(87)90198-6).
- (67) Zeichner, A.; Eldar, B.; Glattstein, B.; Koffman, A.; Tamiri, T.; Muller, D. Vacuum Collection of Gunpowder Residues from Clothing Worn by Shooting Suspects, and Their Analysis by GC/TEA, IMS, and GC/MS. *Journal of Forensic Sciences* **2003**, *48* (5), 2002390. <https://doi.org/10.1520/jfs2002390>.
- (68) Menking-Hoggatt, K.; Ott, C.; Vander Pyl, C.; Dalzell, K.; Curran, J.; Arroyo, L.; Trejos, T. Prevalence and Probabilistic Assessment of Organic and Inorganic Gunshot Residue and Background Profiles Using LIBS, Electrochemistry, and SEM-EDS. *Forensic Chemistry* **2022**, *29* (2022), 100429. <https://doi.org/10.1016/j.forc.2022.100429>.

- (69) Taudte, R. V.; Roux, C.; Blanes, L.; Horder, M.; Kirkbride, K. P.; Beavis, A. The Development and Comparison of Collection Techniques for Inorganic and Organic Gunshot Residues. *Analytical and Bioanalytical Chemistry* **2016**, *408* (10), 2567–2576. <https://doi.org/10.1007/s00216-016-9357-7>.
- (70) O'Mahony, A. M.; Samek, I. A.; Sattayasamitsathit, S.; Wang, J. Orthogonal Identification of Gunshot Residue with Complementary Detection Principles of Voltammetry, Scanning Electron Microscopy, and Energy-Dispersive X-Ray Spectroscopy: Sample, Screen, and Confirm. *Analytical Chemistry* **2014**, *86* (16), 8031–8036. <https://doi.org/10.1021/ac5016112>.
- (71) Kaya, S. I.; Cetinkaya, A.; Ozkan, S. A. Green Analytical Chemistry Approaches on Environmental Analysis. *Trends in Environmental Analytical Chemistry* **2022**, *33*, e00157. <https://doi.org/10.1016/j.teac.2022.e00157>.
- (72) Krishan, K.; Kanchan, T.; Bumrah, G. S. The Fingerprint Sourcebook. *Journal of Forensic and Legal Medicine* **2012**, *19* (3), 182–183. <https://doi.org/10.1016/j.jflm.2011.12.018>.
- (73) Cadd, S.; Islam, M.; Manson, P.; Bleay, S. Fingerprint Composition and Aging: A Literature Review. *Science & Justice* **2015**, *55* (4), 219–238. <https://doi.org/10.1016/j.scijus.2015.02.004>.
- (74) Baker, L. B. Physiology of Sweat Gland Function: The Roles of Sweating and Sweat Composition in Human Health. *Temperature* **2019**, *6* (3), 211–259. <https://doi.org/10.1080/23328940.2019.1632145>.
- (75) Sears, V. G.; Bleay, S. M.; Bandey, H. L.; Bowman, V. J. A Methodology for Finger Mark Research. *Science & Justice* **2012**, *52* (3), 145–160. <https://doi.org/10.1016/j.scijus.2011.10.006>.
- (76) Bansal, H.; Badiye, A.; Kapoor, N. Distribution of Fingerprint Patterns in an Indian Population. *Malaysian Journal of Forensic Sciences* **2014**, *5*(2) (2014), 18–21.

- (77) Roxburgh, T. J. On the Evidential Value of Finger Prints. *Sankhyā: The Indian Journal of Statistics* **1934**, *1* (2/3), 186–214.
- (78) Ashbaugh, D. R. *Quantitative-Qualitative Friction Ridge Analysis : An Introduction to Basic and Advanced Ridgeology.*, 1st ed.; Crc Press: S.L., 1999.
- (79) Jain, L. C. *Intelligent Biometric Techniques in Fingerprint and Face Recognition*; Crc Press: Boca Raton, 1999.
- (80) Parsons, N. R.; Smith, J. Q.; Thonnes, E.; Wang, L.; Wilson, R. Rotationally Invariant Statistics for Examining the Evidence from the Pores in Fingerprints. *Law, Probability and Risk* **2007**, *7* (1), 1–14. <https://doi.org/10.1093/lpr/mgm018>.
- (81) Abhishek, K.; Yogi, A. A Minutiae Count Based Method for Fake Fingerprint Detection. *Procedia Computer Science* **2015**, *58* (2015), 447–452. <https://doi.org/10.1016/j.procs.2015.08.061>.
- (82) Bleay, S. M. Solid Phase Selective Deposition Techniques. *Fingerprint Development Techniques: Theory and Application* **2018**, *Ch 8*, 199–220. <https://doi.org/10.1002/9781119187400.ch8>.
- (83) Bleay, S. M. Optical Detection and Enhancement Techniques. *Fingerprint Development Techniques: Theory and Application* **2018**, *Ch 6*, 111–153. <https://doi.org/10.1002/9781119187400.ch6>.
- (84) Kanokwongnuwut, P.; Kirkbride, K. P.; Kobus, H.; Linacre, A. Enhancement of Fingermarks and Visualizing DNA. *Forensic Science International* **2019**, *300* (2019), 99–105. <https://doi.org/10.1016/j.forsciint.2019.04.035>.
- (85) An, I. Application of Imaging Ellipsometry to the Detection of Latent Fingermarks. *Forensic Science International* **2015**, *253* (2015), 28–32. <https://doi.org/10.1016/j.forsciint.2015.05.009>.
- (86) Bleay, S. M. Amino Acid Reagents. *Fingerprint Development Techniques: Theory and Application* **2018**, *Ch 9*, 221–274. <https://doi.org/10.1002/9781119187400.ch9>.

- (87) Lennard, C. Forensic Sciences : Fingerprint Techniques. In *Encyclopaedia of Analytical Science.*; Elsevier, 2019; pp. 38–47.
- (88) Bleay, S. M. Reagents for Other Eccrine Constituents. *Fingerprint Development Techniques: Theory and Application* **2018**, 275–282. <https://doi.org/10.1002/9781119187400.ch10>.
- (89) Wilkinson, D. Study of the Reaction Mechanism of 1,8-Diazafluoren-9-One with the Amino Acid, L-Alanine. *Forensic Science International* **2000**, 109 (2), 87–103. [https://doi.org/10.1016/S0379-0738\(99\)00219-4](https://doi.org/10.1016/S0379-0738(99)00219-4).
- (90) Bleay, S. M.; Marcel de Puit. Vapour Phase Techniques. *Fingerprint Development Techniques: Theory and Application* **2018**, 155–197. <https://doi.org/10.1002/9781119187400.ch7>.
- (91) Stevenson, R. Characterisation Study of Brass Cartridges for High End Competition Target Shooting. Thesis, University of Strathclyde, 2014.
- (92) Yaqoob, K.; Hashmi, F.; Hassan Tanveer, W. Failure Analysis of Cartridge Brass Shell. *Engineering Failure Analysis* **2022**, 138, 106325. <https://doi.org/10.1016/j.engfailanal.2022.106325>.
- (93) Hajizadeh, K.; Tajally, M.; Emadoddin, E.; Borhani, E. Study of Texture, Anisotropy and Formability of Cartridge Brass Sheets. *Journal of Alloys and Compounds* **2014**, 588, 690–696. <https://doi.org/10.1016/j.jallcom.2013.11.091>.
- (94) Moret, S.; Spindler, X.; Lennard, C.; Roux, C. Microscopic Examination of Fingerprint Residues: Opportunities for Fundamental Studies. *Forensic Science International* **2015**, 255, 28–37. <https://doi.org/10.1016/j.forsciint.2015.05.027>.
- (95) Ramos, A. S.; Vieira, M. T. An Efficient Strategy to Detect Latent Fingermarks on Metallic Surfaces. *Forensic Science International* **2012**, 217 (1-3), 196–203. <https://doi.org/10.1016/j.forsciint.2011.10.047>.

- (96) Wightman, G.; Emery, F.; Austin, C.; Andersson, I.; Marcus, L.; Arju, G.; Steven, C. The Interaction of Fingerprint Deposits on Metal Surfaces and Potential Ways for Visualisation. *Forensic Science International* **2015**, *249*, 241–254. <https://doi.org/10.1016/j.forsciint.2015.01.035>.
- (97) Wightman, G.; O'Connor, D. The Thermal Visualisation of Latent Fingermarks on Metallic Surfaces. *Forensic Science International* **2011**, *204* (1-3), 88–96. <https://doi.org/10.1016/j.forsciint.2010.05.007>.
- (98) Jasuja, O. P.; Singh, G.; Almog, J. Development of Latent Fingermarks by Aqueous Electrolytes. *Forensic Science International* **2011**, *207* (1-3), 215–222. <https://doi.org/10.1016/j.forsciint.2010.10.011>.
- (99) Liu, S.; Pflug, M.; Hofstetter, R.; Taylor, M. The Effect of PH on Electrolyte Detection of Fingermarks on Cartridge Cases and Subsequent Microscopic Examination. *Journal of Forensic Sciences* **2014**, *60* (1), 186–192. <https://doi.org/10.1111/1556-4029.12620>.
- (100) Bond, J. W. On the Electrical Characteristics of Latent Finger Mark Corrosion of Brass. *Journal of Physics D: Applied Physics* **2008**, *41* (12), 125502. <https://doi.org/10.1088/0022-3727/41/12/125502>.
- (101) Bond, J. W. Imaging Fingerprint Corrosion of Fired Brass Shell Casings. *Review of Scientific Instruments* **2009**, *80* (7), 075108. <https://doi.org/10.1063/1.3183578>.
- (102) Bond, J. W. Visualization of Latent Fingerprint Corrosion of Brass. *Journal of Forensic Sciences* **2009**, *54* (5), 1034–1041. <https://doi.org/10.1111/j.1556-4029.2009.01108.x>.
- (103) Sykes, S.; Bond, J. W. A Comparison of Fingerprint Sweat Corrosion of Different Alloys of Brass. *Journal of Forensic Sciences* **2012**, *58* (1), 138–141. <https://doi.org/10.1111/j.1556-4029.2012.02300.x>.

- (104) Sapstead, R. M.; Corden, N.; Robert Hillman, A. Latent Fingerprint Enhancement via Conducting Electrochromic Copolymer Films of Pyrrole and 3,4-Ethylenedioxythiophene on Stainless Steel. *Electrochimica Acta* **2015**, *162*, 119–128. <https://doi.org/10.1016/j.electacta.2014.11.061>.
- (105) Beresford, A. L.; Hillman, A. R. Electrochromic Enhancement of Latent Fingerprints on Stainless Steel Surfaces. *Analytical Chemistry* **2010**, *82* (2), 483–486. <https://doi.org/10.1021/ac9025434>.
- (106) Brown, R. M.; Hillman, A. R. Electrochromic Enhancement of Latent Fingerprints by Poly(3,4-Ethylenedioxythiophene). *Physical Chemistry Chemical Physics* **2012**, *14* (24), 8653–8661. <https://doi.org/10.1039/C2CP40733G>.
- (107) Costa, C. V.; Assis, A. M. L.; Freitas, J. D.; Tonholo, J.; Ribeiro, A. S. A Low-Potential Electrochemical Method for Fast Development of Latent Fingerprints on Brass Cartridge Cases by Electrodeposition of Poly(3,4-Ethylenedioxythiophene). *Nano Select* **2020**, *1* (4), 405–412. <https://doi.org/10.1002/nano.202000040>.
- (108) Broncová, G.; Tereza Slaninová; Miroslava Trchová. Characterization of Electrochemically Visualized Latent Fingerprints on Steel Substrates. *Journal of Solid State Electrochemistry* **2022**, *26* (11), 2423–2433. <https://doi.org/10.1007/s10008-022-05245-4>.
- (109) Broncová, G.; Slaninová, T.; Trchová, M.; Prokopec, V.; Matějka, P.; Shishkanova, T. V. Optimization of Electrochemical Visualization of Latent Fingerprints with Poly(Neutral Red) on Brass Surfaces. *Polymers* **2021**, *13* (19), 3220. <https://doi.org/10.3390/polym13193220>.
- (110) InzeltG. *Conducting Polymers: A New Era in Electrochemistry*; Springer Berlin Heidelberg: Berlin, Heidelberg, 2012.
- (111) John, R. *Electrochemical Studies of Heterocyclic Conducting Polymers*. Thesis, University of Wollongong, 1992.

- (112) Molapo, K. M.; Ndangili, P. M.; Ajayi, R. F.; Gcineka Mbambisa; Mailu, S. M.; Njagi Njomo; Milua Masikini; Baker, P.; Iwuoha, E. I. Electronics of Conjugated Polyaniline. *International Journal of Electrochemical Science* **2012**, *7* (12), 11859–11875. [https://doi.org/10.1016/s1452-3981\(23\)16509-6](https://doi.org/10.1016/s1452-3981(23)16509-6).
- (113) Direksilp, C.; Sirivat, A. Synthesis and Characterization of Hollow-Sphered Poly(N-Methylaniline) for Enhanced Electrical Conductivity Based on the Anionic Surfactant Templates and Doping. *Polymers* **2020**, *12* (5), 1023. <https://doi.org/10.3390/polym12051023>.
- (114) Barsan, M. M.; Ghica, M. E.; Brett, C. M. A. Electrochemical Sensors and Biosensors Based on Redox Polymer/Carbon Nanotube Modified Electrodes: A Review. *Analytica Chimica Acta* **2015**, *881*, 1–23. <https://doi.org/10.1016/j.aca.2015.02.059>.
- (115) Gracia, R.; Mecerreyes, D. Polymers with Redox Properties: Materials for Batteries, Biosensors and More. *Polymer Chemistry* **2013**, *4* (7), 2206. <https://doi.org/10.1039/c3py21118e>.

Chapter 2: Theory Behind Experimental Techniques

Multiple analytical techniques were employed in this work, in both qualitative and quantitative capacities. The following sections describe these techniques in so far as they operate and produce analytical data, starting with electrochemical analysis then continuing into methods employed for material and surface analysis.

2.1 Electrochemical methods

Electrochemistry broadly involves the study of oxidation and reduction (redox) reactions in an electrolytic solution by observing parameters such as current (I), charge (Q) or potential (E)¹. Oxidation (**Equation 2.1**) and reduction (**Equation 2.2**) are fundamental chemical processes that involve the transfer of electrons between species, with oxidation being the loss of electrons while reduction is the gain of electrons.



Species which have the ability to either accept or donate electrons are termed “electroactive” species. This transfer of electrons occurs at the working electrode (WE) in an electrochemical cell and allows for the changes in the above-mentioned parameters (I , Q and E) to be observed and measured².

If undergoing oxidation, the species is supplying electrons to the circuit and thus increasing the current, conversely a species undergoing reduction takes electrons from the circuit effectively decreasing the observed current. There are two main types of current produced during electrochemical reactions: faradaic or non-faradaic (capacitive) currents³. Electron transfer between the analyte and the WE results in faradaic current, which as described by Faradays’ Law (**Equation 2.3**) stating that the amount of electricity that passes through an electrolyte solution during an electrochemical reaction, is proportional to the amount of chemical change³.

$$Q = nFN \quad 2.3$$

Where Q is charge (C), n is the number of electrons and F is Faraday’s constant (F , 96,485 $C \cdot mol^{-1}$) and N is the number of moles of substance converted (mol).

In this research, current and current density are where the current is a rate at which the total charge is collected, as seen in **Equation 2.4**⁴.

$$i = \frac{\Delta Q}{\Delta t} = nF \frac{\Delta N}{\Delta t} \quad 2.4$$

where i is the current measured in amperes (A) and t is time in seconds (s). To convert this value to current density (j) it is simply the current divided by the area of the WE in use (Equation 2.5)⁴.

$$j = \frac{i}{A} \quad 2.5$$

where j is the current density measured in A.cm⁻² and A is the area of the electrode in cm².

Non-faradaic current or capacitive current, is created by both polar and charged species that are present at the interface between the WE surface and the solution, an interface area is known as the electrical double layer. If the electrode holds a negative charge, positively charged ions in close proximity to the electrode surface will arrange next to the positively charged surface and vice versa (Figure 2.1).

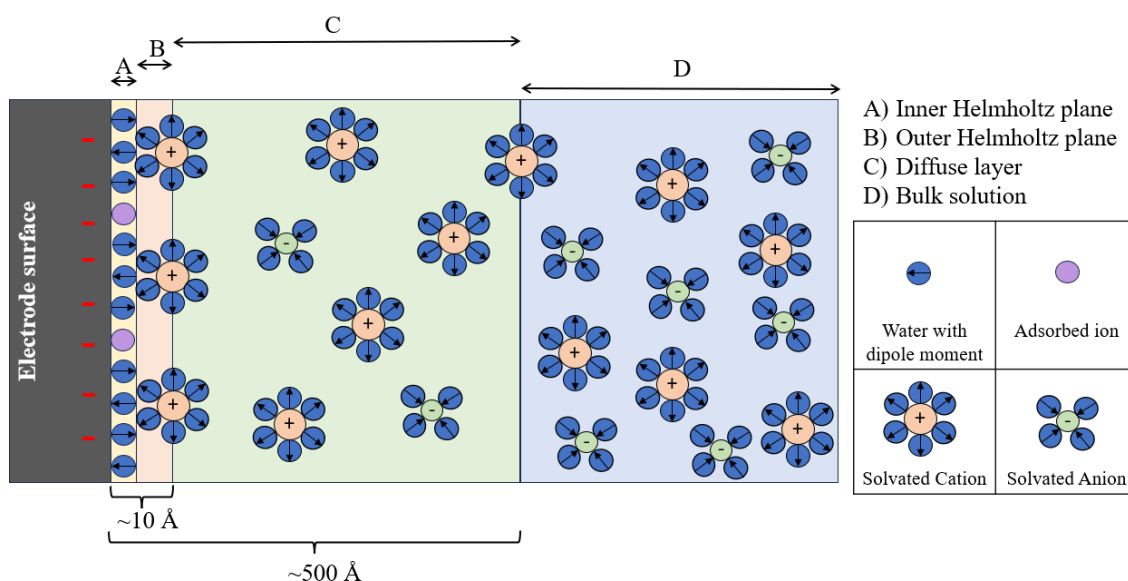


Figure 2.1: Electrical double layer containing the inner and outer Helmholtz planes and diffuse layer interface at an electrode surface, showing continuation into bulk solution.

2.2 Mass Transport

The movement of species within an electrochemical system is predominantly described by the Nernst-Planck equation (**Equation 2.6**)⁴:

$$\vec{J}_i = -D_i \vec{\nabla} c_i - \frac{z_i F D_i c_i}{RT} \vec{\nabla} \phi + c_i \vec{u} \quad 2.6$$

Where in all cases the subscript i refers to the species of interest, while the variables not previously mentioned are \vec{J}_i as the molar flux ($\text{mol}\cdot\text{s}^{-1}$), D_i as the diffusivity ($\text{m}^2\cdot\text{s}^{-1}$), c_i as the concentration ($\text{mol}\cdot\text{cm}^{-2}$), z_i as the relative charge of the species, ϕ as the electric potential and \vec{u} as the fluid velocity.

This equation includes the three principal mechanisms of mass transport: diffusion, migration and convection. Diffusion involves the movement of species across a concentration gradient from an area of high concentration to an area of low concentration. Therefore, if a species undergoes oxidation or reduction due to the applied potential at the electrode, the original concentration at the surface of the electrode will decrease, in turn creating an area of low concentration at the electrode surface during the diffusion process. Migration involves the movement of charged species influenced by an applied potential and depends on the charge and concentration of the species. Its effects can be controlled with the use of high concentrations of electrolytes¹. Convection involves the physical movement of the solution components by either mechanical (stirring) or thermal (convection currents) means. This process allows the species to be replaced at the surface without any physiochemical properties of either the solution or electrochemical species being utilised (**Figure 2.2**).

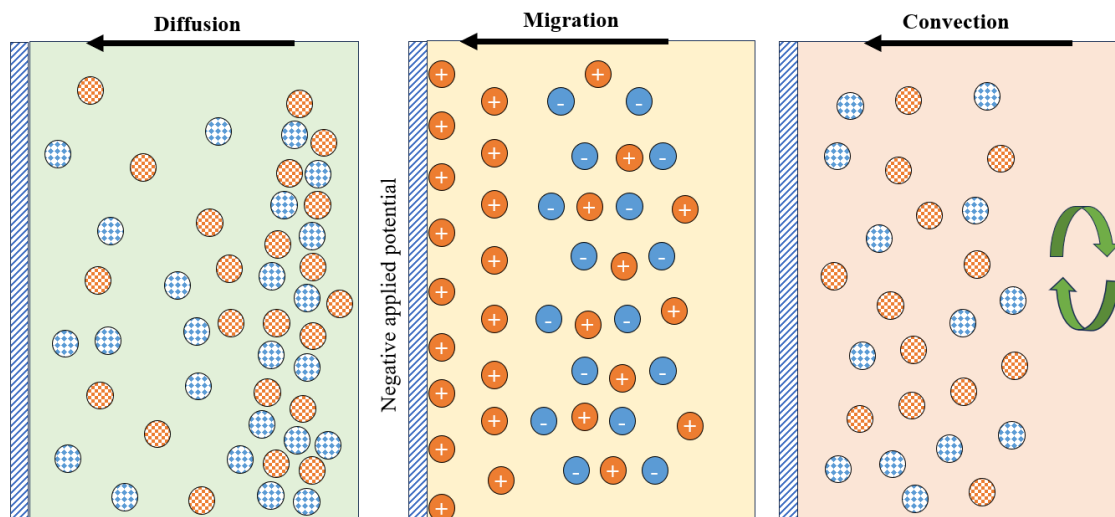


Figure 2.2: Diagrams of the three principal mechanisms of mass transport: diffusion, migration and convection.

Mass transport may be described in a single direction (Figure 2.3), allowing for the simplification of Equation 2.6 to Equation 2.7⁴:

$$J_i = -D_i \frac{\partial c_i}{\partial x} - \frac{z_i F D_i c_i}{RT} \frac{\partial \phi}{\partial x} + c_i u_x \quad 2.7$$

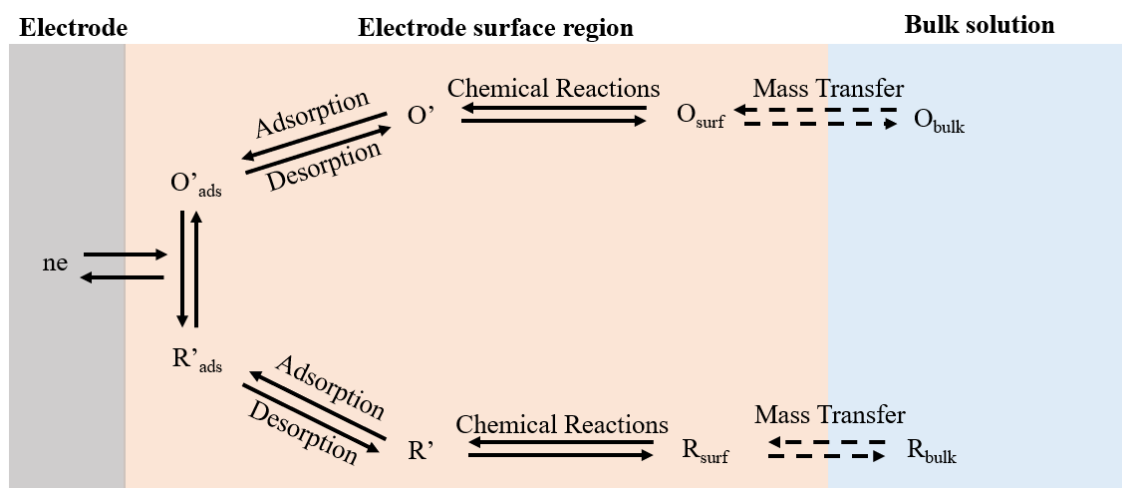


Figure 2.3: Overview of redox processes involved in the generation of an electrochemical signal.

For accurate modelling of electrochemically active species, it is often desirable to isolate diffusion as the sole transport mechanism. Experimentally, this isolation requires the elimination of convection and migration. Firstly, the solution must remain stagnant (i.e. no mixing or stirring) to suppress convection and secondly, introducing a high concentration of a supporting electrolyte that does not undergo redox reactions within the potential range of interest. Consequently, the supporting electrolyte predominantly carries the current, thereby minimising the migration of electrochemically active species.

Under these conditions, mass transport of electrochemically active species occurs solely via diffusion, as described by Fick's first law (**Equation 2.8**)⁴:

$$J_i = -D_i \frac{\partial c_i}{\partial x} \quad 2.8$$

When diffusion is the only transport method, Fick's second law is also applicable and can be simplified to one dimension (**Equation 2.9**)⁴:

$$\frac{\partial c_i}{\partial t} = D_i \frac{\partial^2 c_i}{\partial x^2} \quad 2.9$$

Combining these laws allows for the calculation of the transient flux of electrochemically active species. If a sufficiently large potential step was applied this could lead to the complete depletion of the reactant at the electrode surface, establishing diffusion limitations on the current. Thus, the current can be related to the flux (**Equation 2.10**) further enabling the derivation of a model that describes how current varies with time under diffusion-limited conditions (**Equation 2.11**)⁴:

$$J_i = -\frac{i}{nFA} \quad 2.10$$

$$\frac{i(t)}{nFA} = D_i \left. \frac{\partial c_i(t,x)}{\partial x} \right|_{x=0} \quad 2.11$$

The dynamic model for diffusion-limited conditions is observed through the Cottrell equation (**Equation 2.12**), which predicts that current decays as the inverse square root of time following a potential step⁴:

$$i(t) = nFAc \sqrt{\frac{D}{\pi t}} \quad 2.12$$

This behaviour is attributed to the thickening of the diffusion layer over time, which diminishes the concentration gradient and consequently the diffusion rate, leading to a decrease in diffusion-limited current. Despite its utility, the Cottrell equation has

limitations as it applies solely to diffusion-limited currents, predicts an infinite initial current (which is impractically high to measure), and does not account for convection that may arise over time, invalidating the diffusion limitation assumption. Additionally, it neglects the previously mentioned non-Faradaic currents such as double-layer charging. Nonetheless, the Cottrell equation facilitates several experimental techniques for characterising diffusion in electrochemical systems, the first of which will be discussed in the next section.

2.3 Electrochemical Experimental Techniques

2.3.1 Chronoamperometry

Chronoamperometry (CA) is a large amplitude technique with entails stepping the potential of the working electrode from a value where no faradaic reaction occurs to a potential at which the surface concentration of the electroactive species is effectively zero (**Figure 2.4**).

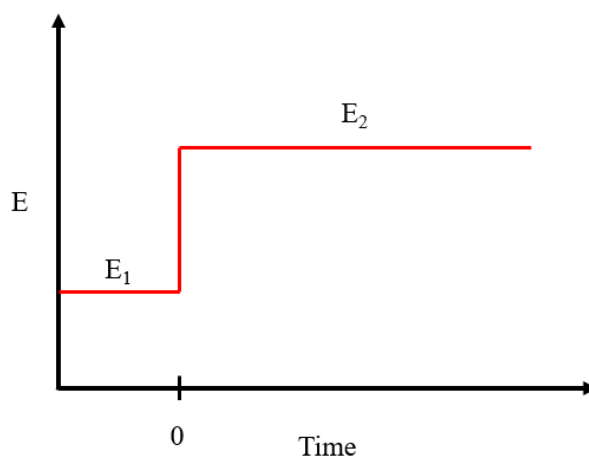


Figure 2.4: Generic graph showing potential step (with respect to time) for a chronoamperometry experiment.

To match the assumptions of the Cottrell equation this experimental method employs a stationary WE and an unstirred solution. The arising current-time dependence is then monitored. Under these conditions, as mentioned previously, mass transport occurs exclusively by diffusion, and the current-time curve (**Figure 2.5**) reflects the evolution of the concentration gradient near the electrode surface.

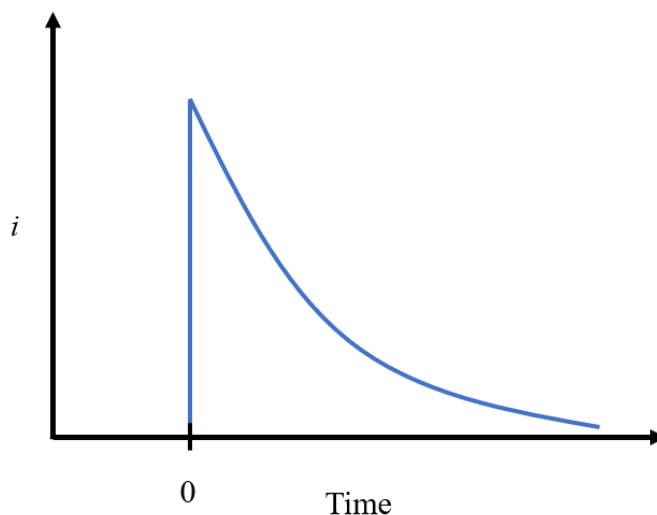


Figure 2.5: Generic graph showing the current response to time during a chronoamperometry experiment.

From this data a plot of i vs. $\frac{1}{\sqrt{t}}$ will result in a slope equal to $nFAc\sqrt{\frac{D}{\pi}}$ which can be useful for determining the diffusivity of a species of interest⁴. Chronocoulometry involves integration of the current response in CA resulting in measurement of Q , after the potential step. The monitored response involves output of charge-time plots. While such techniques are very useful tools in electrochemical measurements, within this thesis the most prominent form of electrochemical methods employed falls under the category of voltammetry.

2.3.2 Linear Sweep Voltammetry

Linear sweep voltammetry (LSV) is a controlled potential electrochemical technique which employs a stationary electrode to investigate the redox behaviour and electrochemical properties of species in a solution. LSV involves applying a linearly increasing (or decreasing) potential to an electrochemical cell while measuring the resulting current⁵. This technique provides insights into the oxidation and reduction processes of analytes, their concentration levels, and their electrochemical kinetics (**Figure 2.6**).

The core principle of LSV centres around the systematic variation of the electrode potential and the observation of the corresponding current response. As the applied potential changes, electrochemical reactions occur at the electrode surface, leading to

changes in the current flowing through the cell. The resulting data is graphed as a voltammogram, where the current is plotted against the applied potential.

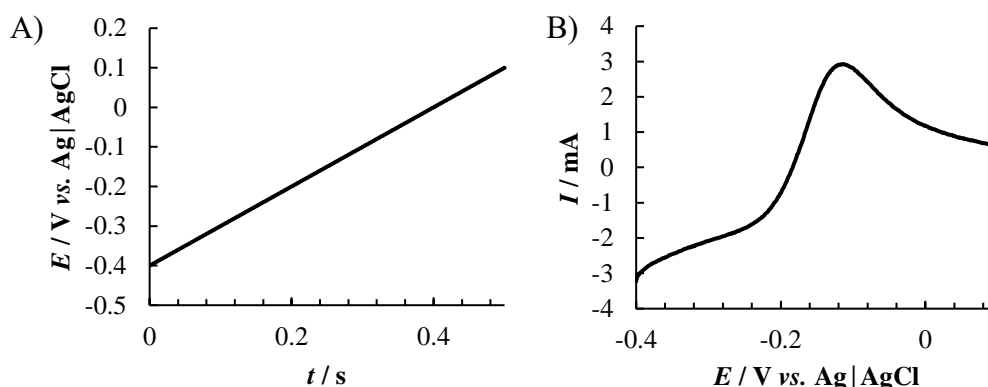


Figure 2.6: Generic examples of A) potential vs. time and B) current vs. potential during a LSV experiment for an oxidative process.

2.3.3 Cyclic Voltammetry

If instead of sweeping in a single direction, the method was employed to sweep to a potential and then return to the original starting potential the method changes from LSV to Cyclic Voltammetry (CV). CV is a very useful and widely applied technique for the exploratory evaluation of redox behaviour or elucidation of electrochemical properties of an analyte of interest⁶. It allows for the observations of cathodic and anodic potentials, at which the species of interest undergoes reduction or oxidation. CV involves applying a potential at a constant rate in a triangular wave form, sweeping from a minimum applied potential to the maximum and returning (**Figure 2.7 (A)**). This sweep is classified as one cycle and within this cycle there are two distinctive processes, the anodic and cathodic sweeps. During the sweep, the potentiostat measures the current (I) resulting from the applied potential (E), and the resulting plot of this measurement is called a cyclic voltammogram (**Figure 2.7 (B)**). Redox active analytes produce signals or peaks from which the peak potentials can be obtained for anodic or cathodic processes (E_p^a and E_p^c respectively), while at these potentials a current which is concentration dependent is also observed (I_p^a and I_p^c).

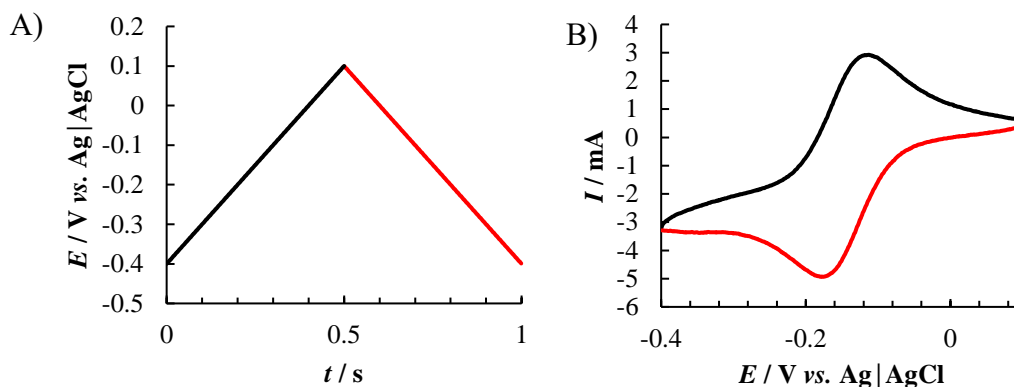


Figure 2.7: Generic examples of A) potential vs. time and B) current vs. potential for a reversible or Nernstian system.

For an electrochemically reversible reaction ($R \rightleftharpoons O + ne^-$) the potential of the electrode can be used to establish the concentration of the electroactive species using (**Equation 2.13**) the Nernst equation⁷:

$$E = E^\circ + \frac{2.3RT}{nF} \log \frac{C_O(0,t)}{C_R(0,t)} \quad 2.13$$

where E° is the standard potential for the redox reaction R is the universal gas constant ($8.314 \text{ J.K}^{-1}.\text{mol}^{-1}$), T is the Kelvin temperature, n is the number of electrons transferred in the reaction, and F is the Faraday constant [$96,487 \text{ C.mol}^{-1}$]. $C_O(0,t)$ and $C_R(0,t)$ are the surface concentration of the reactants⁷. The peak current response for a redox reversible analyte may be described by (**Equation 2.14**) the Randles- Ševčík equation⁴:

$$i_p = (2.69 \times 10^5) n^2 A C D^{\frac{1}{2}} v^{\frac{1}{2}} \quad 2.14$$

where n is the number of electrons involved in the process, A is the electrode surface area in cm^2 , C is the concentration of the analyte in mol.cm^{-3} , D is the diffusion coefficient in $\text{cm}^2.\text{s}^{-1}$ and v is the potential scan rate in V.s^{-1} .

As current is directly proportional to concentration, if a linear response is observed in a plot of I_p vs. \sqrt{v} the process is said to be diffusion controlled, while if the plot of I_p vs. v provides a linear response, this indicates a surface confined process.

In the case of irreversible processes, there is slow electron exchange between the redox species and the working electrode, individual peaks are reduced in size and widely separated. Totally irreversible systems exhibit a peak potential shift with the scan rate (**Equation 2.15**)⁷:

$$E_p = E^o - \frac{RT}{\alpha n_a F} \left[0.78 - \ln \frac{k^o}{\sqrt{D}} + \ln \left(\frac{\alpha n_a F v}{RT} \right)^{\frac{1}{2}} \right] \quad 2.15$$

where α represents the transfer coefficient and n_a is the number of electrons involved in the charge transfer step. Consequently, E_p occurs at potentials higher than E^o , with the overpotential linked to k^o and α . This peak displacement can be compensated by adjusting the scan rate, and the voltammogram contains widely separated peaks as αn decreases⁷.

The peak current given by **Equation 2.16** is still proportional to the bulk concentration, however still lower (about 80%) compared to a reversible process⁷.

$$i_p = (2.99 \times 10^5) n (\alpha n_a)^{\frac{1}{2}} A C D^{\frac{1}{2}} V^{\frac{1}{2}} \quad 2.2.16$$

Quasi-reversible electrochemical processes ($10^{-1} > k^o > 10^{-5} \text{ cm.s}^{-1}$) exist where the current is controlled by both charge transfer and mass transport processes, via the reversibility parameter (**Equation 2.17**) which is effectively the ratio of charge transfer (k^o) to mass transfer rates⁴.

$$\Lambda = \frac{k^o}{\sqrt{\pi \left(\frac{n F v}{RT} \right) D}} \quad 2.17$$

Large values represent a more electrochemical reversible process, while low values indicate electrochemically irreversible behaviour⁴. The voltammograms of quasi-reversible processes appear more drawn out with much larger separation between the peak potentials⁷.

2.3.4 Differential Pulse Voltammetry

Differential Pulse Voltammetry (DPV) is a useful electrochemical technique in the study of redox behaviour of substances in a solution. The fundamental principle of DPV involves the application of a series of fixed magnitude potential pulses, superimposed on a potential ramp (**Figure 2.8**) to an electrochemical cell containing the sample solution^{5,7}.

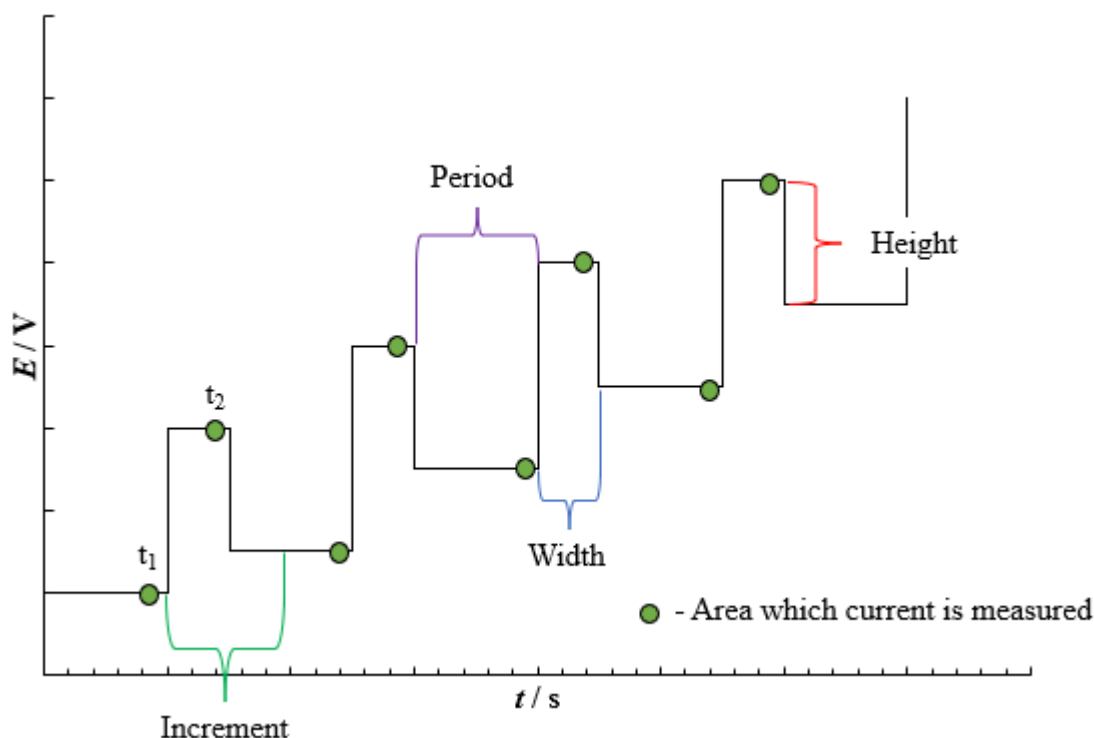


Figure 2.8: Generic example of potential vs. time during DPV analysis, indicating the parameters of pulse increment, period, width, height and the locations of current measuring.

These voltage pulses are applied in rapid succession, with a small-time interval (known as the pulse width) between each pulse. The potential of the working electrode is stepped up and down, resulting in a voltage profile resembling a staircase pattern. The key feature of DPV is that it measures the difference in current (Δi) before (t_1) and near the end of (t_2) each voltage pulse (**Equation 2.18**)⁷:

$$\Delta i = i_{(t_2)} - i_{(t_1)} \quad 2.18$$

This results in lower capacitive current and limits of detection as low as 10^{-8} M^7 . This difference in current is plotted against the base potential, resulting in a differential pulse voltammogram of Δi vs. E and the resulting voltammogram consists of current peaks for the analyte of interest which are directly proportional to their concentration (**Equation 2.19**)⁵:

$$i_p = \frac{nFA\sqrt{DC}}{\sqrt{\pi(t_2-t_1)}} \left(\frac{1-\sigma}{1+\sigma} \right) \quad 2.19$$

Where σ is given by **Equation 2.20**⁵:

$$\sigma = \exp\left(\frac{nF\Delta E}{2RT}\right) \quad 2.20$$

And the term $\left(\frac{1-\sigma}{1+\sigma}\right)$ describes the effect of the pulse height (ΔE) on Δi . DPV is particularly valuable for analysing electroactive species and investigating their concentration levels, kinetics, and electrochemical properties.

2.3.5 Electrodes used in the Electrochemical Cell.

During the previous section reference have been made to electrodes (specifically working electrodes). Within this work the three-electrode electrochemical cell is utilised for electroanalytical experiments. The three electrodes of interest within this set-up are the WE the counter electrode (CE) and the reference electrode (RE). The fundamental purpose of a WE is to facilitate electron transfer, which occurs at its surface during electrochemical reactions. These reactions can involve the oxidation or reduction of a species, resulting in the change in flow of electrons within the circuit and subsequently the observed current. This observed current is passed through a circuit between the WE and CE. The CE's purpose is to complete this circuit and allow the current to flow (acting as a source or sink of electrons). As such, the CE needs to be made of materials which are inert such as carbon or platinum and should be much larger than the WE to ensure that no limitations in current are due to the CE³.

The final type of electrode within the three-electrode cell is the RE, where the potential of the WE is controlled relative to the RE. RE's should have stable and reproducible potentials, preferably using a reversible process. In these reversible RE's a small cathodic current produces a reduction reaction while a small anodic current produces an oxidation reaction⁸. **Equation 2.21** represents the reaction for the type of reference electrode used throughout this PhD thesis the silver/silver chloride (Ag/AgCl) 3M KCl electrode.



Another type of RE which is used in this work was a pseudo-reference electrode, an electrode whereby no appreciable current is allowed to flow through and is used to observe or control the potential at the WE for low current systems. While the pseudo-

reference electrode fulfils the role of a traditional RE the electrochemical processes allowing it to do so are not as well defined as traditional RE's.

2.4 Additional analytical techniques used in this thesis

While electrochemical methods were the main focus of data generation within this thesis, numerous other analytical techniques were employed within the thesis.

2.4.1 *Scanning Electron Microscopy*

Scanning electron microscopy (SEM) is an imaging technique, which employs a focused beam of electrons to probe the surface structure and texture of samples, providing detailed visual information at the micro and nano-scale level compared to traditional lens-based microscopy. The fundamental principle of SEM focuses on the interaction between the electron beam and the sample, allowing for surface characterisation and topological understanding of the sample. **Figure 2.9** shows a simplified diagram of the internal components of a scanning electron microscope. The electron gun generates the beam of electrons with the use of a heated tungsten filament, due to the high temperatures applied, excited electrons of between 1-30 keV are generated. The velocity of electrons can be adjusted by varying the applied accelerated voltage. When directed towards the sample, the electron beam is guided through a Wehnelt cylinder, limiting its diameter to a range of 10-50 μm . To prevent electron dispersion, a vacuum system is maintained within the instrument's chamber. Two condenser lenses work to sustain the electron beam diameter, reducing it to about 2-10 nm. This focused beam then passes through scanning coils positioned along its axis, aligning it to a focal point. Adjusting the current in these coils can influence the electromagnetic strength. The electron beam undergoes its final magnification through a second lens, known as the objective lens, before interacting with the sample.

When the electron beam interacts with the sample of interest, it generates two distinct signals composed of photons and electrons. Typically, the most commonly used signals are secondary and backscattered electrons. SEM instruments often incorporate various signals, such as secondary electrons, backscattered electrons, and x-ray signals.

Secondary electrons, characterised by their scattering from the sample surface, typically exhibit low energy⁹.

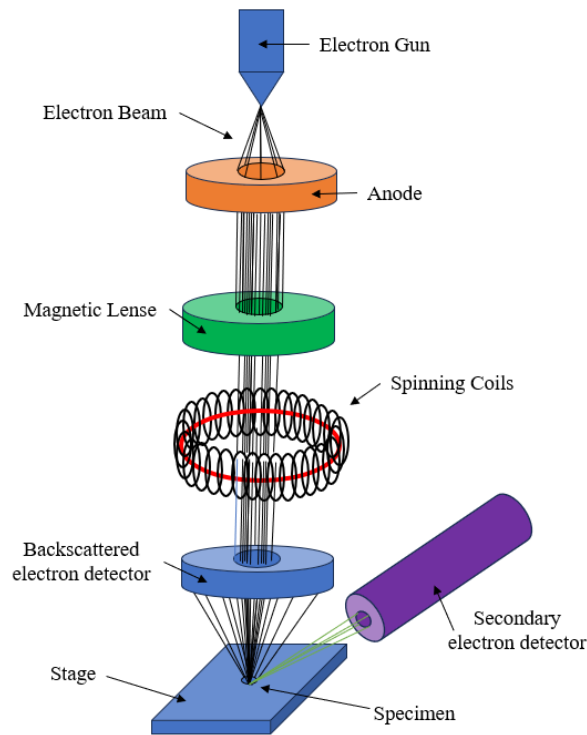


Figure 2.9: Simplified diagram of the components of a SEM.

2.4.2 Energy-dispersive X-ray Spectroscopy

Energy-dispersive x-ray spectroscopy (EDX) is an analytical technique commonly used in conjunction with SEM to characterise the elemental composition of materials at a microscopic scale. EDX provides insights into the types and quantities of elements present in a sample by detecting the X-rays emitted when electrons from the sample's atoms are displaced during interaction with an electron beam. Energy-dispersive X-ray Spectroscopy (EDX) is commonly employed in conjunction with SEM, utilising the generation of X-rays during electron-sample interactions. When the electron beam interacts with the sample, secondary electrons are created, leaving atoms in the sample with “holes” in their electron shells. If these “holes” are in inner shells, the atoms are left in an unstable state. Electrons from higher energy outer shells then drop into the vacant sites, emitting X-rays as they transition from higher to lower energy states (**Figure 2.10**).

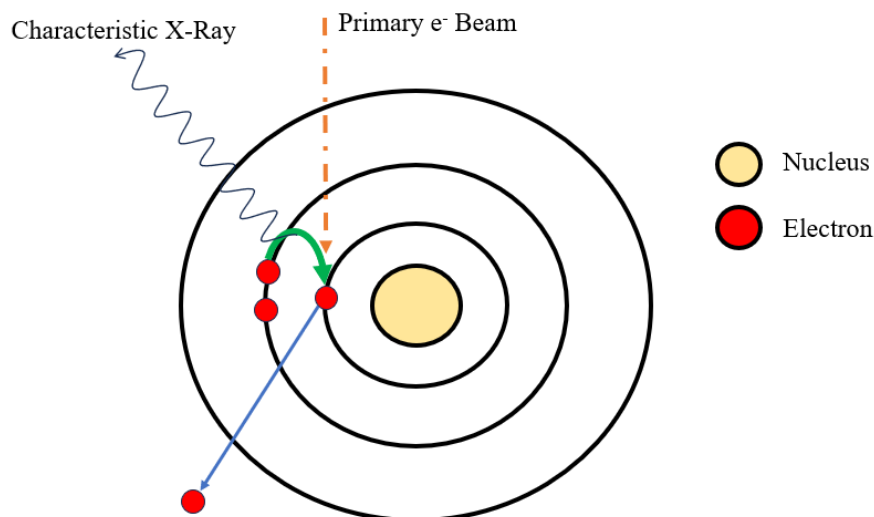


Figure 2.10: Simplified image of X-ray generation during EDX analysis.

This process allows for the identification of the elemental composition of the sample, as each element emits X-rays with characteristic energy and wavelength. EDX is a non-destructive technique, much like SEM. It can perform elemental analysis in small areas, as tiny as $0.5\ \mu\text{m}$. The emitted X-rays originate from a depth determined by the formation depth of the secondary electrons, typically ranging from 0.5 to $2\ \mu\text{m}$ ¹⁰.

Additionally, EDX analysis can quantify the detected elements by calculating the area under the peak of each identified element in the sample spectrum. These calculations convert the area under the peak into weight or atomic percentage. However, the accuracy of quantitative analyses is influenced by the surface roughness of the sample¹¹ therefore within this work only qualitative analysis was performed.

2.4.3 X-ray Photoelectron Spectroscopy

X-ray Photoelectron Spectroscopy (XPS) serves as a crucial technique for unravelling the elemental composition and chemical states within a material, particularly at its surface layers. In the XPS process, soft X-rays, typically in the range of 1 – $3\ \text{keV}$ are directed onto the material, inducing the ejection electrons in orbitals with binding energies less than the energy of the X-rays from surface atoms (**Figure 1.29**). The resulting photoelectrons carry kinetic energy and unique characteristics that unveil both the elements present and their specific chemical states. These ejected photoelectrons are

detected using an energy analyser, to precisely measure their kinetic energy. This analysis determines the binding energy of the electrons, allowing for the identification of corresponding elements within the sample. Detection of the ejected electrons, quantified at various kinetic energies by detectors, generates the XPS spectrum, or survey spectrum. This spectrum provides valuable information about the material's elemental composition. Moreover, high-resolution XPS spectra are obtained for specific elements, offering detailed insights into the chemical states of the atoms. This is essential for understanding the chemical bonding and electronic structure of the material. An inherent characteristic of XPS is its surface sensitivity. The technique typically probes depths of just a few nanometres, making it particularly adept at studying the surface chemistry of materials¹².

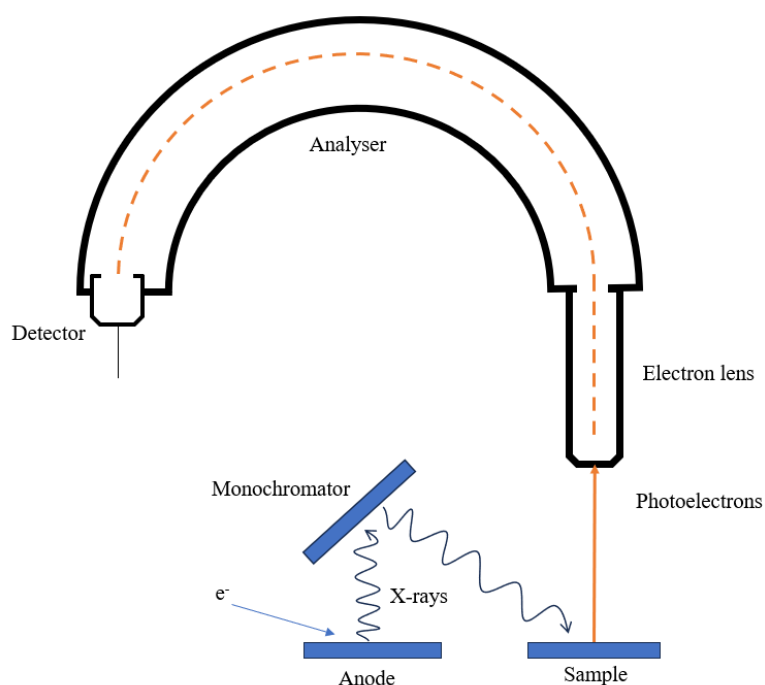


Figure 2.11: Simple diagram of XPS spectrometer.

2.4.4 Ultraviolet–visible spectroscopy

Ultraviolet-Visible (UV-Vis) spectroscopy, a widely employed technique, enables the study of a substance's absorption or transmission of light within the ultraviolet and visible regions of the electromagnetic spectrum. In UV-Vis spectroscopy, a sample is exposed to light in the UV and visible ranges, typically between 190 and 780 nm¹³. As the incident light (and therefore energy) is absorbed by the molecule the electrons within are promoted from an occupied orbital to an unoccupied orbital of greater energy, causing electronic

transitions between energy levels. Notably, these transitions result in the absorption of specific wavelengths of light. Some of the most important transitions are observed in **Figure 2.12** and **Table 2.1**¹⁴.

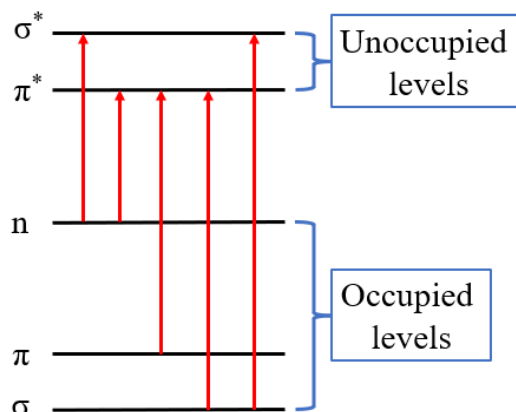


Figure 2.12: Energy level transitions within UV-Vis indicating the occupied and unoccupied orbitals.

Table 2.1: Energy level transitions within UV-Vis analysis with examples of where transitions are commonly found¹⁴.

Transition	Commonly found within
$\sigma \rightarrow \sigma^*$	Alkanes
$\sigma \rightarrow \pi^*$	Carbonyl compounds
$\pi \rightarrow \pi^*$	Alkanes, carbonyl compounds and azo compounds
$n \rightarrow \sigma^*$	Nitrogen, oxygen, sulphur and halogen containing compounds or substituents.
$n \rightarrow \pi^*$	Carbonyl compounds

The absorption spectrum generated displays characteristic peaks and troughs, with each peak corresponding to a specific electronic transition. The intensity of these peaks relates to the concentration of the absorbing species. Additionally, the position of the peaks provides information about the nature of the electronic transitions, contributing to the identification of compounds. Within this work 2nd derivative spectroscopy was used to enhance the resolution of the UV-Vis spectrum. By analysing the second derivative of the absorption spectrum, subtle features and overlapping peaks can be more clearly distinguished. This refinement enables a more detailed examination of the electronic

transitions, providing a higher level of precision in identifying compounds and understanding their electronic structures¹⁵.

2.4.5 Infra-Red Spectroscopy (IR)

Infrared (IR) spectroscopy is a technique that measures the vibrational motions of atoms around their connecting bonds when excited by electromagnetic radiation from the IR region of the electromagnetic spectrum. In IR spectroscopy, atoms are not subject to electronic transitions as IR photons lack sufficient energy for such transitions. However, they possess enough energy to induce vibrational motions within groups of atoms concerning the bonds between them (**Figure 2.13**). As molecules absorb IR radiation at specific frequencies and wavelengths, the resulting vibrations are characteristic of certain energies¹⁶. This characteristic fingerprint provides a means to identify the functional groups and chemical species present in a material. Each group exhibits a unique absorption frequency or band, determined by either the wavelength (λ) or its reciprocal value, wavenumber (cm^{-1}). The frequency of vibrations between two atoms relies on two key factors: the mass of the atoms involved and the rigidity of the bonds between them. Heavier atoms vibrate at slower frequencies than lighter atoms, and stronger bonds, which tend to be more rigid, demand more energy to stretch and/or compress the bonds between them. This leads to the creation of an IR spectrum, resulting in a distinctive and unique fingerprint for each compound¹³.

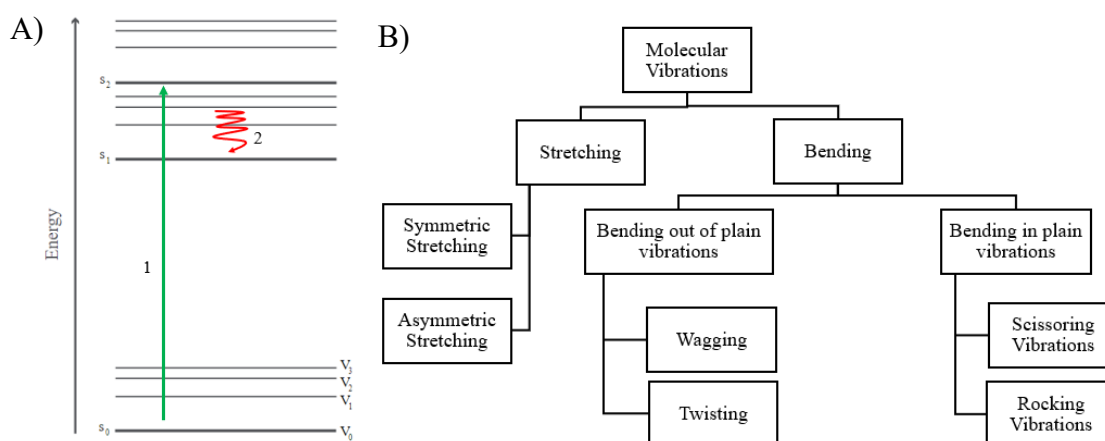


Figure 2.13: A) Simplified Jablonski diagram of 1) promotion of an electron to a higher energy level and 2) the subsequent release of that energy in the form of molecular vibrations with B) a chart of the types of molecular vibrations¹⁴.

2.4.6 *Thermogravimetric analysis*

Thermogravimetric Analysis (TGA) is a thermal analysis technique used to study the mass changes of a material as a function of temperature or time in a controlled environment. This method provides insights into the composition, thermal stability, and decomposition characteristics of a wide range of materials. In a typical TGA experiment, a small amount of the sample is placed in a crucible, and the crucible is subjected to a controlled temperature program. The sample's mass is continuously monitored by a sensitive balance as it undergoes temperature-induced transformations. The temperature is gradually increased, and any changes in the sample's mass is recorded (**Figure 2.14**). The TGA curve obtained displays mass loss or gain as a function of temperature¹⁷. Various thermal events, such as decomposition, oxidation, desorption of volatile components, or phase transitions, can be identified based on the observed weight changes. The onset temperature, peak temperature, and extent of weight change provide crucial information about the material's thermal stability and decomposition kinetics.

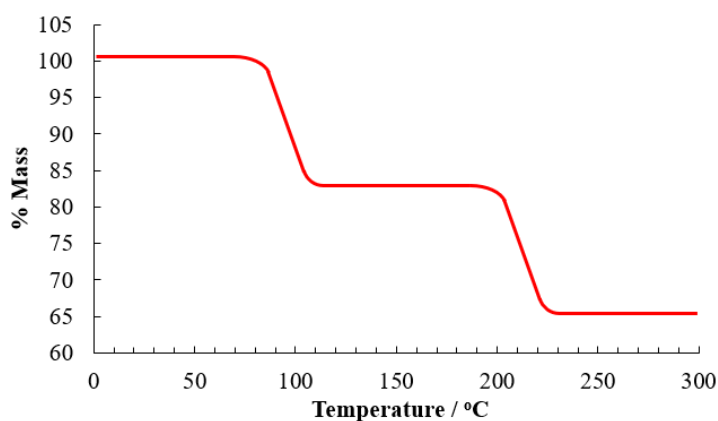


Figure 2.14: Generic example of a TGA thermograph showing a % mass loss with increasing temperature.

2.4.7 *Differential Scanning Calorimetry*

Differential Scanning Calorimetry (DSC) is a technique for observing the thermal properties of materials as they experience temperature variations. In DSC, a small quantity of the sample is deposited in a sample pan alongside a reference pan (inert aluminium/platinum materials) or reference loop. The temperature is then programmed to gradually rise or fall, with the instrument continuously gauging the heat flow disparity between the sample and reference. As the sample undergoes phase transitions or other thermal events, it either absorbs or releases heat. The instrument detects this differential heat flow, constructing a DSC curve that charts heat flow against temperature or time. Peaks or troughs in the curve align with specific thermal events like melting, crystallisation, glass transitions, or chemical reactions. The resultant DSC curve yields valuable insights into the material's thermal behaviour. The position, shape, and area under the peaks provide nuanced information about the energetics of the processes transpiring in the sample. DSC is proficient in delivering quantitative data, encompassing enthalpy changes linked to phase transitions and the heat capacity of the sample¹⁷. The technique aids in comprehending the intricate thermal dynamics of various materials, exploring temperature-induced effects on material behaviour.

2.5 References:

- (1) Brett, C. Fundamentals of Electrochemistry. In *Piezoelectric Transducers and Applications*; Springer Berlin, Heidelberg, 2008; pp. 223–239.
- (2) Holze, R. *Experimental Electrochemistry : A Laboratory Textbook*; John Wiley & Sons, Incorporated: Somerset, 2019.
- (3) Heineman, W. R.; Kissinger, P. T. *Laboratory Techniques in Electroanalytical Chemistry*; M. Dekker: New York ; Basel, 1996.
- (4) Bard, A. J.; Faulkner, L. R.; White, H. S. *Electrochemical Methods*; John Wiley & Sons, 2022.
- (5) Brett, C. M. A.; Vrett, A. *Electrochemistry : Principles, Methods, and Applications*; Oxford University Press: Oxford, 2005.
- (6) Elgrishi, N.; Rountree, K. J.; McCarthy, B. D.; Rountree, E. S.; Eisenhart, T. T.; Dempsey, J. L. A Practical Beginner's Guide to Cyclic Voltammetry. *Journal of Chemical Education* **2017**, *95* (2), 197–206.
<https://doi.org/10.1021/acs.jchemed.7b00361>.
- (7) Wang, J. Fundamental Concepts. In *Analytical Electrochemistry*; John Wiley & Sons, Inc: 1-28, 2006.
- (8) Papavinas, S. Electrochemical Polarization Techniques for Corrosion Monitoring. In *Techniques for Corrosion Monitoring*; Elsevier, 2008; pp. 49–85.
- (9) Mirkin, M. V.; Horrocks, B. R. Electroanalytical Measurements Using the Scanning Electrochemical Microscope. *Analytica Chimica Acta* **2000**, *406* (2), 119–146.
[https://doi.org/10.1016/s0003-2670\(99\)00630-3](https://doi.org/10.1016/s0003-2670(99)00630-3).
- (10) Goldstein, J. I.; Newbury, D. E.; Michael, J. R.; Ritchie, N. .W.M; Scott, J. H. J. Secondary Electrons. In *Scanning Electron Microscopy and X-Ray Microanalysis*; Springer New York, 2018; pp. 29–37.

Chapter 2: Theory Behind Experimental Techniques

- (11) Goldstein, J. I.; Newbury, D. E.; Michael, J. R.; Ritchie, N. W. M.; Scott, J. H. J. Quantitative Analysis: The SEM/EDS Elemental Microanalysis K-Ratio Procedure for Bulk Specimens, Step-By-Step. In *Scanning Electron Microscopy and X-Ray Microanalysis*; Springer New York; pp. 309–399.
- (12) Vickerman, J. C.; Gilmore, I. S. *Surface Analysis : The Principal Techniques*; Wiley: Chichester, U.K., 2009.
- (13) Skoog, D. A.; West, D. M.; Holler, F. J.; Crouch, S. R. *Fundamentals of Analytical Chemistry*, 9th ed.; Brooks/Cole Cengage Learning: Australia, 2014.
- (14) Malhotra, P. *Analytical Chemistry*; Springer Nature, 2023.
- (15) Xu, W.; Yu, H.; Yang, F.; Yang, F.; Liu, D.; Lu, K.; Gao, H.; Song, Y. Second Derivative UV–Visible Spectroscopy Characterizing Structural Components of Dissolved and Particulate Organic Matter in an Urbanized River. *Environmental Sciences Europe* **2022**, *34* (1). <https://doi.org/10.1186/s12302-022-00609-z>.
- (16) Pavia, D. L.; Lampman, G. M.; Kriz, G. S.; Vyvyan, J. R.; Lin, T.-C. *Introduction to Spectroscopy*; Cengage Learning Asia Pte. Ltd: Taipei, 2015.
- (17) Ebnesajjad, S. Surface and Material Characterization Techniques. In *Handbook of Adhesives and Surface Preparation*; Elsevier, 2011; pp. 31–48.

Chapter 3: Electroanalysis of Organic Firearm Residue Species

*Note: Research data within Chapters 3 & 4 directly correlate with two publications produced from the PhD research:

- McKeever, C.; Callan, S.; Warren, S.; Dempsey, E. Magnetic nanoparticle modified electrodes for voltammetric determination of propellant stabiliser diphenylamine. *Talanta* 2022, 238, 123039. <https://doi.org/10.1016/j.talanta.2021.123039>.
 - McKeever, C.; Dempsey, E. Electroanalysis of ethyl-centralite propellant stabiliser at magnetic nanoparticle modified glassy carbon and screen-printed electrodes with extension to forensic firearm residue analysis. *Sensors and Actuators. B, Chemical* 2023, 396, 134604. <https://doi.org/10.1016/j.snb.2023.134604>.
-

3.1 Chapter Aims

The objective of this chapter is to enhance our understanding of the electrochemical behaviour of analytes, DPA and EC, and to observe the effect of MNP-modified electrodes on sensing these molecules. This exploration aids in the development of a suitable method for electrochemically sensing in a real FAR matrix.

3.2 Introduction

As discussed in **Chapter 1**, the organic fraction of firearms residue (OFAR) comprises a complex mixture of species originally present in the propellant formulation and degradation products, produced after the firing event. The firearms residue (FAR) contains burnt and unburnt particles from the primer/propellant. The inorganic fraction typically includes Ba, Sb, and Pb particles, while the organic fraction consists of burnt or unburnt particles containing propellants like nitro-glycerine, nitrocellulose, as well as stabilisers such as methyl or ethyl centralite (1,3-diethyl-1,3-diphenylurea (EC)) and diphenylamine (DPA)¹. Decomposition products include N-nitroso diphenylamine, 2-nitrodiphenylamine and 2,4-dinitro-N-ethylaniline² and gunpowder-specific mono-, di-, and trinitro-DPA derivatives. These, along with centralite, as identified, serve as compelling evidence for FAR³. The two main analytes of interest in this work, which exist within the complex matrix of OFAR are DPA and EC.

DPA analysis has garnered attention in both forensic⁴ and environmental^{5,6} contexts in recent years. Primarily employed as a stabilising agent in propellant systems for ammunition, DPA binds to propellant degradation products, thereby extending the shelf life of the ammunition. Additionally, DPA finds common use in preserving harvested apples, preventing a storage disorder known as "scald"^{7,8}. DPA has become more prevalent in recent years as a contaminate of emerging concern with regards to environmental pollution. The European Union first implemented a limit on the use of DPA in 2008 and limits the presence of DPA on nearly all food items to 0.05 mg/kg, implemented from 1st of May 2019⁹. EC appears to have its industrial uses confined to the ammunition industry being used primarily as a propellant stabiliser, which increases the shelf life of the ammunition¹⁰. This specificity makes EC a crucial compound in OGSR analysis.

Chapter 3: Electroanalysis of Organic Firearm Residue Species

Currently, OFAR analysis relies on solid-phase micro-extraction¹¹, often coupled with liquid¹² or gas chromatography^{13,14}. Mass spectroscopy, a pivotal technique^{3,15-17} along with capillary electrophoresis¹⁸ and Raman spectroscopy¹⁹, is integral to the process. However, these methods necessitate expensive, laboratory-confined instrumentation and skilled operators. Although electroanalysis related to the metallic fraction of FAR has been extensively reviewed and reported^{20,21}, there is a notable scarcity of reports on the electrochemistry of these stabilisers and their redox behaviour as mixtures. Bratin and Kissinger implemented an electrochemical detection method coupled with liquid chromatography (LC), where the individual organic components of a OFAR sample were separated through LC and then tested individually at Hg|Au and glassy carbon electrodes (GCE)²². Other examples including FAR, used screen printed electrodes (SPE)²³, as a precursor to confirmation by SEM/EDX while Dalzell et al. reported a comparative study of electrochemical instruments in authentic shooter samples²⁴. Renewed interest as forensically significant target molecules is the incentive behind this work and it is thus an important starting point for the development of an analytical method for the complex array of compounds found in organic component of the residue. Evaluating the redox electrochemistry of DPA and EC at glassy carbon electrodes and examining magnetic nanoparticles (MNP) as electrode modifiers, to aid OFAR detection, is a key goal of research presented in this chapter.

MNP have a wide variety of uses, allowing ease of separation in solution²⁵ while acting as effective electrode modifiers²⁶ with applications in medical imaging²⁷ drug delivery²⁸ biosensing^{29,30} and bioanalytical devices³¹. The latter are the subject of a recent review by Hasanzadeh et al.³². MNP can have particle size ranging 10–50 nm³³ and present different physio/chemical properties compared to their bulk size, due to the size differences. The material has been successfully modified or doped with Cobalt³⁴ and Manganese³⁵, however sensor approaches based on the unmodified form have received little attention. Among these materials, magnetite (Fe₃O₄), a Fe²⁺ and Fe³⁺ complex oxide, is one of the most commonly studied super-paramagnetic nanoparticles, being widely used in magnetic resonance imaging contrast enhancement, tissue specific release of therapeutic agents³⁶, in addition to *in vitro* binding of proteins and enzymes³⁷.

3.3 Experimental

3.3.1 *Materials and Reagents*

Ethanol (anhydrous $\geq 99.5\%$), Methanol (ACS Reagent, 99.8%), diphenylamine (ACS Reagent $\geq 99\%$), 1,3 diethyl-1,3 diphenyl urea (ACS Reagent $\geq 99\%$), acetic acid (ACS Reagent $\geq 95.0\%$), lithium perchlorate (ACS Reagent $\geq 95.0\%$) were all purchased from Sigma-Aldrich and required no further purification. Electrode polishing solution was a 1 μm monocrystalline diamond suspension (Akasol). The sacrificial iron anode and cathode rods ($3 \times 12 \text{ cm}^2$) were purchased from Goodfellow (purity 99.5%). Rare earth neodymium magnets (grade N35) were purchased from Farnell. A glassy carbon electrode (GCE) (3 mm disk 0.0706 cm^2) (IJ Cambria Scientific) served as the working electrode, while platinum wire and a standard Ag/AgCl electrode (internal solution 3 M KCl) were employed as the counter and reference electrodes, respectively. The Ag/AgCl reference electrode was stored in 3 M KCl when not in use. A non-aqueous reference electrode was prepared using silver nitrate (10 mM) and lithium perchlorate (0.1 M) in methanol/acetonitrile.

3.3.2 *Instrumentation and Software*

The surface morphology of the magnetic nanoparticles was measured using SEM (Hitachi SU-70 FE-SEM with Oxford instruments X-max 50 mm² solid-state detector performed by Susan Warren at the CREST centre within the Technological University of Dublin. XRD was performed by Wynette Redington at University of Limerick using a PANalytical Empyrean-reflection instrument. ATR was performed on a Thermo Scientific iS50 ATR. Thermal analysis was performed using a PerkinElmer STA 6000 DSC/TGA analyser. All electrochemical experiments were carried out using the Solartron Potentiostat Model 1285 operated by Scribner Associates CorrWare software package with data analysis using CorrView Version 2.3a. An IR lamp was used to dry the magnetic nanoparticle suspensions on GCEs and a ThermoFisher thermostatic oven was used for drying the magnetic nanoparticles following preparation. UV-Vis studies were performed using a PerkinElmer Lambda 35 UV/VIS Spectrophotometer, and a spectroelectrochemical (SEC) cell (Path length 0.1 cm) with platinum gauze working electrode (geometric area 0.96 cm^2).

3.3.3 *Procedures*

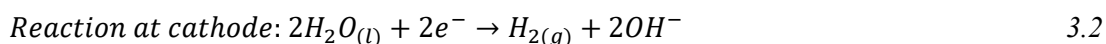
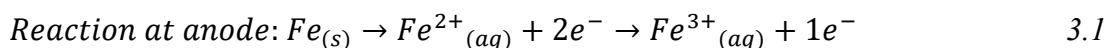
3.3.3.1 Electrochemical procedures

All aqueous electrochemical methods were carried out using a standard Ag|AgCl reference electrode with an internal filling solution of 3 M KCl. Therefore, all quoted potentials are + 0.197 V vs. the standard hydrogen electrode unless otherwise stated. After brief solubility studies varying the ratios, the aqueous electrolyte employed was 0.1 M LiClO₄ in methanol and sodium acetate buffer solution pH 4.5 (30:70) (37 mL sodium acetate (0.1 M) and 63 mL acetic acid (0.1 M) realised a solution of pH ~ 4.5) while the non-aqueous electrolyte was 0.1 M LiClO₄ in methanol and acetonitrile (50:50). Linear sweep (LSV) & Cyclic voltammetry (CV) was performed over the relevant potential range with bare and modified GCEs used as working electrode. Differential pulse voltammetry (DPV) was performed at bare and modified GCEs in supporting electrolyte with initial potential -1 V final potential 1.5 V, incremental potential 0.004 V, amplitude 0.05 V, pulse width 0.05 s, sample width 0.0167 s, pulse period 0.5 s. The working electrodes were prepared by polishing with monocrystalline diamond suspension (1.0 μm), followed by an ethanol and subsequent deionised water rinse, followed by drying with compressed air.

3.3.3.2 Synthesis of Magnetite Particles

The facile electrochemical preparation of magnetic iron oxide nanoparticles was achieved via electrooxidation of an iron anode in the presence of an amine surfactant pH 5.7 (adapted from method by Cabrera et al.³⁸ and Rahimdad et al.³⁹). The sacrificial iron anode and cathode rods (99.5% purity) were first polished mechanically using sandpaper to remove impurities, then transferred into a water/ethanol mixture (50:50 v/v) followed by ultrasonication for 20 min to ensure no further impurities were present. A potential of 5 V was applied for 1800 s in 0.04 M tetramethylammonium chloride as electrolyte/capping agent with temperature control using a water bath held at 60 °C. The interelectrode spacing was 8 mm (edge to edge) using a 9.4 mm diameter iron anode and cathode with immersion depth 3 cm (see **Figure 3.1**). During the electro-synthetic process, the solution changed from yellow to brown with eventually a black precipitate forming according to the processes below:

Chapter 3: Electroanalysis of Organic Firearm Residue Species



Total reaction in two steps:

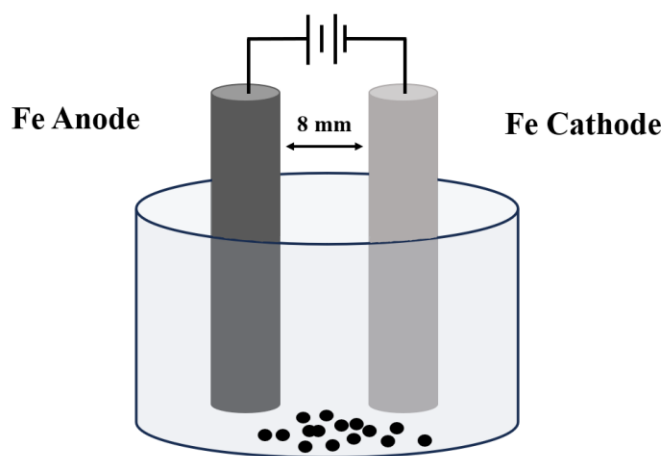
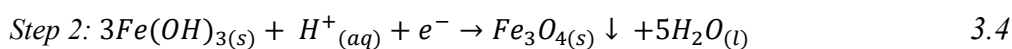
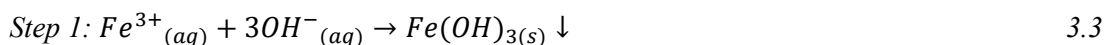
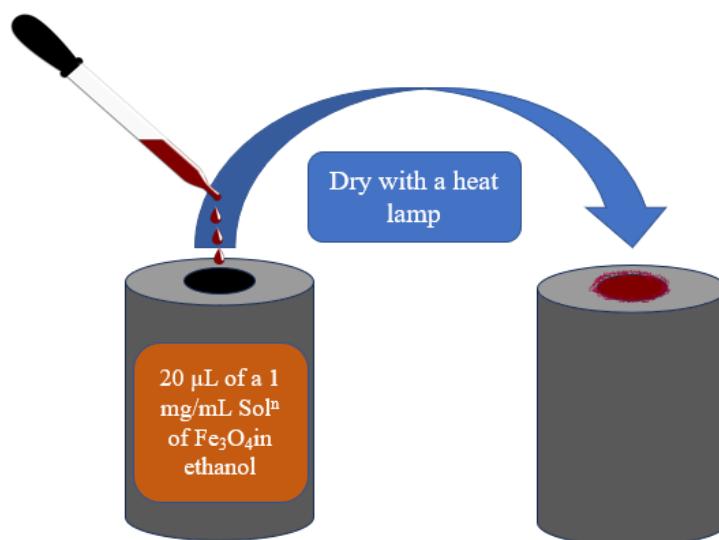


Figure 3.1: Representation of iron anode and cathode rods immersed in tetramethylammonium chloride with electrochemical formation of Fe_3O_4 upon application of 5 V for 30 min at 60 °C.

The MNPs were allowed to settle in the solution (aided by neodymium magnets of grade N35), decanted and washed with water three times, followed by three ethanol rinses. This process was repeated until the supernatant was clear with a final ethanol wash. The particles were collected and allowed to dry in an oven at 80 °C for 3 h followed by suspension in ethanol at 1 mg.mL⁻¹.

3.3.3.3 Electrode Modification

A polished GCE was rinsed with ethanol and allowed to dry under an IR heat lamp. The magnetite suspension (1 mg.mL⁻¹ in ethanol) was sonicated to ensure an even dispersion of particles and drop casted onto the electrode surface in 5 × 20 μL increments with drying in between with loading at 1.416 mg.cm⁻². Lower loadings (2 × 20 μL) resulted in poor signal and surface stability.



Scheme 3.1: Typical example for a single step of drop cast modification of macroelectrode using a solution of $1 \text{ mg}\cdot\text{mL}^{-1}$ magnetite based MNP suspended in ethanol.

3.3.3.4 Spectroelectrochemistry UV-Vis Studies

A platinum gauze electrode was electrochemically cleaned in $0.5 \text{ M H}_2\text{SO}_4$ by cycling for 20 cycles at $200 \text{ mV}\cdot\text{s}^{-1}$ followed by mechanical polishing using $1 \text{ }\mu\text{m}$ monocrystalline diamond suspension. Film formation for study utilised the spectroelectrochemical cell (**Figure 3.2**) over the potential range -1 to 1 V at $100 \text{ mV}\cdot\text{s}^{-1}$ for 100 cycles in the aqueous electrolyte in the presence of 1 mM DPA . Both the modified electrode and the solution remaining following deposition were analysed by UV-Vis spectroscopy over the range $200\text{--}700 \text{ nm}$.

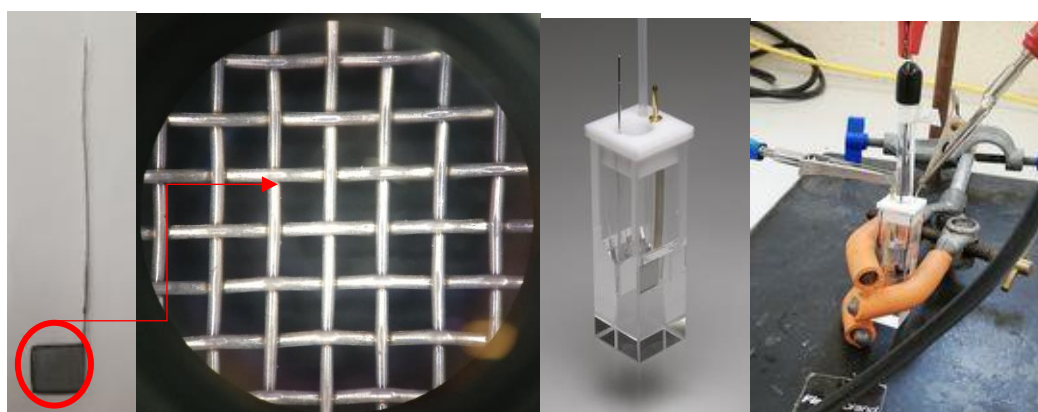


Figure 3.2: Equipment for spectroelectrochemistry. From left to right, platinum mesh electrode, magnified image of mesh, spectroelectrochemical quartz cuvette used and an in-situ image of equipment.

3.3.3.5 Surface Analysis

Scanning electron microscopy (SEM) was performed by Susan Warren in Technological University Dublin and employed for particle size and morphology was analysis using a Hitachi SU-70 FE-SEM from a 1 mg/mL MNP sample in ethanol. Average particle size was determined based on measurement of 100 particles.

3.4 Results and Discussion

3.4.1 Optimisation of Electrochemical Synthesis for Magnetic Nanoparticle Formation

Iron based magnetic nanoparticles (MNP) have been utilised in a variety of systems to enhance electrochemical sensing capabilities⁴⁰⁻⁴³. One such method of MNP preparation was developed by Cabrera et al.³⁸. This work builds on this method and considers further optimisation of the conditions for MNP production including, the impact of temperature (45 °C, 60 °C, and 75 °C) at 5 V (for 30 minutes), and a subsequent study of applied potentials (1 V, 2.5 V, and 5 V) at 60 °C (for 30 minutes) investigated during the electrochemical preparation process.

3.4.1.1 Effect of Temperature during electrochemical synthesis of MNP

The temperature of the water bath was adjusted during the electrosynthesis process (45, 60 and 75 °C). E_{app} of 5 V was consistent throughout the study however, the temperature of the bath was set to 15 °C above and below the temperature stated in the literature³⁸. In **Figure 3.3** the effect of temperature of the solution on current density alone is clear (area = 8.47 cm²), with an observed increase in temperature resulting in an increase in current density. **Table 3.1** shows the initial, maximum and final current densities achieved during the experiment.

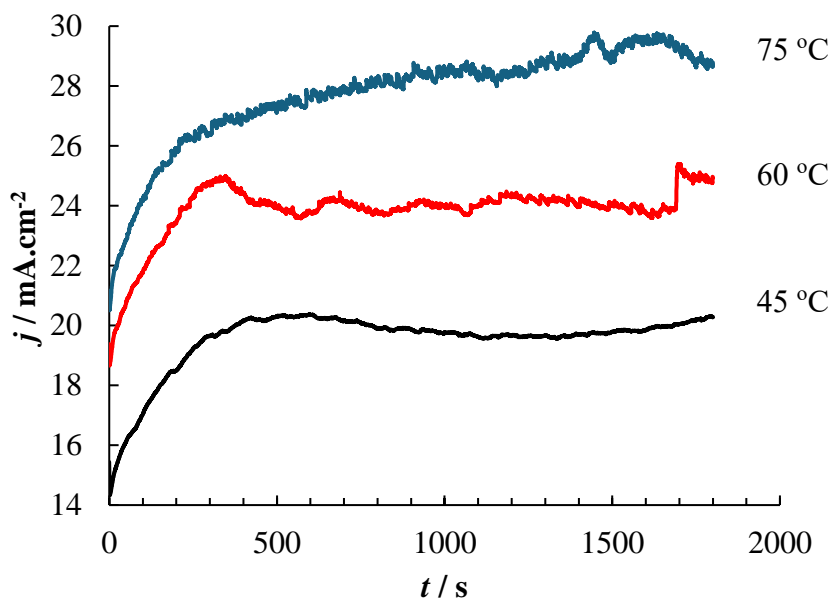


Figure 3.3: Current-time response at $E_{app} = +5 V$ for 1800 s, at three different temperatures of 45 °C (black), 65 °C (red) and 75 °C (blue), showing the process of MNP production at an iron cathode in 0.04 M tetramethylammonium chloride (typical trace).

Table 3.1: Current density values throughout temperature study during MNP formation ($n=2$).

Temperature (°C)	Starting Current Density (mA.cm ⁻²)	Maximum Current Density (mA.cm ⁻²)	Final Current Density (mA.cm ⁻²)
45	15.4	20.3 @ 417 seconds	20.3
60	19.4	25.2 @ 1705 seconds	24.9
75	21.1	29.7 @ 1646 seconds	28.8

Figure 3.4 displays the IR spectra for the material produced at different temperatures. The purple region highlighted, indicates a response for the Fe-O bond observed within the material (517 cm⁻¹ at 45 °C, 554 cm⁻¹ at 60 °C and 535 cm⁻¹ at 75 °C) with literature values of 572 and 377 cm⁻¹ being attributed to Fe-O vibrations⁴⁴. Responses observed from material generated at 45 and 75 °C showed an area of high response across the range of 1600 to 750 cm⁻¹, indicating remaining material from the tetramethyl ammonium chloride with C-H from methyl groups evident around 1450 cm⁻¹, along with O-H bending across the range of 1420 to 1330 cm⁻¹. The material generated at 45 °C also had a much more apparent O-H response at 3190 cm⁻¹ indicating hydroxide formation or presence within the material.

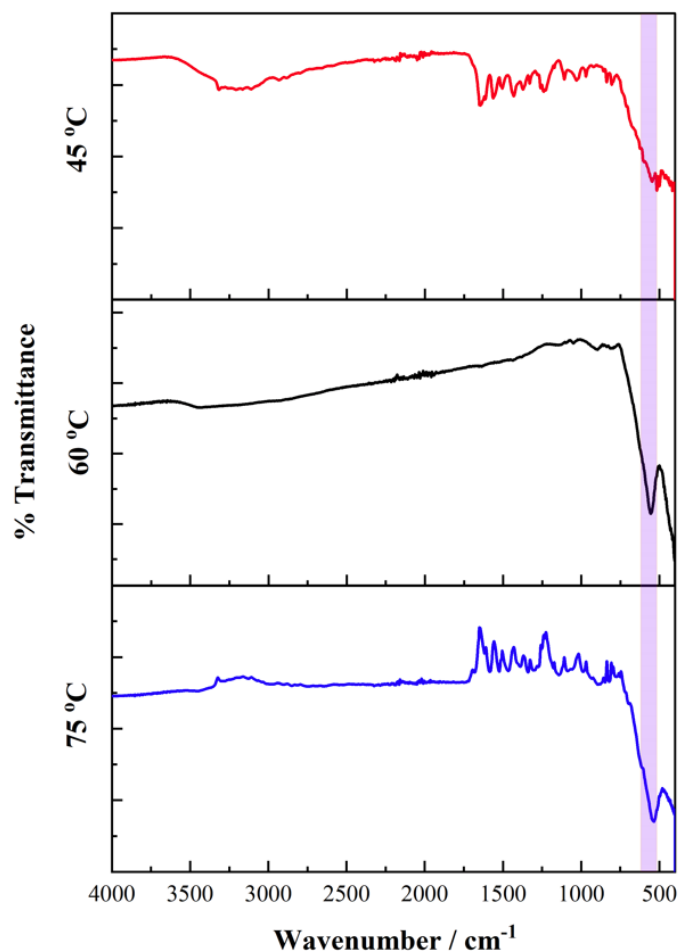


Figure 3.4: IR spectra for the MNP material produced at $E_{app} = +5$ V for 1800 s held at temperatures of 45, 60 and 75 °C during electrochemical synthesis, highlighting the region (purple) which the Fe-O bond is found (approximately 570 cm^{-1}).

The spectra observed from the material generated at 60 °C appeared to have far less peaks within it, indicating less contamination than the other temperatures examined. This was matched in the necessity for additional cleaning cycles of water and subsequent ethanol washes of the materials generated at 45 and 75 °C to obtain black material free from orange/red impurities. This indicated that Fe was present at higher than desired oxidation states and that a different form of iron oxide, maghemite [Fe_2O_3], was formed during the process as opposed to the desired magnetite [Fe_3O_4]. To further understand optimisation of the methodology the applied potential was then varied.

3.4.1.2 Effect of Applied Potential During Electrochemical Synthesis of MNP

Figure 3.5 illustrates the current vs. time response observed during MNP electrochemical formation under three applied potential conditions, displaying a gradual stabilisation of the current over the 30-minute electrosynthesis period. As expected, the increase in the applied potential resulted in an increase in the current density at the iron electrode. An E_{app} of 1 V and 2.5 V resulted in a much smoother j ($\text{mA}\cdot\text{cm}^{-2}$) vs. time plot (**Figure 3.5**) compared to that of 5 V. Data within **Table 3.2** also indicates the stability of the current density across the time period employed. The highest current densities at $E_{app} = 1$ V and 2.5 V observed as the final measurements, while $E_{app} = 5$ V resulted in the highest value 95 seconds before the experiment was completed. Product yields also varied with applied potentials with 98 mg, 254 mg, and 141 mg obtained for 1, 2.5 and 5 V respectively.

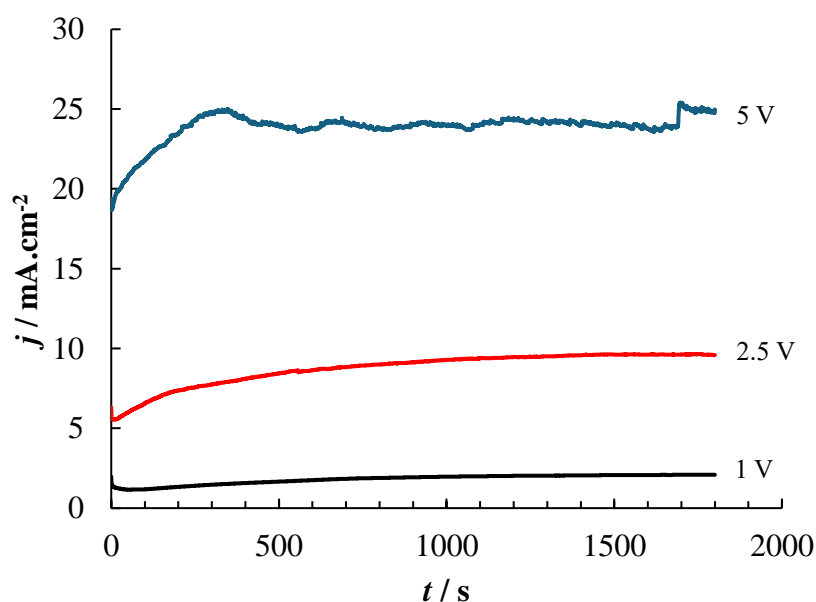


Figure 3.5: Current-time response at held potentials of $E_{app} = +1$ V (black) , $+2.5$ V (red) and $+5$ V (blue) for 1800 s, at 60°C , observing the process of MNP production at an iron cathode in 0.04 M tetramethylammonium chloride (typical trace).

Chapter 3: Electroanalysis of Organic Firearm Residue Species

Table 3.2 Current density values at Fe anode throughout the applied potential study of MNP formation ($n=2$).

Applied Potential (V)	Starting Current Density (mA.cm⁻²)	Maximum Current Density (mA.cm⁻²)	Final Current Density (mA.cm⁻²)
1	1.98	2.10 @ 1800 seconds	2.10
2.5	6.31	9.60 @ 1800 seconds	9.60
5	19.4	25.21 @ 1705 seconds	24.9

FTIR spectroscopy was used once more to obtain information about the nature of surface hydroxyl groups and adsorbed water (**Figure 3.6**). Hydroxylation of iron oxides is followed by further adsorption of water molecules which interact via H bonding to the surface OH groups. Tertiary amine C–N stretch 1125 cm^{-1} ($1250\text{--}1020\text{ cm}^{-1}$)⁴⁵, intermolecular bonded O–H stretching 3409 cm^{-1} ($3550\text{--}3200\text{ cm}^{-1}$)⁴⁵ and OH bending vibration 1636.8 cm^{-1} (1652.88 cm^{-1})⁴⁵ were evident. The characteristic vibrational bands of pure Fe₃O₄ mainly appeared at 561 and 421 cm^{-1} (literature values of 572 and 377 cm^{-1} being attributed to Fe–O vibrations, and those at 422 and 611 cm^{-1} ascribed to Fe–O bending vibrations of Fe₃O₄⁴⁴.

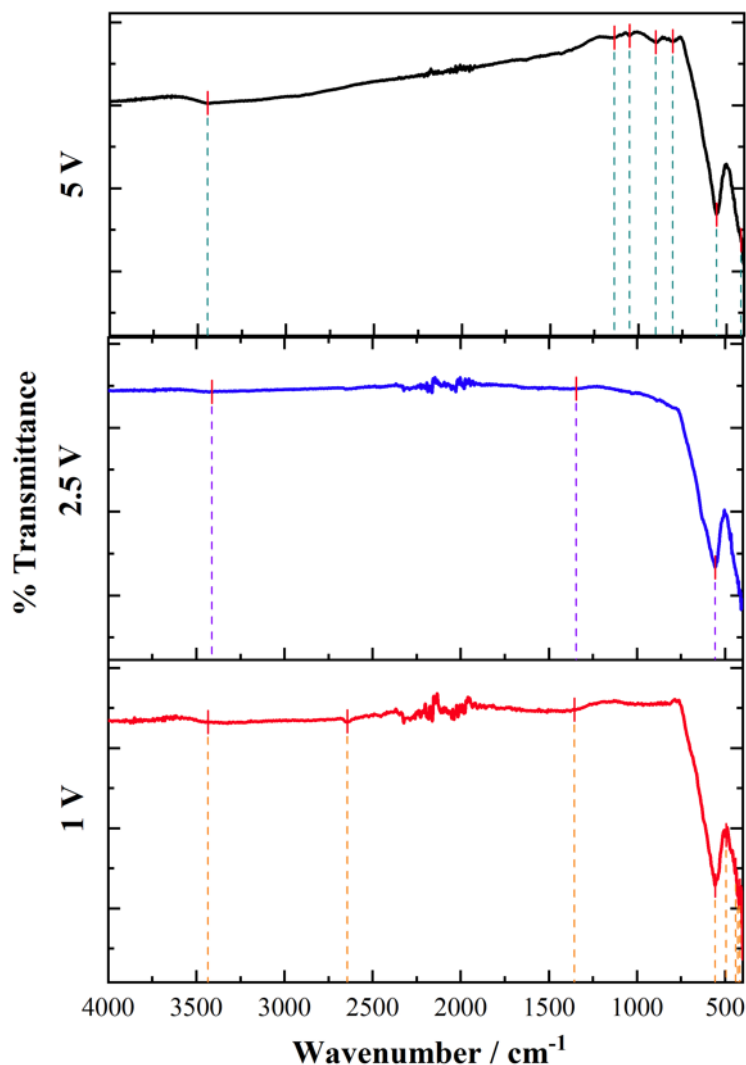


Figure 3.6: IR spectra for the MNP material produced at $E_{app} = +1, +2.5$ and $+5$ V while being heated at 60°C , highlighting peaks of interest with dropped dotted lines.

Scanning electron microscopy (SEM) and energy dispersive spectroscopy (EDS) together provided information regarding morphology and elemental composition of the MNP with micrometric sized aggregates of the nanoparticles evident. SEM images (**Figure 3.7**) confirm the nanoparticle size and spherical nature of particles prepared using application of 1, 2.5 and 5 V for 30 min at 60°C with median distribution plot (**Figure 3.7 (E)**) and average values 55.1 ± 16.0 , 49.6 ± 13.7 and 50.7 ± 12.4 nm respectively (**Table 3.3**). The nanomaterial prepared from 5 V resulted in relatively tighter size distribution.

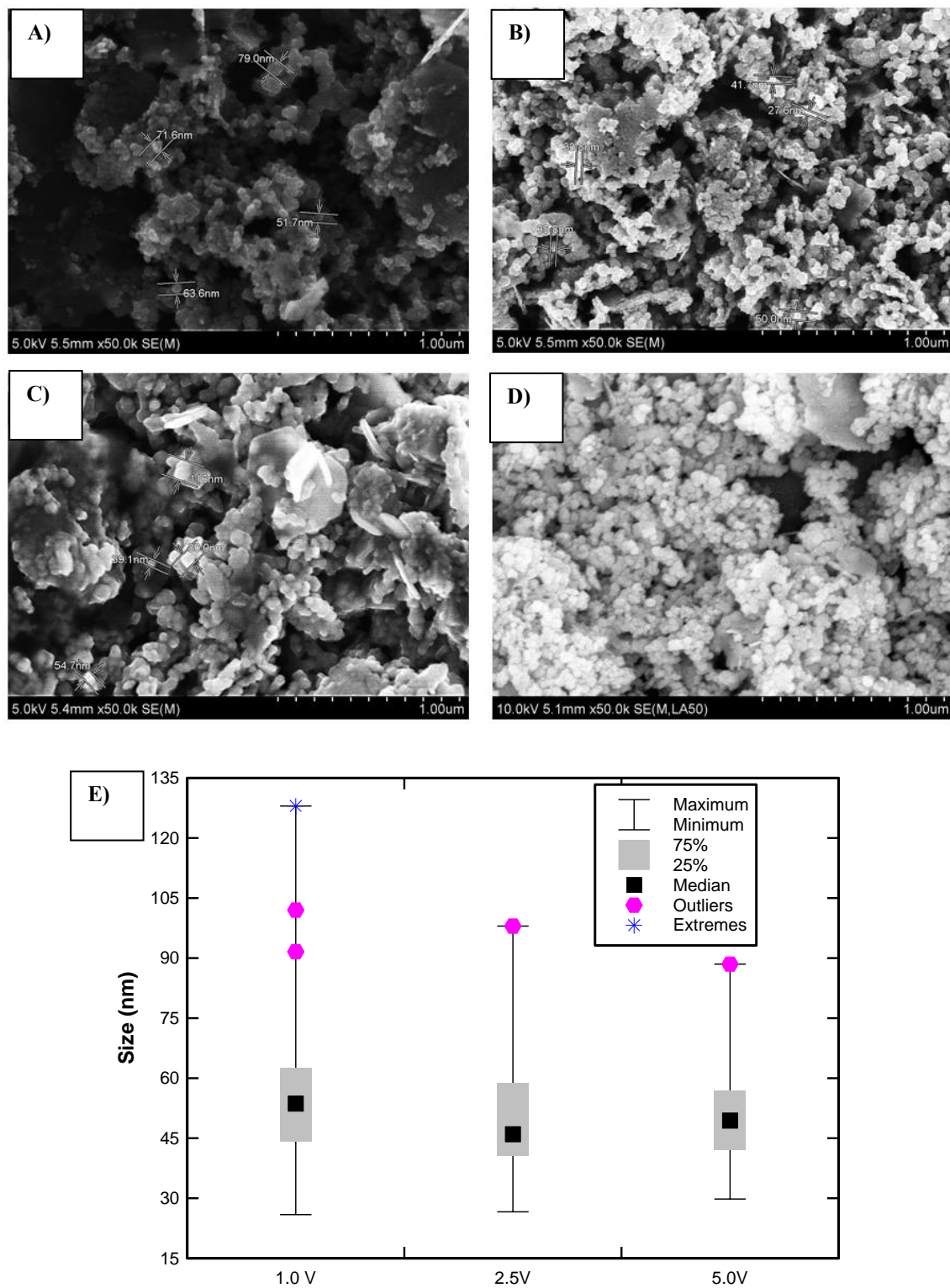


Figure 3.7: High resolution SEM images of MNP electrosynthesis via application of A) 1 V, B) 2.5 V and C & D) 5 V. With E) a particle size distribution based on 100 particles (1 V), 50 particles (2.5 and 5 V) samples.

Chapter 3: Electroanalysis of Organic Firearm Residue Species

Table 3.3: Average particle size of MNP prepared via electrosynthesis.

	1 V	2.5 V	5 V
Average (nm)	55.1	49.6	50.7
Standard Deviation	16.0	13.7	12.4
Max (nm)	128.0	98.0	88.5
Min (nm)	25.9	26.6	29.8

Elemental identification was in agreement with the synthetic composition. EDS spectra (**Figure 3.8**) for each material were normalised by oxygen stoichiometry resulting in 75.4 Fe: 23.3 O (1 V MNP), 75.5 Fe:23 O (2.5 V MNP) and 77.1 Fe: 22.5 O (5 V), which are in good agreement with the theoretical atomic mass ratio for Fe₃O₄ (72.4 Fe:27.6 O) (with standard deviations of ± 1.70 for Fe and ± 2.00 for O).

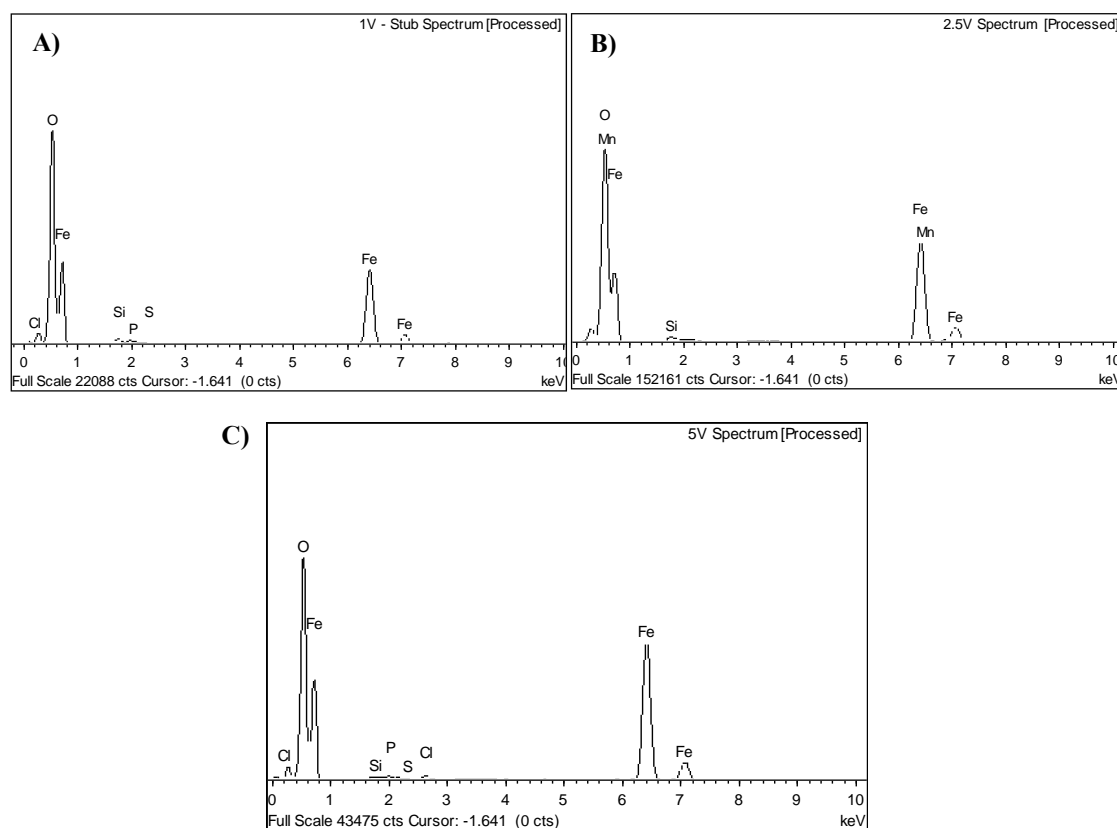


Figure 3.8: EDX spectrum confirming Fe and O atomic composition from A) 1 V, B) 2.5 V and C) 5 V preparations.

Given that the more uniform particle size distribution was the key difference between the generated material with different applied potentials, $E_{app} = 5$ V at 60 °C was employed henceforth.

3.4.1.3 Thermal Analysis of Magnetic Nanoparticles

Thermogravimetric analysis (TGA) and differential scanning calorimetry (DSC) (**Figure 3.9**) (30–640 °C) were employed to assess the thermal stability of the MNP, a characteristic influenced by grain size and the synthetic process⁴⁶. The initial mass variation loss (**Red curve, Figure 3.9.**) may be due to an overlap of the exothermic process of H₂O and surface –OH group elimination with an exothermic DSC change (**Blue curve, Figure 3.9**) at 100 °C followed by the oxidation of Fe(II) to Fe(III) as magnetite [Fe²⁺Fe³⁺]₄O₄ changes to maghemite γ Fe₂³⁺O₃. The second DSC exothermic (oxidation) signal was a weak process at 290.39 °C and finally an endothermic event at 606.74 °C ($\Delta H = -4.157$ J g⁻¹) occurred close to the upper temperature limit of the sample crucible employed. Across the range 170–650 °C the overall mass loss was 2.05%, below that of the theoretical 3.1% expected for conversion of magnetite to maghemite.

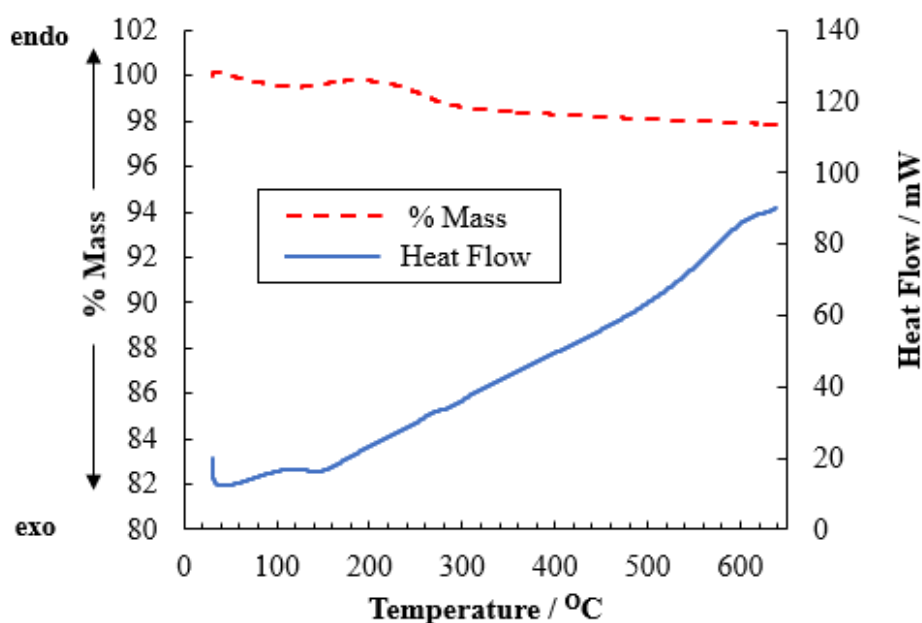


Figure 3.9: Plots of thermogravimetric (red-dash) and differential scanning calorimetry (blue-solid) data of a 12.35 mg Fe₃O₄ sample (generated at $E_{app} = +5$ V at 60 °C) in air at a flow rate of 10 ml.s⁻¹ with a temperature programme with an initial hold of 30 °C for 1 minute and an increasing ramp of 30 °C to 600 °C at 5 °C.min⁻¹ (typical trace shown).

3.4.1.4 X-Ray Diffraction Analysis of Magnetic Nanoparticles

X-Ray diffraction analysis (XRD) (**Figure 3.10**) was performed with broadening peaks visible, indicating small crystallites with characteristic peaks matching well with literature values^{47,48} for 220, 311, 400, 511 and 440 (**Table 3.4.**) crystal planes of Fe₃O₄ spinal face centred cubic crystal structure⁴⁹, with both Fe²⁺ and Fe³⁺ occupying octahedral sites and Fe³⁺ tetrahedral sites.

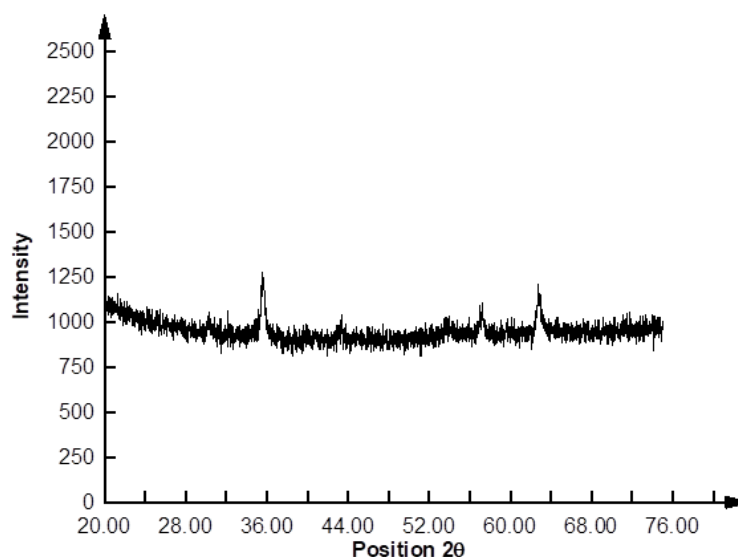


Figure 3.10: X-ray diffraction pattern of MNP generated from an electrosynthetic method of $E_{app} = +5$ V at 60 °C for 1800 s in 0.04 M tetramethylammonium chloride.

Table 3.4: XRD data for Magnetite MNP.

<i>Pos.</i> [°2θ]	Crystal planes	d-spacing [Å]	FWHM [°2θ]	Left	Rel. [%]	Int.	Matched by*
30.2655	220	2.95	0.4015		19.18		01-084-
35.6951	311	2.51	0.2676		65.78		01-084-
43.2728	400	2.09	0.4015		14.71		01-084-
57.1870	511	1.61	0.4015		22.87		01-084-
62.8044	440	1.47	0.3346		43.95		01-084-

* Matched against the International Centre for Diffraction Data database PDF-4 database

Phase identification of magnetite and maghemite (γ -Fe₂O₃) is challenging, as both have the same cubic structure with close lattice parameters⁵⁰. However, XRD analysis further confirms the generation of Fe₃O₄ based MNP in line with literature values.

3.4.1.5 Electrochemical investigation of MNP modified GCE.

Figure 3.11 shows voltammograms of the bare and modified GCEs (as described in section 2.2.3) examined in 0.1 M KCl, over the potential range -1 to $+1$ V vs. Ag|AgCl at $50 \text{ mV}\cdot\text{s}^{-1}$. **Figure 3.11 (A)** shows CVs for electrodes modified with MNP synthesised at different applied potentials, while **Figure 3.11 (B)** examines the redox properties of the materials prepared under different temperatures. Hydrogen adsorption/desorption was evident in all cases between -0.5 and -1.0 V which corresponds to literature⁵¹. An irreversible anodic wave was observed at 1.0 V vs Ag|AgCl. During a cathodic scan, it has been shown that Fe_3O_4 can undergo dissolution with release of Fe^{2+} which can be electrochemically re-oxidised (1.0 V vs Ag|AgCl in this electrolyte) with this process more evident at lower pH, and dependent on both the presence of oxygen in solution and the cathodic potential limit. Further studies focused on use of methanol/sodium acetate buffer (3:7) as electrolyte to provide compatibility with the optimum DPA dissolution solvent and more clearly defined Fe^{2+} reoxidation signals.

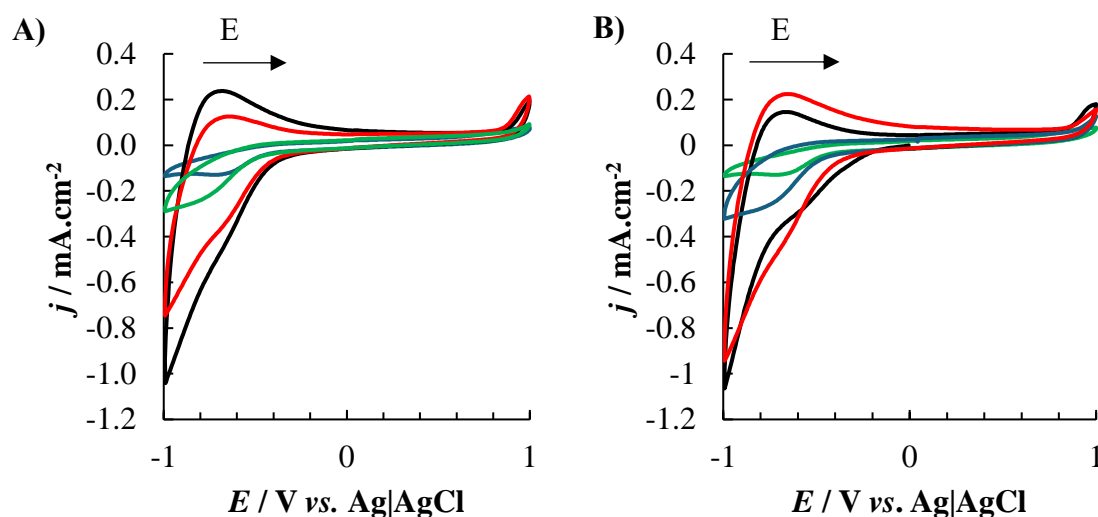


Figure 3.11: Cyclic voltammogram (showing cycle 3) of MNP modified GCE and bare electrode over the potential range -1 to $+1$ V vs. Ag|AgCl at $50 \text{ mV}\cdot\text{s}^{-1}$ in 0.1 M KCl including A) modification material generated at different potentials, showing bare GCE (green), 5 V MNP modified GCE (blue), 2.5 V MNP modified GCE (red), and 1 V MNP modified GCE (black). And B) with modification material generated at different temperatures showing bare GCE (green), MNP modified GCE with material generated at 60 °C (blue), 75 °C (red) and 45 °C (black) (typical traces throughout).

Cyclic voltammetry of bare and modified electrodes was performed in aerated, and nitrogen bubbled degassed aqueous electrolyte (in methanol/sodium acetate buffer (3:7)) (Figure 3.12) ($n=1$). The black trace representing the MNP modified GCE in aerated electrolyte (Figure 3.12 (A)) resulted in a strong irreversible redox process at $E_p^a = 0.5$ V (I) with small reduction wave at $E_p^c = 0.0$ V (II) vs. Ag|AgCl. This was thought to represent re-oxidation of Fe^{2+} released from $[Fe^{2+}Fe_2^{3+}]O_4$ following the cathodic sweep and the signal was suppressed in degassed electrolyte (Figure 3.12 (B)). It has been shown previously that this anodic peak increased upon addition of Fe^{2+} to the cell and was found to be pH dependent⁴⁸.

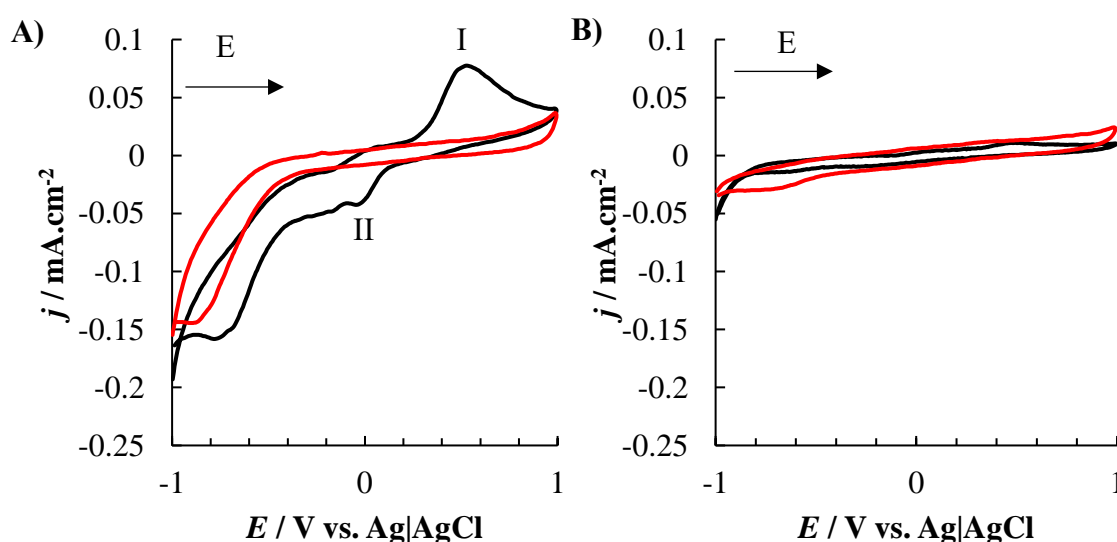


Figure 3.12: Cyclic voltammograms (showing cycle 3) over the potential range -1 to $+1$ V vs. Ag|AgCl at 50 mV.s^{-1} in 3:7 methanol:sodium acetate buffer ($\text{pH} \sim 4.5$) of bare (black) and MNP modified (red) GCE in A) aerated and B) degassed solutions (typical traces).

Figure 3.13 shows the influence of the cathodic limit on this anodic process with no couple evident when swept from 0.0 V (Blue Trace) and a weak process following -0.5 V (red trace), indicating that the -1.0 V (black trace) cathodic limit was required to register this anodic process (I).

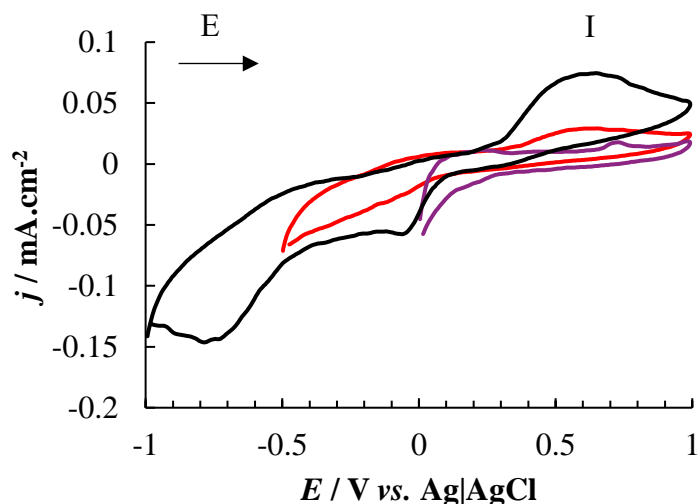


Figure 3.13: Cyclic voltammograms (showing cycle 3) of MNP modified GCE showing the influence of cathodic potential limit on MNP redox behaviour (typical traces). Potential ranges 0 to 1 V (blue), -0.5 to +1 V (red) and -1 to +1 V (black) vs. Ag|AgCl at a scan rate of 50 mV.s⁻¹ in 3:7 methanol:sodium acetate buffer (pH ~4.5) (typical traces).

Figure 3.14 shows a scan rate study (20–200 mV.s⁻¹) of the MNP modified GCE resulting in a linear relationship ($r^2 = 0.993$) between current taken at 0.6 V and scan rate with slope of $1.01 \times 10^{-3} \text{ A.cm}^{-2} \cdot \text{V}^{-1} \cdot \text{s}$ resulting in a surface coverage value of $1.08 \times 10^{-9} \text{ mol.cm}^{-2}$ using the relationship below (**Equation 3.5**⁵²) for a one electron surface confined species. A plot of current vs. square root scan rate showed linearity (up to 0.3 V.s⁻¹) indicating a mixed diffusional system, correlating with the concept that Fe²⁺ release diffuses to the electrode for re-oxidation at 0.5 V vs. Ag|AgCl. Log current vs. log scan rate plots resulted in a slope of 0.82 over the range 0.05–0.5 V.s⁻¹ which was more typical of an adsorbed species (slope 1.0). The magnetite layer exhibited capacitance of $2 \times 10^{-4} \text{ F.cm}^{-2}$ which was 3.3 times that of the electric double layer capacitance, being in line with recent literature⁵³.

$$I_p = \frac{n^2 F^2}{4RT} A \nu \Gamma$$

3.5

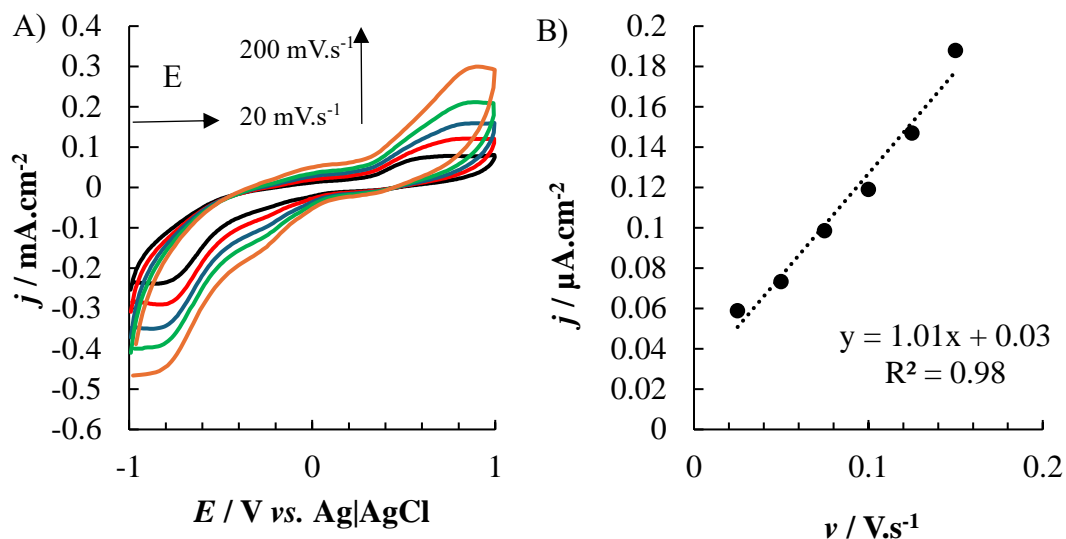


Figure 3.14: A) Cyclic voltammograms (showing cycle 3) over the potential range of -1 to +1 V vs. Ag|AgCl for a scan rate study for MNP modified GCE using scan rates from 20 to 200 mV.s⁻¹ in 3:7 methanol:sodium acetate buffer (pH ~4.5)(typical traces). B) Corresponding plot of current density vs. scan rate using data from (A) (n=2).

A stability study was performed by cycling the modified electrode over the range -1 to +1 V vs. Ag/AgCl for 40 cycles in 3:7 methanol:sodium acetate buffer at 100 mVs⁻¹. A continuous decrease in current was evident (data not shown) which possibly reflects a transformation process upon cycling resulting in lower Fe²⁺ release following the first reduction step. The experiment was repeated following addition of 20 μL of 1% Nafion to the MNP layer in an attempt to improve stability; however similar reduction in the main redox process was evident with a 96% loss of the initial current after 20 cycles at 100 mVs⁻¹. The lower potential limit was required in order to visualise impact on the anodic process (Fe²⁺/Fe³⁺) to the detriment of the signal. The electrocatalytic effect of the surface confined material was thought to be intact despite these surface alterations

3.4.2 *Electrochemical Analysis of Diphenylamine*3.4.2.1 *Voltammetric Investigations*

Non-aqueous electrochemistry of diphenylamine was examined in methanol:acetonitrile (1:1) in 0.1 M LiClO₄ over the concentration range 0.05–1 mM at 50 mV.s⁻¹ (**Figure 3.15 (A)**). The anodic peak at E_p^a 0.6 V (I) corresponded to the one electron oxidation of the aromatic amine resulting in diphenylamine radical cation formation (stabilised in resonance forms) with recombination resulting in formation of a diphenylbenzidine dimer (DPB). Dimerisation occurs via C–C addition in the para position (**Scheme 3.3**) and the DPB species itself was electroactive displaying a weak oxidation ($E_p^a = 0.45$ V) and reduction process ($E_p^c = 0.3$ V) being most evident at higher concentrations^{50,54}. A plot of j vs. concentration DPA (**Figure 3.15 (B)**) was linear (0.05–1 mM) based on the main anodic process at 0.65 V with sensitivity 0.374 mA.cm⁻².M⁻¹ ($r^2 = 0.996$).

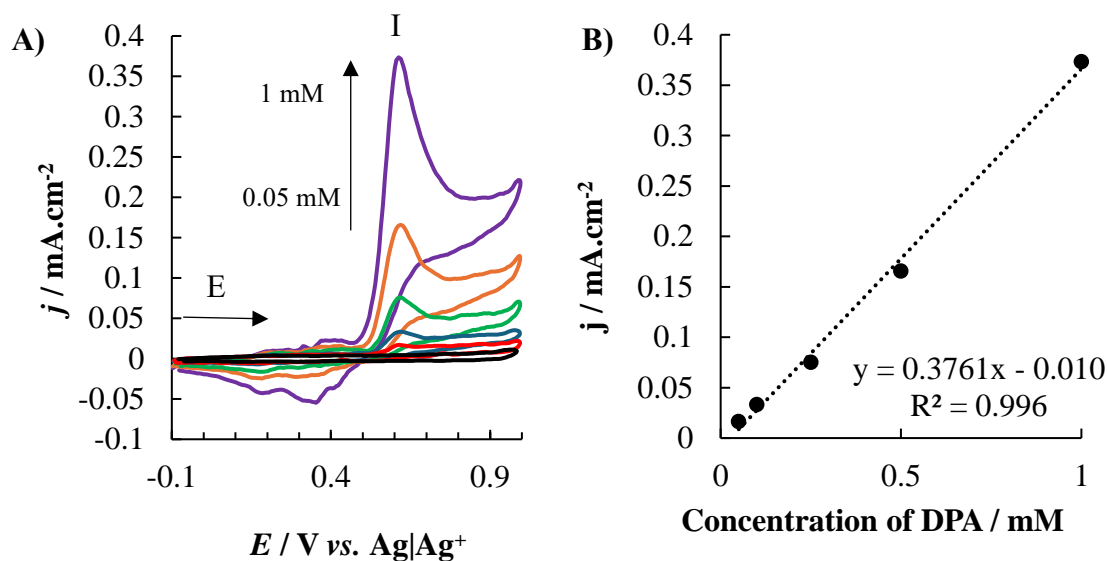
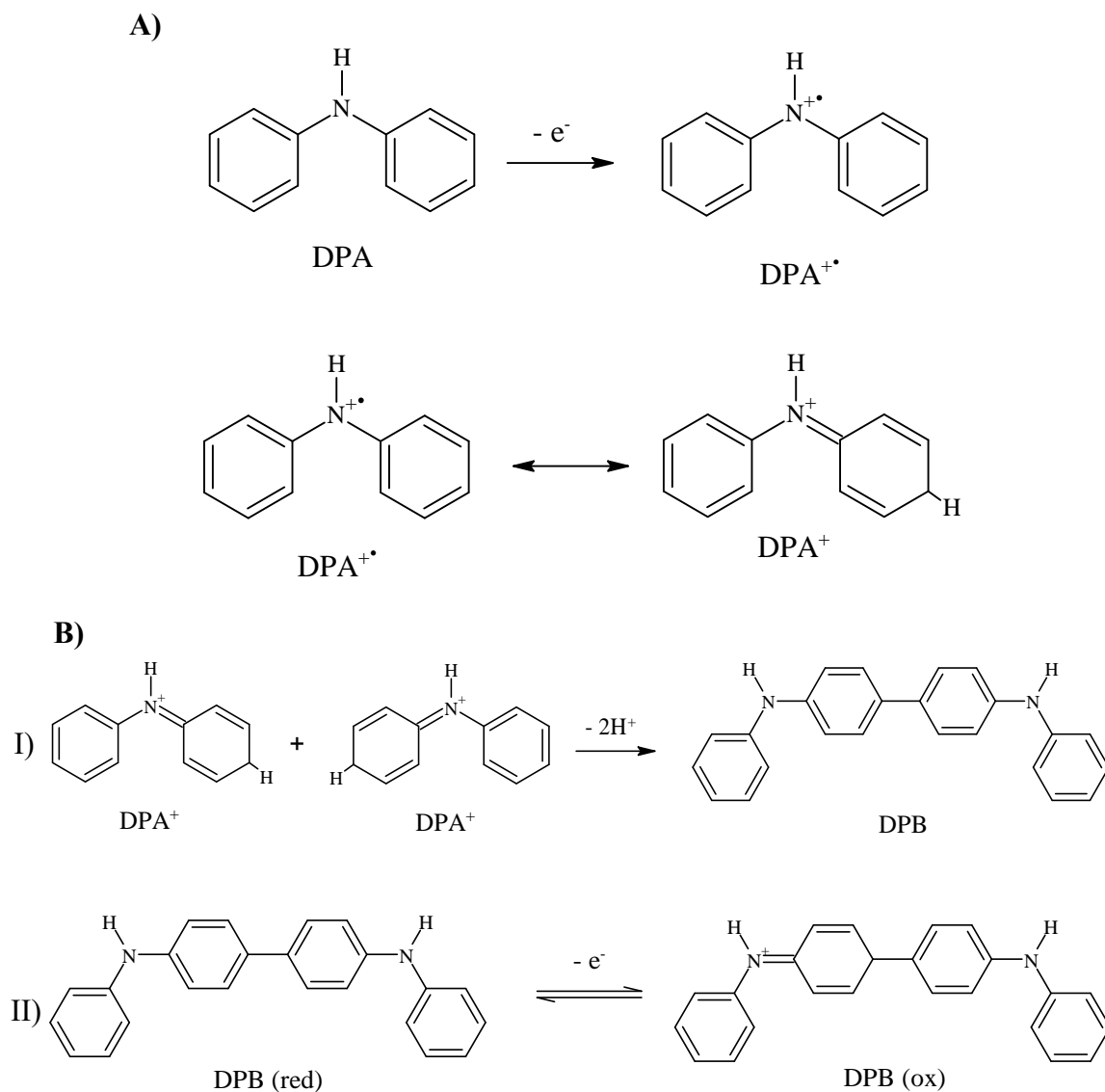


Figure 3.15: A) Cyclic voltammogram (showing cycle 1) at an unmodified GCE over the potential range of -0.1 to +1 V vs. Ag|AgCl at a scan rate of 50 mV.s⁻¹. Concentration range of DPA was 0.05 to 1 mM in a 1:1 solution of acetonitrile:methanol with 0.1 M LiClO₄. B) corresponding plot of j (from peak I) vs. concentration of DPA ($n=1$).

The ratio of anodic and cathodic currents for this process plotted vs. scan rate indicates an electron transfer, chemical reaction and further electron transfer (ECE) process – irreversible electron transfer followed by a homogeneous chemical reaction where the ratio decreased as the oxidised species was consumed by the subsequent chemical reaction (formation of diphenylbenzidine).



Scheme 3.2: Mechanism of diphenylbenzidine formation from diphenylamine showing (A) One electron oxidation of DPA to a radical cation (electrochemical step) followed by dimerisation (B (I)) (chemical step), and leads to the electroactive diphenylbenzidine species (electrochemical step) in non-aqueous electrolyte (B (II)).

Scan rate studies verified a diffusion controlled chemically irreversible process which may be described by **Equations (3.6 & 3.7)**⁵⁵. The expressions below allowed estimation of diffusion coefficient (D) and transfer coefficient (α) (assuming $n = 1$) as $5.47 \times 10^{-8} \text{ cm}^2 \cdot \text{s}^{-1}$ with $\alpha n_a = 0.49$.

$$i_p = 2.99 \times 10^5 \times n \times \sqrt{\alpha n_a} \times A \times C \times \sqrt{D} \times \sqrt{v} \quad 3.6$$

$$E_p - E_{p(\frac{1}{2})} = \frac{1.857 \times R \times T}{\alpha n_a \times F} \quad 3.7$$

where α is the transfer coefficient, n_a is the number of electrons in the rate determining step, D is the diffusion co-efficient ($\text{cm}^2 \cdot \text{s}^{-1}$) and v is scan rate ($\text{V} \cdot \text{s}^{-1}$). **Equation 3.8** allows determination of k^o (standard heterogeneous rate constant) for an irreversible process⁵⁵.

$$k^o = 2.415 \exp\left(-0.02 \frac{F}{RT}\right) \sqrt{D_o} \frac{1}{\sqrt{(E_p - E_{p/2})}} \sqrt{v} \quad 3.8$$

where k^o is the standard heterogeneous rate constant, R is the gas constant, T is temperature (K) and F is Faraday's constant. Taking E_p at $50 \text{ mV} \cdot \text{s}^{-1}$ as 0.61 V and at 0.561 V this results in a k^o value of $1.23 \times 10^{-3} \text{ cm} \cdot \text{s}^{-1}$.

Following dissolution testing of DPA, the most suitable aqueous solvent system was found to be 3:7 methanol: sodium acetate buffer (pH 4.5) representing a more suitable electrolyte for practical DPA sensing applications. A scan rate study in 1 mM DPA (**Figure 3.16 (A)**) showed oxidation at 0.7 V vs. Ag|AgCl with more dominant electrochemistry evident for the surface confined follow-on product of the initial oxidation step at $E_p^a = 0.47$ and $E_p^a = 0.40 \text{ V}$ vs. Ag|AgCl. The diffusion coefficient was calculated as $1.4 \times 10^{-6} \text{ cm}^2 \cdot \text{s}^{-1}$ with $\alpha n_a = 0.7$ and $k^o = 4.08 \times 10^{-4} \text{ cm} \cdot \text{s}^{-1}$ which was 3 times lower than the rate constant in the organic electrolyte (literature D value $2.5 \times 10^{-5} \text{ cm}^2 \cdot \text{s}^{-1}$)⁵⁶. A plot of $\log j$ for the surface confined anodic and cathodic processes ($E_p^a = 0.47 \text{ V}$ (peak I) and $E_p^c = 0.40 \text{ V}$ (peak II)) vs. \log scan rate (**Figure 3.16 (B)**) resulted in slopes of 0.78 and 0.7 respectively, while a plot of j vs. scan rate was found to be linear with r^2 values of 0.991 and 0.981 respectively (**Figure 3.16 (C)**).

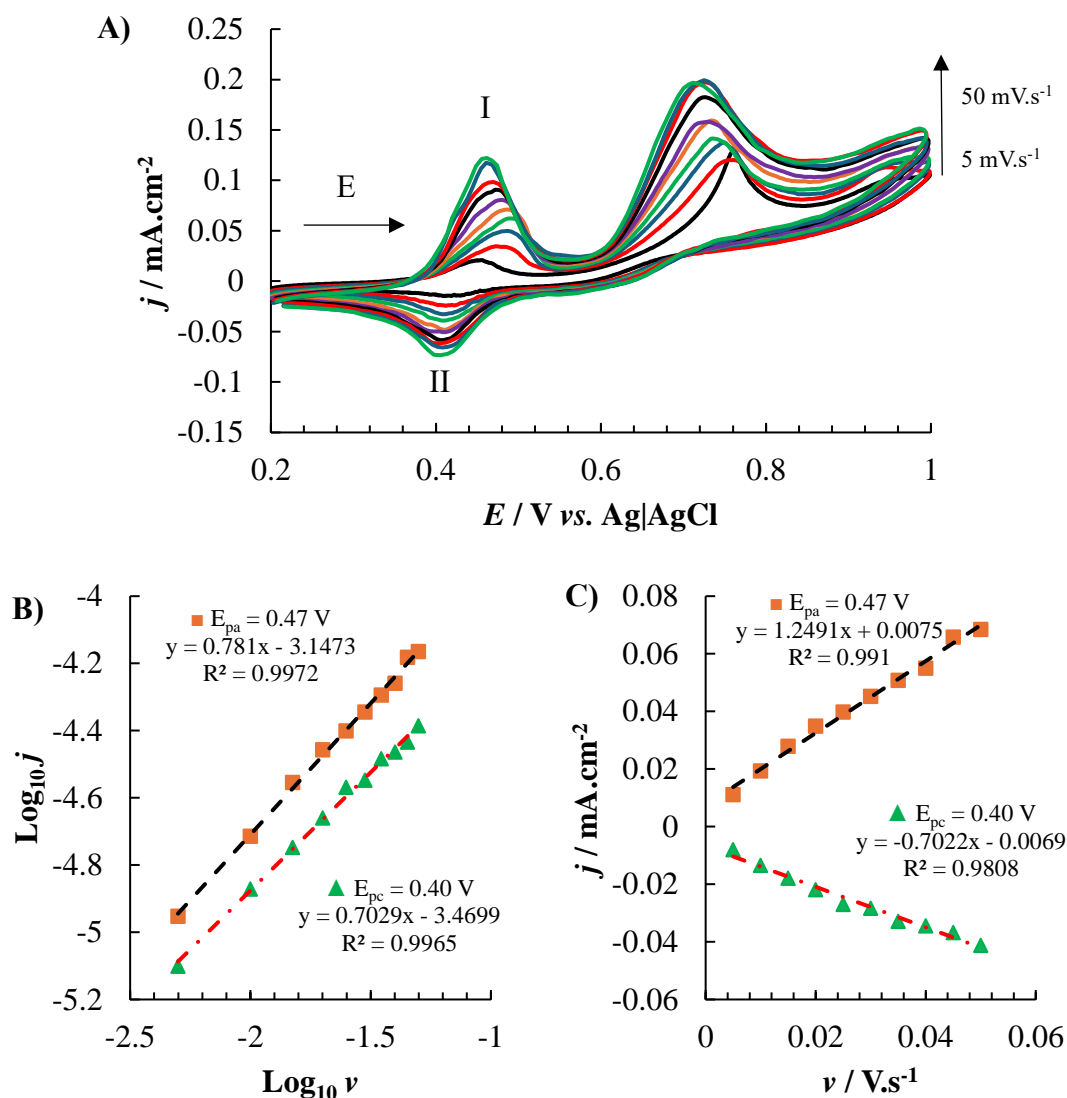


Figure 3.16: Cyclic voltammogram (showing cycle 3) over the potential range of 0.2 to 1 V vs. Ag|AgCl for scan rate study using a fresh GCE surface with each new scan rate over 5 to 50 mV \cdot s $^{-1}$ for 1 mM DPA in a 3:7 methanol:sodium acetate buffer (pH ~4.5). Corresponding plots (for peaks I and II) of B) $\log j_p$ vs. $\log \nu$ confirming surface confined behaviour of the signal for the dimeric species formed following the first anodic sweep. C) Plot of j_p vs. ν confirming surface confined behaviour of the signal for the dimeric species formed following the first anodic sweep.

The DPA concentration (**Figure 3.17**) dependence of the anodic process resulted in a linear relationship ($r^2 = 0.998$) over the range 0.1–0.5 mM.

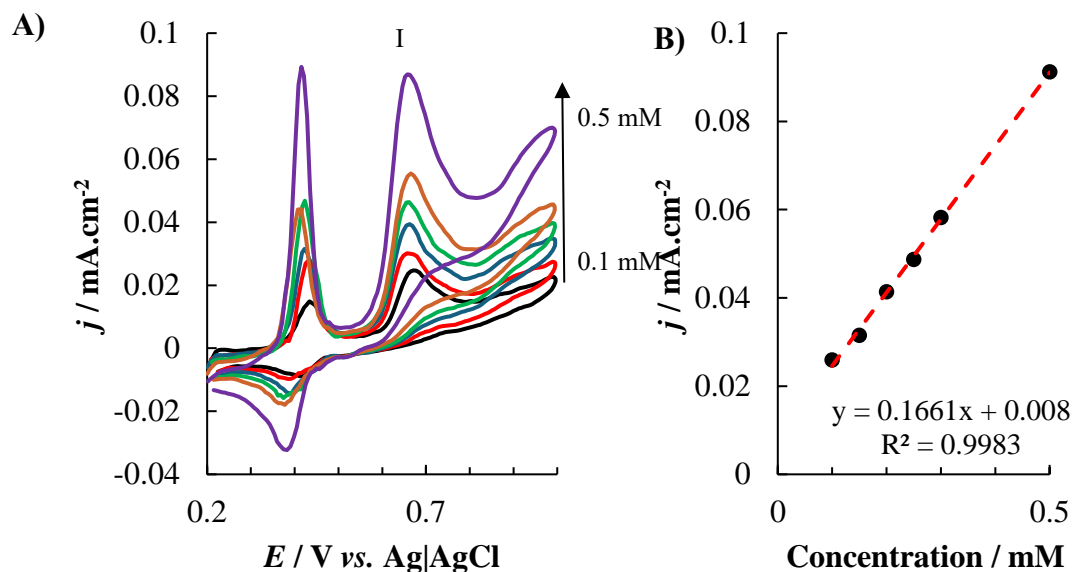


Figure 3.17: A) Cyclic voltammogram (showing cycle 3) over the potential range of 0.2 to 1 V vs. Ag|AgCl for a DPA concentration study using a fresh GCE surface with each concentration over the range 0.1 to 0.5 mM DPA in a 3:7 methanol:sodium acetate buffer (pH ~4.5). B) Corresponding plot of j_p vs. concentration for response at $E_p^a = 0.7$ V (peak I).

In **Figure 3.18 (A)** the voltammogram of the deposited layer is shown with a response at $E_p^c = 0.4$ V, together with dark field reflectance microscopy image **Figure 3.18 (B)** indicating a textured surface of the GCE.

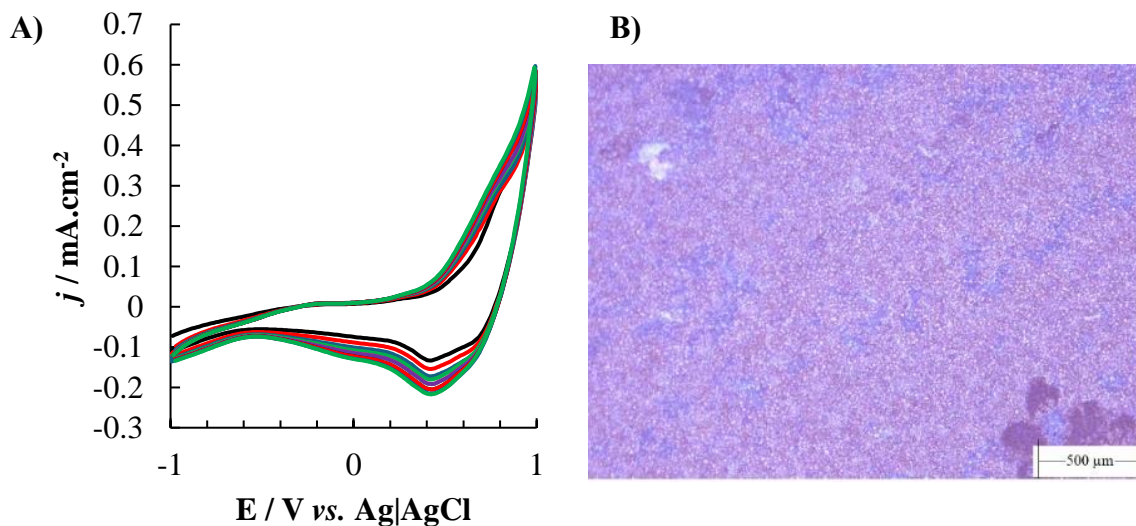


Figure 3.18: A) Cyclic voltammogram over the potential range of -1 to +1 V vs. Ag|AgCl at 100 mV.s^{-1} in a solution of 3:7 methanol:sodium acetate buffer (pH ~4.5) showing cycles 1-10 for the film formed after repeated cycling in 1 mM DPA in 3:7 methanol:sodium acetate buffer (pH ~4.5) ($n=1$). B) Reflectance microscopy image of formed film, pre-electrochemical measurements (of A), on a GCE (x1000 using dark field polarisation).

3.4.2.2 UV-Vis Spectroscopy of Films Formed from Diphenylamine Cycling

The visible appearance of films formed on the GCE surface in the methanol/sodium acetate buffer (3:7) indicate that polymeric by-products of the DPA oxidation may form and contribute to this signal⁵⁷, resulting in electrochemical processes in line with previous diphenylamine electropolymerisation studies^{58,59}. Formation of phenolic or benzoquinone products, the latter of which are common degradation species found in polyaniline films⁶⁰, may also occur in the acidic aqueous conditions examined and such derivatives may be responsible for the process evident at $E_p^a = 0.47$ V.

In order to examine this further, UV-Vis studies involved potential cycling in a 1 mM solution of the DPA monomer at a Pt gauze spectroelectrochemical working electrode. Absorption spectra (average $n = 4$) are shown (**Figure 3.19**) and include (I) spectra taken of the solution following polymerisation and (II) spectra recorded at the Pt gauze electrode in a spectroelectrochemical cell. **Figure 3.19 (A)** shows the absorbance spectrum before and after cycling in 1 mM DPA with reduction in the DPA signals (indicative λ_{\max} for DPA are 204 and 284 nm)⁶¹, and appearance of a shoulder at 332 nm and a weak absorbance at 455 nm (region II is shown in inset for clarity). **Figure 3.19 (B)** presents the data in absorbance ratio format with relative changes post cycling being evident at regions I and II of the spectra (Abs ratio >1) corresponding to 339 and 452 nm respectively. **Figure 3.19 (C)** shows the spectrum over the range subject to most change at the Pt gauze electrode pre and post cycling with λ_{\max} at 456 nm. In the case of the latter, background correction was ensured by using 1 mM DPA in the reference cuvette. Deposition from 1 mM DPA onto Pt results in an unstable film which, apparently evident on the electrode at 456 nm (black curve **Figure 3.19 (B) and (C)**). This results in a stronger signal for the solution spectrum (in the absence of electrode (red curve **Figure 3.19 (C)**), with increase in the overall absorbance of the formed products (>312 nm). The UV studies point towards solution phase poly(diphenylamine) formation with λ_{\max} that aligns well with literature values between 424 to 514 nm subject to pH effects⁶²⁻⁶⁵ resulting from coupling of diphenylbenzidine species and appearing less adherent on platinum relative to carbon. Additionally, an understanding of the diphenylbenzidine formation is advantageous with respect to optical detection methods via the reaction of diphenylamine with nitrite and nitrate ions from nitrocellulose⁶⁶ with oxidation to the blue diamine.

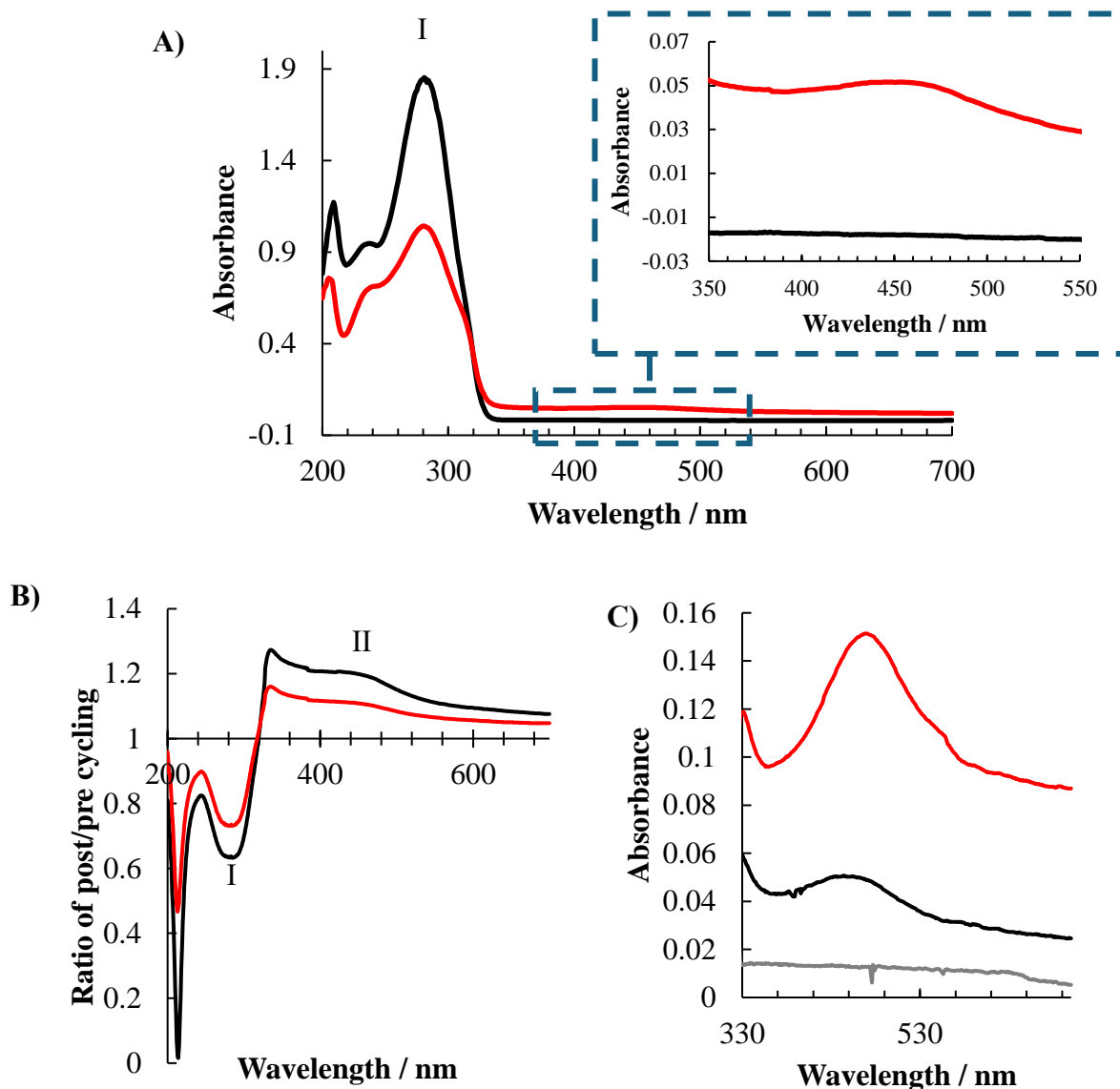


Figure 3.19: Averaged UV-Vis spectra ($n=4$) of A) 1 mM DPA in a solution of 3:7 methanol:sodium acetate buffer (pH ~4.5) before (black) and after (red) cycling 100 times over the potential range -1 to $+1$ V at $100 \text{ mV}\cdot\text{s}^{-1}$. Inset: zoomed in region between 350 and 550 nm. Indicative λ_{max} for DPA are 204 and 284 nm which decrease following film formation. B) Absorbance ratio spectra for pre and post cycling solution with (red) and without (black) platinum gauze. C) Overlaid spectra for Pt gauze in background electrolyte (grey) and following cycling (black). Red curve represents solution only spectrum (background reference cuvette containing 1 mM DPA).

Having established insights into the DPA oxidation process from cycling, an evaluation of the influence of the electrosynthesised MNP on the DPA electrochemistry and quantitative signals follows, with the view to establishing optimum analytical performance parameters for the transducer prior to real sample analysis.

3.4.2.3 Voltammetric Response of Diphenylamine at MNP Modified Electrode

Figure 3.20 shows the third cycle response to 1 mM DPA in aqueous electrolyte at $50 \text{ mV}\cdot\text{s}^{-1}$ over the potential ranges of 0 to +1 V, -0.5 to +1 and -1 to +1 V. The MNP modified electrode resulted in an enhanced signal relative to the bare response (black curve vs. red curve) with lowering of the anodic process which appeared from cycle 2 onwards evident at 0.5 V (II) (34–63%). Under optimum conditions, over the range -1 to 1 V at $50 \text{ mV}\cdot\text{s}^{-1}$ there was an 87–97% ($n = 3$) increase in the DPA oxidation at $E_p^a = 0.7 \text{ V}$ (I) relative to unmodified GCEs.

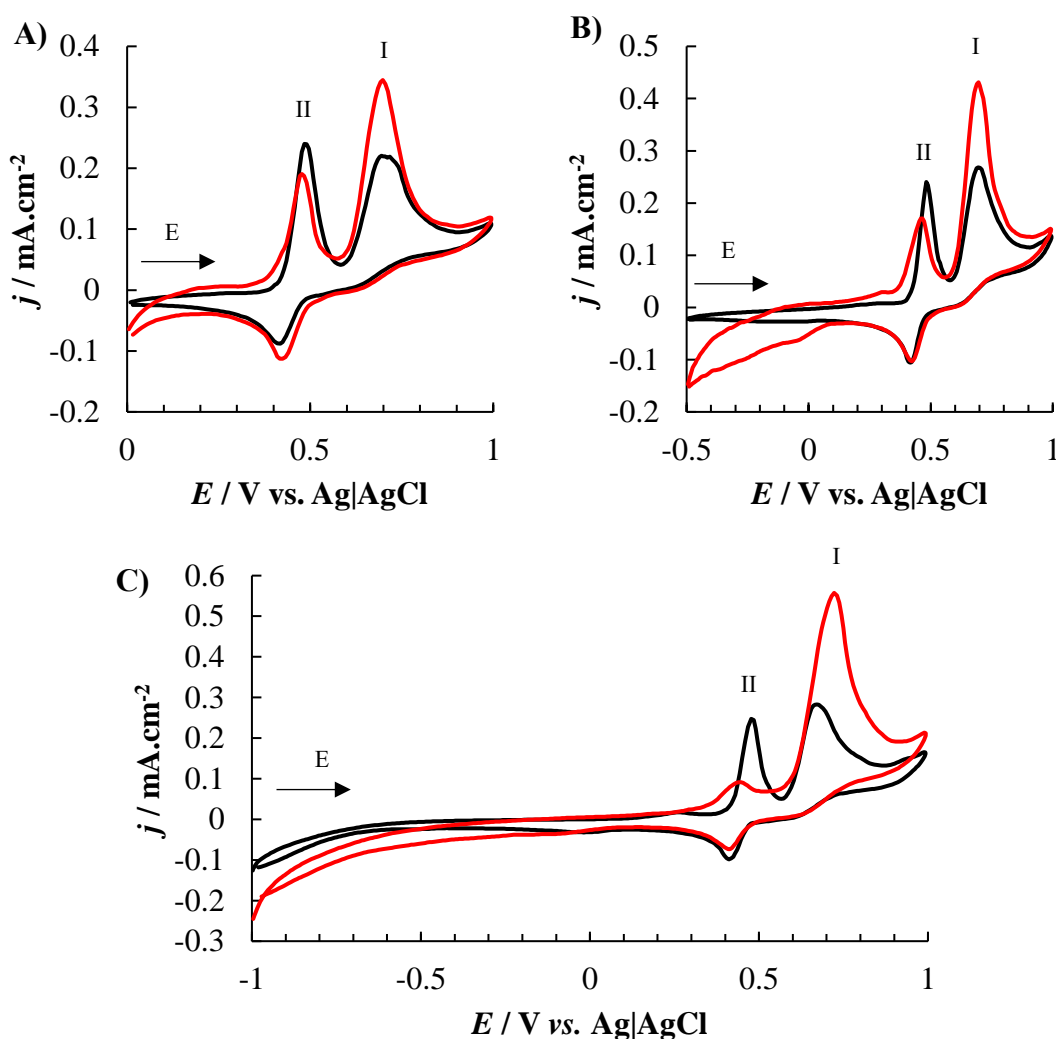


Figure 3.20: Cyclic voltammogram (showing cycle 3) of a 1 mM DPA solution in 3:7 methanol:sodium acetate buffer (pH ~4.5) at $50 \text{ mV}\cdot\text{s}^{-1}$ over the potential range of A) 0 to 1, B) -0.5 to +1 V and C) -1 to +1 V vs. Ag|AgCl at bare (black) and MNP modified (red) (typical traces).

The apparent ability of the MNP layer to impede the diphenylbenzidine dependent polymer redox process (possibly due to stabilisation of DPA^+) was evident and can aid in sensor selectivity and reusability/surface regeneration as required. Linear sweep voltammograms resulted in calibration plots over the range 0.01–1 mM DPA (**Figure 3.21**) with sensitivity of $0.510 \pm 0.02 \text{ mA cm}^{-2}.\text{mM}^{-1}$ ($n=3$) which is 1.51-fold increase relative to the bare electrode response ($0.336 \pm 0.005 \text{ mA.cm}^{-2}.\text{mM}^{-1}$ ($n=3$)) at 0.65 V vs. Ag|AgCl, a statistically significant increase in sensitivity ($p = 0.0001$). This is in part due to enhanced surface to volume ratio on the electrode surface and enhanced electron transfer, but selectivity and surface reusability is also an important concern for a future multiplexed device.

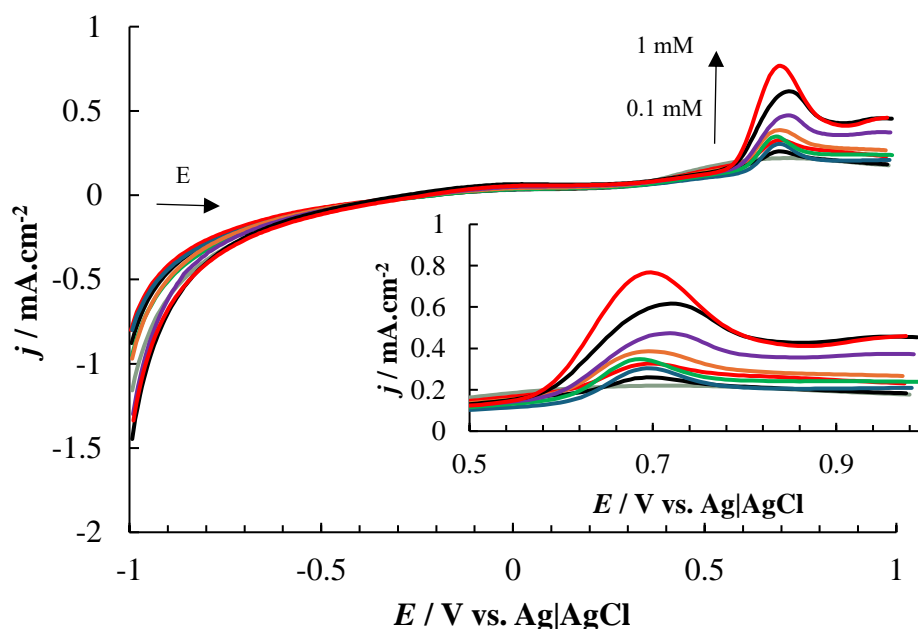
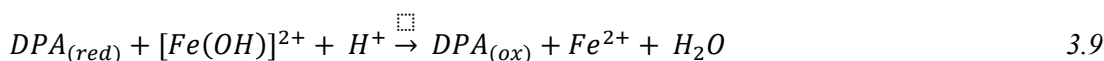


Figure 3.21: Linear sweep voltammogram over the potential range of -1 to +1 V vs. Ag|AgCl at 50 mV.s^{-1} for DPA concentration series (0.1 to 1 mM) in 3:7 in methanol:sodium acetate buffer (pH ~4.5) at a MNP modified GCE (typical trace). Inset: zoomed in region of 0.5 to 1 V for DPA oxidation.

A postulated mechanism for this signal enhancement is given below (**Equation 3.9**), with DPA generating Fe^{2+} from Fe^{3+} species (dominant at pH 4.5)⁵¹.



In order to examine lower analytical ranges, differential pulse voltammetry (DPV) was employed. **Figure 3.22** shows differential pulse voltammograms over the range -1 to 1.5 V with focus on relevant potential range of DPA oxidation at bare (**Figure 3.22 (A)**) and modified (**Figure 3.22 (B)**) GCEs ($n=3$).

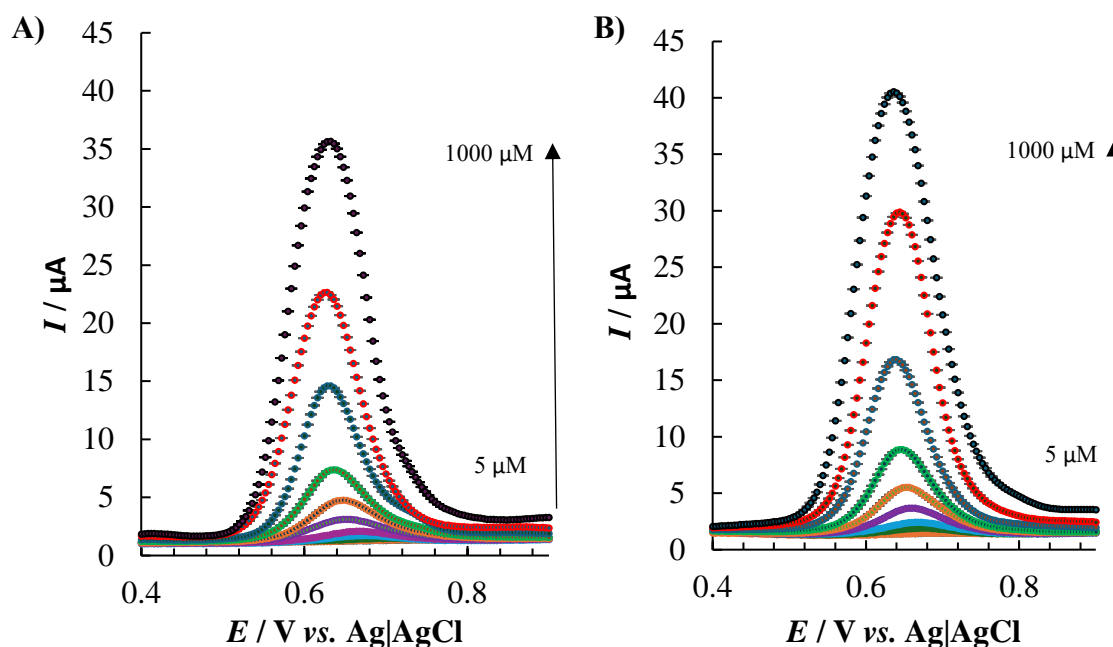


Figure 3.22: Averaged data ($n=3$) for differential pulse voltammetry over the potential range of -1 to $+1.5$ V vs. Ag|AgCl with additional parameters as per electrochemical procedures section (region of DPA peak 0.4 V to 0.9 V only shown). DPA concentration series (5 to 1000 μM) at A) bare and B) MNP modified GCE (with current standard deviations of ± 0.12 μA at bare and ± 0.16 μA at modified electrodes across the entire series).

The corresponding calibration curves for the bare and MNP modified electrodes (**Figure 3.23**) show a second order polynomial response across the entire concentration range (**Figure 3.23 (A)**). Two linear series were derived, a higher series over the concentrations of 100 to 1000 μM (**Figure 3.23 (B)**) and lower series over the range 5 to 50 μM (**Figure 3.23 (C)**), with the highest sensitivity being achieved at the lower concentration series. Sensitivities of 0.0629 ± 0.009 and 0.0801 ± 0.003 $\mu\text{A} \cdot \mu\text{M}^{-1}$ for bare and modified electrodes respectively were obtained showing a statistically significantly improved measurement with the use of a modified electrodes ($p = 0.0233$).

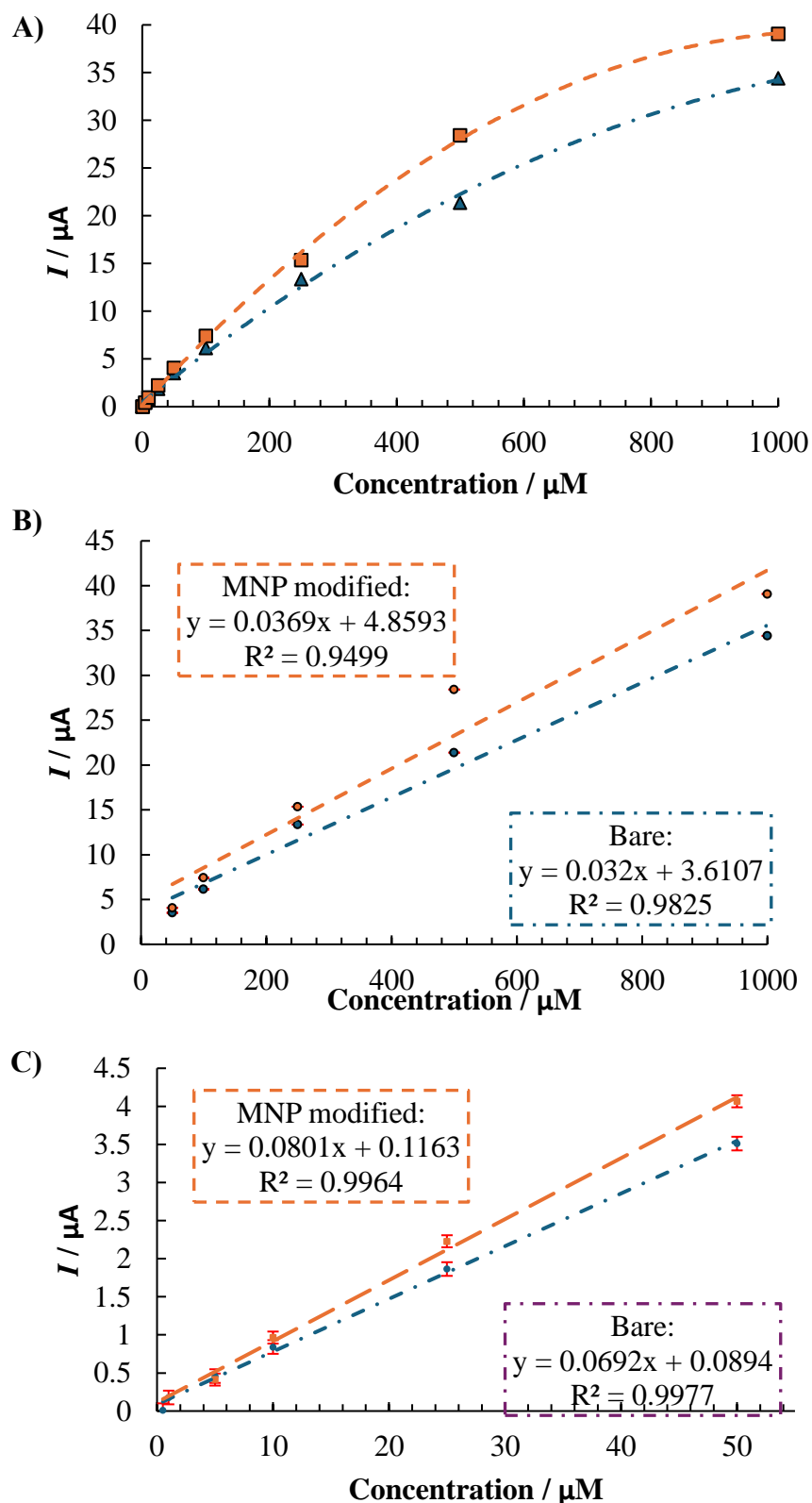


Figure 3.23: Averaged data plots ($n=3$) of current vs. concentration of DPA in 3:7 methanol:sodium acetate buffer ($\text{pH} \sim 4.5$) (from Figure 3.21) at bare (blue) and modified (red) GCE over the concentrations of A) 5 to 1000 μM B) 50 to 1000 μM and C) 5 to 50 μM .

Calculations of the LOD and LOQ were performed using **Equations 3.10 and 3.11**:

$$LOD: \frac{3.3 \times \sigma}{m} \quad 3.10$$

$$LOQ: \frac{10 \times \sigma}{m} \quad 3.11$$

Where σ is the standard deviation of the bare and MNP modified electrodes in the background solution of 3:7 methanol:sodium acetate buffer (n=9) (± 0.052 and $\pm 0.093 \mu\text{A}$ respectively), while m is the slope or sensitivity of the calibration.

Calculation with a MNP modified electrode resulted in an LOD = $3.51 \mu\text{M} \pm 0.15 \mu\text{M}$, LOQ = $11.7 \mu\text{M} \pm 0.47 \mu\text{M}$, relative to unmodified electrode with LOD = $2.27 \mu\text{M} \pm 0.03 \mu\text{M}$, LOQ = $7.57 \mu\text{M} \pm 0.10 \mu\text{M}$, with a significant difference found between both the LOD ($p = 0.001$) and the LOQ ($p=0.001$). It was proposed that the higher standard deviation observed with the MNP modified electrode was due to the inherent variability of the simplistic method of drop cast modification, subsequently influencing LOD and LOQ estimations even with increased sensitivity. Alternative methods of immobilisation such as the use of ferrofluids/inks have the potential to improve variation, standardising the deposition process of the material.

Overall, the observed decrease in current signal associated with the follow-on oxidation species provides reason to believe that this modified surface can assist where multiple components are of interest e.g. in presence of 1,3-diethyl-1,3-diphenylurea (ethyl centralite) as a co-target in forensic analysis, which is explored in the next section.

3.4.3 *Electrochemical Analysis of Ethyl-Centralite*

In order to gain insights into the redox behaviour of ethyl-centralite (EC) and to contribute to the depth of literature on the electrochemistry of this species, its behaviour was examined in acetonitrile (0.1 M LiClO₄) using cyclic voltammetry. The first cycle showed an irreversible wave at 1.0 V vs Ag|Ag⁺ with a reduction process at 0.7 V (peak III). Subsequent cycles 2 and 3 (**Figure 3.24**) revealed a new weak anodic process at 0.75 V (Peak II). Plots of j_p^a vs. scan rate resulted in a decrease in current ratio with increasing scan rate indicating a competing follow-on chemical process which follows the initial oxidation.

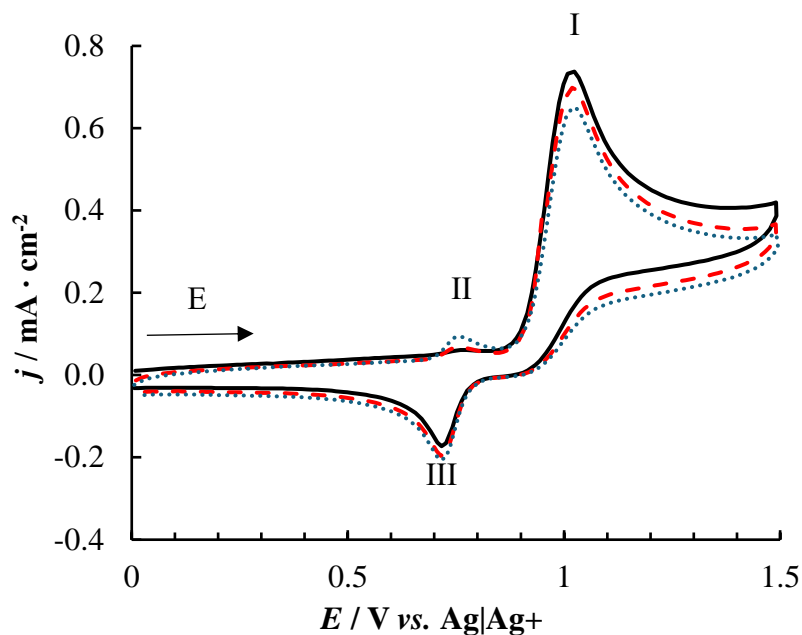


Figure 3.24: Cyclic voltammogram of 1 mM EC in 0.1 M LiClO₄ in acetonitrile for 3 cycles at a GCE over the potential range 0 to 1.5 V vs. Ag|Ag⁺ (10 mM AgNO₃) at 100 mV·s⁻¹. (Cycle 1: black/solid, Cycle 2: red/dash, Cycle 3: blue/dots) (typical trace).

Faster scan rates restore reversibility of the cathodic process (Peak II/III), (**Figure 3.25 (A)**) and all peaks reflected a diffusion-controlled process with current density vs scan rate^{1/2} being linear (**Figure 3.25 (B)**). Research by Bergens *et al* reflects one of the few reports on the non-aqueous electrochemistry of EC in this solvent system and the data presented here advances this work⁵, by further identifying the effects of scan rate, cycle number and solution pH on EC.

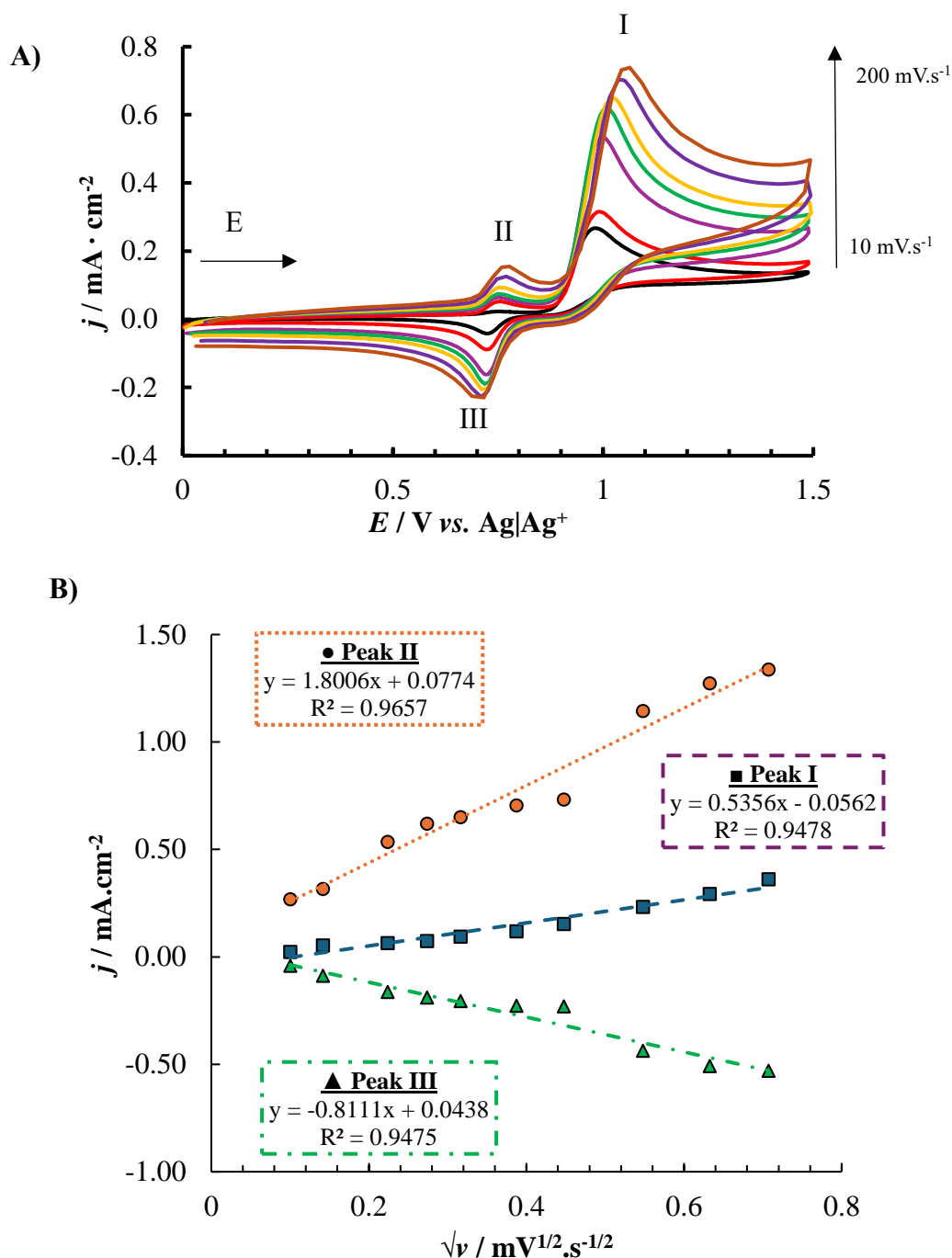


Figure 3.25: A) Cyclic voltammogram (showing cycle 3) of 1 mM EC in 0.1 M LiClO₄ in acetonitrile at various scan rates 10 to 200 mV·s⁻¹ (typical trace) with B) corresponding plot of current density vs. $\sqrt{\text{scan rate}}$ for peaks I, II, III. Potential range 0 to 1.5 V vs. Ag|Ag⁺ (10 mM AgNO₃).

Investigations in an aqueous electrolyte which provided sufficient solubility for EC (Figure 2.26) resulted in an irreversible wave at $E_p^a = 1.2 \text{ V vs. Ag/AgCl}$ which decreased upon cycling (Figure 2.26 (A)). Investigation into the influence of a lower starting

potential resulted in no significant effect on the anodic process ($\pm 0.015 \text{ mA}\cdot\text{cm}^{-2}$) (**Figure 2.26 (B)**).

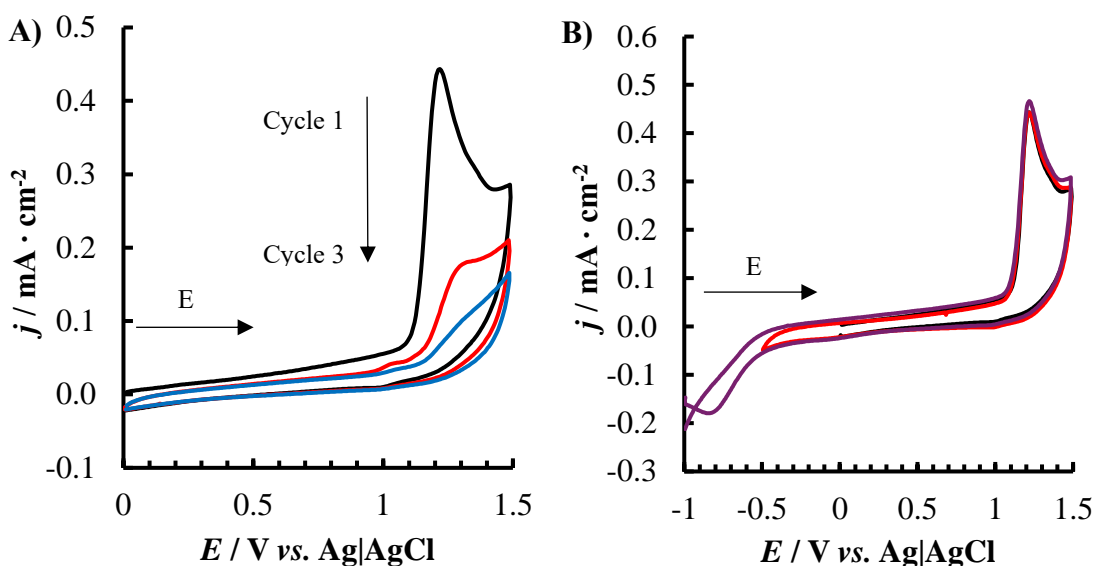


Figure 3.26: Cyclic voltammogram of A) 1 mM EC in 3:7 methanol:sodium acetate buffer (pH ~4.5) at a GCE over the potential range 0 to 1.5 V at $50 \text{ mV}\cdot\text{s}^{-1}$ (showing all three cycles) (typical trace). B) Influence of the cathodic limit on the anodic process (first cycle shown) at $50 \text{ mV}\cdot\text{s}^{-1}$ over the potential range -1 (blue), 0 (black) and -0.5 (red) to +1.5 V (typical traces).

In order to examine any film/redox product deposition which might influence subsequent analytical work, **Figure 3.27 (A)** shows the effect of continuous potential sweeping in 1 mM EC at the GCE, with a decrease of peak I ($E_p^a = 1.2 \text{ V}$) evident from 406.8 to 65.36 $\text{mA}\cdot\text{cm}^{-2}$. Within cycle 2 of the voltammogram the emergence of the new process at 1.06 V(III) was observed. An investigation in 3:7 methanol: phosphate buffer pH 7.25 resulted in an anodic shift (100 mV) of peak I to 1.3 V vs. Ag|AgCl (**Figure 3.27 (B)**), being suggestive of a pH effect with no evidence of new redox couples upon cycling.

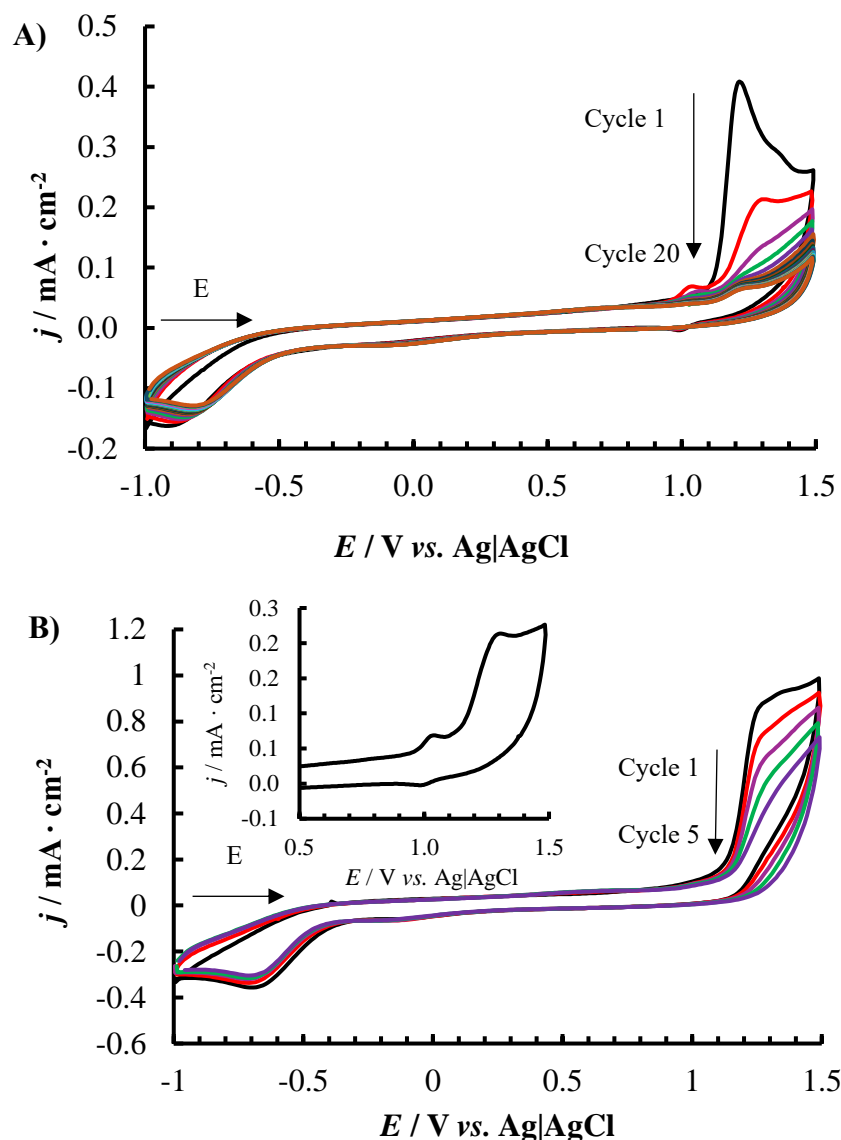


Figure 3.27: Cyclic voltammogram over the potential range of -1 to +1.5 V vs. Ag|AgCl of A) 1 mM EC in 3:7 methanol:sodium acetate buffer (pH ~4.5) at a GCE (20 cycles shown) (typical trace) and B) 1 mM EC in 3:7 methanol:phosphate buffer (pH ~7.25) at a GCE (5 cycles shown) (typical trace). Inset: cycle 2 shown at $50 \text{ mV}\cdot\text{s}^{-1}$

Following potential cycling in 1 mM EC, a golden hue was visible on the surface of the GCE (**Figure 3.28 (A(2))**) relative to control surface (**A(1)**). This was interesting and warranted further investigations. Film formation in 5 mM EC (over 50 cycles) followed, as shown in **Figure 3.28 (B)** with peaks at 1.0, 1.2 and 0.98 V evident. The resultant more purple, less uniform film is shown in image **Figure 3.28 (A(3))** with evidence of bubble formation. From the voltammetry, the redox **peaks I, II III** were found to be much more defined in the case of deposition from 5 mM EC relative to 1 mM (**(Figure 3.28 (B) and (C) respectively)**) with an additional peak at -0.19 V observed (**IV**). Following cycling,

the electrodes were gently rinsed with water and dried with nitrogen before testing in the background electrolyte (it was noted that the film was easily removed with a gentle wash of ethanol).

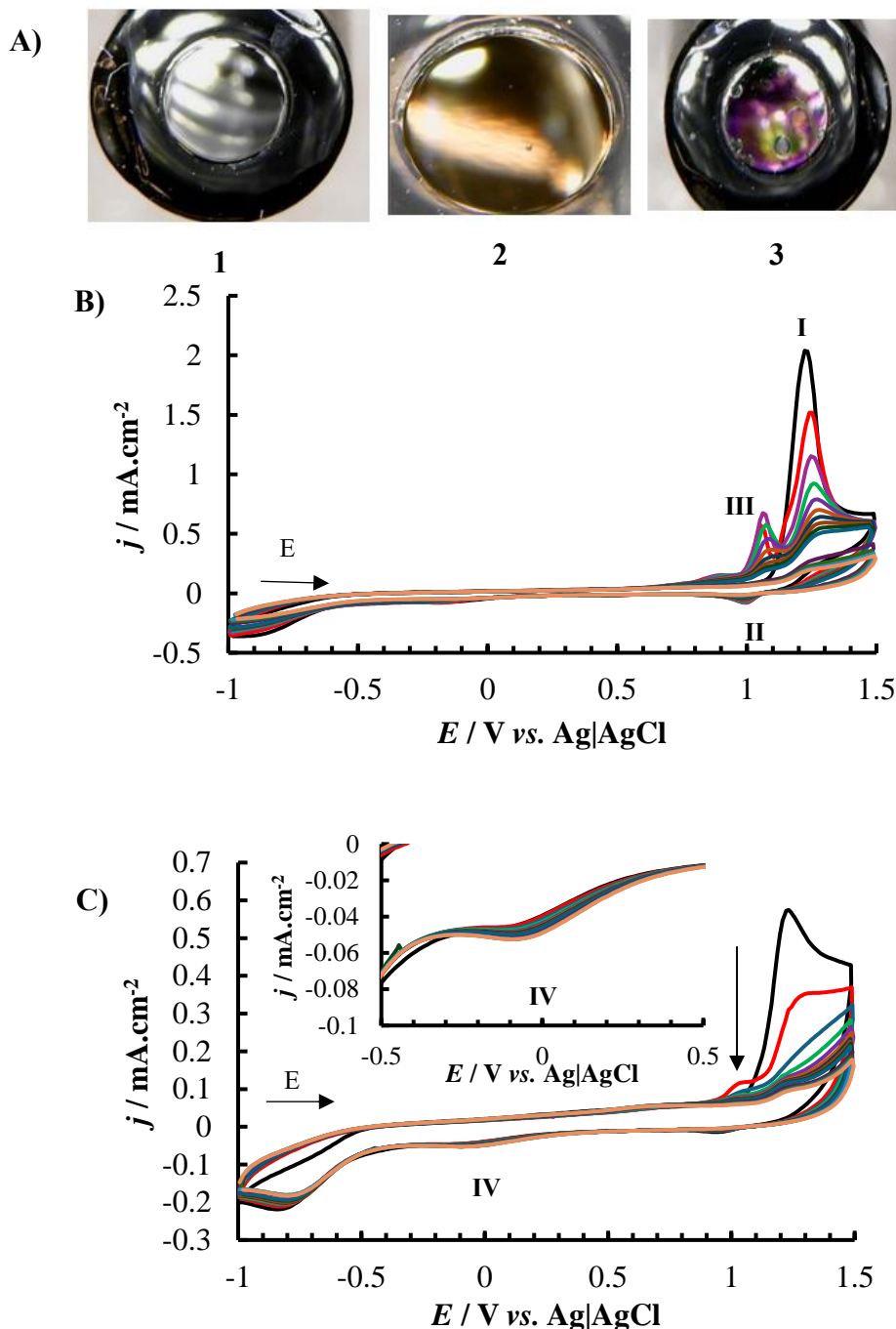


Figure 3.28: A) Photographs (x40 magnification) of 1) bare GCE polished surface and a GCE surface following 50 cycles in 2) 1 mM and 3) 5 mM EC in 3:7 methanol:sodium acetate buffer (pH ~4.5) at $100 \text{ mV}\cdot\text{s}^{-1}$ over the range -1 to +1.5 V. Cyclic voltammogram over the potential range of -1 to +1 V vs. Ag|AgCl at $50 \text{ mV}\cdot\text{s}^{-1}$ for B) 5 mM EC and C) 1 mM EC in 3:7 methanol:sodium acetate buffer (pH ~4.5) at a GCE (50 cycles, showing cycles 1 to 10 and then every subsequent tenth cycle) (typical trace) Inset: zoomed in region of -0.5 to 0.5 V vs. Ag/AgCl for clarity of peak IV

The resultant film formed from 1 mM EC resulted in weak signals evident at 1.0 and -0.04 V vs. Ag|AgCl (**Figure 3.29**) due to the soluble nature of the deposited material. Peak I ($E_p^a = 1.0$ V) decreased by 64% over 5 cycles ($0.087 \text{ mA}\cdot\text{cm}^{-2}$ to $0.055 \text{ mA}\cdot\text{cm}^{-2}$) while peak II ($E_p^c = -0.04$ V) showed a steady increase over 5 cycles ($\sim -0.045 \text{ mA}\cdot\text{cm}^{-2}$).

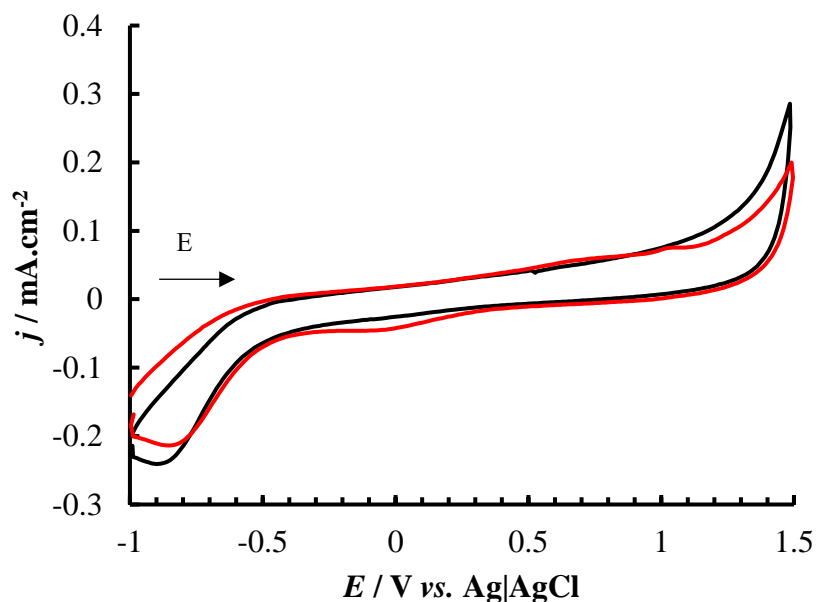
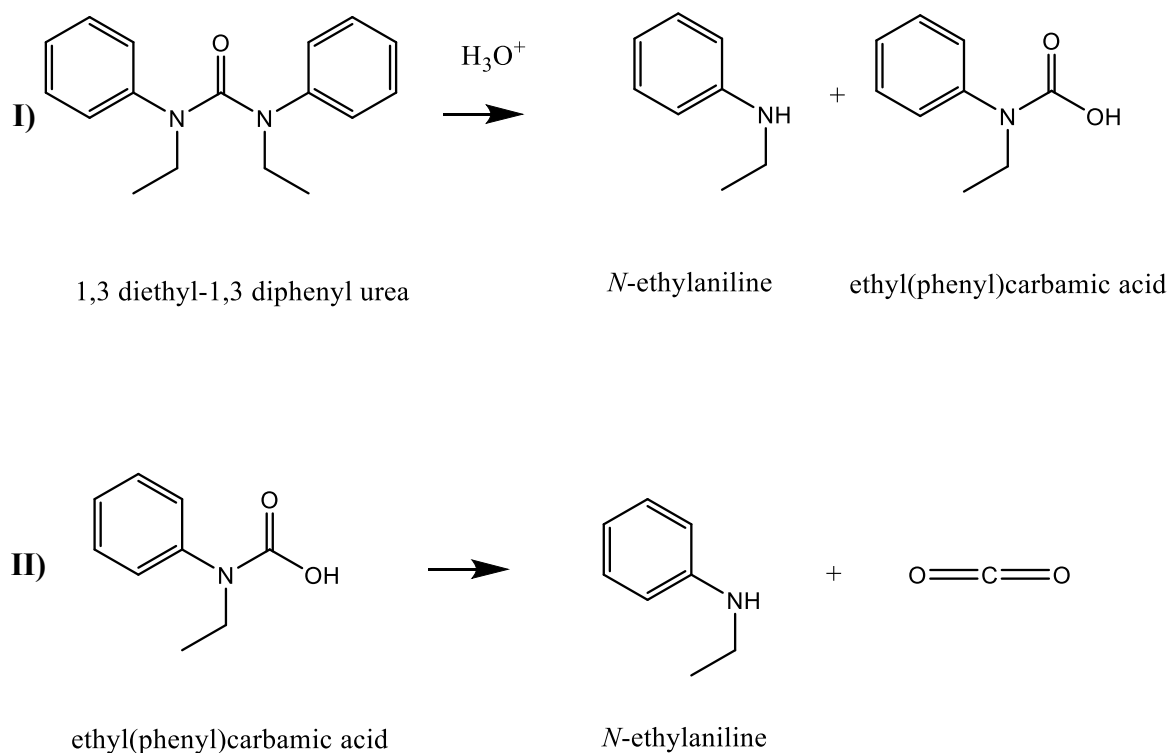


Figure 3.29: Cyclic voltammogram (showing cycle 1) over the potential range of -1 to +1.5 V vs. Ag|AgCl at $100 \text{ mV}\cdot\text{s}^{-1}$ in 3:7 methanol:sodium acetate buffer (pH ~ 4.5) of film formed following cycling in 1 mM EC (red) relative to bare GCE (black) ($n=1$).

Given the acidic pH conditions employed in the studies thus far, a hydrolysis reaction was proposed to explain breakdown of EC⁶⁷ and subsequent deposition of decomposition products (see **Scheme 3.4** for proposed mechanism) which is suggested to result in *N*-ethyl-aniline and ethyl(phenyl)carbamic acid. Salvestrini *et al.*, state that bifunctional acid-base buffers are particularly efficient catalysts, such as the acetate buffer ($\text{CH}_3\text{COOH}/\text{CH}_3\text{COO}^-$) implemented here⁶⁷. In their work, nonlinear dependence of the rate constant on buffer concentrations suggested the existence of an intermediate (an aryl-isocyanate), with this intermediate formation being the rate determining step. However, given the disubstituted N atoms in EC, formation of this intermediate may prove difficult as both the ethyl group ($\text{p}K_a: 50$) and the aromatic ring ($\text{p}K_a: 43$) on the nitrogen are poor leaving groups. Laudien *et al.* propose a possible mechanism of hydrolytic decomposition of phenylureas in acidic media as an addition-elimination mechanism with the attack of

the protonated nitrogen by water as the rate determining step, forming a tetrahedral intermediate⁶⁸. Regardless of the intermediate pathway both mechanisms result in the formation and subsequent breakdown of a carbamic acid to its corresponding aniline under acidic conditions.

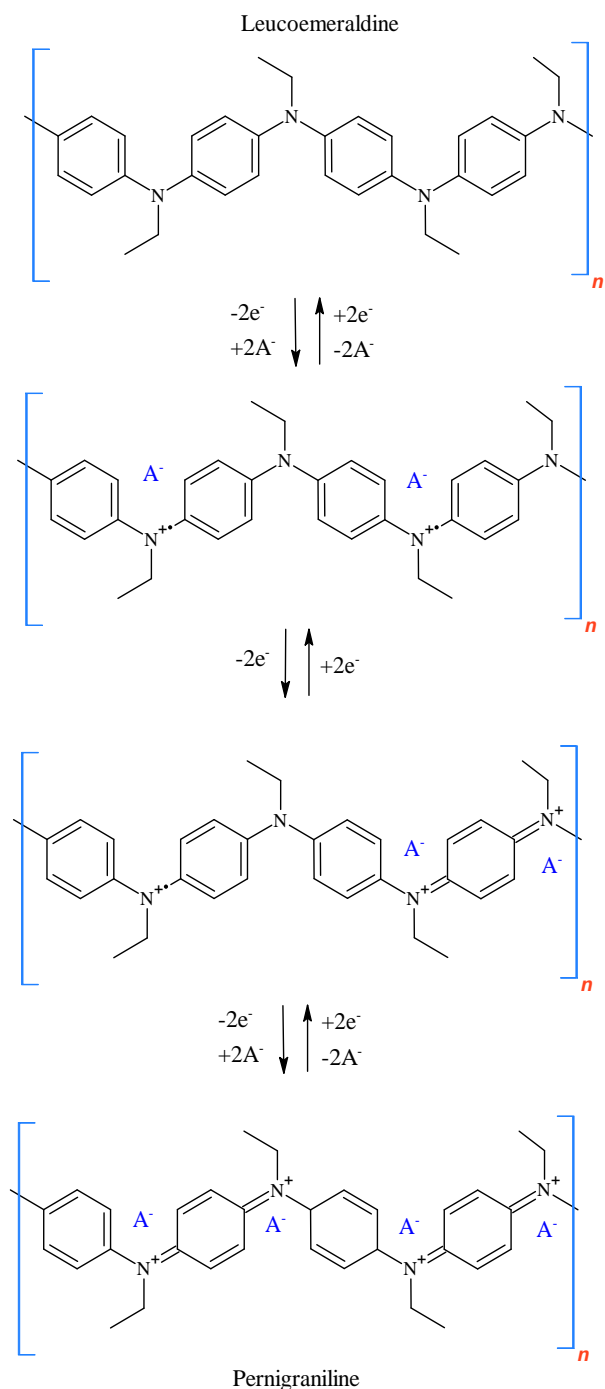
The second potential product, ethyl(phenyl)carbamic acid is a type of carbamic acid. As carbamic acids are generally unstable and revert to their parent amine and CO₂⁶⁹ (**Scheme 3.3**), this may explain the bubbles observed during the experiments, particularly for electrodes cycled in 5 mM EC. Dimerisation of *N*-ethylaniline⁷⁰ and resultant poly(*N*-ethylaniline) (**Scheme 3.4**) may explain the yellow colour observed on the electrode surface⁷¹.



Scheme 3.3: I) Acid catalysed hydrolysis of EC with breakdown of ethyl(phenyl)carbamic acid, and II) further reaction of N-ethylaniline formed from hydrolysis and breakdown of carbamic acid.

Both breakdown compounds are readily soluble in ethanol⁷² but have some retention on the electrode surfaces in the aqueous electrolyte employed here. The CVs shown in **Figure 3.27** in particular bear an interesting resemblance to that of electropolymerisation of *N,N* dimethylaniline at carbon paste electrodes⁷³ where SDS acted as a surfactant to stabilise the aniline radical cation, thus improving the rate of polymerisation. Solubility effects due to the ethyl group may explain the weak film forming processes evident, together with steric effects due to the ethyl substituent which can distort the π system and lower conjugation^{74,75}.

The redox mechanism of poly(*N*-alkyl anilines) includes $2e^-/2H^+$ oxidation processes of the leucoemeraldine (fully reduced) - emeraldine - pernigraniline (fully oxidised) forms with the aid of the mobile acetate counterion⁷⁵. Following the initial irreversible oxidation (**Peak I in Figure 3.27 (B)**), in subsequent cycles, redox peaks possibly associated with poly(*N*-ethylaniline) (III & II 1.05 V and 0.99 V respectively) increase (cycles 2 to 3) followed by a decrease (cycles 4 to 20). This may be due to soluble products⁷³ or loss of electroactivity upon overoxidation of the poly(*N*-ethylaniline) pernigraniline form. The bulky ethyl substituent may decrease conjugation, and can increase the energy of the semioxidised emeraldine, increasing the oxidation potential of the leucoemeraldine form⁷⁴, with this reduced form possibly featuring in the weak cathodic process (IV) at -0.11 V.



Scheme 3.4: Various structures of poly(*N*-methylaniline) undergoing oxidation and reduction⁷⁶.

Due to the weak nature of the adsorbed species observed upon cycling under these conditions, a scan rate study was not possible. However, scan rate investigations for GCEs in 1 mM EC were performed (**Figure 2.30 (A)**). The effect of scan rate on the current at 10 mV.s⁻¹ and 200 mV.s⁻¹ are shown for the first three cycles (**Figure 2.30 (B & C)**). At slow scan rates the processes at 1.05 V (**II**) and 1.00 V (**III**) were not visible due to the

experimental timescale while at $200 \text{ mV}\cdot\text{s}^{-1}$ a clear couple was observed with $E_p^a = 0.05 \text{ V}$. A current density vs $v^{1/2}$ plot for the peak at 1.2 V (**I**) was linear over the range $10\text{-}500 \text{ mV}\cdot\text{s}^{-1}$ while the $\log I$ vs $\log v$ resulted in a slope of 0.55 with equation $\text{Log } j_p = 0.549 \text{ Log } n + 3.343$ ($r^2 = 0.997$) reflecting the diffusion-controlled nature of the process.

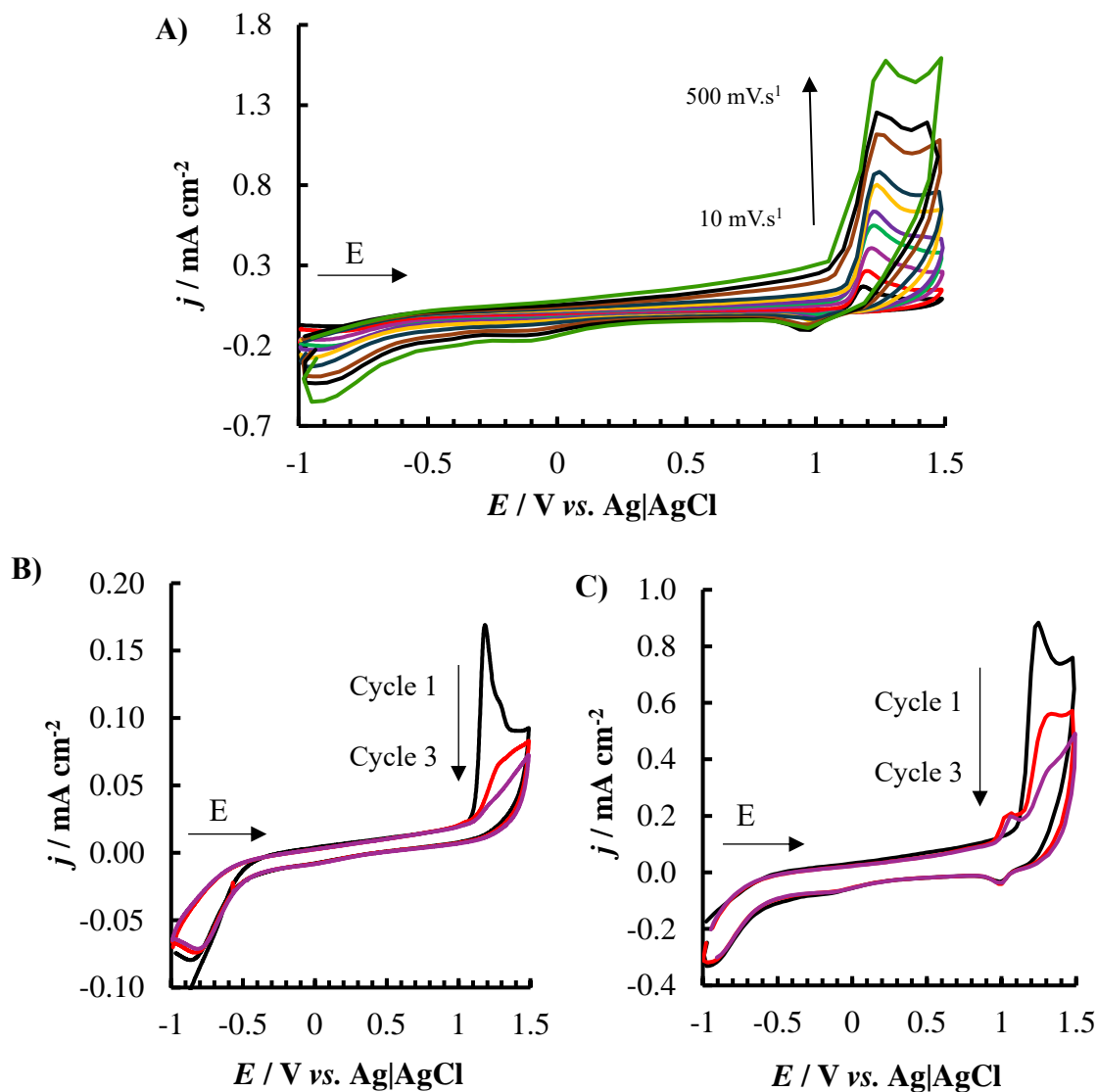


Figure 3.30: A) Cyclic voltammograms (showing cycle 1) for scan rate study of EC at a bare GCE over the potential range of -1 to $+1.5 \text{ V vs. Ag|AgCl}$, scan rates of 10 to $500 \text{ mV}\cdot\text{s}^{-1}$. First 3 cycles of 1 mM EC with 0.1 M LiClO_4 in $3:7$ methanol:sodium acetate buffer ($\text{pH} \sim 4.5$) at B) $10 \text{ mV}\cdot\text{s}^{-1}$ and C) $200 \text{ mV}\cdot\text{s}^{-1}$

The average value of $E_p - E_{p/2}$ as a function of scan rate was 65.9 mV and the αn_α term was estimated (**Equation (2.7)**) as 0.72. Taking α as 0.5 this results in n_α of 1.4. The diffusion coefficient D_0 was estimated from Cycle 1 data using **Equation (2.6)** resulting in $3.35 \times 10^{-5} \text{ cm}^2 \cdot \text{s}^{-1}$. When scan rate data from cycle 3 was examined, linearity was improved for current density vs scan rate plots with peaks II and III exhibiting surface confined behaviour ($r^2 = 0.977$ and 0.998 respectively) and $\log j_p^a$ vs. $\log \nu$ plots for peak (I) resulting in a slope of 0.7 indicating a mixed diffusion effect. Such first time voltammetric studies of the redox behaviour and mechanism for EC electrooxidation in these media offers novel insights which inform the follow on electroanalytical and sensor development stage, exploiting glassy carbon electrodes modified with the magnetic nanoparticles synthesised as described in **section 2.2.2**.

Differential pulse voltammetry was employed to minimise the complications observed above upon cycling and to isolate the main anodic oxidation peak for analytical purposes. **Figure 3.31 (A) and (B)** shows the concentration dependent DPV response at bare and modified (magnetic nanoparticle) GCEs over the range 0.5-1000 μM .

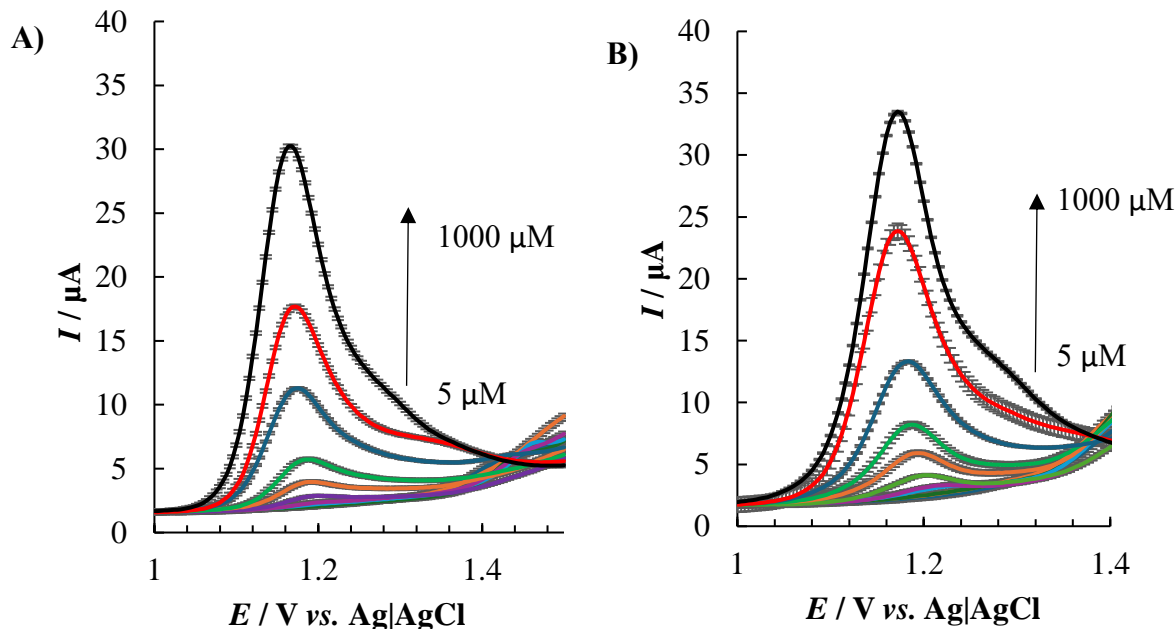


Figure 3.31: Average DPV data ($n=3$) of EC over the potential range of -1 to $+1.5$ V vs. Ag|AgCl with additional parameters as per electrochemical procedures section (region of EC peak 1 to 1.5 V only shown) for a concentration series (5 to 1000 μM) at A) bare and B) MNP modified GCE (with current standard deviations of $\pm 0.15 \mu\text{A}$ for bare and $\pm 0.20 \mu\text{A}$ for modified across the entire series).

When the concentration series was plotted, a polynomial response was observed, indicating that more than one linear series may be present in the set **Figure 3.32 (A)**. Two linear series were derived ($n=3$), a higher series (**Figure 3.32 (B)**) over the range 100 to 1000 μM and lower series (**Figure 3.32 (C)**) across the region of 5 to 50 μM , with the highest sensitivity being achieved at the lower concentration series of 0.0386 ± 0.0026 and $0.0637 \pm 0.0044 \mu\text{A} \cdot \mu\text{M}^{-1}$ for bare and modified electrodes respectively. Limits of detection and quantification values were calculated in the same way in which the values for DPA were achieved and LODs of 4.07 ± 0.25 and $4.39 \pm 0.28 \mu\text{M}$ and LOQs of 13.6 ± 0.85 and $14.6 \pm 0.95 \mu\text{M}$ were obtained for both bare and modified electrode respectively.

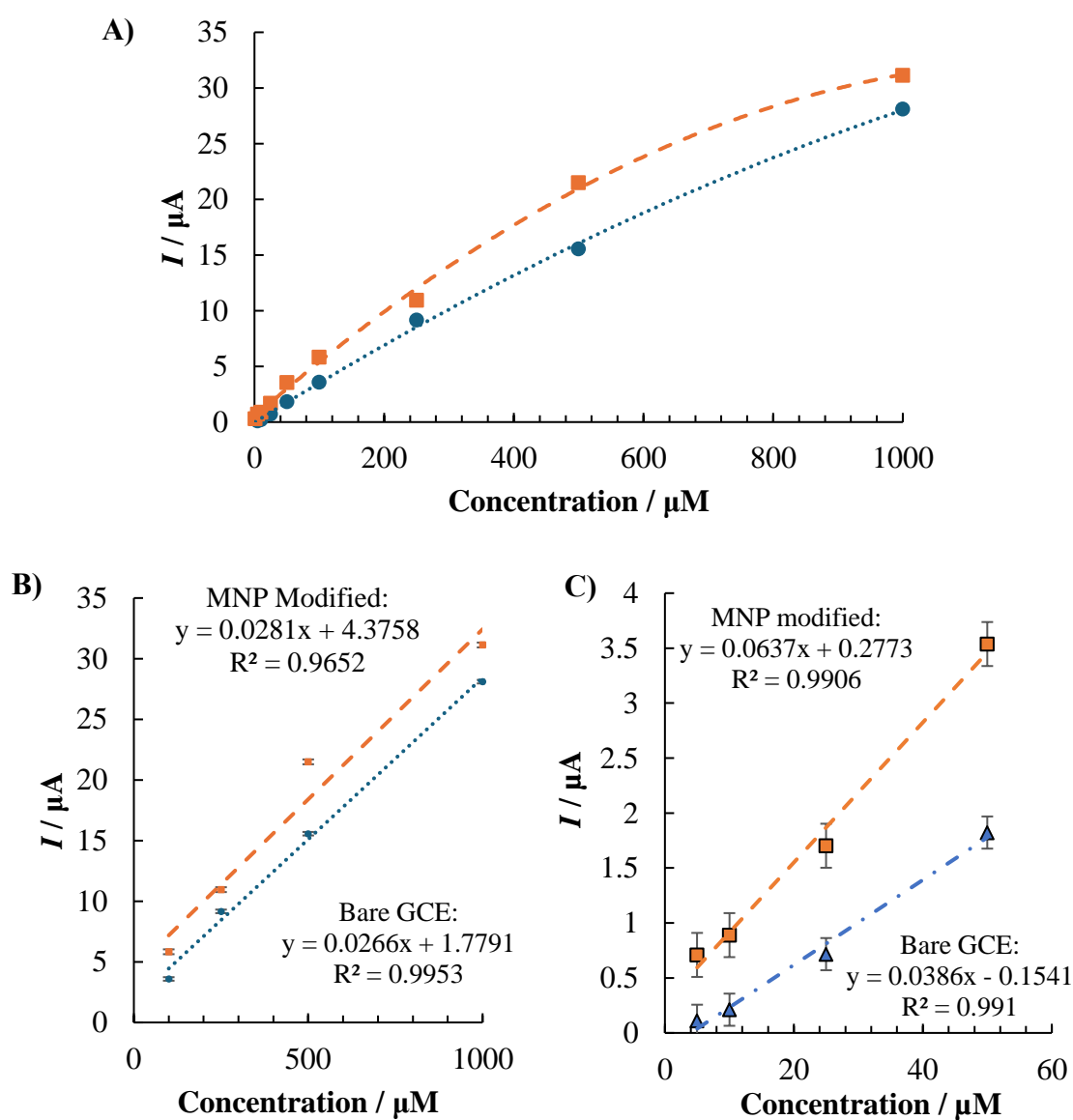


Figure 3.32: Average data plots ($n=3$) of current vs. concentration of EC in 3:7 methanol:sodium acetate buffer ($\text{pH} \sim 4.5$) at bare (blue) and modified (red) GCE over the concentrations of A) 5 to 1000 μM , B) 50 to 1000 μM and C) 5 to 50 μM .

Table 3.5: Comparison of LOD and LOQ values for DPA and EC at bare and MNP modified GCEs.

<i>Electrode</i>	LOD (μM)	LOQ (μM)
<i>Diphenylamine</i>		
<i>Bare GCE</i>	2.27 ± 0.03	7.57 ± 0.10
<i>MNP modified GCE</i>	3.51 ± 0.15	11.7 ± 0.47
<i>Ethyl-centralite</i>		
<i>Bare GCE</i>	4.07 ± 0.25	13.6 ± 0.85
<i>MNP modified GCE</i>	4.39 ± 0.28	14.6 ± 0.95

3.5 Conclusion

In this chapter, new insights into the electrooxidation of DPA and EC in organic and aqueous electrolytes have been discovered, realising key knowledge into follow-up products and processes which could arise during degradation.

The work presented within this chapter, progresses this via a successful study into the electrochemistry of DPA and EC coupled with the first-time use of iron oxide magnetic nanoparticles, positively influencing the sensing capabilities of the modified GCE. MNPs were prepared using the accessible and controlled process of electrooxidation at iron anodes followed by characterisation via surface, thermal, spectroscopic, and electrochemical techniques.

Follow-up products were proposed, with the generation of DPB through the oxidation and subsequent dimerisation of DPA and degradation of EC to its primary amine. In both instances deposition of some material was confirmed with either surface confined processes ($\text{Log } j_p^a$ vs. Log scan rate) or visual inspection of the electrode surface. It appeared that the modified electrode hindered the generation of the DPB formation or at least adsorption to the electrodes surface. These processes were present primarily using

Chapter 3: Electroanalysis of Organic Firearm Residue Species

CV and so the use of DPV was more advantageous, with LOD and LOQ for both analytes calculated at bare and MNP modified GCE.

In the next chapter, investigation into the electrochemical behaviour of both analytes within the same sample matrix is progressed, being key for developing an electroanalytical method for OFAR analysis.

3.6 References

- (1) Shaw, L.; Dennany, L. Applications of Electrochemical Sensors: Forensic Drug Analysis. *Current Opinion in Electrochemistry* **2017**, *3* (1), 23–28. <https://doi.org/10.1016/j.coelec.2017.05.001>.
- (2) Karahacane, D. S.; Dahmani, A.; Khimeche, K. Raman Spectroscopy Analysis and Chemometric Study of Organic Gunshot Residues Originating from Two Types of Ammunition. *Forensic Science International* **2019**, *301* (2019), 129–136. <https://doi.org/10.1016/j.forsciint.2019.05.022>.
- (3) Benito, S.; Abrego, Z.; Sánchez, A.; Unceta, N.; Goicolea, M. A.; Barrio, R. J. Characterization of Organic Gunshot Residues in Lead-Free Ammunition Using a New Sample Collection Device for Liquid Chromatography–Quadrupole Time-of-Flight Mass Spectrometry. *Forensic Science International* **2015**, *246* (2015), 79–85. <https://doi.org/10.1016/j.forsciint.2014.11.002>.
- (4) Argente-García, A.; Hakobyan, L.; Guillem, C.; Campíns-Falcó, P. Estimating Diphenylamine in Gunshot Residues from a New Tool for Identifying Both Inorganic and Organic Residues in the Same Sample. *Separations* **2019**, *6* (1), 16. <https://doi.org/10.3390/separations6010016>.
- (5) Arne Bergens; Lundström, K.; Asplund, J. Voltammetric Determination of the Stabilizing Additives Acardite II, Centralite I and Diphenylamine in Propellants. *Talanta* **1985**, *32* (9), 893–899. [https://doi.org/10.1016/0039-9140\(85\)80203-4](https://doi.org/10.1016/0039-9140(85)80203-4).
- (6) Wang, C.-Y.; Ge, Q.; Jiang, N.; Cong, H.; Tao, Z.; Liu, M.; Fan, Y. A Label-Free Electrochemical Sensor Constructed with Layer-By-Layer Assembly of GCE-AuNPs-Q[7]·HAuCl₄ for Detection of Diphenylamine. *Analytical Sciences* **2022**, *38* (9), 1181–1188. <https://doi.org/10.1007/s44211-022-00141-3>.
- (7) Denmead, C. F.; Vere-Jones, N. W.; Atkinson, J. D. A Commercial Method of Controlling Apple Scald with Diphenylamine Emulsions. *Journal of Horticultural Science* **1961**, *36* (2), 73–84. <https://doi.org/10.1080/00221589.1961.11514001>.

Chapter 3: Electroanalysis of Organic Firearm Residue Species

- (8) Donadel, J. Z.; Thewes, F. R.; Ferreira, L.; Schultz, E. E.; Pasquetti, R.; Ludwig, V.; Mesadri, J.; Klein, B.; Thewes, F. R.; Prediger, F.; Both, V.; Brackmann, A.; Neuwald, D. A.; Wagner, R. Superficial Scald Development in “Granny Smith” and “Nicoter” Apples: The Role of Key Volatile Compounds When Fruit Are Stored under Dynamic Controlled Atmosphere. *Food Research International* **2023**, *173* (2023), 113396–113396. <https://doi.org/10.1016/j.foodres.2023.113396>.
- (9) European Union. *COMMISSION REGULATION (EU) 2018/1515 of 10 October 2018 Amending Annexes III and V to Regulation (EC) No 396/2005 of the European Parliament and of the Council as Regards Maximum Residue Levels for Diphenylamine and Oxadixyl in or on Certain Product*.
- (10) Curtis, N. J.; Berry, P. Derivatives of Ethyl Centralite in Australian Gun Propellants. *Propellants Explosives Pyrotechnics* **1989**, *14* (6), 260–265. <https://doi.org/10.1002/prop.19890140609>.
- (11) Dalby, O.; Butler, D.; Birkett, J. W. Analysis of Gunshot Residue and Associated Materials-A Review. *Journal of Forensic Sciences* **2010**, *55* (4), 924–943. <https://doi.org/10.1111/j.1556-4029.2010.01370.x>.
- (12) Ferdowsi, M.; Abolfazl Taghian; Najafi, A.; Moradi, M. Application of a Nanostructured Supramolecular Solvent for the Microextraction of Diphenylamine and Its Mono-Nitrated Derivatives from Unburned Single-Base Propellants. *Journal of separation science* **2014**, *38* (2), 276–282. <https://doi.org/10.1002/jssc.201401023>.
- (13) Pigou, P.; Dennison, G. H.; Johnston, M.; Kobus, H. An Investigation into Artefacts Formed during Gas Chromatography/Mass Spectrometry Analysis of Firearms Propellant That Contains Diphenylamine as the Stabiliser. *Forensic Science International* **2017**, *279* (2017), 140–147. <https://doi.org/10.1016/j.forsciint.2017.08.013>.
- (14) Burleson, G. L.; Gonzalez, B.; Simons, K.; Yu, J. C. C. Forensic Analysis of a Single Particle of Partially Burnt Gunpowder by Solid Phase Micro-Extraction–Gas Chromatography–Nitrogen Phosphorus Detector. *Journal of Chromatography A* **2009**, *1216* (22), 4679–4683. <https://doi.org/10.1016/j.chroma.2009.03.074>.

Chapter 3: Electroanalysis of Organic Firearm Residue Species

- (15) McKenzie-Coe, A.; Bell, S.; Fernandez-Lima, F. Detection of Firearm Discharge Residue from Skin Swabs Using Trapped Ion Mobility Spectrometry Coupled to Mass Spectrometry. *Analytical Methods* **2018**, *10* (35), 4219–4224. <https://doi.org/10.1039/c8ay00658j>.
- (16) Castellanos, A.; Bell, S.; Fernandez-Lima, F. Characterization of Firearm Discharge Residues Recovered from Skin Swabs Using Sub-Micrometric Mass Spectrometry Imaging. *Analytical Methods* **2016**, *8* (21), 4300–4305. <https://doi.org/10.1039/c6ay00096g>.
- (17) MacCrehan, W. A.; Bedner, M. Development of a Smokeless Powder Reference Material for Propellant and Explosives Analysis. *Forensic Science International* **2006**, *163* (1-2), 119–124. <https://doi.org/10.1016/j.forsciint.2005.11.027>.
- (18) MacCrehan, W. A.; Layman, M. J.; Secl, J. D. Hair Combing to Collect Organic Gunshot Residues (OGSR). *Forensic Science International* **2003**, *135* (2), 167–173. [https://doi.org/10.1016/s0379-0738\(03\)00207-x](https://doi.org/10.1016/s0379-0738(03)00207-x).
- (19) Zeng, J.; Qi, J.; Bai, F.; Chung Yu, J. C.; Shih, W.-C. Analysis of Ethyl and Methyl Centralite Vibrational Spectra for Mapping Organic Gunshot Residues. *The Analyst* **2014**, *139* (17), 4270–4278. <https://doi.org/10.1039/c4an00657g>.
- (20) Wang, J.; O'Mahony, A. M. Electrochemical Detection of Gunshot Residue for Forensic Analysis. *Forensic Science: A Multidisciplinary Approach* **2016**, 103–124. <https://doi.org/10.1002/9783527693535.ch6>.
- (21) Bandodkar, A. J.; O'Mahony, A. M.; Ramírez, J.; Samek, I. A.; Anderson, S. M.; Windmiller, J. R.; Wang, J. Solid-State Forensic Finger Sensor for Integrated Sampling and Detection of Gunshot Residue and Explosives: Towards “Lab-On-a-Finger.” *The Analyst* **2013**, *138* (18), 5288. <https://doi.org/10.1039/c3an01179h>.

Chapter 3: Electroanalysis of Organic Firearm Residue Species

- (22) Bratin, K.; Kissinger, P. T.; Briner, R. C.; Bruntlett, C. S. Determination of Nitro Aromatic, Nitramine, and Nitrate Ester Explosive Compounds in Explosive Mixtures and Gunshot Residue by Liquid Chromatography and Reductive Electrochemical Detection. *Analytica Chimica Acta* **1981**, *130* (2), 295–311. [https://doi.org/10.1016/s0003-2670\(01\)93007-7](https://doi.org/10.1016/s0003-2670(01)93007-7).
- (23) Ott, C. E.; Dalzell, K. A.; Calderón-Arce, P. J.; Alvarado-Gámez, A. L.; Trejos, T.; Arroyo, L. E. Evaluation of the Simultaneous Analysis of Organic and Inorganic Gunshot Residues within a Large Population Data Set Using Electrochemical Sensors. *Journal of Forensic Sciences* **2020**, *65* (6), 1935–1944. <https://doi.org/10.1111/1556-4029.14548>.
- (24) Dalzell, K. A.; Ott, C. E.; Trejos, T.; Arroyo, L. E. Comparison of Portable and Benchtop Electrochemical Instruments for Detection of Inorganic and Organic Gunshot Residues in Authentic Shooter Samples. *Journal of Forensic Sciences* **2022**, *67* (4), 1450–1460. <https://doi.org/10.1111/1556-4029.15049>.
- (25) Theamdee, P.; Traiphol, R.; Rutnakornpituk, B.; Wichai, U.; Rutnakornpituk, M. Surface Modification of Magnetite Nanoparticle with Azobenzene-Containing Water Dispersible Polymer. *Journal of nanoparticle research* **2011**, *13* (10), 4463–4477. <https://doi.org/10.1007/s11051-011-0399-7>.
- (26) Wen, W.; Xie, F.; Hu, R. Carbon-Coated Nickel Magnetic Nanoparticles Modified Electrodes as a Sensor for Determination of Acetaminophen. *Sensors and Actuators B-chemical* **2007**, *123* (1), 495–500. <https://doi.org/10.1016/j.snb.2006.09.031>.
- (27) Wallyn, J.; Anton, N.; Vandamme, T. F. Synthesis, Principles, and Properties of Magnetite Nanoparticles for in Vivo Imaging Applications—a Review. *Pharmaceutics* **2019**, *11* (11), 601. <https://doi.org/10.3390/pharmaceutics11110601>.
- (28) Guo, S.; Li, D.; Zhang, L.; Li, J.; Wang, E. Monodisperse Mesoporous Superparamagnetic Single-Crystal Magnetite Nanoparticles for Drug Delivery. *Biomaterials* **2009**, *30* (10), 1881–1889. <https://doi.org/10.1016/j.biomaterials.2008.12.042>.

- (29) Doaga, R.; McCormac, T.; Dempsey, E. Functionalized Magnetic Nanomaterials for Electrochemical Biosensing of Cholesterol and Cholesteryl Palmitate. *Microchimica Acta* **2020**, *187* (4). <https://doi.org/10.1007/s00604-020-4203-1>.
- (30) Lu, B.-W.; Chen, W.-C. A Disposable Glucose Biosensor Based on Drop-Coating of Screen-Printed Carbon Electrodes with Magnetic Nanoparticles. *Journal of Magnetism and Magnetic Materials* **2006**, *304* (1), e400–e402. <https://doi.org/10.1016/j.jmmm.2006.01.222>.
- (31) Martín-Yerga, D. Electrochemical Detection and Characterization of Nanoparticles with Printed Devices. *Biosensors* **2019**, *9* (2), 47. <https://doi.org/10.3390/bios9020047>.
- (32) Hasanzadeh, M.; Shadjou, N.; de la Guardia, M. Iron and Iron-Oxide Magnetic Nanoparticles as Signal-Amplification Elements in Electrochemical Biosensing. *TrAC Trends in Analytical Chemistry* **2015**, *72*, 1–9. <https://doi.org/10.1016/j.trac.2015.03.016>.
- (33) Priyadarshana, G.; Kottegoda, N.; Senaratne, A.; de Alwis, A.; Karunaratne, V. Synthesis of Magnetite Nanoparticles by Top-down Approach from a High Purity Ore. *Journal of Nanomaterials* **2015**, *2015*, 1–8. <https://doi.org/10.1155/2015/317312>.
- (34) Gahrouei, Z. E.; Labbaf, S.; Kermanpur, A. Cobalt Doped Magnetite Nanoparticles: Synthesis, Characterization, Optimization and Suitability Evaluations for Magnetic Hyperthermia Applications. *Physica E: Low-dimensional Systems and Nanostructures* **2020**, *116*, 113759. <https://doi.org/10.1016/j.physe.2019.113759>.
- (35) Del Bianco, L.; Spizzo, F.; Barucca, G.; Ruggiero, M. R.; Geninatti Crich, S.; Forzan, M.; Sieni, E.; Sgarbossa, P. Mechanism of Magnetic Heating in Mn-Doped Magnetite Nanoparticles and the Role of Intertwined Structural and Magnetic Properties. *Nanoscale* **2019**, *11* (22), 10896–10910. <https://doi.org/10.1039/c9nr03131f>.
- (36) Abdelhamid, H. N. Nanoparticle-Based Surface Assisted Laser Desorption Ionization Mass Spectrometry: A Review. *Microchimica Acta* **2019**, *186* (10). <https://doi.org/10.1007/s00604-019-3770-5>.

- (37) Kouassi, G. K.; Irudayaraj, J.; McCarty, G. Examination of Cholesterol Oxidase Attachment to Magnetic Nanoparticles. *Journal of Nanobiotechnology* **2005**, *3* (1), 1. <https://doi.org/10.1186/1477-3155-3-1>.
- (38) Cabrera, L.; Gutierrez, S.; Menendez, N.; Morales, M. P.; Herrasti, P. Magnetite Nanoparticles: Electrochemical Synthesis and Characterization. *Electrochimica Acta* **2008**, *53* (8), 3436–3441. <https://doi.org/10.1016/j.electacta.2007.12.006>.
- (39) Rahimdad, N.; Khalaj, A.; Azarian, G.; Nematollahi, D. Electrochemical Device for the Synthesis of Fe₃O₄ Magnetic Nanoparticles. *Journal of The Electrochemical Society* **2019**, *166* (2), E1–E6. <https://doi.org/10.1149/2.0231902jes>.
- (40) Beitollahi, H.; Safaei, M.; Shishehbore, M. R.; Tajik, S. Application of Fe₃O₄@SiO₂/GO Nanocomposite for Sensitive and Selective Electrochemical Sensing of Tryptophan. *Journal of Electrochemical Science and Engineering* **2018**, *9* (1), 45–53. <https://doi.org/10.5599/jese.576>.
- (41) Habibi, B.; Pashazadeh, S.; Pashazadeh, A.; Lotf Ali Saghatforoush. An Amplified Electrochemical Sensor Employing One-Step Synthesized Nickel–Copper–Zinc Ferrite/Carboxymethyl Cellulose/Graphene Oxide Nanosheets Composite for Sensitive Analysis of Omeprazole. *RSC advances* **2023**, *13* (43), 29931–29943. <https://doi.org/10.1039/d3ra04766k>.
- (42) Poo-arporn, Y.; Pakapongpan, S.; Poo-arporn, R. P. Electrochemical Determination of Diethylstilbestrol by Using a Magnetic Nanoparticle/Graphene Composite Film Electrode. *IOP Conference Series: Materials Science and Engineering* **2019**, *625*, 012015. <https://doi.org/10.1088/1757-899x/625/1/012015>.
- (43) Amani, S.; Sohrabi, N.; Mohammadi, R.; Ahadzadeh, I. Synthesis and Investigation of CoMnFeO₄/Reduced Graphene Oxide as Ecofriendly Electrode Material for Supercapacitor and Its Electrochemical Performances. *Journal of Alloys and Compounds* **2023**, *937*, 168020. <https://doi.org/10.1016/j.jallcom.2022.168020>.

- (44) Habibi, N.; Karimi, B. Fabrication and Characterization of Zinc Oxide Nanoparticle Coated Magnetic Iron Oxide: Effect of S-Layers Adsorption on Surface of Oxide. *Journal of Industrial and Engineering Chemistry* **2014**, *20* (5), 3033–3036. <https://doi.org/10.1016/j.jiec.2013.11.039>.
- (45) Stuart, B. H. *Infrared Spectroscopy: Fundamentals and Applications* Stuart/*Infrared Spectroscopy: Fundamentals and Applications*; Chichester, Uk John Wiley & Sons, Ltd, 2004.
- (46) Sun, B.; Ni, X.; Cao, Y.; Cao, G. Electrochemical Sensor Based on Magnetic Molecularly Imprinted Nanoparticles Modified Magnetic Electrode for Determination of Hb. *Biosensors and Bioelectronics* **2017**, *91*, 354–358. <https://doi.org/10.1016/j.bios.2016.12.056>.
- (47) Starowicz, M.; Starowicz, P.; Żukrowski, J.; Przewoźnik, J.; Lemański, A.; Kapusta, C.; Banaś, J. Electrochemical Synthesis of Magnetic Iron Oxide Nanoparticles with Controlled Size. *Journal of Nanoparticle Research* **2011**, *13* (12), 7167–7176. <https://doi.org/10.1007/s11051-011-0631-5>.
- (48) Wright, J. P.; Bell, A. M. T.; Attfield, J. Paul. Variable Temperature Powder Neutron Diffraction Study of the Verwey Transition in Magnetite Fe₃O₄. *Solid State Sciences* **2000**, *2* (8), 747–753. [https://doi.org/10.1016/s1293-2558\(00\)01107-9](https://doi.org/10.1016/s1293-2558(00)01107-9).
- (49) Fleet, M. E. The Structure of Magnetite: Symmetry of Cubic Spinels. *Journal of Solid State Chemistry* **1986**, *62* (1), 75–82. [https://doi.org/10.1016/0022-4596\(86\)90218-5](https://doi.org/10.1016/0022-4596(86)90218-5).
- (50) Ristić, M.; Fujii, T.; Hashimoto, H.; Opačak, I.; Svetozar Musić. A Novel Route in the Synthesis of Magnetite Nanoparticles. *Materials Letters* **2013**, *100*, 93–97. <https://doi.org/10.1016/j.matlet.2013.03.013>.
- (51) Yuan, K.; Renock, D.; Ewing, R. C.; Becker, U. Uranium Reduction on Magnetite: Probing for Pentavalent Uranium Using Electrochemical Methods. *Geochimica et Cosmochimica Acta* **2015**, *156*, 194–206. <https://doi.org/10.1016/j.gca.2015.02.014>.

Chapter 3: Electroanalysis of Organic Firearm Residue Species

- (52) Bard, A. J.; Faulkner, L. R.; White, H. S. *Electrochemical Methods*; John Wiley & Sons, 2022.
- (53) Min Hwan Kim; Dong Hun Bae; Hyoung Jin Choi; Seo, Y. Synthesis of Semiconducting Poly(Diphenylamine) Particles and Analysis of Their Electrorheological Properties. *Polymer* **2017**, *119*, 40–49. <https://doi.org/10.1016/j.polymer.2017.05.017>.
- (54) Vuki, M.; Shiu, K.-K.; Galik, M.; O'Mahony, A. M.; Wang, J. Simultaneous Electrochemical Measurement of Metal and Organic Propellant Constituents of Gunshot Residues. *The Analyst* **2012**, *137* (14), 3265. <https://doi.org/10.1039/c2an35379b>.
- (55) Heineman, W. R.; Kissinger, P. T. *Laboratory Techniques in Electroanalytical Chemistry*; M. Dekker: New York ; Basel, 1996.
- (56) Yang, H.; Bard, A. J. The Application of Rapid Scan Cyclic Voltammetry and Digital Simulation to the Study of the Mechanism of Diphenylamine Oxidation, Radical Cation Dimerization, and Polymerization in Acetonitrile. *Journal of Electroanalytical Chemistry and Interfacial Electrochemistry* **1991**, *306* (1-2), 87–109. [https://doi.org/10.1016/0022-0728\(91\)85224-d](https://doi.org/10.1016/0022-0728(91)85224-d).
- (57) Sakthivel, M.; Sukanya, R.; Chen, S. Fabrication of Europium Doped Molybdenum Diselenide Nanoflower Based Electrochemical Sensor for Sensitive Detection of Diphenylamine in Apple Juice. *Sensors and Actuators B: Chemical* **2018**, *273*, 616–626. <https://doi.org/10.1016/j.snb.2018.06.094>.
- (58) Tsai, T.; Ku, S.; Chen, S.; Lou, B.; Ajmal Ali, M.; Al-Hemaid, F. M. A. Electropolymerized Diphenylamine on Functionalized Multiwalled Carbon Nanotube Composite Film and Its Application to Develop a Multifunctional Biosensor. *Electroanalysis* **2014**, *26* (2), 399–408. <https://doi.org/10.1002/elan.201300495>.

Chapter 3: Electroanalysis of Organic Firearm Residue Species

- (59) Krishnan, R. G.; Beena Saraswathyamma. Simultaneous Resolution and Electrochemical Quantification of Tyrosine and Tryptophan at a Poly (Diphenylamine) Modified Electrode. *Journal of the Electrochemical Society* **2021**, *168* (2), 027509–027509. <https://doi.org/10.1149/1945-7111/abe1dd>.
- (60) Golczak, S.; Kancierzewska, A.; Fahlman, M.; Langer, K.; Langer, J. Comparative XPS Surface Study of Polyaniline Thin Films. *Solid State Ionics* **2008**, *179* (39), 2234–2239. <https://doi.org/10.1016/j.ssi.2008.08.004>.
- (61) European Food Safety Authority. Conclusion on the Peer Review of the Pesticide Risk Assessment of the Active Substance Diphenylamine. *EFSA Journal* **2012**, *10* (1), 2486. <https://doi.org/10.2903/j.efsa.2012.2486>.
- (62) Nagarajan, S.; Santhosh, P.; Sankarasubramanian, M.; Vasudevan, T.; Gopalan, A.; Lee, K.-P. UV–Vis Spectroscopy for Following the Kinetics of Homogeneous Polymerization of Diphenylamine in P-Toluene Sulphonic Acid. *Spectrochimica acta. Part A, Molecular and Biomolecular Spectroscopy* **2005**, *62* (1-3), 420–430. <https://doi.org/10.1016/j.saa.2005.01.010>.
- (63) Naqvi, I. I.; Perveen, A. Investigation of Electron Transfer Reaction between Diphenylbenzidine and Ascorbic Acid. *Turkish Journal of Chemistry* **2005**, *96* (3), 627–634.
- (64) Tsai, Y.-T.; Wen, T.-C.; Gopalan, A. Tuning the Optical Sensing of PH by Poly(Diphenylamine). *Sensors and Actuators B: Chemical* **2003**, *96* (3), 646–657. <https://doi.org/10.1016/j.snb.2003.07.009>.
- (65) Wu, M.-S.; Wen, T.-C.; Gopalan, A. In Situ UV–Visible Spectroelectrochemical Studies on the Copolymerization of Diphenylamine with Anthranilic Acid. *Materials Chemistry and Physics* **2002**, *74* (1), 58–65. [https://doi.org/10.1016/s0254-0584\(01\)00406-0](https://doi.org/10.1016/s0254-0584(01)00406-0).
- (66) Hoffer, R.; Wyss, P. The Use of Unburned Propellant Powder for Shooting-Distance Determination. Part II: Diphenylamine Reaction. *Forensic Science International* **2017**, *278* (2017), 24–31. <https://doi.org/10.1016/j.forsciint.2017.06.022>.

Chapter 3: Electroanalysis of Organic Firearm Residue Species

- (67) Stefano Salvestrini; Paola Di Cerbo; Capasso, S. Kinetics and Mechanism of Hydrolysis of Phenylureas. *Journal of the Chemical Society Perkin Transactions 2* **2002**, No. 11, 1889–1893. <https://doi.org/10.1039/b205850b>.
- (68) Laudien, R.; Mitzner, R. Reply to the “Comment on ‘Phenylureas. Part 1. Mechanism of the Basic Hydrolysis of Phenylureas and Part 2. Mechanism of the Acid Hydrolysis of Phenylureas’ ” by S. Salvestrini, P. Di Cerbo and S. Capasso, *J. Chem. Soc., Perkin Trans. 2*, 2002, 8481,2. *Journal of the Chemical Society Perkin Transactions 2* **2002**, No. 4, 849–849. <https://doi.org/10.1039/b201281m>.
- (69) Adams, P.; Baron, F. A. Esters of Carbamic Acid. *Chemical Reviews* **1965**, 65 (5), 567–602. <https://doi.org/10.1021/cr60237a002>.
- (70) Zuman, P. Chapter VIII - Practical Applications. In *Organic Polarographic Analysis Volume 12 in International Series of Monographs on Analytical Chemistry*; Elsevier Ltd. , 1964; pp. 185–226.
- (71) Sarı, B.; Gök, A.; Şahin, D. Synthesis and Properties of Conducting Polypyrrole, Polyalkylanilines, and Composites of Polypyrrole and Poly(2-Ethylaniline). *Journal of Applied Polymer Science* **2006**, 101 (1), 241–249. <https://doi.org/10.1002/app.23247>.
- (72) Chabukswar, V. V.; Bhavsar, S. V.; Mohite, K. C. Synthesis of Poly(N-Ethylaniline) Nanoparticles Synthesis and Characterization of Organically Soluble Conducting Poly(N-Ethylaniline) Nanoparticles Using Acrylic Acid as a Soft Template. *Journal of Macromolecular Science Part A* **2012**, 49 (7), 547–553. <https://doi.org/10.1080/10601325.2012.687682>.
- (73) Fathi, S.; Mahdavi, M. R. Electropolymerization of N,N-Dimethylaniline in Presence of Sodium Dodecyl Sulfate and Its Electrochemical Properties. *Russian Journal of Electrochemistry* **2014**, 50 (11), 1077–1084. <https://doi.org/10.1134/s1023193514090031>.

Chapter 3: Electroanalysis of Organic Firearm Residue Species

- (74) Andriianova, A. N.; Biglova, Y. N.; Mustafin, A. G. Effect of Structural Factors on the Physicochemical Properties of Functionalized Polyanilines. *RSC Advances* **2020**, *10* (13), 7468–7491. <https://doi.org/10.1039/c9ra08644g>.
- (75) Lindfors, T.; Ivaska, A. Potentiometric and UV–Vis Characterisation of N-Substituted Polyanilines. *Journal of Electroanalytical Chemistry* **2002**, *535* (1-2), 65–74. [https://doi.org/10.1016/s0022-0728\(02\)01172-5](https://doi.org/10.1016/s0022-0728(02)01172-5).
- (76) Direksilp, C.; Sirivat, A. Synthesis and Characterization of Hollow-Sphered Poly(N-Methylaniline) for Enhanced Electrical Conductivity Based on the Anionic Surfactant Templates and Doping. *Polymers* **2020**, *12* (5), 1023. <https://doi.org/10.3390/polym12051023>.

Chapter 4: Electrochemical Analysis of Analytes Found Within OFAR with the Extension to Real Sample Analysis

*Note: Research data within Chapters 3 & 4 directly correlate with two publications produced from the PhD research:

- McKeever, C.; Callan, S.; Warren, S.; Dempsey, E. Magnetic nanoparticle modified electrodes for voltammetric determination of propellant stabiliser diphenylamine. *Talanta* 2022, 238, 123039. <https://doi.org/10.1016/j.talanta.2021.123039>.
 - McKeever, C.; Dempsey, E. Electroanalysis of ethyl-centralite propellant stabiliser at magnetic nanoparticle modified glassy carbon and screen-printed electrodes with extension to forensic firearm residue analysis. *Sensors and Actuators. B, Chemical* 2023, 396, 134604. <https://doi.org/10.1016/j.snb.2023.134604>.
-

4.1 Chapter Aims

In this chapter the three main aims were:

- To develop an understanding of how two different analytes found within the organic fraction of FAR behave as they undergo analysis within a single matrix.
- To apply the developed methodologies to an unburnt propellant sample and real case FAR.
- To extend this methodology to a low cost on-site disposable screen-printed electrode configuration.

4.2 Introduction

With an understanding of how the analytes behave electrochemically in aqueous media (**Chapter 3**), the initial steps in the development of an electrochemical method for O-FAR have been presented. While O-FAR is not a regularly used component for FAR analysis, as discussed in **Chapter 1**, there is increased interest in developing analytical methods for reliable detection of the characteristic compounds found within a sample matrix. Examples of conventional methods of analysis can be seen in **Table 4.1**, with chromatographic methods being a common choice for forensic science researchers/practitioners.

Table 4.1: Non-electrochemical methods of analysis for DPA or EC.

Method	Analyte	Linear range (ng.mL ⁻¹)	LOD (ng.mL ⁻¹)	Ref
<i>Solid phase microextraction GC</i>	DPA & EC		qualitative	1
<i>Ion mobility spectrometry</i>	DPA		qualitative	2
<i>Transfer to TLC with luminescence detection</i>	DPA		qualitative	3
<i>GC-MS</i>	DPA	10 – 5000	2.09	4
	EC	10 – 5000	0.382	4
<i>UHPLC-ESI-MS/MS</i>	DPA	–	95.64	5
	EC	-	11.06	5
<i>Surface enhanced Raman spectroscopy</i>	DPA		qualitative	6
<i>MS/MS</i>	DPA	5 – 200	1	7
<i>Solid phase microextraction with ion mobility spectrometer^a</i>	DPA	–	0.12 ng	8
	EC	-	1.2 ng	8
<i>Thermal desorption GC-MS^a</i>	DPA	-	0.05 ng (Vial) 5 ng (Swab)	9
	EC	-	0.05 ng (Vial & Swab)	8
<i>LC-EC detector (Au/Hg)^a</i>	DPA	–	0.039 ng	10
<i>HPLC tandem MS/MS</i>	DPA	5-500	0.03	11

^a LOD values quoted as mass not concentration values.

However, with the lab confined nature of these methods of analysis and the generally large costs associated with routine use, electroanalytical methods have experienced interest as a more viable approach for the determination of analytes of interest (specifically DPA and EC in this work). Though the use of electrochemical methods for EC are very limited, DPA has been the subject of great interest in electroanalytical method development. This is due in part to the reclassification of the allowed concentrations in the environment. Since this, many different electrochemical methods have been developed with some examples shown in **Table 4.2**.

Table 4.2: Electrochemical methods for analysis of DPA or EC.

<i>Electrode</i>	Method	Analyte	Linear Range (μM)	Sensitivity ($\mu\text{A}\cdot\mu\text{M}^{-1}$)	LOD (μM)	Ref
<i>PMo₁₂/GO/GCE</i>	DPV	DPA	0.05–400	2.00	0.006	12
<i>EuMoSe₂/GCE</i>	DPV	DPA	0.01–243.17	2.32	0.008	13
<i>DPA/MIP/CPE</i>	DPV	DPA	500–3000	–	10.0	14
<i>TiC/f-CNF/CSPE</i>	LSV	DPA	0.04–56.82	16.47	0.003	15
<i>RGO/Fe₃O₄-MIP/GCE</i>	DPV	DPA	0.1–30	–	0.05	16
<i>La₂(WO₄)₃/SPCE</i>	DPV	DPA	0.01–58.06	0.094	0.0024	17
<i>Mg_xNi_{9-x}S₈@C/GCE</i>	DPV	DPA	0.1–76	–	0.016	18
<i>AgNP/GG/CSPE</i>	DPV	DPA	0.01–9.09	6.879	0.0054	19
<i>Bare Carbon SPE</i>	SWASV	DPA	5.9 – 47	-	27.3	20*
<i>Bare Carbon SPE</i>	SWASV	EC	1.8 – 29.8	-	1.67	20*
<i>Bare GCE</i>	C-SWV	DPA	–	-	-	21*
<i>Bare GCE</i>	DPV	DPA	0.5 – 50	0.0629	2.27	<i>This work</i>
<i>MNP modified GCE</i>	DPV	DPA	0.5 – 50	0.0801	3.51	<i>This work</i>
<i>Bare GCE</i>	DPV	EC	0.5 – 50	0.0386	4.07	<i>This work</i>
<i>MNP modified GCE</i>	DPV	EC	0.5 – 50	0.0637	4.39	<i>This work</i>

*Forensic application

With the wide variety of methods available for O-FAR analysis, electrochemical methods are a growing interest in the research space. Within this chapter, further development and optimisation of the method was undertaken with a goal to further develop the method for on-site capabilities, with a simple low-cost modification material, which has not been undertaken by the methods given in the above table.

4.3 Experimental

4.3.1 Materials and Reagents

Ethanol (anhydrous $\geq 99.5\%$), methanol (ACS Reagent, 99.8%), diphenylamine (ACS Reagent $\geq 99\%$), 1,3 diethyl-1,3 diphenyl urea (ACS Reagent $\geq 99\%$), acetic acid (ACS Reagent $\geq 95.0\%$), lithium perchlorate (ACS Reagent $\geq 95.0\%$), hexamineruthenium(II), potassium chloride were all purchased from Sigma-Aldrich and required no further purification. Electrode polishing solution was a 1 μm monocrystalline diamond suspension (Akasel). The sacrificial iron anode and cathode rods ($3 \times 12 \text{ cm}^2$) were purchased from Goodfellow (purity 99.5%). Rare earth neodymium magnets (grade N35) were purchased from Farnell. For the chemical precipitation of magnetic nanoparticles,

Chapter 4: Electrochemical Analysis of Analytes Found Within OFAR with the Extension to Real Sample Analysis

iron(III) chloride hexahydrate (97 -102%, Alfa Aesar), iron(II) chloride tetrahydrate (\geq 99%, Fluka) and ammonium hydroxide (25% solution in water, Acros organics) were employed.

4.3.2 Instrumentation and Software

All electrochemical experiments were carried out using a Solartron Potentiostat Model 1285 operated by Scribner Associates Corrware software package with data analysis using CorrView Version 2.3a and a CHI Electrochemical workstation model (660E) operated by CHI software (version 19.10) with Microsoft excel 365 software package for data analysis. A glassy carbon electrode (IJ Cambria Scientific) (GCE) (3 mm disk, area = 0.0707 cm²) served as the working electrode, while platinum wire and a standard Ag|AgCl electrode (internal solution 3 M KCl) were employed as the counter and reference electrodes, respectively. The Ag|AgCl reference electrode was stored in 3 M KCl when not in use. An IR lamp was used to dry the magnetic nanoparticle suspensions on working electrodes and a ThermoFisher thermostatic oven was used for drying the magnetic nanoparticles following synthesis. Scanning Electron Microscopy with Energy Dispersive X Ray spectroscopy was performed on a Hitachi SU-70 FE-SEM with Oxford instruments X-max 50 mm² solid-state detector. Atomic Force Microscopy (AFM) measurements were taken on an Agilent 5500 AFM in Acoustic AC mode. Tap300A1-G cantilevers from Budget Sensors were used with resonant frequency of \sim 300 kHz and a spring constant of 40 N/m. Screen printed strips were fabricated using DuPont BQ242 polymer thick film (PTF) carbon ink, Gwent Silver/Silver Chloride ink, Polyethylene terephthalate (PET) substrate and a ThermoScientific HERAtherm Incubator.

4.3.3 Procedures

4.3.3.1 Electrochemical Procedures

Electrochemical procedures utilised within this chapter follow those seen in **Chapter 3 section 3.3.3.1**

4.3.3.2 Synthesis of Magnetic Nanoparticles

Electrosynthesis of magnetic nanomaterials (MNP) was employed per **Chapter 3 section 3.3.3.2**.

Chapter 4: Electrochemical Analysis of Analytes Found Within OFAR with the Extension to Real Sample Analysis

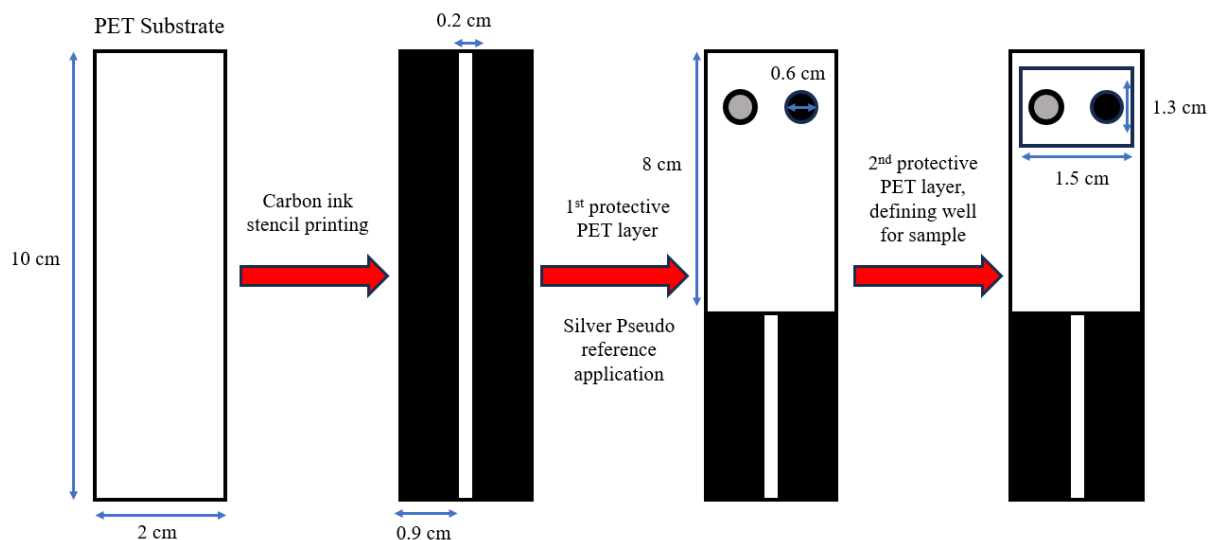
For the purposes of the screen-printed electrode modification, and due to the larger quantities required, a chemical coprecipitation method was employed²². This involved dissolving $\text{FeCl}_3 \cdot 6\text{H}_2\text{O}$ (5.833 g) and $\text{FeCl}_2 \cdot 4\text{H}_2\text{O}$ (2.149 g) in 100 mL of DI water, followed by stirring under N_2 gas, while heating to 72°C . This was followed by addition of 10 mL of 25% ammonium hydroxide. The magnetic particles precipitated instantaneously, and the mixture was further stirred at 72°C for a further 20 minutes and then allowed to cool to room temperature. The material isolation and washing procedure followed that of the electrosynthesis approach.

4.3.3.3 Glassy Carbon Electrode Modification

As per **section 3.3.3.3**

4.3.3.4 Screen Printed Electrodes

Screen printed electrodes (SPE) were fabricated in a multistep process (*in house* developed protocol using stencil printing) - see **Scheme 4.1**. Once the base PET substrate was measured to size, protective masks (with adhesive backing) were cut to 8 x 2 cm with a 1.5 x 1.3 cm sample well. Carbon ink was then applied to the surface and allowed to dry at 60°C for 2 hours. Following curing, the protective mask was removed to expose the channel, and the printed layers were applied to the dried electrode base with the aid of adhesive backed tape. The pseudo reference electrode was formed from silver/silver chloride ink which was cured at 60°C for 2.5 hours. The electrode was ready for use once cooled to room temperature with an exposed geometric working electrode area of 0.283 cm^2 . Magnetic nanoparticle modification of the SPE prototype was achieved via drop casting in a similar fashion to that of GCE with the volume reduced to 10 μL increments to facilitate the dimensions of the sample well (total volume 100 μL).



Scheme 4.1: Schematic showing fabrication process for screen printed electrode utilised within this work.

4.3.3.5 Surface Analysis

Scanning electron microscopy sample analysis required carbon tape lift recovery of the OFAR from the textile target sample over an area of approximately 20 cm² taken radially from the hole produced from the ammunition penetration, followed by sputter coating (Au/Pd) and EDS analysis. Atomic force microscopy analysis was performed by Dr. Shane Murphy of Technological University Dublin, on the same sample type using the same recovery method with tapping mode employed.

4.3.3.6 Firearm Residue Extraction and Analysis

A portion of fabric (polyester/cotton blend (65/35)) was subjected to close range firing using a shotgun - cartridge of ELEY Super game, branded ammunition (**Figure 4.1**) containing Maxam[®] CSB 3 powder, a single base powder that is fast-burning specially indicated for loading low shot weight shotshells (up to 32 g). The unfired propellant specifications are given below (**Table 4.1**)²³



Figure 4.1: Photograph of ELEY super game shotgun cartridges box with spent cartridges.

Table 4.3: Maxam[®] CSB 3 powder specifications as per manufacturer.

Parameter of Propellant	Value
Gauge	12
Powder	1.65 g
Lead	30
Velocity	409 m.s ⁻¹
Pressure	52.2 Mpa
Shape	Disc
Colour	Grey
Diameter	1.7 mm
Thickness	0.3 mm
Density	535 g.L ⁻¹

Firearm recovery involved application of a methanol-soaked cotton swab over a designated area (50 cm²) of the textile sample (**Figure 4.2**). The swab was added to a volume of methanol and sonicated for 30 min. The extracted solution was filtered (gravity filtration) to remove remaining particulates and the solvent removed under nitrogen. The remaining white solid was reconstituted in 1.5 mL methanol and brought up to 5 mL with 0.1 M LiClO₄ sodium acetate buffer pH 4.4 (retaining the 3:7 electrolyte employed with the standards).



Figure 4.2: Photograph of gunshot hole in 65% polyester 35% cotton fabric.

DPV followed in all cases and samples were subjected to spiking for quantitative analysis via standard addition. In the case of the screen-printed electrode sample analysis, 60 mg of propellant disks was dissolved in 5 mL of methanol and the solution was then applied to a 40 cm² portion of polyester fabric, which was allowed to air dry for 1 hour before being recovered using a methanol-soaked cotton swab.

4.4 Results and Discussion

4.4.1 *Dual Analyte Analysis*

In the previous chapter, analytes were examined electrochemically on an individual basis with the formation of secondary products clearly observed with cyclic electrochemical methods. Due to the follow-on chemical processes involved in the case of both DPA and EC, DPV was selected as the electroanalytical method for dual analyte quantitation.

DPV was performed in a standard test mixture and the response examined at both the bare and MNP modified GCEs. As may be seen in **Figure 4.3 (A & B)** both analytes showed good response resolution with peak potentials of 0.654 V and 1.26 V for DPA and EC anodic signals respectively, with I_p^a evaluation over the range 1-1000 μ M. In the mixed

Chapter 4: Electrochemical Analysis of Analytes Found Within OFAR with the Extension to Real Sample Analysis

standard analysis, the MNP modifier impacted the sensitivity for DPA (1.22 ± 0.077 - fold increase ($n=3$)) with no significant difference ($p = 0.3013$) in relation to the EC signal, though a more well-defined EC peak shape was evident. A polynomial response was observed here to a greater extent relative to EC alone (Figure 4.3 (C & D)).

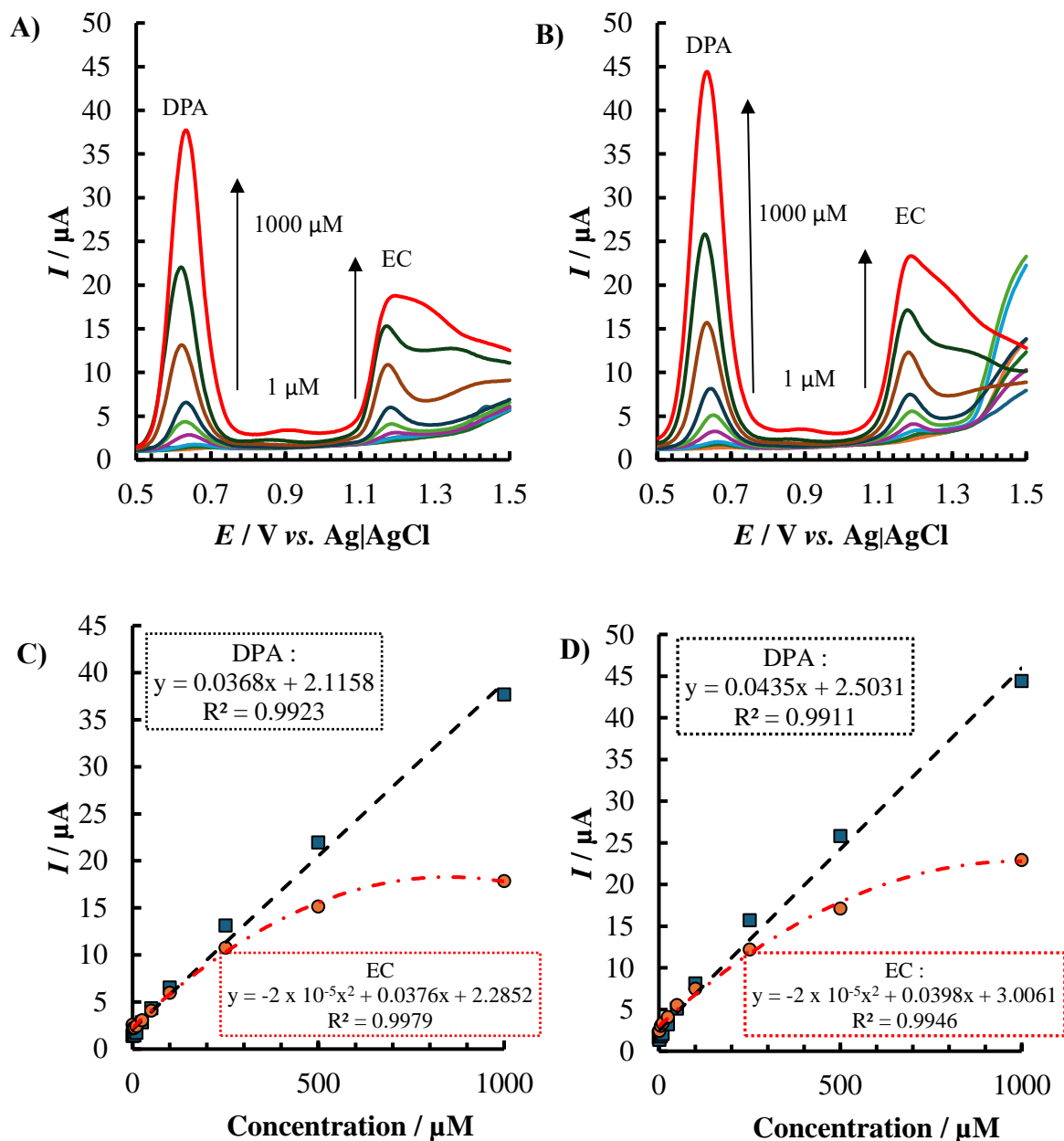


Figure 4.3: Average data ($n=3$) for DPV over the potential range -1 to $+1.5$ V vs. $Ag|AgCl$ (region of peaks 0.5 to 1.5 V only shown) with additional parameters as per electrochemical procedures section. Equal concentrations of DPA and EC over the range 1 to 1000 μM in a 3:7 methanol:sodium acetate buffer ($pH \sim 4.5$) at A) bare and B) MNP modified GCE (with current standard deviations of ± 0.15 μA for bare and ± 0.24 μA for modified across the entire series) with corresponding calibration curves for C) bare and D) modified electrodes.

Chapter 4: Electrochemical Analysis of Analytes Found Within OFAR with the Extension to Real Sample Analysis

As DPA was subject to polymerisation to diphenylbenzidine^{24,25}, upon oxidation, the presence of both analytes caused an alteration in the shape of the more positive response for EC (Figure 4.4 (A)). The MNP modified electrode impacted positively on this effect, resulting in a sharper peak. The change from cyclic methods to a pulse technique and continuous use of MNP modification was implemented to reduce the effect of polymerisation of the analytes on the electrode surface. While the effect may have been reduced, the change in signal of EC compared to when the analyte is by itself may indicate that some hindrance to the surface remained. Concurrently, no difference was observed in the shape of the anodic response for DPA while EC was present (Figure 4.4 B).

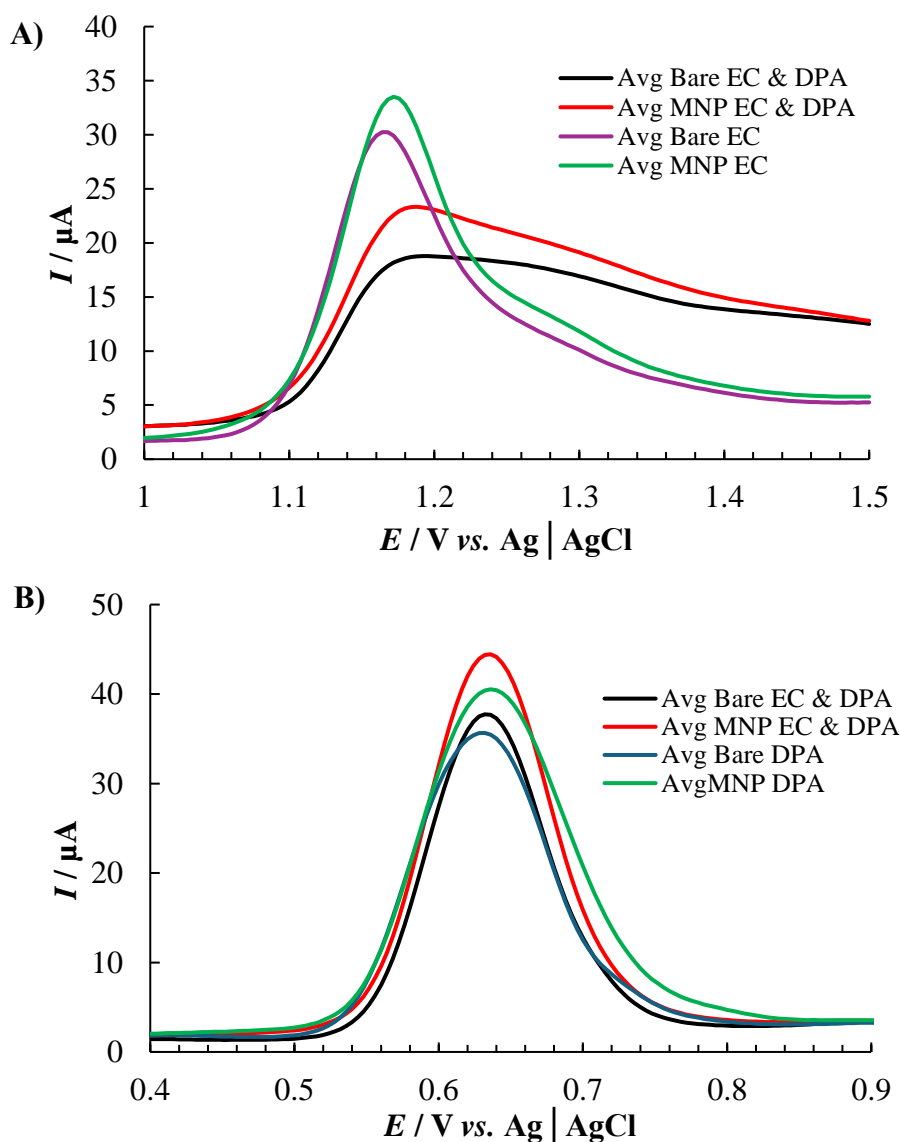


Figure 4.4: Average DPV ($n=3$) over the potential range of -1 to $+1.5$ V vs. Ag|AgCl for both individual and dual analyte systems with additional parameters as per electrochemical procedures section showing A) 1 mM EC peak and B) 1 mM DPA peak under the same conditions at both a bare and MNP modified GCE.

Chapter 4: Electrochemical Analysis of Analytes Found Within OFAR with the Extension to Real Sample Analysis

As observed with the analytes individually, two linear ranges existed across the concentration range used in the analysis. Calibration curves for the analytical range of interest (**Figure 4.5**) are shown to result in sensitivities $7.49 \times 10^{-2} \pm 0.0012 \mu\text{A} \cdot \mu\text{M}^{-1}$ and $5.49 \times 10^{-2} \pm 0.0014 \mu\text{A} \cdot \mu\text{M}^{-1}$ for DPA and EC respectively. This represents a small decrease in DPA and EC sensitivity relative to individual analysis over the same range ($8.01 \times 10^{-2} \pm 0.0034$ and $6.37 \times 10^{-2} \pm 0.0044 \mu\text{A} \cdot \mu\text{M}^{-1}$ respectively) ($n=3$).

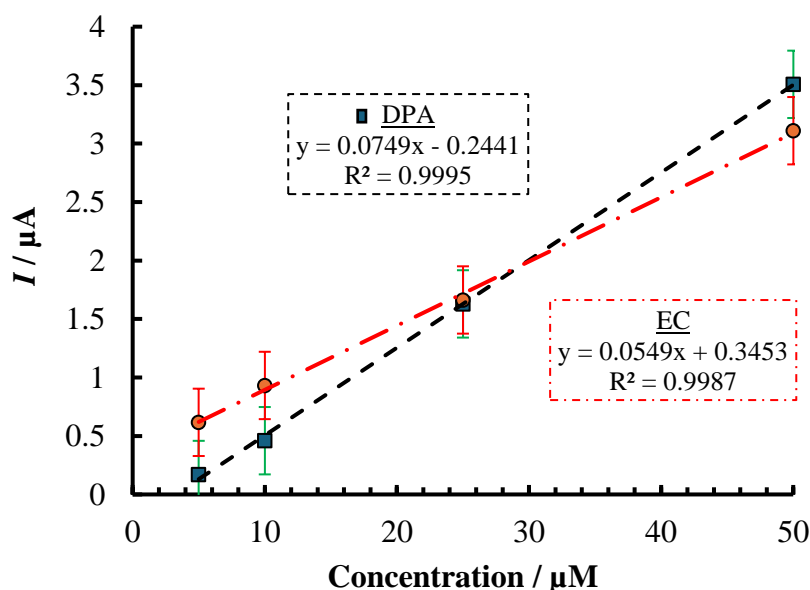


Figure 4.5: Plot of current vs. concentration for both DPA and EC in a mixed analyte system over the concentration range of 5 to 50 μM at MNP modified GCE.

Using the data from the lower calibration range, values for limits of detection and quantification (**Equation 3.10 and 3.11**) can be compared for both single and mixed analyte standards along with a comparison of bare and modified GCEs (**Table 4.4.**) with the MNP modified electrode realising a lower LOD for EC alone and in the presence of DPA relative to the bare electrode.

Table 4.4: LOD and LOQ comparison for bare and MNP modified electrodes.

<i>Electrode</i>	<i>System</i>	<i>Analyte</i>	<i>LOD (μM)</i>	<i>LOQ (μM)</i>
<i>Bare GCE</i>	Single analyte	Ethyl Centralite	4.07 ± 0.25	13.6 ± 0.85
	Single analyte	Diphenylamine	2.27 ± 0.03 ^{a,b}	7.57 ± 0.10 ^{a,b}
	Mixed analytes	Ethyl Centralite	7.06 ± 2.52	23.5 ± 8.40
	Mixed analytes	Diphenylamine	4.48 ± 0.83 ^a	14.9 ± 1.94 ^a
<i>MNP modified GCE</i>	Single analyte	Ethyl Centralite	4.39 ± 0.28	14.6 ± 0.95
	Single analyte	Diphenylamine	3.51 ± 0.15 ^b	11.7 ± 0.47 ^b
	Mixed analytes	Ethyl Centralite	4.76 ± 0.28	15.9 ± 1.28
	Mixed analytes	Diphenylamine	3.75 ± 0.06	12.5 ± 0.19

Table 4.5 shows the overall comparison of LOD and LOQ values obtained for single vs. mixed analyte systems and the bare vs. MNP modified electrodes. In general, no statistical significance (via unpaired t-test) was found with the exception of LOD's and LOQ's calculated for (a) DPA in bare electrode single vs. mixed systems (values ^a in **Table 4.4**) and (b) bare vs. MNP modified electrodes in the single analyte system (values ^b in **Table 4.4**).

Chapter 4: Electrochemical Analysis of Analytes Found Within OFAR with the Extension to Real Sample Analysis

Table 4.5: Comparison of statistically significant differences for LOD and LOQ values obtained for DPA and EC at different electrode modifications.

<i>Modification</i>	<i>Comparison</i>	<i>P value</i>	<i>Statistically Significant Difference</i>
<i>Bare</i>	EC single vs. mixed - LOD	0.1103	No
	EC single vs. mixed - LOQ	0.1121	No
	DPA single vs. mixed - LOD	0.0100	Yes
	DPA single vs. mixed - LOQ	0.0028	Yes
<i>MNP</i>	EC single vs. mixed - LOD	0.2461	No
	EC single vs. mixed - LOQ	0.2306	No
	DPA single vs. mixed - LOD	0.0618	No
	DPA single vs. mixed - LOQ	0.0523	No
<i>System-Analyte Comparison</i>		<i>P value</i>	<i>Statistically significant Difference</i>
<i>Single analyte-EC</i>	Bare vs. MNP LOD	0.2138	No
	Bare vs. MNP LOQ	0.2485	No
<i>Single analyte-DPA</i>	Bare vs. MNP LOD	0.0001	Yes
	Bare vs. MNP LOQ	0.0001	Yes
<i>Mixed analyte-EC</i>	Bare vs. MNP LOD	0.1931	No
	Bare vs. MNP LOQ	0.1963	No
<i>Mixed analyte-DPA</i>	Bare vs. MNP LOD	0.2033	No
	Bare vs. MNP LOQ	0.0999	No

Consideration of competing electroactive signals from co-existing species was important in advance of real sample analysis and an interference study examined diphenyl urea (DPU) and dimethyl phthalate (DMP) (MNP modified electrodes) in the same electrolyte at 0.25 mM in each case. **Figure 4.6** shows that individually, DPA, DPU and EC were adequately resolved $E_p^a = 0.64, 0.96$ and ~ 1.20 V respectively. DMP was found to be non-electroactive over this range and had no impact on propellant stabiliser current response signals.

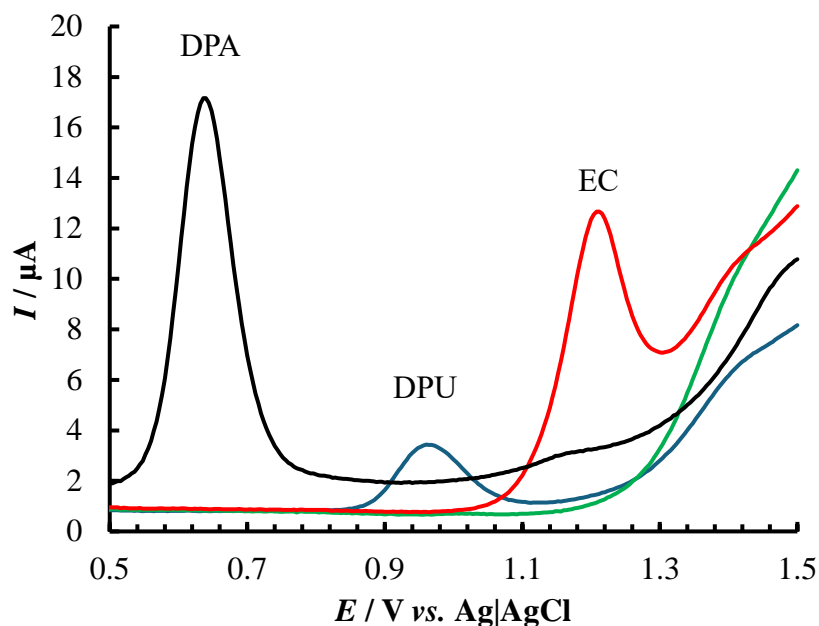


Figure 4.6: Overlaid DPVs over the potential range of -1 to +1.5 V vs. Ag|AgCl with additional parameters as per electrochemical procedures section (region of peaks: 0.5 to 1.5 V only shown). MNP modified GCE response to 0.25 mM DPA (black), 0.25 mM EC (red), 0.25 mM DPU (blue) and 0.25 mM DMP (green) in individual solutions (typical traces).

In summary, both EC and DPA were successfully determined both qualitatively and quantitatively within a mixed solution, with LODs and LOQ calculated. Slight variation was observed in the results when compared to the values obtained when analysis was performed individually with the analytes, however, MNP modification did still provide an increased signal response. The signals realised did not show an overlap at potentials with other common analytes found within OFAR and the methodology was ready to be tested with a real sample of FAR.

4.4.2 Analysis of Firearms Residue generated from the Discharge of a Shotgun.

Real samples were obtained from the discharge from a shot gun using the Eley 12 Super game cartridges filled with Maxam[®] CSB 3 powder as per section 3.3.3.6. To ensure that the FAR samples obtained were capable of being processed by traditional methodologies of FAR analysis FAR, SEM, EDX and AFM were employed for tape lifts acquired around the hole on the fabric.

4.4.2.1 Traditional Analysis of FAR

In order to provide verification of the FAR metallic composition, via conventional surface analysis, tape lift samples were employed for SEM/EDX analysis along with atomic force microscopy (AFM). **Figure 4.7 (A & B)** show the particles (spheres approximately 17 μm in diameter), while the EDX showed evidence of characteristic inorganic metal fraction of FAR to include lead, barium and antimony as shown in **Figure 4.7 (C)**. These results are in line with the Organisation of Scientific Area Committee for Forensic Science (OSAC) criteria for FAR particle analysis via SEM/EDX²⁶.

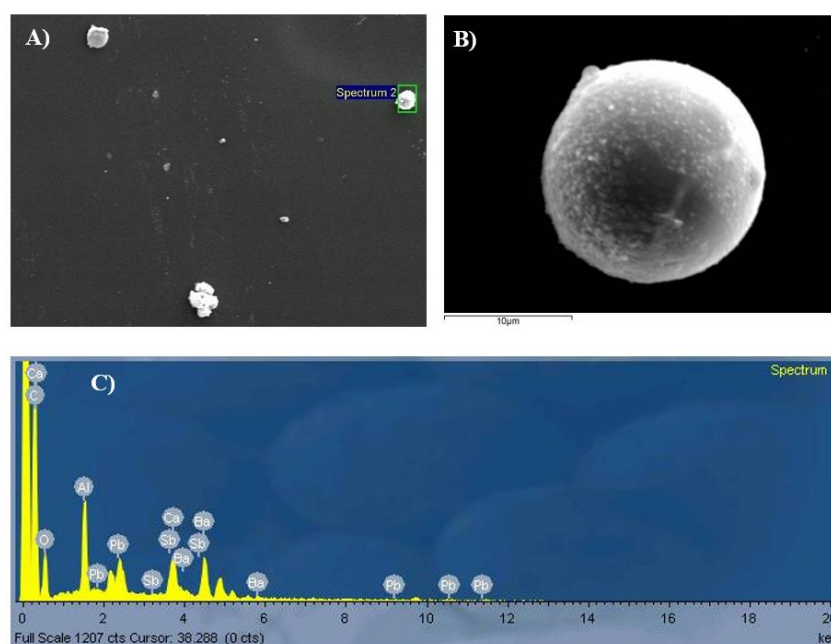


Figure 4.7: SEM photographs of IFAR particles recovered from fabric via tape lifts using a carbon stub showing particles at A) $\times 450$ and B) $\times 4000$ magnification with EDX spectral analysis for IFAR particle in (B) showing presence of lead, antimony and barium.

AFM analysis (**Figure 4.8**) focused on a single particle of 4 μm diameter with height 1.5 μm - topography, amplitude and phase shown. The phase image shows phase shifts at different points decorating the surface of the particle, possibly corresponding to materials of different hardness. These are forward trace images, but the same details are reproduced in the backward retrace images. Interpreting the phase images is complex due to the convolution of sample topography and interaction forces. Tapping-mode operation was chosen in the repulsive regime, providing improved contrast in the phase image by setting the oscillation amplitude slightly below the cantilever's resonance frequency. Darker

Chapter 4: Electrochemical Analysis of Analytes Found Within OFAR with the Extension to Real Sample Analysis

regions in the phase image may suggest areas with higher elastic modulus or increased surface adhesion.

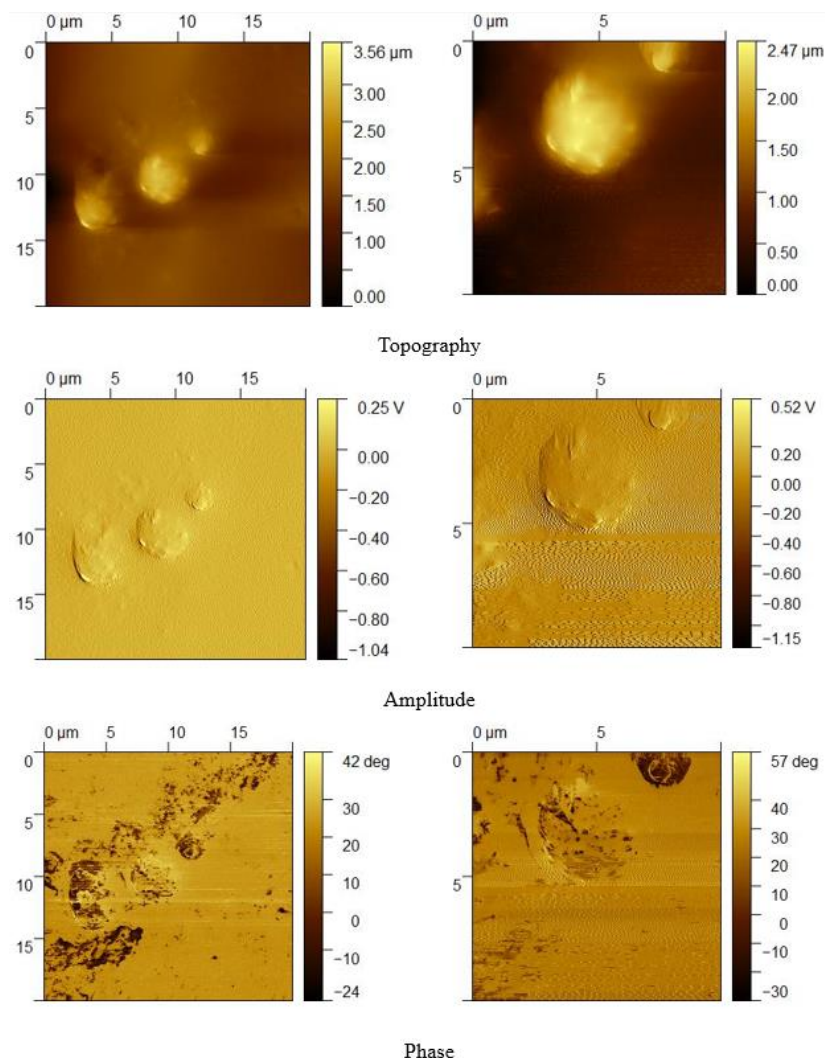


Figure 4.8: Atomic force microscopy of tape lifted sample performed by Dr. Shane Murphy of Technological University Dublin, taken under ambient conditions using a benchtop AFM in tapping mode with 300 kHz, 40 N.m^{-1} cantilever using a scan speed of 0.2 lines.s^{-1} , drive frequency of 272 kHz and drive amplitude of 0.4 V.

Through each form of analysis, confirmation of shape, size and composition of the particles found within the tape lifts are in line with the recommended criteria for I-FAR. With this confirmation, there was confidence that the sample procedure would be suitable to test the electrochemical approach for OFAR determination.

4.4.2.2 Electrochemical Detection of Organic Analytes in a Sample of Unburnt Propellant.

5 mg of unburnt propellant discs (**Figure 4.9**) were dissolved and reconstituted to undergo DPV analysis (**Figure 4.10**). The results showed that DPA was qualitatively identified by the signal at $E_p^a = 0.676$ V vs. Ag|AgCl by overlaying with a 10 μ M DPA standard DPV, in the case of both bare and MNP modified electrodes. A wave representing lead oxidation appeared at $E_p^a = -0.492$ V, which matches previous reports under similar experimental conditions²⁷ and the signal was observed to be significantly amplified at the MNP modified electrode with an average 37-fold increase in current observed. This was thought to be due to the co-ordination of Pb^{2+} ions to the surface hydroxy groups of the magnetic nanomaterials, with the lead response being sensitive to nanomaterial loading/dispersion with intra electrode variations. Xiong et al., 2013 demonstrated a similar effect at amine functionalised magnetite nanoparticles with a 10-fold enhancement in signal using a stripping square wave approach²⁸. Wu et al. also reported a mixed metal quantitative system made possible at Fe_3O_4 modified functionalised multiwalled carbon nanotubes²⁹.



Figure 4.9: Photograph of unburnt propellant discs recovered from shotgun cartridge.

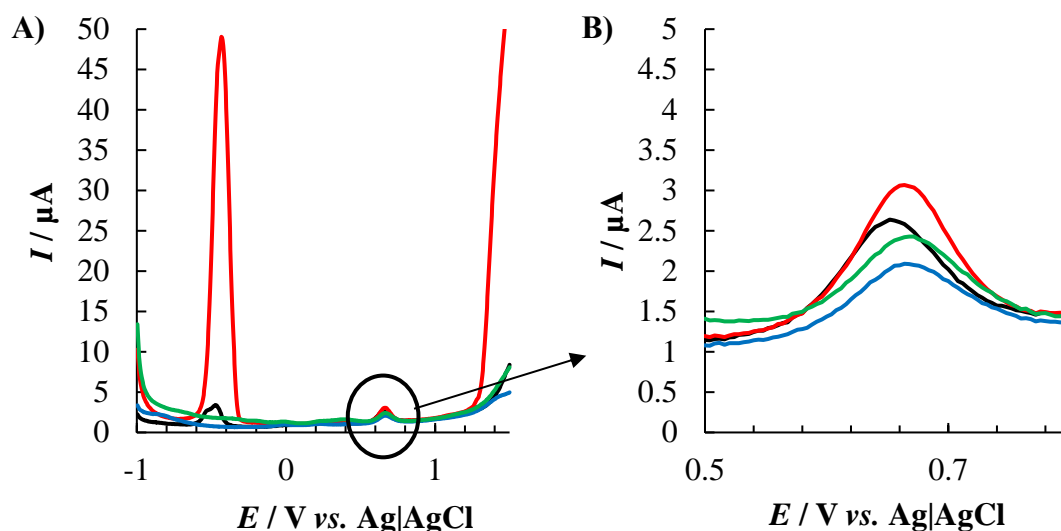


Figure 4.10: Average DPV data ($n=3$) over the potential range of -1 to +1.5 vs. Ag/AgCl with additional parameters as per electrochemical procedures section. A) unburnt propellant sample at bare (black) and MNP modified (red) electrodes and 10 μM DPA standard at bare (blue) and MNP modified (green) electrodes with B) zoomed in region of interest for DPA peak.

The absence of EC within the sample may be partly due to the changes in formulation from ammunition types and brands. Most shotgun propellants are single base formulations, which may favour the presence of 1-5% w/w of the stabiliser with no clearly defined preference on the stabiliser used. However, lists are provided in the patents of propellant formulations with the phrase “at least one” normally including DPA or EC³⁰⁻³³. Regardless, as there was a possibility that EC was present even if only in low concentrations, standard addition analysis was performed to estimate the quantities of stabilisers present in the unburnt propellant.

Standard addition for DPA quantification at bare (**Figure 4.11 (A)**) and MNP modified (**Figure 4.11 (B)**) electrodes with additions of DPA over the range 19.6–56.6 μM were performed, with calculations (**Figure 4.11 C**) realising 1.08 and 1.06 % w/w for bare and modified respectively for DPA in the unburnt propellant.

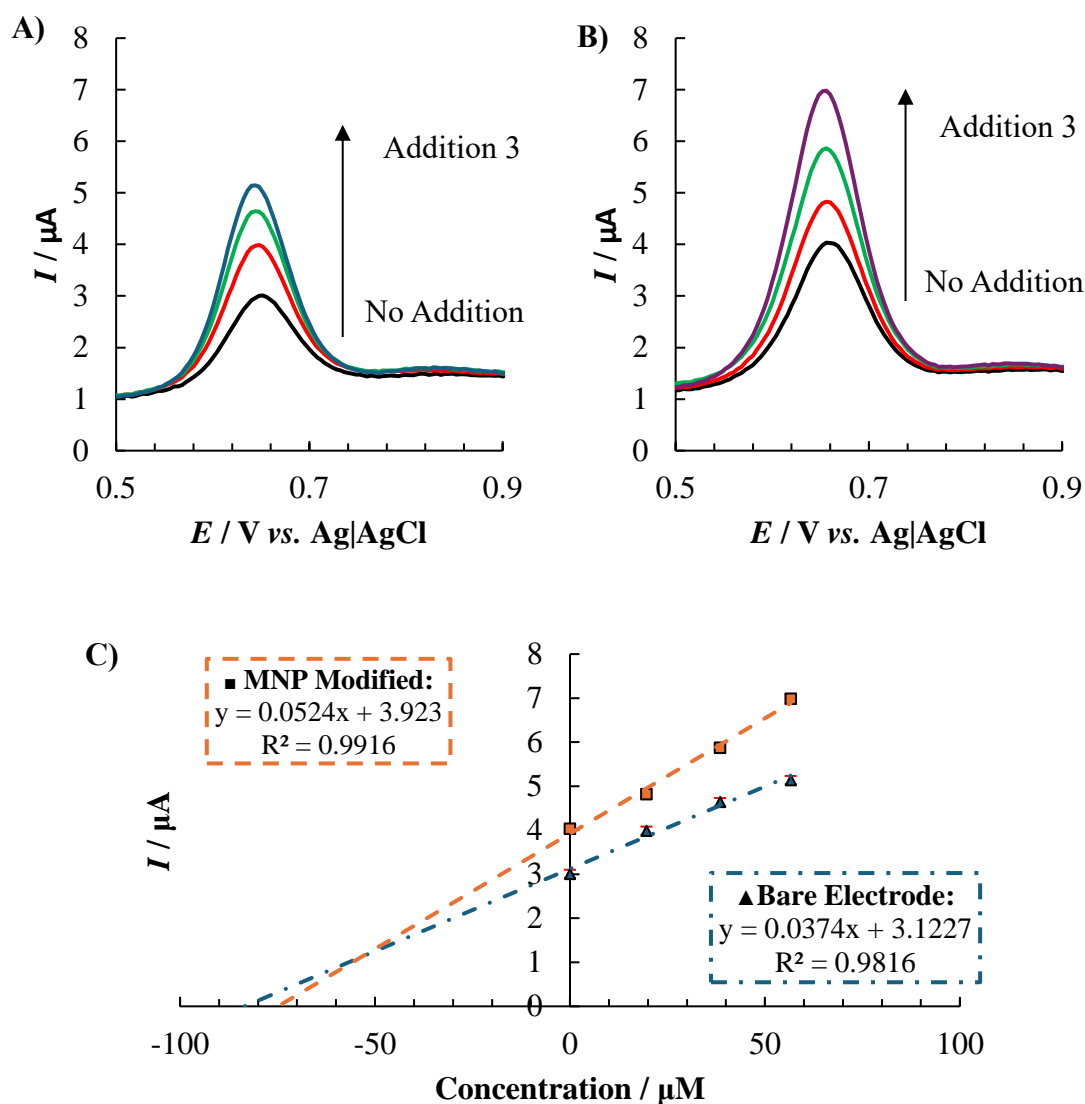


Figure 4.11: Average DPV data ($n=3$) over the potential range of -1 to $+1.5$ V vs. Ag|AgCl with additional parameters as per electrochemical procedures section of A) bare and B) MNP modified GCE with standard addition of DPA 19.6 to 56.6 μM in a solution of 5.91 mg unburnt propellant discs with C) standard addition analysis plots generated from DPV data in (A) and (B) (with current standard deviations of ± 0.092 μA for bare and ± 0.11 μA for modified across the entire series).

Standard addition for EC was also performed at a bare (Figure 4.12 (A)) and MNP modified electrode (Figure 4.12 (B)). However, as the initial testing indicated that the level of EC may be absent or below the LOD, a much larger quantity of unburnt propellant discs (32.2 mg) was used to allow for the best chance for detection, hence the clear presence of DPA within the signal. Standard addition calculations (Figure 4.12 C) realised 0.21 and 0.25 % w/w for bare and modified respectively for EC in the unburnt propellant.

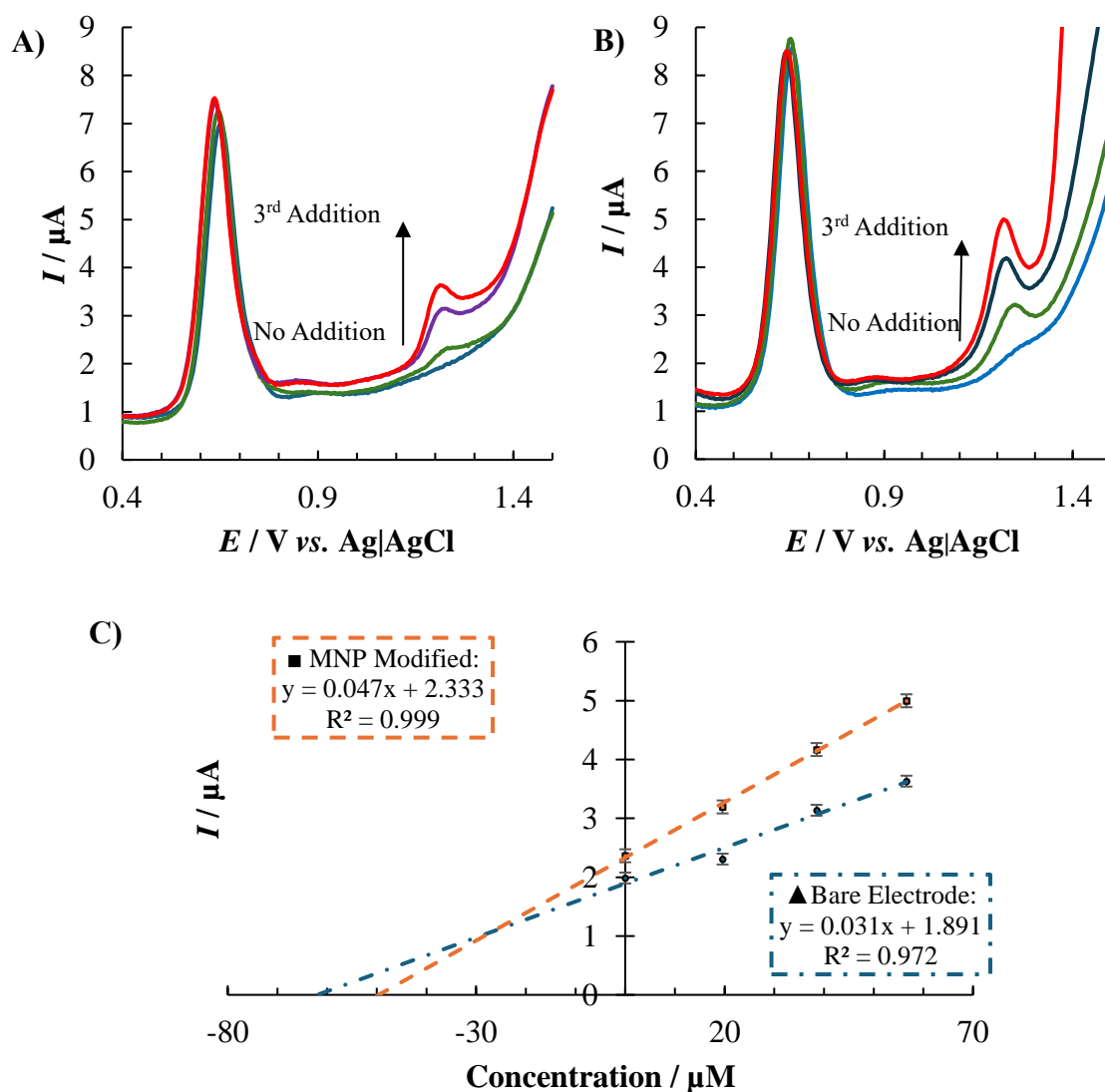


Figure 4.12: Average DPV data ($n=3$) over the potential range of -1 to $+1.5$ V vs. Ag|AgCl with additional parameters as per electrochemical procedures section. A) bare and B) MNP modified GCE with standard addition of EC 19.6 to 56.6 μM in a solution of 32.2 mg unburnt propellant discs with C) standard addition analysis plots generated from DPV data in (A) and (B) (with current standard deviations of ± 0.14 μA for bare and ± 0.4 μA for modified across the entire series).

The quantitative data for the standard addition analysis for DPA and EC (Table 4.6) are within the previously calculated LOQ for both analytes in mixed systems at bare and modified electrodes, increasing the confidence in the obtained values. The total calculated % w/w of stabilisers in the samples were within the 1-5% w/w value quoted by multiple patents for propellant formulation.

Chapter 4: Electrochemical Analysis of Analytes Found Within OFAR with the Extension to Real Sample Analysis

Table 4.6: Averaged results of standard addition analysis with unburnt propellant (n=3).

Electrode	DPA recovered (μM)	% w/w DPA	EC recovered (μM)	% w/w EC	Total % w/w observed stabilisers in sample
Bare	86.5 ± 2.5	1.08 ± 0.036	62.0 ± 3	0.21 ± 0.013	1.29
Modified	76.3 ± 0.7	1.06 ± 0.010	49.6 ± 2.4	0.25 ± 0.010	1.31

The results obtained gave an excellent estimation of the quantities of DPA and EC present within the propellant formulations prior to firing. The next steps were to move on to a recovered FAR sample to show if the concentrations present are still within the defined LOD and LOQ for successful analysis.

4.4.2.3 Electrochemical Detection of Organic Analytes in a Real Sample of FAR.

Figure 4.13 shows the firearm residue DPV trace following recovery via methanol swabbing of the textile surface. MNP modified electrodes resulted in a wave at 0.672 V indicative of DPA which was confirmed by spiking (19.6–56.6 mM DPA additions). Quantitation realised 0.512 and 0.426 $\mu\text{g}\cdot\text{cm}^{-2}$ DPA for bare and MNP modified electrode respectively.

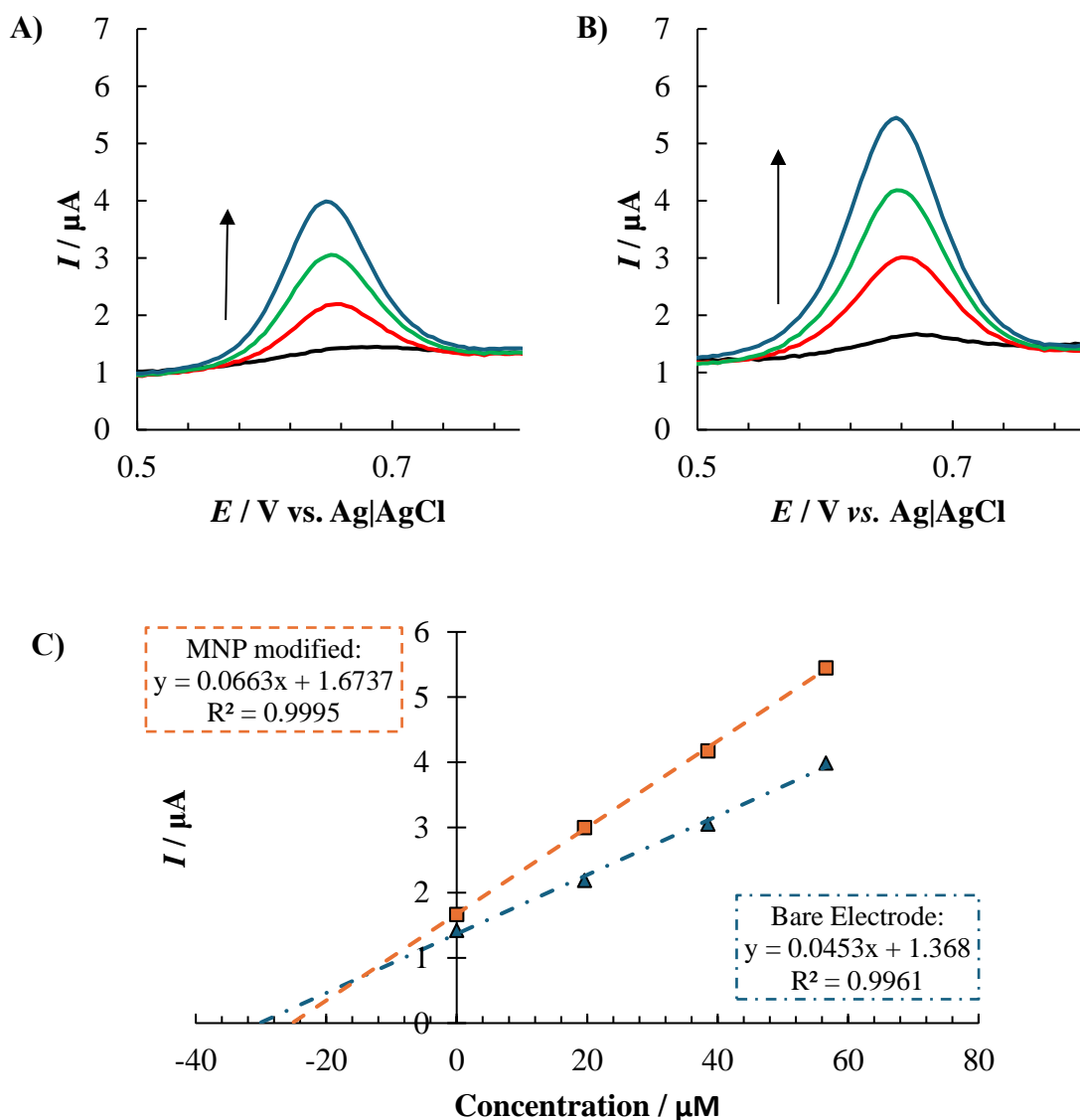


Figure 4.13: Average DPV data ($n=3$) over the potential range of -1 to $+1.5$ V vs. Ag|AgCl with additional parameters as per electrochemical procedures section. A) bare and B) MNP modified GCE with standard addition of DPA 19.6 to 56.6 μM in a solution of FAR swabbed over an area of 50 cm^2 with C) standard addition analysis plots generated from DPV data in (A) and (B) (current standard deviations of ± 0.02 μA for bare and ± 0.01 μA for modified across the entire series).

Figure 4.14 shows the DPVs corresponding to the recovered OFAR from the actual FAR sample recovered from a fabric textile at both bare (Figure 4.14 (A)) and MNP (Figure 4.14(B)) modified GCEs with corresponding EC standard addition data Figure 4.14 (C) (no DPA was observed in this case). Recovery of 1.52 ± 0.27 and 1.17 ± 0.3 $\mu\text{g cm}^{-2}$ was realised at bare and MNP modified electrodes respectively.

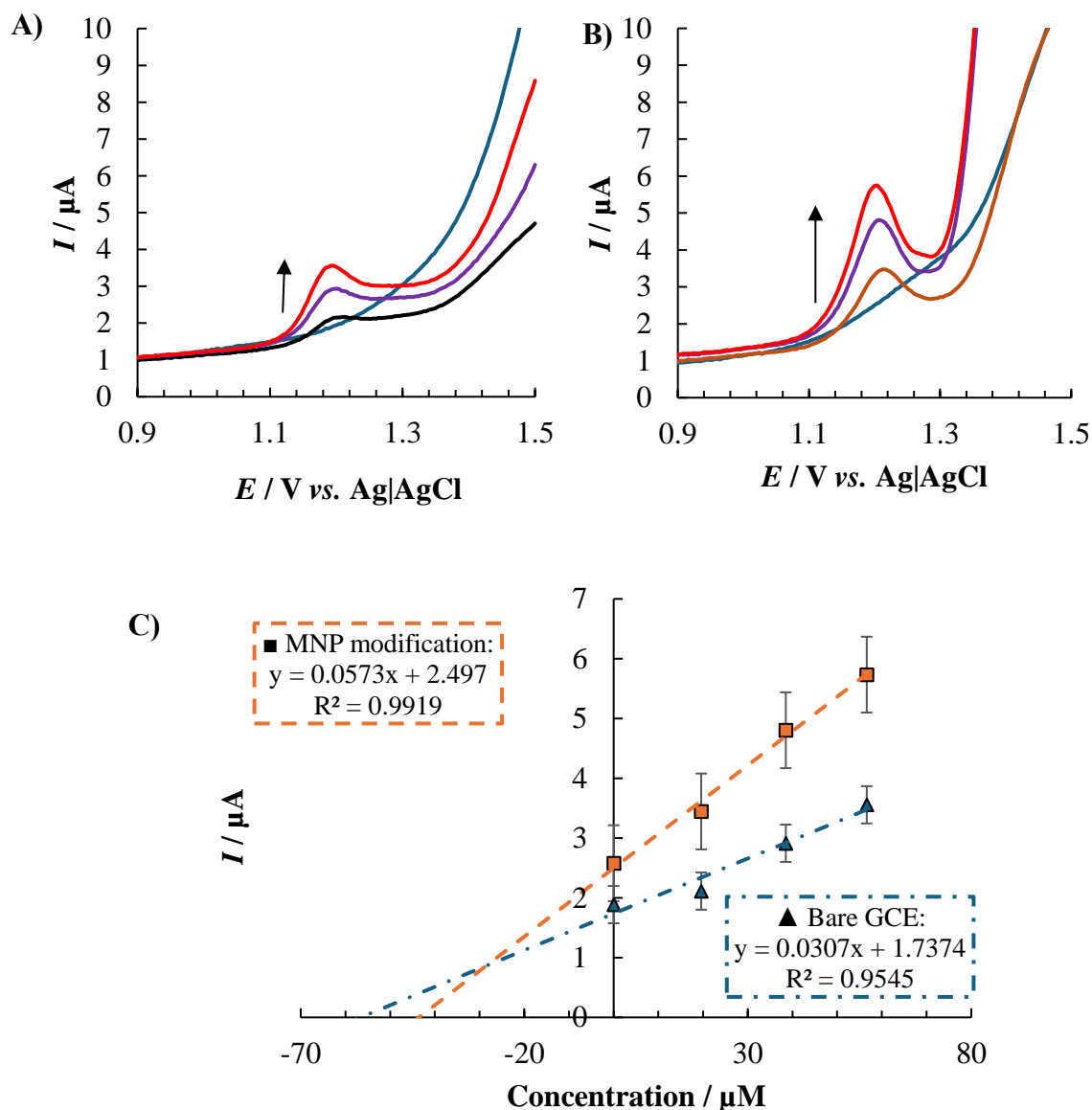


Figure 4.14: Average DPV data ($n=3$) over the potential range of -1 to $+1.5$ V vs. Ag|AgCl with additional parameters as per electrochemical procedures section. A) bare and B) MNP modified GCE with standard addition of EC 19.6 to 56.6 μM in a solution of FAR swabbed over an area of 50 cm^2 . C) standard addition analysis plots generated from DPV data in (A) and (B) (with current standard deviations of ± 0.31 μA for bare and ± 0.63 μA for modified across the entire series).

In all instances, the concentration of the analytes obtained from real FAR samples (Table 4.7) were above the previously calculated LOQs while being less than the original unburnt propellant samples. Trache *et al.* have reported on the stability of the stabilisers of energetic material showing that the DPA stabilisation mechanism produces a variety of nitro and nitrite substituted compounds while on the shelf³⁴. The act of firing may catalyse this process, lowering residual DPA levels. In relation to EC shelf-life stability, the breakdown to a carbamic acid and N-ethylaniline, are also proposed³⁴, and based on our

Chapter 4: Electrochemical Analysis of Analytes Found Within OFAR with the Extension to Real Sample Analysis

voltammetric studies, the method can report residue levels of EC which remain on clothing following firearm discharge.

Table 4.7: Results of standard addition analysis with FAR sample swabbed from textile surface ($n=3$).

Electrode	DPA recovered μM	DPA recovery $\mu\text{g cm}^{-2}$	EC recovered μM	EC recovery $\mu\text{g cm}^{-2}$
Bare	30.2 ± 1.4	0.512 ± 0.024	56.6 ± 10.1	1.52 ± 0.27
Modified	25.2 ± 5.6	0.426 ± 0.094	43.6 ± 11	1.17 ± 0.30

The data presented here provides a strong lab-based method for the analysis of OFAR. However forensic scientists already have deeply established methodologies in SEM and EDX for FAR analysis. To provide a realistic alternative to laboratory-based analysis, an onsite, portable approach utilising screen printed electrodes for FAR analysis was proposed.

4.4.3 *Development of Screen-Printed Electrodes for OFAR Detection*

Following successful determination of the analytes of interest within a conventional three electrode cell, the development of screen-printed electrodes (SPE) which could use the previously developed method was the next step in the development of a methodology which forensic professionals could potentially use on site for FAR analysis.

The initial fabrication process for the SPEs underwent two iterations prior to the finalised design (as seen in **Section 3.3.3.4**). In **Figure 4.15** the designs of the SPE are shown. Design #1 was initially used; however, the singular large opening was difficult to reproduce for the second PET layer and tears were commonplace due to the opening's proximity to the edge. Design #2 was implemented with the use of a hole punch allowing for a uniform opening, however, when applying MNP for modification the solution ran from the working electrode side to the counter and pseudo reference side, causing loss of material and in some instances short circuiting of the SPE due to iron nanomaterial

creating a conductive bridge between the electrodes. Design #3 was developed with the idea of minimising the likelihood of MNP materials accidentally being applied to the reference and counter electrodes. Due to the separation of the electrode active areas, an additional layer of PET acting as a sample well was added to allow for the sample solution to be held on the electrode surface. As the most successful, design #3 was utilised for the analysis.

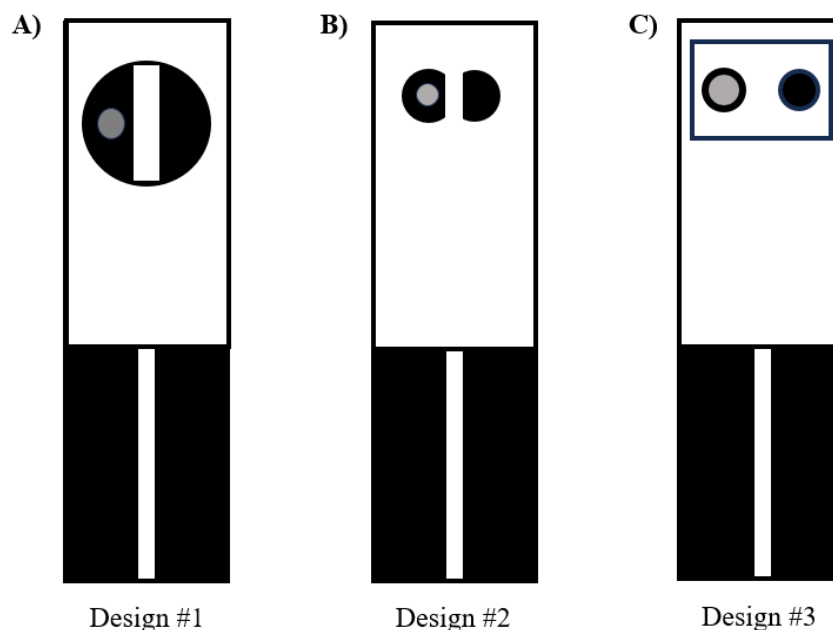


Figure 4.15: Three iterations of the SPE prototype design for the analysis of OFAR.

MNP modification of the SPE was performed with the same final volume of solution, however, due to the size of the exposed working electrode area, the application volume was changed from 5 applications of 20 μL of a 1 $\text{mg}\cdot\text{mL}^{-1}$ solution of MNP in ethanol to 10 applications of 10 μL for a final volume of 100 μL of solution.

4.4.3.1 Comparison of Electrosynthesised and Coprecipitated Magnetic Nanoparticles

Due to the low yields of material obtained from the electrosynthesis method of MNP formation, a different method of material synthesis was used. IR and TGA/DSC analysis was performed to compare the materials. As shown in **Figure 4.16**, indicative functional group Fe-O (magnetite) at 560.71 and 437.28 cm^{-1} were observed for the original

Chapter 4: Electrochemical Analysis of Analytes Found Within OFAR with the Extension to Real Sample Analysis

electrosynthesised material, which shifted to 545.28 and 425.23 cm^{-1} for the material prepared using the chemical co-precipitation method.

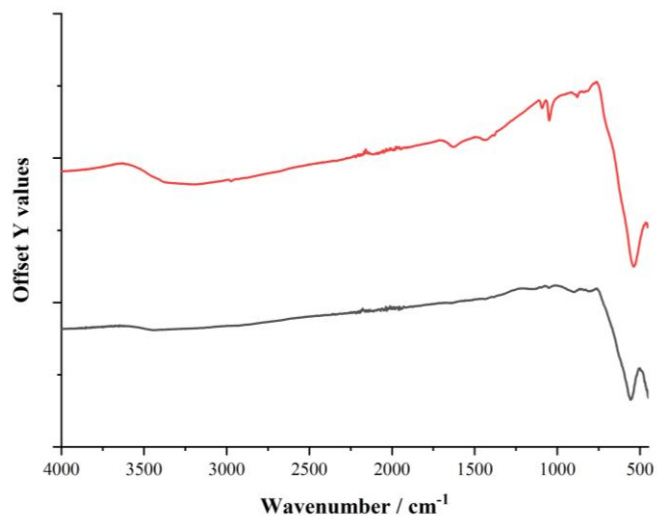


Figure 4.16: FTIR spectra of (black) electrochemically and (red) chemically synthesised MNP.

Thermogravimetric analysis (TGA) coupled with differential scanning calorimetry (DSC) was employed to examine thermal stability which can depend on grain size and the synthetic process (Figure 4.17). The initial mass variation loss (red TG curves) may be due to an overlap of the exothermic process of H_2O and surface $-\text{OH}$ group elimination.

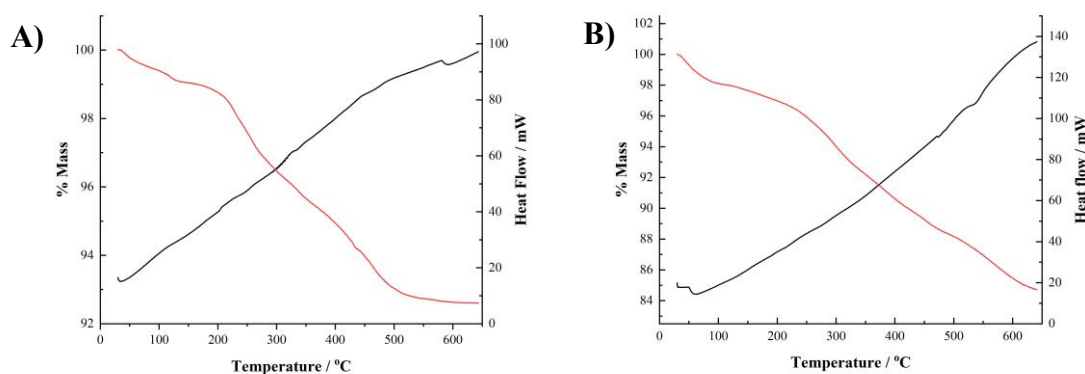


Figure 4.17: Thermal analysis (DSC/TGA) in air at a flow rate of $10 \text{ mL}\cdot\text{s}^{-1}$ with a temperature programme of an initial hold at $30 \text{ }^{\circ}\text{C}$ for 1 minute and an increasing temperature ramp of $30 \text{ }^{\circ}\text{C}$ to $600 \text{ }^{\circ}\text{C}$ at $5 \text{ }^{\circ}\text{C}\cdot\text{min}^{-1}$ for A) chemically prepared and B) electrochemically prepared MNPs.

The material was comparable from the results of FTIR and TGA/DSC analysis and deemed appropriate for use with the SPE methods.

4.4.3.2 Analysis of Individual Analytes at SPE

Given the success with the previous methods, DPV analysis was once more utilised for the initial exploration into the SPE's ability to detect the analytes of interest. In **Figure 4.18**, the difference between the bare and modified SPE were observed. Within the individual analyte solutions (**Figure 4.18 (A & B)**) the bare SPE (solid black trace) on average (n=3) reported higher current values than the modified counterpart, with $I_p^a = 6.92 \pm 0.14 \mu\text{A}$ for DPA and $6.99 \pm 0.19 \mu\text{A}$ for EC at the bare SPE, and, $I_p^a = 5.25 \pm 0.80 \mu\text{A}$ for DPA and $5.84 \pm 0.53 \mu\text{A}$ for EC at the modified SPE. The modified SPE reported a signal of ~76% and ~84% for DPA and EC respectively compared to the bare SPE. A statistically significant difference was observed when comparing DPA bare and modified values ($p = 0.0236$) and EC bare and modified values ($p = 0.0241$) using an unpaired t-test.

Upon observing the results for the solution with both analytes present (**Figure 4.18 (C)**), the same trend of MNP modification producing signals less than the bare SPE continued. Modified SPEs produced signals of ~93% and ~91% for DPA and EC respectively compared to the bare SPE.

In both instances, there was a reported loss of signal comparing the multi-analyte solutions to their individual counterparts even though the concentration remained the same. However, even with the loss of current for the analytes, the introduction of the MNP modified SPE appeared to produce more defined analyte peaks.

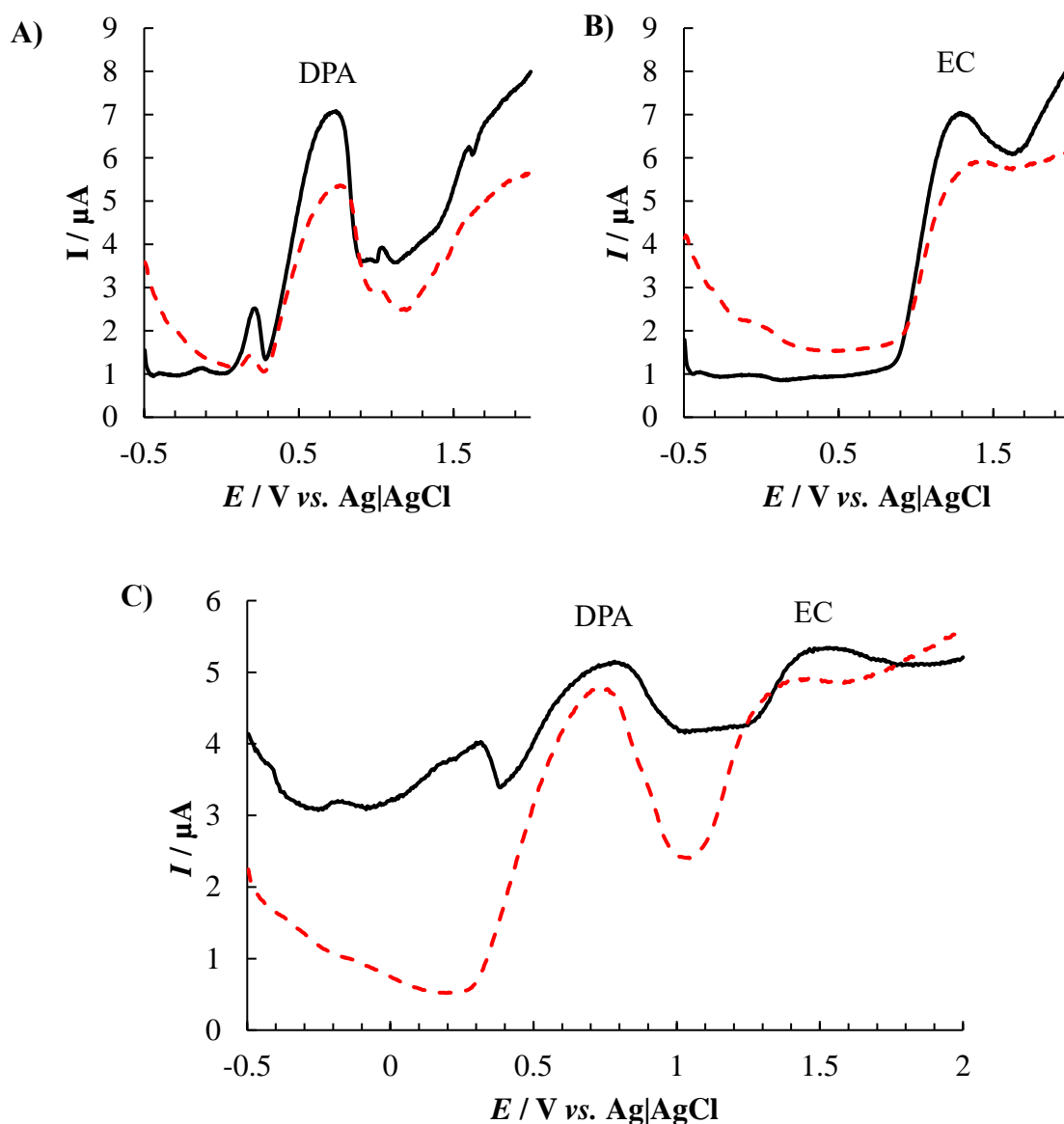


Figure 4.18: Average DPV data ($n=3$) over the potential range of -0.5 to $+2$ V vs. Ag|AgCl with additional parameters as per electrochemical procedures section. A) 1 mM DPA, B) 1 mM EC and C) 1 mM DPA and 1 mM EC in 3:7 methanol:sodium acetate buffer ($\text{pH} \sim 4.5$) comparing a bare (solid) and MNP modified (dash) SPE.

To explore the change in trend, from that previously observed in the three-electrode cell, a closer look at the background voltammograms was required. In **Figure 4.19 (A)** the comparison between the average background DPV scans ($n=4$) in aqueous electrolyte for bare and MNP modified SPE are shown. At the expected potential region for DPA reaction ($E_p^a \approx 0.78$ V) average bare SPE resulted in a current of $2.16 \pm 0.25 \mu\text{A}$ while average MNP modified SPE resulted in a current of $0.329 \pm 0.62 \mu\text{A}$, a 70.4% drop in current between the bare and modified SPE. Due to the shift in EC position within a multi analyte

solution and the position of the analyte signal in a region of increasing anodic current for both bare and MNP modified SPE, the backgrounds could not be compared accurately.

To obtain a more accurate representation of how the background signal affected the analyte signal, a background subtraction was performed (**Figure 4.19 (B)**). This involved performing the analysis with the SPE in the electrolyte solution, then subsequently removing and drying the solution and adding the solution for analysis. The initial data was then subtracted from the analyte data to realise background subtracted results. The background subtraction resulted in a change in the average trend, with the modified SPEs reporting a 1.76-fold increase for DPA and 2.12-fold increase for EC. The trend was much more in line with the previously observed trend at the macro GCE, leading to the background subtraction being integrated into the methodology going forward.

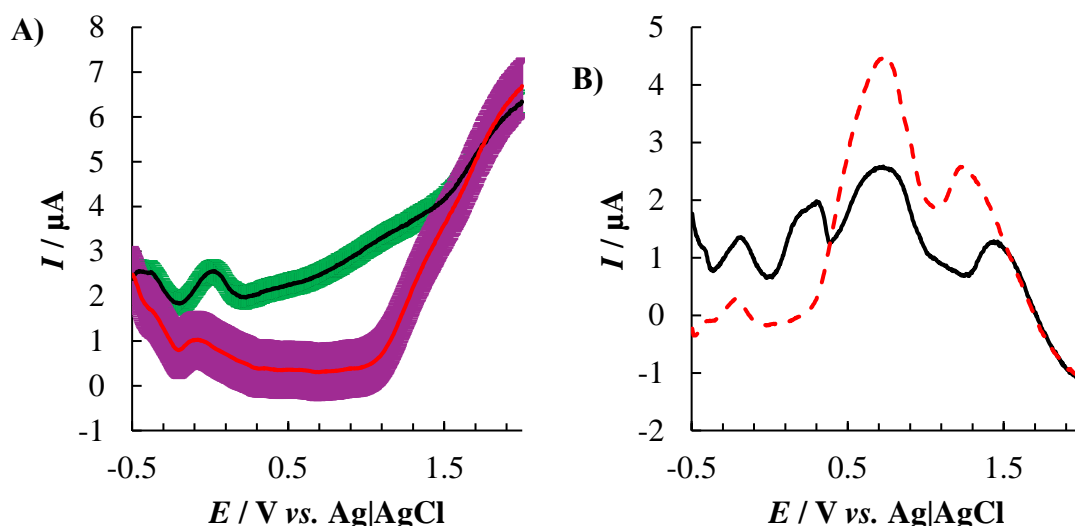


Figure 4.19: Average DPV data ($n=4$) over the potential range of -0.5 to $+2$ V vs. Ag/AgCl with additional parameters as per electrochemical procedures section. A) background electrolyte solution at bare (black) and MNP modified (red) SPE and B) 1 mM DPA and 1 mM EC in 3:7 methanol:sodium acetate buffer (pH ~ 4.5) background subtracted (using data from (A)) comparing a bare (solid) and MNP modified (dash) SPE.

4.4.3.3 Reproducibility of SPE's

As the background subtraction was necessary to observe a clear increase in signal comparing the bare and MNP modified SPE, the reproducibility of the SPE was relevant due to the *in-house* fabrication of the electrodes. Robust signal reproducibility was demonstrated (**Figure 4.20 (A & B) and Table 4.8**) with intra SPE variation ($n=4$) being

Chapter 4: Electrochemical Analysis of Analytes Found Within OFAR with the Extension to Real Sample Analysis

highly promising at % RSD = 3.9 and 4.8% for the bare electrode response and 3.8 and 2.6% for the MNP modified SPE.

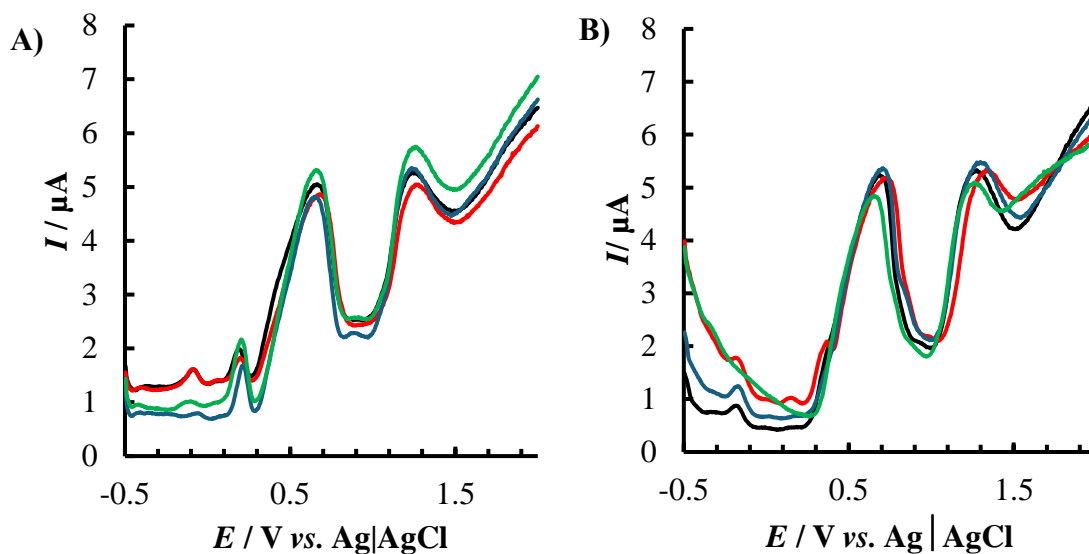


Figure 4.20: DPV over the potential range of -0.5 to +2 V vs. Ag/AgCl with additional parameters as per electrochemical procedures section. Of A) bare and B) modified SPE for 1 mM EC and DPA in 3:7 methanol:sodium acetate buffer (pH ~4.5) showing inter-electrode variability for $n=4$ individual strips.

Table 4.8: DPA and EC peak data at four different SPEs.

<i>Bare</i>					<i>MNP Modified</i>				
<i>SPE</i>	<i>DPA</i>		<i>EC</i>		<i>SPE</i>	<i>DPA</i>		<i>EC</i>	
	E_p^a (V)	I_p^a (μ A)	E_p^a (V)	I_p^a (μ A)		E_p^a (V)	I_p^a (μ A)	E_p^a (V)	I_p^a (μ A)
1	0.59	4.78	1.25	5.00	1	0.66	4.83	1.27	5.07
2	0.62	4.90	1.24	5.71	2	0.74	5.14	1.35	5.34
3	0.60	5.01	1.22	5.23	3	0.67	5.28	1.25	5.32
4	0.66	5.31	1.22	5.31	4	0.71	5.34	1.31	5.45
<i>Average</i>	0.62	5.00	1.23	5.31	<i>Average</i>	0.70	5.15	1.29	5.30
<i>StDev</i>	0.03	0.20	0.01	0.26	<i>StDev</i>	0.03	0.20	0.04	0.14
<i>RSD</i>	4.3%	3.9%	0.8%	4.8%	<i>RSD</i>	4.6%	3.8%	2.9%	2.6%

4.4.3.4 Analysis of Unburnt Propellant with SPE

To further explore the capabilities of the SPE pertaining to actual forensic samples, the unburnt propellant samples were used to test the SPE with a more complex matrix. The previously mentioned quantitative data with a GCE (**Table 4.3**) confirmed trace amounts of EC in the unburnt propellant and the results in **Figure 4.21** provided evidence of the printed prototype's ability to perform dual propellant stabiliser measurement.

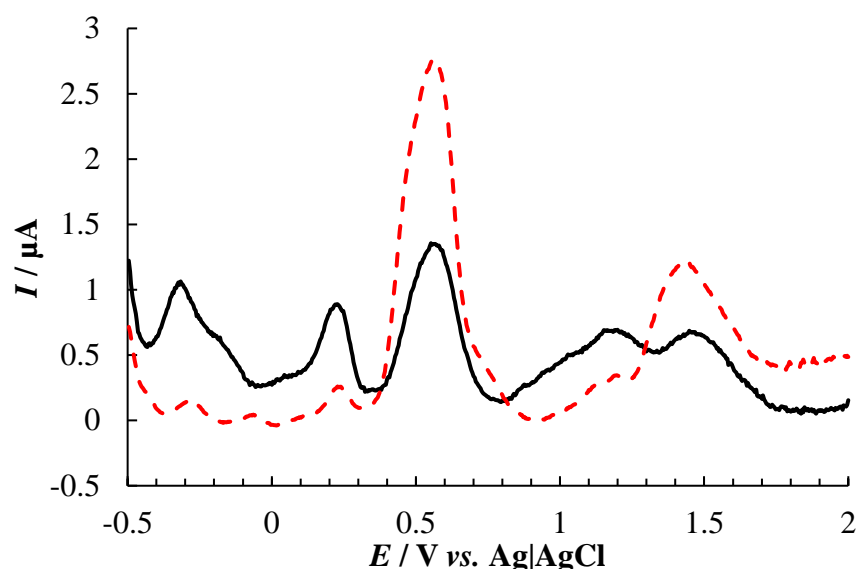


Figure 4.21: Average DPV data ($n=3$) over the potential range of -0.5 to $+2$ V vs. Ag/AgCl with additional parameters as per electrochemical procedures section, of a sample of unburnt propellant at bare (solid) and MNP modified (dash) SPE (background subtracted).

Due to the lack of remaining FAR sample, an analogue sample was produced by dissolving unburnt propellant and applying the solution to a textile and further using the swabbing recovery procedure for generation of the samples. Qualitative measurement of unburnt propellant recovered from a textile sample may be seen in the DPVs presented in **Figure 4.22** (background subtracted signals). A peak was observed at 0.244 V, which was suppressed in the presence of MNP. This may relate to other propellant breakdown/degradation products and requires further investigation.

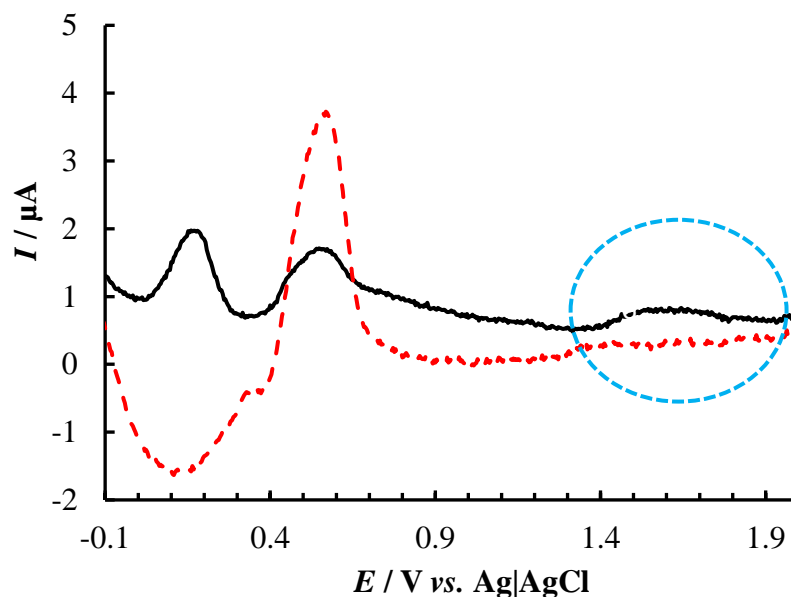


Figure 4.22: Average DPV data ($n=3$) over the potential range of -0.5 to $+2$ V vs. Ag|AgCl with additional parameters as per electrochemical procedures section of a sample of unburnt propellant recovered from a textile at bare (solid) and MNP modified (dash) SPE (both background subtracted).

4.5 Conclusion

While confirmatory testing of the organic fraction of FAR is largely laboratory confined, on-site testing/screening of this fraction can be facilitated using electroanalysis as a timely, viable triage tool at crime scenes.

Testing and recovery of OFAR from a target cloth (from a single base shotgun shell), together with unburnt propellant served to demonstrate robust operational performance of the method with recovery of both stabilisers achieved. SEM and AFM surface analyses verified the presence of the typical unburnt metal particles with the presence of Pb, Ba, Sb confirmed by EDS. The work culminated in proof of principle studies at a custom designed screen-printed electrode which achieved selectivity and reproducibility with respect to OFAR recovered sample analysis with intra SPE variation ($n=4$) being highly promising at % RSD = 3.9 and 4.8% for the bare electrode response and 3.8 and 2.6% for the MNP modified electrodes. The prototype can be adapted to include an integrated membrane/solvent for OFAR recovery from a surface with integrated electroanalysis with possibility to extend to analysis of the inorganic metallic fraction of FAR through stripping voltammetry. Our ongoing work on MNP in relation to metal analysis

Chapter 4: Electrochemical Analysis of Analytes Found Within OFAR with the Extension to Real Sample Analysis

demonstrated very significant metal amplification signals (e.g. Pb) thought to be due to co-ordination to surface hydroxide groups of the iron oxide particles. Further work would be required to advance this aspect and establish optimal screening of both inorganic and organic fractions of the FAR. Overall, the work has laid a solid foundation for OFAR electrochemical sensing with an understanding of the redox behaviour of key propellant components at carbon and MNP modified electrodes, with strong potential for advancement of rapid on-site analysis.

4.6 References

- (1) Burleson, G. L.; Gonzalez, B.; Simons, K.; Yu, J. C. C. Forensic Analysis of a Single Particle of Partially Burnt Gunpowder by Solid Phase Micro-Extraction–Gas Chromatography–Nitrogen Phosphorus Detector. *Journal of Chromatography A* **2009**, *1216* (22), 4679–4683. <https://doi.org/10.1016/j.chroma.2009.03.074>.
- (2) Arndt, J.; Bell, S.; Crookshanks, L.; Lovejoy, M.; Oleska, C.; Tulley, T.; Wolfe, D. Preliminary Evaluation of the Persistence of Organic Gunshot Residue. *Forensic Science International* **2012**, *222* (1-3), 137–145. <https://doi.org/10.1016/j.forsciint.2012.05.011>.
- (3) Hofer, R.; Wyss, P. The Use of Unburned Propellant Powder for Shooting-Distance Determination. Part II: Diphenylamine Reaction. *Forensic Science International* **2017**, *278* (2018), 24–31. <https://doi.org/10.1016/j.forsciint.2017.06.022>.
- (4) Maitre, M.; Horder, M.; Kirkbride, K. P.; Gassner, A.-L.; Weyermann, C.; Roux, C.; Beavis, A. A Forensic Investigation on the Persistence of Organic Gunshot Residues. *Forensic Science International* **2018**, *292*, 1–10. <https://doi.org/10.1016/j.forsciint.2018.08.036>.
- (5) Bonnar, C.; Moule, E. C.; Lucas, N.; Seyfang, K. E.; Dunsmore, R. P.; Popelka-Filcoff, R. S.; Redman, K.; Paul Kirkbride, K. Tandem Detection of Organic and Inorganic Gunshot Residues Using LC–MS and SEM-EDS. *Forensic Science International* **2020**, *314*, 110389. <https://doi.org/10.1016/j.forsciint.2020.110389>.
- (6) López-López, M.; de la Ossa, M. Á. F.; García-Ruiz, C. Fast Analysis of Complete Macroscopic Gunshot Residues on Substrates Using Raman Imaging. *Applied Spectroscopy* **2015**, *69* (7), 889–893. <https://doi.org/10.1366/14-07816>.
- (7) Tong, Y.; Wu, Z.; Yang, C.; Yu, J.; Zhang, X.; Yang, S.; Deng, X.; Xu, Y.; Wen, Y. Determination of Diphenylamine Stabilizer and Its Nitrated Derivatives in Smokeless Gunpowder Using a Tandem MS Method. *The Analyst* **2001**, *126* (4), 480–484. <https://doi.org/10.1039/b010183o>.

- (8) Joshi, M.; Delgado, Y.; Guerra, P.; Lai, H.; Almirall, J. R. Detection of Odor Signatures of Smokeless Powders Using Solid Phase Microextraction Coupled to an Ion Mobility Spectrometer. *Forensic Science International* **2009**, *188* (1-3), 112–118. <https://doi.org/10.1016/j.forsciint.2009.03.032>.
- (9) Stevens, B.; Bell, S.; Adams, K. Initial Evaluation of Inlet Thermal Desorption GC–MS Analysis for Organic Gunshot Residue Collected from the Hands of Known Shooters. *Forensic Chemistry* **2016**, *2*, 55–62. <https://doi.org/10.1016/j.forc.2016.10.001>.
- (10) Bratin, K.; Kissinger, P. T.; Briner, R. C.; Bruntlett, C. S. Determination of Nitro Aromatic, Nitramine, and Nitrate Ester Explosive Compounds in Explosive Mixtures and Gunshot Residue by Liquid Chromatography and Reductive Electrochemical Detection. *Analytica Chimica Acta* **1981**, *130* (2), 295–311. [https://doi.org/10.1016/s0003-2670\(01\)93007-7](https://doi.org/10.1016/s0003-2670(01)93007-7).
- (11) Mei, H.; Quan, Y.; Wang, W.; Zhou, H.; Liu, Z.; Shi, H.; Wang, P. Determination of Diphenylamine in Gunshot Residue by HPLC-MS/MS. *Journal of Forensic Science and Medicine* **2016**, *2* (1), 18. <https://doi.org/10.4103/2349-5014.162808>.
- (12) Gao, J.; Yang, T.; Wang, X.; He, Q.; He, P.; Jia, L.; Du, L.; Deng, H.; Zhang, H.; Jia, B.; He, X.; Tang, B. Spherical Phosphomolybdic Acid Immobilized on Graphene Oxide Nanosheets as an Efficient Electrochemical Sensor for Detection of Diphenylamine. *Microchemical Journal* **2020**, *158*, 105158–105158. <https://doi.org/10.1016/j.microc.2020.105158>.
- (13) Sukanya Ramaraj; Mani Sakthivel; Chen, S.-M.; Ho, K.-C. Ultrasound-Assisted Synthesis of Two-Dimensional Layered Ytterbium Substituted Molybdenum Diselenide Nanosheets with Excellent Electrocatalytic Activity for the Electrochemical Detection of Diphenylamine Anti-Scald Agent in Fruit Extract. *Ultrasonics sonochemistry* **2019**, *50*, 265–277. <https://doi.org/10.1016/j.ultrsonch.2018.09.028>.

- (14) Hande, P. E.; Samui, A. B.; Kulkarni, P. S. An Efficient Method for Determination of the Diphenylamine (Stabilizer) in Propellants by Molecularly Imprinted Polymer Based Carbon Paste Electrochemical Sensor. *Propellants, Explosives, Pyrotechnics* **2017**, *42* (4), 376–380. <https://doi.org/10.1002/prop.201600118>.
- (15) Ramki, S.; Sukanya, R.; Chen, S.-M.; Sakthivel, M.; Ye, Y.-T. Electrochemical Detection of Toxic Anti-Scald Agent Diphenylamine Using Oxidized Carbon Nanofiber Encapsulated Titanium Carbide Electrocatalyst. *Journal of Hazardous Materials* **2019**, *368*, 760–770. <https://doi.org/10.1016/j.jhazmat.2019.01.110>.
- (16) Liu, L.; Zhu, X.; Zeng, Y.; Wang, H.; Lu, Y.; Zhang, J.; Yin, Z.; Chen, Z.; Yang, Y.; Li, L. An Electrochemical Sensor for Diphenylamine Detection Based on Reduced Graphene Oxide/Fe₃O₄-Molecularly Imprinted Polymer with 1,4-Butanediyl-3,3'-Bis-1-Vinylimidazolium Dihexafluorophosphate Ionic Liquid as Cross-Linker. *Polymers* **2018**, *10* (12), 1329–1329. <https://doi.org/10.3390/polym10121329>.
- (17) Sundaresan, P.; Gnanaprakasam, P.; Chen, S.-M.; Mangalaraja, R. V.; Lei, W.; Hao, Q. Simple Sonochemical Synthesis of Lanthanum Tungstate (La₂(WO₄)₃) Nanoparticles as an Enhanced Electrocatalyst for the Selective Electrochemical Determination of Anti-Scald-Inhibitor Diphenylamine. *Ultrasonics Sonochemistry* **2019**, *58*, 104647–104647. <https://doi.org/10.1016/j.ultsonch.2019.104647>.
- (18) Nehru, R.; Murugesan, R. C.; Chen, S.-M.; Sankar, R. Electrochemical Sensing of Free Radical Antioxidant Diphenylamine Cations (DPAH^{•+}) with Carbon Interlaced Nanoflake-Assembled Mg_xNi_{9-x}S₈ Microspheres. *CrystEngComm* **2019**, *21* (4), 724–735. <https://doi.org/10.1039/c8ce02004c>.

- (19) Sangili, A.; Vinothkumar, V.; Chen, S.-M.; Veerakumar, P.; Lin, K.-C. Efficient and Green Synthesis of Silver Nanocomposite Using Guar Gum for Voltammetric Determination of Diphenylamine. *Journal of Materials Science Materials in Electronics* **2021**, *32* (1), 1289–1302. <https://doi.org/10.1007/s10854-020-04902-6>.
- (20) Ott, C. E.; Dalzell, K. A.; Calderón-Arce, P. J.; Alvarado-Gómez, A. L.; Trejos, T.; Arroyo, L. E. Evaluation of the Simultaneous Analysis of Organic and Inorganic Gunshot Residues within a Large Population Data Set Using Electrochemical Sensors. *Journal of Forensic Sciences* **2020**, *65* (6), 1935–1944. <https://doi.org/10.1111/1556-4029.14548>.
- (21) Vuki, M.; Shiu, K.-K.; Galik, M.; O'Mahony, A. M.; Wang, J. Simultaneous Electrochemical Measurement of Metal and Organic Propellant Constituents of Gunshot Residues. *The Analyst* **2012**, *137* (14), 3265. <https://doi.org/10.1039/c2an35379b>.
- (22) Ristić, M.; Fujii, T.; Hashimoto, H.; Opačak, I.; Musić, S. A Novel Route in the Synthesis of Magnetite Nanoparticles. *Materials Letters* **2013**, *100*, 93–97. <https://doi.org/10.1016/j.matlet.2013.03.013>.
- (23) Maxam. *Maxam CSB 3 Powder | Load Data*. xxl-reloading.com. <https://www.xxl-reloading.com/Maxam-CSB-3> (accessed 2024-02-16).
- (24) Tsai, T.; Ku, S.; Chen, S.; Lou, B.; Ali, M. A.; Al-Hemaid, F. M. A. Electropolymerized Diphenylamine on Functionalized Multiwalled Carbon Nanotube Composite Film and Its Application to Develop a Multifunctional Biosensor. *Electroanalysis* **2014**, *26* (2), 399–408. <https://doi.org/10.1002/elan.201300495>.

- (25) Wu, M.-S.; Wen, T.-C.; Gopalan, A. Electrochemical Copolymerization of Diphenylamine and Anthranilic Acid with Various Feed Ratios. *Journal of the Electrochemical Society* **2001**, *148* (5), D65–D65. <https://doi.org/10.1149/1.1366625>.
- (26) Gunshot Residue Subcommittee. Practice for Gunshot Residue Analysis by Scanning Electron Microscopy/Energy Dispersive X-Ray Spectrometry. *ASTM 14.02* **2017**. <https://doi.org/10.1520/e1588-17>.
- (27) Segura, R.; Díaz, K.; Pizarro, J.; Placencio, A.; Tapia, D.; Fajardo, Á. Anodic Stripping Voltammetric Determination of Lead Using a Chemically Modified Electrode Based on Aza Crown Ether. *Journal of the Chilean Chemical Society* **2017**, *62* (4), 3726–3730. <https://doi.org/10.4067/s0717-97072017000403726>.
- (28) Wang, L.; Luo, J.; Fan, Q.; Suzuki, M.; Suzuki, I. S.; Engelhard, M. H.; Lin, Y.; Kim, N.; Wang, J.; Zhong, C.-J. Monodispersed Core–Shell Fe₃O₄@Au Nanoparticles. *Journal of Physical Chemistry B* **2005**, *109* (46), 21593–21601. <https://doi.org/10.1021/jp0543429>.
- (29) Wu, W.; Jia, M.; Wang, Z.; Zhang, W.; Zhang, Q.; Liu, G.; Zhang, Z.; Li, P. Simultaneous Voltammetric Determination of Cadmium(II), Lead(II), Mercury(II), Zinc(II), and Copper(II) Using a Glassy Carbon Electrode Modified with Magnetite (Fe₃O₄) Nanoparticles and Fluorinated Multiwalled Carbon Nanotubes. *Microchimica Acta* **2019**, *186* (2). <https://doi.org/10.1007/s00604-018-3216-5>.
- (30) Stiles, S.; Luense, J. Methods of Making Double Base Casting Powder, November 30, 2010. <https://patents.google.com/patent/US7842144B1/en>.
- (31) Haury, V.; Frankel, M. Gun Propellant Containing Nitroplasticized Nitrocellulose and Triaminoguanidine Nitrate, May 8, 1973. <https://patents.google.com/patent/US3732131A/en>.

Chapter 4: Electrochemical Analysis of Analytes Found Within OFAR with the Extension to Real Sample Analysis

- (32) Pierce, E. Nitrocellulose Solid Propellant Composition with Load Additive to Reduce Radar Attenuation, April 30, 1974. <https://patents.google.com/patent/US3808061A/en>.
- (33) Hafner, M. T.; Balangue, R.; Clark, D.; Westbrook, J. W. Propellant Compositions Including Stabilized Red Phosphorus and Methods of Forming Same, May 22, 2014. <https://patents.google.com/patent/US20140137996A1/en>.
- (34) Trache, D.; Tarchoun, A. F. Stabilizers for Nitrate Ester-Based Energetic Materials and Their Mechanism of Action: A State-of-The-Art Review. *Journal of Material Science* **2018**, *53* (1), 100–123. <https://doi.org/10.1007/s10853-017-1474-y>.

**Chapter 5: Latent Finger-Mark Visualisation at a
Brass Surface via Deposition of Conducting
and Redox Polymers**

5.1 Chapter Aims

The overall goal of this chapter was to appreciate the electrochemical degradation of brass under the conditions required for monomer deposition. This included an examination of the most appropriate electrolyte, deposition conditions and monomer combinations.

5.2 Introduction

As mentioned in **Chapter 1**, the most common material used for the manufacture of ammunition casings is brass. Brass is an alloy of mostly copper and zinc, along with other trace elements depending on the application of material and the need for machinability or thermal conductivity¹. The use of brass alloy as an electrochemical transducer can introduce a multitude of challenges that are not normally encountered with traditional electrodes. Metals with low formal potentials, such as zinc, tend to exhibit high reactivity, passivation, surface oxide formation and hydrogen evolution². This high reactivity can call the material's stability into question. An electrode substrate containing such material may suffer from degradation or corrosion, reducing performance over the course of the electrochemical measurements in aqueous electrolytes. As a result, we understand that brass is a challenging material electrochemically, however its use is a requirement in relation to the forensic application proposed. The type of brass used by the ammunition industry is known as cartridge brass, with typical composition shown in **Table 5.1**.

Table 5.1: Composition of common metals and averaged compositions found in cartridge brass.
^{3,4}

<i>Element</i>	Mass %
<i>Cu</i>	71.21
<i>Zn</i>	28.50
<i>Fe</i>	0.050
<i>Pb</i>	0.070
<i>Other</i>	0.17

Chapter 5: Latent Finger-Mark Visualisation at a Brass Surface via Deposition of Conducting and Redox Polymers

In countries with highly regulated firearms laws, material such as cartridge brass is difficult to obtain. In **Chapter 6**, cartridge brass will be used for analysis, however, this research was undertaken in a country in which acquisition of such materials is controlled. While ammunition casings were obtained by donation from a military history collection, they were classified as a limited sample type, meaning that the possible damage to the samples upon exploratory testing should be avoided. As a result, an alternative type of brass (α alloy CZ108/CW508L) was used for the majority of the analysis presented in this chapter. This form of the alloy has a slightly lower copper and slightly higher zinc composition, relative to the cartridge brass, at ~62 and 37% respectively. Brass in this form would be most commonly available, being used for all manner of applications from screws to locks, jewellery and instrument components⁵.

As a result of the higher percentage zinc composition in the brass plates used as electrodes, the dezincification process becomes more significant. Dezincification is a form of selective leaching or dealloying which is the selective removal of a particular element from an alloy due to the occurrence of corrosion⁶. Copper-zinc alloys containing more than 15% zinc are susceptible to dezincification⁷.

In this process, there are three possible mechanisms:

1. The most active component (**Table 5.2**) of the alloy (zinc) will selectively enter into the surrounding solution, while the remaining material exists as a porous and mechanically highly weakened mass⁸.
2. The entire alloy (copper and zinc) enters into solution after which the Cu^{2+} ions are expelled from the solution by zinc and the Cu^{2+} ions then deposit as porous copper⁸.
3. A combination of processes 1 and 2, in a multi-step mechanism.

Table 5.2: Galvanic series of some example metals indicating nobility or activity⁷.

<i>Cathodic (Nobel)</i>
<i>Platinum</i>
<i>Gold</i>
<i>Titanium</i>
<i>Silver</i>
<i>Copper</i>
<i>Brasses</i>
<i>Tin</i>
<i>Lead</i>
<i>Cadmium</i>
<i>Zinc</i>
<i>Magnesium</i>
<i>Anodic (Active)</i>

Opinions differ on whether the mechanism is selective dissolution of the most active zinc component or complete dissolution and redeposition of the copper component⁹. Primarily dezincification is observed in the natural exposure from interactions between ion-containing water (mostly chloride {Cl⁻}) and brass^{10,11}, aqueous electrochemical analysis can easily speed up this process and has been used to try and understand the mechanism.

Pathway one as reported by Weisser states that the removal of zinc is selective, or at least preferential, from the surface of brass in contact with any corrosive medium¹². In this mechanism, zinc is believed to be preferentially attacked at active sites, progressing deeper from the surface. While this mechanism does propose the loss of zinc only, it is noted that this is only in theory and that in practice, some copper is unavoidably removed together with zinc. For pathway two, Evans performed a study that indicated zinc atoms need to be accompanied by copper atoms in order to easily leave the alloy¹³. In micro-areas of non-uniform zinc rich regions on the brass surface, copper remains in residual amounts. These copper rich sites act as a cathode, turning the alloy into a galvanic cell which further allows for the redeposition of copper from the solution to the surface. Warraky¹⁴ further investigated the copper and zinc ratio by solution analysis, suggesting a ratio more favourable to zinc than in the bulk alloy. This indicated the dissolution of

Chapter 5: Latent Finger-Mark Visualisation at a Brass Surface via Deposition of Conducting and Redox Polymers

both copper and zinc with the subsequent redeposition of copper. The final proposed pathway for this process involves a combination of both pathway one and two.

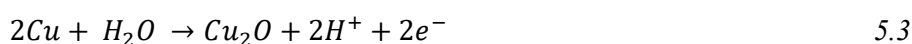
In general, if following the second proposed mechanism, the corrosion of α -Brass in neutral chloride solutions involves the cathodic reduction of oxygen on the electrode surface according to the following steps¹⁵:



For alloys containing zinc, a further passivation process occurs through the formation of a zinc oxide film during the dezincification phase, as follows:



Subsequently, copper dissolves to form copper oxides (Cu_2O and CuO):



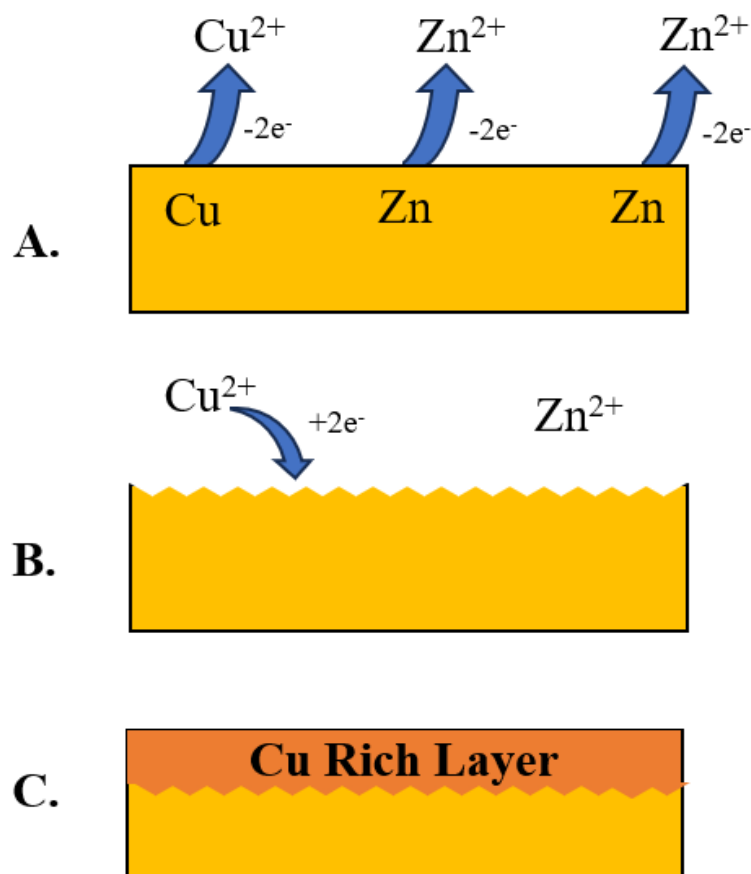
When the surface is covered with ZnO , CuO , and Cu_2O , $CuCl$ can form according to the reaction:



$CuCl$ then undergoes further reaction:



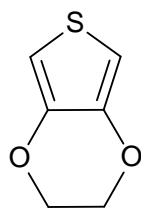
Pchel'nikov proposed a two-step mechanism using electrochemical techniques in a sodium chloride rich medium, which involved a short period of preferential dissolution of zinc, generating a copper rich surface and a subsequent simultaneous dissolution of both metals¹⁶. This was followed by a secondary preferential dissolution due to the redeposition of copper which commenced when a threshold level of copper in the solution had been reached. Broadly, as seen in **Scheme 5.1**, the entire dezincification process can be classified as **(A)** preferential dissolution of zinc from the alloy *and/or* simultaneous dissolution of both copper and zinc, resulting in the removal of material from the brass surface and subsequently, a rougher surface. This is followed by **(B)** the redeposition of copper from solution, while the zinc remains. The processes seem to be dictated by a variety of criteria such as **(C)** surface oxide formation¹⁷, temperature^{18,19}, solution ion concentration¹⁶ and type of brass alloy used.



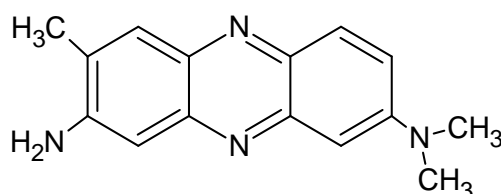
Scheme 5.1: Scheme showing a basic overview of the steps involved in the dezincification process.

Therefore, the experimental parameters selected in this work will minimise or exploit such processes at the brass surface while facilitating the electro-deposition of visualisation materials.

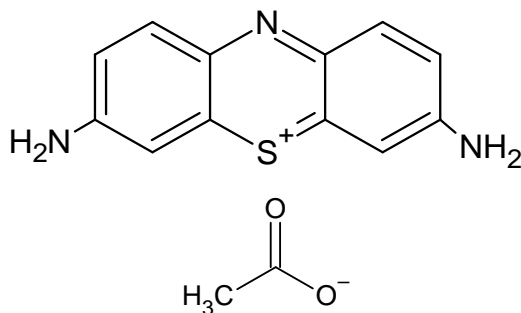
In **Chapter 1**, the underlying processes by which conducting and redox polymers are deposited and behave electrochemically was discussed. Three compounds were selected, 3,4-ethylenedioxythiophene (EDOT), a conducting polymer, together with the phenazine and phenothiazine species, Neutral Red (NR) and Thionine Acetate (Th) (**Figure 5.1**).



3,4-ethylenedioxythiophene (EDOT)



Neutral Red (NR)



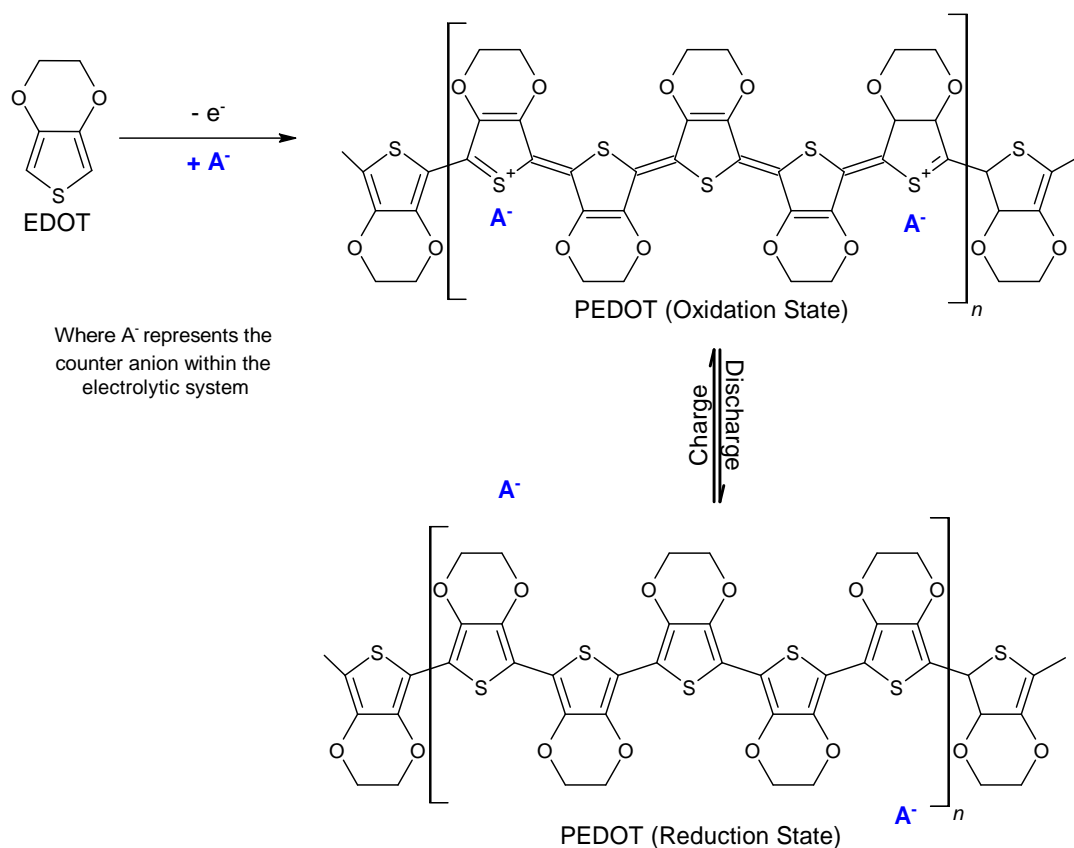
Thionine Acetate (Th)

Figure 5.1: Chemical structures of monomers of interest for deposition.

The polymerised form of EDOT (PEDOT) is a highly studied conducting polymer which can be formed electrochemically on various substrates, such as Indium Tin Oxide (ITO)^{20–22} and glassy carbon^{23,24} electrodes along with nontraditional electrochemical surfaces such as hydrogels or stainless steel^{25,26}. Polymerisation can occur under a range of experimental conditions^{26–29} and a generic schematic of the electrochemical polymerisation process can be seen in **Scheme 5.2**. When sufficient potentials are applied to the electrode substrate, EDOT monomers are rapidly oxidised by electron transfer. This process leads them to combine and create dimeric cations, which are stabilised through a deprotonation process. The dimer is further oxidised and forms a positively charged cationic group³⁰. Through successive rounds of coupling and deprotonation, these cations gradually form into a conjugated PEDOT chain³¹. Concurrently, the counter anion (A^-) enters the conjugate chain as a dopant to achieve charge balance. Consequently, different

Chapter 5: Latent Finger-Mark Visualisation at a Brass Surface via Deposition of Conducting and Redox Polymers

modes of electrodeposition (e.g. constant potential, cyclic voltammetry, or current density experiments) and parameters (such as different anions³²) may induce different morphological results. PEDOT has been used in latent finger-mark visualisation in copolymeric films at stainless steel surfaces³³ and also as an individual polymer at a brass ammunition casing surface, where Costa et al. developed a fast chronocoulometric method which resulted in successful results with finger-marks on a brass substrate aged up to 30 days, making it a strong choice for this work²⁶.



Scheme 5.2: Initial oxidation of EDOT and possible polymeric forms of PEDOT obtained via electrochemical means³².

Phenazine or phenothiazine dyes are related compounds, in that both families contain fused aromatic ring structures with a nitrogen within the central ring and at least two amine groups each attached to positions 3 and 7 of the outer ring. These amines can be primary, secondary or tertiary, differing by the presence of either a second nitrogen or sulphur within the central ring (Figure 5.2). In Scheme 4.3 a generic process for dimerisation of these compounds is shown involving a deprotonated unit attaching through the cationic amine group and undergoing a further deprotonation resulting in the

Chapter 5: Latent Finger-Mark Visualisation at a Brass Surface via Deposition of Conducting and Redox Polymers

dimer. This dimer would then undergo further deprotonation forming the repeating structure as seen in **Figure 5.2** causing repeating linkage through the amine group to the fused ring backbone.

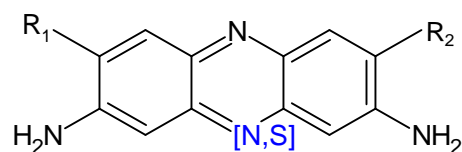
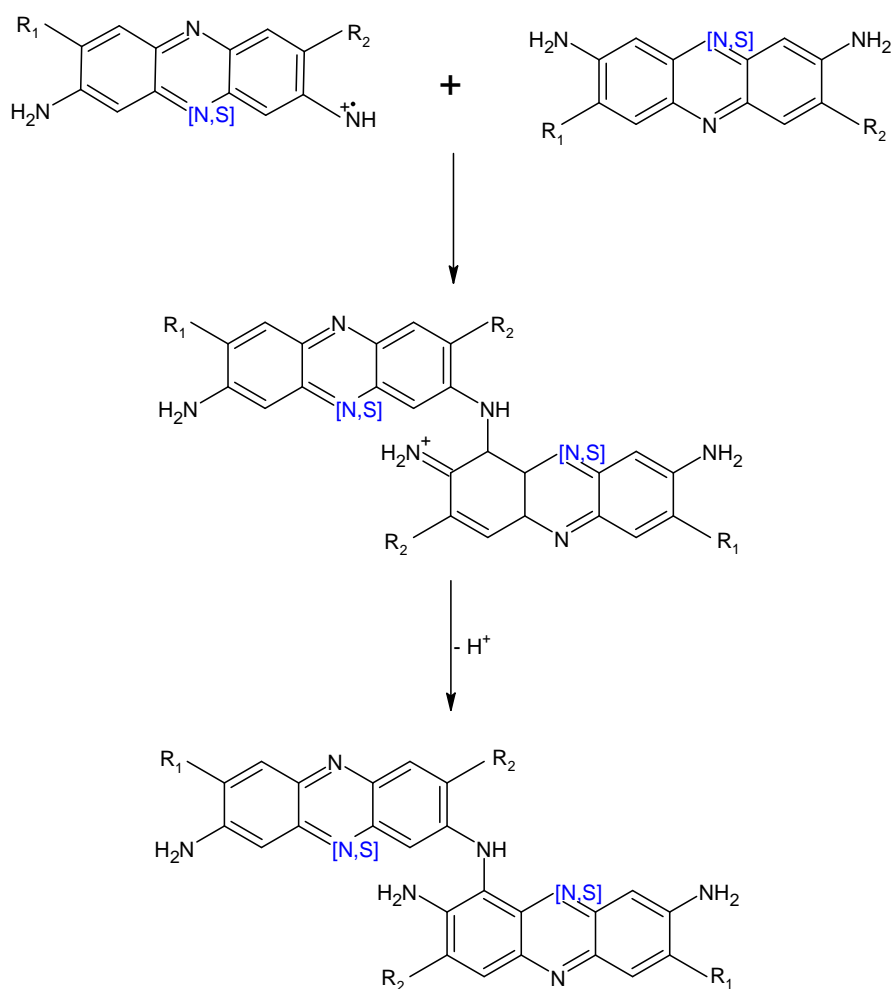


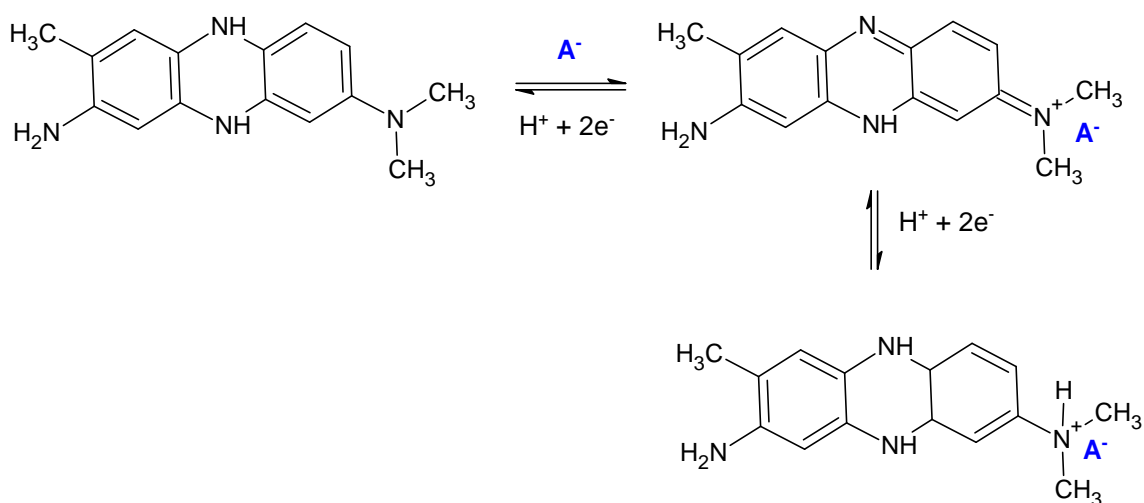
Figure 5.2: Generic structure of a phenazine and phenothiazine, where R groups ($-\text{H}$, $-\text{CH}_3$ etc.) may or may not be present³⁴.



Scheme 5.3: Generic dimerisation of phenazine and phenothiazines³⁴.

Chapter 5: Latent Finger-Mark Visualisation at a Brass Surface via Deposition of Conducting and Redox Polymers

As mentioned previously, the two species of interest which fall under this category are NR and Th. Deposition of the redox monomer NR has been explored for many applications including DNA sensing³⁵, stabilisation of biosensors³⁶, carbon dioxide reduction³⁷ and pharmaceutical analyte sensing^{38,39}. Electropolymerisation of NR has been observed to be highly pH sensitive, with initial protonation varying greatly with the pH of the solution. The polymerisation mechanism includes an initial radical formation due to oxidation with subsequent dimerisation and tetramerisation to combine to form the polymer through C-N coupling⁴⁰. Counter ions within the solution play a role in stabilisation of the charge during doping and de-doping much like that observed with PEDOT (Scheme 5.4).



Scheme 5.4: Mechanism of doping and de-doping of neutral red monomer.

There is, to the best of our knowledge, only one report of electropolymerisation of NR in relation to finger-mark visualisation on forensically relevant substrates, where Broncová et al. developed a cyclic voltammetry method for the visualisation of latent finger-marks on brass ammunition casings, resulting in level 2 features within the finger-mark being visualised⁴¹.

Th and polythionine (pTh) modified electrodes have been used for quantitation of species of interest such as heparin⁴² and uric acid⁴³. Th films have been studied at a wide variety of conditions and surfaces^{23,44,45} but thus far have not been used in the visualisation of latent finger-marks. Th polymerisation follows a similar mechanism as NR with the initial

radical cation formation and subsequent linkage through C-N coupling producing the repeating unit as seen in **Figure 5.3**, with additional studies showing that a larger anion (A^-) present during the electrochemical formation of films favours the production of these cations, but overall decreases mobility and hinders uniform film formation⁴⁶.

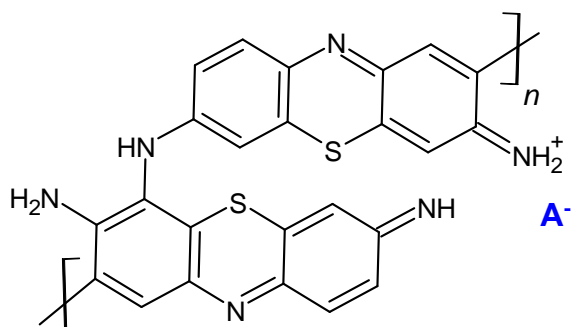


Figure 5.3: Structure of repeating unit of polythionine⁴⁷.

The use of these three species individually and more specifically in combination, to develop latent finger-marks on a brass surface will enhance the body of work currently in the literature of latent finger-mark development on brass surfaces, realising a novel approach to this challenge.

5.3 Experimental

5.3.1 *Materials and Reagents*

Brass (CZ108/CW508L) sheets were obtained from Farnell Ltd. UK in 100 x 250 mm sized sheets. Sodium nitrate was purchased from VWR chemicals. Thionine Acetate (>85%) and Neutral Red (>90%) were purchased from ThermoScientific while 3,4-ethylenedioxythiophene (EDOT) (95%) was purchased from Flurochem. All compounds were used without further purification. Sulfuric acid (96% pure solution in water) and 5 M hydrochloric acid solution were obtained from Acro Organics. Ethanol (anhydrous $\geq 99.5\%$) was obtained from Sigma-Aldrich and all deionised water was obtained from the lab Millipore Milli-Q water system with a Progard[®] TS2 filter attached. 1 μ M diamond suspension purchased from ThermoScientific. Brasso[®] was purchased from a local store.

5.3.2 *Instrumentation and software*

All electrochemical experiments were carried out using a Solartron Potentiostat Model 1285 operated by Scribner Associates Corrware software package with data analysis using CorrView Version 2.3a and a CHI Electrochemical workstation model (660E) operated by CHI software (version 19.10) with Microsoft excel 365 software package and Origin Pro2023b for data analysis. A platinum mesh (square area 1.32 cm²) was used for the counter electrode and a standard Ag|AgCl electrode (internal solution 3 M KCl) was employed as the reference electrode. The Ag|AgCl reference electrode was stored in 3 M KCl when not in use. A HUAWEI P20 lite mobile phone, running EMUI version 9.1.0 in addition with a LED desk lamp were used for photography. Ultra-violet - visible (UV-vis) spectrophotometric analysis was performed with a USB-650UV Spectrometer attached to a DH-2000-S-DUV-TTL lamp via a QR4000-7-SR-BX reflection probe from Ocean Insight controlled via OceanView software version 2.0.12. Infra-Red spectrophotometric analysis was performed with a Thermo Scientific Nicolet iS50 Spectrophotometer with an ATR attachment controlled via OMNIC 9 software version 9.9.471. X-Ray Photoelectron spectroscopy was performed with a Kratos AXIS 165 instrument at the Bernal institute within the University of Limerick.

5.3.3 *Procedures*

5.3.3.1 *Brass Preparation and Cleaning*

Brass strips of size 2.5 x 7 cm were cut from the larger sheet with the use of metal shears. An exposed working area of 2.5 x 2.5 cm (6.25 cm²) was formed on one side of the sheet with the use of insulating tape (**Figure 5.4**). The brass sheets were replenished with polishing. The polishing method involved removal of the tape from the strip and a small amount of Brasso[®] (isopropyl alcohol 3–5%, ammonia 5–10%, silica powder 15–20% and oxalic acid 0–3%) was applied to a rough cloth. This was used as the initial abrasive, removing the most loosely bound material. The sheet was then brought to a lustre finish with 1 µm diamond suspension and a polishing pad. The strips were rinsed with deionised water and sonicated in a beaker of ethanol for 10 minutes to ensure all adsorbed residual material on the surface was removed. The brass strips were finally dried via compressed air and, once the area was defined with tape again, were ready for use.

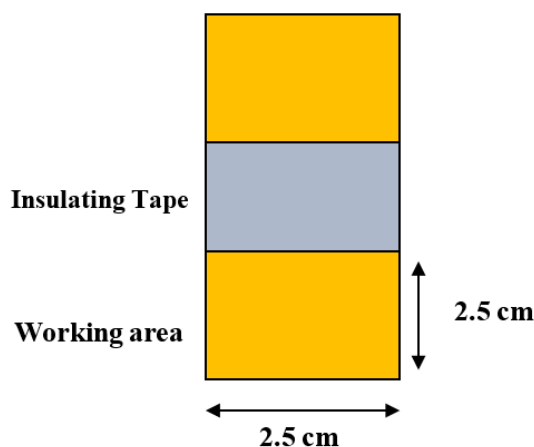


Figure 5.4: Diagram of brass strip with working area sectioned via insulating tape prior to electrochemical use.

5.3.3.2 Glassy Carbon Electrode Preparation and Cleaning

After each use, glassy carbon electrodes (GCE) were cleaned with 1 μm diamond suspension and a micro-cloth polishing pad. The polished surface was then rinsed with a strong jet of deionised water, followed by ethanol to ensure that no polishing material remained on the surface. The electrode was then dried via a jet of compressed air.

5.3.3.3 Indium Tin Oxide (ITO) Preparation and Cleaning

Prior to each use indium tin oxide (ITO) electrodes were gently wiped clean with a piece of lint free tissue in three steps, dampened with deionised water, ethanol and finally acetone. The electrode was further sonicated in ethanol for 10 minutes and dried via a jet of compressed air. The working area was defined via insulating tape to give an area of 6.25 cm^2 .

5.3.3.4 Preparation of Monomer Solutions

To ensure homogeneous solutions of the monomers, once the correct amount of compound was measured out [see **Table 5.3** for concentrations used] it was transferred to the flask with the minimal volume of solvent. Sufficient solvent was added to the flask to approximately fill a quarter of the total volume. This was then sonicated for 10 minutes, placed in the fridge for 5 minutes and then sonicated for an additional 10 minutes. The solution was then brought up to the mark of the vessel and was allowed to stir for 30

Chapter 5: Latent Finger-Mark Visualisation at a Brass Surface via Deposition of Conducting and Redox Polymers

minutes. The solutions were stored in the fridge at 4 °C and stirred at room temperature for 5 minutes before use.

Table 5.3: Combinations of EDOT monomer, thionine acetate and neutral red employed.

<i>Monomer</i> → <i>Solution</i> ↓	EDOT* (2 mM)	Thionine Acetate (1 mM)	Neutral Red (1 mM)
1	X	/	/
2		X	
3			X
4	X		X
5	X	X	
6		X	X

* EDOT was initially used at a concentration of 10 mM when in the solution of 0.1 M H₂SO₄, however, due to solubility issues with subsequent electrolytes, this concentration was reduced to 2 mM.

5.3.3.5 Electrochemical Methods

Over the course of this chapter cyclic voltammetry and chronoamperometry were implemented as the principal electroanalytical techniques. In all instances, the reference electrode was a 3 M KCl Ag | AgCl and the counter electrode was a platinum gauze (~ 1.32 cm² in total area only, not taking increased area of mesh into account).

5.3.3.6 X-Ray Photoelectron Spectroscopy

Samples were sent to the *Bernal Institute* within *University of Limerick* for analysis carried out by *Dr Fattima Laffir*. Two samples (**Figure 5.5**) were prepared via cyclic voltammetry across the range of -0.2 to 0.5 V at 50 mV.s⁻¹ for 3 cycles. Sections of the brass surface were protected with insulating tape prior to electrochemical analysis, to allow for an accurate representation of how the procedure altered the brass surface.

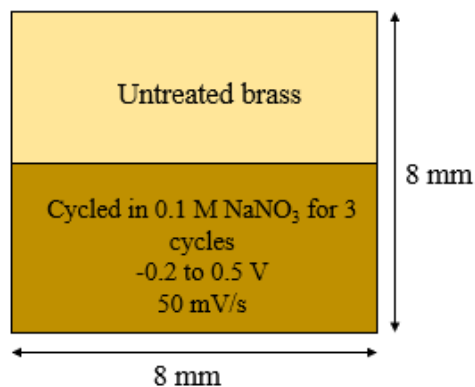


Figure 5.5: Diagram of brass samples for XPS analysis.

5.3.3.7 Ultraviolet / Visible Spectroscopy

The lamp was allowed to heat up at least 30 minutes prior to use. The instrument was blanked with a dried surface of interest (e.g. ITO/GCE/Brass) which was cycled in the electrolyte only, using the same parameters used for the film formations. Film samples were gently dried with a jet of compressed air, post formation, and placed on a level surface. The reflectance probe was lowered as close to the surface as possible without making contact. The room was darkened as much as possible to minimise diffuse extraneous environmental light, which may enter the probe. To ensure an accurate measurement, the readings were taken at three different locations at the surface with an average of 4 scans at each location. While the wavelength range of the instrument was 200 to 800 nm, due to noise visible within the raw data, the observed range within the analysis was reduced to 220 to 650 nm. Data was analysed and 2nd derivative was calculated within OriginPro2023.

5.3.3.8 Attenuated Total Reflection Infrared Spectroscopy

The diamond surface was cleaned with methanol-dampened lint free tissue and allowed to dry for 5 minutes prior to use. The instrument was blanked to the environmental conditions of the room and background data of the clean surface of interest was obtained for manual background subtraction within OriginPro2023. Sample data was obtained with an average of 16 scans, as, in general, films appeared thin.

5.3.3.9 Application of a Groomed Print onto a Surface

The donor's hands were initially washed with soap and warm water. The finger, which was intended to provide the finger-mark, was rubbed across sebaceous oil rich areas (forehead, down the side of the nose and behind the ear). This finger was then rubbed two to three times on the forearm, to remove any excess oils or skin cells which may have become trapped between the ridges, to lessen the likelihood of smudges or errors on the ridges. The finger was then gently placed on the surface of interest for one to two seconds.

5.3.3.10 Scoring of a Visualised Finger-mark

As mentioned in **Chapter 1**, finger-marks quality can be quantified via the use of grades and level features. Due to the manual application of the finger-marks, the use of grades as a scoring metric was not useful, as intentionally applied marks without external degradation factors, (heat, time etc.) would be of grade 3 or 4 (highest scores). Therefore, the scoring metric for the visualisation in this section was limited only to the levels of details with level 3 being the highest score. A digitised image of the print employed for all analysis presented is shown in **Figure 5.6** with common features shown.

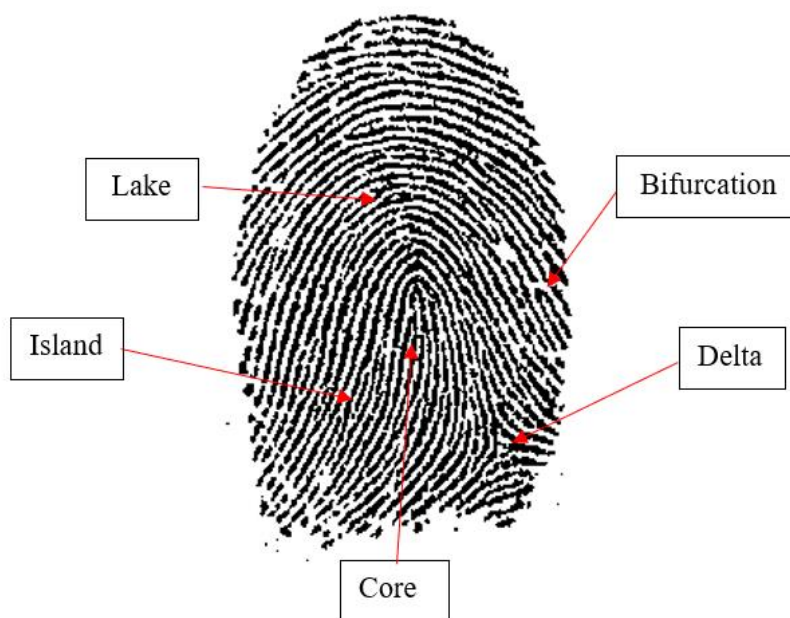


Figure 5.6: Digitised finger-mark of finger used in analysis with common features labelled.

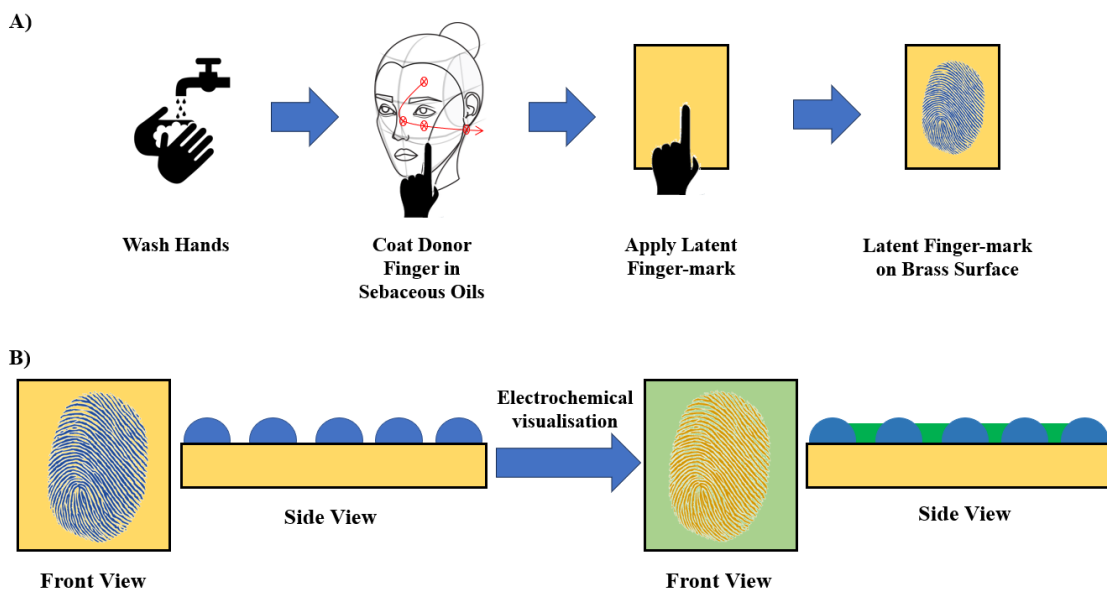
5.4 Results and Discussion

5.4.1 *Electrochemical Investigation of Brass Substrate*

5.4.1.1 3,4-ethylenedioxythiophene Deposition on Brass in Sulfuric Acid

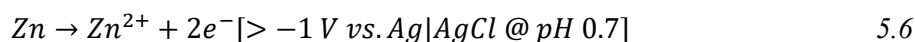
Sulfuric acid (H_2SO_4) has classically been used as an etching agent for brass ornamental pieces or circuitry design⁴⁸. To our knowledge, the work of Costa et al. is the only published report of successful deposition of PEDOT onto a brass surface²⁶ for the specific goal of latent finger-mark visualisation. However, the deposition of PEDOT with the use of H_2SO_4 onto a metallic surface (stainless steel) for the use in latent finger-mark visualisation has been reported^{33,49} with level 2 details observed. The process of monomer deposition for visualisation on the surface relies on the finger-mark acting as a protective layer or stencil in the presence of the aggressive ions of strong acids, SO_4^{2-} and NO_3^- , given that classically, stencils are used to etch ornamental designs into brass. In **Scheme 5.5** the initial application process is shown (**Scheme 5.5 (A)**), the resulting latent finger-mark can be seen to have stencil-like properties with the ridge detail being transferred to the surface by means of natural sebaceous oils. These sebaceous oils protect the brass surface from the incoming deposition material, allowing the material to be deposited in the negative space of the finger-mark (valleys) (**Scheme 5.5 (B)**). Subsequently this means that the visualised finger-mark is a negative of the original fingerprint, i.e. areas containing colour pertaining to the material were not in contact with the finger during deposition.

Chapter 5: Latent Finger-Mark Visualisation at a Brass Surface via Deposition of Conducting and Redox Polymers



Scheme 5.5: A) Application of a latent finger-mark on a brass surface and B) basic view of electrochemically deposited material onto the surface of brass using the latent finger-mark as a stencil.

Initial exploration into the behaviour of brass in 0.1 M H₂SO₄ was performed via cyclic voltammetry (**Figure 5.7**). A starting potential of -0.60 V was employed with an anodic sweep, resulting in evident passivity until $E_p^a = 0.20$ V, past which apparent breakdown of the material was observed. Comparing to a Pourbaix diagram of zinc in a room temperature aqueous system (**Figure 5.8**)⁵⁰, the experimental conditions indicate the formation of Zn²⁺. This suggests a loss of zinc, via oxidation, from the bulk alloy is highly likely to contribute to the strong increase in current, until the maximum of 1.1 V is reached.



Within the return sweep of cycle one, a crossover event was evident at 0.11 V (**Figure 5.7** inset) with other crossovers at approximately 0.35 V in all three cycles. An observed crossover in cyclic voltammetry is due to a subsequent electrodeposition at the surface, in this case possibly due to copper oxide (CuO), which could be further reduced back to Cu - the response observed with $E_p^c -0.2$ V. Observationally, some blue material was produced over the course of the experiment, which could indicate the presence of copper sulphate (CuSO₄). A possible set of chemical equations (Equation 5.X to 5.X) of the mechanism are given below⁵¹:

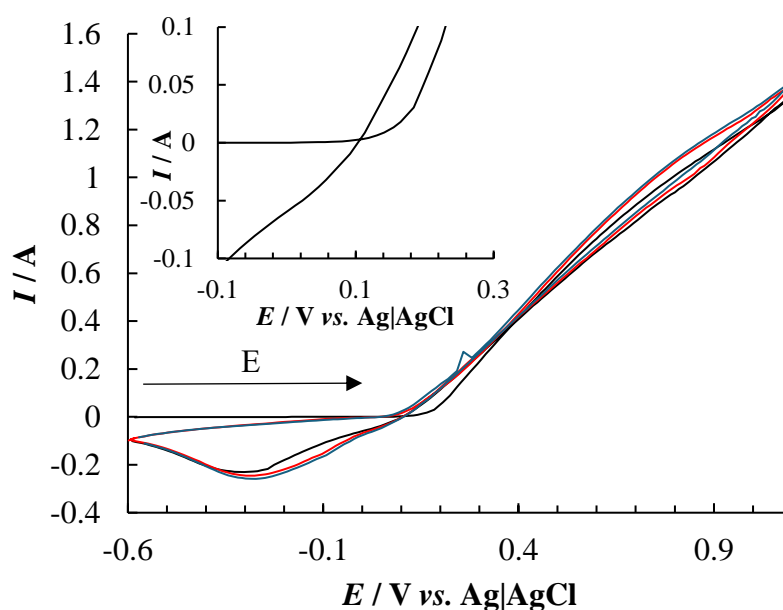
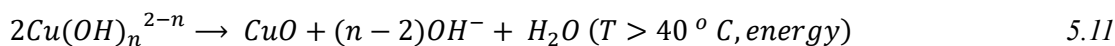
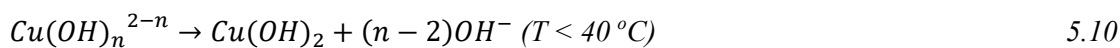
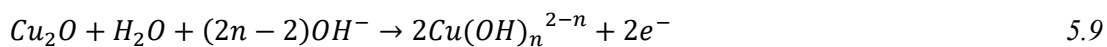


Figure 5.7: Cyclic voltammogram over the potential range -0.6 to +1 V vs. Ag|AgCl for a brass sheet in 0.1 M H_2SO_4 at $100 \text{ mV}\cdot\text{s}^{-1}$ for 3 cycles (Cycle 1: black, Cycle 2: red and Cycle 3: blue). Inset: showing crossover in cycle 1 at 0.11 V (typical trace).

Chapter 5: Latent Finger-Mark Visualisation at a Brass Surface via Deposition of Conducting and Redox Polymers

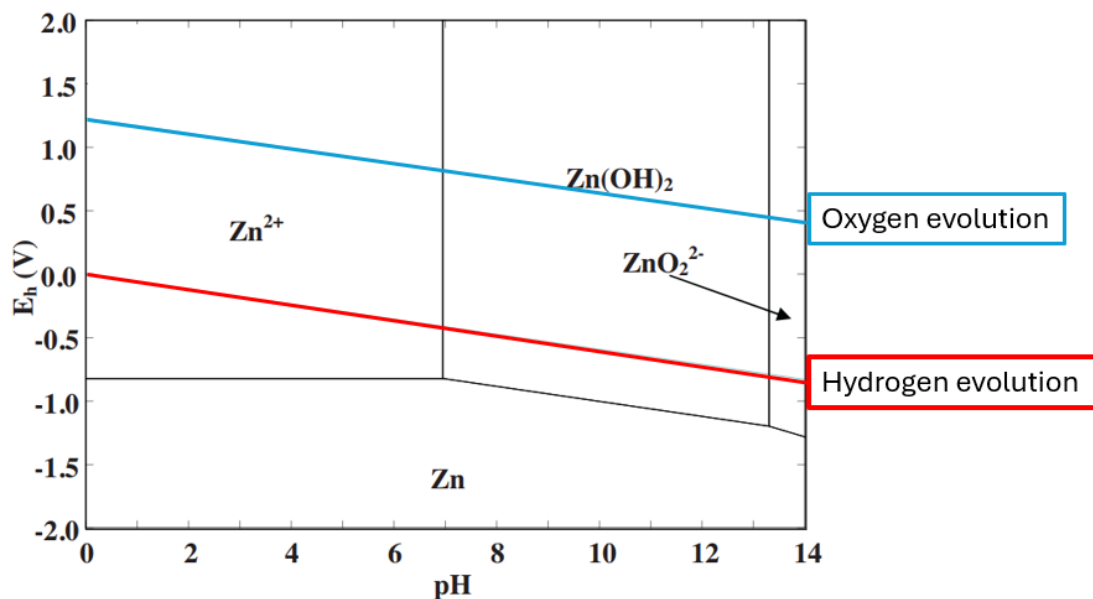


Figure 5.8: Pourbaix diagram of zinc in an aqueous system at 25 °C⁵⁰.

Groomed finger-marks were applied to the brass surface and the potential cycling method was repeated. The visualisation of the finger-mark was successful (**Figure 5.9**) clearly identified as loop (level 1 feature) and level 2 features visible with the naked eye.

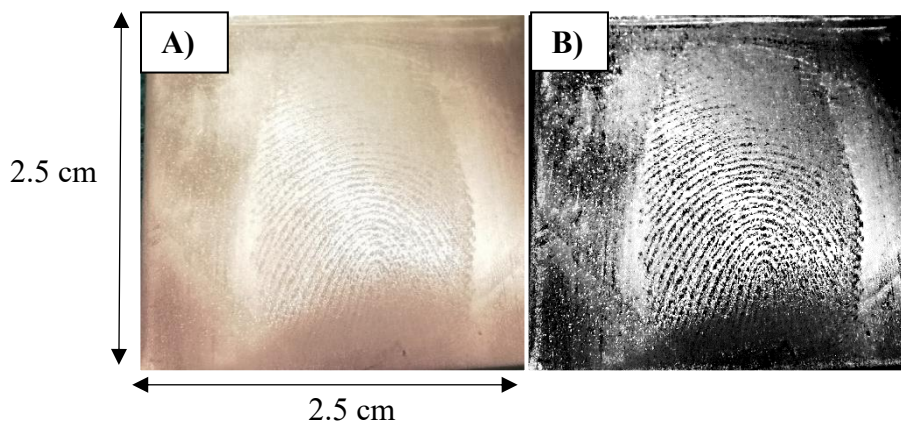


Figure 5.9: Photograph of sebaceous finger-mark on a brass sheet visualised via cyclic voltammetry over the potential range of -0.6 to +1 V vs. Ag|AgCl for 3 cycles at 100 $mV \cdot s^{-1}$ in 0.1 M H_2SO_4 with B) high contrast black and white.

Chapter 5: Latent Finger-Mark Visualisation at a Brass Surface via Deposition of Conducting and Redox Polymers

The process, however, resulted in gaseous activity at the counter electrode at $E_p^a > 0.3$ V vs. Ag|AgCl. This vigorous reaction may result in altered pH during scanning and the production of bubbles which may adhere to the substrate, thus interfering with the process. As a result, constant potential coulometry was employed. The applied potentials of -0.5, -0.1, 0.3, 0.5 and 1.1 V (**Figure 5.10**) were selected from the cyclic voltammetry range previously employed. In all cases, the potential was applied for 60 seconds.

The use of chronoamperometry gave interesting insights into how the brass behaves. The most anodic potential (1.1 V) resulted in a dark brown colouration on the brass while the solution turned blue, to a greater extent than observed in the cyclic method, indicating, again, the production of soluble CuSO_4 in solution. The current density vs. time plot at this potential (**Figure 5.10 (A)**) resulted in relatively more noise in comparison to the other anodic potentials, $E_{\text{app}} = 0.5$ and 0.3 V. This was attributed to the higher levels of activity. The applied potentials of 0.5 and 0.3 V resulted in smoother traces, and, upon application of 0.5 V, a pink colour was observed at the brass surface, while a dull yellow/grey was obtained at the 0.3 V. In all the above experiments, the surface of the brass became pitted and roughened due to the corrosion process. When compared to a Pourbaix diagram for copper (**Figure 5.11**)⁵² in a solution of concentrated sulfuric acid at ambient temperature, the selected experimental anodic potentials are firmly placed within the corrosion region and increase the likelihood of generation of CuSO_4 . However, with the less anodic potentials of 0.5 and 0.3 V, the blue hue of the solution was less apparent. This may indicate some incomplete reaction as Cu_2O is formed within the steps and the pink colour could be attributed to this.

When the voltage was held at the cathodic potentials of -0.1 and -0.5 V, there were no visible effects at either the brass surface or the CE.

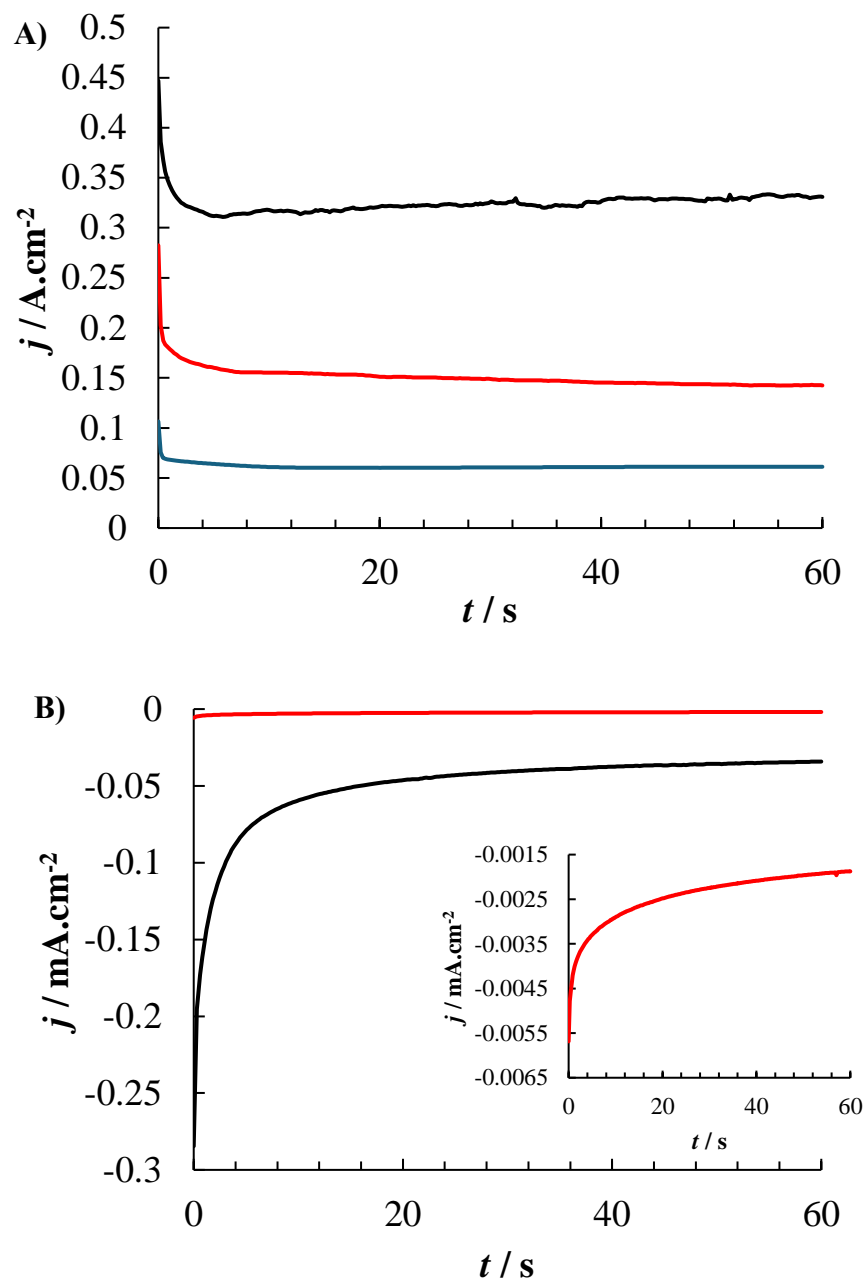


Figure 5.10: Chronoamperometry of brass sheets in 0.1 M H₂SO₄ showing $E_{app} =$ A) +1.1 V (black), +0.5 V (red) and +0.3 V (blue) and B) -0.5 V (black) and -0.1 V (red). Inset: zoomed in plot of -0.1 V.

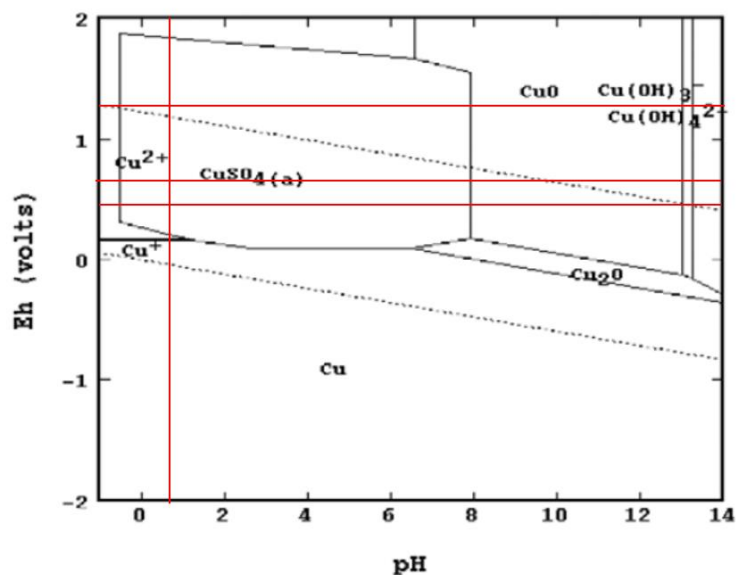


Figure 5.11: Pourbaix diagram of copper in a SO_4^{2-} rich environment⁵² with the horizontal red lines indicating the potentials held (corrected for conversion to SHE) with vertical line representing pH of solution employed in this work.

An applied potential of 0.1 V was selected for further analysis. The effect of the applied potential as shown in **Figure 5.12** resulted in no gaseous release at the CE, however, a faint line where the solution met the air was observed on the surface of the brass (**inset Figure 5.12**). This was an apparent etch of the surface as it was not removable by wiping. Using the same strip of brass without employing the cleaning method, the experiment was repeated for a longer period of 5 minutes. Following this period, no gaseous release was observed at the counter electrode and, when removed, a new line indicating the solution height was visible on the brass strip. There was no notable colour difference at the brass surface, however, the surface did slightly lose the lustre associated with an unused brass strip. The time periods employed did result in some variation within the chronoamperograms. Upon application of 0.1 V for $t = 1.0$ min, a starting current density of $1.80 \text{ mA}\cdot\text{cm}^{-2}$ and a final value of $0.29 \text{ mA}\cdot\text{cm}^{-2}$ were obtained at the one-minute mark. In the case of $E_{\text{app}} = 0.1 \text{ V}$ for $t = 5.0$ min, an initial current density of $1.0 \text{ mA}\cdot\text{cm}^{-2}$, was observed, decreasing to $0.25 \text{ mA}\cdot\text{cm}^{-2}$ at the $t=1.0$ min mark and finishing with $0.61 \text{ mA}\cdot\text{cm}^{-2}$ at 5.0 minutes. This slight variation in the current densities could be associated with the observed loss in lustre at the brass surface. While the parameters are not within range of any observed zinc passivation from Pourbaix diagrams, the loss of material was most likely across the entire brass surface which was submerged. This loss from the initial

one-minute-long experiment could have slightly altered the surface, decreasing the current density which was observed in the subsequent run.

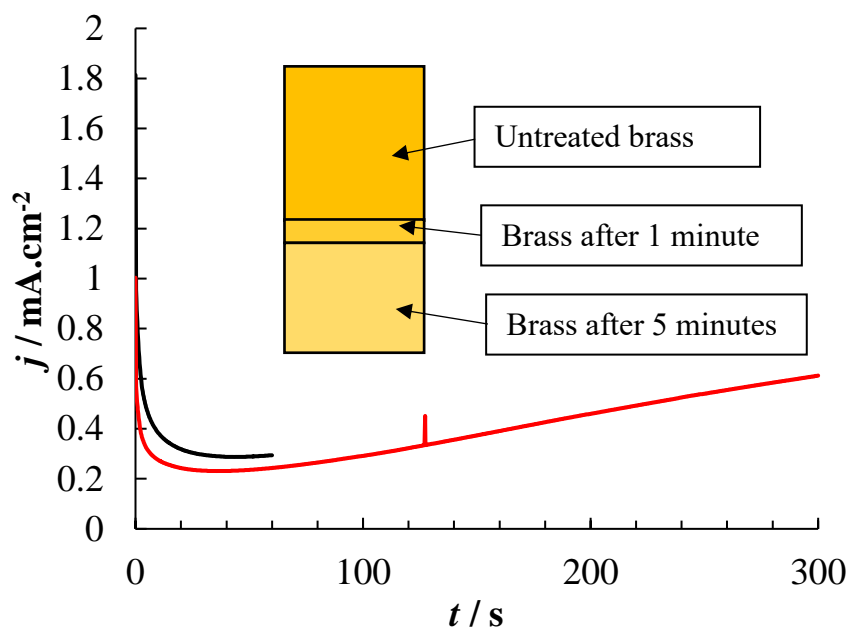


Figure 5.12: Chronoamperometry of a brass sheet in 0.1 M H_2SO_4 at $E_{app} = 0.1$ V for 60 s (black) and 300 s (red). Inset: representation of solution lines on a strip of brass post analysis in 0.1 M H_2SO_4 .

To exploit the possible corrosion process, while paving the way for improved finger-mark visualisation with the aid of phenothiazine monomers, a “low and slow” chronoamperometric method was proposed. **Figure 5.13 (A)** shows the chronoamperometry trace for $E_{app} = 0.1$ V and 0.2 V at $t = 300$ seconds. During the experiment, at 0.1 V, small quantities of gas were intermittently produced at the CE. Initially, the change in current density could be due to the increased activity of the material due to the activation process which was observed. Concurrently, 0.2 V was observed to be the potential at which onset initially occurred. The corrosion onset of the brass does include the oxidation of at least zinc within the bulk alloy releasing 2 electrons per zinc atom, resulting in increased current flow. **Figure 5.13 (B)** shows the corresponding finger-mark for the experiment involving $E_{app} = 0.2$ V, being lightly etched onto the surface of the brass with very little colour change of the surrounding surface. The surface was gently wiped with an ethanol-dampened lint free tissue to ensure that the visible print was, in-fact, etched into the surface and not just remaining sebaceous oil material from the initial contact. This did not change the quality of the visualised finger-mark. When

Chapter 5: Latent Finger-Mark Visualisation at a Brass Surface via Deposition of Conducting and Redox Polymers

the potential was increased to 0.2 V for a new brass surface and finger-mark, the gas evolution was much more uniform and controlled. In this case, there was a much more obvious change in the surface colour as the brass changed to a grey/brown colour after the experiment. The finger-mark was lightly etched onto the surface with the loosely bound brown material being easily removed with a gentle wipe as before. The surface appeared to be duller relative to that produced upon application of 0.1 V. The quality of the finger-marks was low, and while overall shape was visible (level 1) no discernible level 2 features were observed, under these conditions.

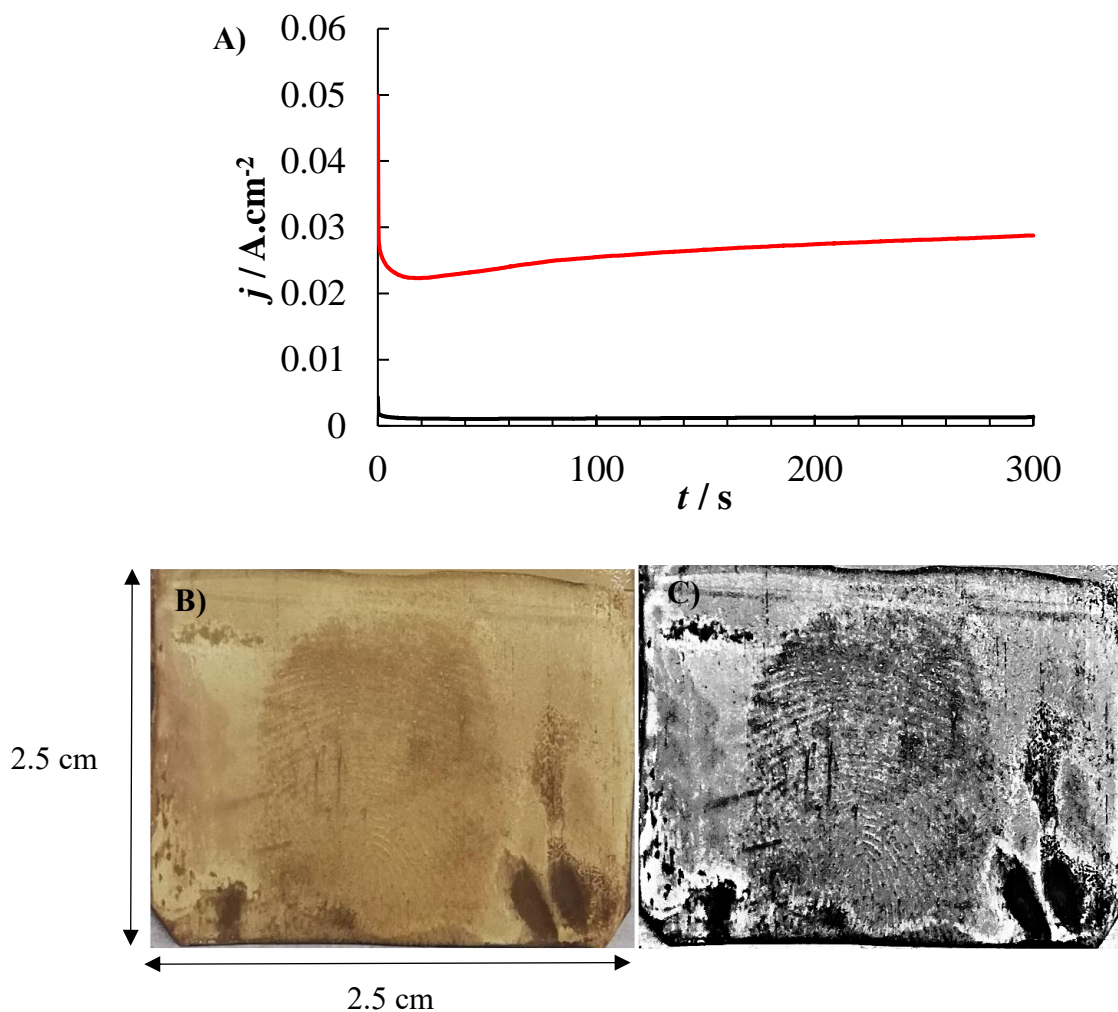


Figure 5.13: A) Chronoamperometry of a brass sheet with a latent print of $E_{app} = +0.1 \text{ V}$ (black) and $E_{app} = +0.2 \text{ V}$ (red) for 300 s in 0.1 M H_2SO_4 and corresponding photograph of visualised finger-marks via $E_{app} = +0.2 \text{ V}$ in B) full colour and C) high contrast black and white.

Based upon these investigations using 0.1 M H_2SO_4 , the inclusion of EDOT monomer in this electrolyte followed. **Figure 5.14 (A)** shows the same current-time profile methods

of applied potential experiments (0.1 V & 0.2 V for 5 minutes). The clear difference in current density was still observed with the use of this solution under the same conditions.

The surface of the brass did develop a mild dull grey colouration as well as a dark coloured (navy) vertical streak pattern, seemingly more concentrated to the side closest to the counter electrode. This facilitated a slight visualisation of the finger-mark which, was deposited onto the surface prior to the experiment. When the potential was increased to 0.2 V, a much more steady and visible bubbling was observed from the CE, reflecting an overall deeper colouration visible on the brass surface. Development of the print was visible during the process and a slight blue colour was observed in the solution after the experiment was complete. Upon replication of the methods, without altering the solution, the blue colour became much more prominent reflecting the collective release of CuSO_4 or, perhaps, desorbed PEDOT. Finger-marks visualised in previously used solution provided much lower quality (nearly non-visible) results. The surface of the brass developed a mud/clay pink colour, which appeared “thicker” in some areas. When visualisation was repeated with a fresh solution, the finger-marks’ appearance following the experiment was much darker, leading to the assumption that the quantity of monomer consumed during the deposition process, or the release of secondary material into the solution, was significant enough to warrant a fresh solution each time. Regardless of this effect, finger-mark visualisation, as shown in **Figure 5.14 (B)**, using this EDOT-sulfuric acid approach was poor relative to sulfuric acid alone (see **Figure 5.10 (B)**) with not even level 1 features observed.

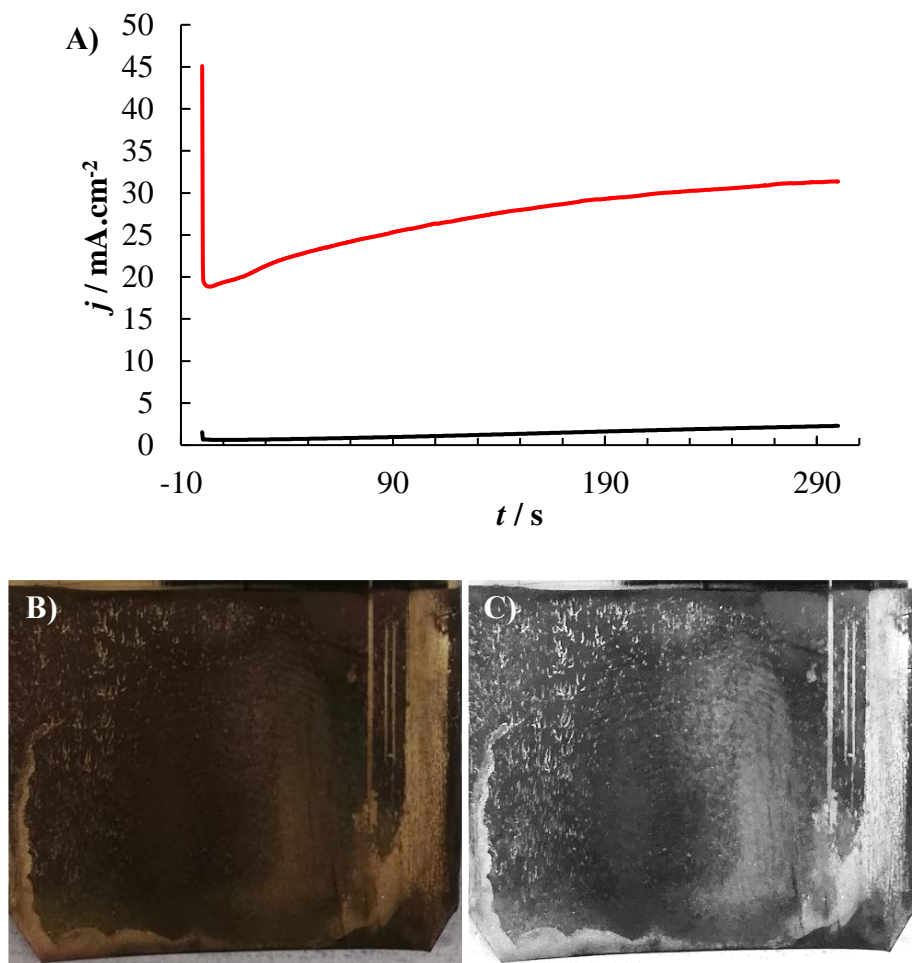


Figure 5.14: A) Chronoamperometry of a brass sheet of $E_{app} = +0.1$ V (black) and $E_{app} = +0.2$ V (red) for 300 s in 0.01 M EDOT with 0.1 M H_2SO_4 and corresponding photograph of visualised finger-marks via $E_{app} = +0.2$ V in B) full colour and C) high contrast black and white.

In order to improve upon the potentiostatic approach, the next steps involved potential sweeping over the range -0.2 to 0.5 V. **Figure 5.15** shows the cyclic voltammograms of brass sheets in 0.1 M H_2SO_4 (A) and 0.1 M H_2SO_4 with 0.01 M EDOT (B). Gas evolution at the CE was evident in the anodic region and increased with increasing potential as expected. The voltammograms retained the characteristic shape of that in **Figure 5.7** with less noise evident with the second crossover observed at 0.25 V for the H_2SO_4 and 0.33 V for the EDOT in cycle 1, and not observed in the subsequent cycles, for both solutions. The current density was also quite comparable in each case, indicating that much of the activity observed by the electrochemical measurements was, in fact, due to the brass activity. The brass surface did exhibit a pale pink colour, as observed previously, when held at 0.5 V, again, indicating the presence of some material at the surface, possibly from

the expected dezincification process. When wiped with an ethanol-dampened lint free tissue, the surface was mostly unaffected other than some unevenly distributed dark spots which were removed.

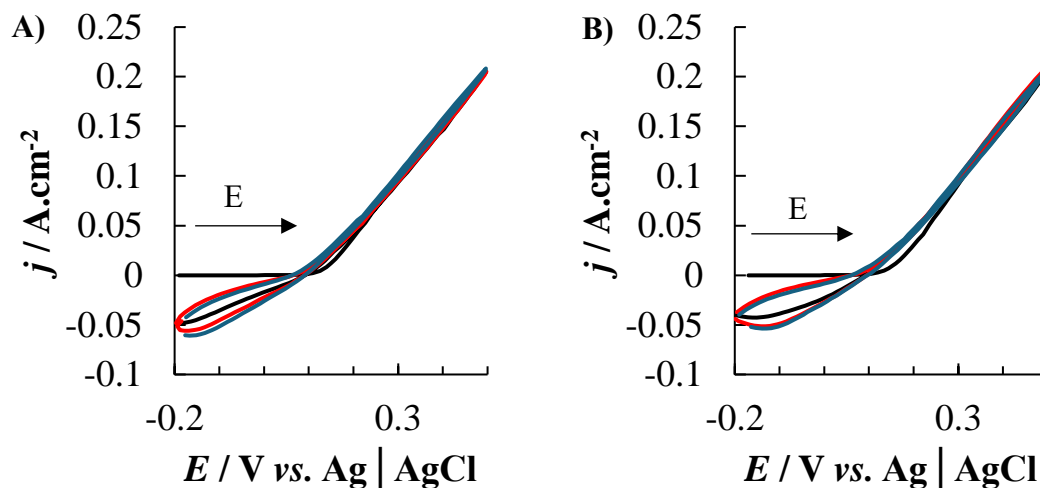


Figure 5.15: Cyclic voltammogram over the potential range of -0.2 to $+0.5 \text{ V vs. Ag} | \text{AgCl}$ for 3 cycles at $100 \text{ mV}\cdot\text{s}^{-1}$ for a brass sheet in A) $0.1 \text{ M H}_2\text{SO}_4$ and B) 0.01 M EDOT with $0.1 \text{ M H}_2\text{SO}_4$.

Finger-mark visualisation (**Figure 5.16**) was partly visible during cycling and produced visible finger-marks of the highest quality in comparison to previous methods, with level 1 and 2 features easily visible to the naked eye for both solutions. The addition of EDOT appeared to display a much higher contrast between the visualised finger-mark and the brass surface compared to electrolyte only. This led to much more defined ridges and an overall more easily discernible finger-mark, strengthening the reasoning for including such monomers. Additionally, during the cleaning process (**Section 5.3.3.1**), the finger-mark remained etched on the surface indicating that this method may preserve the finger-marks as well as visualising them, allowing for a more thorough forensic examination and retention of the evidence. This indicates that while the process may etch and degrade the brass surface, this method may also preserve finger-mark evidence after the initial visualisation.

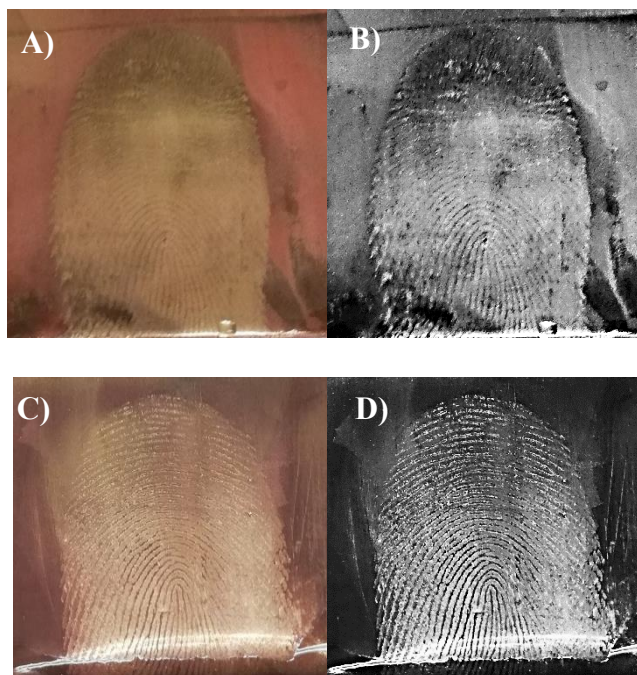


Figure 5.16: Photographs of finger-marks on brass visualised via cyclic voltammetry over the potential range of -0.2 to $+0.5$ V vs. $\text{Ag}|\text{AgCl}$ for 3 cycles at $100 \text{ mV}\cdot\text{s}^{-1}$ showing A) the full colour image and B) the high contrast counterpart of a finger-mark visualised in $0.1 \text{ M H}_2\text{SO}_4$ and C) a full colour and D) the high contrast counterpart visualised in 0.01 M EDOT in $0.1 \text{ M H}_2\text{SO}_4$.

Overall, investigations into the use of H_2SO_4 , with and without EDOT, resulted in level 2 features with characteristic ridge patterns of the donor being evident. However, the process introduced gas evolution at the CE (most likely H_2) which can interfere with the visualisation quality of the working electrode and the colouration resulted in dull ridge details due to the use of sulfuric acid. Accordingly, our attention turned to the use of sodium nitrate (NaNO_3), in place of H_2SO_4 , which has been reported previously for similar samples in combination with neutral red (NR)^{53,54}

The combination of aggressive nitrate (NO_3^-) ion, with deposition of redox and optically active phenazine and phenothiazine monomers (thionine & neutral red), was pursued in order to realise further opportunities to exploit both corrosion and deposition processes, each of which may contribute to high contrast finger-mark enhancement.

5.4.1.2 3,4-ethylenedioxythiophene Deposition in Sodium Nitrate

As mentioned above Bracová et al. reported successful visualisation of latent finger-marks on a brass substrate with sodium nitrate as electrolyte^{53,54}. While a potential range of -0.3 to 0.6 V was implemented, based on previous analysis, this range was reduced to match the parameters which were deemed successful with the H₂SO₄ studies, with **Figure 5.17** showing the cyclic voltammogram of a brass sheet in 0.1 M NaNO₃. Starting at -0.2 V the potential was swept anodically with passivity evident until 0.19 V, following which, like that observed in the H₂SO₄, dissolution or breakdown of the material occurred with increasing the current density until the maximum potential of 0.5 V was reached. On the reverse sweep, while an increased anodic current was observed which resulted in a crossover at E_p^c 0.071 V, characteristic of passivity breakdown, this was the only observable crossover, unlike H₂SO₄ which displayed two crossover events. Reduction of the oxide layer at $E_p^c = -0.05$ V, became more difficult in subsequent cycles decreasing to a potential of $E_p^c = -0.1$ V in cycles 2 and 3 with an increase in current density of 2.5 mA.cm⁻². Behaviour of the brass sheet in this electrolyte was indicative of the activity relative to the studies performed in H₂SO₄. Overall, behaviour in NaNO₃ resulted in less vigorous gaseous release at the CE, under the experimental conditions used, while retaining the desirable colour change apparent following potential sweeping.

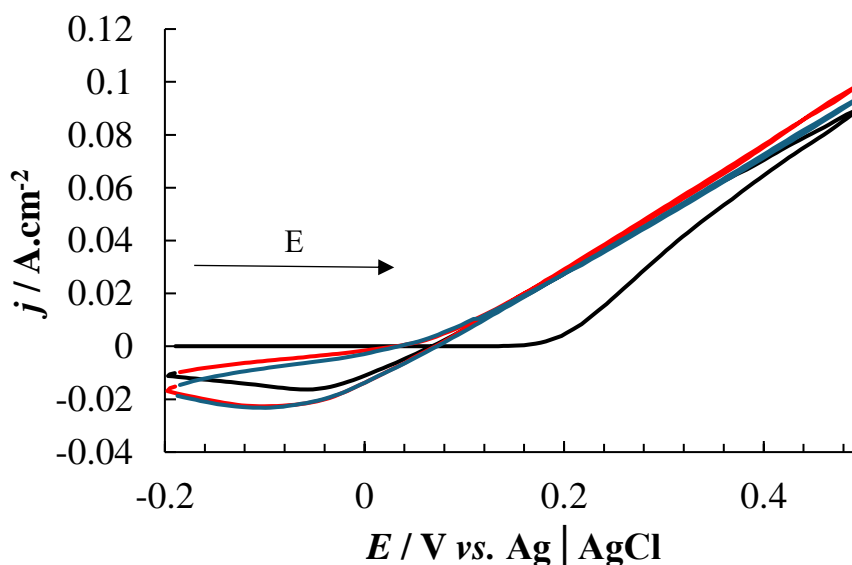


Figure 5.17: Cyclic voltammogram of a brass sheet over the potential range of -0.2 to +0.5 V vs. Ag|AgCl for 3 cycles (Cycle 1: black, Cycle 2: red and Cycle 3: blue) at 50 mV.s⁻¹ in 0.1 M NaNO₃.

Chapter 5: Latent Finger-Mark Visualisation at a Brass Surface via Deposition of Conducting and Redox Polymers

Subsequent finger-mark deposition and visualisation (**Figure 5.18 (A)**) resulted in the clearest contrast thus far, encouraging the continued use of NaNO_3 . An even surface colour was evident, and preliminary testing with latent finger-marks indicated a reproducible visualisation method with all the finger-marks containing level 2 features and two of the marks exhibiting excellent contrast between the ridges and valleys of the finger-mark. When observed individually the finger-mark visualised in 0.1 M NaNO_3 under these conditions (**Figure 5.18 (B)**) showed the presence of pores along the ridges which are level 3 features and among the highest scoring details to be visualised⁵⁵.

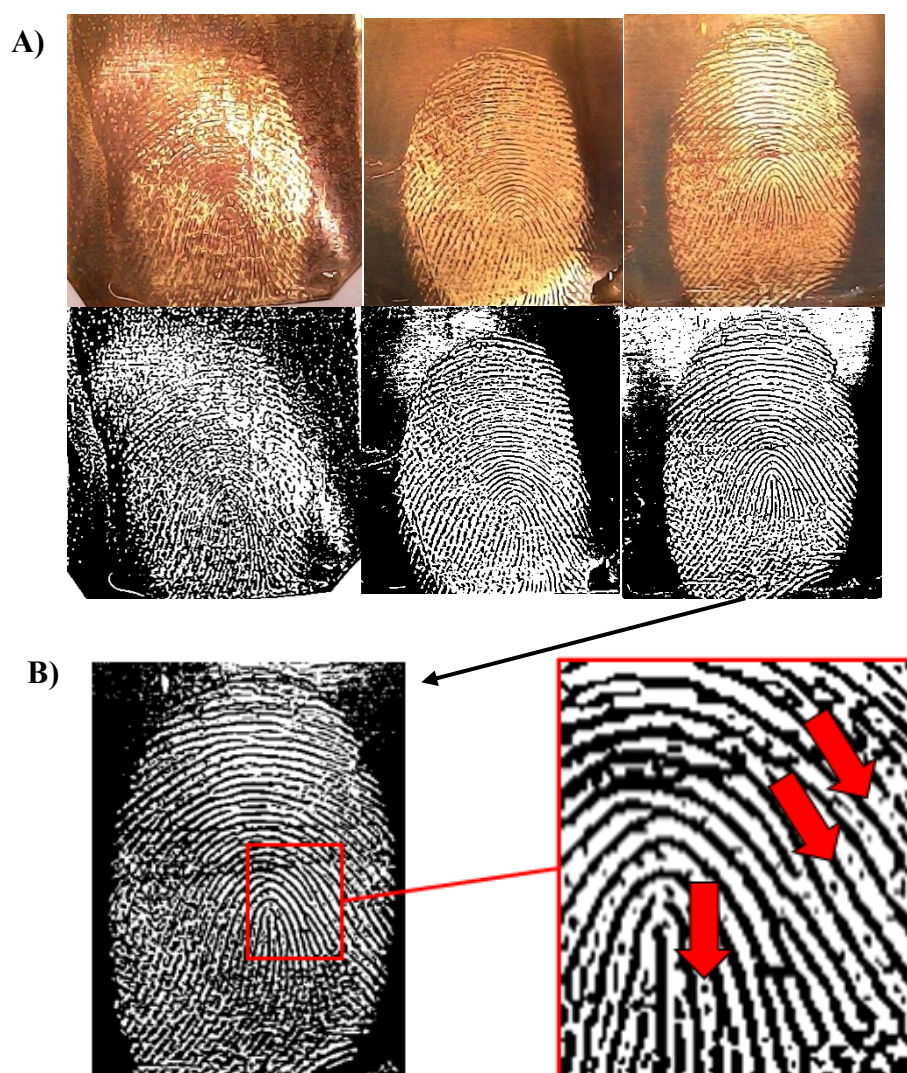
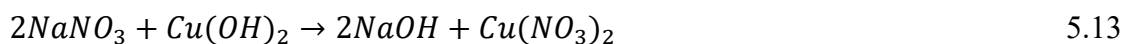


Figure 5.18: Photographs of A) finger-marks on brass visualised via cyclic voltammetry over the potential range of -0.2 to $+0.5$ V at $50 \text{ mV}\cdot\text{s}^{-1}$ for three cycles in 0.1 M NaNO_3 with high contrast images underneath and B) level 3 features indicated by arrows on zoomed in region of one of the previously visualised finger-marks.

Chapter 5: Latent Finger-Mark Visualisation at a Brass Surface via Deposition of Conducting and Redox Polymers

Upon repeated use of the solution, a blue hue was observed, indicative of a copper salt formation in line with that observed with the use of H_2SO_4 . Pourbaix diagrams of copper within aqueous conditions (**Figure 5.19**) suggest generation of copper hydroxide ($\text{Cu}(\text{OH})_2$) under these experimental conditions. A possible copper salt which is formed in the cell is *Copper (II) nitrate*, which is blue in colour and highly soluble in water and may be formed through the below process:



Further evidence which strengthens the likelihood of this reaction is the change in pH of the solution post cyclic voltammetry. Initially the pH of the 0.1 M NaNO_3 solution was observed to be a pH of 5.01, however, when measured post analysis, this pH increased to 6.5. The alkaline shift may reflect the production of sodium hydroxide (NaOH) due to the above reaction (**Equation 5.13**) suggesting that the potential range and pH employed was within both protection and passivation zones for copper.

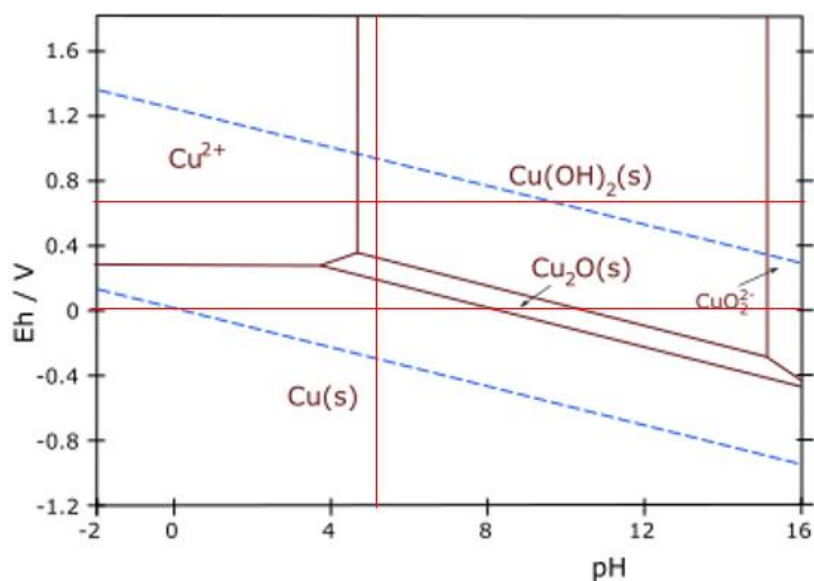


Figure 5.19: Pourbaix diagram of copper in an aqueous environment with the red intersecting lines showing the maximum and minimum of the potential ranges with the experimental parameters (corrected for conversion to SHE).

Having established possible brass behaviour in 0.1 M NaNO₃, cyclic voltammetry was employed with the addition of 2 mM EDOT into the solution. The produced voltammogram (Figure 5.20) was of a similar shape to that obtained in the electrolyte alone (Figure 5.17), with passivation occurring on the initial anodic sweep from -0.2 to 0.19 V and a steady increase in current density until the maximum of 0.5 V was reached. A cross over was once again observed at 0.070 V which increased to 0.13 V in subsequent cycles. The similarities between both voltammograms suggests that electrochemical measurements (at least cyclic voltammetry) were not a discernible technique for comparing the electrochemistry of the EDOT monomer with this brass alloy as the working electrode.

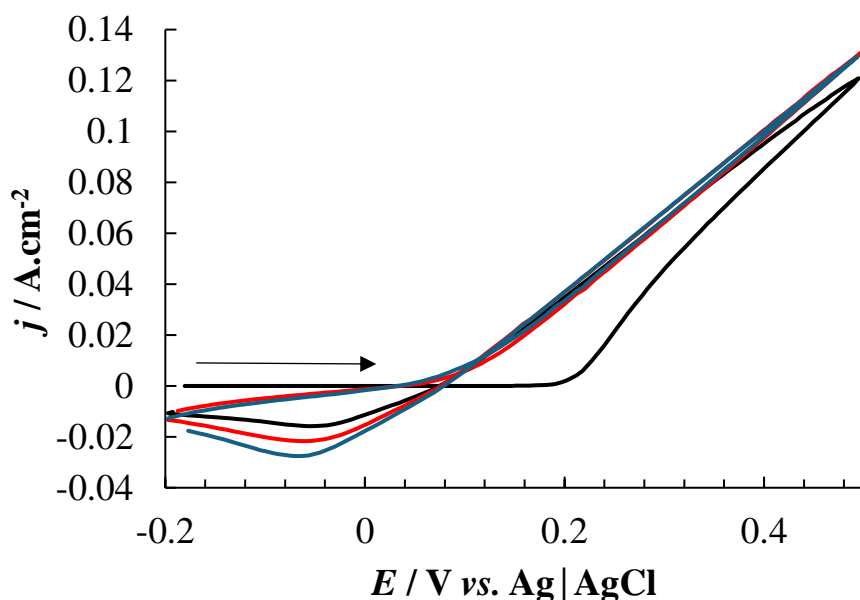


Figure 5.20: Cyclic voltammogram of a brass strip over the potential range -0.2 to +0.5 V vs. Ag|AgCl showing three cycles at 50 mV.s⁻¹ in a solution of 2 mM EDOT in 0.1 M NaNO₃.

The visualised finger-marks that were produced from this method (Figure 5.21) contained level 2 features which were visible to the naked eye, with an indication of level 3 features (Figure 5.21 (C)) when zoomed into the image. The valleys between the ridges (approximately 300 μm in diameter) appeared to be narrower than those observed in 0.1 M NaNO₃, and this may lead to a loss in definition in a more complex finger-mark sample. However, given that level 3 features were present this visualisation method was deemed to be successful.

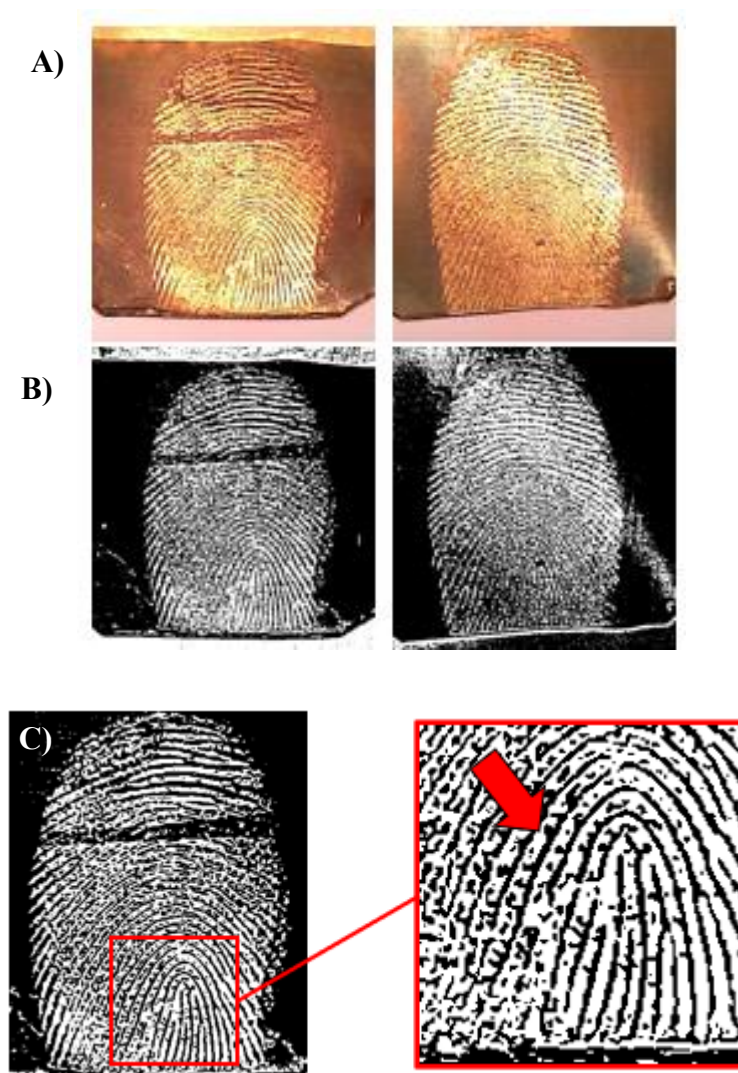


Figure 5.21: Photographs of A) finger-marks visualised with 2 mM EDOT in 0.1 M NaNO₃ with B) high contrast photographs C) zoomed in image of core of visualised finger-mark showing level 3 features (pores).

In comparing electrolytes thus far, H₂SO₄ resulted in the highest visualisation of level 2 features while an average level of 1.7 (n = 15 finger-marks, with nine instances of level 2 visualisation and a single instance of failed visualisation, grade 0) across all electrochemical methods, while NaNO₃ generated the highest visualisation of level 3 features with an average level feature of 2.2 (n = 20 finger-marks with six instances of level 3 visualisation and three instances of level 1 with no failed visualisations). Therefore, NaNO₃ alone appeared to be more suited to an electrochemical visualisation process for latent finger-marks on a brass surface and can be successfully used in conjunction with a monomer of interest for deposition. It was the obvious choice to

proceed with this electrolyte for further optimisation. Overall, possible corrosion of brass in the areas defined by the fingerprint was exploited for visualisation, which was further improved with the presence of EDOT, and subsequent XPS investigations were employed to examine this further.

5.4.2 *X-ray Photoelectron Spectroscopy of a Brass Surface*

XPS was performed on two samples of brass, with sample one being untreated brass which was protected by insulating tape and sample two being brass which was cycled in 0.1 M NaNO₃ as shown in **Figure 5.22**. This tape protection, allowed for the sample to be from the exact same piece of brass and mitigated any deviations of surface composition which may be observed across the entire sheet of brass. **Table 5.4** shows an overview of the signals found within untreated brass across the full survey, with the presence of copper (Cu) and zinc (Zn). Additionally, this gives an indication as to the other metals which are contained within the alloy. The presence of tin (Sn), iron (Fe) and lead (Pb) all fall in line with additional metals found in brass in literature¹.

Table 5.4: Binding energies and species found in full XPS survey data (untreated brass).

Binding Energy (eV)	Identity	Binding Energy (eV)	Identity
9.74	Zn 3d	310.00	Rh 3d 5/2
24.49	Sn 4d	713.44	Fe 2 p 3/2
75.42	Cu 3p	718.80	Fe 2 p 3/2
88.82	Zn 3p 3/2	931.92	Cu 2p 3/2
122.33	Cu 3s	952.03	Cu 2p 1/2
	Cu ₂ O	1021.73	Zn 2p 3/2
138.47	Pb 4f 7/2	1044.51	Zn 2p 1/2
284.52	C 1s		

In order to further understand the processes which were taking place at the surface during visualisation, the elemental regions of Cu, Zn and O were provided with a more in-depth XPS scan. Starting with the copper region, a clear difference in peak area was observed in **Figure 5.22 (A)**, indicating a larger concentration of copper at the surface of the treated

brass, strengthening the view that the dezincification process was playing a role in the surface change. When comparing the forms of existing copper (Figure 5.22 (B & C)) the red trace was associated with Cu^0 in a $2p_{3/2}$ state which saw an increase from 1.3 % to 9.8% composition of the surface, while the red, blue trace was associated with Cu^{2+} within CuO and, this too resulted in an increase from 0.8 % to 4 % composition. The increase of both elemental copper and the oxide suggested the redeposition of the metal and oxidation of some material during the experiment.

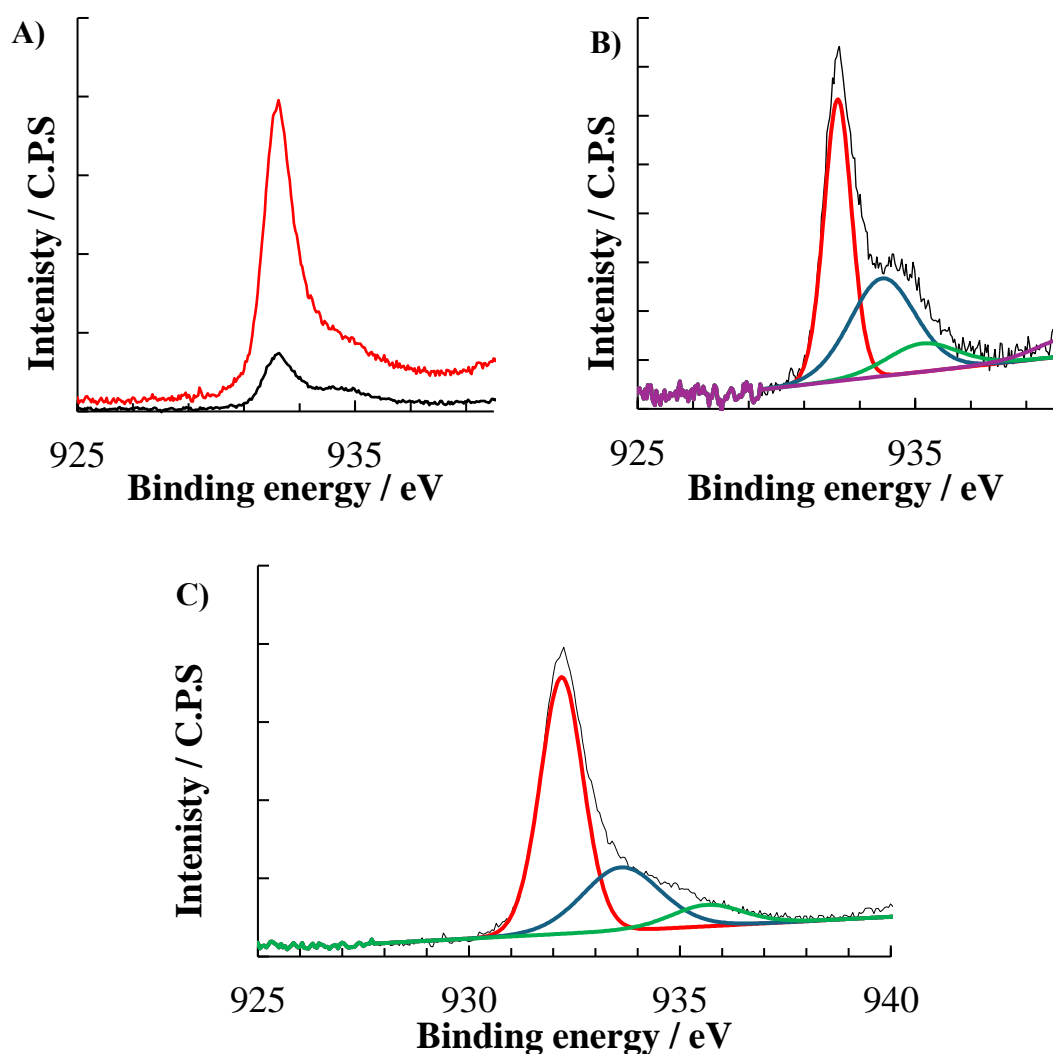


Figure 5.22: XPS spectra of brass showing A) full copper area scan of untreated (black) and treated in 0.1 M NaNO_3 over the potential range -0.2 to $+0.5$ V vs. $\text{Ag}|\text{AgCl}$ for three cycles at 100 mV.s^{-1} (red) samples with B) untreated and C) treated brass.

Chapter 5: Latent Finger-Mark Visualisation at a Brass Surface via Deposition of Conducting and Redox Polymers

When observing the zinc persistence (**Figure 4.23 (A)**), the relative peak areas suggest a drop in the zinc concentration at the surface. There was relatively no change in how the zinc was bound within the surface matrix and it appeared that there was no redeposition or additional surface activity with zinc, other than its removal. In terms of oxygen **Figure 4.23 (B & C)**) the most drastic difference was the oxygen from oxide, which increased from 3.1 % to 11.3% composition at the surface, matching with the trend observed with the increase of the copper oxide post analysis.

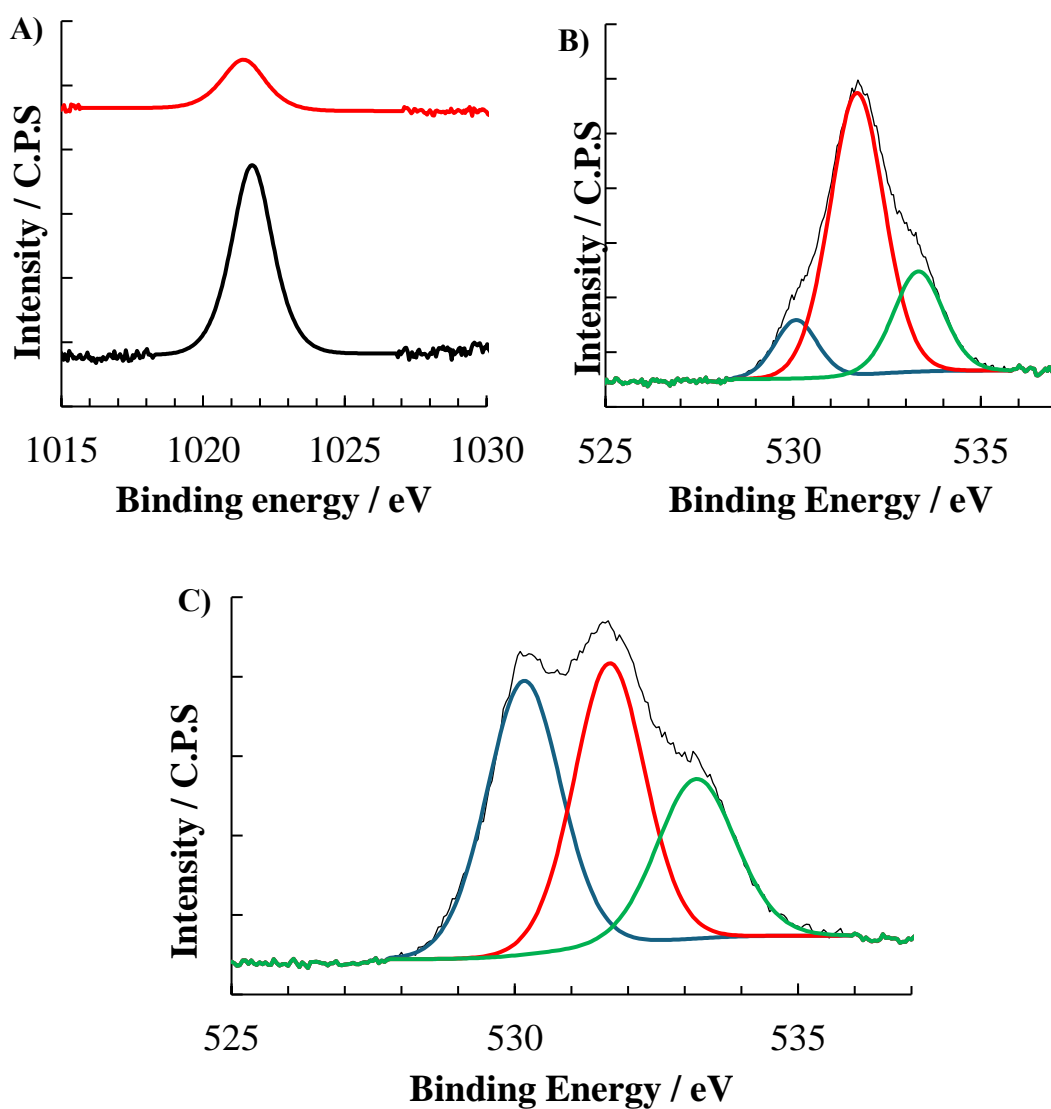


Figure 5.23: XPS data of brass sheets showing the A) zinc region with untreated (black) and treated (red) brass B) the oxygen region of untreated brass and C) the oxygen region of treated brass.

Chapter 5: Latent Finger-Mark Visualisation at a Brass Surface via Deposition of Conducting and Redox Polymers

Overall, the general trend as seen in **Table 5.6** suggests a significant decrease in zinc composition with an increase in both copper and oxygen composition at the surface. This links back to the dezincification effect and the colour change observed at the surface post analysis with the use of 0.1 M NaNO₃ only.

Table 5.5: Averaged total percentage of elements at the surfaces of brass samples

	O 1s	C 1s	N 1s	Cu 2p	Zn 2P
Untreated Brass	25.9	69.7	0.9	2.2	1.3
NaNO ₃ Cycled Brass	28.4	63.7	1	6.2	0.8

*Brass was cycled in 0.1 M NaNO₃ over the potential range of -0.2 to 0.5 V at 100 mV.s⁻¹, untreated brass was within the same solution, however, protected from the solution via insulation tape.

Following these electrochemical and surface (XPS) insights, the work progressed with phenazine and phenothiazine combinations with the goal to further enhance finger-mark visualisation including high level features via electrodeposition.

5.4.3 Electrochemical and Optical Investigations of Phenazine, Phenothiazine and EDOT Deposition.

Studies on brass electrochemistry and polymer (EDOT) deposition thus far concluded the most appropriate electrochemical conditions for use in NaNO₃ and indicated promising data in the presence of EDOT. Introduction of a phenazine and phenothiazine, such as neutral red (NR) and thionine acetate (Th) respectively in the proposed combinations below (**Table 4.7**) followed, with electrochemical studies initially focusing on glassy carbon electrodes (GCE) and indium tin oxide (ITO) electrodes prior to an electrochemical examination at brass for finger-mark visualisation experiments.

Chapter 5: Latent Finger-Mark Visualisation at a Brass Surface via Deposition of Conducting and Redox Polymers

Table 5.6: Reagent combinations employed for electrodeposition experiments using conducting and redox polymers.

<i>Solution</i>	EDOT (2 mM)	Thionine Acetate (Th) (1 mM)	Neutral Red (NR) (1 mM)
1	X		
2		X	
3			X
4	X		X
5	X	X	
6		X	X

5.4.3.1 Characterisation of Phenazine, Phenothiazine and EDOT Combinations in NaNO₃ at a Glassy Carbon Electrode

Initial testing at a GCE involved a potential sweep method for film growth at the surface of the electrode. The potential range for this experiment set was found to be most successful at -0.8 to 1.2 V. **Figure 5.24 (A)** shows electro-polymerisation of PEDOT from a 2 mM EDOT solution in 0.1 M NaNO₃. An initial oxidation of 1.23 V and 10.26 mA.cm⁻² (I) was observed which was not present in subsequent cycles 1 – 5, being in line with the necessary anodic process for initiation of polymer formation. A secondary redox couple (**Figure 5.24 (A) inset II & III**) of E_p^a 0.31 and E_p^c 0.07 V was visible in cycles 3 and 5, and these responses may represent the oxidation and reduction (or charging and discharging) of the PEDOT film as seen in **Scheme 5.2**. The observed currents did not change as cycling continued. However, the voltammetry observed in **Figure 5.24 (B)** suggests the presence of some material at the electrode surface, with the presence of a weak anodic wave at $E_p^a = 0.35$ V (I) and overall higher current density when compared to a clean GCE in a 0.1 M NaNO₃ solution.

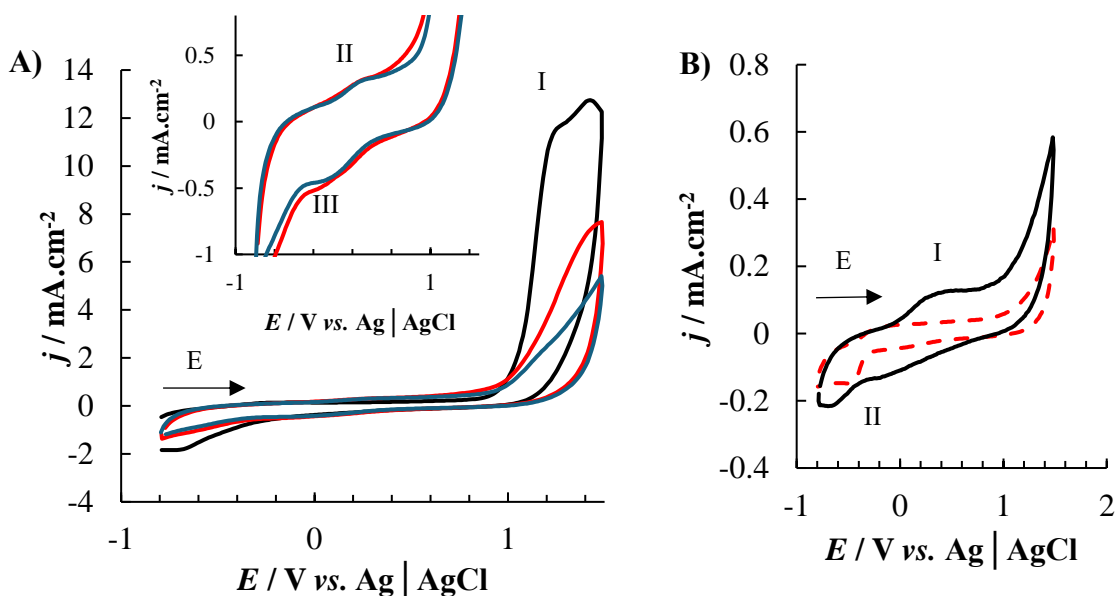


Figure 5.24: A) Cyclic voltammogram of 2 mM EDOT in 0.1 M NaNO₃ at a GCE over the potential range -0.8 to +1.2 V vs. Ag|AgCl at 100 mV.s⁻¹ showing cycles one (black), three (red) and five (blue). Inset of cycles three and five. B) PEDOT film on a GCE showing third cycle (black) against third cycle of a clean electrode (red dash) over the potential range -0.8 to +1.5 V vs. Ag|AgCl at 100 mV.s⁻¹ in 0.1 M NaNO₃.

In the case of thionine acetate at a GCE (**Figure 5.25 (A)**), indicative anodic responses at $E_p^a = -0.26$ (I), 0.62 and 1.06 V (II) were observed within cycle one, with cathodic responses observed at $E_p^c = -0.077$ (III) and -0.58 V (IV). The irreversible oxidation at 1.06 V may reflect the formation of Th radical cation species, as the response remained in the subsequent cycles, however, with a diminished current density dropping from 174 to 81 $\mu\text{A.cm}^{-2}$ very weak cathodic waves at $E_p^c = 0.13$ (I) and -0.069 (II) V were also visible which resulted in a single cathodic process at 0.059 V when the formed film (**Figure 5.25 (B)**) was cycled in the electrolyte. The film displayed no discernible features in the voltammogram other than a slightly increased current density, however, observationally the surface did appear to have a blue hue when dried. There are few literature reports for the electropolymerisation of Th, by itself, on a GCE. It is more normally employed as a mediator within much more complex electrode transduction configurations such as Th electrochemically deposited on a graphene modified GCE, Th modified carbon nanotubes^{56,57}, Th modified gold nano particles^{58,59} or a combination of both⁶⁰ deposited on a glassy carbon surface. As the goal was the deposition of a material for contrast and not for the electrochemical properties it may provide, the poor

electrochemical response observed in **Figure 5.25 (B)** may be the reason that the scope of the literature was not interested in Th alone on a GCE due to the poor conductive properties which were observed in this work.

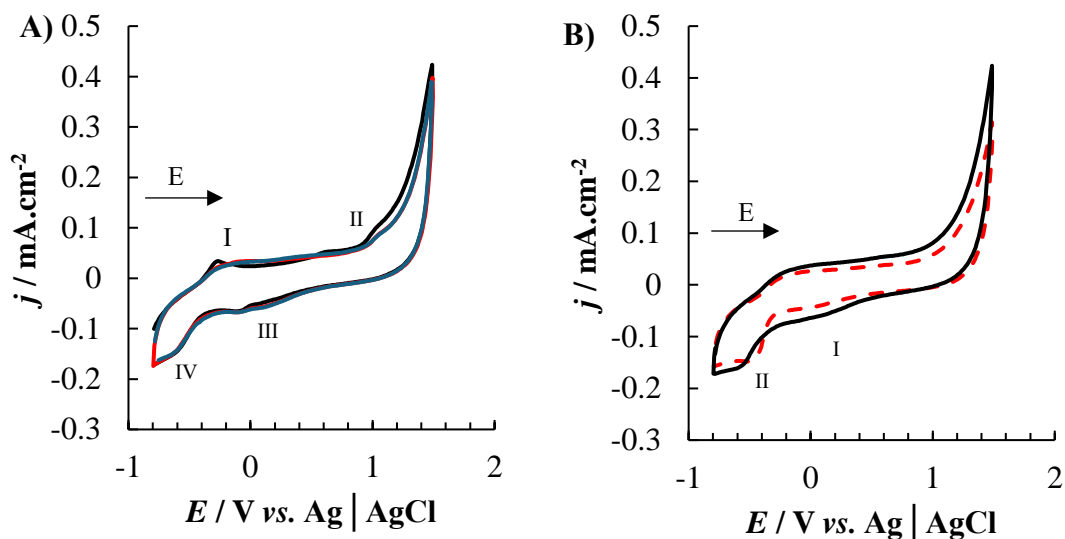


Figure 5.25: A) Cyclic voltammogram of 1 mM Th in 0.1 M NaNO_3 at a GCE over the potential range of -0.8 to +1.2 V vs. Ag|AgCl at $100 \text{ mV}\cdot\text{s}^{-1}$ showing cycles one (black), three (red) and five (blue) and B) Th film on a GCE showing third cycle (black) against third cycle of a clean electrode (red dash) over the potential range of -0.8 to +1.5 V vs. Ag|AgCl at $100 \text{ mV}\cdot\text{s}^{-1}$ in 0.1 M NaNO_3 .

Potential cycling of NR (**Figure 5.26 (A)**) shows an initial oxidative response at $E_p^a = -0.64$ (I) and 1.02 (II) V in cycle 1 with the initial anodic response not reappearing on subsequent cycles and the response at 1.02 V diminishing from $0.29 \text{ mA}\cdot\text{cm}^{-2}$ in cycle 1 to $0.19 \text{ mA}\cdot\text{cm}^{-2}$ in cycle 5. A new redox couple at $E_p^a = 0.16$ V and $E_p^c = 0.21$ V (III & IV) was observed in cycles 3 and 5, indicating the presence of a couple which was not present in the initial cycle. Anodic responses at 0.080 V and 1.02 V and a cathodic response at 0.14 V in the film formed from cycling (**Figure 5.26 (B)**) suggest clearer evidence of a redox film present at the surface (**Scheme 5.6**) than any of the other individual monomers under these conditions. Given the slightly acidic conditions ($\text{pH} \sim 5.6$), a possible tetramer suggested by Pauliukaite et al. may be present at the surface⁴⁰. This allows for multiple points of chemical linkage and a much more complex polymeric repeating structure perhaps facilitating polymer deposition on the electrode.

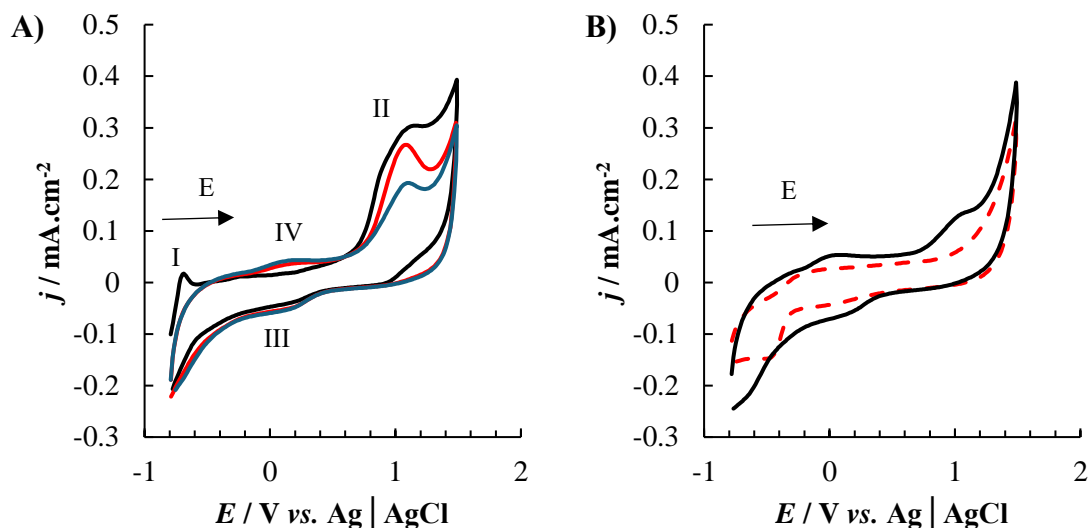
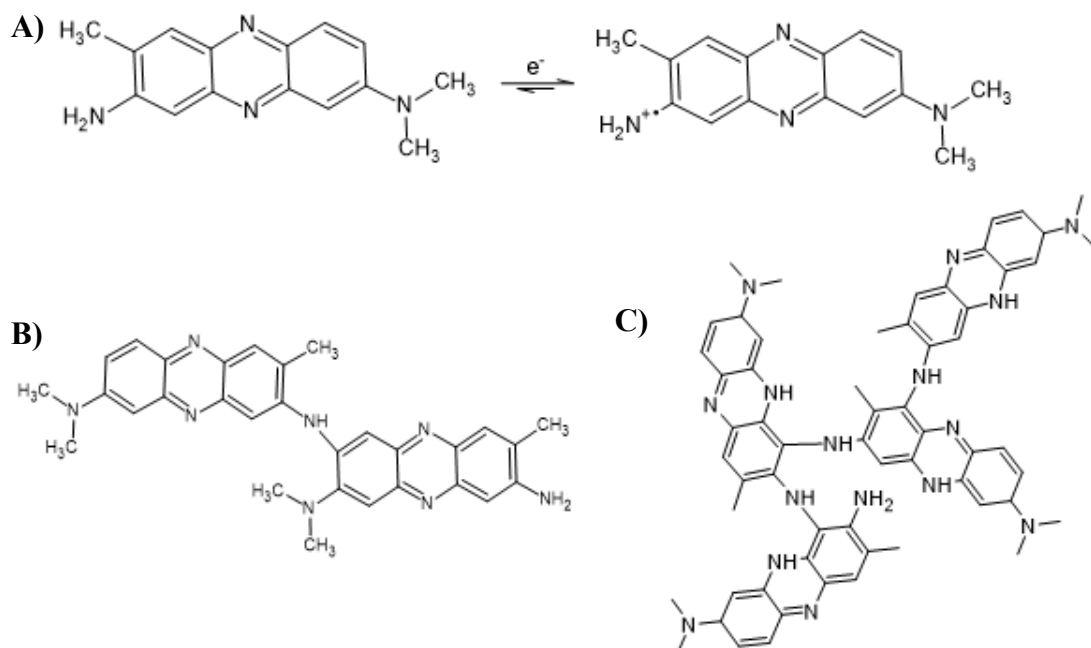


Figure 5.26: A) Cyclic voltammogram of 1 mM NR in 0.1 M NaNO_3 at a GCE over the potential range -0.8 to +1.2 V vs. Ag|AgCl at $100 \text{ mV}\cdot\text{s}^{-1}$ showing cycles one (black), three (red) and five (blue) B) NR film on a GCE showing third cycle (black) against third cycle of a clean electrode (red dash) over the potential range -0.8 to +1.5 V vs. Ag|AgCl at $100 \text{ mV}\cdot\text{s}^{-1}$ in 0.1 M NaNO_3 .



Scheme 5.6: A) Initial reduction of neutral red with B) possible dimer and C) oligomer structures⁴⁰.

Chapter 5: Latent Finger-Mark Visualisation at a Brass Surface via Deposition of Conducting and Redox Polymers

In the first combination of the monomers, EDOT and neutral red (EDOT-NR), 2 mM and 1 mM respectively, were examined (**Figure 5.27**) with some of the characteristics of both individual components. (**Figure 5.28 (A)**) In cycle 1, anodic responses at $E_p^a = 0.7, 0.89$ (I) and 1.35 (II) V were observed along with a weak cathodic response at $E_p^c = 0.18$ V. Subsequent cycles appeared as traces of the individual monomers with cycle 3 taking the previously observed characteristics of PEDOT formation with a redox couple of $E_p^a = 0.39$ V and $E_p^c = 0.0079$ V (III & IV). Cycle 5 resulted an anodic response at 1.18 V like that observed in the case of NR alone. Voltammetry of the film (**Figure 5.28(B)**) indicated that some material was formed at the surface with a weak anodic response at $E_p^a = 1.02$ V (I).

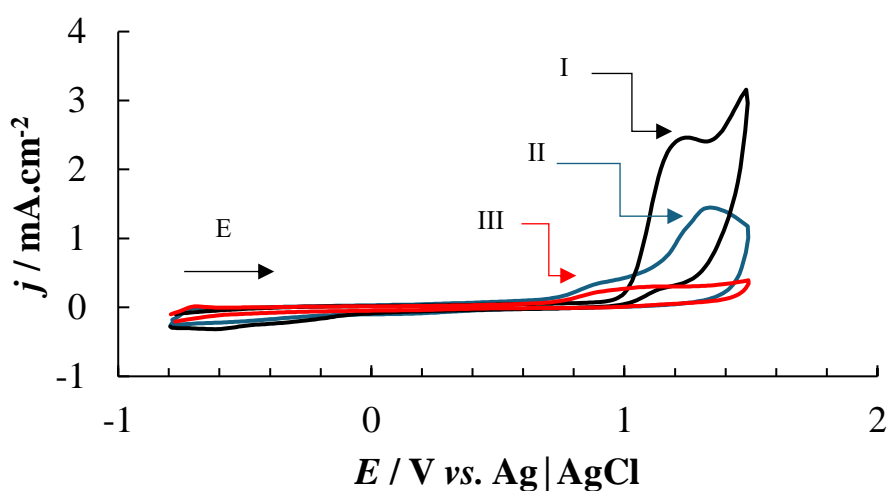


Figure 5.27: Cyclic voltammogram (showing cycle 1) over the potential range of -0.8 to +1.5 V vs. Ag|AgCl at $100 \text{ mV}\cdot\text{s}^{-1}$ of 2 mM EDOT (black), 1 mM NR (blue) and EDOT-NR (2:1 mM) (red) in 3:7 methanol:sodium acetate buffer (pH ~ 4.5) (typical traces).

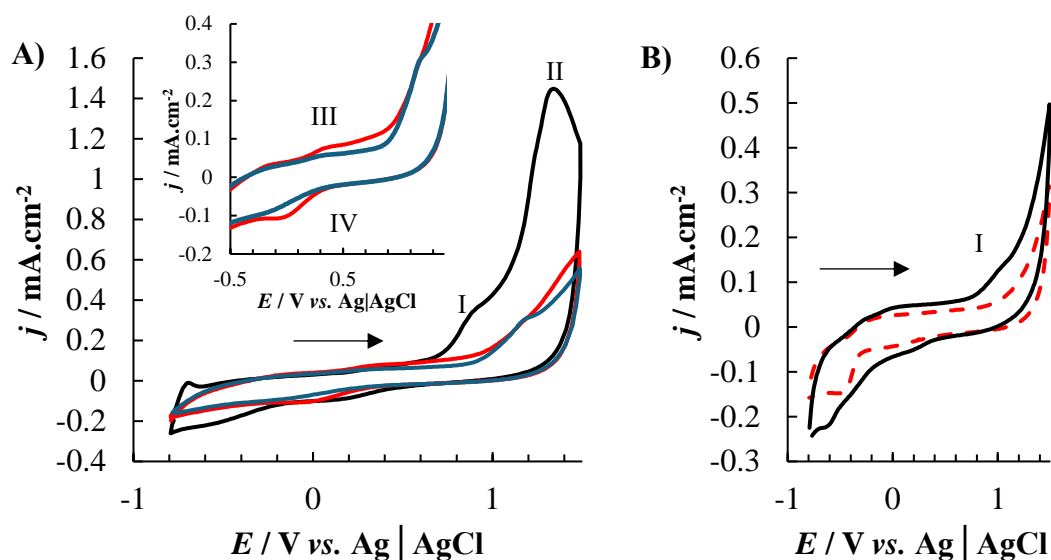


Figure 5.28: Cyclic voltammogram of A) 2 mM EDOT and 1 mM NR in 0.1 M NaNO₃ at a GCE across the range of -0.8 to +1.2 V vs. Ag|AgCl at 100 mV.s⁻¹ showing cycles one (black), three (red) and five (blue). Inset: cycles three and five. B) PEDOT-NR film on a GCE showing third cycle (black) against third cycle of a clean electrode (red dash) across the range of -0.8 to +1.5 V vs. Ag|AgCl at 100 mV.s⁻¹ in 0.1 M NaNO₃.

The second combination observed was a mix of EDOT and thionine acetate (PEDOT-Th). **Figure 5.29** shows that the initial cycle contains a much more characteristic shape of PEDOT than Th. While the film formation of the combination (**Figure 5.30 (A)**) resulted in an EDOT characteristic oxidation process at $E_p^a = 1.22$ V (I) in cycle one, cycle 3 contained a weak couple at $E_p^a = 0.28$ V and $E_p^c = -0.013$ V (II & III), along with an anodic response not previously observed in any solution thus far at $E_p^a = 1.4$ V. The latter may be indicative of a monomer couple formed from the electropolymerisation of the combination of both species. Cycle 5 showed an anodic response at $E_p^a = 0.41$ V with a subsequent reduction at $E_p^c = -0.18$ V. **Figure 5.30 (C)** shows a weak anodic response at $E_p^a = 0.6$ V (I), suggesting this redox active material was different to that observed with PEDOT alone (response at $E_p^a = 0.35$ V was observed for PEDOT film), and was adsorbed to the surface when compared to the clean GCE trace.

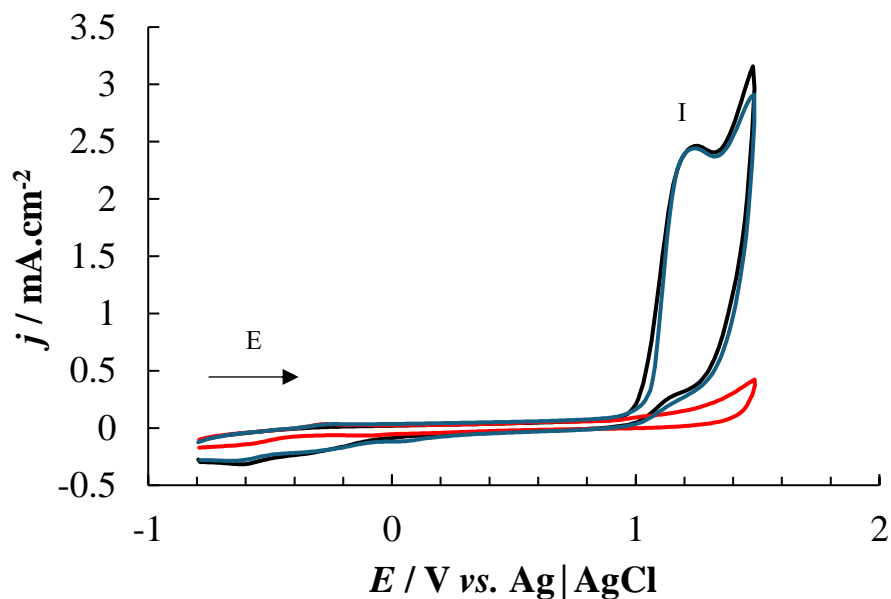


Figure 5.29: Cyclic voltammogram (showing cycle 1) over the potential range -0.8 to $+1.5$ V vs. Ag|AgCl at 100 mV.s^{-1} of 2 mM EDOT (black), 1 mM Th (blue) and EDOT-Th ($2:1 \text{ mM}$) (red) in $3:7$ methanol:sodium acetate buffer ($\text{pH} \sim 4.5$) (typical traces).

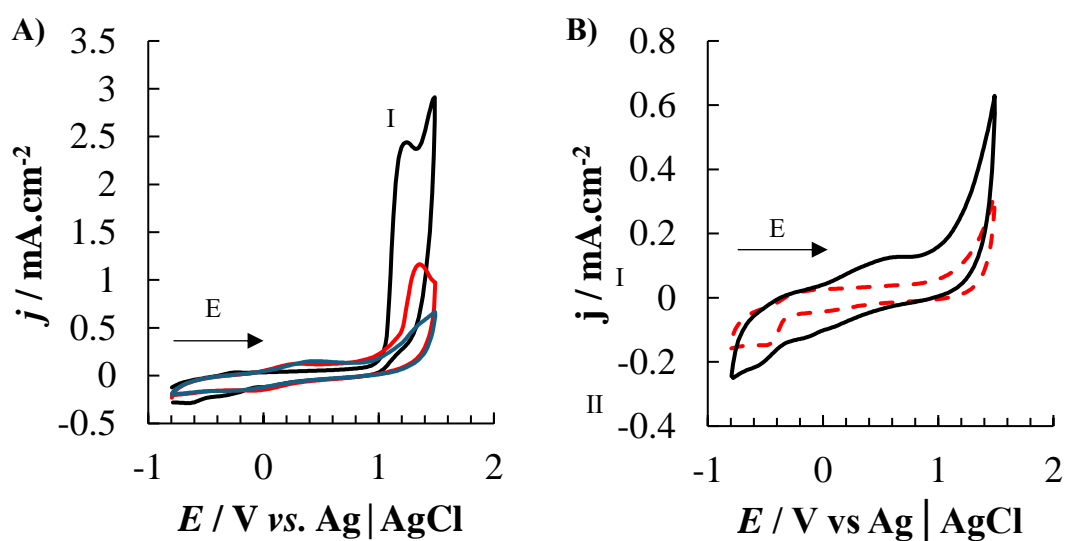


Figure 5.30: Cyclic voltammogram of A) 2 mM EDOT and 1 mM Th in 0.1 M NaNO_3 at a GCE over the potential range -0.8 to $+1.2$ V vs. Ag|AgCl at 100 mV.s^{-1} showing cycles one (black), three (red) and five (blue). B) PEDOT-Th film on a GCE showing third cycle (black) against third cycle of a clean electrode (red dash) over the potential range -0.8 to $+1.5$ V vs. Ag|AgCl at 100 mV.s^{-1} in 0.1 M NaNO_3 .

Chapter 5: Latent Finger-Mark Visualisation at a Brass Surface via Deposition of Conducting and Redox Polymers

The neutral red – thionine acetate (NR-Th) cyclic voltammogram (**Figure 5.31**) initially shows characteristic responses of both NR and Th, with responses at $E_p^a = -0.66$ and 1 V being attributed to NR and the response at $E_p^c = -0.22$ V also being observed for Th alone. During cycling (**Figure 5.32 (A)**) initial anodic responses were observed at $E_p^a = -0.66$ V -0.23 V and 1.0 V with the first and last responses being attributed to the presence of neutral red in the solution. Cycle 1 resulted in a cathodic response at $E_p^c = -0.02$ V (I). In subsequent cycles an anodic response at $E_p^a = 0.26$ V (III) and a diminished response at 1.13 V (II) were observed. A seemingly double cathodic response at $E_p^c = 0.17$ and -0.036 V (IV & V) was visible, with the cycled surface (**Figure 5.32 (B)**) indicating a weak anodic response, like all responses observed with neutral red films at $E_p^a = 1$ V (I).

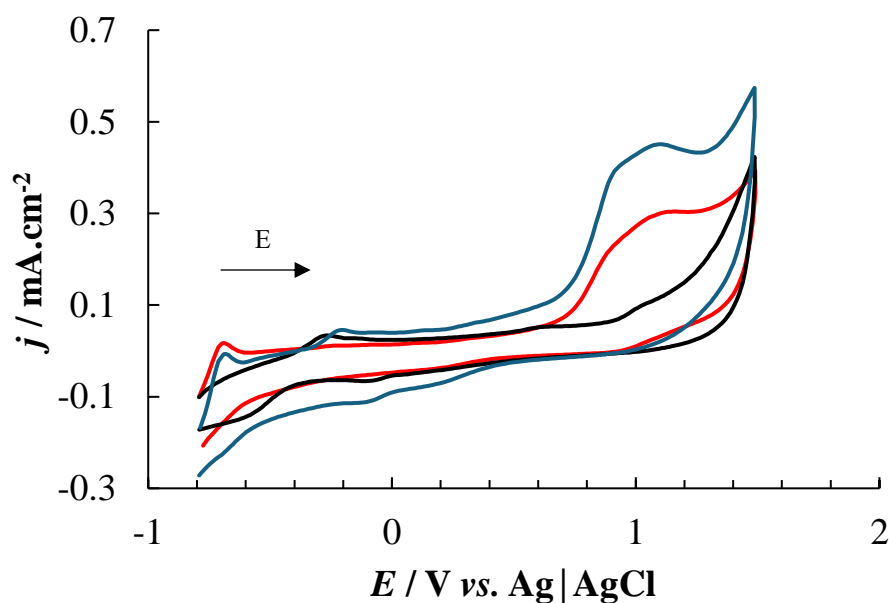


Figure 5.31: Cyclic voltammogram (showing cycle 1) over the potential range -0.8 to +1.5 V vs. Ag|AgCl at $100 \text{ mV}\cdot\text{s}^{-1}$ of 1 mM NR (black), 1 mM Th (blue) and NR-Th (1:1 mM) (red) in 3:7 methanol:sodium acetate buffer (pH ~ 4.5) (typical traces).

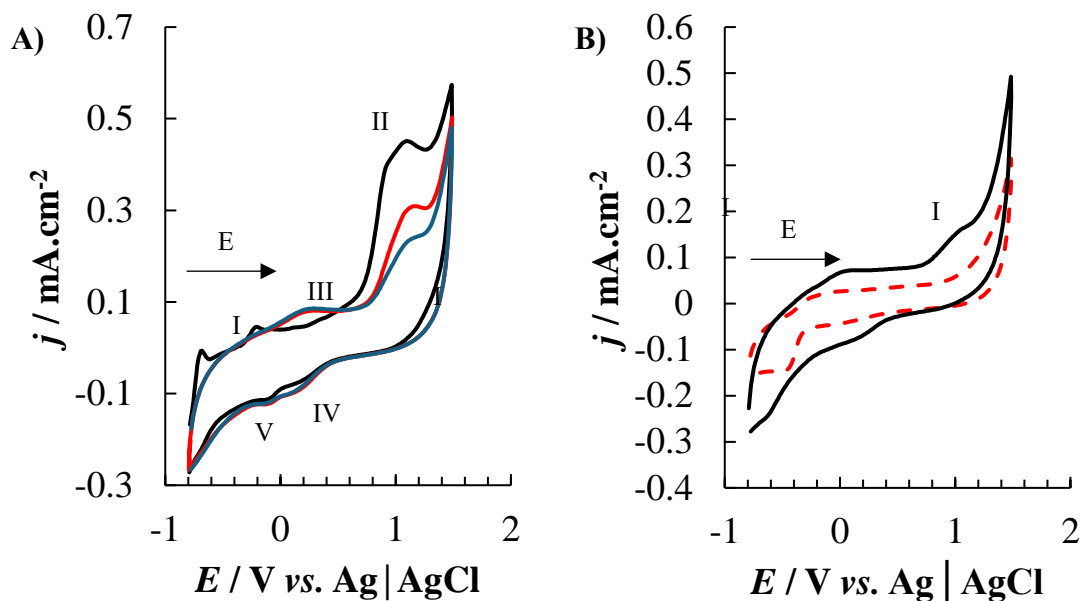


Figure 5.32: Cyclic voltammogram of A) 1 mM NR and 1 mM Th in 0.1 M NaNO_3 at a GCE over the potential range -0.8 to $+1.2\text{ V vs. Ag|AgCl}$ at $100\text{ mV}\cdot\text{s}^{-1}$ showing cycles one (black), three (red) and five (blue) and B) NR-Th film on a GCE showing third cycle (black) against third cycle of a clean electrode (red dash) over the potential range -0.8 to $+1.5\text{ V vs. Ag|AgCl}$ at $100\text{ mV}\cdot\text{s}^{-1}$ in 0.1 M NaNO_3 .

Overall, electrochemical activity was observed with all individual monomers and their respective combinations at a GCE, with successful deposition of material in all instances. In **Table 5.7** an overview of the electrochemical responses shows that some of the monomers exhibit characteristic redox features when combined.

Table 5.7: Overview of electrochemical responses observed in cycle one of the various solutions used for this analysis.

<i>Solution</i>		Anodic Response (E_p^a) (V)			Cathodic Response (E_p^c) (V)	
<i>EDOT</i>	Peak	I	II		III	
		1.23	0.31		0.07	
<i>Th</i>	Peak	I	II		III	IV
		-0.26	1.06		-0.77	-0.58
<i>NR</i>	Peak	I	II	IV	III	
		0.64	1.02	0.21	0.16	
<i>EDOT-NR</i>	Peak	I	II	III	IV	
		0.89	1.32	0.37	-0.05	
<i>EDOT-Th</i>	Peak	I	II	III	IV	
		0.89	1.35	0.39	0.01	
<i>NR-Th</i>	Peak	I	II		III	
		1.22	0.28		-0.013	

In order to further characterise the surface, UV-Vis absorbance spectroscopy was employed. As described in **Chapter 1** light interactions with films can shift the responses either way (red shift {bathochromic} / blue shift {hypsochromic})⁶¹ the intensity of which is directly related to the majority unit or form of unit present within the polymeric structure⁶², incurring some discrepancies when comparing individually formed films and films derived from combinations of materials.

Given the understanding that the films produced contain complex polymeric chains, a 2nd derivative process was utilised to gather more comprehensive knowledge of the spectra, resolving overlapping peaks which may be lost in standard UV-Vis spectroscopy. In **Figure 5.33** a comparison between a solution of EDOT and the 2nd derivative is shown with response at 260 nm in the original EDOT spectra containing two unique peaks at 252 nm and 265 nm. As an important side note, the use of the 2nd derivative inverts the peaks of interest, so instead of a peak being the peak of interest, it is instead a trough.

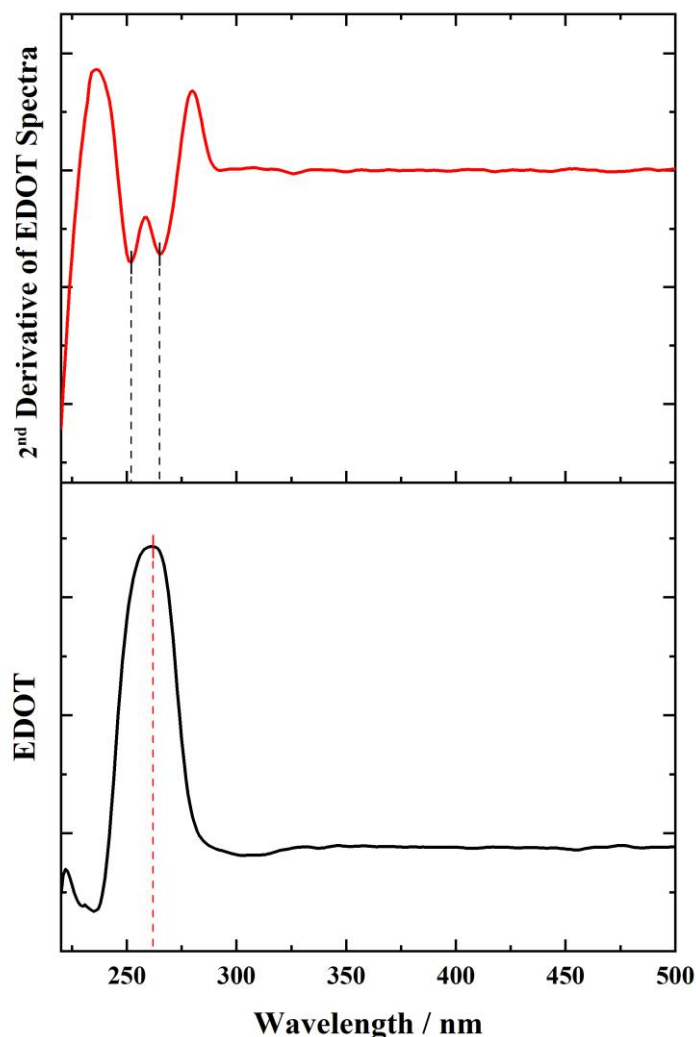


Figure 5.33: Example spectra of a 2 mM EDOT solution in 0.1 M NaNO₃ showing how second derivative analysis can resolve a spectral peak.

Comparative reflectance probe measurements of the PEDOT film against the combination films containing PEDOT are shown in **Figure 5.34** with the dashed lines indicating matched peaks from the PEDOT film to the combined films. PEDOT contained six of the same responses as the PEDOT-Th film matching at 220, 416, 471, 498, 525 and 558 nm, with the wavelengths between 400 and 600 nm being representative of PEDOT in a neutral state^{63,64}, while comparative peaks at 262 and 358 nm were observed within both PEDOT and PEDOT-NR films.

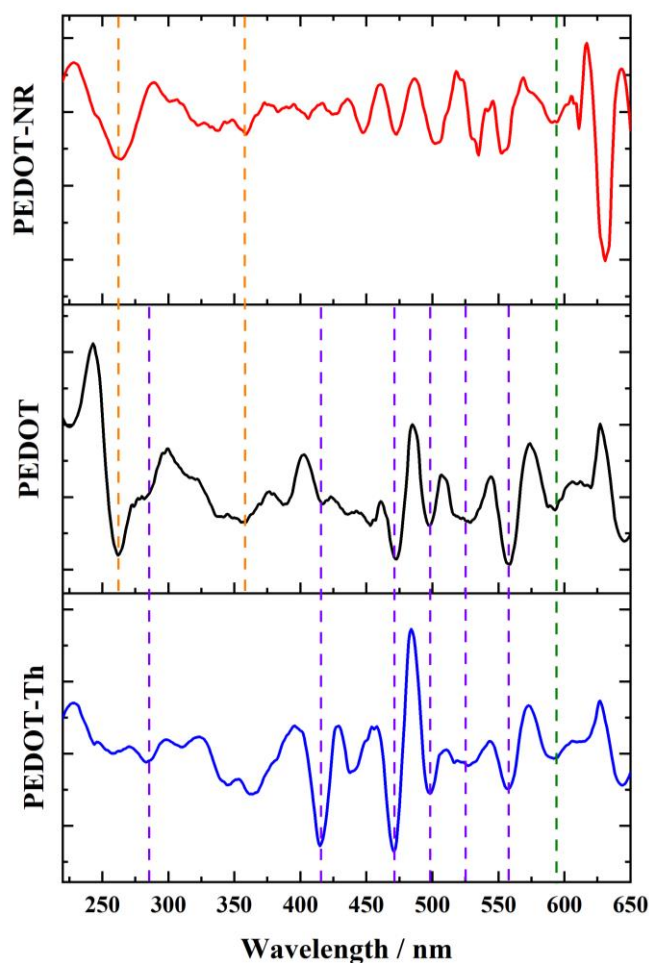


Figure 5.34: Second derivative UV-Vis absorbance spectra of PEDOT and PEDOT containing films on a GCE using reflectance probe spectroscopy.

When comparing the Th and Th containing films (**Figure 5.35**) peaks at 302 and 366 nm can be observed in both Th and NR-Th films, while peaks at 259 and 340 nm were in both Th and EDOT-Th films. The strong reference wavelength of 520 nm for thionine acetate⁶⁵ was observed in the Th film (518 nm) indicating the polymeric structure may contain Th in a lower number of polymeric units within the chain. While direct overlaps of responses were minimal, there are multiple instances where there was a slight offset between the responses observed in Th and the Th containing films. When comparing the Th and PEDOT-Th films, peaks at 435, 525 and 606 nm and 440, 550 and 617 nm respectively may match. Considering changes in the polymeric structure, an increase in conjugation or a change in delocalisation caused by a less uniform repeating unit can produce bathochromic shifts, such as those observed here^{66,67}. Similarly, when observing the NR-

Th film, responses within 10 to 20 nm of the Th film were observed, indicative of the same shifts and potentially the change in colour of the film at the surface as the unmatched peaks were mainly within the visible range of the spectra.

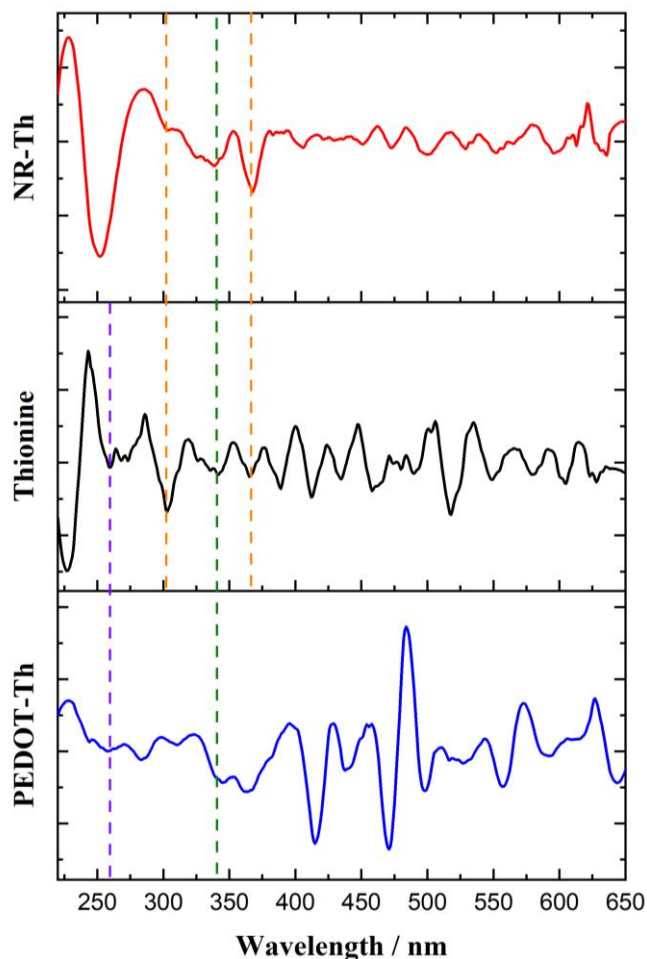


Figure 5.35: Second derivative UV-Vis absorbance spectra of Th and Th containing films on a GCE using reflectance probe spectroscopy.

The NR containing films (**Figure 5.36**) most notably have the fewest direct matches in wavelength relative to the NR film alone; absorbances at wavelengths of 255 and 261 nm match with the NR-Th and PEDOT-NR films respectively. The most likely reason for the lack of matching to the original film is due to the fact that NR is a red compound, while both others produce blue polymeric films. The usual shifts due to changes in the polymeric structure can be a reason for the lack of direct overlap. However, the films formed from NR combined solutions typically have more of a purple to burgundy hue, as opposed to the deep orange/red colour obtained from NR films alone.

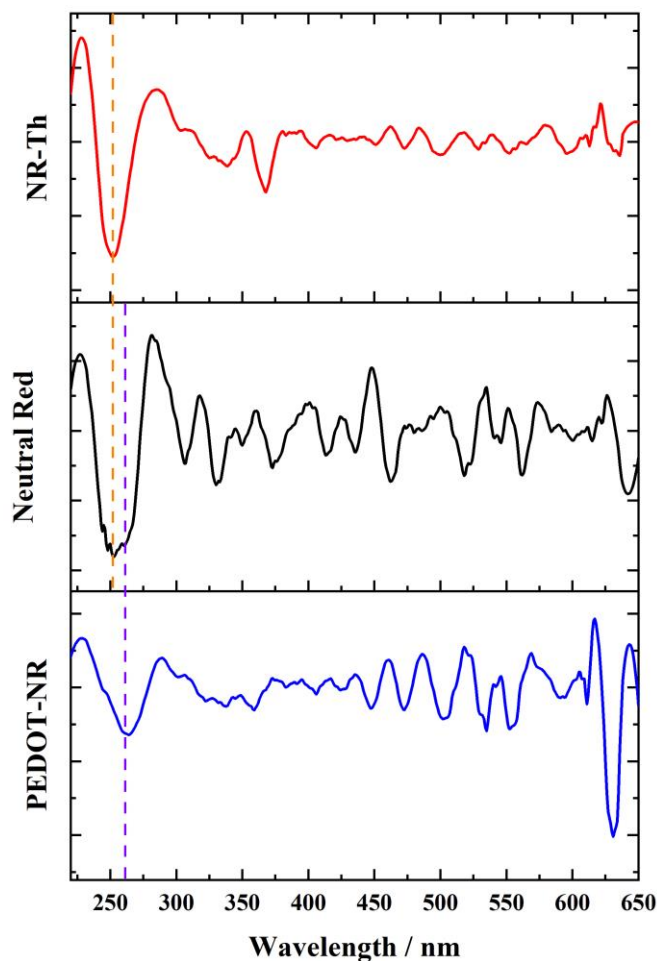


Figure 5.36: Second derivative UV-Vis absorbance spectra of NR and NR containing films on a GCE using reflectance probe spectroscopy.

A more detailed analysis of the matching wavelengths can be seen in **Table 5.8** matching results based on an understanding that slight shifts may have happened due to the mix of individual units in the overall polymeric film*, with the dash (-) (blue highlight) indicating that a response would have been expected due to the monomers present within the mixture, and the bold numbers (orange highlight) indicating that the response was not expected due to the components of the combination. Deviations from these colours shows that the response was observed in multiple individual films, as evidenced by this thorough first-time spectral investigation of such materials using these techniques.

Chapter 5: Latent Finger-Mark Visualisation at a Brass Surface via Deposition of Conducting and Redox Polymers

Table 5.8: Table of observed absorbance wavelengths within polymeric films on a GCE.

PEDOT	Th	NR	PEDOT-Th	PEDOT-NR	NR-Th
Wavelength / nm					
		253		-	252
262	260	261	264	264	-
282			283	-	
	303	306	310	301	304
	326	330		323	325
	336			332	332
342	341	341	345	345	-
358				359	
	365		362		368
387	389		-	-	388
417	412	413	415	424	421
436	435	435	438	-	436
453			456	-	451
473	474	474	471	473	473
498		495	498	-	-
	503	504	-	502	500
522	518	518	517	-	-
529		523	527		529
		541		542	-
559			557		557
		562		-	565
593		593	592	591	-
610		609	609	607	608
615		615	-	611	613
620	623	622	-	-	618
	638		-	631	636
646		642	644	-	-

* Wavelengths were classified as a match if they were ± 10 nm

In order to further characterise the films at the surface, infra-red spectroscopy was employed. Infra-red spectroscopic analysis of polymeric films presents a multitude of challenges such as suffering a low signal-to-noise ratio for thin films⁶⁸ as well as issues regarding penetration of the light and subsequent nonuniform return of the light beam, while thick films may introduce constructive or destructive interference of the light due to refraction as light passes through the film. Hydrogen bonding is also known to vary spectral responses within the magnitude of 100's of cm^{-1} ^{61,69}. The films of interest within this work have clear capabilities of having hydrogen bonding within the structures due to the presence of oxygen and nitrogen in the main structure and amine substituent groups present within the phenazine and phenothiazine. The “stacking” of the polymeric layers could increase the influence of hydrogen bonding on these possible shifts in wavenumbers. This presents the possible “*catch 22*” problem of a film being too thin for analysis to be performed or a film being too thick such that hydrogen bonding interferes with the results.

The IR spectra for all films on a GCE are shown in **Figure 5.37**. Across all spectra, the upper limits of the IR data (blue box) appear to be shifted left, as the assumed N-H stretching response was not visible within its expected range of ~ 3500 to 3200 cm^{-1} for any form. Instead, a strong response at $\sim 3700 \text{ cm}^{-1}$, or higher, was observed. If this value was matched to a literature table alone, it would indicate the presence of an alcoholic O-H bond. Additionally, the signal does not have the characteristic broad response of an O-H which could be attributed to the sample containing water. Only two possibilities remain, firstly a shift in wavenumber for the expected N-H bonds and, if this was the case, a shift may be possible for other expected bond values, or, as shown in **Equation 5.13** the process may produce NaOH, which could be the leading cause of the pH change from pre and post analysis. This may allow for dissociated OH^- to be contained within the polymeric structure during the forming process as a counter anion leading to the response visible within the spectra.

The orange highlighted area in **Figure 5.37** appears to have nearly identical responses across all spectra. This may be attributed to a contamination or defect on the surface, however, with each instance the electrode was cleaned and polished in preparation for the new film and the spectra were background subtracted with the IR spectra of a clean GCE surface, hence this is unlikely. Within this box, responses may be assigned to bending of singly bound hydrogens and double bonds. This area would have a lot of comparative

peaks and may not be useful for the determination of unique bonds within the polymer films and was disregarded for this analysis.

The area of most interest for the comparative analysis of the films on a GCE surface was the blue highlighted region (Figure 5.37) which is expanded further in Figure 5.38.

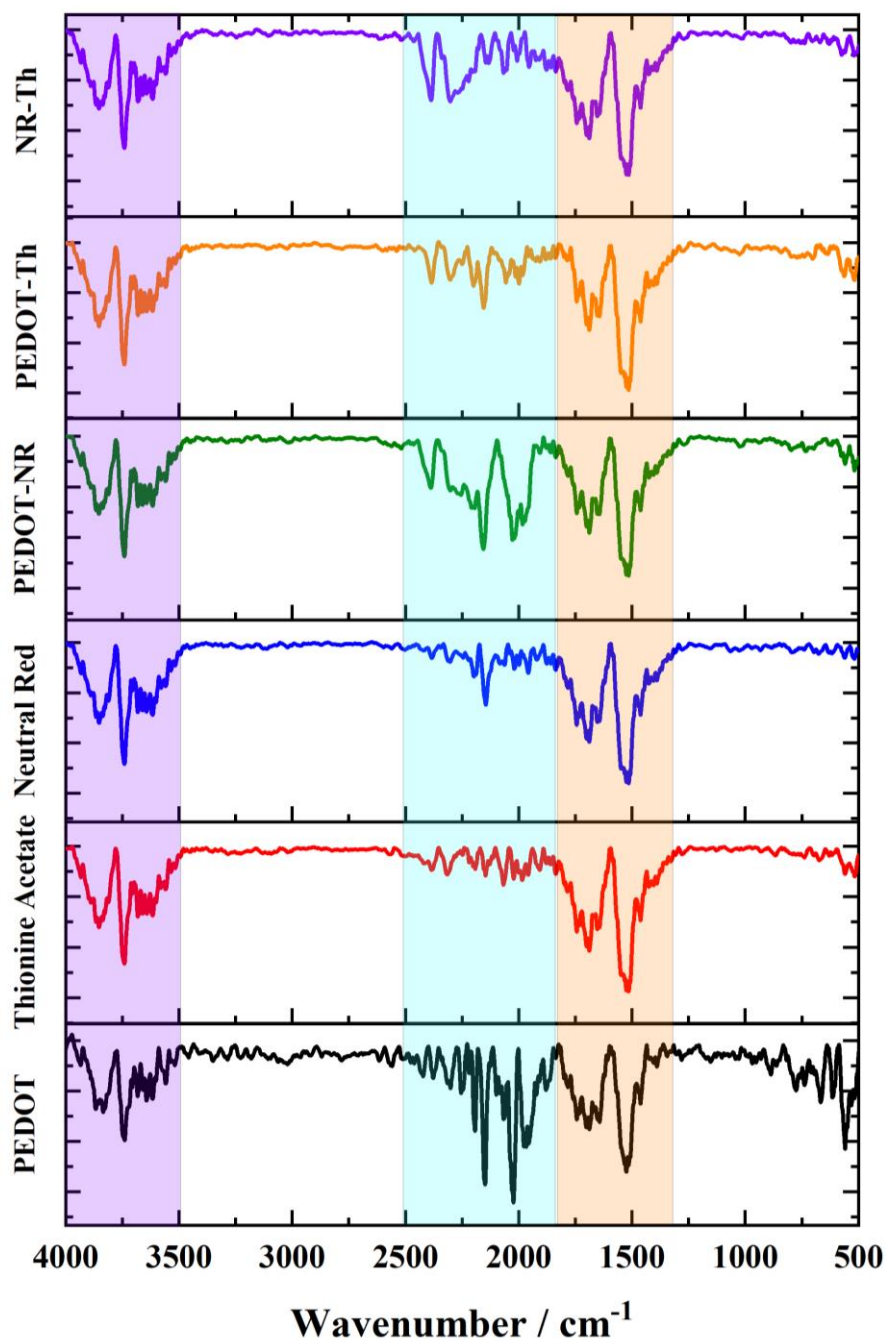


Figure 5.37: IR spectra of electrochemically deposited films on a GCE surface.

In **Figure 5.38** the expanded spectra of the films across 2600 to 1750 cm^{-1} on a GCE surface, show subtle differences which may further indicate the structure of the main units of the polymeric films. Peaks from the mixed systems, have been matched to their individual counterparts showing the relationship.

Within the NR set of films (**Figure 5.38 (A)**), peaks at 2380, 2300, 2200 & 2190 (double headed peak) and, 2145 cm^{-1} were matched between the individual and combined films. Peaks at 2190, 2148 and 1970 cm^{-1} were matched between PEDOT and the combinations (**Figure 5.38 (B)**), while Th had peaks of 2385, 2320, 2065, 1878 and 1858 cm^{-1} (**Figure 5.38 (C)**). In the majority of these cases, the peaks are within a region which is not generally characterised by reference tables outside of C=C within aromatic systems. Peaks within the region 2300 to 2400 cm^{-1} are quoted to indicate the presence of CO_2 , and therefore while it is not impossible that the films somehow managed to contain CO_2 , it is a general response across all spectra of films thus not useful in the comparative identity analysis.

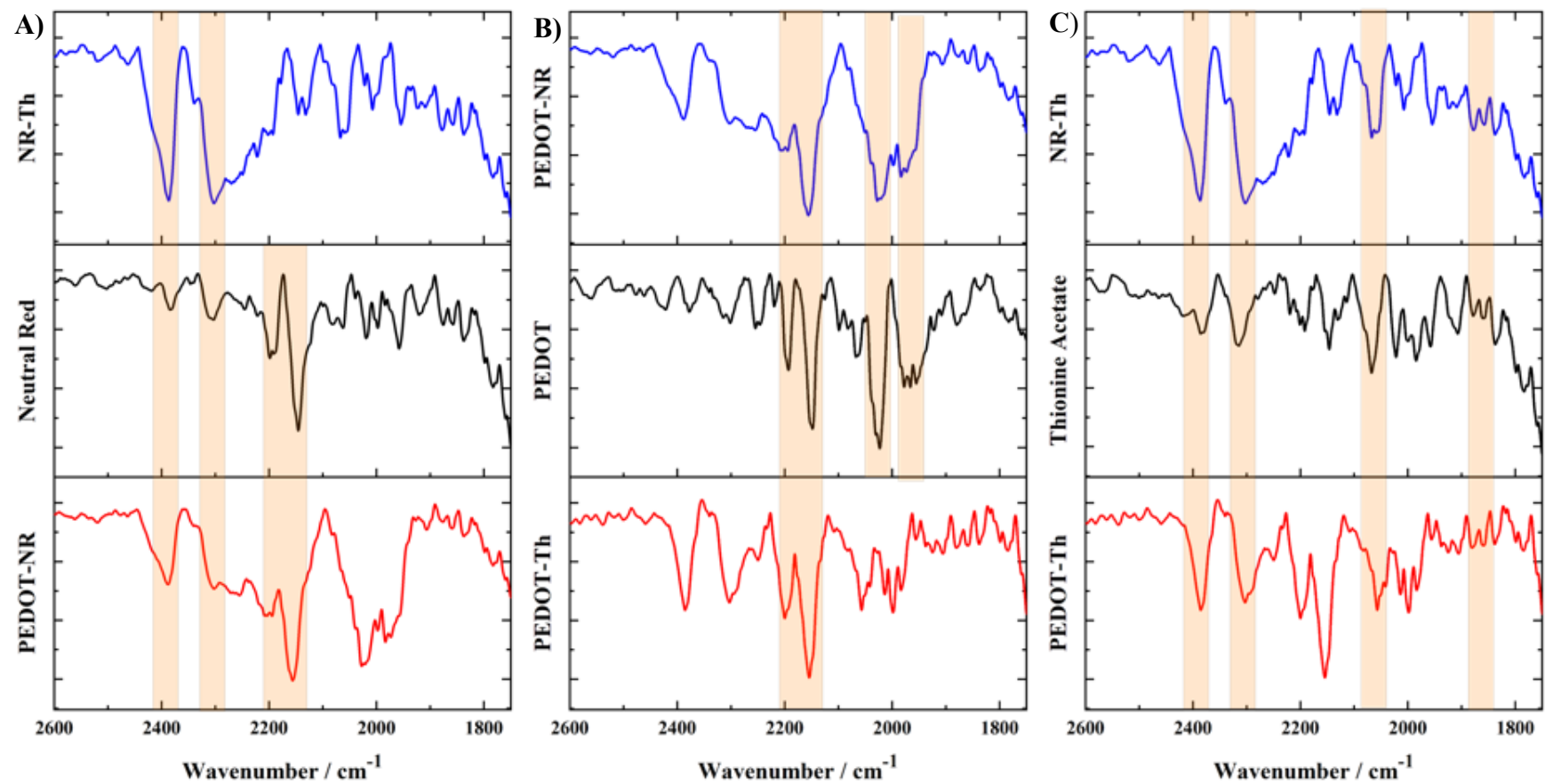


Figure 5.38: Series of IR spectra of films on a GCE with A) comparison of NR containing films, B) comparison of PEDOT containing films and C) comparison of Th containing films.

Film formation of various monomers and their combinations was successfully performed at a GCE surface. Characteristic peaks of the individual monomers were observed in the combinations, confirming the uptake of both components of the combination within the formed film. Electrochemically, all of the mechanisms proposed for polymerisation required an initial anodic process which allowed for subsequent polymerisation and film formation. At the GCE surface, NR dominated the characteristics of the electrochemical processes for which it was present, while spectroscopic analysis discerned that Th provided the dominant features across the UV, visible and IR light ranges. This indicates that even though Th films on GCE may provide poor sensing performances, which may be why they are studied to a little extent in the literature, the films formed by the process may have a sufficient amount of Th units within the polymeric structure to provide useful spectral data.

5.4.3.2 Characterisation of Phenazine, Phenothiazine and EDOT at an Indium Tin Oxide Electrode

With successful results achieved at a GCE, further examination at a metallic electrode was required as a closer step to understanding the monomer behaviour on brass. Initially platinum was considered, however, due to the likelihood of nitrate ions degrading the surface⁷⁰⁻⁷² Indium Tin Oxide (ITO) electrodes were selected.

At the ITO electrode, the voltammogram of EDOT (**Figure 5.39 (A)**) displayed a crossover behaviour in the early cycles (2, 3, and 4) at 1.03 V in cycle 2 and 0.97 V in cycles 3 and 4. This crossover phenomenon indicated the development of a large capacitive current, which increased as the cycles progressed. A subsequent scan rate study in 0.1 M NaNO₃ revealed a large rectangular shaped capacitance current which increased with scan rate, characteristic of voltammograms of PEDOT films on electrode surfaces^{29,73,74}.

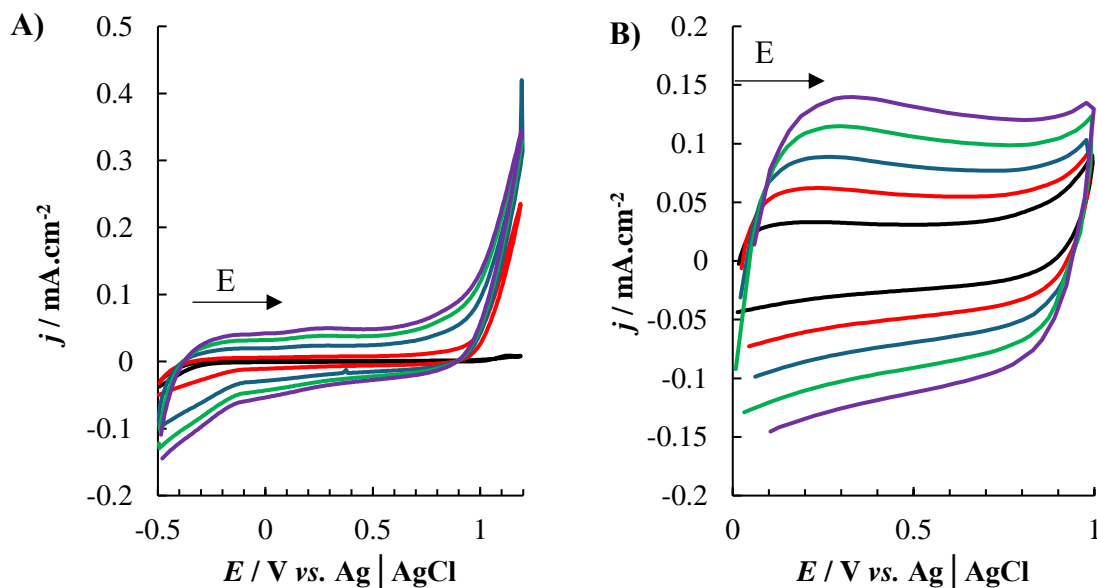


Figure 5.39: Cyclic voltammograms of an ITO electrode in A) 2 mM EDOT in 0.1 M NaNO₃ over the potential range -0.5 to +1.2 V vs. Ag|AgCl at 100 mV.s⁻¹ showing cycles one (black), five (red), ten (blue), fifteen (green) and twenty (purple) (typical traces) and B) scan rate study of the film formed in (A) in 0.1 M NaNO₃ over the potential range 0 to 1 V vs. Ag|AgCl at 50 (black), 100 (red), 150 (blue), 200 (green) and 250 (purple) mV.s⁻¹ (typical traces).

For thionine acetate growth, (**Figure 5.40 (A)**), an initial anodic response was observed at $E_p^a = -0.15$ V, accompanied by a double cathodic response at $E_p^c = 0.029$ and -0.24 V. These responses exhibited an increase in current with subsequent cycling, particularly the $E_p^c = -0.24$ V cathodic response, which experienced a potential shift that ended at $E_p^c = 0.23$ V in cycle 20. Additionally, a second anodic response appeared initially at $E_p^a = 0.19$ V in cycle 3, shifting positively to 0.24 V, and displayed an increase in current by cycle 20. The subsequent scan rate study (**Figure 5.40 (B)**) was observed to contain a prominent redox response with $E_p^a = 0.067$ V, $E_p^c = -0.33$ and $E_{1/2} = -0.145$ V at a scan rate of 250 mV.s⁻¹.

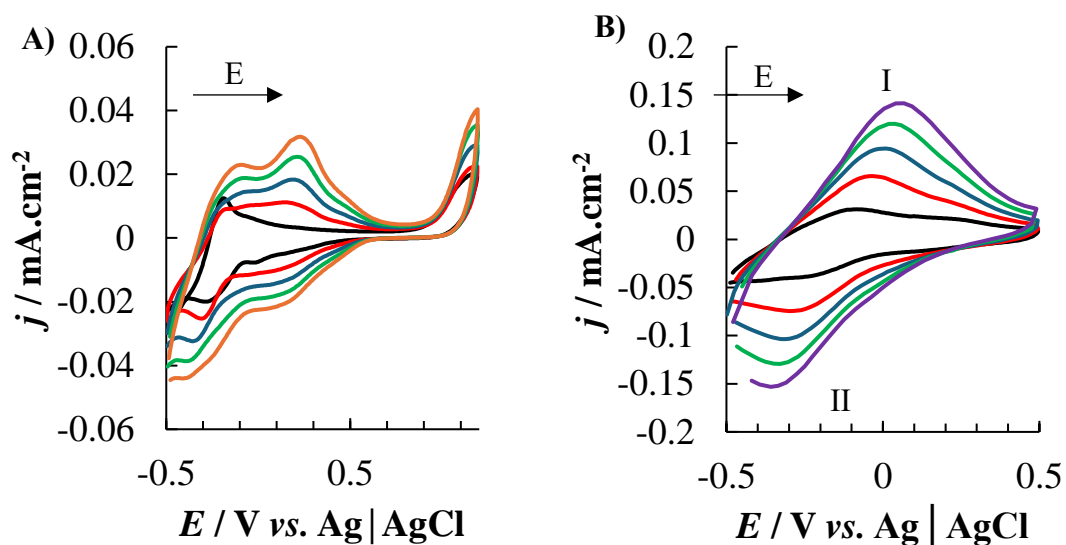


Figure 5.40: Cyclic voltammograms of an ITO electrode in A) 1 mM Th in 0.1 M NaNO₃ over the potential range -0.5 to +1.2 V vs. Ag|AgCl at 100 mV.s⁻¹ showing cycles one (black), five (red), ten (blue), fifteen (green) and twenty (purple) (typical traces) and B) scan rate study of the Th film formed in (A) in 0.1 M NaNO₃ over the potential range -0.5 to +0.5 V vs. Ag|AgCl at 50 (black), 100 (red), 150 (blue), 200 (green) and 250 (purple) mV.s⁻¹ (typical traces).

When plotted as j vs. scan rate (**Figure 5.41 (A)**) and j vs square root scan rate (**Figure 5.41 (B)**), a linear response was obtained in both instances for both anodic and cathodic responses, suggesting that the redox mechanism (**Scheme 5.7**) followed both a mixed adsorption surface controlled and diffusion controlled process, indicating the presence of material at the surface of the electrode and a thick layer of redox material through which diffusion of ions may occur.

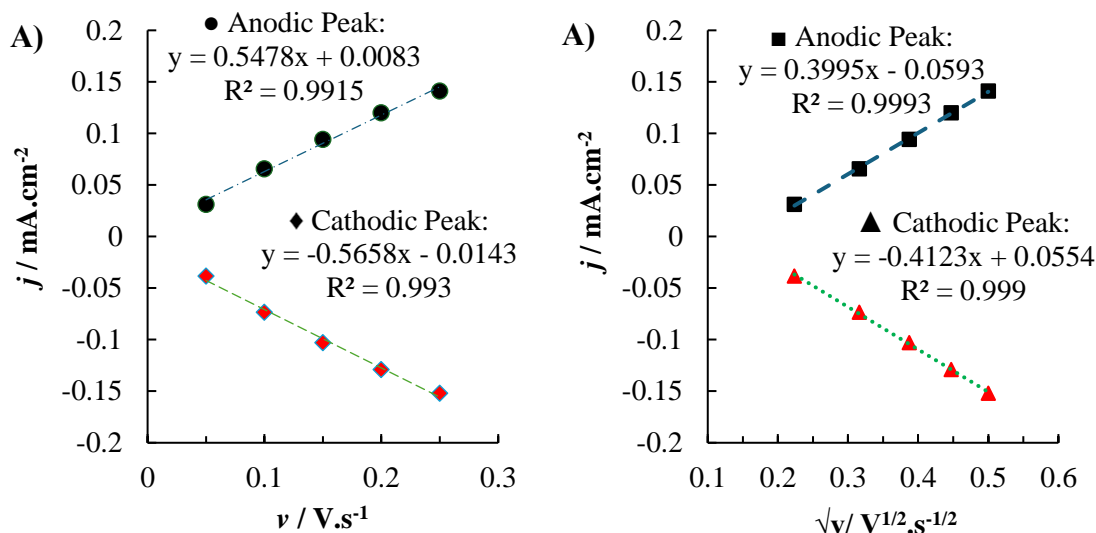
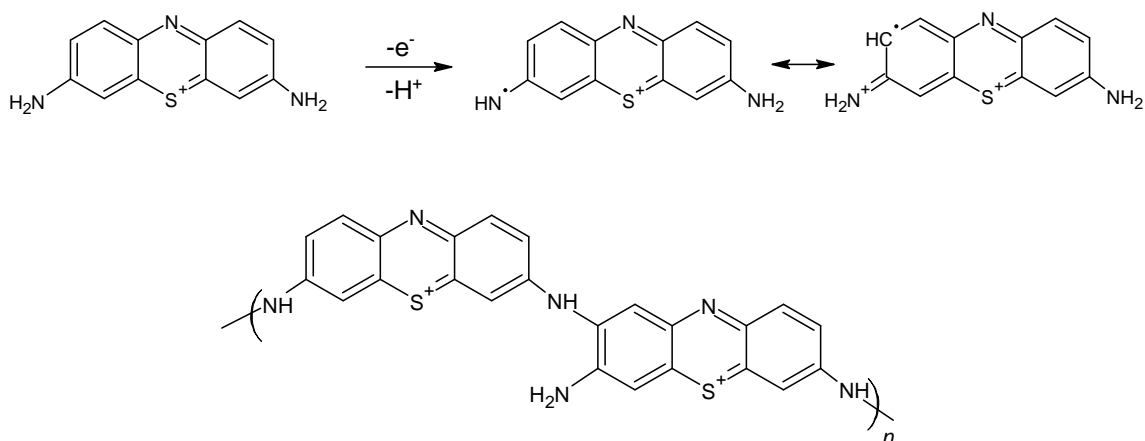


Figure 5.41: Plot of j_p values I and II from Figure 5.40 vs. A) scan rate and B) $\sqrt{\text{scan rate}}$.



Scheme 5.7: Initial oxidation and dimerisation of thionine⁷⁵.

In the case of neutral red (Figure 5.42 (A)), an initial anodic response was observed at 1 V, which steadily decreased as cycling continued. Simultaneously, a redox couple with $E_p^a = 0.22$ V and $E_p^c = 0.048$ V was observed in subsequent cycles. The following scan rate (Figure 5.42 (B)) study did not show any notable redox processes.

The polymerisation of neutral red takes place around 0.8 V in Britton-Robinson buffer (pH 5.15)⁷⁶, while the potential is shifted more positive, and this may be the identity of the peak observed at 1 V within this work. The common absence of the corresponding reduction peak indicates the formation of a radical cation that in turn reacts with another

cation species forming a dimer. For general phenothiazines such as Th, the dimer is linked via the secondary amino group.

This dimer can result in a radical cation when oxidised and react with other radicals forming the overall polymeric structure⁷⁶. The secondary redox process can be attributed to the polymer itself, with an indicative response visible on cycle 1, which would contain monomer only, and this redox process may involve the phenazine ring⁷⁶.

The NR polymer has been observed as a colourless film in low pH and has thus been classified as in a deprotonated state⁷⁶. As the films produced from these methods are coloured red it would suggest that they are in their protonated state.

The lack of notable responses of the film alone on the ITO surface (**Figure 5.42 (B)**) may be attributed to the transport capabilities of the film. The film can be divided into two layers: an inner layer that undergoes oxidation and reduction, and an outer layer that functions as a membrane for the transport of water and hydrogen ions⁷⁶. The presence of electroactive groups in a solid material slightly alters the behaviour of the polymer compared to its behaviour as a monomer in a solution. Specifically, the reduction process of the polymer involves the reduction and saturation of the phenazine ring, which may be indicated by the anodic response observed at approximately 0.22 V.

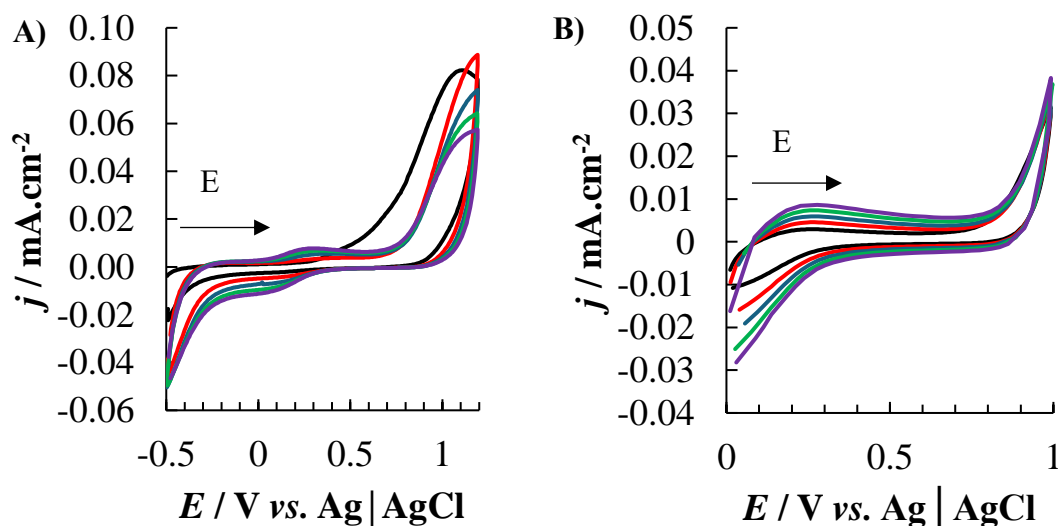


Figure 5.42: Cyclic voltammograms of an ITO electrode in A) 1 mM NR in 0.1 M NaNO₃ over the potential range -0.5 to +1.2 V vs. Ag|AgCl at 100 mV.s⁻¹ showing cycles one (black), five (red), ten (blue), fifteen (green) and twenty (purple) (typical traces) and B) scan rate study of the NR film formed in (A) in 0.1 M NaNO₃ over the potential range 0 to 1 V vs. Ag|AgCl at 50 (black), 100 (red), 150 (blue), 200 (green) and 250 (purple) mV.s⁻¹ (typical traces).

Similarly, for the EDOT-NR mixture (**Figure 5.43 (A)**), an initial anodic response was observed at 1 V, which also decreased as cycling progressed. The voltammogram displayed a redox couple with $E_p^a = 0.28$ V and $E_p^c = 0.008$ V which could be the central phenazine ring of the NR. The scan rate study (**Figure 5.43 (B)**) resulted in a similar response to that obtained from neutral red alone, with more uniform increase in current density, perhaps due to the PEDOT deposition.

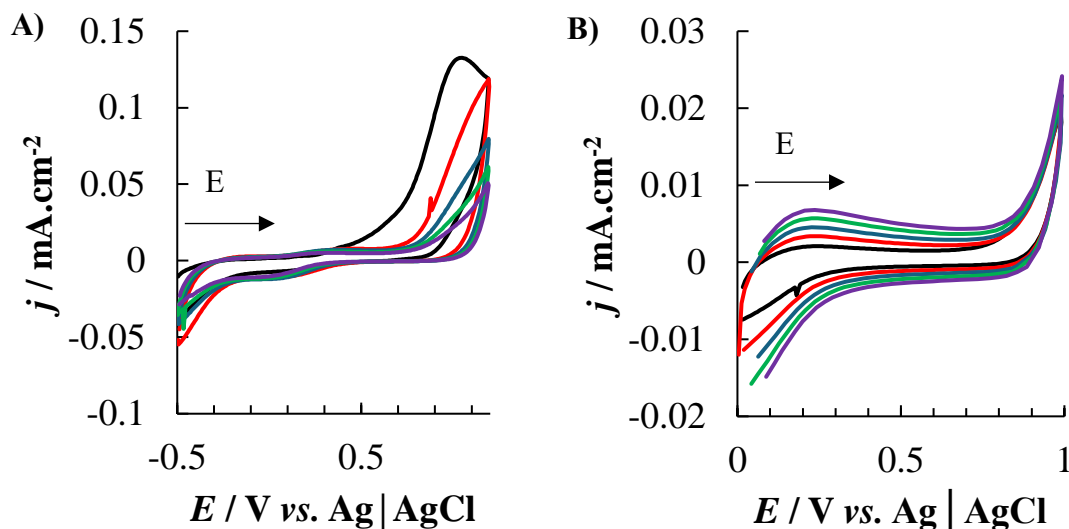


Figure 5.43: Cyclic voltammograms of an ITO electrode in A) 2 mM EDOT and 1 mM NR in 0.1 M NaNO₃ over the potential range -0.5 to +1.2 V vs. Ag|AgCl at 100 mV.s⁻¹ showing cycles one (black), five (red), ten (blue), fifteen (green) and twenty (purple) (typical traces) and B) scan rate study of the film formed in (A) in 0.1 M NaNO₃ over the potential range 0 to 1 V vs. Ag|AgCl at 50 (black), 100 (red), 150 (blue), 200 (green) and 250 (purple) mV.s⁻¹ (typical traces).

In the case of EDOT-TH (**Figure 5.44 (A)**), an initial oxidation response appeared at -0.046 V in cycle 1, accompanied by reduction responses at 0.065 and -0.11 V. However, the initial oxidation response vanished by the final cycle. A second anodic response emerged at 0.17 V from cycle 3 onwards, while the reduction responses exhibited an increase in current as cycling continued. The shape of the obtained voltammogram indicates that the thionine redox response is more prominent than that of the EDOT. Both characteristics of PEDOT and thionine can be observed with the scan rate study (**Figure 5.44 (B)**) with a redox couple of $E_p^a = 0.19$ V and $E_p^c = -0.2$ V on the conducting polymer non-faradaic current steadily increasing with scan rate. The plot of j vs square root scan rate (**Figure 5.44 (C)**) resulted in a linear trend suggesting a diffusion-controlled process within the film produced.

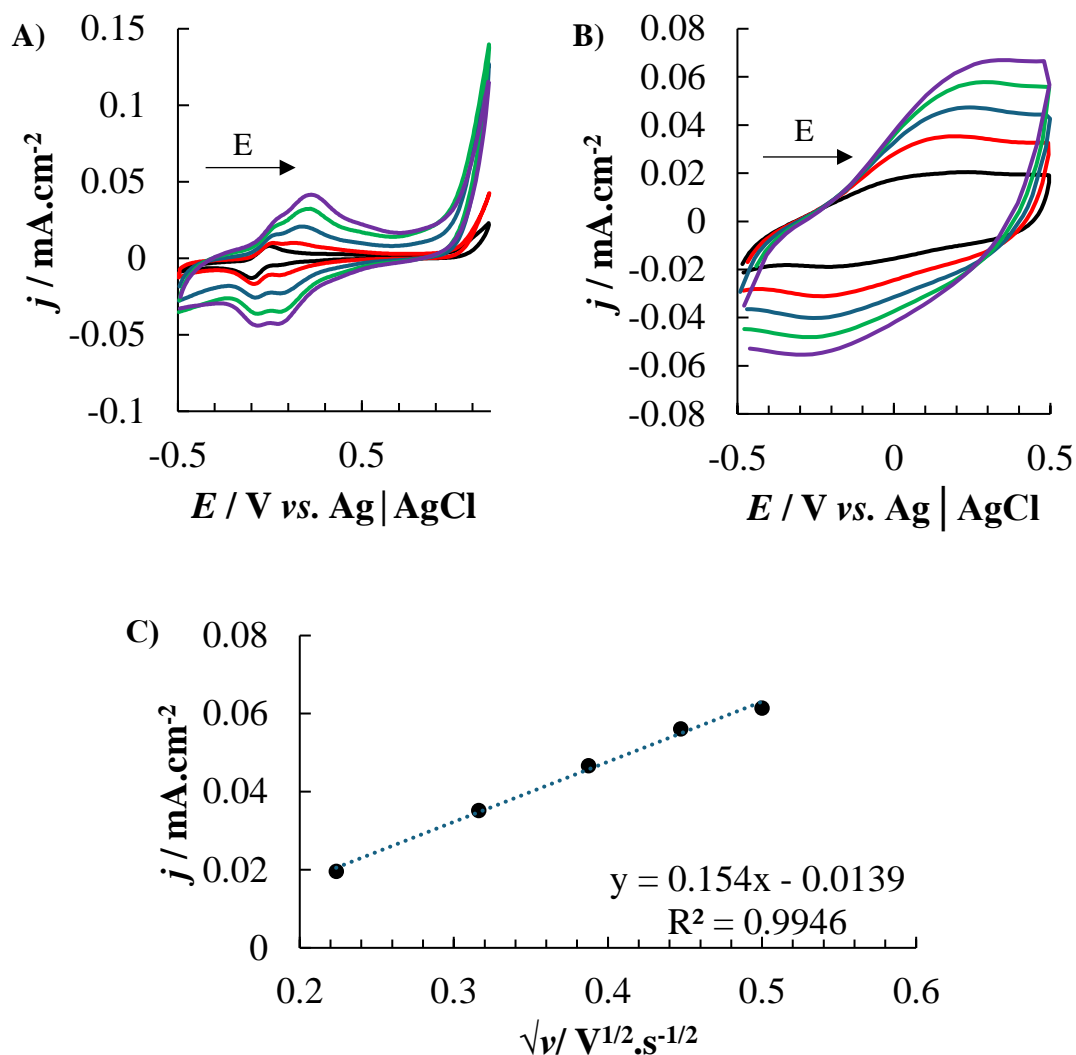


Figure 5.44: Cyclic voltammograms of an ITO electrode in A) 2 mM EDOT and 1 mM Th in 0.1 M NaNO₃ over the potential range -0.5 to +1.2 V vs. Ag|AgCl at 100 mV.s⁻¹ showing cycles one (black), five (red), ten (blue), fifteen (green) and twenty (purple) (typical traces) and B) scan rate study of the film formed in (A) in 0.1 M NaNO₃ over the potential range -0.5 to +0.5 V vs. Ag|AgCl at 50 (black), 100 (red), 150 (blue), 200 (green) and 250 (purple) mV.s⁻¹ (typical traces) and C) plot of I_p^c vs. $\sqrt{\text{scan rate}}$.

The voltammograms of neutral red and thionine acetate in absence of conducting polymers (Figure 5.45 (A)) matched their individual redox signals quite well. Initial anodic responses were observed at -0.12 and 1 V, accompanied by a reduction response at -0.13 V. However, the response at -0.12 V diminished as cycling continued, and the response at 1 V progressively decreased. A new anodic response appeared at 0.21 V, along with a reduction response at 0.05 V. with the scan rate study (Figure 5.45 (B)) containing a redox couple of $E_p^a = 0.21$ V and $E_p^c = -0.15$ V. The anodic response of this couple

observed a linear response of I_p^a vs. square root scan rate (Figure 5.45 (C)) indicating a diffusion-controlled process.

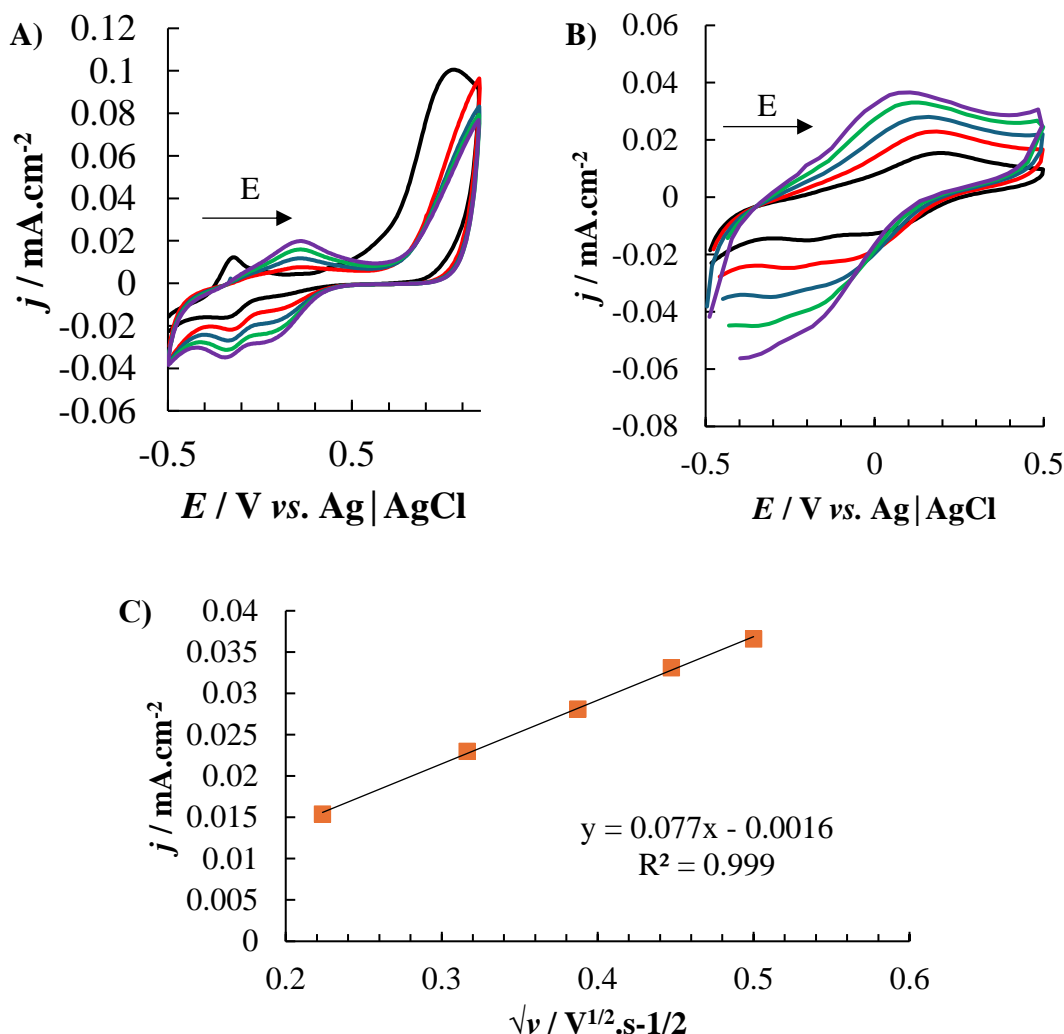


Figure 5.45: Cyclic voltammograms of an ITO electrode in A) 1 mM NR and 1 mM Th in 0.1 M NaNO_3 over the potential range -0.5 to +1.2 V vs. $\text{Ag}|\text{AgCl}$ at $100 \text{ mV}\cdot\text{s}^{-1}$ showing cycles cycles one (black), five (red), ten (blue), fifteen (green) and twenty (purple) (typical traces) and B) scan rate study of the film formed in (A) in 0.1 M NaNO_3 over the potential range -0.5 to +0.5 V vs. $\text{Ag}|\text{AgCl}$ at 50 (black), 100 (red), 150 (blue), 200 (green) and 250 (purple) $\text{mV}\cdot\text{s}^{-1}$ (typical traces) and C) plot of I_p^a vs. $\sqrt{\text{scan rate}}$.

Second derivative UV-Vis absorbance spectroscopy was also performed on all formed films at an ITO surface (Figure 5.46). Responses for all combinations were matched with their individual counterparts, with the responses of Th and NR containing films at 300 and 325 nm being attributed to a $\text{N}=\text{C}$ chromophore within the structure. The difference in the absorbance of this chromophore shifted depending on whether part of a

phenothiazine or phenazine ring structure. While the majority of this response within the NR-Th film was attributed to NR and thus a phenazine core, 2nd derivative spectroscopy allowed for the observation of a shoulder within this response (circled) which corresponds with the wavelength of the Th response, further indicating the presence of both monomeric structures within the overall polymer.

While stronger absorbances would have been expected above 400 nm as the films did possess colour, indicative absorbances such as Th showing a response at 573 nm representing the blue colour the film contained, and NR absorbing at 446 nm for its red/orange colour. However, the noise of the spectra for the combination films was too great to define absorbance values within this region.

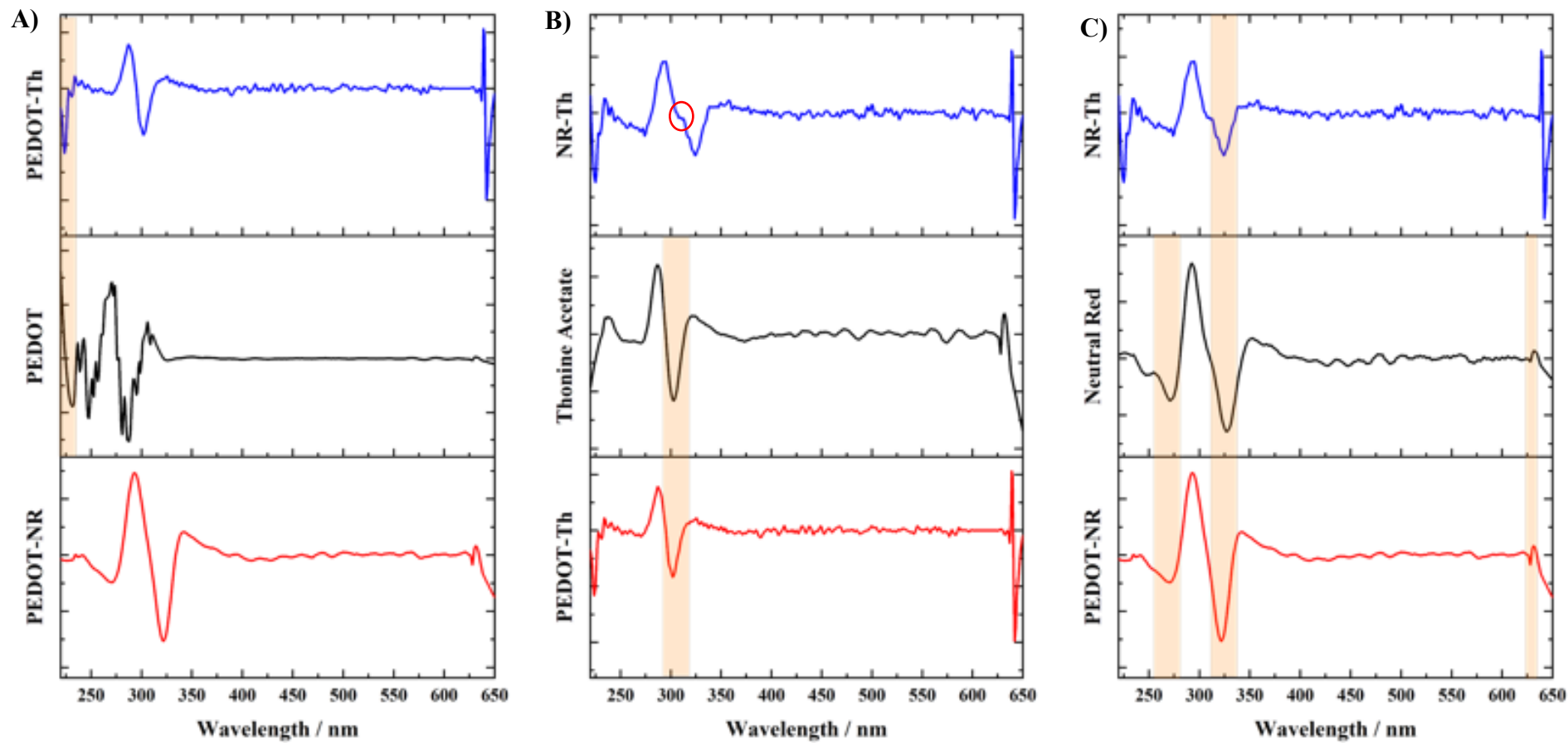


Figure 5.46: UV-Vis absorbance spectra for A) PEDOT containing films, B) Th containing films and C) NR containing films at an ITO surface.

IR Spectroscopy was performed on the films deposited on an ITO surface as seen in **Figure 5.47** and similar issues which arose with the films on the GCE exist. Except for the film containing NR alone, a characteristic three peak response at about 3850, 3735 and 3620 cm^{-1} was observed in all other spectra with varying degrees of intensity. As mentioned in the analysis of the GCE IR data, again the case for two distinct reasons behind this response may be a N-H which has been red shifted due to hydrogen bonding, or it may be trapped O-H responses from the NaOH generated from the polymerisation process. As the response was present in the PEDOT film alone, the presence of O-H may be more likely. In all cases a weak response was observed at about 2300 cm^{-1} similar to that in the case of the GCE, indicating the presence of CO_2 . This may mean that CO_2 is trapped within the polymeric structure, similar to the OH. In a comparative sense, the PEDOT-NR film appears to contain spectral features for both the individual monomers, while Th dominates the responses for the Th containing films.

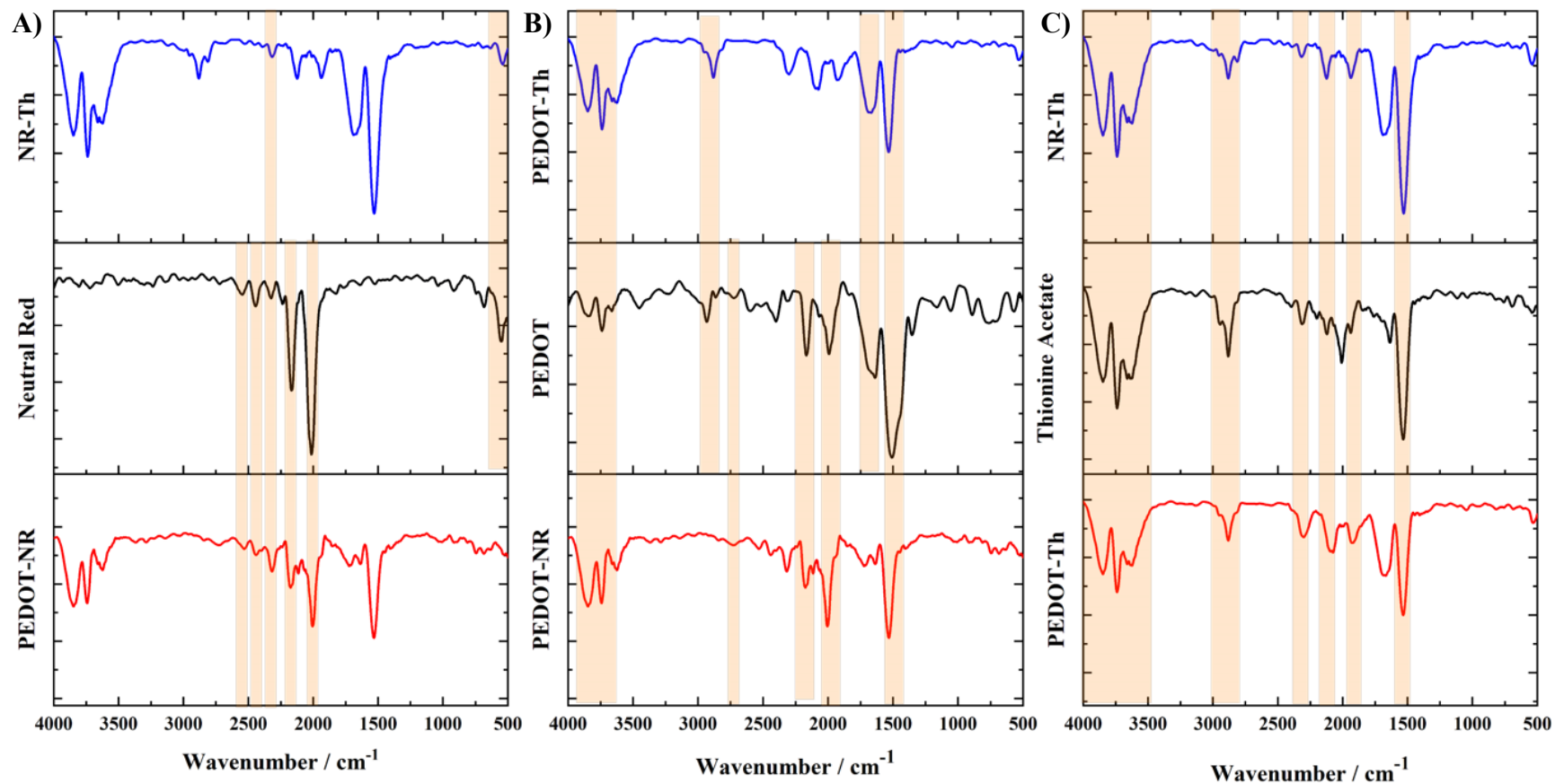


Figure 5.47: IR spectra of A) NR containing films B) PEDOT containing films and C) Th containing films at an ITO surface.

At the ITO surface, films were successfully deposited and characterised via electrochemical, and spectroscopic techniques. The analysis with thicker films proved more successful than the GCE counterpart. Electrochemically, successful redox couples were found within the Th containing films, which were generally found to follow diffusion-controlled processes likely due to diffusion of charge balancing counter ions through the thick film. Films containing EDOT generally resulted in an increase in current response per signal when compared to the individual monomers. Spectral analysis proved slightly more difficult in terms of the number of signals observed. This may be due to the thickness of the film, however, signals within the combination films were matched successfully to their individual counterparts.

5.4.3.3 Proposed Structures of Polymeric Films

Literature comparatives of the possible polymeric structures for any of the combined monomer solutions show very few examples. The only known literature of one of these combinations was reported by Murphy et al. combining EDOT and thionine to form electrochemically deposited films at a GCE surface²³. A comparative mix of species was reported by Ergun and Eroglu, in which a film containing EDOT and a phenazine species was electrochemically deposited on a platinum surface⁷⁷.

Therefore, proposed structures of the individual species films formed, described EDOT combining through the carbons attached to the sulphur and NR and Th forming polymeric units joined via C-N coupling through the amine group and the carbon of the fused ring central structure. Multi-species films without literature counterparts could be proposed with linkages as seen below in **Figure 5.48**. As the electrochemical analysis at both GC and ITO surfaces indicated that the initial oxidation event required for polymerisation of the monomers to occur it would be safe to assume that the linkages between the units would follow the same process as the homogenous polymers. The additional characterisation via spectroscopy indicated that in the case of PEDOT-NR films, the majority of the film was made up of NR repeating units, while PEDOT-Th films contained a majority of Th units and NR-Th films contained a majority of Th units.

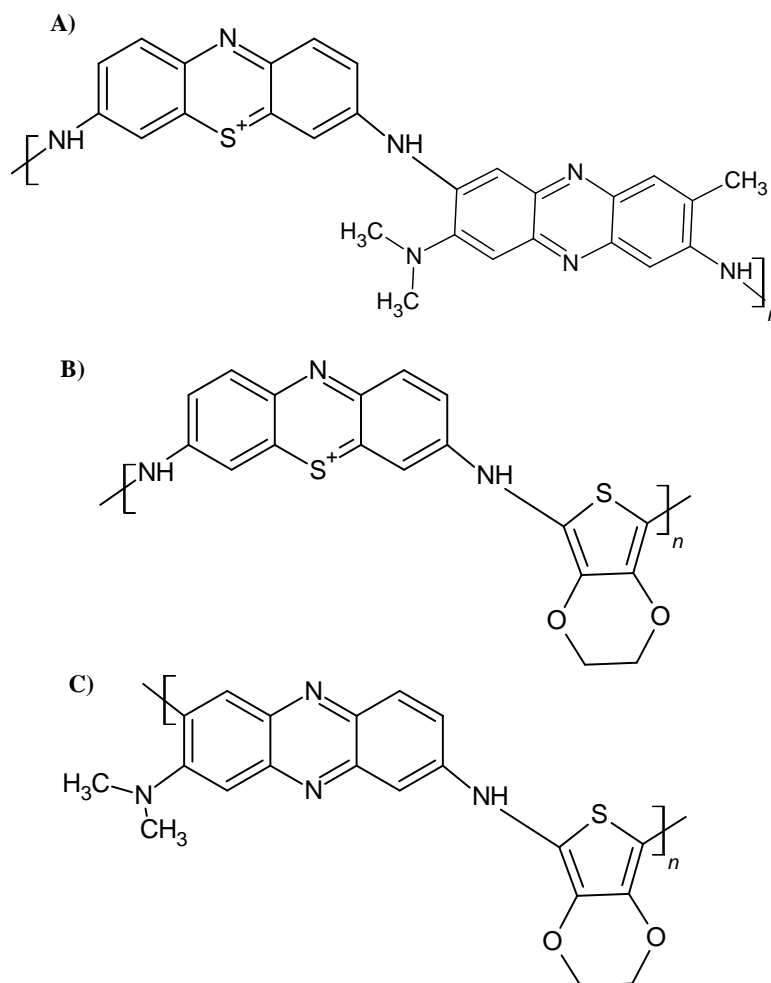


Figure 5.48: Proposed structures indicating linkages between monomer units in combined films showing A) NR-Th, B) PEDOT-Th and C) PEDOT-NR.

5.4.3.4 Characterisation of Phenazine, Phenothiazine and EDOT Combinations in NaNO₃ at a Brass Surface

Voltammograms obtained from the deposition of monomers and mixtures onto a brass surface (**Figure 5.49**) did not show significant differences compared to voltammograms arising from the electrolyte alone, over the range stated. The electrochemical characteristics of the brass electrode dominated the voltammogram, overshadowing any observable features of the monomers. Consequently, the voltammograms obtained from the brass electrode were not useful for comparing the electrochemical activity of the monomers of interest. The only point of change within the data was the potential at which the crossovers were observed within cycle 1. **Table 5.9** shows the potentials of these events.

Chapter 5: Latent Finger-Mark Visualisation at a Brass Surface via Deposition of Conducting and Redox Polymers

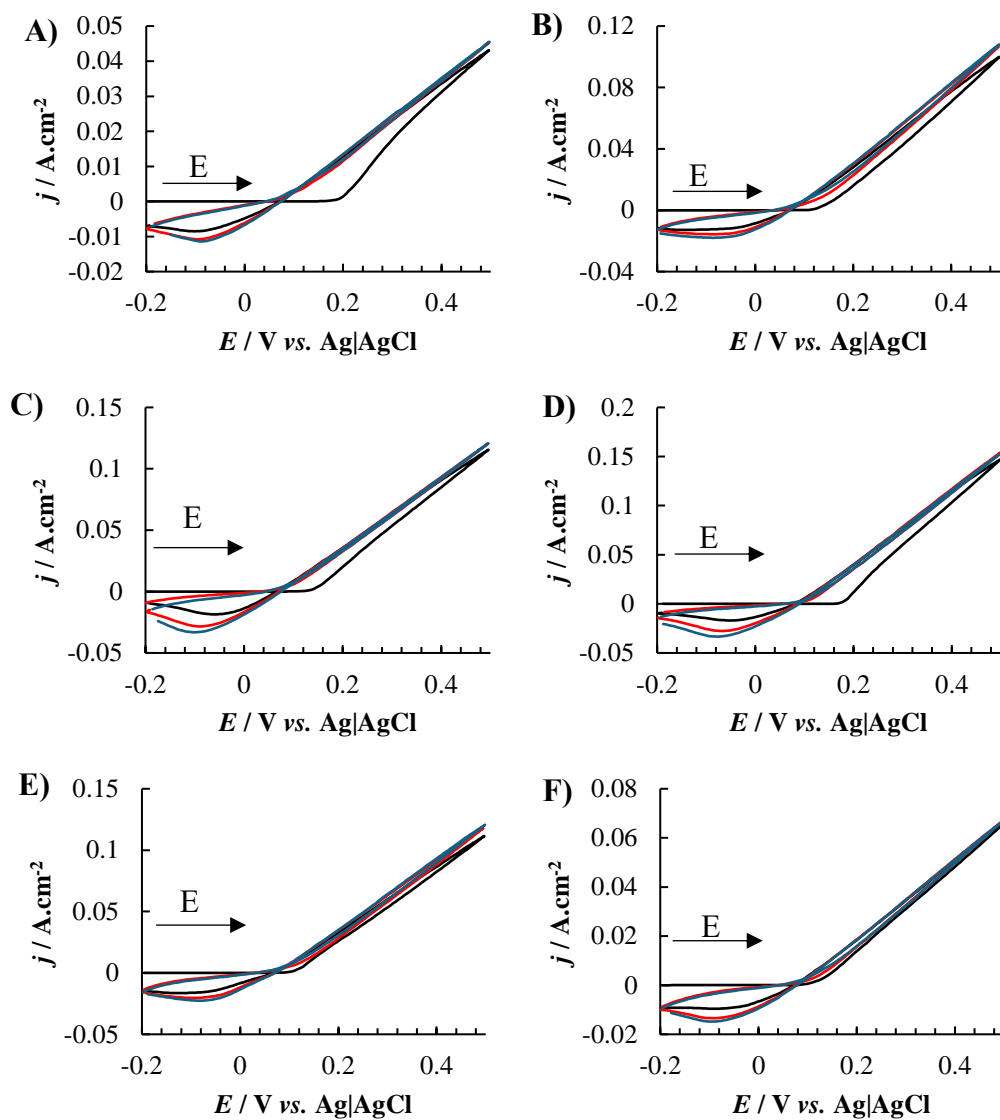


Figure 5.49: Cyclic voltammograms of A) 2 mM EDOT, B) 1 mM Th, C) 1 mM NR, D) 2 mM EDOT and 1 mM NR, E) 2 mM EDOT and 1 mM Th and F) 1 mM NR and 1 M Th in 0.1 M NaNO_3 at a brass surface over the potential range -0.2 to +0.5 V vs. Ag|AgCl at 100 mV.s^{-1} (typical traces).

Chapter 5: Latent Finger-Mark Visualisation at a Brass Surface via Deposition of Conducting and Redox Polymers

Table 5.9: Table of crossover and breakdown potentials observed in cycle 1 with a brass surface in various solutions of monomers.

<i>Solution</i>	Crossover potential (V)	Onset Potential (V)
<i>NaNO₃</i>	0.075	0.164
<i>EDOT</i>	0.079	0.199
<i>Thionine Acetate</i>	0.080	0.129
<i>Neutral Red</i>	0.066	0.141
<i>EDOT-NR</i>	0.074	0.179
<i>EDOT-Th</i>	0.063	0.099
<i>NR-Th</i>	0.072	0.142

Absorbance UV-Vis spectroscopy (film probe spectra studies) were unsuccessful, with noise evident in the spectra. However, reflectance spectroscopy (**Figure 5.50**) without the use of 2nd derivative produced suitable data for analysis. The optical properties of NR dominate in the reflectance spectra for mixed films, with 261, 318, 351 and 577 nm and 236, 261, 318 and 352 nm being attributed to its presence in the EDOT-NR and NR-Th films respectively. Th appeared to be lost at the brass surface, only being attributed to one signal at 243 nm in the neutral red mixture and two signals at 312 and 318 nm in the EDOT mixture.

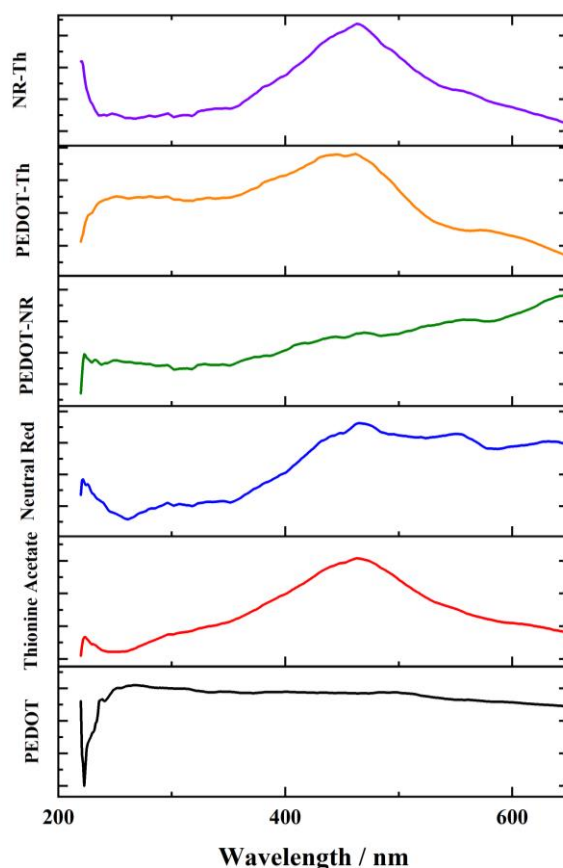


Figure 5.50: UV-vis absorbance spectra of all individual and mixed monomer films at a brass surface, using reflectance probe spectroscopy.

IR spectroscopy analysis at the brass surface (**Figure 5.51**) produced some of the most promising results for each film formed. Similar spectral features to those obtained at the other surfaces were observed. PEDOT-NR and NR-Th films produced similar spectra with the main peaks observed at 2030, 2120 and 2200 cm^{-1} , perhaps indicating the phenazine ring structures containing C=C. Similar peaks were observed in the case of NR alone at 1990, 2100 and 2210 cm^{-1} . Within the PEDOT and Th individual films, a characteristic peak for C=O was observed at 1701 cm^{-1} , along with an indicative peak for N-O at 1531 cm^{-1} which may be from NO_3^- ions in the electrolyte. These peaks were not observed on any of the other films.

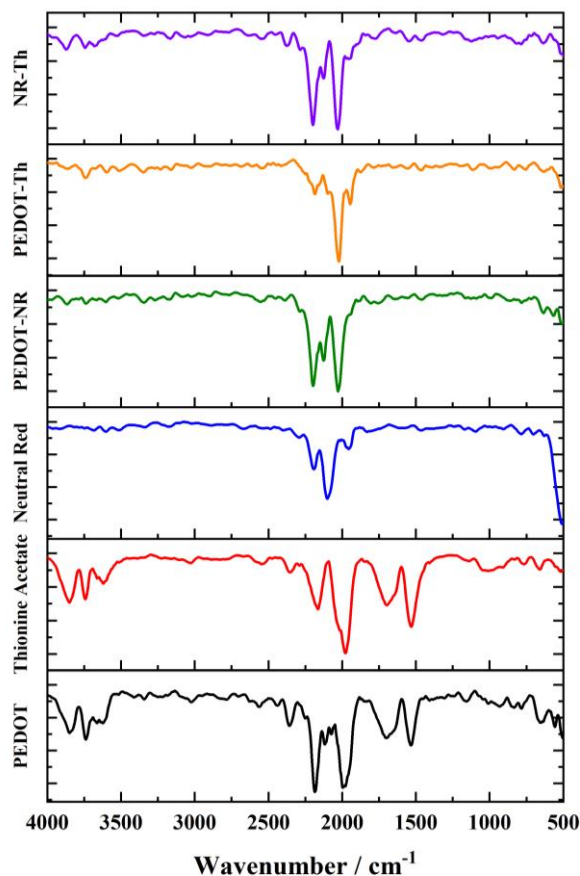


Figure 5.51: IR spectra of electrochemically deposited films on a brass surface.

Overall, at the brass surface, films were successfully deposited via electrochemical deposition. While the electrochemical data did not produce unique voltammograms which could determine electrochemical processes unique to the monomer used spectroscopic analysis did reveal that the films produced were unique to the material deposited. Additional cations and anions which may have been present in the solution from the breakdown of the brass surface most likely played a role in the polymeric structure of the films.

This thorough examination of conducting and redox polymer mixtures paves the way for visualisation of finger-marks on brass surfaces and is to the best of our knowledge the first such comprehensive investigation of these materials using these techniques.

5.5 Conclusion

Data presented here has advanced our understanding of the brass substrate intended for finger-mark visualisation using electrochemical means. While the exact dezincification mechanism was not investigated in detail, XPS data pointed to increased copper concentration at the surface, copper and zinc presence in the formed precipitate. In addition, a blue hue in the solution post analysis and a change to the surface, which removed some material (etch) post analysis, show that a corrosion process, possibly dezincification, was taking place during electroanalytical measurements.

Sodium nitrate provided the most promising electrolyte for brass studies, minimising gaseous release at the counter electrode and providing a mild etch effect for successful visualisation of a latent finger-mark at a brass surface without the need for additional material or monomers.

The desire for only mild etches was in part due to the end case use, with a branch of tool mark analysis which can be performed on ammunition casing, matching scratches on the casing to the barrel of the firearm from which it was fired. If the electrolyte provided a strong etch, such as the H_2SO_4 , the marks which are generated from firing the ammunition could become much deeper and ruin the print, removing much needed detail.

The monomers of interest have been studied and shown to undergo successful oxidation and subsequent polymerisation/deposition at both a glassy carbon and indium tin oxide surfaces. Characterisation of the films deposited on the surfaces suggested proposed structures of the repeating units of the polymer. The deposition of this material at a brass surface did not show any significant changes in the electrochemical results due to the dominance of the brass electrochemical signature. However, spectral analysis and an observable colour change has shown indicative results (due to the challenging nature of the brass surface) that material was successfully deposited on the surface of the brass allowing for a better contrast of colours at the surface for visualisation of latent finger-marks.

In the next chapter, optimisation of these methods, focuses on visualisation quality and subsequent scoring of the prints in order to select the most appropriate system and parameters for latent finger-mark visualisation.

5.6 References

- (1) Vilarinho, C.; Davim, J. P.; Soares, D.; Castro, F.; Barbosa, J. Influence of the Chemical Composition on the Machinability of Brasses. *Journal of Materials Processing Technology* **2005**, *170* (1-2), 441–447. <https://doi.org/10.1016/j.jmatprotec.2005.05.035>.
- (2) Zagal, J.; Ponce, I.; Oñate, R. Redox Potentials as Reactivity Descriptors in Electrochemistry. In *Redox*; IntechOpen, 2020.
- (3) Hajizadeh, K.; Tajally, M.; Emadoddin, E.; Borhani, E. Study of Texture, Anisotropy and Formability of Cartridge Brass Sheets. *Journal of Alloys and Compounds* **2014**, *588*, 690–696. <https://doi.org/10.1016/j.jallcom.2013.11.091>.
- (4) Yaqoob, K.; Hashmi, F.; Hassan Tanveer, W. Failure Analysis of Cartridge Brass Shell. *Engineering Failure Analysis* **2022**, *138*, 106325. <https://doi.org/10.1016/j.engfailanal.2022.106325>.
- (5) Thames Stockholders. *Brass CZ108 | Thames Stockholders*. www.thamesstock.com. <https://www.thamesstock.com/cz108-brass-alloy.htm> (accessed 2024-01-07).
- (6) Khoshnaw, F.; Gubner, R. Part II: Corrosion Topics. In *Corrosion Atlas Case Studies*; Elsevier: xiii - xviii, 2019.
- (7) Cramer, S. D.; Covino, B. S.; Asm International. Handbook Committee. *ASM Handbook. Volume 13B, Corrosion : Materials*; Asm International: Materials Park, Oh, 2005.
- (8) Khoshnaw, F.; Gubner, R. Part I: General Aspects of Corrosion, Corrosion Control, and Corrosion Prevention. In *Corrosion Atlas Case Studies*; Elsevier: xxv -xli, 2019.
- (9) Talbot, D.; Talbot, J. *Corrosion Science and Technology*, 3rd ed.; Crc Press: Boca Raton, 2020.

Chapter 5: Latent Finger-Mark Visualisation at a Brass Surface via Deposition of Conducting and Redox Polymers

- (10) Mattsson, E. Corrosion of Copper and Brass: Practical Experience in Relation to Basic Data. *British Corrosion Journal* **1980**, *15* (1), 6–13. <https://doi.org/10.1179/000705980798318708>.
- (11) Mattsson, E. Stress Corrosion in Brass Considered against the Background of Potential/PH Diagrams. *Electrochimica Acta* **1961**, *3* (4), 279–291. [https://doi.org/10.1016/0013-4686\(61\)85004-4](https://doi.org/10.1016/0013-4686(61)85004-4).
- (12) Weisser, T. S. The De-Alloying of Copper Alloys. *Studies in Conservation* **1975**, *20* (sup1), 207–214. <https://doi.org/10.1179/sic.1975.s1.035>.
- (13) Goldstein, E. M. The Corrosion and Oxidation of Metals: Scientific Principles and Practical Applications (Evans, Ulick R.). *Journal of Chemical Education* **1960**, *37* (12), 662–662. <https://doi.org/10.1021/ed037p662.2>.
- (14) El Warraky, A.; El Shayeb, H. A.; Sherif, E. M. Pitting Corrosion of Copper in Chloride Solutions. *Anti-Corrosion Methods and Materials* **2004**, *51* (1), 52–61. <https://doi.org/10.1108/00035590410512735>.
- (15) R. Lachhab; M. Galai; A. Ech-chebab; R.A. Belakhmima; M. Ebn Touhami; Mansouri, I. Comparative Study of the Corrosion Behavior of Three Alpha Brass Alloys Used in Potable Water Distribution Equipment in Aggressive Soil Using Electrochemical Measurements. *Ceramics International* **2024**, *50* (3), 4282–4295. <https://doi.org/10.1016/j.ceramint.2023.10.185>.
- (16) Pchel'nikov, A. P.; Sitnikov, A. D.; Marshakov, I. K.; Losev, V. V. A Study of the Kinetics and Mechanism of Brass Dezincification by Radiotracer and Electrochemical Methods. *Electrochimica Acta* **1981**, *26* (5), 591–600. [https://doi.org/10.1016/0013-4686\(81\)80025-4](https://doi.org/10.1016/0013-4686(81)80025-4).

Chapter 5: Latent Finger-Mark Visualisation at a Brass Surface via Deposition of Conducting and Redox Polymers

- (17) El-Reuim, S. S. A.; Assaf, F. H.; El-Sayed, A.; Zaky, A. M. Cyclic Voltammetric Behaviour of Copper Rich Brasses in NaCl Solution. *British Corrosion Journal* **1995**, *30* (4), 297–301. <https://doi.org/10.1179/000705995798113727>.
- (18) Abbas, M. I. Effects of Temperature on Dezincification and Electrochemical Behaviour of 70–30 Brass in Sulphuric Acid. *British Corrosion Journal* **1991**, *26* (4), 273–278. <https://doi.org/10.1179/000705991798269017>.
- (19) Itoh, I.; Takeo Hikage. Dezincification Mechanism of Brass in Vacuum at High Temperature. *Transactions of the Japan Institute of Metals* **1976**, *17* (3), 165–169. <https://doi.org/10.2320/matertrans1960.17.165>.
- (20) Muhammad Farhan Zainal; Mohd, Y. Characterization of PEDOT Films for Electrochromic Applications. *Polymer-Plastics Technology and Engineering* **2015**, *54* (3), 276–281. <https://doi.org/10.1080/03602559.2014.977422>.
- (21) Abaci, U.; Guney, H. Y.; Kadiroglu, U. Morphological and Electrochemical Properties of PPy, PANi Bilayer Films and Enhanced Stability of Their Electrochromic Devices (PPy/PANi–PEDOT, PANi/PPy–PEDOT). *Electrochimica Acta* **2013**, *96*, 214–224. <https://doi.org/10.1016/j.electacta.2013.02.120>.
- (22) Eduard Nasybulin; Wei, S.; Ioannis Kymissis; Levon, K. Effect of Solubilizing Agent on Properties of Poly(3,4-Ethylenedioxythiophene) (PEDOT) Electrodeposited from Aqueous Solution. *Electrochimica acta* **2012**, *78*, 638–643. <https://doi.org/10.1016/j.electacta.2012.06.083>.
- (23) Murphy, B.; Singh, B.; Delaney, A.; Warren, S.; Dempsey, E. Phenothiazine Redox Active Conducting Polymer Films at Nanocomposite Surfaces. *Journal of The Electrochemical Society* **2020**, *167* (2), 027525. <https://doi.org/10.1149/1945-7111/ab6a83>.

- (24) Anindya, W.; Wahyuni, W. T.; Rafi, M.; Putra, B. R. Electrochemical Sensor Based on Graphene Oxide/PEDOT:PSS Composite Modified Glassy Carbon Electrode for Environmental Nitrite Detection. *International Journal of Electrochemical Science* **2023**, *18* (3), 100034. <https://doi.org/10.1016/j.ijoes.2023.100034>.
- (25) Fu, F.; Wang, J.; Yu, J. Interpenetrating PAA-PEDOT Conductive Hydrogels for Flexible Skin Sensors. *Journal of Materials Chemistry C* **2021**, *9* (35), 11794–11800. <https://doi.org/10.1039/d1tc01578h>.
- (26) Costa, C. V.; Assis, A. M. L.; Freitas, J. D.; Tonholo, J.; Ribeiro, A. S. A Low-Potential Electrochemical Method for Fast Development of Latent Fingerprints on Brass Cartridge Cases by Electrodeposition of Poly(3,4-Ethylenedioxythiophene). *Nano Select* **2020**, *1* (4), 405–412. <https://doi.org/10.1002/nano.202000040>.
- (27) Zhu, D.; Lu, X.; Lu, Q. Electrically Conductive PEDOT Coating with Self-Healing Superhydrophobicity. *Langmuir* **2014**, *30* (16), 4671–4677. <https://doi.org/10.1021/la500603c>.
- (28) Zhao, Q.; Jamal, R.; Zhang, L.; Wang, M.; Abdiryim, T. The Structure and Properties of PEDOT Synthesized by Template-Free Solution Method. *Nanoscale Research Letters* **2014**, *9* (1). <https://doi.org/10.1186/1556-276x-9-557>.
- (29) Chhin, D.; Polcari, D.; Le Guen, C. B. -; Tomasello, G.; Cicoira, F.; Schougaard, S. B. Diazonium-Based Anchoring of PEDOT on Pt/Ir Electrodes via Diazonium Chemistry. *Journal of the Electrochemical Society* **2018**, *165* (12), G3066–G3070. <https://doi.org/10.1149/2.0061812jes>.
- (30) Nabilah Azman, N. H.; Lim, H. N.; Sulaiman, Y. Effect of Electropolymerization Potential on the Preparation of PEDOT/Graphene Oxide Hybrid Material for Supercapacitor Application. *Electrochimica Acta* **2016**, *188*, 785–792. <https://doi.org/10.1016/j.electacta.2015.12.019>.

- (31) Pandey, G. P.; Rastogi, A. C. Synthesis and Characterization of Pulsed Polymerized Poly(3,4-Ethylenedioxythiophene) Electrodes for High-Performance Electrochemical Capacitors. *Electrochimica Acta* **2013**, *87*, 158–168. <https://doi.org/10.1016/j.electacta.2012.08.125>.
- (32) Ren, M.; Zhou, H.; Zhai, H.-J. Obvious Enhancement in Electrochemical Capacitive Properties for Poly(3,4-Ethylenedioxythiophene) Electrodes Prepared under Optimized Conditions. *Journal of Materials Science Materials in Electronics* **2021**, *32* (8), 10078–10088. <https://doi.org/10.1007/s10854-021-05666-3>.
- (33) Sapstead, R. M.; Corden, N.; Robert Hillman, A. Latent Fingerprint Enhancement via Conducting Electrochromic Copolymer Films of Pyrrole and 3,4-Ethylenedioxythiophene on Stainless Steel. *Electrochimica Acta* **2015**, *162*, 119–128. <https://doi.org/10.1016/j.electacta.2014.11.061>.
- (34) Pauliukaite, R.; Ghica, M. E.; Barsan, M. M.; Brett, C. M. A. Phenazines and Polyphenazines in Electrochemical Sensors and Biosensors. *Analytical Letters* **2010**, *43* (10-11), 1588–1608. <https://doi.org/10.1080/00032711003653791>.
- (35) Kappo, D.; Shurpik, D.; Padnya, P.; Stoikov, I.; Rogov, A.; Evtugyn, G. Electrochemical DNA Sensor Based on Carbon Black—Poly(Methylene Blue)—Poly(Neutral Red) Composite. *Biosensors* **2022**, *12* (5), 329–329. <https://doi.org/10.3390/bios12050329>.
- (36) Pauliukaite, R.; Ghica, M. E.; Barsan, M.; Brett, C. M. A. Characterisation of Poly(Neutral Red) Modified Carbon Film Electrodes; Application as a Redox Mediator for Biosensors. *Journal of Solid State Electrochemistry* **2007**, *11* (7), 899–908. <https://doi.org/10.1007/s10008-007-0281-9>.

- (37) Seelajaroen, H.; Haberbauer, M.; Hemmelmaier, C.; Aljabour, A.; Dumitru, L. M.; Hassel, A. W.; Sariciftci, N. S. Enhanced Bio-Electrochemical Reduction of Carbon Dioxide by Using Neutral Red as a Redox Mediator. *ChemBioChem* **2019**, *20* (9), 1196–1205. <https://doi.org/10.1002/cbic.201800784>.
- (38) Sun, W.; Jiao, K.; Han, J.; Lu, L. Linear Sweep Voltammetric Determination of Heparin Based on Its Interaction with Neutral Red. *Analytical Letters* **2005**, *38* (7), 1137–1148. <https://doi.org/10.1081/al-200057217>.
- (39) Liang, X.; Zhou, Y.; Almeida, J. M. S.; Brett, C. M. A. A Novel Electrochemical Acetaminophen Sensor Based on Multiwalled Carbon Nanotube and Poly(Neutral Red) Modified Electrodes with Electropolymerization in Ternary Deep Eutectic Solvents. *Journal of Electroanalytical Chemistry* **2023**, *936*, 117366. <https://doi.org/10.1016/j.jelechem.2023.117366>.
- (40) Pauliukaite, R.; Brett, Christopher M. A. Poly(Neutral Red): Electrosynthesis, Characterization, and Application as a Redox Mediator. *Electroanalysis* **2008**, *20* (12), 1275–1285. <https://doi.org/10.1002/elan.200804217>.
- (41) Broncová, G.; Tereza Slaninová; Miroslava Trchová. Characterization of Electrochemically Visualized Latent Fingerprints on the Steel Substrates. *Journal of Solid State Electrochemistry* **2022**, *26* (11), 2423–2433. <https://doi.org/10.1007/s10008-022-05245-4>.
- (42) Huo, H. Y.; Luo, H. Q.; Li, N. B. Electrochemical Sensor for Heparin Based on a Poly(Thionine) Modified Glassy Carbon Electrode. *Microchimica Acta* **2009**, *167* (3-4), 195–199. <https://doi.org/10.1007/s00604-009-0240-5>.
- (43) Gao, X.; Gui, R.; Xu, K. Q.; Guo, H.; Jin, H.; Wang, Z. A Bimetallic Nanoparticle/Graphene Oxide/Thionine Composite-Modified Glassy Carbon Electrode Used as a Facile Ratiometric Electrochemical Sensor for Sensitive Uric Acid Determination. *New Journal of Chemistry* **2018**, *42* (18), 14796–14804. <https://doi.org/10.1039/c8nj02904k>.

- (44) Warren, S.; Rathod, D. G.; McCormac, T.; Dempsey, E. Investigations into the Use of a Thionine/PEDOT Layer as an NADH Electrocatalyst with Applications in Glutamate Sensing. *ECS Transactions* **2010**, *25* (28), 21–32. <https://doi.org/10.1149/1.3309674>.
- (45) Warren, S.; Munteanu, G.; Rathod, D.; McCormac, T.; Dempsey, E. Scanning Electrochemical Microscopy Imaging of Poly (3,4-Ethylendioxythiophene)/Thionine Electrodes for Lactate Detection via NADH Electrocatalysis. *Biosensors and Bioelectronics* **2019**, *137*, 15–24.
- (46) André Olean-Oliveira; Oliveira, G. A.; Celso Xavier Cardoso; Marcos F.S. Teixeira. Role of Anion Size in the Electrochemical Performance of a Poly(Thionine) Redox Conductive Polymer Using Electrochemical Impedance Spectroscopy. *Polymer* **2022**, *258*, 125291–125291. <https://doi.org/10.1016/j.polymer.2022.125291>.
- (47) Medvedeva, A. S.; Dyakova, E. I.; Kuznetsova, L. S.; Mironov, V. G.; Gurkin, G. K.; Rogova, T. V.; Kharkova, A. S.; Melnikov, P. V.; Naumova, A. O.; Butusov, D. N.; Arlyapov, V. A. A Two-Mediator System Based on a Nanocomposite of Redox-Active Polymer Poly(Thionine) and SWCNT as an Effective Electron Carrier for Eukaryotic Microorganisms in Biosensor Analyzers. *Polymers* **2023**, *15* (16), 3335–3335. <https://doi.org/10.3390/polym15163335>.
- (48) Bumbulis, J.; Graydon, W. F. Dissolution of Brass in Sulfuric Acid Solutions. *Journal of The Electrochemical Society* **1962**, *109* (12), 1130. <https://doi.org/10.1149/1.2425258>.
- (49) Brown, R. M.; Hillman, A. R. Electrochromic Enhancement of Latent Fingerprints by Poly(3,4-Ethylendioxythiophene). *Physical Chemistry Chemical Physics* **2012**, *14* (24), 8653–8661. <https://doi.org/10.1039/C2CP40733G>.

- (50) Al-Hinai, A. T.; Al-Hinai, M. H.; Dutta, J. Application of Eh-PH Diagram for Room Temperature Precipitation of Zinc Stannate Microcubes in an Aqueous Media. *Materials Research Bulletin* **2014**, *49*, 645–650. <https://doi.org/10.1016/j.materresbull.2013.10.011>.
- (51) Scherzer, M. T.; Girgsdies, F.; Stotz, E.; Willinger, M. G.; Frei, E.; Schlögl, R.; Pietsch, U.; Lunkenbein, T. Electrochemical Surface Oxidation of Copper Studied by in Situ Grazing Incidence X-Ray Diffraction. *Journal of Physical Chemistry C* **2019**, *123* (21), 13253–13262. <https://doi.org/10.1021/acs.jpcc.9b00282>.
- (52) Groot, D. R.; van der Linde, J. A. N. The Processing of EWaste. Part 2. The Electrochemical Leaching Behaviour of a Metallic Alloy Derived from Waste Printed Circuit Boards. *Journal of the Southern African Institute of Mining and Metallurgy* **2009**, *109* (12), 701–707.
- (53) Broncová, G.; Slaninová, T.; Dendisová, M. Poly(Neutral Red) Modified Metal Substrates for Fingerprint Visualization. *Chemical Papers* **2021**, *75* (12), 6673–6676. <https://doi.org/10.1007/s11696-021-01794-6>.
- (54) Broncová, G.; Slaninová, T.; Trchová, M.; Prokopec, V.; Matějka, P.; Shishkanova, T. V. Optimization of Electrochemical Visualization of Latent Fingerprints with Poly(Neutral Red) on Brass Surfaces. *Polymers* **2021**, *13* (19), 3220. <https://doi.org/10.3390/polym13193220>.
- (55) Jain, A. K.; Chen, Y.; Demirkus, M. Pores and Ridges: High-Resolution Fingerprint Matching Using Level 3 Features. *IEEE Transactions on Pattern Analysis and Machine Intelligence* **2007**, *29* (1), 15–27. <https://doi.org/10.1109/tpami.2007.250596>.
- (56) Xu, Y.; Yang, L.; He, P.; Fang, Y. Electrochemical DNA Biosensor Based on a Thionine–Carbon Nanotube Modified Electrode. *Journal of Biomedical Nanotechnology* **2005**, *1* (2), 202–207. <https://doi.org/10.1166/jbn.2005.022>.

- (57) Shobha Jeykumari, D. R.; Ramaprabhu, S.; Sriman Narayanan, S. A Thionine Functionalized Multiwalled Carbon Nanotube Modified Electrode for the Determination of Hydrogen Peroxide. *Carbon* **2007**, *45* (6), 1340–1353. <https://doi.org/10.1016/j.carbon.2007.01.006>.
- (58) Zhuo, Y.; Yu, R.; Yuan, R.; Chai, Y.; Hong, C. Enhancement of Carcinoembryonic Antibody Immobilization on Gold Electrode Modified by Gold Nanoparticles and SiO₂/Thionine Nanocomposite. *Journal of Electroanalytical Chemistry* **2009**, *628* (1-2), 90–96. <https://doi.org/10.1016/j.jelechem.2009.01.016>.
- (59) Fan, Y.; Shi, S.; Ma, J.; Guo, Y. A Paper-Based Electrochemical Immunosensor with Reduced Graphene Oxide/Thionine/Gold Nanoparticles Nanocomposites Modification for the Detection of Cancer Antigen 125. *Biosensors and Bioelectronics* **2019**, *135*, 1–7. <https://doi.org/10.1016/j.bios.2019.03.063>.
- (60) Li, S.; Zhu, X.; Zhang, W.; Xie, G.; Feng, W. Hydrogen Peroxide Biosensor Based on Gold Nanoparticles/Thionine/Gold Nanoparticles/Multi-Walled Carbon Nanotubes–Chitosans Composite Film-Modified Electrode. *Applied Surface Science* **2012**, *258* (7), 2802–2807. <https://doi.org/10.1016/j.apsusc.2011.10.138>.
- (61) Joseph, J.; Jemmis, E. D. Red-, Blue-, or No-Shift in Hydrogen Bonds: A Unified Explanation. *Journal of the American Chemical Society* **2007**, *129* (15), 4620–4632. <https://doi.org/10.1021/ja067545z>.
- (62) Yang, C.; Yi, J.; Tang, X.; Zhou, G.; Zeng, Y. Studies on the Spectroscopic Properties of Poly(Neutral Red) Synthesized by Electropolymerization. *Reactive and Functional Polymers* **2006**, *66* (11), 1336–1341. <https://doi.org/10.1016/j.reactfunctpolym.2006.03.015>.
- (63) Bredas, J. L.; Street, G. B. Polarons, Bipolarons, and Solitons in Conducting Polymers. *Accounts of Chemical Research* **1985**, *18* (10), 309–315. <https://doi.org/10.1021/ar00118a005>.

- (64) Guay, J.; Kasai, P.; Diaz, A.; Wu, R.; Tour, J. M.; Dao, L. H. Chain-Length Dependence of Electrochemical and Electronic Properties of Neutral and Oxidized Soluble α,α -Coupled Thiophene Oligomers. *Chemistry of Materials* **1992**, *4* (5), 1097–1105. <https://doi.org/10.1021/cm00023a031>.
- (65) Owino, J.; Arotiba, O.; Hendricks, N.; Songa, E.; Jahed, N.; Waryo, T.; Ngece, R.; Baker, P.; Iwuoha, E. Electrochemical Immunosensor Based on Polythionine/Gold Nanoparticles for the Determination of Aflatoxin B1. *Sensors* **2008**, *8* (12), 8262–8274. <https://doi.org/10.3390/s8128262>.
- (66) Li, M.; Bin, H.; Jiao, X.; Wienk, M. M.; Yan, H.; Janssen, J. Controlling the Microstructure of Conjugated Polymers in High-Mobility Monolayer Transistors via the Dissolution Temperature. *Angewandte Chemie International Edition* **2019**, *59* (2), 846–852. <https://doi.org/10.1002/anie.201911311>.
- (67) Hayashi, S. Highly Crystalline and Efficient Red-Emissive π -Conjugated Polymer Film: Tuning of Macrostructure for Light-Emitting Properties. *Materials Advances* **2020**, *1* (4), 632–638. <https://doi.org/10.1039/d0ma00218f>.
- (68) Ceccacci, A. C.; Cagliani, A.; Marizza, P.; Schmid, S.; Boisen, A. Thin Film Analysis by Nanomechanical Infrared Spectroscopy. *ACS Omega* **2019**, *4* (4), 7628–7635. <https://doi.org/10.1021/acsomega.9b00276>.
- (69) Fornaro, T.; Burini, D.; Biczysko, M.; Barone, V. Hydrogen-Bonding Effects on Infrared Spectra from Anharmonic Computations: Uracil-Water Complexes and Uracil Dimers. *The Journal of Physical Chemistry. A* **2015**, *119* (18), 4224–4236. <https://doi.org/10.1021/acs.jpca.5b01561>.
- (70) Amertharaj, S.; Hasnat, M. A.; Mohamed, N. Electroreduction of Nitrate Ions at a Platinum-Copper Electrode in an Alkaline Medium: Influence of Sodium Inositol Phytate. *Electrochimica Acta* **2014**, *136*, 557–564. <https://doi.org/10.1016/j.electacta.2014.05.128>.

Chapter 5: Latent Finger-Mark Visualisation at a Brass Surface via Deposition of Conducting and Redox Polymers

- (71) Begum, H.; Islam, Md. N.; Aoun, S. B.; Safwan, J. A.; Shah, S. S.; Aziz, Md. A.; Hasnat, M. A. Electrocatalytic Reduction of Nitrate Ions in Neutral Medium at Coinage Metal-Modified Platinum Electrodes. *Environmental Science and Pollution Research* **2022**, *30* (12), 34904–34914. <https://doi.org/10.1007/s11356-022-24372-z>.
- (72) de Groot, M. T.; Koper, M. T. M. The Influence of Nitrate Concentration and Acidity on the Electrocatalytic Reduction of Nitrate on Platinum. *Journal of Electroanalytical Chemistry* **2004**, *562* (1), 81–94. <https://doi.org/10.1016/j.jelechem.2003.08.011>.
- (73) Ouyang, L.; Wei, B.; Kuo, C.; Pathak, S.; Farrell, B.; Martin, D. C. Enhanced PEDOT Adhesion on Solid Substrates with Electrografted P(EDOT-NH₂). *Science Advances* **2017**, *3* (3), e1600448. <https://doi.org/10.1126/sciadv.1600448>.
- (74) Wustoni, S.; Hidalgo, T. C.; Hama, A.; Ohayon, D.; Savva, A.; Wei, N.; Wehbe, N.; Sahika Inal. In Situ Electrochemical Synthesis of a Conducting Polymer Composite for Multimetabolite Sensing. *Advanced Materials Technologies* **2019**, *5* (3). <https://doi.org/10.1002/admt.201900943>.
- (75) Yang, R.; Ruan, C.; Dai, W.; Deng, J.; Kong, J. Electropolymerization of Thionine in Neutral Aqueous Media and H₂O₂ Biosensor Based on Poly(Thionine). *Electrochimica Acta* **1999**, *44* (10), 1585–1596. [https://doi.org/10.1016/s0013-4686\(98\)00283-7](https://doi.org/10.1016/s0013-4686(98)00283-7).
- (76) Benito, D.; García-Jareño J. J.; Navarro-Laboulais, J.; Vicente, F. Electrochemical Behaviour of Poly(Neutral Red) on an ITO Electrode. *Journal of Electroanalytical Chemistry* **1998**, *446* (1-2), 47–55. [https://doi.org/10.1016/s0022-0728\(97\)00565-2](https://doi.org/10.1016/s0022-0728(97)00565-2).

Chapter 5: Latent Finger-Mark Visualisation at a Brass Surface via Deposition of Conducting and Redox Polymers

- (77) Cansu Ergun, E. G.; Eroglu, D. An Electrochemically and Optically Stable Electrochromic Polymer Film Based on EDOT and 1,2,3,4-Tetrahydrophenazine. *Organic Electronics* **2019**, *75*, 105398. <https://doi.org/10.1016/j.orgel.2019.105398>.

Chapter 6: Visualisation of Latent Finger-Marks on Brass Surfaces

6.1 Chapter Aims

The overall aim of this chapter is, to enhance the visualisation process of a finger-mark with the view to achieve the highest possible score of the visualised finger-mark (Grade-4 and level-3). Secondly, the aim is to refine and optimise experimental parameters to mitigate risk by professionals who may adopt the technique, and finally, to achieve visualisation of a finger-mark on an ammunition casing to the extent of donor identification.

6.2 Introduction

The goal of the previous experimental chapter was to establish an understanding of how redox and conducting polymers behave at brass surfaces under electrochemical conditions with the aim to extend this information to a latent finger-mark visualisation technique. While some latent finger-marks were previously developed and scored, in this chapter, the main focus of any analysis performed was enhancement of the quality of the visualised finger-mark achieved on a brass surface. As mentioned in **Chapter 1**, previously successful latent finger-mark visualisation on metallic surfaces have been described in the literature¹⁻¹⁰, with varying degrees of success, in some cases requiring very high applied potentials and long analysis times.

Degradation of a latent finger-mark is a key issue for forensic professionals, as the ammunition casings are rarely analysed directly after use in real cases. Multiple factors such as time, humidity, heat and secondary contamination can hinder current methods of visualisation¹¹. In this work, two of these factors (time and temperature) were selected to understand how the methods proposed behave relative to analogues of “real case” finger-mark evidence.

One of the initial findings which generated the interest in electrochemical visualisation of latent finger-marks on metallic substrates was that of the natural etching of sweat on metals¹². Forge workers who produced salt rich sweat, were observed to work with machinery which would have indicative finger-marks present due to the sweat generated from working in such hot environments, these workers were referred to as “rusters”¹². This was due to the natural salts present within mostly eccrine sweat corroding and

degrading the metallic surface¹³. The age of the latent finger-mark may also affect the surface naturally, perhaps inducing a mild etch effect with sweat and time alone.

Heat was also a factor of importance, as the end goal of this methodology was to visualise finger-marks on ammunition casings after the discharge of the weapon. The heat generated from the discharge of a firearm depends on many factors, such as type of ammunition used (single, double or triple base), the diameter of the barrel of the firearm and how many repeated firing events were performed. These exact values are difficult to find within the literature, as the focus on firing stress is placed on largely automatic weapons, to avoid unexpected detonation of the ammunition.

6.3 Experimental

6.3.1 *Materials and Reagents*

Brass (CZ108/CW508L) sheets were obtained from Farnell Ltd. UK in 100 x 250 mm sized sheets. Sodium nitrate (NaNO₃) was purchased from VWR chemicals, Thionine Acetate (Th) and Neutral Red (NR) were purchased from ThermoScientific while 3,4-ethylenedioxythiophene (EDOT) was purchased from Flurochem. All compounds required no further purification. Ethanol (anhydrous $\geq 99.5\%$) was obtained from Sigma-Aldrich and all deionised water was obtained from the lab Millipore Milli-Q water system with a Progard[®] TS2 filter attached. Electrode polishing solution was a 1 μ M Monocrystallin diamond suspension (Akasel). Brass ammunition casings were donated from a private collection, showing the headstamp of “*HXP 85*” indicating their manufacturing origin from the Greek Powder and Cartridge Company in 1985.

6.3.2 *Instrumentation and Software*

All electrochemical experiments were carried out using a Solartron Potentiostat Model 1285 operated by Scribner Associates Corrware software package with data analysis using CorrView Version 2.3a and a CHI Electrochemical workstation model (660E) operated by CHI software (version 19.10) with Microsoft excel 365 software package and Origin Pro 2023b for data analysis. A platinum mesh (square area 1.32 cm²) was used for the counter electrode and a standard Ag|AgCl electrode (internal solution 3 M KCl) was employed as the reference electrode. The Ag|AgCl reference electrode was stored in 3 M

KCl when not in use. A HUAWEI P20 lite mobile phone, running EMUI version 9.1.0 in addition with a LED desk lamp were used for photography. X-Ray Photoelectron spectroscopy was performed with a Kratos AXIS 165 instrument at the University of Limerick (Dr. Fattima Laffir). Heat degradation experiments were carried out using a Gallenkamp, size 2, Muffle Furnace. A bespoke electrochemical cell was fabricated with chemical resistant PET material (maximum volume 250 mL) and a Teflon inlet tube, containing copper wire ($d = 1 \text{ mm}$) with the attachment point manipulated into a corkscrew spiral ($d = 5 \text{ mm}$), allowing for an ammunition casing to be screwed into the connection to act as a working electrode, sealed to a watertight finish with Araldite 2-part epoxy adhesive.

6.3.3 Procedures

6.3.3.1 Brass Preparation and Cleaning

Brass strips were prepared and cleaned as per section **5.3.3.1** in **Chapter 5**.

As ammunition casings were significantly different in shape compared to brass sheets used previously, a drill was employed to house the ammunition casings (**Figure 6.1**). Ammunition casings were held within the chuck of the drill and rotated on the polishing surface in three steps. Firstly, the casing was rotated on p1200 grit polishing paper with Brasso as lubricant. The casing was then further rotated on a cloth with Brasso and finally was rotated on a fine polishing pad with $1 \mu\text{m}$ diamond suspension to bring it to a mirror finish. The rotation of the drill allowed for even coverage across the entire casing.

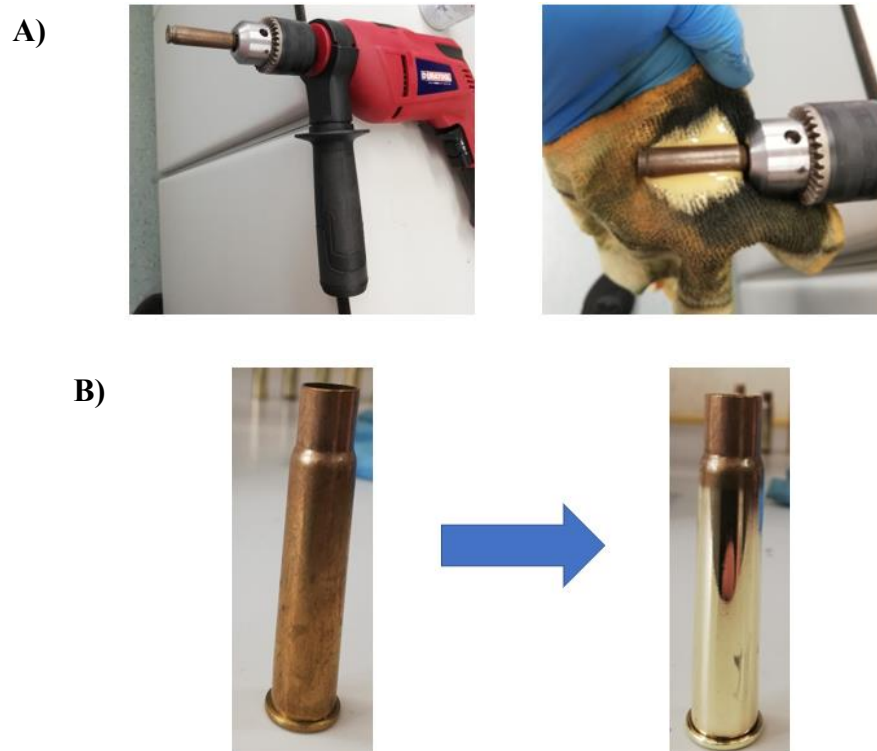


Figure 6.1: A) Photographs of ammunition casings in a drill B) before and after polishing surface of ammunition casings.

6.3.3.2 Groomed Sebaceous finger-mark generation

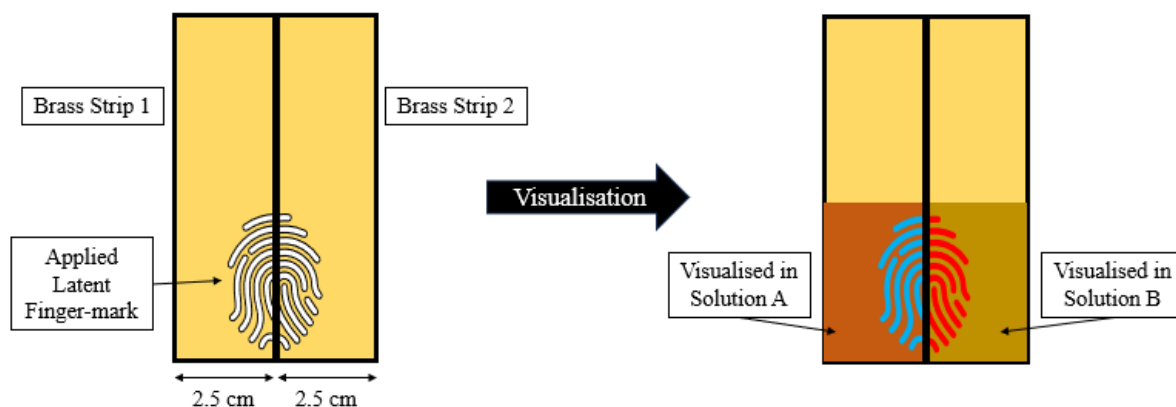
As described earlier in Chapter 5 section 5.3.3.9

6.3.3.3 Groomed Eccrine finger-mark generation

The hands were initially washed with soap and warm water. The cleaned hand was then placed into two gloves and the gloves were worn for a minimum of thirty minutes while doing light activity around the lab (solution preparation, cleaning etc.). The gloves were removed, and a finger was then gently placed on the surface of interest for one to two seconds.

6.3.3.4 Split Printing of Finger-marks

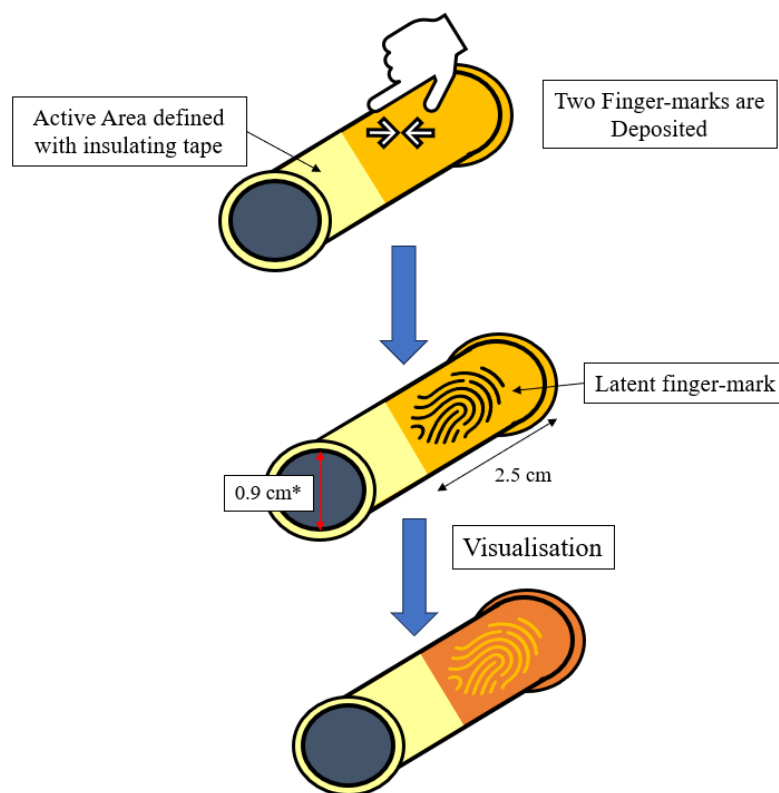
Latent finger-marks were applied in the same manner as previously stated in section 5.3.3.2, with the deviation being that the mark was applied between two different brass sheets as per **Scheme 6.1**.



Scheme 6.1: Visualisation of the “split print” method for comparison of visualisation solutions.

6.3.3.5 Application of finger-marks to ammunition casings

While the method of application of latent finger-marks did not deviate greatly from previously mentioned procedures, a slight variation occurred due to the way in which the casing was connected into the system. To ensure that the applied finger-marks were not damaged, the ammunition casing was cleaned (as in section 5.3.3.1), then attached to the corkscrew adaptor. Once in place, the latent finger-mark was applied in a pinch, meaning that two prints were applied (the index finger and thumb) one on the side closest to the reference electrode and one on the side of the counter electrode.



Scheme 6.2: Application of finger-marks to ammunition casings.

*Due to the taper within the form of the ammunition casing, the diameter indicated on the above scheme is taken from the central point of the active area.

6.3.3.6 Electrochemical Methods

Over the course of this chapter cyclic voltammetry and constant potential techniques are implemented as the principle electroanalytical techniques. Cyclic voltammetry was employed across the range of -0.2 to 0.5 V at $50 \text{ mV}\cdot\text{s}^{-1}$, while constant potential techniques were set at $E_{app} = 0.1, 0.25$ and 0.5 V under different time or maximum charge parameters. A bespoke electrochemical cell was fabricated for visualisation techniques on the ammunition casings (**Figure 6.2**). This allowed the ammunition casing to act as the working electrode, within the 3-electrode cell with an approximate distance of $\sim 1.5 \text{ cm}$ between WE and CE.

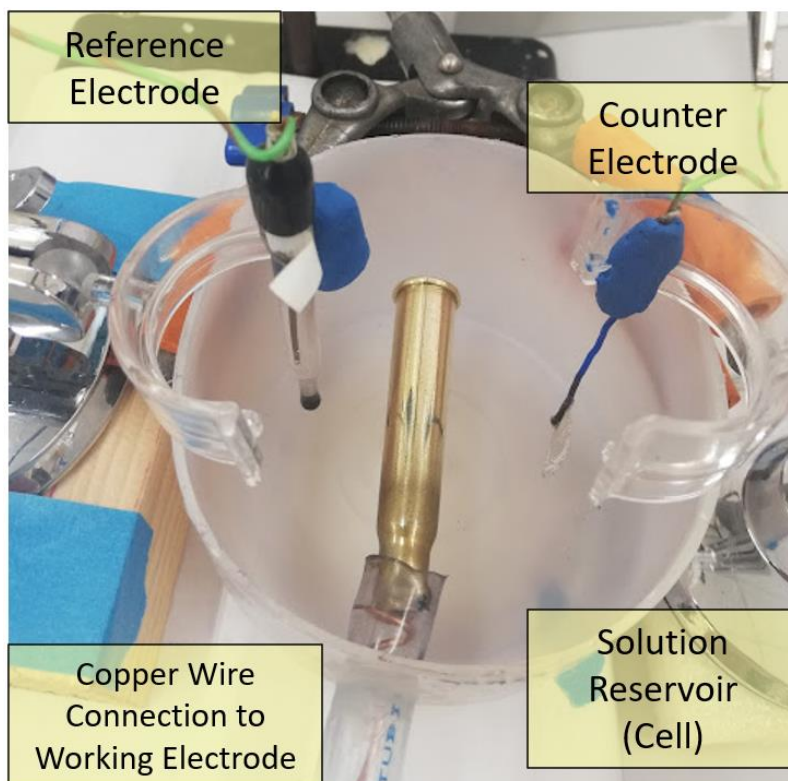


Figure 6.2: Photograph of three electrode cell set-up with ammunition casing acting as the working electrode.

6.3.3.7 Reflectance Microscopy

Reflectance microscopy was performed in a dark room with the only light available to the subject being that from the microscope lamp. The camera attached to the microscope contained a magnification setting, which allowed a minimum magnification of x1000. Due to the high magnification, for more representative images of the finger-marks, imaging through the eyepiece was employed with a camera to allow for the x50 magnification.

6.3.3.8 X-Ray Photoelectron Spectroscopy

Samples of brass with electrochemically deposited films were analysed by *Dr. Fattima Laffir* at the *Bernal Institute* within *University of Limerick*. Samples of brass sheets were prepared via potential sweeping over the range of -0.2 to 0.5 V at 50 mV.s^{-1} for 3 cycles in a solution of 1 mM thionine acetate and 2 mM EDOT with thionine acetate made up in 0.1 M NaNO_3 .

6.3.3.9 Examination of Heat Degradation on Finger-mark visualisation

Using a Gallenkamp, size 2, Muffle Furnace, temperature was set and allowed to stabilise over the course of an hour. The temperature was taken with a thermocouple inserted into the furnace. Once the desired temperature was reached, the furnace was left for a further twenty minutes to ensure homogeneous heat within the entire chamber. This was to ensure the initial temperature was representative of the entire chamber. Finger-marks were applied in the same manner as that described for either the sebaceous or eccrine mark procedures. The sample was then placed into the chamber and a timer was commenced once the door was closed. Once the required time was complete, the sample was removed with tongs and left to rest and cool down on a piece of ceramic.

6.3.3.10 Examination of the effect of Aging Process of Finger-mark

Both natural finger-marks (contact of the finger to the surface without any preparation) and a groomed sebaceous finger-marks were collected from various donors on flat brass surfaces. These finger-marks were stored in a cool dry place away from direct light. The area was not temperature or humidity controlled. The samples were then tested at the 5 month and 16-month time period.

6.3.3.11 Scoring of Visualised Finger-marks

Scoring of the visualised finger-marks was performed, focusing solely on the level of features observable, with the common level of features being between 1-3. To have a more quantifiable values, additional levels were added. These half levels (1.5 & 2.5) were employed when some of the features of the upper level were observed, though not sufficient to classify as that level (apparent in > 50% of finger-mark). As a result, finger-mark visualisation which resulted, for example, in only 2-3 visible pores was not given the same weighting as a method which produced a finger-mark with level 3 features throughout the mark.

6.3.3.12 Finger-mark photography

Finger-mark photographs were taken using a phone camera under a set of conditions as seen in **Figure 6.3**. The light may have been manoeuvred for clarity of the end

photograph, however, all efforts were made to keep a consistent photography process, to ensure fair comparison between visualised finger-marks.

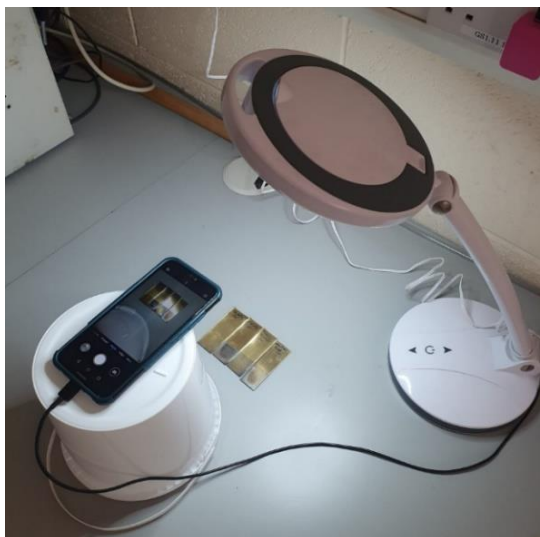


Figure 6.3: Photograph of photographic set-up of imaging for visualised finger-marks.

Colour manipulation was employed to create images of higher clarity, by changing brightness, temperature, contrast, and saturation levels of the image. No image manipulation such as filling in blank spaces with assumed features or merging multiple images to create a composite finger-mark was employed in this work.

6.4 Results and Discussion

6.4.1 Screening of Monomers and Combinations for Effectivity of Visualisation

6.4.1.1 Cyclic Voltametric Methods for Finger-mark Visualisation

All initial depositions were performed on freshly cut brass sheets, which had only undergone an initial cleaning step (ethanol rinse and jet of compressed air), to ensure any material which may have been deposited on the surface during the cutting process was removed. As with the electrochemical results discussed in **Chapter 5**, the voltammograms produced when the brass sheets underwent potential cycling did not indicate any uniquely identifiable redox features. The shape of the voltammogram was

attributed mainly to the electrochemical properties of brass¹⁰. The addition of a latent finger-mark did not alter the electrochemical results of the brass in any of the solutions tested. Crossover potentials, or the onset potential of the reduction process, did not develop to a noticeable degree when comparing untouched brass to a surface with a latent finger-mark present. In some instances, a notable change in the maximum cathodic current reached was observed, however, this value did result in some variability between replicates in addition to the hand cut nature of the brass sheets (**Figure 6.4**).

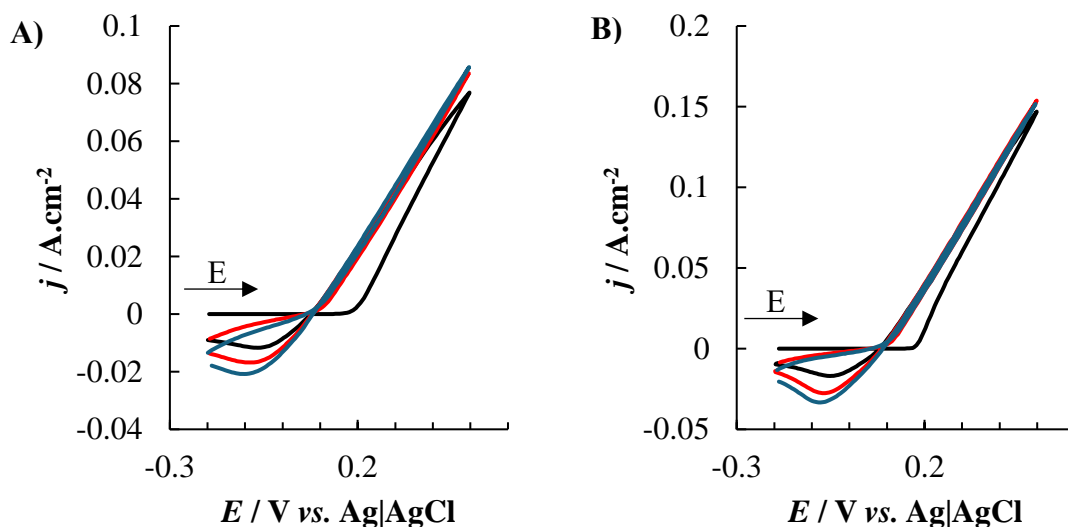


Figure 6.4: Cyclic voltammogram of a brass sheet A) without and B) with a latent finger-mark in 2 mM EDOT and 1 mM NR in 0.1 M NaNO₃ over the potential range -0.2 to +0.5 V vs. Ag|AgCl at 50 mV.s⁻¹ for three cycles (Cycle 1: black, Cycle 2: red and Cycle 3: blue-dash) (typical traces).

Visualisation of a groomed finger-mark was performed in triplicate, via cyclic voltammetry across the range of -0.2 to 0.5 V at 50 mV.s⁻¹ for 3 cycles in each solution and mixture. In **Figure 6.5** and **Figure 6.6**, each of the visualised finger-marks are presented as high contrast black and white images with the specific test solution.

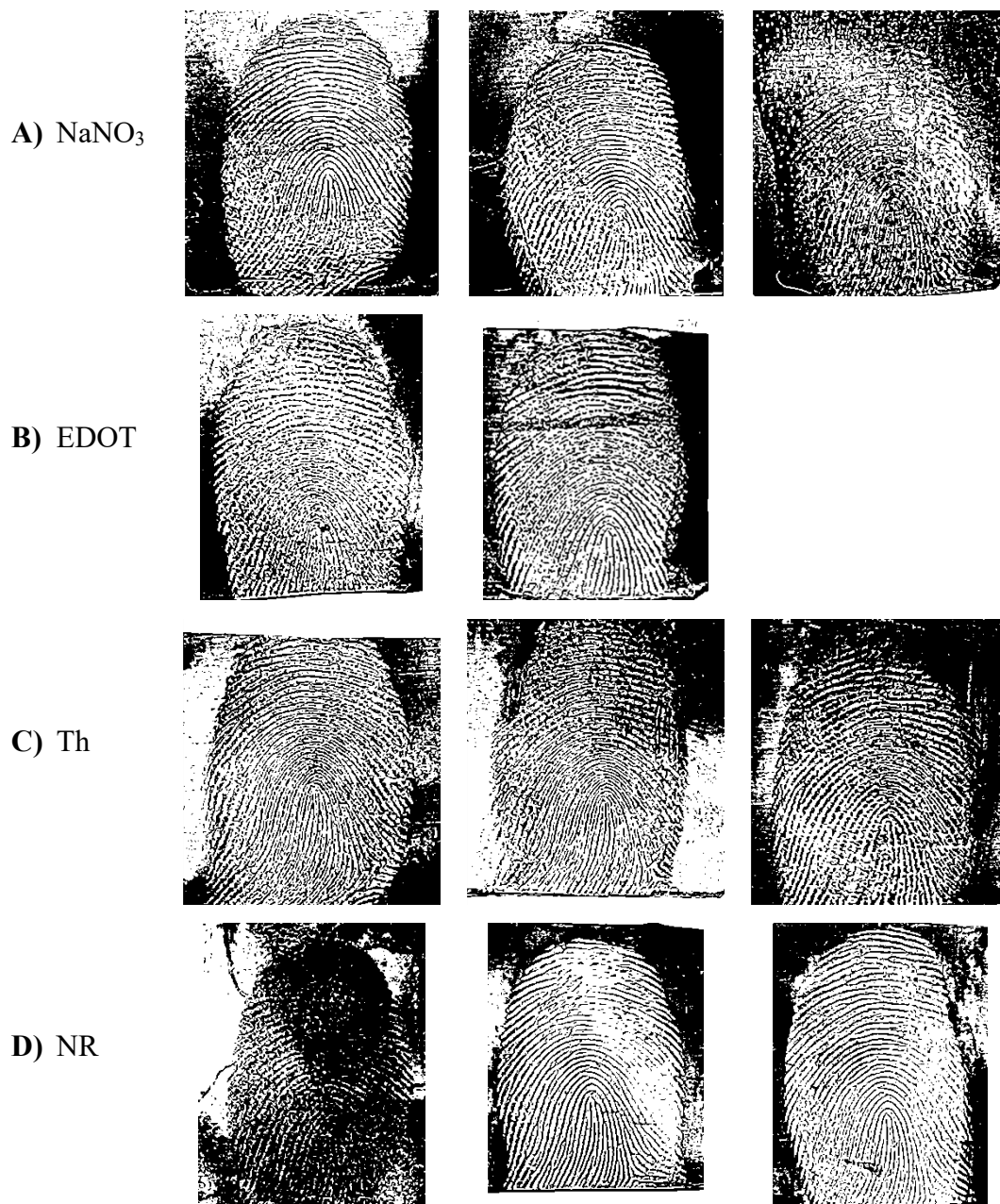


Figure 6.5: High contrast photographs of latent finger-marks visualised at a brass sheet via cyclic voltammetry over the potential range -0.2 to $+0.5$ V vs. $\text{Ag}|\text{AgCl}$ at $50 \text{ mV}\cdot\text{s}^{-1}$ for three cycles in A) 0.1 M NaNO_3 , and subsequent monomer solutions of 0.1 M NaNO_3 with B) 2 mM EDOT , C) 1 mM Th and D) 1 mM NR .

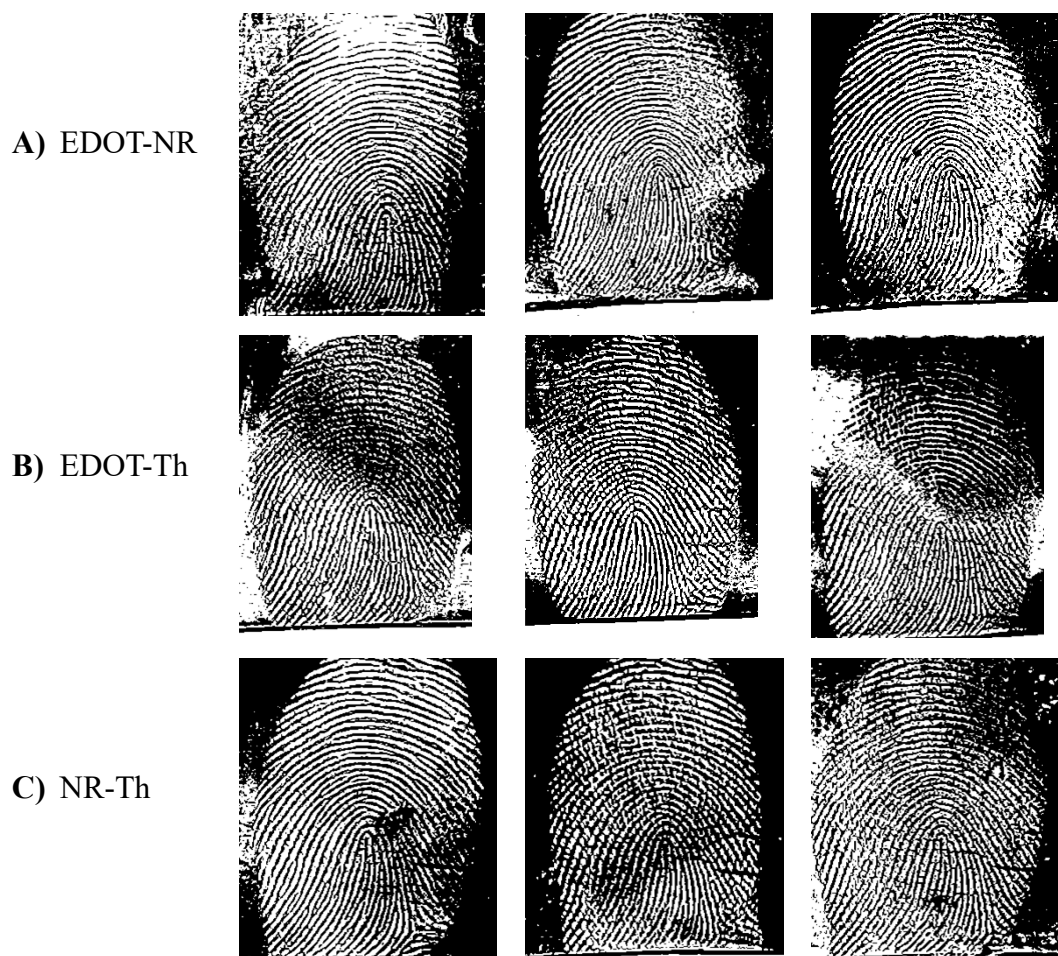


Figure 6.6: High contrast photographs of latent finger-marks visualised at a brass sheet via cyclic voltammetry over the potential range -0.2 to $+0.5$ V vs. $\text{Ag}|\text{AgCl}$ at $50 \text{ mV}\cdot\text{s}^{-1}$ for three cycles in 0.1 M NaNO_3 with mixed monomer solutions of A) EDOT-NR (2:1 mM), B) EDOT-Th (2:1 mM), C) NR-Th (1:1 mM).

In all instances finger-marks were successfully visualised in triplicate, using the CV method at the brass surface. In **Table 6.1** a cross comparison of levels of detail obtained from the visualisation methods is presented. Th was the most successful individual monomer, providing marks with an average of level 2.5 details observed post visualisation. All monomer mixes produced much more visually reproducible visualisations, with an average level feature of 2.3 for the EDOT-NR and NR-Th mixtures while EDOT-Th resulted in an average level feature of 2.5. Upon examination of the individual values within each set, EDOT-Th appeared to have the highest likelihood of level 3 features from visualisation, while NR-Th appeared to be the least reproducible, with both maximum and almost minimum visualisation of the finger-marks.

Table 6.1: Comparison of level features obtained from the visualisation of a groomed latent finger-mark on a brass surface in various solutions via cyclic voltammetry.

Solution	Level of Feature in Finger-mark 1	Level of Feature in Finger-mark 2	Level of Feature in Finger-mark 3	Average level of feature in Finger-Mark
<i>NaNO₃</i>	2.5	2.5	1	2
<i>EDOT</i>	1.5	2.5	2	2
<i>Th</i>	3	3	1.5	2.5
<i>NR</i>	1.5	2.5	2	2
<i>EDOT-NR</i>	2	3	2	2.3
<i>EDOT-Th</i>	2.5	2.5	2.5	2.5
<i>NR-Th</i>	3	1.5	2.5	2.3

A closer look at the visualised finger-marks with the use of reflectance microscopy followed. This involved taking the most successfully visualised finger-mark from each method and observing the core at a magnification of x1000. In **Figure 6.7** each of these cores are seen; the general images of the cores contain 4 visible ridges, if counting 1-4 left to right. Ridge 1 and 2 are connected and would be classified as the exact core of the finger-mark, these ridges contain 5-6 pores across in total. Ridge 3 was a ridge ending containing a single pore just at the end of the ridge and ridge 4 continues the overall finger-mark pattern containing a possible 2-3 pores down its length.

EDOT visualisation (**Figure 6.7 (A)**) at x1000 magnification produced highly textured ridges (diameter approximately 450 µm) with a mixture of deposited material (dark area) and protected surface (light area) across the entirety of the ridge. Pores were somewhat visible but did not appear to have definitive shapes and there was “bleed” into the ridges. This also appeared to affect the ridge edges with ridge 3 and 4 appearing to be connected, removing the ridge ending characteristic from ridge 3.

Th visualisation (**Figure 6.7 (B)**), interestingly, appeared to have increased the sizes of the pores within the ridges, almost appearing as corridors within the ridges (ridge diameter approximately 450 µm, pore diameter approximately 150 µm). This could easily be mistaken for additional ridges if the endings or connection points were not visible at this location. This may be the reason why level 3 features were so prominent within this visualisation technique when photographed with a standard camera. Definition of the

ridge edges was successful and while the area between the ridges was small (approximately 50-100 μm), the contrast between protected metal surface (light area) and deposited material (dark area) was large enough to define the boundaries.

With NR (**Figure 6.7 (C)**) visualisation at this magnification appeared to generate ridge detail at a fine level, while the boundary of the ridge to the metal surface (light to dark respectively) appeared rough or textured, the shape or curvature of the ridge was still visible. Fingerprints are not perfectly straight lines on the fingers; therefore, visualisation may be more representative of the fingerprint which applied the mark (diameter approximately 150 – 300 μm). Pores within the ridges were well defined with the same contrast as the metal surface, indicating that the pore was in fact an area of no contact and thus capable of having material deposited onto it.

EDOT-NR (**Figure 6.7 (D)**) produced a visualised mark which in some cases was difficult to see. Ridge details with defined boundaries were visible. However, it appeared that the pores within the ridges break the ridge creating lagoon-like structures, making characterisation of the ridge shape difficult when a pore was present.

EDOT-Th (**Figure 6.7 (E)**) produced immaculate visualisation of the ridges with crisp ridge boundaries and defined ridge and pore shape throughout the core. The fine details observed in this visualisation asks the question whether one of the pores on ridge 1 was actually a ridge break, which could not be seen with the other methods and whether there was a small lake feature on ridge 4, previously thought to be a pore.

NR-Th (**Figure 6.7 (F)**) also produced ridges of fine detail similar to that produced with NR alone. Pores within the ridges are defined, as is the boundary between the ridge and the metal surface. One issue was the apparent smudging of the ridges; however, this may have been due to the application process of the finger-mark and not the visualisation method.

Considering both the print contrast and clarity of the cores, split print comparison was performed with EDOT-Th and NR-Th selected as likely candidates for the optimisation of methodologies. Th alone was also promising. In order to achieve a closer comparison of these methods, the split print method (using two brass sheets) of comparison was performed, removing the variability of the mark application and allowing for the

visualisation methods to be compared directly via the quality of visualisation without the variation in the finger-mark.

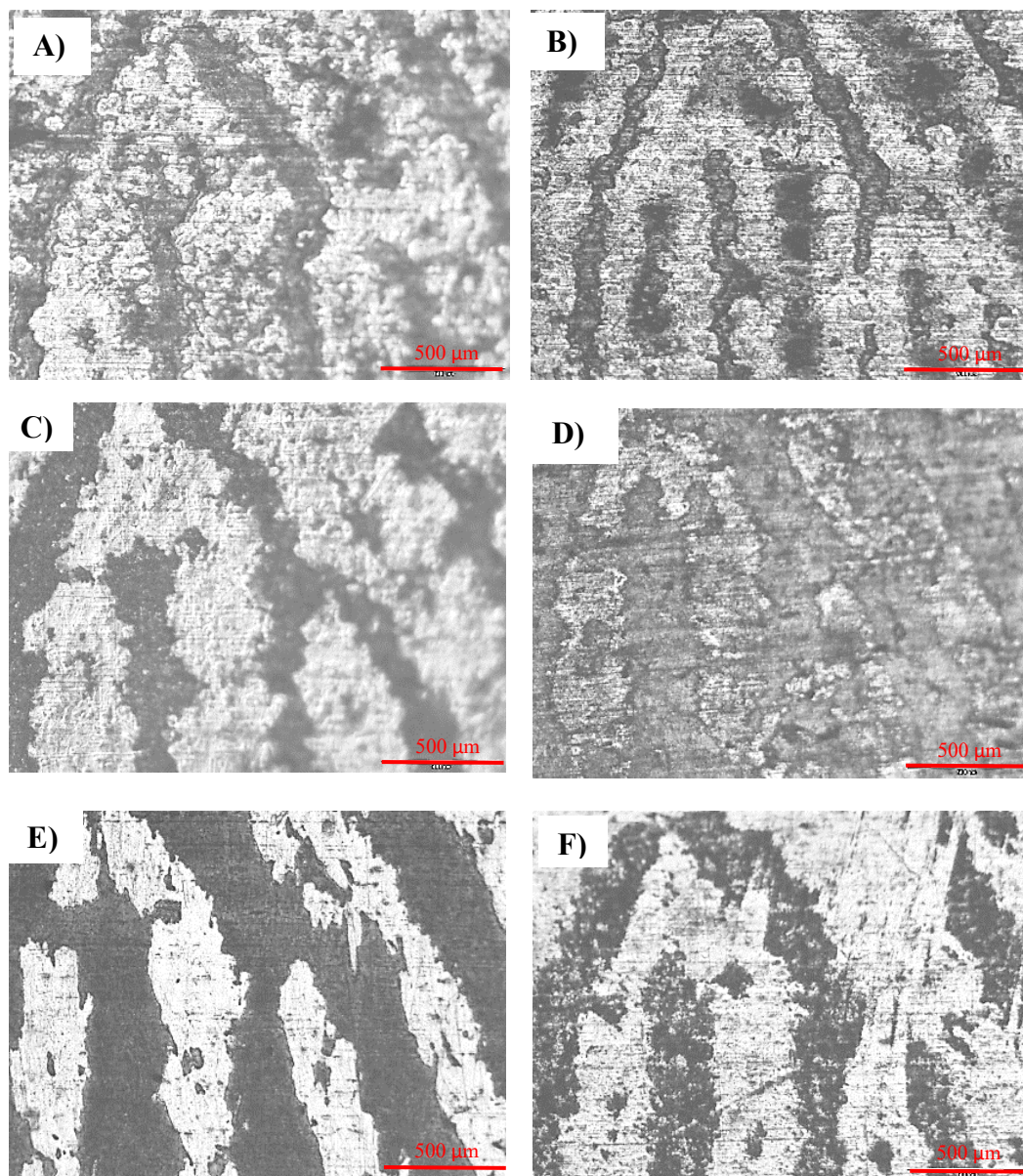





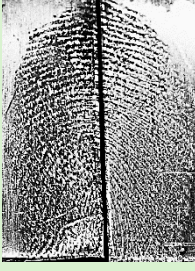
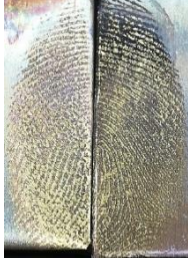






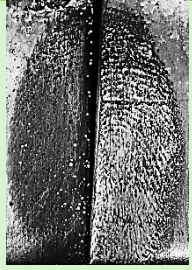




Figure 6.7: Photographs of microscope images ($\times 1000$ magnification) of finger-mark cores visualised at a brass sheet via cyclic voltammetry over the potential range -0.2 to $+0.5$ V vs. Ag|AgCl at $50 \text{ mV}\cdot\text{s}^{-1}$ for three cycles in 0.1 M NaNO_3 containing the monomers A) 2 mM EDOT , B) 1 mM Th , C) 1 mM NR and the mixed monomer solutions of D) EDOT-NR ($2:1 \text{ mM}$), E) EDOT-Th ($2:1 \text{ mM}$) and F) NR-Th ($1:1 \text{ mM}$).

Table 6.2 shows the complete overview of comparative visualised finger-marks. The split print method produced the first cases of unsuccessful visualisation (deemed level 0) at the brass surface. NaNO_3 and NR-Th solutions in some cases, did alter the colour of the surface of the brass, however, they did not produce visualisation to the point where the

general pattern (loop, arch, whorl, etc.) was discernible. Th and EDOT-Th solutions were the most successful methods as they resulted in visualisation of partial level 3 features (level 2.5). Reproducibility of the finger-mark visualisation with the split prints was noticeably different to that of the full finger-mark visualisation previously discussed, with NaNO₃ having an average of level 1.00, NR-Th an average of level 1.17, Th an average of level 1.83 and EDOT-Th an average of level 1.67.

Table 6.2: Table of results from the split print method of application of finger-marks visualised via cyclic voltammetry.

<i>Print</i>	Left	Right	Image	High Contrast Image
1	EDOT-Th Level 2-3	NaNO ₃ Level 1		
2	Thionine Level 2-3	NR-Th Level 2		
3	EDOT-Th Level 1	NaNO ₃ Level 2		
4	NR-Th Level 1-2	Th Level 2		

<i>Print</i>	Left	Right	Image	High Contrast Image
5	NR-Th Level 0	EDOT- Th Level 1- 2		
6	NaNO ₃ Level 0	Thionine Level 1		
7	Thionine Level 2-3	EDOT- Th Level 2- 3		
8	NaNO ₃ Level 1	NR-Th Level 0		

The sudden variation within the average level of features visualised may be attributed to the new position of the finger-marks on the surface. When the finger-marks were placed entirely on the surface, they were positioned within the centre of the brass strip, while in this case they were placed at the edge of the brass sheet to allow for the single finger-mark to be on multiple strips. While the exact rationale for this variation was not fully understood, two theories can be presented.

Firstly, the proximity of the finger-marks to the counter electrode had altered slightly. Initial optimisation of the set of electrodes within the cell, found that a close proximity of the counter electrode to the surface improved the visualisation quality. However, if the counter electrode was too close, the gaseous release at the upper potentials of the cyclic

method ($E_p^a = > 0.3$ V) would allow for bubbles to adhere to the surface of the brass, thus producing an area in which no visualisation occurs. While the counter electrode was in the normal position for the cell setup, the finger-marks were now slightly further away, and this may have influenced the visualisation quality.

Another parameter which may have changed the finger-mark visualisation could also be due to the new positioning of the finger-marks. As the finger-marks are now at the edge of the strip, they are positioned right next to the freshly cut sides of the brass sheets. As mentioned in the previous section, the process of dezincification occurs during electrochemical measurements, and surface topology would be much more complex, due to the manual cutting process with the tools used in this methodology. A sheering method of cut introduces multiple changes to the surface parameters such as flatness, roughness and may also introduce micro-fractures within the surface as well¹⁴. This produces a much higher surface area than would be previously expected based on the geometric area. Concurrently, this surface would also have had less time to react to produce surface oxides allowing for a more active surface, which when undergoing the stresses of electrochemical analysis, may have expedited the dezincification process. This may result in areas of high activity and metal ion movement, perhaps interfering with the deposition process of the materials. While unexpected, the change in parameters did shine a light on the robustness of the methods currently employed and prompted reflection upon the end goal of the methodologies being developed within this work. The use of solutions of Th and EDOT-Th appear to be able to deal with variations more effectively than the other solutions employed. Deposition of these species produced the highest average level features on the full print and once more on the split prints.

In order to further understand what may be happening at the surface once deposited, XPS was employed using brass sheet samples modified electrochemically within i) Th and ii) EDOT-Th solutions using the optimised cyclic voltametric method.

6.4.1.2 X-Ray Photoelectron Spectroscopy of a Brass Surface Post Visualisation Methods

As in the previous chapter (**Chapter 5**) XPS analysis was utilised to further understand what materials may have been deposited on the brass surface. With Th and EDOT-Th being the most successful solutions in the visualisation of latent finger-marks on the brass

surfaces, deposition was performed via the previously used cyclic voltametric method over the range of -0.2 to 0.5 V at 50 mV.s⁻¹ for 3 cycles.

In **Figure 6.8 (A)** the binding energies of nitrogen are observed, with both Th and EDOT-Th showing two nitrogen responses at 398.4 and 399.8 eV, with the lower being representative of the C=N of a phenazine ring and the upper of a N-C, possibly of aromatic nature¹⁵, such as the amine groups attached to the ring structure of the phenothiazine core of thionine. The presence of these responses in both the Th and EDOT-Th cycled surfaces indicated that Th was still deposited onto the surface when combined with a different species in solution.

The more interesting of the elemental differences between the deposited materials from the different solutions was the sulphur composition at the surface. Both monomers of interest contain sulphur within the molecular structures but these responses (**Figure 6.8 (B)**) varied slightly. The lower end of the binding energies observed gave indications of copper and zinc interactions with the sulphur, with the matches shown below in **Table 6.3**.

The quantification scan of the atoms at the surface (**Figure 6.8 (C)**) shows the variation of the elemental composition of the surface when compared to the bare brass and NaNO₃ cycled samples originally observed in **Chapter 5**. The increase in sulphur was clearly due to both sulphur containing compounds of Th and EDOT, while the slight increase in the zinc presence may be due to these sulphur zinc interactions (**Table 6.3**). Most notable is the variation in the copper persistence at the surface when Th alone was deposited. As described in the previous chapter (**Section 5.4.2**), the dezincification process results in an increase in copper concentrations at the surface of the brass once cycling has occurred. One potential explanation for the increase of copper is its removal and subsequent redeposition. During the removal it is proposed that free copper cations are present in solution which, during the visualisation process (cyclic voltammetry) allows Cu-S bonds to form¹⁶, with copper ions acting as a catalytic site¹⁷.

This increase in the copper persistence may indicate a more available form of sulphur within the thionine subunits of the deposited material compared to material generated from electrochemical methods with EDOT-Th solutions. While not confirmed as yet, these results indicated a clear change in the structure of the material deposited and perhaps

if a polymeric/oligomeric film is produced, it may contain unreacted monomer units of both species.

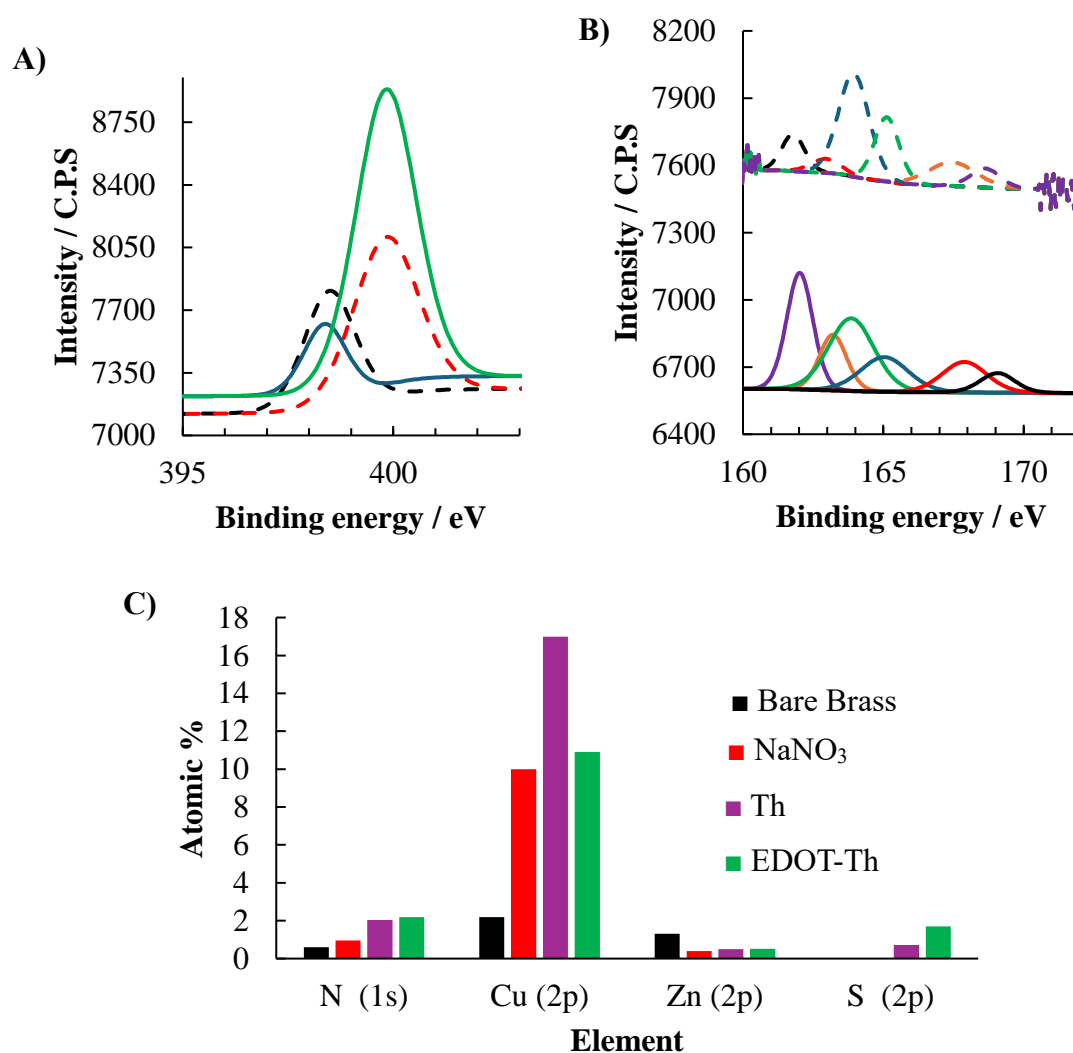


Figure 6.8: XPS graphs from brass surface following cyclic voltammetry over the potential range -0.2 to +0.5 V vs. Ag|AgCl at 50 mV.s⁻¹ for three cycles in 0.1 M NaNO₃ with EDOT-Th (solid lines) and Th (dashed lines), showing the binding energies of A) Nitrogen and B) Sulphur. C) Histogram showing the elemental % atomic quantification at surface for untreated brass (black) and brass surface following cyclic voltammetry over the potential range -0.2 to +0.5 V vs. Ag|AgCl at 50 mV.s⁻¹ for three cycles in 0.1 M NaNO₃ (red), 2 mM Th (purple) and EDOT-Th (2:1 mM)(green).

Table 6.3: Identity of some sulphur binding energies found with Th and EDOT-Th deposition layers on a brass surface.

Binding Energy	Spectral Line	Identity	Reference
161.8	2p _{3/2}	Sulphide - CuS	18
161.9	2p _{3/2}	Sulphide - ZnS	19
162.0	2p _{3/2}	Sulphide - CuS	20
163.1	2p _{1/2}	CuFeS ₂	21

6.4.2 Potentiostatic Methods for Finger-mark Visualisation

In the previous sections, successful visualisation was achieved with the cyclic voltammetric methods. However, the proposition of a simplified method of visualisation would appeal more to forensic professionals, which in turn would require less complex instrumentation. A method which can be attractive to forensic professionals who may not have experience in electrochemistry is advantageous. Hence, a potentiostatic method where $E_{app} = 0.5$ V was employed with subsequent investigations below.

This potential (0.5 V vs. Ag|AgCl) was selected as it was the maximum potential reached in the cathodic sweep of the cyclic voltammetric methods. A brass surface, without a latent finger-mark, was then held at 0.5 V in solutions of NaNO₃, Th and EDOT-Th until charges of 1, 5 and 10 C were passed (**Figure 6.9**).

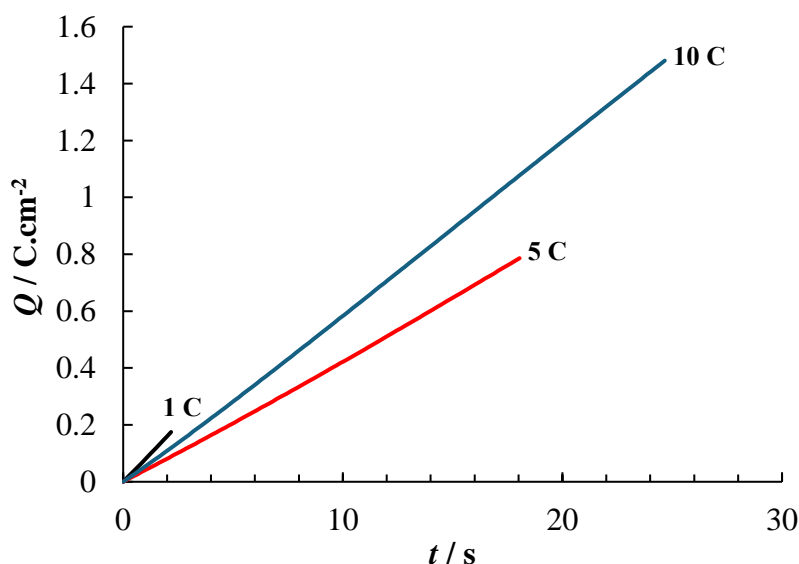


Figure 6.9: Charge density vs. time plot for brass sheets held at $E_{app} = +0.5$ V vs. Ag|AgCl in 1 mM Th with 0.1 M NaNO₃ until a charge of 1 (black), 5 (red) and 10 (blue) C was reached.

In **Table 6.4** the results of the investigation are displayed, with a clear indication that a charge of 1 C does not change the surface enough while 10 C induces loosely bound material to the brass surface which may hinder visualisation of a latent finger-mark.

Table 6.4: Data from survey of $E_{app} = 0.5 V$ at brass sheets in different visualisation solutions.

NaNO₃			
Charge (C)	Maximum Charge Density (C.cm⁻²)	Time to reach Charge (s)	Surface description
1	0.174	4.44	Mild colour change on surface easily removed.
5	0.836	26.53	Strong colour change on surface with no change in surface texture
10	1.657	10.37	Deep colour change on surface, with increase of texture and easily removable material.
Thionine Acetate			
Charge (C)	Maximum Charge Density (C.cm⁻²)	Time to reach Charge (s)	Surface description
1	0.179	2.18	Mild colour change on surface easily removed
5	0.786	18.05	Strong colour change on surface with no change in surface texture
10	1.481	24.66	Deep colour change on surface, with increase of texture and easily removable material.
EDOT-Th			
Charge (C)	Maximum Charge Density (C.cm⁻²)	Time to reach Charge (s)	Surface description
1	0.015	3.53	Mild colour change on surface easily removed
5	0.759	13.98	Strong colour change on surface with no change in surface texture
10	1.666	27.79	Deep colour change on surface, with increase of texture and easily removable material.

It was concluded that films formed upon passage of 5 C resulted in the most successful deposition of material, with minimal damage to the brass surface. To further optimise the deposition parameters, films formed via 4, 5 and 6 C were selected to observe the effect they had on visualisation quality of latent finger-marks on the brass sheets.

In the solution of NaNO_3 at 4 C (**Figure 6.10 (A)**) an even coverage was seen across the bare surface, ridge detail was clear with a purple/blue hue seen between the ridges. Using dark field polarisation, the clarity of the pores was more pronounced within the ridges, however, they were larger in size than expected. Using 5 C (**Figure 6.10 (B)**) the bare surface appeared more textured than previously observed at 4 C, a blue hue was observed between the ridge details and indicative pores (level 3) were observed within the ridges. This was also evident in the dark field polarisation images, which made the ridges and troughs appear much more defined. At 6 C (**Figure 6.10 (C)**) the surface was much more highly textured, with instances of what appeared to be material agglomerated onto the surface. The ridge details appeared to show a purple/red hue within the trough and in both the regular and dark field polarisation images. The pores within the ridges appeared to “bleed” to a large degree, particularly at the upper end of the core feature imaged, losing some of the clarity which would have been expected with these level 3 features.

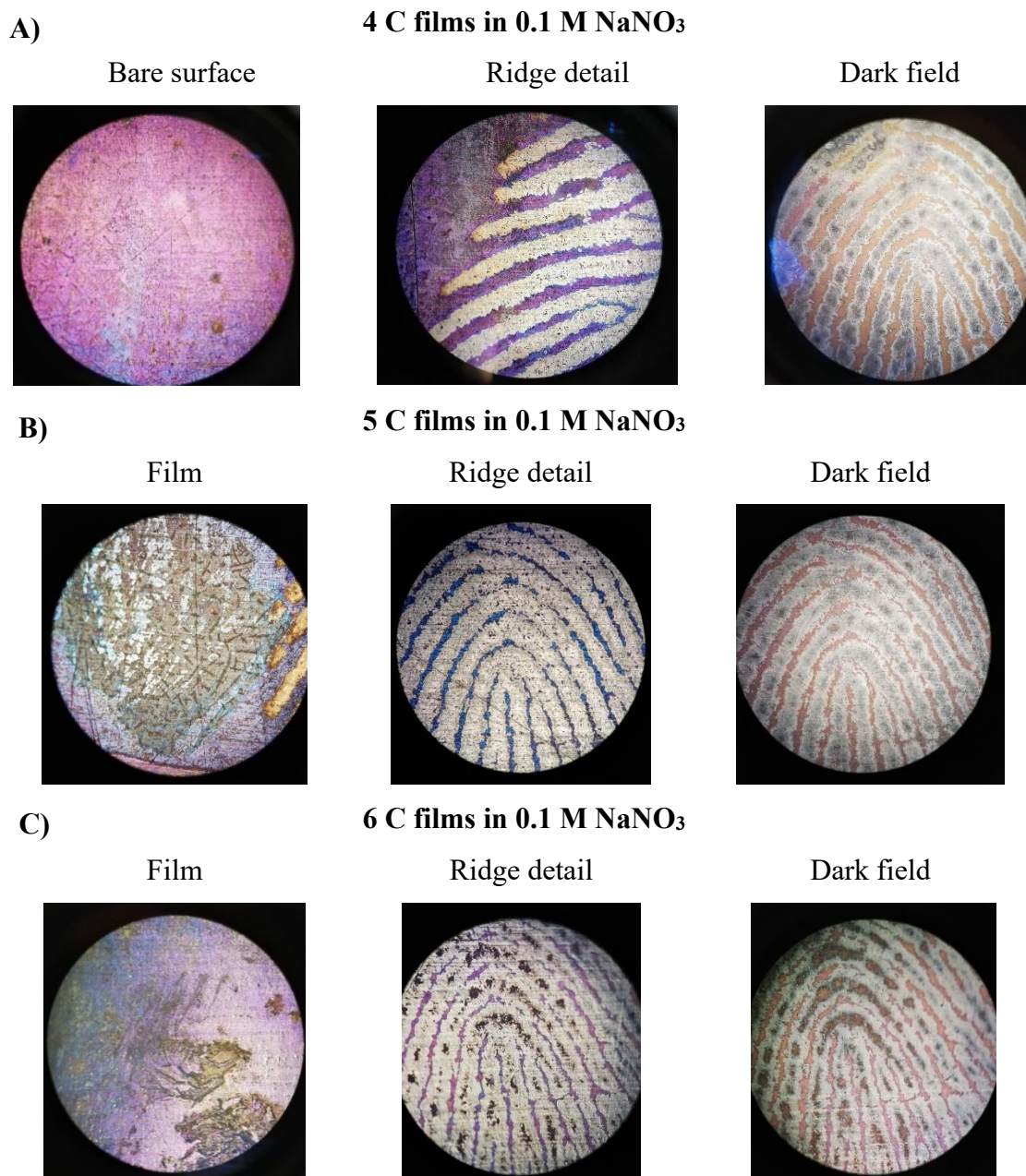


Figure 6.10: Photographs $\times 100$ magnification of untouched surface, ridge details and dark field of a visualised latent finger-mark visualised upon $E_{app} = +0.5 V$ vs. $Ag|AgCl$ in $0.1 M NaNO_3$ until a charge of A) 4, B) 5 and C) 6 C was reached.

When visualised in the Th solution, following the passing of 4 C (**Figure 6.11 (A)**) the bare surface was uniform, like that observed in the $NaNO_3$. The detail between the ridges appeared with a purple/blue hue and the pores within the ridges appeared to “bleed” into each other, almost making it appear as if the ridges were hollow channels. In the case of 5 C films (**Figure 6.11 (B)**), the bare surface did appear to have an even coverage with some instances of material agglomerated across the surface. The ridge detail showed a

much more defined distance between the ridges than observed in the case of 4 C, however, there was a loss of some definition in the pore shapes along the ridges. Passage of 6 C (Figure 6.11 (C)) produced a highly textured surface, which could be described as “rough”. Definition between the ridges were very clear and defined, however, pore features along the ridges were not observed.

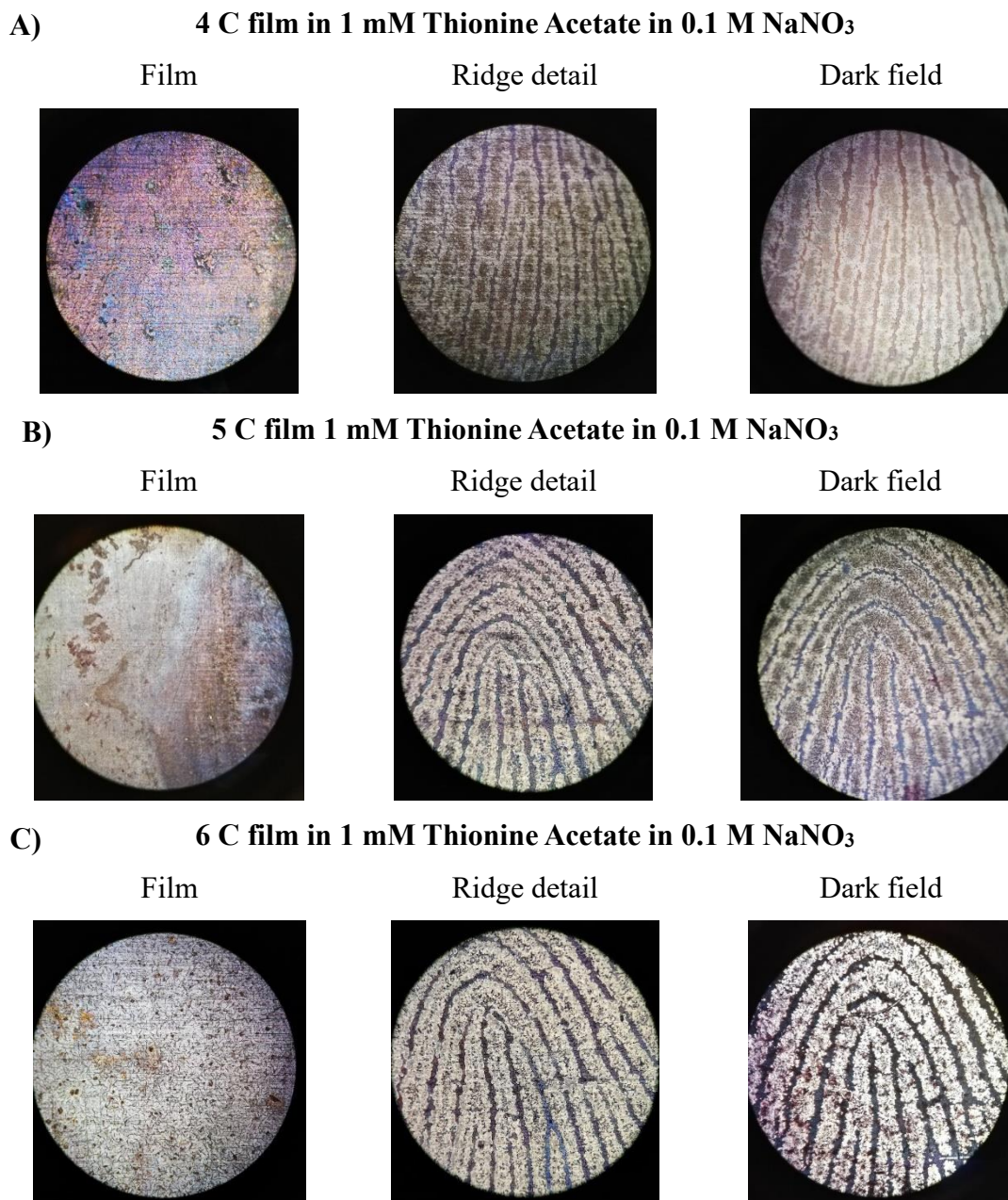
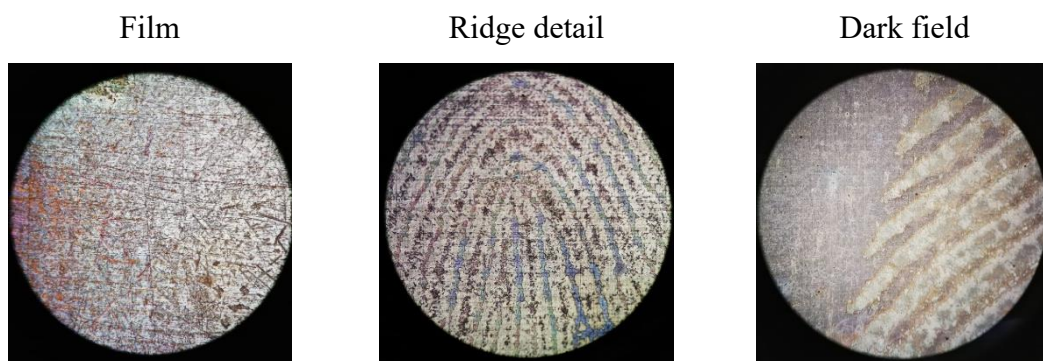


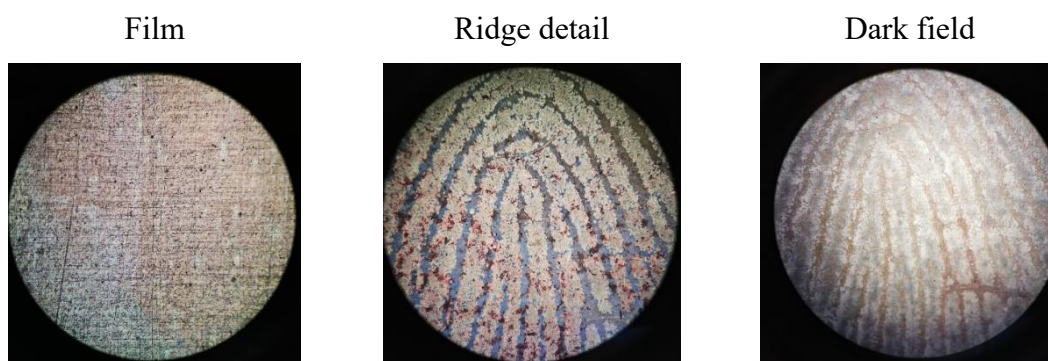
Figure 6.11 Photographs $\times 100$ magnification of untouched surface, ridge details and dark field image of a visualised latent finger-mark visualised with $E_{app} = +0.5$ V vs. Ag|AgCl in 1 mM Th in 0.1 M NaNO₃ until a charge of A) 4, B) 5 and C) 6 C was reached.

The final solution of EDOT-Th produced an even coverage at the bare surface for all charge values tested. Development of ridges using 4 C (**Figure 6.12 (A)**), appeared successfully defined, with a blue hue observed between the ridges and indicative presence of pores within the ridges. In the case of 5 C (**Figure 6.12 (B)**) this produced excellent definition between the ridges, with indicative pores, while also introducing a red hue across the defined ridge detail. The implementation of 6 C films (**Figure 6.12 (C)**), produced ridges, from which the general shape of the detail could be obtained, however, clear definition between the ridges was not visible. Extensive bleeding of the pores was also observed along the ridge pattern.

A) 4 C film in 1 mM Thionine Acetate and 2 mM EDOT in 0.1 M NaNO₃



B) 5 C film in 1 mM Thionine Acetate and 2 mM EDOT in 0.1 M NaNO₃



C) 6 C film in 1 mM Thionine Acetate and 2 mM EDOT in 0.1 M NaNO₃



Figure 6.12 Photographs x100 magnification of untouched surface, ridge details and dark field image of a visualised latent finger-mark visualised with $E_{app} = +0.5 V$ vs. Ag|AgCl in 2 mM EDOT with 1 mM Th in 0.1 M NaNO₃ until a charge of A) 4, B) 5 and C) 6 C charge was reached.

Throughout the results of this constant potential study, use of a charge of 5 C appeared to be the most successful cutoff point, while once more, EDOT-Th produced the clearest visualisation of the ridge detail within the finger-mark. While still not achieving the clarity observed with some of the cyclic methods, the indicative pores would be deemed successful for individual matching purposes, although diameter could not be used as a comparative aspect.

While the simplification of the method appeared to be successful, upon application of 0.5 V, some gaseous release was observed at the counter electrode, with the possibility of bubble adsorption to the brass surface. This can decrease the effectiveness of the finger-mark visualisation, as the bubbles would leave circular areas on the surface which did not undergo visualisation.

Applied potentials of 0.25 and 0.1 V were thus examined for $t = 60$ seconds, to observe whether gaseous production at the counter electrode diminished while simultaneously achieving successful visualisation of a latent finger-mark.

In **Figure 6.13** a latent finger-mark, visualised at $E_{app} = 0.25$ V for 60 seconds in the EDOT-Th solution is shown. The method produced a finger-mark with level 2 details present and a highly contrasted finger-mark, comparative to the deposited material. Unfortunately, gaseous release still occurred at the counter electrode, and therefore the potential was lowered further to 0.1 V.



Figure 6.13: Photograph and high contrast image of latent finger-mark on a brass surface visualised in 2 mM EDOT and 1 mM Th in 0.1 M NaNO₃ at $E_{app} = +0.25$ V vs. Ag|AgCl for 60 s.

When initially holding at $E_{app} = 0.1$ V for 60 seconds, minimal visualisation occurred, however, the indicative presence of a latent finger-mark and no gaseous generation at the counter electrode prompted lengthening the time as a next step. In **Figure 6.14** latent finger-marks visualised after $E_{app} = 0.1$ V for 120 seconds are shown, with clearly defined ridge details and level 2 features across the entire finger-mark.



Figure 6.14: Photograph and high contrast image of a latent finger-mark on a brass surface visualised in 2 mM EDOT and 1 mM Th in 0.1 M NaNO₃ at $E_{app} = +0.1$ V vs. Ag|AgCl for 120 s.

With the successful decrease in applied potential and removal of gaseous production at the counter electrode, the method was repeated in just the supporting electrolyte 0.1 M NaNO₃ to ensure that the EDOT-Th did in fact play a role in the successful visualisation of the latent finger-mark (**Figure 6.15**). While successful visualisation did occur, it was clear that the contrast between the visualised finger-mark and the brass surface was not as clear as when visualised in the solution of EDOT-Th. This resulted in level 2 features, however, appearing more fragmented with less contrast before colour corrections were applied.



Figure 6.15: Photograph and high contrast image of a latent finger-mark on a brass surface visualised in 0.1 M NaNO₃ at $E_{app} = +0.1$ V vs. Ag|AgCl for 120 s.

Throughout the entire process, the monomer combination of EDOT-Thionine acetate resulted in the most reproducible visualisation of the highest quality, with an average of

level 2.3 details being observed across multiple finger-mark visualisations. This was the selected solution for further analysis with more challenging latent finger-mark samples.

6.4.3 Visualisation of Analogous Real Case Latent Finger-marks

With all practical research, the end goal or “use case” must be kept at the forefront of the mind when examining samples. Unfortunately, the scope of this work did not allow for the application of a latent finger mark to live ammunition and subsequent firing to observe the efficacy of the visualisation methods proposed.

To understand the robustness of the method proposed, samples had to be degraded by influential parameters which forensic professionals may come across in their professional lives. As mentioned previously in the introduction, two of the factors which may hinder the visualisation methods are the time or age of the latent finger-mark on the surface, and the potential degradation of the sample due to the heat experienced during the discharge of the firearm.

6.4.3.1 Visualisation of Aged Finger-marks

With nearly all analytical forensic techniques, the time that has passed between the “event” and the analysis is a major contributing factor to the efficacy of the method. Natural degradation, contamination, dilution and destruction of evidence all increase in likelihood the longer it takes a sample to be analysed. One aspect examined was the natural degradation of the sample, as latent finger-marks were applied to brass surfaces and stored at room temperature in a dark and dry place for two distinct time periods i.e. 5 and 16 months.

Finger-marks were supplied by eight donors (taken at random due to availability) and two samples were obtained from each donor, a “natural” finger-mark which was acquired from the donors’ hand when asked to supply the mark and a subsequent groomed finger-mark. These finger-marks were obtained from both male and female donors, as it is observed that female finger-marks are more difficult to visualise than males. This is due, in part, to the general size difference in the hands of both and subsequent increase in ridge density compared to male hands²². This in turn makes the area available for deposition of material smaller and likelihood for smudging of the finger-mark higher.

Finger-marks stored for 5 months were applied via the split print method, in total 8 donors submitted marks which were then visualised via the potentiostatic method of $E_{app} = 0.1$ V for 120 s (**Figure 6.16**).

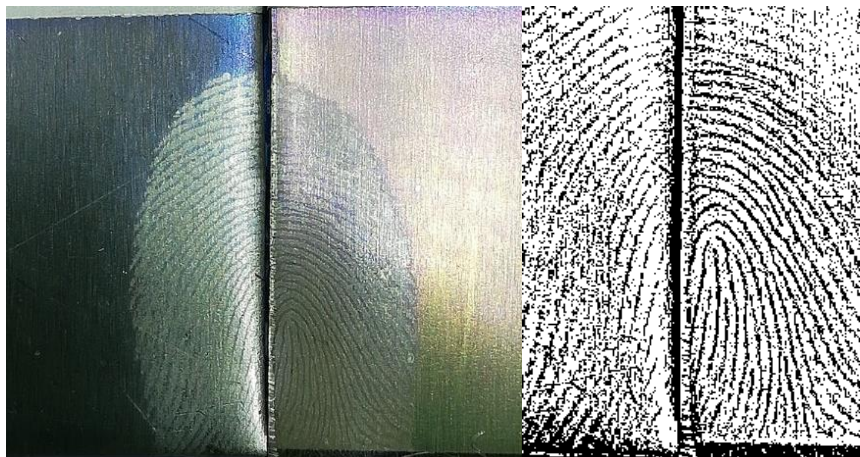


Figure 6.16: Photograph and zoomed in high contrast image of visualised 5-month-old groomed latent finger-mark at $E_{app} = +0.1$ V vs. Ag|AgCl for 120 s split across two brass sheets showing, left visualised in 0.1 M NaNO₃ and right visualised in 2 mM EDOT with 1 mM Th in 0.1 M NaNO₃.

Table 6.5 shows the level of features obtained from the visualised aged finger-marks. Comparatively, electrolyte alone achieved an average level feature of 2.25 while the EDOT-Th solution observed an average level feature of 2.38. While the average level features observed for both solutions was quite similar, the solution of EDOT-Th never fell below level 2 and boasted the greatest number of clear level 3 presence within the visualisation of the latent finger-marks.

Table 6.5: Level features observed from visualisation of 5-month-old latent finger-marks.

<i>Donor</i> (Male(M)/Female (F))	Visualisation with NaNO ₃ (level features obtained)	Visualisation with EDOT-Th (level features obtained)
1 (M)	2.5	2
2 (M)	2-3	3
3 (F)	2	2
4 (M)	2	2
5 (M)	2.5	3
6 (M)	3	2.5
7 (F)	1.5	2
8 (M)	2	2.5
<i>Total average visualisation</i>	2.25	2.38

With successful finger-mark visualisation observed at this time point, the next time point of interest was 16 months. **Figure 6.17** shows natural and groomed prints visualised with the EDOT-Th solution. Aged latent finger-marks were successfully visualised both in the groomed and natural forms from male and female donors. Level 2 features were observed in all cases, with indicative level 3 features observed in the natural male finger-mark (**Figure 6.17 (A)**) and groomed female finger-mark (**Figure 6.17 (D)**).

Comparatively, at the 16-month time point the visualisation performed in NaNO₃ alone, did not produce a single instance of level 3 features within the visualised finger-marks, with a single instance of unsuccessful visualisation. However, this unsuccessful visualisation was with a “natural” finger-mark, and the donor may have been a poor producer of latent finger-marks.

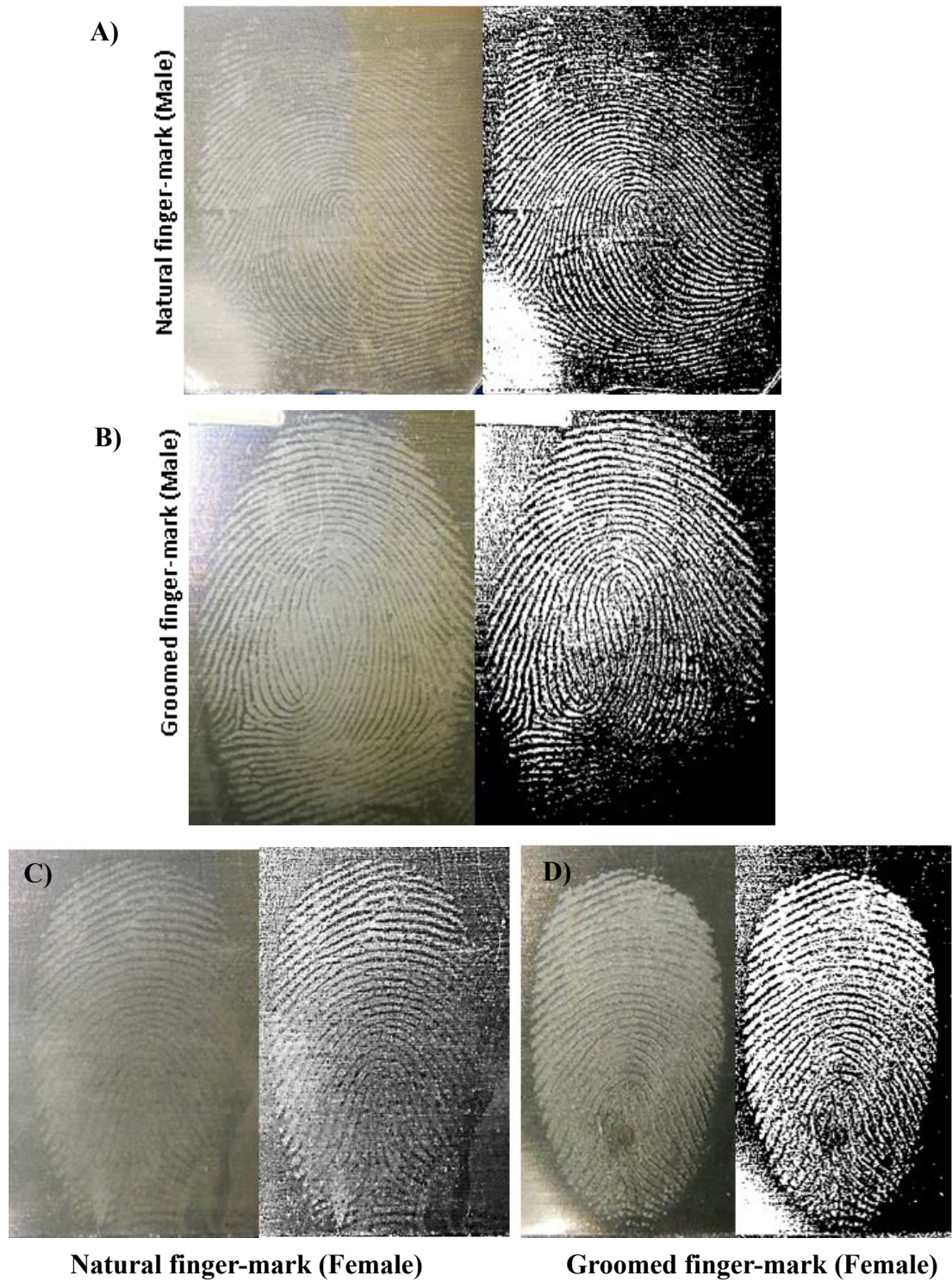


Figure 6.17: Natural (A and C) and groomed (B and D) 16-month-old latent finger-marks on a brass surface visualised in 2 mM EDOT with 1 mM Th in 0.1 M NaNO₃ at $E_{app} = +0.1$ V vs. Ag|AgCl for 120 s.

Table 6.6: Level features observed from visualisation of 16-month-old latent finger-marks

Finger-Mark	Visualisation Solution	Apparent Level of Detail
<i>1 – Male, Natural</i>	NaNO ₃	2
<i>2 – Male, Groomed</i>	EDOT-Th	2-3
<i>3 – Female, Natural</i>	EDOT-Th	2
<i>4 – Female, Groomed</i>	NaNO ₃	2
<i>5 – Male, Natural</i>	EDOT-Th	2-3
<i>6 – Male, Groomed</i>	NaNO ₃	2
<i>7 – Female, Natural</i>	NaNO ₃	0-1
<i>8 – Female, Groomed</i>	EDOT-Th	2-3

The time allotted for “aged” finger-marks on brass vary a great deal in the literature, with successful visualisation reported via electrostatic adsorption of finger-marks on ammunition casings which were 10 days old²³, cyanoacrylate fuming for natural and groomed prints which were 2 weeks old²⁴ and silver electroless deposition on 6-week-old finger-marks²⁵. Lam et al. reported successful visualisation on a 22-week-old latent finger-mark on ammunition casings via disulphur dinitride fuming.

Using electrochemical methods, Costa et al. reported successful finger-mark visualisation up to 30 days for sebaceous marks and 15 days for eccrine marks with a constant potential method of $E_{app} = 0.9 \text{ V}$ for 180 s⁵. The work presented in this thesis shows some of the longest aged latent finger-marks (both groomed and natural) visualised by electrochemical means when compared with current literature.

6.4.3.2 Visualisation of Heat-Treated Finger-marks

While the heat generated from the discharge of a firearm varies significantly depending on size and power of the firearm used, studies performed on small calibre firearms (which would be more likely for street level crimes), can achieve temperatures of approximately 540 °C within the bore of the firearm²⁶. These temperatures could increase greatly if an automatic weapon was employed, with multiple rounds being fired in a short period of time. Anecdotally, temperatures of 260 °C have been observed within bullets being fired, however, stringent testing on these temperatures have not been performed. Regardless of this, temperatures of approximately 600 °C can be expected at the surface of the ammunition casing for smaller calibre weapons with little change to the brass surface composition (**Figure 6.18**), which will eventually cool over time. The initial explosion of a the propellant lasts <1 ms, however, to fully stress test the latent finger-marks much greater time periods were employed in this work.

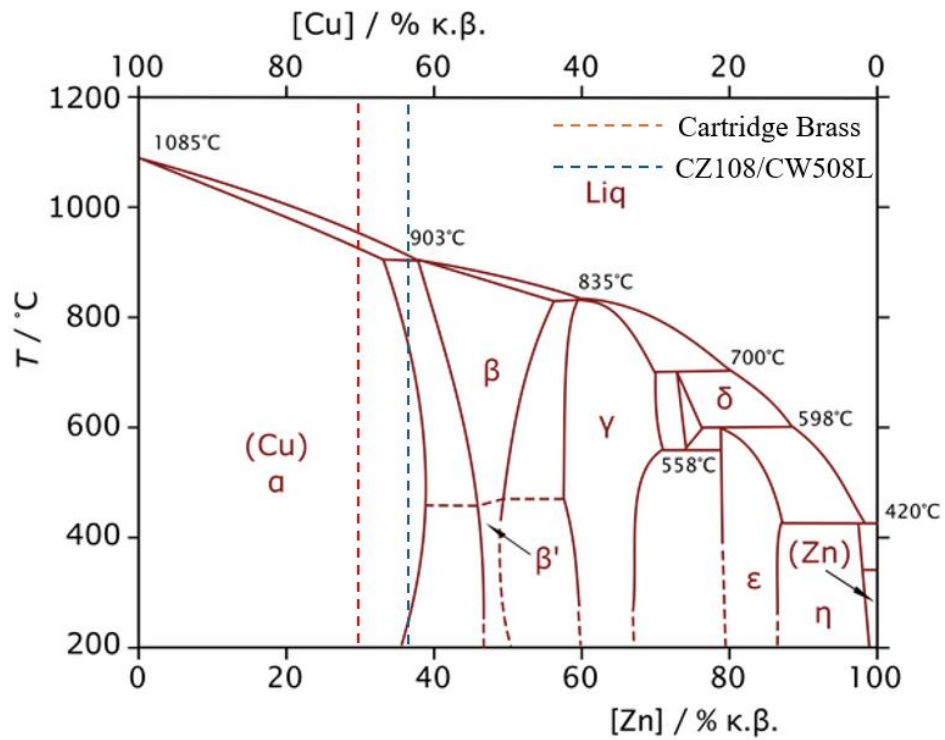


Figure 6.18: Phase diagram for brass with different compositions of copper and zinc, indicating both types of brass used within this work.

Groomed sebaceous latent finger-marks and groomed eccrine finger-marks were employed within the temperature study, however, only the sebaceous finger-marks were successfully visualised. This may be due in part to the high-water content which would be present within eccrine sweat, meaning that all the material was removed from the surface of the brass due to the high heat.

Initially latent finger-marks ($n=4$) were held at 100 °C for 25 minutes. This was carried out to ensure that all the water present within the finger-mark was removed. **Figure 6.19** shows a visualised finger-mark, where there was a lack of clear contrast to the ridges and troughs within the finger-mark observed under these conditions. The length of time employed may have allowed the sebaceous material to spread out slightly thus deforming the tight ridge lines and decreasing the space between the ridges. Regardless of this issue, level 2 features were still visible within the finger-marks, which, with enough points of comparison, would still allow for a match with a reference finger-mark.



Figure 6.19: Photograph and high contrast image of latent finger-mark visualised in 2 mM EDOT with 1 mM Th in 0.1 M NaNO₃ at $E_{app} = +0.1$ V vs. Ag|AgCl for 120 s post heating to 100 °C for 25 minutes.

The next temperature employed was 300 °C, with successful visualisation obtained up to level 2 (**Figure 6.20**) features in all samples ($n=4$). The shorter time employed than the previous temperature allowed for the visualised finger-marks to regain the clear definition between the ridges.



Figure 6.20: Photograph and high contrast image of latent finger-mark visualised in 2 mM EDOT with 1 mM Th in 0.1 M NaNO₃ at $E_{app} = +0.1$ V vs. Ag|AgCl for 120 s post heating to 300 °C for 0.5 minutes.

The final temperature which was employed was 700 °C. This temperature visually altered the brass surface before visualisation to a silver colour. Observationally, temperatures of the furnace dropped dramatically when the door was open while placing the samples within; in some instances, the temperature would drop to 690 °C. In those instances, the silver colour at the surface was not achieved, and so it appears that brass can be annealed at temperatures of 700 °C, a process which was employed to change the structure of the brass to make it stronger. When samples were correctly heated to 700 °C, it is assumed that a structural change at the upper surface of the brass occurred with this partial annealing process changing the brass. Latent finger-marks were not visible once the sample was removed from the furnace, however, potentiostatic visualisation produced visualised latent finger-marks as shown in **Figure 6.21**

Finger-marks of clear level 2 features were achieved three times, while in one instance an indicative finger-mark was observed which would not even be classified as level 1 features, as the overall shape of the finger-mark was unclear.

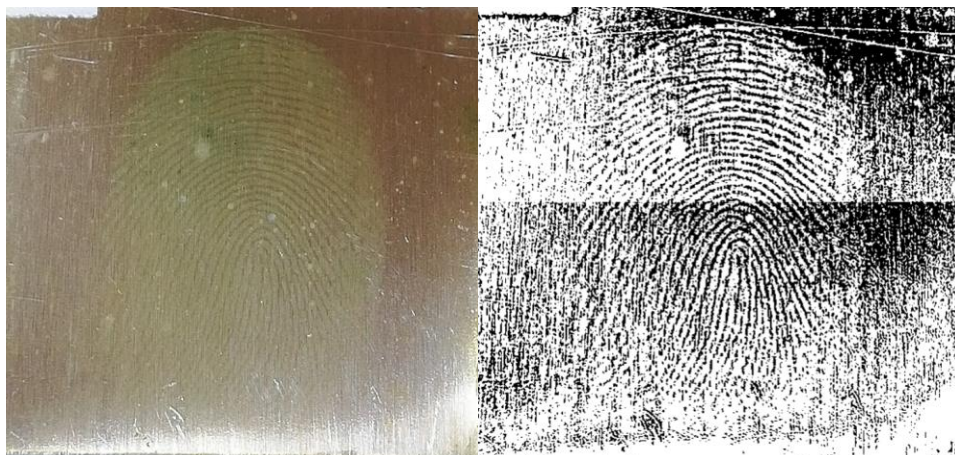


Figure 6.21: Photograph and high contrast image of latent finger-mark visualised in 2 mM EDOT with 1 mM Th in 0.1 M NaNO₃ at $E_{app} = +0.1$ V vs. Ag|AgCl for 120 s post heating to 700 °C for 0.5 minutes.

Table 6.7: Overview of level features achieved from heat treated latent finger-marks on brass.

Temperature Held at	Time held for	Level features achieved				Avg. Level of features
100 °C	25 minutes	1-2	2	2	2	1.88
300 °C	0.5 minutes	1-2	1-2	2	2	1.75
700 °C	0.5 minutes	0-1	1-2	2	2	1.50

Temperature degradation studies of latent finger-marks have been reported in the literature in a wide variety of scenarios. Latent finger-marks on the surface of lightbulbs which were allowed reach temperatures of 156.3 °C have been successfully visualised with black powders²⁷. Bleay et al. reported successful visualisation of latent finger-marks on brass via cyanoacrylate fuming with basic yellow 40 dye and gun blueing methods after reaching temperatures of 600 °C for 5 minutes²⁸. The application of high temperatures to metal surfaces has also been investigated as a visualisation technique, using the protective nature of the latent finger-mark to hinder surface oxidation creating a contrast at the metal surface. There have also been reports of enhanced visualisation of a grade 2 finger-marks on a brass surface heated to 600 °C²⁹. Girelli et al. performed an intensive investigation into the visualisation of latent finger-marks on ammunition casing which had fired with the mark present before firing, using brass sheets heated to 200 °C as the control, reporting successful visualisation with a cyanoacrylate, gun blueing and fluorescent dye method for groomed prints applied to both surfaces³⁰. To our knowledge

there are no reports in the literature of electrochemical methods used to develop heat degraded latent finger-marks on a metallic surface. Overall, finger-marks were visualised up to the temperatures expected during firing of ammunition.

Across multiple types of challenging finger-mark samples, EDOT-Th was successful in generating visualised finger-marks of high quality via a potentiostatic approach with $E_{app} = 0.1$ V for 120 seconds. In the case of data generated it is understood that there is an inherited variability to the deposition of these finger-marks, due to numerous factors, mainly the donors. Some people are just naturally better at producing latent finger-marks, or one may deposit a “better” finger-mark once and subsequently have the quality of the mark drop on subsequent depositions. However, this study is an important stepping stone towards the validation of this methodology.

6.4.4 Visualisation of Finger-marks on Ammunition Casings

While a potentiostatic method was optimised for brass strips, it is important to note that the composition of cartridge brass differs slightly from the CZ108/CW508L utilised in previous studies. To gain a comprehensive understanding of influence of the ammunition casing, both cyclic voltammetric methods and potentiostatic techniques were employed.

Given the success of the EDOT-Th solution with brass strips, this solution was selected for the studies involving ammunition casings. The change in surface curvature prompted the incorporation of additional grading vectors in the assessment of visualised finger-marks on ammunition casing surfaces. This adjustment was necessary due to the higher likelihood of smudging on the curved surface compared to the flat brass surface.

Furthermore, considering the method of application, two finger-marks were applied to the ammunition casing, as illustrated in **Scheme 6.2**. In all instances successful visualisation was closely linked to the proximity to the counter electrode; however, partial visualisations were achievable in some instances.

6.4.4.1 Electrochemistry of Brass Ammunition Casings

In a continuation with the previously successful visualisation method, a potentiostatic method with $E_{app} = 0.1$ V for 120 seconds was employed for groomed latent finger-marks on a brass ammunition casing surface. In **Figure 6.22** a representative finger-mark was observed, of grade 3 containing level 2 features. **Table 6.8** shows the quality of prints produced ($n=4$). Overall, the potentiostatic method of $E_{app} = 0.1$ V, was successful in the visualisation of the finger-marks. However, level 3 features were not visualised within any of the replicates.

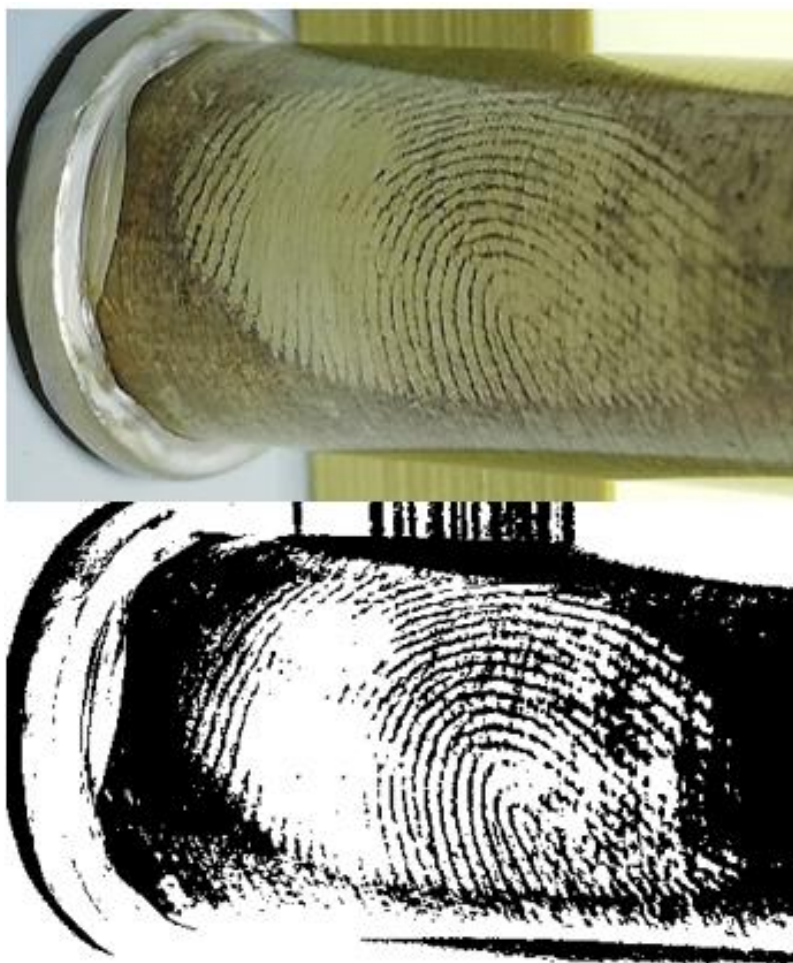


Figure 6.22: Photograph and high contrast image of latent finger-mark on a brass ammunition casing visualised at $E_{app} = +0.1$ V vs. Ag|AgCl for 120 s in 2 mM EDOT with 1 mM Th in 0.1 M NaNO₃.

Table 6.8: Results of replicates of visualisation in EDOT-Th solution with $E_{app} = 0.1$ V for 120 s.

Visualisation	Observed Grade	Observed level of detail
1	3	2
2	2	1.5
3	3	2
4	3	2

In order to establish whether level 3 features could be observed within visualised finger-marks on brass ammunition casings, the previously successful method of cyclic voltammetry was employed. Initial methods across the range of -0.2 to 0.5 V at $50 \text{ mV}\cdot\text{s}^{-1}$ employed 3 cycles for successful visualisation. However, initial exploration with this method, revealed partially visualised finger-marks, with little contrast between the brass surface and the finger-mark. To improve contrast, an increase in the number of cycles was examined (from 3 to 6 cycles), aligned with the doubling of time which proved beneficial for the potentiostatic method at 0.1 V. Upon changing this condition, some of the most impressive, visualised finger-marks were observed. In **Figure 6.23** a latent finger-mark visualised in a solution of EDOT-Th over the potential range -0.2 to 0.5 V at $50 \text{ mV}\cdot\text{s}^{-1}$ for 6 cycles is shown. Within this mark of clear grade 4, level 3 features were observed across the entire finger-mark. Pore details along the ridge structures are clear, even with the coloured photograph without the need for colour manipulation.

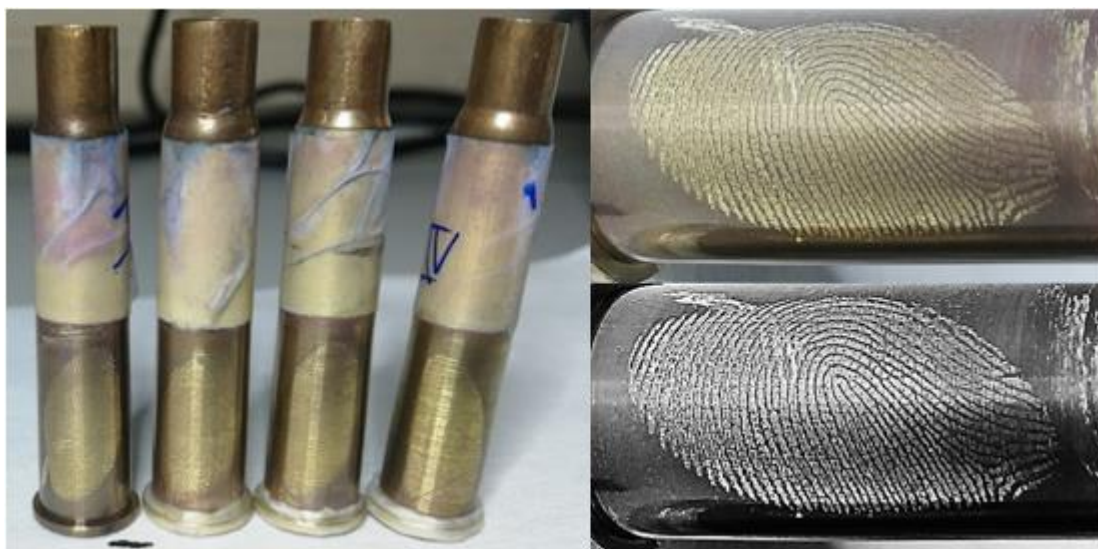


Figure 6.23: Visualised latent finger-mark on ammunition casing using cyclic voltammetry over the potential range of -0.2 to $+0.5$ V vs. $Ag|AgCl$ at $50\text{ mV}\cdot\text{s}^{-1}$ for 6 cycles in 2 mM EDOT with 1 mM Th in 0.1 M $NaNO_3$.

Successful visualisation was even observed with the secondary finger-mark on the casing (thumb print on opposite side of index print). In **Table 6.9** the visualising results within replicates ($n=4$) are presented. High quality visualised finger-marks were observed across all replicates, indicating that the method employed was extremely successful in the visualisation of these latent finger-marks.

Table 6.9: Results of replicates of visualisation in EDOT-Th solution via cyclic voltammetry.

Visualisation	Observed Grade	Observed level of detail
1	4	3
2	4	2-3
3	4	2-3
4	3	2

Owing to the constrained supply of ammunition casings, it was not feasible to conduct an in-depth study as originally intended. However, a visualised finger-mark of the highest possible quality was obtained from the cyclic voltammetric method conducted on the surface of brass ammunition casings. The findings presented here represent highly

encouraging initial steps towards the complete development of a rapid latent finger-mark visualisation technique.

6.5 Conclusion

Various electrochemical methods were employed to visualise latent finger-marks on a diverse range of brass surfaces. The study focused on solutions containing EDOT, thionine acetate, and neutral red, as well as their combinations, to assess their efficacy in revealing latent finger-marks on brass. The results indicated that the EDOT-Th solution emerged as the most reliable, consistently revealing latent finger-marks at level 3 features, including the pores within the ridges.

Significantly, to our knowledge, this study is the first instance of electrochemically polymerising thionine, and consequently, the EDOT-Th mixture onto the surface of brass. In summary, successful visualisation of latent finger-marks, encompassing grade 4 and level 3 features, was achieved on the surfaces of brass ammunition casings through electrochemical methods. Even the slowest methodology implemented in this study yielded successful visualisation within 168 seconds.

Both natural and groomed finger-marks, aged up to 16 months, were effectively visualised on brass surfaces, displaying level 3 features. Crucially, for the intended end application, finger-marks subjected to a temperature of 700 °C were successfully visualised at level 2 features, overcoming challenges posed by brass annealing temperatures and potential structural alterations to the surface.

This research has demonstrated the establishment of a rapid and low-potential visualisation method for latent finger-marks deposited on brass surfaces, requiring no sample preparation. Nevertheless, further scrutiny of the sample type, particularly ammunition casings, is recommended for comprehensive analysis and application.

6.6 References

- (1) Bond, J. W. Imaging Fingerprint Corrosion of Fired Brass Shell Casings. *Review of Scientific Instruments* **2009**, *80* (7), 075108. <https://doi.org/10.1063/1.3183578>.
- (2) Bond, J. W. Visualization of Latent Fingerprint Corrosion of Metallic Surfaces. *Journal of Forensic Sciences* **2008**, *53* (4), 812–822. <https://doi.org/10.1111/j.1556-4029.2008.00738.x>.
- (3) Bond, J. W. Effect That the Relative Abundance of Copper Oxide and Zinc Oxide Corrosion Has on the Visualization of Fingerprints Formed from Fingerprint Sweat Corrosion of Brass. *Journal of Forensic Sciences* **2011**, *56* (4), 999–1002. <https://doi.org/10.1111/j.1556-4029.2011.01759.x>.
- (4) Sykes, S.; Bond, J. W. A Comparison of Fingerprint Sweat Corrosion of Different Alloys of Brass. *Journal of Forensic Sciences* **2012**, *58* (1), 138–141. <https://doi.org/10.1111/j.1556-4029.2012.02300.x>.
- (5) Costa, C. V.; Assis, A. M. L.; Freitas, J. D.; Tonholo, J.; Ribeiro, A. S. A Low-Potential Electrochemical Method for Fast Development of Latent Fingerprints on Brass Cartridge Cases by Electrodeposition of Poly(3,4-Ethylenedioxythiophene). *Nano Select* **2020**, *1* (4), 405–412. <https://doi.org/10.1002/nano.202000040>.
- (6) Brown, R. M.; Hillman, A. R. Electrochromic Enhancement of Latent Fingerprints by Poly(3,4-Ethylenedioxythiophene). *Physical Chemistry Chemical Physics* **2012**, *14* (24), 8653–8661. <https://doi.org/10.1039/C2CP40733G>.
- (7) Beresford, A. L.; Hillman, A. R. Electrochromic Enhancement of Latent Fingerprints on Stainless Steel Surfaces. *Analytical Chemistry* **2010**, *82* (2), 483–486. <https://doi.org/10.1021/ac9025434>.
- (8) Lam, R.; Hockey, D.; Williamson, J.; Hearn, N. G. R. Latent Fingermark Development on Fired and Unfired Brass Ammunition under Controlled and Blind

- Conditions. *Forensic Science International* **2022**, 337, 111369. <https://doi.org/10.1016/j.forsciint.2022.111369>.
- (9) Broncová, G.; Tereza Slaninová; Miroslava Trchová. Characterization of Electrochemically Visualized Latent Fingerprints on the Steel Substrates. *Journal of Solid State Electrochemistry* **2022**, 26 (11), 2423–2433. <https://doi.org/10.1007/s10008-022-05245-4>.
- (10) Broncová, G.; Slaninová, T.; Trchová, M.; Prokopec, V.; Matějka, P.; Shishkanova, T. V. Optimization of Electrochemical Visualization of Latent Fingerprints with Poly(Neutral Red) on Brass Surfaces. *Polymers* **2021**, 13 (19), 3220. <https://doi.org/10.3390/polym13193220>.
- (11) Christofidis, G.; Morrissey, J.; Birkett, J. W. Detection of Fingermarks- Applicability to Metallic Surfaces: A Literature Review. *Journal of Forensic Sciences* **2018**, 63 (6), 1616–1627. <https://doi.org/10.1111/1556-4029.13775>.
- (12) Burton, J. L.; Pye, R. J.; Brookes, D. B. Metal Corrosion by Chloride in Sweat. *British Journal of Dermatology* **1976**, 95 (4), 417–422. <https://doi.org/10.1111/j.1365-2133.1976.tb00843.x>.
- (13) Collins, K. J. The Corrosion of Metal by Palmar Sweat. *Occupational and Environmental Medicine* **1957**, 14 (3), 191–197. <https://doi.org/10.1136/oem.14.3.191>.
- (14) Stephenson, D. A.; Agapiou, J. S. *Metal Cutting Theory and Practice*, 3rd ed.; CRC Press, 2018.
- (15) Losito, I.; Cosimino Malitesta; Isabella De Bari; Cosima Damiana Calvano. X-Ray Photoelectron Spectroscopy Characterization of Poly(2,3-Diaminophenazine) Films Electrosynthesised on Platinum. *Thin Solid Films* **2005**, 473 (1), 104–113. <https://doi.org/10.1016/j.tsf.2004.07.059>.

- (16) Jayagopi Gayathri; Kumar Sangeetha Selvan; Sangilimuthu Sriman Narayanan. A Novel Sensor for the Determination of Hg²⁺ in Waters Based on Octadentate Ligand Immobilized Multi-Walled Carbon Nanotube Attached to Paraffin Wax Impregnated Graphite Electrodes (PIGE). *Journal of Solid State Electrochemistry* **2018**, 22 (9), 2879–2888. <https://doi.org/10.1007/s10008-018-3984-1>.
- (17) Pandey, I.; Bairagi, P. K.; Verma, N. Electrochemically Grown Polymethylene Blue Nanofilm on Copper-Carbon Nanofiber Nanocomposite: An Electrochemical Sensor for Creatinine. *Sensors and actuators. B, Chemical* **2018**, 277, 562–570. <https://doi.org/10.1016/j.snb.2018.09.036>.
- (18) Deroubaix, G.; Marcus, P. X-Ray Photoelectron Spectroscopy Analysis of Copper and Zinc Oxides and Sulphides. *Surface and Interface Analysis* **1992**, 18 (1), 39–46. <https://doi.org/10.1002/sia.740180107>.
- (19) Buckley, A. N.; Wouterlood, H. J.; Woods, R. The Surface Composition of Natural Sphalerites under Oxidative Leaching Conditions. *Hydrometallurgy* **1989**, 22 (1-2), 39–56. [https://doi.org/10.1016/0304-386x\(89\)90040-6](https://doi.org/10.1016/0304-386x(89)90040-6).
- (20) Nefedov, V. I.; Salyn, Ya. V.; Solozhenkin, P. M.; Pulatov, G. Yu. X-Ray Photoelectron Study of Surface Compounds Formed during Flotation of Minerals. *Surface and Interface Analysis* **1980**, 2 (5), 170–172. <https://doi.org/10.1002/sia.740020503>.
- (21) Yin, Q.; Kelsall, G. H.; Vaughan, D. J.; England, K. E. R. Atmospheric and Electrochemical Oxidation of the Surface of Chalcopyrite (CuFeS₂). *Geochimica et Cosmochimica Acta* **1995**, 59 (6), 1091–1100. [https://doi.org/10.1016/0016-7037\(95\)00026-v](https://doi.org/10.1016/0016-7037(95)00026-v).
- (22) Sharma, S.; Shrestha, R.; Krishan, K.; Kanchan, T. Sex Estimation from Fingerprint Ridge Density. A Review of Literature. *Acta Biomedica Atenei Parmensis* **2021**, 92 (5), e2021366–e2021366. <https://doi.org/10.23750/abm.v92i5.11471>.

- (23) Xu, J.; Zhang, Z.; Zheng, X.; Bond, J. W. A Modified Electrostatic Adsorption Apparatus for Latent Fingerprint Development on Unfired Cartridge Cases. *Journal of Forensic Sciences* **2016**, *62* (3), 776–781. <https://doi.org/10.1111/1556-4029.13344>.
- (24) Pitera, M.; Sears, V. G.; Bleay, S. M.; Park, S. Fingermark Visualisation on Metal Surfaces: An Initial Investigation of the Influence of Surface Condition on Process Effectiveness. *Science & Justice* **2018**, *58* (5), 372–383. <https://doi.org/10.1016/j.scijus.2018.05.005>.
- (25) Payne, I. C.; McCarthy, I.; Almond, M. J.; Baum, J. V.; Bond, J. W. The Effect of Light Exposure on the Degradation of Latent Fingerprints on Brass Surfaces: The Use of Silver Electroless Deposition as a Visualization Technique. *Journal of Forensic Sciences* **2014**, *59* (5), 1368–1371. <https://doi.org/10.1111/1556-4029.12524>.
- (26) Jacob, A. M.; Foltz, A. L.; Florio, L. *Characterization of Bore Temperatures and Stresses in Small Calibre Gun Barrels*; U.S Army Armament Research, Development and Engineering Centre, 2019; pp. 1–10.
- (27) Colella, O.; Miller, M.; Boone, E.; Buffington-Lester, S.; Curran, F. J.; Simmons, T. The Effect of Time and Temperature on the Persistence and Quality of Latent Fingerprints Recovered from 60-Watt Incandescent Light Bulbs. *Journal of Forensic Sciences* **2019**, *65* (1), 90–96. <https://doi.org/10.1111/1556-4029.14133>.
- (28) Bleay, S. M.; Kelly, P. F.; King, R. S. P.; Thorngate, S. G. A Comparative Evaluation of the Disulfur Dinitride Process for the Visualisation of Fingermarks on Metal Surfaces. *Science & Justice* **2019**, *59* (6), 606–621. <https://doi.org/10.1016/j.scijus.2019.06.011>.

(29) Wightman, G.; O'Connor, D. The Thermal Visualisation of Latent Fingermarks on Metallic Surfaces. *Forensic Science International* **2011**, *204* (1-3), 88–96. <https://doi.org/10.1016/j.forsciint.2010.05.007>.

(30) Girelli, C. M. A.; Vieira, M. A.; Singh, K.; Cunha, A. G.; Freitas, J. C. C.; Emmerich, F. G. Recovery of Latent Fingermarks from Brass Cartridge Cases: Evaluation of Developers, Analysis of Surfaces and Internal Ballistic Effects. *Forensic Science International* **2018**, *290*, 258–278. <https://doi.org/10.1016/j.forsciint.2018.07.026>.

Chapter 7: Conclusions and Future work

7.1 Conclusion:

As discussed in **Chapter 1**, current methodologies for the analysis of forensic evidence generated from the discharge of a firearm vary widely. Throughout the research presented in this thesis the development of electrochemical methods for the improvement of analysis for this type of evidence has been demonstrated within two research themes:

- The development of an electroanalytical method for the detection of organic firearms residue and,
- The development of an electrochemical method for the visualisation of latent finger-marks on brass ammunition casings.

Within the following sections general conclusions are made based on the work presented within this thesis and proposed future work which could be used for the further development of each analytical approach.

7.1.1 Development of an Electroanalytical Method for the Detection of Organic Firearms Residue

7.1.1.1 General Conclusions

Chapter 3 and **Chapter 4** described the development of an electroanalytical method for the detection of O-FAR. The studies significantly advanced our understanding of the electrooxidation of DPA and EC in both organic and aqueous electrolytes, shedding light into potential degradation products and associated processes.

The investigation revealed subsequent products, including the generation of DPB through the oxidation and subsequent dimerisation of DPA, as well as the degradation of EC to its primary amine with concurrent CO₂ release.

This research employed a novel approach, integrating Fe₃O₄ MNPs into the electrochemical study, via simple drop casting modification of the electrodes surface. The MNPs prepared through a controlled electrooxidation process and chemical co-precipitation process, were characterised comprehensively through surface, thermal, spectroscopic, and electrochemical techniques. The addition of the MNPs appeared to influence the secondary product formation processes, hindering DPB formation or adsorption to the electrode surface, as indicated by cyclic voltammetry.

With the understanding that the cyclic methods may be hindered by secondary processes, even if the processes were diminished by the MNP modification, DPV proved advantageous. In terms of sensitivity LODs and LOQs were calculated at 4.39 ± 0.28 and 14.6 ± 0.95 μM and 3.51 ± 0.15 and 11.7 ± 0.47 μM for EC and DPA respectively. It was also observed that these values changed when both analytes were present within the same matrix, with LOD and LOQ for EC and DPA found to be 4.76 ± 0.38 and 15.9 ± 1.28 μM and 3.75 ± 0.06 and 12.5 ± 0.19 μM respectively.

It was found that selectivity for the analytes with this method could be developed further for more analytes of interest within the O-FAR matrix, and the work showed that diphenyl urea and dimethyl phthalate do not overlap in terms of E_p values, with adequate resolution between the signals, indicating a clear route for further method development.

Application of the method to unburnt ammunition propellant resulted in a clear DPA presence in only 5 mg of sample, while a larger value of 32.2 mg was required for an indicative response to EC. In both cases, with the use of a standard addition method the original concentration of each analyte could be successfully estimated. This indicates that the original propellant formulation contained 1.31 % w/w of stabilisers, being within the expected range of between 1-5 %.

The method was extended to real FAR samples, which were confirmed to be genuine samples with traditional FAR analysis (SEM/EDX). These samples were found to contain DPA and EC which were quantified by the previously mentioned standard addition method.

Proof-of-principle studies with a custom-designed screen-printed electrode highlighted the potential for O-FAR electrochemical sensing with integrated electroanalysis. Selectivity and reproducibility of recovered samples resulted in intra sensor variation % RSD = 3.9 and 4.8% for the bare electrode response and 3.8 and 2.6% for the MNP modified electrodes.

The research presented in **Chapter 3** and **Chapter 4** led to the publication of two research articles, offering insights into the electrochemical behaviour of characteristic compounds in O-FAR. Notably, this research marked the first instance to our knowledge of EC being electrochemically studied in an aqueous supporting electrolyte. Furthermore, the study explored surface deposition of materials arising the analytes of interest, shedding light on

potential surface fouling issues in more complex matrices, which had not been addressed in other articles using electroanalytical methods for O-FAR analysis. Another significant milestone was the introduction of magnetic nanoparticles as a modification material for sensing O-FAR, alongside the development of *in-house* fabricated screen-printed electrodes featuring a sample well in their design. Using relatively simple electrochemical methods and the portability of screen-printed electrodes, these chapters lay the groundwork for on-site screening of FAR samples, with prospects for further advancements towards on-site quantitation.

7.1.1.2 Future work

While the work presented within this thesis, provides insight into novel avenues for electrochemically analysing O-FAR, forensic science is a strict discipline requiring methodologies with sensitivity, selectivity and robustness at their core. Before implementing the methods developed here, future work will be required.

Future experimental work should aim to further explore and refine the electrooxidation processes of DPA and EC in aqueous electrolytes. Detailed investigations into the degradation mechanisms and identification of additional by-products could provide a more comprehensive understanding of these key propellant components and possibly their nitrated derivatives in the full sample matrix. The role of MNPs in diminishing this formation should also be explored to understand if it is caused by the change in surface type or by the material itself. Exploring various electrode modification techniques and materials could help identify the most effective approaches for hindering these processes.

Enhancing the robustness of the technique is essential for its effective application. To achieve this, the introduction of additional analytes, specifically characteristic compounds like methylcentralite, nitroglycerine, nitroguanidine, 2-nitrodiphenylamine, 4-nitrodiphenylamine, 2,4-dinitrotoluene, akardite II, nitrocellulose, and other diphenylamine derivatives, is imperative. This expansion of analytes aims to determine selectivity of the method for a broader range of compounds associated with firearm discharge residue. By incorporating these additional analytes into the analytical framework, the method can be fine-tuned to detect a comprehensive set of characteristic compounds commonly found in gunshot residue. This step is crucial for building a versatile method that can analyse the diverse chemical composition of residues resulting

from firearm discharges. The objective is to establish a robust and selective method capable of identifying a spectrum of compounds associated with gunshot residue, enabling a more comprehensive forensic analysis. Selectivity is key to distinguishing between different components, and the inclusion of various characteristic compounds contributes to the development of a method with broad applicability in forensic investigations.

To further develop the method future work may also involve extending the electroanalytical method to simultaneously analyse the inorganic metallic fraction of firearm discharge residue through techniques such as stripping voltammetry. This expansion could provide a more holistic understanding of the composition of FAR. Ongoing work on MNPs in relation to metal analysis suggests promising avenues for the enhancement of screening capabilities for both inorganic and organic fractions of firearm discharge residue. Overall, the research lays a solid foundation for the electrochemical sensing of OFAR, providing insights into the redox behaviour of key propellant components at carbon and MNP-modified electrodes, with significant potential for advancing rapid on-site analysis.

However, achieving a more reproducible modification method is crucial for advancing the electroanalytical sensing of FAR. One potential avenue for improvement involves exploring the integration of MNPs with inks, developing ferrofluids tailored for printing applications. This approach would aim to enhance the consistency and reliability of the production of SPEs used in FAR sensing. Ferrofluids, which are colloidal suspensions of magnetic nanoparticles in a carrier fluid, offer unique properties that can be used for controlled and uniform deposition on electrode surfaces. Developing ferrofluids compatible with printing technologies would allow for the precise and reproducible application of MNPs, addressing the observed challenges associated with variability in the modification process.

Ultimately, the method's validation should encompass a diverse array of FAR types. As previously highlighted in **Chapter 1**, propellant formulations exhibit significant variation, both in composition and the timescale required for successful analysis. A thorough validation process involving a broad spectrum of samples and diverse collection styles is essential. This comprehensive validation would establish the method's suitability for forensic applications and pave the way for its routine use in such investigations. The

incorporation of various FAR types ensures that the method's efficacy extends across the spectrum of gunshot residue scenarios encountered in forensic casework.

7.1.2 Development of an Electrochemical Method for the Visualisation of Latent Finger-marks on Brass Ammunition Casings

7.1.2.1 General Conclusions

Chapter 5 and **Chapter 6** presented the development of an electrochemical method for the visualisation of latent finger-marks on brass ammunition casings. The resulting data enhanced our understanding of visualising finger-marks on brass substrates through electrochemical means. XPS data suggested an increased copper concentration at the surface, presence of copper and zinc in the formed precipitate, a post-analysis blue hue in the solution, and surface changes indicating a corrosion process taking place during electroanalytical measurements.

Notably, sodium nitrate emerged as the most successful electrolyte for brass, providing a mild etch effect without significant gaseous release at the counter electrode, crucial for visualising latent finger-marks in tool mark analysis without compromising detail. The study emphasised the importance of mild etches due to the potential application in tool mark analysis for ammunition casings. Strong etches, like H_2SO_4 , could adversely affect fired ammunition marks, reducing crucial details. The investigation into monomers demonstrated successful polymerisation/deposition at GCE and ITO surfaces. Despite the dominance of brass's electrochemical signature diminishing the characteristic signals of the monomers used in the study, deposition of these materials on brass surfaces facilitated improved colour contrast for latent finger-mark visualisation, as evident in spectral analysis and observable colour changes.

Cyclic voltammetry and chronoamperometry were employed to visualise latent finger-marks on various brass surfaces. The investigation focused on solutions containing EDOT, Thionine Acetate, Neutral Red, and their combinations to evaluate their effectiveness in visualising latent finger-marks on brass. Among the monomers used, EDOT-Th consistently proved to be the most reliable, revealing latent finger-marks at level 3 features, including pores within the ridges, on a flat brass surface through a rapid (120 s) and low-potential (0.1 V) method. Notably, this study, to the best of our

knowledge, marks the first instance of electrochemically polymerising a mixture of EDOT and Thionine, onto a brass surface.

The successful visualisation of groomed latent finger-marks, even after exposure to high temperatures of 700 °C was observed, and both natural and groomed latent finger-marks aged for up to 16 months were successfully visualised. This underscores the effectiveness and versatility of the method suggesting its applicability to conditions experienced by fired ammunition casings.

Bespoke electrochemical cells were designed to facilitate the use of ammunition casings as working electrodes. Among the electrochemical methods applied, cyclic voltammetry proved most successful, producing a pristine visualised latent finger-mark of grade 4 with visible level 3 features.

This research established the first steps to a rapid, low-potential visualisation method for latent finger-marks on brass surfaces, especially ammunition casings, without the need for sample preparation. However, further exploration of this sample type is essential for a comprehensive understanding and application.

The research presented in **Chapter 5** and **Chapter 6** have made major contributions to the development of an electrochemical method for the visualisation of latent finger-marks on spent brass ammunition casings. Indicating that with the method proposed pristine finger-marks can be visualised on ammunition casings, natural finger-marks can be visualised after 16 months and finger-marks which had been heated to 700°C (more than the proposed surface temperature of ammunition during discharge) are still viable for this visualisation method.

Once more, as mentioned above, forensic professionals require rigorous testing to be performed before a new method can be introduced into routine use. In the future work section, the criteria are described which are required before this method is utilised by forensic professionals along with research avenues which are of interest.

7.1.2.2 Future work

Future research in electrochemical methods for latent finger-mark visualisation on brass surfaces should gain a deeper understanding of the structure of EDOT-Th on this substrate, a critical component in the electrochemical process. A comprehensive investigation into the characteristics and behaviour of this polymer could contribute to

refining the electrochemical approach, enhancing its film thickness and ability for contrast with the surface.

Expanding the scope of the study to include a larger and more diverse pool of finger-mark samples on various ammunition casings would provide a more robust foundation for the method's applicability. This could involve analysing finger-marks from different individuals, considering variations in pressure, moisture, and other potential influencing factors (for example gender).

The visualisation of latent finger-marks on pre-fired ammunition casings is a crucial step in validating the method's efficacy under realistic forensic scenarios. Understanding how the firing process affects the visibility and characteristics of finger-marks is essential for establishing the method's reliability in practical applications.

Comparative studies with established forensic methods, such as cyanoacrylate fuming, can offer insights into the strengths and limitations of electrochemical visualisation. This comparative analysis could help forensic professionals choose the most effective technique based on specific case requirements and conditions.

Investigating the long-term stability and performance of the deposited material on brass surfaces is paramount. This involves assessing how well the visualised finger-marks endure over time, considering factors like environmental exposure and potential degradation. Such studies are crucial for ensuring the sustained and reliable application of the electrochemical method in forensic scenarios.

Expanding the application of electrochemical visualisation to different types of tool marks on ammunition casings represents an intriguing avenue for research. Understanding how the method responds to various markings and indentations can broaden its scope, potentially making it a versatile tool for forensic investigators.

Additionally, considering the unique challenges posed by ammunition casings, further research may involve exploring the potential structural alterations to the brass surface under various conditions. This could lead to the development of tailored methodologies that account for the specific characteristics of ammunition casings, ensuring accurate and reliable results in forensic applications.

In summary, future experimental work should aim to deepen our understanding of the electrochemical processes involved, explore new materials and methodologies, and

address specific challenges associated with ammunition casings to advance the field of latent finger-mark visualisation on brass and other surfaces.

7.2 Additional Components Completed During the PhD Programme

7.2.1 Modules Completed and Credits Achieved.

Over the course of the PhD programme, the modules below have been completed, gaining a total of 35 credits, fulfilling the credit requirements for the structured PhD programme at Maynooth University.

Table 7.1: Modules completed, and credits awarded.

Module Code	Module Name	Credits
CH801	Core Skills and Research Techniques in Chemistry	5
CH803	Teaching Skills in Chemistry	5
FM801	Conference Organisation	5
FM805	Outreach and Communication	5
GST13	Research Funding Application	5
FM809	Advanced Communication Skills (publication)	5
CTL1	Professional Certificate in Teaching and Learning	5
Total	35 ECTs	

Additionally, certifications have been attained in research integrity from Epigeum's online courses and from the startup experience provided by Spin up Science.

7.2.2 Presentations

7.2.2.1 Poster Presentations:

1. RSC Electrochemistry twitter poster competition #Electrochem21Poster, Title: Electroanalysis of Organic Gunshot Residue in a Propellant Sample using Magnetic Nano Particle Modified Electrodes.
2. 239th ECS meeting, Online <https://www.electrochem.org/239>, May 30-June 3, 2021, under the Sensors Session, (With Recorded Presentation), Title: Carbon Nano-Onion Modified Electrodes for Voltammetric Detection of Propellant Stabiliser 1,3-Diethyl-1,3-Diphenyl Urea (Ethyl Centralite).
3. PortASAP COST EU meeting early, online, 24th of May 202, Title: Firearm Residue Analysis and Latent Fingerprint Enhancement – The Role of Electrochemistry in Portable Forensic Solutions.
4. Chartered Society of Forensic Science “back in action” conference, Leeds, UK, 4th November 2022 Title: Voltammetric Analysis of Propellant Stabilisers found in the Organic Fraction of Firearms Residue via Iron Oxide Modified Carbon Based Electrodes.
5. 74th Irish Universities Chemistry Research Colloquium, in University of Galway, Galway, Co. Galway, 14-15th June 2023, Title: Advancement of Electroanalytical Techniques for use in Forensic Evaluation of Firearms Generated Evidence.

7.2.2.2 Oral Presentations:

1. COST action PortASAP final meeting in Tallinn, presented online, 15th of February 2022 Title: Firearm Residue Analysis and Latent Fingerprint Enhancement – The Role of Electrochemistry in Portable Forensic Solutions.
2. SCI Electrochemistry Postgraduate Conference 2022, Loughborough University, Loughborough, UK, 25th of May.
3. 18th International Conference on Electroanalysis ESEAC 2022, Vilnius, Lithuania, 5-9 June 2022, Title: Latent Fingerprint Enhancement on Brass Substrates with the aid of Electrochromic and Redox Polymer Deposition.

4. 73rd Irish Universities Chemistry Research Colloquium, University College Dublin, Dublin 4, Co. Dublin, 15-16th June 2022 Title: Latent Fingerprint Enhancement on Brass Substrates with the aid of Electrochromic and Redox Polymer Deposition.
5. Maynooth University Community and Industrial Engagement: Chemistry Research Symposium, Maynooth University, Maynooth, Co. Kildare, 2nd November 2022, Title: The use of Electroanalytical Methods in the Forensic Evaluation of Evidence Generated from the Discharge of a Firearm.
6. RSC Early Career Researcher Regional Symposium on Electrochemistry, Queens University, Belfast, Co. Antrim, 4th November 2022, Title: The use of Electroanalytical Methods in the Forensic Evaluation of Evidence Generated from the Discharge of a Firearm.

7.2.3 Publications

1. Colm McKeever, Sarah Callan, Susan Warren, Eithne Dempsey, Magnetic nanoparticle modified electrodes for voltammetric determination of propellant stabiliser diphenylamine, *Talanta*, Volume 238, Part 2, 2022, 123039, ISSN 0039-9140, <https://doi.org/10.1016/j.talanta.2021.123039>.
2. Colm McKeever, Eithne Dempsey, Electroanalysis of ethyl-centralite propellant stabiliser at magnetic nanoparticle modified glassy carbon and screen-printed electrodes with extension to forensic firearm residue analysis, *Sensors and Actuators B: Chemical*, Volume 396, 2023, 134604, ISSN 0925-4005, <https://doi.org/10.1016/j.snb.2023.134604>.
3. Colm McKeever, Eithne Dempsey, Latent finger-mark enhancement on brass ammunition casings utilising electrochemical deposition of conducting and redox polymers – *Forensic Science International*, in preparation.
4. Colm McKeever, Eithne Dempsey, Comparative electrochemical and optical examination of films formed from c-deposition of Neutral Red/Thionine Copolymers, *Electrochemical Acta*, in preparation.

7.2.4 *Outreach*

Over the course of the PhD programme, I have been involved in numerous outreach events including four talks at secondary schools about learning chemistry at 3rd level and the possibilities of careers available to chemistry graduates in Ireland.

I was involved in public outreach, taking part in Pint of Science 2023 in Maynooth, talking about my PhD research to the general public.

I was one of the founding members of the Institute of Chemistry of Irelands Young Chemists' Network (ICIYCN) and served as the chairperson for two years. In this we provided free events for postgraduate students in chemistry on the island of Ireland in a wide range of subjects including career preparation, mental health and pathways chemistry graduates had undertaken to get where they are in their careers.

I was the European Young Chemists' Network representative for Ireland which I liaised with a broad range of chemists across the continent providing events for all early-stage chemists.

7.2.5 *Funding Awards*

- Maynooth University Graduate Teaching Studentship 2019-2021.
- Irish Research Council Government of Ireland Postgraduate Scholarship Programme, GOIPG/2021/250, 2021-2023.
- Maynooth University Covid Extension Grant 2023-2024.
- Analytical Chemistry Trust Fund, Covid Disruption Grant, 2022.

7.2.6 *Prizes and Awards*

7.2.6.1 *Poster Awards*

- RSC Electrochemistry twitter poster competition #Electrochem21Poster (Poster presentation).

7.2.6.2 Oral Presentation Awards

- 18th International Conference on Electroanalysis ESEAC 2022, Vilnius, Lithuania, 5-9 June 2022.
- Maynooth University Community and Industrial Engagement: Chemistry Research Symposium, Maynooth University, Maynooth, Co. Kildare, 2nd November 2022.

7.2.6.3 Additional Awards

- Maynooth University Teaching Award 2023.